

WL-TR-93-3105

PROCEEDINGS OF DAMPING '93

VOL 3 OF 3

**AD-A274 228**



B.L. PORTIS, COMPILER

CSA ENGINEERING, INC.  
2850 W. BAYSHORE ROAD  
PALO ALTO, CALIFORNIA 94303-3843

JUNE 1993

INTERIM REPORT FOR 02/01/93-02/28/93

APPROVED FOR PUBLIC RELEASE; DISTRIBUTION IS UNLIMITED.

DTIC  
ELECTE  
DEC 23 1993  
A

FLIGHT DYNAMICS DIRECTORATE  
WRIGHT LABORATORY  
AIR FORCE MATERIEL COMMAND  
WRIGHT PATTERSON AFB OH 45433-7562

**93-31148**

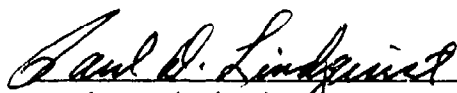


**93 12 23 005**

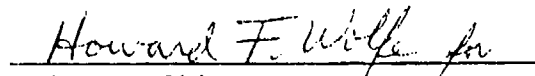
## NOTICE

WHEN GOVERNMENT DRAWINGS, SPECIFICATIONS, OR OTHER DATA ARE USED FOR ANY PURPOSE OTHER THAN IN CONNECTION WITH A DEFINITELY GOVERNMENT-RELATED PROCUREMENT, THE UNITED STATES GOVERNMENT INCURS NO RESPONSIBILITY OR ANY OBLIGATION WHATSOEVER. THE FACT THAT THE GOVERNMENT MAY HAVE FORMULATED OR IN ANY WAY SUPPLIED THE SAID DRAWINGS, SPECIFICATIONS, OR OTHER DATA, IS NOT TO BE REGARDED BY IMPLICATION, OR OTHERWISE IN ANY OTHER PERSON OR CORPORATION; OR AS CONVEYING ANY RIGHTS OR PERMISSION TO MANUFACTURE, USE, OR SELL ANY PATENTED INVENTION THAT MAY IN ANY WAY BE RELATED THERETO.

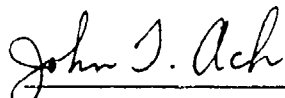
THIS TECHNICAL REPORT HAS BEEN REVIEWED AND IS APPROVED FOR PUBLICATION.



Paul D. Lindquist  
Aerospace Engineer  
Acoustics and Sonic Fatigue



Ralph M. Shimovetz  
Section Leader  
Acoustics and Sonic Fatigue



John Ach, Acting Chief  
Aerospace Engineer  
Acoustics and Sonic Fatigue

IF YOUR ADDRESS HAS CHANGED, IF YOU WISH TO BE REMOVED FROM OUR MAILING LIST, OR IF THE ADDRESSEE IS NO LONGER EMPLOYED BY YOUR ORGANIZATION PLEASE NOTIFY WL/FIBG, WRIGHT-PATTERSON AFB, OH 45433-6553 TO HELP MAINTAIN A CURRENT MAILING LIST.

COPIES OF THIS REPORT SHOULD NOT BE RETURNED UNLESS RETURN IS REQUIRED BY SECURITY CONSIDERATIONS, CONTRACTUAL OBLIGATIONS, OR NOTICE ON A SPECIFIC DOCUMENT.

# REPORT DOCUMENTATION PAGE

Form Approved  
OMB No 0704-0188

Public reporting burden for this collection of information is estimated to average 1 hour per response, including the time for reviewing instructions, searching existing data sources, gathering and maintaining the data needed, and completing and reviewing the collection of information. Send comments regarding this burden estimate or any other aspect of this collection of information, including suggestions for reducing this burden, to Washington Headquarters Services, Directorate for Information Operations and Reports, 1215 Jefferson Davis Highway, Suite 1204 Arlington, VA 22202-4302, and to the Office of Management and Budget, Paperwork Reduction Project (0704-0188) Washington, DC 20503.

1. AGENCY USE ONLY (Leave blank)	2. REPORT DATE JUN 1993	3. REPORT TYPE AND DATES COVERED FINAL FEB 91 - FEB 93
4. TITLE AND SUBTITLE PROCEEDINGS OF DAMPING '93 VOLUME 3 OF 3		5. FUNDING NUMBERS C F33615-89-C-3201 PE 63215C PR L502 TA 00 WU 20
6. AUTHOR(S) BONNIE L. PORTIS, COMPILER		8. PERFORMING ORGANIZATION REPORT NUMBER
7. PERFORMING ORGANIZATION NAME(S) AND ADDRESS(ES) CSA ENGINEERING, INC. 2850 W. BAYSHORE RD. PALO ALTO, CA 94303-3843		10. SPONSORING/MONITORING AGENCY REPORT NUMBER WL-TR-93-3105
9. SPONSORING/MONITORING AGENCY NAME(S) AND ADDRESS(ES) WL/ FIBGC (CAPT JOHN R. MACKAMAN) FLIGHT DYNAMICS DIRECTORATE WRIGHT LABORATORY AIR FORCE MATERIEL COMMAND WRIGHT PATTERSON AFB OH 45433-7006		11. SUPPLEMENTARY NOTES

12a. DISTRIBUTION AVAILABILITY STATEMENT  APPROVED FOR PUBLIC RELEASE; DISTRIBUTION UNLIMITED	12b. DISTRIBUTION STATEMENT
---	-----------------------------

13. ABSTRACT (Maximum 200 words)  PRESENTED ARE INDIVIDUAL PAPERS OF DAMPING '93, HELD 24-26 FEBRUARY 1993 IN SAN FRANCISCO. THE SUBJECTS INCLUDED: PASSIVE DAMPING CONCEPTS; PASSIVE DAMPING ANALYSIS AND DESIGN TECHNIQUES; OPTIMIZATION; DAMPED CONTROL/STRUCTURE INTERACTION; VISCOELASTIC MATERIAL TESTING AND CHARACTERIZATION; HIGHLY DAMPED MATERIALS; VIBRATION SUPPRESSION TECHNIQUES; DAMPING IDENTIFICATION AND DYNAMIC TESTING; APPLICATIONS TO AIRCRAFT; SPACE STRUCTURES; MARINE STRUCTURES; AND COMMERCIAL PRODUCTS; DEFENSE APPLICATIONS; AND PAYOFFS OF VIBRATION SUPPRESSION.
--

14. SUBJECT TERMS VIBRATION DAMPING, PASSIVE DAMPING CONTROL/STRUCTURES INTERACTION	15. NUMBER OF PAGES 380
16. PRICE CODE	
17. SECURITY CLASSIFICATION OF REPORT UNCLASSIFIED	18. SECURITY CLASSIFICATION OF THIS PAGE UNCLASSIFIED
19. SECURITY CLASSIFICATION OF ABSTRACT UNCLASSIFIED	20. LIMITATION OF ABSTRACT III

## Workshop Administration

### Director

Dr. Lynn C. Rogers  
Oak Ridge National Lab

### Technical Chairman

Dr. Conor D. Johnson  
CSA Engineering, Inc.

### Administrative Chairman

Bonnie L. Portis  
CSA Engineering, Inc.

### Session Chairmen

Dr. Mohan Aswani, *Aerospace Corporation*  
Mr. Eric M. Austin, *CSA Engineering, Inc.*  
Mr. L. Porter Davis, *Honeywell, Inc.*  
Mr. William Driscoll, *3M*  
Mr. Robert Dunning, *Lockheed*  
Dr. John P. Henderson, *Materials and Vibration Engineering*  
Dr. Darel E. Hodgson, *E\*Sorb Systems*  
Dr. Robert Holman, *Hughes Aircraft Company*  
Mr. J. Warren Hoskins, *Lockheed Missiles and Space Company*  
Dr. Roy Ikegami, *Boeing Aerospace and Electronics*  
Dr. Conor D. Johnson, *CSA Engineering, Inc.*  
Dr. James Kelly, *EERC, University of California at Berkeley*  
Dr. Edward Kerwin, *Bolt, Beranek and Newman, Inc.*  
Dr. John Kirby, *McDonnell Douglas Aerospace Company*  
Mr. Robert Krumme, *CMS, Inc.*  
Lt. Col. Steve Lamberson, *AFWL/ARDI*  
Capt. Vincent J. Levraea, *Wright Laboratory, Flight Dynamics Directorate*  
Mr. Salvatore Liguore, *McDonnell Douglas Aerospace Company*  
Mr. Paul Lindquist, *Wright Laboratory, Flight Dynamics Directorate*  
Capt. John R. Mackaman, *Wright Laboratory, Flight Dynamics Directorate*  
Mr. Rory Ninneman, *Phillips Laboratory*  
Mr. Ted Nye, *TRW Space and Technology Group*  
Mr. Jerome Pearson, *Wright Laboratory, Flight Dynamics Directorate*  
Mr. Ken Qassim, *Phillips Laboratory*  
Dr. Mohan Rao, *Michigan Technological University*  
Mr. Stanley Sattinger, *Westinghouse Science and Technology Center*

DTIC QUALITY INSPECTED \*

Accession For	
NTIS	CRA&I
DTIC	TAB
Unannounced	
Justification	
By	
Dist. Location /	
Availability Codes	
Dist	Avail. and/or Special
A-1	



Dr. Daniel Segalman, *Sandia National Labs*  
Dr. Jaak Soovere, *Lockheed Aeronautical*  
Capt. Daniel Stech, *United States Air Force Academy*  
Mr. Ralph Tate, *Loral Vought Systems*  
Dr. John Tracy, *McDonnell Douglas Aerospace Company*  
Dr. Ben Wada, *Jet Propulsion Laboratory*  
Ms. Catherine Wong, *Naval Surface Warfare Center*  
Mr. Michael Zeigler, *Wright Laboratory, Flight Dynamics Directorate*

## FOREWORD

This publication includes individual papers of **Damping '93** held February 24-26, 1993, San Francisco, California. The Conference was sponsored by the Air Force Wright Laboratory, Flight Dynamics Directorate, Wright-Patterson Air Force Base, Ohio.

## TABLE OF CONTENTS

	<u>Paper No.</u>
<b>The Role of Damping and Durability in Secondary Structure for Air Vehicles</b> (Keynote Address) Dr. John W. Lincoln	AAA*
<b>Non-obstructive Particle Damping Technology</b> (Invited Speaker) Dr. Hagop Panossian	AAB
<div style="border: 1px solid black; padding: 2px 10px; display: inline-block;"> <b>SESSION BA - Various Vibration Suppression Technologies</b> </div>	
<b>Energy Absorption Due to Cyclic Deformation of Shape Memory Alloys</b> Dr. Darel E. Hodgson	BAA
<b>Passive Damping Applications</b> Dr. Stepan S. Simonian	BAB
<b>Design of Passive Piezoelectric Damping for Space Structures</b> Dr. Andreas H. von Flotow, J. Aldrich, Nesbit Hagood, and David W. Vos	BAC
<div style="border: 1px solid black; padding: 2px 10px; display: inline-block;"> <b>SESSION CA - Space Applications I</b> </div>	
<b>An Advanced Controls Technology Flight Experiment</b> R. A. Manning, R. E. Wyse, and S. R. Schubert	CAA
<b>Optimized Passive Vibration Isolator Design for the Space Station Freedom Exercise Treadmill</b> Richard Armentrout and Harold H. Doiron	CAB
<b>Design of Spacecraft Damped Precision Platform</b> Dennis Hill, John Molnar, John Chionchio, Clyde Stahle, and Michael Zeigler	CAC*
<b>Elastomeric Materials Applied Internally to Turbine Blades</b> Eric M. Austin and Lyn M. Greenhill	CAD*

\*Not available for publication

## TABLE OF CONTENTS (continued)

### Paper No.

#### **SESSION CB - Analysis and Design I**

- |  |             |
|--|-------------|
| <b>Consistent Damping Method for Space Structural Systems</b><br>Wan T. Tsai, Joseph T. Leang, and Richard S. Chao   | <b>CBA</b>  |
| <b>Transient Solution of Coupled Structural Components Using System<br/>Modal Coordinates with and without Coupled System Damping</b><br>Edwin E. Henkel and Raymond Mar | <b>CBB</b>  |
| <b>Multiple Scales Methods for Structural Dynamics</b><br>Wing Kam Liu   | <b>CBC*</b> |
| <b>Formulation of a Frequency Dependent Damping Matrix</b><br>Antonio M. Claret and Fernando Venancio-Filho  | <b>CBD*</b> |

#### **SESSION CC - Viscoelastic Material Measurements**

- |  |            |
|--|------------|
| <b>Fourier Transform Mechanical Analysis (FTMA) Technique to<br/>Determine Dynamic Mechanical Properties of Viscoelastic Materials</b><br>Dr. Surendra N. Ganeriwala       | <b>CCA</b> |
| <b>Dynamic Compressibility Apparatus</b><br>Wayne T. Reader, N. Scott Emery, and Fred Schloss  | <b>CCB</b> |
| <b>Dynamic Durometer Measurement of Young's Modulus and Loss Factor</b><br>Dr. Walter Madigosky and Dr. Ralph Fiorito  | <b>CCC</b> |
| <b>Integrated Direct Stiffness Test System for Viscoelastic Material<br/>Properties (Work in Progress)</b><br>Bryce L. Fowler, Bradley R. Allen, and Dr. David A. Kienholz | <b>CCD</b> |

#### **SESSION DA - Space Applications II**

- |  |             |
|--|-------------|
| <b>Passive Damping Analysis for an Advanced Space Interceptor</b><br>Eric M. Austin, Victor J. Wagner, and David H. Merchant | <b>DAA*</b> |
|--|-------------|

## TABLE OF CONTENTS (continued)

	<u>Paper No.</u>
<b>Variations in the Damping of Space Structures in One Gravity and Zero Gravity</b> Dr. A. S. Bicos, Dr. E. F. Crawley, M. S. Barlow, M. C. van Schoor, and B. Masters	DAB
<b>Impact of Interface Stiffness and Damping on Payload Responses in Space Systems</b> Dr. Wan T. Tsai	DAC

### SESSION DB - Analysis and Testing

<b>Modal Parameter Estimation Effects on Damping Matrix Identification</b> Dr. A. Agneni, Dr. L. Balis-Crema, Dr. A. Castellani, and F. M. Onorati	DBA
<b>The Relation Between Internal Friction in Metals and Elastic Wave Velocities</b> Dr. Augusto Capecchi	DBB
<b>Some Frequency and Damping Measurements of Laminated Beryllium Beams</b> Dr. Lynn C. Rogers and John Andriulli	DBC

### SESSION DC - Characterization of Polymeric Materials

<b>Accurate Characterization of Passive Damping Materials with Database Storage and Retrieval on Different Computer Platforms</b> Bryce L. Fowler and Dr. Lynn C. Rogers	DCA
<b>Results of Recent Analysis of the Frequency-Temperature Behavior of Polyisobutylene</b> Dr. David I. G. Jones	DCB
<b>Estimation of Dynamic Properties of Rubber Materials and their Applications to Vibration Isolation</b> Chun-hwa Ryu, Hyeong-oh Kweon, Gyu-Seop Lee, and Sang-Kyu Park	DCC

## TABLE OF CONTENTS (continued)

### Paper No.

#### **SESSION EA - Damping/Isolation for the Launch Environment**

- |   |            |
|---|------------|
| <b>Performance/Sizing Tradeoffs in Active and Passive Launch Isolation</b><br>David C. Cunningham   | <b>EAA</b> |
| <b>A Launch Isolation System for the Shuttle Resupplied Hubble Space Telescope Solar Array</b><br>L. Porter Davis, Terry Allen, and John Vise                       | <b>EAB</b> |
| <b>A New Structural Design Concept for Launch Vehicle Shrouds to Decrease Payload Noise Environment</b><br>Jefferson Newton, Dr. Roy Ikegami, and Paul D. Nedervelt | <b>EAC</b> |
| <b>Protection of Attitude Control Thrusters Against Pyrotechnic Stage Separation Shock</b><br>Dr. Ernst Hornung and Huba Oery                                       | <b>EAD</b> |

#### **SESSION EB - Analysis and Design II**

- |   |             |
|---|-------------|
| <b>A Boundary Element Formulation for Dynamic Analysis of Viscoelastic Fluid-Dampers</b><br>Dr. Nicos Makris, Dr. G. F. Dargush, and Dr. M. C. Constantinou | <b>EBA</b>  |
| <b>Vibration Responses of Viscoelastically Damped Plates</b><br>Dr. Sung Yi, M. F. Ahmad, Dr. H. Hilton, and G. D. Pollock                                  | <b>EBB</b>  |
| <b>Damping Capacity of Scarf-Joints</b><br>Dr. Mohan Rao and Haiming Zhou   | <b>EBC</b>  |
| <b>Similtude and Modelling Damping Forces in Bolted Connections</b><br>Dr. M. Groper  | <b>EBD*</b> |

## TABLE OF CONTENTS (continued)

### Paper No.

#### **SESSION EC - Shape Memory Alloys**

- Low Frequency Damping and Ultrasonic Attenuation in  $Ti_3Sn$ -Based Alloys** ECA  
Catherine Wong and Rober L. Fleischer
- Fully Cyclic Hysteresis of a Ni-Ti Shape Memory Alloy** ECB  
Dr. Edward J. Graesser and Dr. Francis A. Cozzarelli
- Design and Seismic Testing of Shape Memory Structural Dampers** ECC  
P. R. Witting and Dr. Francis A. Cozzarelli
- The Vibration Characteristics of Composites with Embedded Shape Memory Alloy** ECD  
Lee Chin Hai and Dr. C. T. Sun

#### **SESSION FA - Aircraft Applications**

- A Magnetic Tuned-Mass Damper for Buffet-Induced Airfoil Vibration** FAA  
Joseph R. Maly and Kevin L. Napolitano
- Attenuation of Empennage Buffet Response Through Active Control of Damping Using Piezoelectric Material** FAB  
Jennifer Heeg, Jonathon Miller, and Robert V. Doggett, Jr.
- Analytical Evaluation of Damping Treatments for F-15 Wing** FAC  
Scott R. Schroeder

#### **SESSION FB - Nonlinear Structures**

- The Influence of Constrained-Layer Damping Treatment on Parametric and Autoparametric Resonances in Nonlinear and Internally Resonant Nonlinear Structures** FBA  
Lawrence D. Zavodney and Joseph Schudt

## TABLE OF CONTENTS (continued)

	<u>Paper No.</u>
<b>Incorporating a Full Damping Matrix in the Transient Analyses of Nonlinear Structures</b> J. Michael Chapman	<b>FBB</b>
<b>Treatment of Structural and Frequency Dependent Damping on Nonlinear Systems by a Step-by-Step Linearization Procedure in Frequency Domain</b> Dr. Antonio M. Claret	<b>FBC*</b>

### SESSION FC - Friction

<b>Analysis of Dry Friction Hysteresis in Cables under Uniform Bending</b> Dr. X. Huang and Dr. O. Vinogradov	<b>FCA</b>
<b>On the Linearization of Structures Containing Linear-Friction Dissipating Devices</b> Jose A. Inaudi and Dr. James M. Kelly	<b>FCB</b>
<b>Analysis of Dry Friction Hysteresis in Tension Cables</b> Dr. X. Huang and Dr. O. Vinogradov	<b>FCC</b>

### SESSION GA - Tuned Mass Dampers/Vibration Energy Absorbers

<b>Increasing the Impact Energy Absorption of Containment Structures with Viscoelastic Materials</b> R. G. Holm, M. A. Mendelsohn, and S. S. Sattinger	<b>GAA</b>
<b>The Effect of Viscoelasticity on the Performance of Reaction Mass Actuators</b> Dr. H. Hilton, L. A. Bergman, and T. C. Tsao	<b>GAB</b>
<b>Enhanced Passive Vibration Absorbers Using Acceleration Feedback</b> Capt. D. Stech and Dr. R. Quan	<b>GAC</b>
<b>Improved Precipitation Static Discharge (PSD) Unit Attachment Method</b> T. Gerardi, J. Weiher, Lt. G. Agnes, J. Shaw, and C. Hitchcock	<b>GAD*</b>

\*Not available for publication



## TABLE OF CONTENTS (continued)

Paper No.

### SESSION 3B - Smart Structures

- Finite Element Modeling of Sensors/Actuators for Smart Structure Applications** **GBA\***  
Salvatore L. Liguore and Jack H. Jacobs
- Piezoelectric Composites for Use in Adaptive Damping Concepts** **GBB**  
Wayne T. Reader and David F. Sauter
- Damping in Smart Materials and Structures** **GBC**  
Nisar Shaikh and Sam D. Haddad
- Actively Damped Piezoelectric Composite Wing** **GBD**  
Dr. P. Santini, F. Betti, P. Gasbarri, and A. Rossi

### SESSION GC - Composites

- Stratified Layer Model for Composite Laminates** **GCA\***  
Capt. Vincent Levraea and Col. Ronald Bagley
- Damping Analysis for Thick Composite Laminates and Structures** **GCB**  
Dr. D. A. Saravanos
- Vibration Responses of a Composite Shell Made of a Metallic Material with Damping Treatments** **GCC**  
Dr. Y. P. Lu, A. J. Roscoe, and H. C. Neilson
- Damping Thin-Walled Composite Structures with Embedded Constraining Layers** **GCD**  
Stanley Sattinger and Z. N. Sanjana

### SESSION HA - Civil Structures

- Analytical and Experimental Study of a Mass Damper Using Shape Memory Alloys** **HAA**  
J. A. Inaudi, Dr. J. M. Kelly, W. Taniwangsa, and Robert Krumme

\*Not available for publication

## TABLE OF CONTENTS (continued)

	<u>Paper No.</u>
<b>High Damping of Antique Walls</b> Dr. Juval Mantel	HAB
<b>Temperature Control in Viscoelastic Dampers for Buildings</b> Dr. Warren C. Gibson, Kevin L. Napolitano, Bradley R. Allen, and Dr. Roger Scholl	HAC

### **SESSION HB - Control Structure Interaction**

<b>Response Study of Optimum Structural and Control Design</b> Dr. Narendra Khot	HBA
<b>Uniform Modal Damping of an Elastic Ring by the Natural Control Law</b> Dr. J. Q. Sun and Dr. J. Rossetti	HBB
<b>Two-DOF Small Structures-Optics-Controls System, A Parametric Study</b> Dr. Ernest B. Paxson, Jr.	HBC

### **SESSION HC - High Damping Materials**

<b>Damping Behavior of 6061 Al/SiC/Gr Metal Matrix Composites</b> Robert J. Perez, Jinmin Zhang, M. N. Gungor, and Dr. E. Lavernia	HCA
<b>Development of Room Temperature Vibration Damping Steel</b> Dr. Shian-Ing Chen	HCB*
<b>A Simple Approach to Design, Installation, and Testing of Passive Damping for an Optical System</b> Eric M. Austin and James C. Goodding	HCC

### **SESSION IA - Industrial Applications**

<b>Vibration Attenuation by Configuration Variation of Machines and Structures</b> Dr. Z. Parszewski, J. M. Krodkiewski, and K. Krynicki	IAA
---	-----

\*Not available for publication

## TABLE OF CONTENTS (continued)

	<u>Paper No.</u>
<b>Stiffness and Damping in Automobile Seats</b> Dr. W. M. Patten, Dr. B. Yang, and Li Liu	<b>IAB*</b>
<b>Noise Standardization in Machine Design</b> Ilja D. Tsukernikov and Boris A. Seliverstov	<b>IAC*</b>
<b>Damping in the Noise Reduction of Liquid Separators</b> Boris A. Seliverstov	<b>IAD*</b>

### **SESSION IB - Active Damping**

<b>Active Vibration Control Using Parallel Processing Techniques</b> Dr. G. S. Virk	<b>IBA</b>
<b>Active Contrained Layer Damping</b> Dr. Amr Baz	<b>IBB</b>
<b>Comparing Passive Damping and Active Control on Flexible Structures with Either Closely Spaced or Coincident Modes</b> Major Steven Webb and 2Lt Dean Cibotti	<b>IBC</b>
<b>Damping of Structural Vibration with Piezoelectric Materials and Parameter Optimization</b> T. Yongjie, Z. Shenbi, H. Xieqing, and H. Xuanli	<b>IBD</b>

### **SESSION IC - Damping Properties and Materials**

<b>Damping Properties of PTMG/PPG Blends</b> Gilbert Lee, John D. Lee, Dr. B. Hartmann, and Dr. D. Rathnamma	<b>ICA</b>
<b>Investigation of Damping Properties for the Fiber Enhanced Viscoelastic Damping Polymers</b> Dr. Thomas Alberts and Houchun Xia	<b>ICB</b>
<b>On the Dynamic Properties of Natural Rubber and Epoxidized Natural Rubber</b> H. A. Ahmadi, Dr. A. H. Muhr, and Dr. K. N. G. Fuller	<b>ICC</b>

\*Not available for publication

## TABLE OF CONTENTS (continued)

	<u>Paper No.</u>
<b>Effect of Long Space Exposure upon Properties of Viscoelastic Materials</b> Dr. John Kirby, Dr. Donald Edberg, and Dr. David I. G. Jones	<b>ICD</b>

### **SESSION JB - Analysis and Design**

<b>A Modal Strain Energy Approach to the Prediction of Resistively-Shunted Piezoceramic Damping</b> Christopher Davis and Dr. George Lesieutre	<b>JBA</b>
<b>A Refined Theory of Flexural Vibration for Viscoelastic Damped Sandwich Beams</b> J. M. Bai and Dr. C. T. Sun	<b>JBB</b>
<b>A Simple Approach to Design, Fabrication, and Testing of Passive Damping for an Optical System</b> Eric M. Austin and James C. Goodding	<b>JBC*</b>

### **SESSION JC - Characterization**

<b>A Constitutive Equation for Thermoviscoelastic Behavior of Polymeric Materials</b> Dr. Surendra Ganeriwala	<b>JCA</b>
<b>Relating the Complex Moduli of Viscoelastic Materials to the Complex Stiffness Characteristics of Anti-Vibration Mounts</b> Dr. S. O. Oyadiji and G. R. Tomlinson	<b>JCB*</b>
<b>Sensitivity Analysis For Estimation of Complex Modulus of Viscoelastic Materials by Non-Resonance Method</b> Dr. Kwang-Joon Kim and Tai-Kil Ahn	<b>JCC</b>

The following is a list of authors and their addresses who were unable to submit their papers for publication in the Damping '93 Proceedings.

Dr. John W. Lincoln  
USAF/ASC/ENFS  
Area B, Building 125  
2335 Seventh Street, Suite 6  
Wright-Patterson AFB, OH 454433-7809  
telephone: (513) 255-2576  
fax: (513) 476-4546

John Molnar  
GE Astro Space  
P.O. Box 800  
MS NP 1A  
Princeton, NJ 94303-0800  
telephone: (609) 951-7804  
fax: (609) 951-7911

Eric M. Austin  
CSA Engineering, Inc.  
2850 West Bayshore Road  
Palo Alto, CA 94303-3843  
telephone: (415) 494-7351  
fax: (415) 494-8749

Wing Kam Liu  
Northwestern University  
Department of Mechanical Engineering  
Evanston, IL 60208-3111  
telephone: (708) 491-7094  
fax: (708) 491-3915

Antonio M. Claret  
Escola de Minas / UFOP  
Pc Tiradentes No. 20  
CEP 35400-000 Ouro Preto, MG  
Brasil  
telephone: (031) 551-1139  
fax: (031) 551-1689

Dr. Lynn C. Rogers  
Oak Ridge National Lab  
USAF/WL/FIBG (Center for Passive Damping)  
Area B, Building 24C, Room 220  
2145 Fifth Street, Suite 2  
Wright-Patterson AFB< OH 45433-7006  
telephone: (513) 255-6622 extension 252  
fax: (513) 255-6684

John Andriulli  
Oak Ridge National Lab  
K-25, Site/K-1225, MS-7294  
P.O. Box 2003  
Oak Ridge, TN 37831-7294  
telephone: (615) 576-0424  
fax: (615) 574-8481

Dr. M. Groper  
Western Michigan University  
College of Engineering and Applied Sciences  
Department of Mechanical and Aeronautical Engineering  
Kalamazoo, MI 49008-5065  
telephone: (616) 387-3380  
fax: (616) 387-4024

Salvatore L. Liguore  
McDonnell Douglas Aerospace  
P.O. Box 516  
St. Louis, MO 63166-0516  
telephone: (314) 232-3109  
fax: (314) 777-1171

Capt. Vincent Levraea  
WL/FIBG, Wright Laboratory  
2145 Fifth Street, Suite 2  
Wright-Patterson AFB, OH 45433-7006  
telephone: (513) 255-5229 extension 452  
fax: (513) 255-6685

Col. Ronald Bagley  
WL/FIB, Wright Laboratory  
Wright-Patterson AFB, OH 45433-7006  
telephone: (513) 255-5200 extension 457  
fax: (513) 255-6684

Dr. Shian-Ing Chen  
China Steel Corporation  
Lin Hai Industrial District  
P.O. Box 47-29  
Hsiao Kang, Kaohsiung  
81233 Taiwan, Republic of China  
telephone: 07-802-1111 extension 3353  
fax: 07-802-2511

Dr. W. M. Patten  
The University of Oklahoma  
School of Aerospace and Mechanical Engineering  
865 Asp Avenue, Room 212  
Norman, OK 73019-0601  
telephone: (405) 325-5011  
fax: (405) 325-1088

Ilja D. Tsukernikov  
Head of Vibroacoustics Sector  
123308 Moscow, Marshal Zhukov Avenue, 1  
Russia  
telephone: (095) 195-6974  
fax: (095) 195-1043

Boris A. Seliverstov  
Chief of Laboratory  
123308 Moscow, Marshal Zhukov Avenue, 1  
Russia  
telephone: (095) 195-6974  
fax: (095) 195-1043

H. A. Ahmadi  
Malaysian Rubber Producer's Research Association  
Brickendonbury  
Hertford SG13 8NL, England  
telephone: (0992) 584-966  
fax: (0992) 554-837

Dr. S. O. Oyadiji  
University of Manchester  
Engineering Department  
Simon Building  
Manshester M13 9PL, United Kingdom  
telephone: (44) 61-275-4444  
fax: (44) 61-275-3844

# DAMPING ANALYSIS FOR THICK COMPOSITE LAMINATES AND STRUCTURES

by

D. A. Saravanos<sup>1</sup>

NASA Lewis Research Center  
21000 Brookpark Rd., MS 49-8  
Cleveland, Ohio 44135

## Abstract

*Recent developments on generalized damping mechanics for predicting the dynamic characteristics of composite structures are summarized. The mechanics can handle a broad array of composite structures where interlaminar shear is important, such as, thick composite sections and specialty composite laminates with embedded interlaminar damping layers. A discrete layer laminate damping theory is described. An exact semi-analytical method for simply-supported composite plates and a finite element based method for the prediction of damping in composite structures of general geometry, lamination and boundary conditions are also presented. Experimental correlations and evaluations of the mechanics are included. The beneficial and coupled effects on structural damping in the cases of high thicknesses, alternating ply angles, and embedded damping layers are illustrated.*

## 1. Introduction

The passive damping of polymer matrix composites is receiving current attention. Because of their high stiffness and strength and low specific weight, composite materials are readily preferred in many light-weight flexible structures, where low levels of passive damping typically improve the dynamic and acoustic performance. Various damping mechanics theories for unidirectional composites, laminates and structures have been reported and a representative selection is mentioned here [1-12]. However, most of the previously mentioned work is limited to the classical laminate theory assumptions which neglect the contributions of interlaminar shear damping, which may be significant in thicker sections, or laminates with high interlaminar inhomogeneity.

---

<sup>1</sup> Senior Research Associate, Ohio Aerospace Institute.



For applications requiring higher levels of damping, specialty composite laminates with co-cured damping layers may provide combinations of low weight and superior damping performance. The high interlaminar shear stresses resulting within the embedded viscoelastic layers, as a result of discontinuous variations in the anisotropic properties between the restraining plies result in very high damping values. Work has been reported towards the analysis of composite beams and plates with embedded compliant damping layers [13-18].

Hence, it appears that composite materials, either individually or with the addition of passive damping layers may provide a wide spectrum of damping values, in combination with low-weight and excellent mechanical properties. Yet, a unified and generalized damping theory for composite structures with either thin or thick sections, or with embedded interlaminar damping layers is still required for the accurate prediction of damping and other dynamic characteristics of composite structures.

Consequently, this paper presents integrated generalized mechanics and analytical methods developed for the unified prediction and characterization of damping in a vast array of composite laminates and laminated structures. The mechanics have been generalized, such that, they can handle laminates of variable thickness, interlaminar compliant damping layers and angle-ply laminates. Novel laminate damping mechanics have been developed allowing for variable in-plane displacement fields through the thickness of the laminate. The overall damping capacity of the laminate includes contributions from extension, flexure, interlaminar shear, and material coupling from possible asymmetries that may exist due to the heterogeneous nature of the composite laminate.

Exact semi-analytical solutions have been developed based on the previous discrete laminate damping theory for the case of specialty composite plates. For more complex structures and boundary conditions, a novel 4-node finite element was developed used to simulate the damped characteristics of composite structures of general thickness, shape, lamination, and boundary conditions. Results demonstrate the merit of the developed damping mechanics and investigate issues of current interest, such as: (1) the contributions of interlaminar shear damping in thick composite structures; (2) the effects of embedded interlaminar damping layers; and (3) the enhancement of damping (in structures with or without damping layers) in angle-ply laminates.

## 2. Composite Mechanics

This section briefly reviews the synthesis of damping for composite plies and composite laminates of general stacking sequence and lamination. The measures of damping used in this paper will be primarily the loss factor  $\eta$ , and secondarily the specific damping

capacity (SDC)  $\Psi$  ( $\eta = \Psi/2\pi$ ).

## 2.1. Composite plies

For a composite ply loaded along the material axes (Fig. 1), closed-form expressions are used for the synthesis of elastic and dissipative properties [7]. Five independent elastic parameters completely characterize the stiffness of a unidirectional composite. An additional four independent damping loss factors characterize the composite damping, that is, longitudinal loss factor  $\eta_{111}$ , transverse in-plane damping  $\eta_{122}$ , transverse through-the-thickness damping  $\eta_{133} = \eta_{122}$ , in-plane shear damping  $\eta_{166}$  (direction 12), interlaminar shear damping  $\eta_{144}$  (direction 23), and interlaminar shear damping  $\eta_{155} = \eta_{166}$  (direction 13). For composite plies loaded at an angle  $\theta$  (Fig. 1), a 6 by 6 damping matrix  $[\eta_c]$  is used to describe the damping of the composite [7,8].

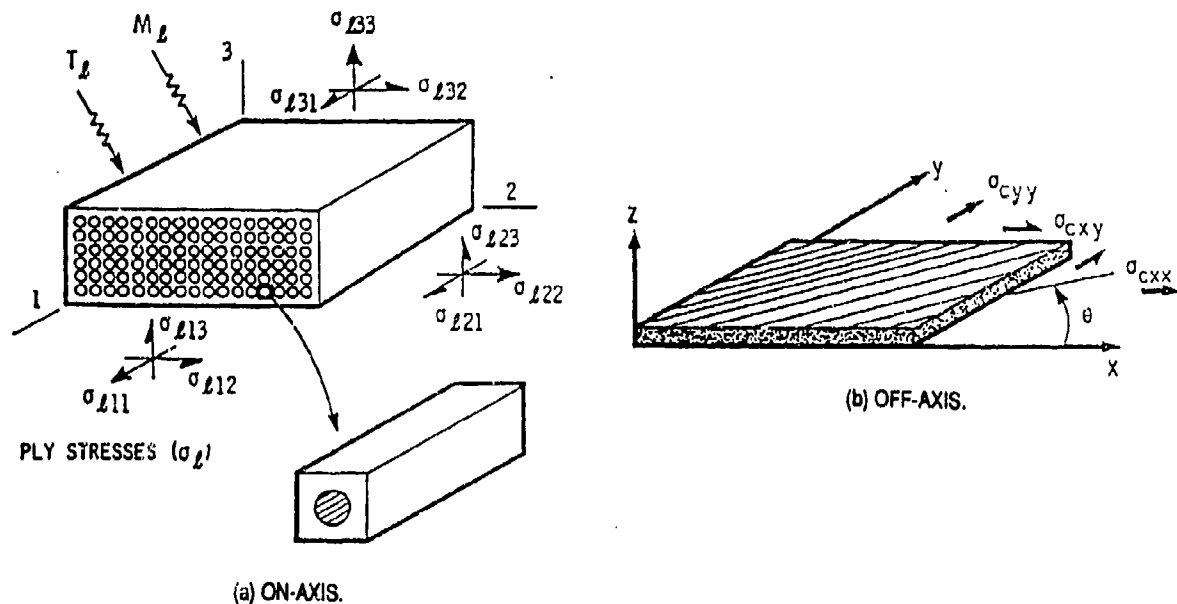
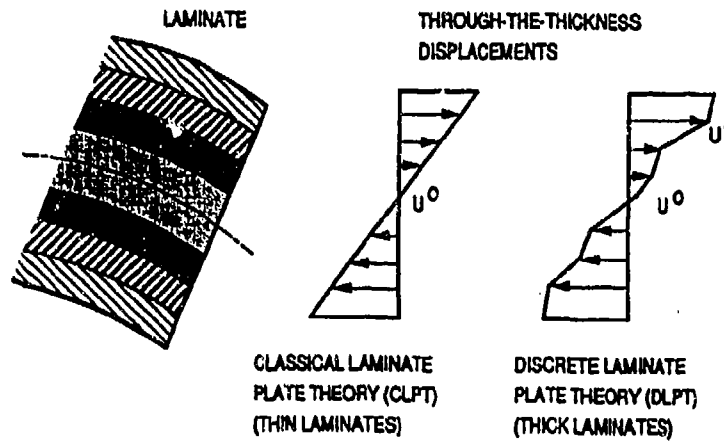


Figure 1 Composite material geometry

## 2.2. Composite Laminates

To model the damping of thick composite laminates with or without embedded damping layers, a discrete layer damping theory (DLDT) incorporating a piecewise continuous displacement field through-the-thickness was developed. The kinematic assumptions for the laminate theory are schematically shown in Fig. 2. The DLDT combines the potential for accurate damping predictions in composite laminates while maintaining generality and



**Figure 2** Kinematic assumptions: (a) DLDT (b) CLDT

elegance. The assumed displacement field has the form,

$$\begin{aligned}
 u(x,y,z,t) &= u^o(x,y,t) + \bar{u}(x,y,z,t) \\
 v(x,y,z,t) &= v^o(x,y,t) + \bar{v}(x,y,z,t) \\
 w(x,y,z,t) &= w^o(x,y,t)
 \end{aligned} \tag{1}$$

Assuming that the displacements are separable functions of  $z$ , the previous equations take the form suggested by Barbero and Reddy [19]:

$$\begin{aligned}
 u(x,y,z,t) &= u^o(x,y,t) + \sum_{j=1}^N u^j(x,y,t) F^j(z) \\
 v(x,y,z,t) &= v^o(x,y,t) + \sum_{j=1}^N v^j(x,y,t) F^j(z) \\
 w(x,y,z,t) &= w^o(x,y,t)
 \end{aligned} \tag{2}$$

where,  $u^j$ , and  $v^j$ , are the in-plane displacements, along the  $x$  and  $y$  directions respectively, at the interfaces between composite plies or sublaminae (group of plies).  $F^j(z)$  are interpolation functions. In this manner, the assumed in-plane displacement field is general, in that it may represent extensional, flexural, shear, and coupled deformations. It also may represent interlaminar shear strains through the thickness of the laminate.

The engineering strains  $\{\epsilon_c\}$  in each composite ply are directly derived from eqs. (2)

$$\begin{aligned}
\epsilon_{ci} &= \epsilon_{ci}^o + \sum_{j=1}^N \epsilon_{ci}^j F^j(z) & i=1,2,6 \\
\epsilon_{ci} &= \epsilon_{ci}^o + \sum_{j=1}^N \epsilon_{ci}^j F_z^j(z) & i=4,5 \\
\epsilon_{c3} &= 0
\end{aligned} \tag{3}$$

The normal strain  $\epsilon_{c3}$  is zero because constant through-the-thickness deflection  $w$  is assumed, hence, the effects of dilatational damping in the case of damping layers are mostly neglected. The expressions of the generalized strains  $\{\epsilon_c^o\}$ ,  $\{\epsilon_c^j\}$  are given in ref. [18].

The dissipated strain energy per unit area, per cycle of the laminate  $\Delta S_L$  is

$$\Delta S_L = 1/2 \int_{-h/2}^{h/2} 2\pi \epsilon_c^T [Q_c] [\eta_c] \epsilon_c dz \tag{4}$$

where  $[Q_c]$ ,  $[\eta_c]$  are the off-axis composite stiffness and damping matrices respectively (see Appendix). The dissipated energy is proved to take the form [18],

$$\Delta S_L = \frac{1}{2} 2\pi (\epsilon_c^{oT} [A_d] \epsilon_c^o + 2 \epsilon_c^{oT} \sum_{j=1}^N [B_d^j] \epsilon_c^j + \sum_{j=1}^N \sum_{m=1}^N \epsilon_c^{jT} [D_d^{jm}] \epsilon_c^m) \tag{5}$$

where:  $[A_d]$  are the extensional laminate damping matrix, which includes out-of-plane shear terms;  $[B_d^j]$  and  $[D_d^{jm}]$  are the generalized coupling and flexural/shear matrices damping matrices. Similarly, the laminate strain energy per unit area  $S_L$  is:

$$S_L = 1/2 (\epsilon_c^{oT} [A] \epsilon_c^o + 2 \epsilon_c^{oT} \sum_{j=1}^N [B^j] \epsilon_c^j + \sum_{j=1}^N \sum_{m=1}^N \epsilon_c^{jT} [D^{jm}] \epsilon_c^m) \tag{6}$$

where,  $[A]$  is the extensional laminate stiffness matrix with additional out-of-plane shear terms,  $[B^j]$  are the generalized coupling stiffness matrices, and  $[D^{jm}]$  the flexural/shear matrices [15]. The laminate kinetic energy per unit area takes the form

$$K_L = 1/2 (\{\dot{u}^o\}^T [A_M] \{\dot{u}^o\} + 2 \{\dot{u}^o\}^T \sum_{j=1}^N [B_M^j] \{\dot{u}^j\} + \sum_{j=1}^N \sum_{m=1}^N \{\dot{u}^j\}^T [D_M^{jm}] \{\dot{u}^m\}) \tag{7}$$

where the generalized laminate mass and inertia matrices are also given in ref. 18. The kinetic energy in eq. (7) includes contributions of rotational inertia. The proposed laminate damping mechanics are general and they can handle any laminate configuration in terms of composite plies, ply angles, laminate stacking sequence, and thickness.

### 2.3. Simply-Supported Composite Plates

Based on the previously described laminate mechanics, exact solutions of the damped dynamic characteristics for specialty composite plates have been obtained [18] and summarized herein for the sake of completeness. These exact and computationally inexpensive predictions of static and dynamic characteristics (modal damping and natural frequencies) have provided valuable insight in the mechanics of the problem and establish a baseline for validating approximate numerical methods. Most other laminations, boundary conditions, and structural configurations require approximate discretized solutions, and such finite element based computational mechanics, which are described in the next section.

For a rectangular  $\alpha$  by  $\beta$  simply supported (SS) composite plate with negligible coupling ( $A_{16} = A_{26}=0$ ,  $B_{16}^j = B_{26}^j=0$ ,  $D_{16}^{jm} = D_{26}^{jm}=0$ ), the following fundamental solutions form a complete set of mode shapes in the x-y plane which satisfy the boundary conditions of the plate:

$$\begin{aligned} u_{mn}^o(x,y,t) &= U_{mn}^o \cos(ax) \sin(by) e^{i\omega t} \\ v_{mn}^o(x,y,t) &= V_{mn}^o \sin(ax) \cos(by) e^{i\omega t} \\ w_{mn}^o(x,y,t) &= W_{mn}^o \sin(ax) \sin(by) e^{i\omega t} \\ u_{mn}^j(x,y,t) &= U_{mn}^j \cos(ax) \sin(by) e^{i\omega t} \\ v_{mn}^j(x,y,t) &= V_{mn}^j \sin(ax) \cos(by) e^{i\omega t} \end{aligned} \quad (8)$$

where,  $a = m\pi/\alpha$ ,  $b = n\pi/\beta$ .

Combination of eqs. (2,3,8) yields the modal mid-plane and generalized strains as separable functions of x, y coordinates, time, and amplitudes.

$$\{\epsilon^o\}_{mn} = [B_{mn}^o] \{U_{mn}^o\} e^{i\omega t} \quad \{\epsilon^j\}_{mn} = [B_{mn}^j] \{U_{mn}^j\} e^{i\omega t} \quad (9)$$

where, the terms in matrices  $[B_{mn}]$  are sinusoidal functions of x, y coordinates and mode order. The amplitude displacement vectors are  $\{U^o\} = \{U^o, V^o, W^o\}^T$  and  $\{U^j\} = \{U^j, V^j\}^T$ .

Utilizing the expressions of strain and kinetic energy, and applying Lagrangian dynamics, the modal analysis (free vibration) solution of the plate takes the form:

$$-\omega_{mn}^2 [M_{mn}] U_{mn} + [K_{mn}] U_{mn} = 0 \quad (10)$$

where, the through-the-thickness modal displacements are  $\{U_{mn}\} = \{U_{mn}^0; U_{mn}^1, \dots, U_{mn}^N\}$  and subscripts m, n indicate the mode order. Numerical solution of this eigenvalue problem provides the natural frequencies  $\omega_{mn}$  and the through-the-thickness modes  $\{U_{mn}\}$  for each order mn of plane modes, in the context of eqs. (8).

The modal damping associated with the mn-th vibration mode  $\eta_{mn}$  is:

$$\eta_{mn} = \frac{1}{2\pi} \frac{\int_A \Delta S_{Lmn} dA}{\int_A S_{Lmn} dA} \quad (11)$$

where  $\Delta S_{Lmn}$  and  $S_{Lmn}$  are respectively the dissipated and maximum laminate strain energies, respectively of the associated mode.

## 2.4. Finite Element Damping Mechanics

Computational finite-element based mechanics for the damping analysis of thick composite structures of general laminations and shapes were also developed, based on the DLDT and are summarized herein (for more information see refs. 20 and 21). A variational formulation of the equilibrium equations for the candidate structure is used. The constitutive viscoelastic law between generalized stresses and strains at the laminate level was eventually expressed in the frequency domain as a complex laminate stiffness product,

$$\begin{aligned} N^o(\omega) &= [\tilde{A}(\omega)] \epsilon^o(\omega) + \sum_{m=1}^N [\tilde{B}^m(\omega)] \epsilon^m(\omega) \\ N^j(\omega) &= [\tilde{B}^j(\omega)] \epsilon^o(\omega) + \sum_{m=1}^N [\tilde{D}^{jm}(\omega)] \epsilon^m(\omega), \quad j=1, \dots, N \end{aligned} \quad (12)$$

where tilde indicates complex laminate stiffnesses. The storage laminate stiffnesses are  $[A]$ ,  $[B^j]$  and  $[D^{jm}]$ , while the loss stiffness matrices are  $[A_d]$ ,  $[B_d^j]$  and  $[D_d^{jm}]$  respectively.

The variational relationship was discretized to an approximate equivalent system of dynamic equations. The damping, stiffness and mass matrices of the element,  $[C_{eij}]$ ,  $[K_{eij}]$  and  $[M_{eij}]$  respectively, were formulated. Subsequently, the dissipated and maximum stored strain energies of the element are calculated from:

$$\Delta S_{eij} = 1/2 U_i^T [C_{eij}] U_j, \quad S_{eij} = 1/2 U_i^T [K_{eij}] U_j \quad (13)$$

and the modal damping of the n-th mode  $\eta_n$  is expressed as the ratio of the dissipated over the maximum modal strain energy of the structure.

$$\eta_n = \frac{1}{2\pi} \frac{\sum \Delta S_{eijn}}{\sum S_{eijn}} \quad (14)$$

A bilinear four-node plate element was developed based on the previous formulation. Selective integration was utilized to avoid overstiffening of the element in the case of low thickness.

### 3. Applications and Results

#### 3.1. Thick Composite Structures

To demonstrate the quality and versatility of the composite mechanics, applications on Graphite/Epoxy composite plates and beams without interlaminar damping layers are presented. The numerical results obtained with the aforementioned method (DLDT) are compared with either exact or finite element results using the classical laminate damping theory (CLDT) assumptions [11]. The composite material used in the applications of this subsection is HM-S Graphite/Epoxy of 0.50 fiber volume ratio (FVR). Measured data for this composite are provided in Ref. 9. Unless otherwise stated, the nominal thickness of each composite ply was taken as 0.254 mm (0.01 inches).

**[0<sub>4</sub>/90<sub>4</sub>]<sub>s</sub> Simply-Supported Composite Plate.** Fig. 3 shows predicted natural frequencies and modal damping values of the fundamental mode of a [0<sub>4</sub>/90<sub>4</sub>]<sub>s</sub> square composite SS plate as functions of thickness aspect ratio ( $\alpha/h$ ), where h is the plate thickness. The modal characteristics of the first 4 modes, that is, modes (1,1), (1,2), (2,1), and (2,2) are shown respectively. It is pointed out, that this laminate has different flexural damping and stiffness characteristics in x and y directions, thus, modes (1,2) and (2,1) have different natural frequencies and modal loss factors. The finite element model consisted of a uniform mesh of 8 by 8 element subdivisions. Clearly, there is excellent agreement between the exact DLDT solutions and the finite element model in the shown thickness regime. The exact CLDT solution is also shown, to illustrate the significant differences between the two theories in damping prediction at high thicknesses. The differences between DLDT and CLDT predictions provide the estimate of interlaminar shear damping.

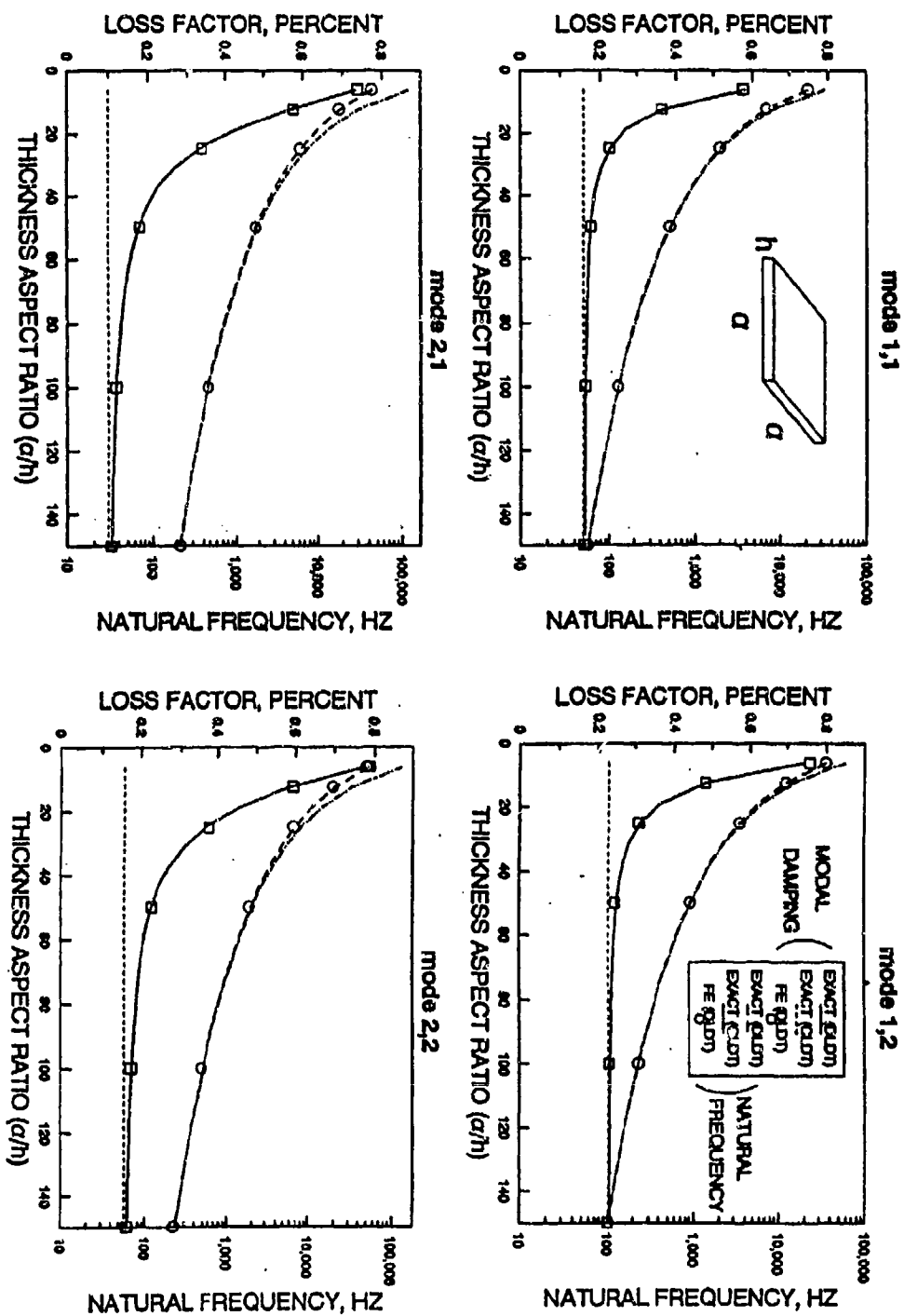
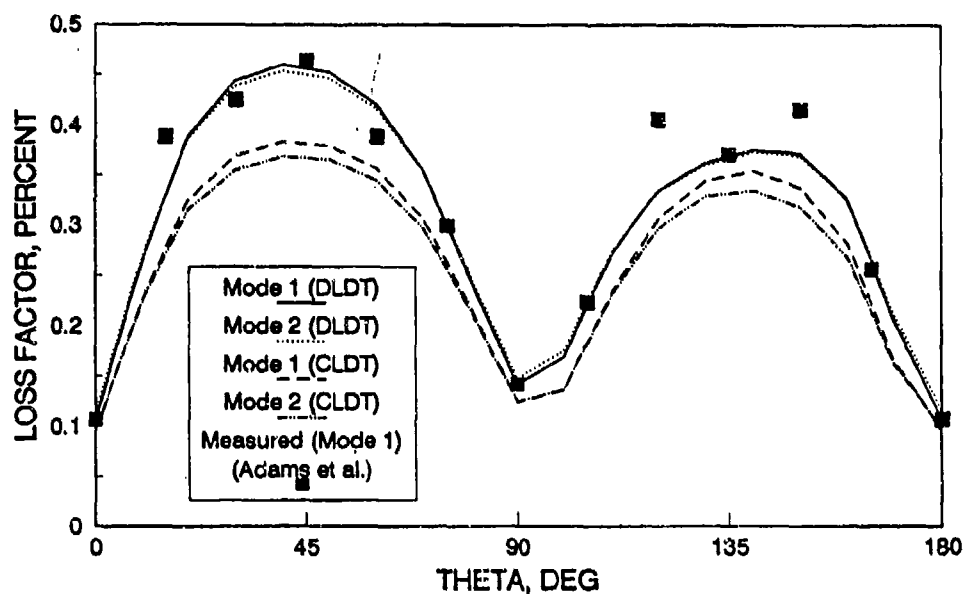


Fig. 3 Modal characteristics of a  $[0,90]_s$  Gr/Epoxy simply-supported plate.





**Fig. 4** Modal characteristics of a  $[0/90+0/45+0/-45+0]_s$  cantilever beam ( $l/h=125$ ;  $l=8$  in). First and second bending modes.

**$[0/90/45/-45]_s$  Free-Free Composite Beam.** Fig. 4 presents the modal damping and natural frequencies of the first and second bending modes of an unsupported (free-free)  $[0/90+0/45+0/-45+0]_s$  thin beam ( $l/h=125$ ). The dimensions of the beam were approximately equal to specimens used by Ni and Adams [9], that is, 200 mm (8 in) long, 12 mm (0.5 in) wide, and 1.60 mm (0.064 in) thick. As seen in Fig. 4, the DLDT has succeeded in capturing the interlaminar shear damping contributions in the range of high interlaminar shear stresses and relative rotation between outer plies ( $\theta \approx 45^\circ, 135^\circ$ ). The interlaminar shear damping is mostly the result of inhomogeneities in the material anisotropy between the plies of alternating fiber orientation.

**$[0_4/-0_4]_s$  Simply-Supported Composite Plate.** The dependence of modal damping on thickness and laminate lay-up is shown in Fig. 5 for a simply supported  $[0_4/-0_4]_s$  Graphite/Epoxy plate. A uniform 8 by 8 finite element mesh was used to model the plate. The modes are identified with their mode shape at  $\theta=0$ . The damping predictions of the CLDT model, which are independent of thickness, are also plotted. The differences between DLDT and CLDT predictions are higher at  $\pm 45$  degs. where the interlaminar stresses are highest.

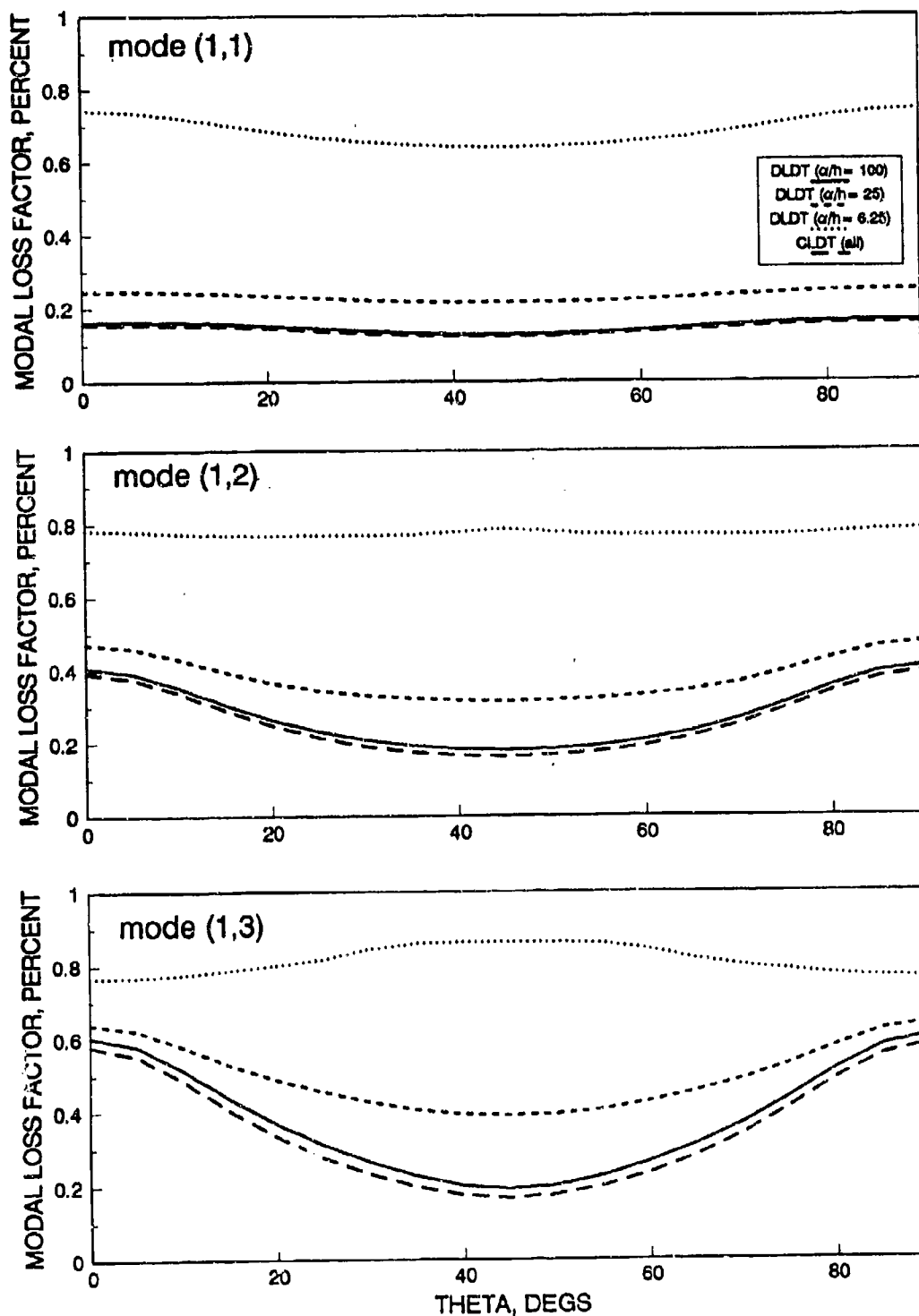


Fig. 5 The effect of thickness aspect ratio on the modal damping of  $[\theta_4/\theta_4]_s$  Gr/Epoxy simply-supported plate.

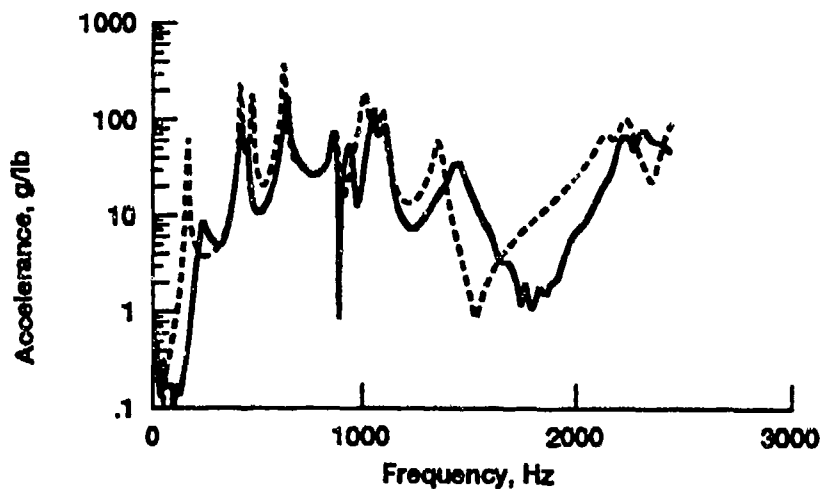
### 3.2 Composite Plates with Embedded Damping Layers

#### Experimental Correlations.

To validate the accuracy of the method and experimentally verify the effects of damping layers on the dynamic response of composite plates, composite plates with interlaminar damping layers were fabricated in-house and tested either at simply-supported or unsupported conditions [18,22]. In all experiments the plates were 11 in by 11 in (28 cm by 28 cm) and consisted of 0.6 FVR T300/934 Graphite/Epoxy plies, combined with layers of ScotchDamp ISD110 damping film (3M Corp., St. Paul, MN) which are indented with letter i in the standard laminate notation. Unless otherwise stated, the shear modulus and shear loss factor of the damping polymer were assumed 5.5 kpsi and 0.16 respectively, and they represent average values of the polymer at 500 Hz and 30° C as provided by the manufacturer's data sheet. Due to non-existing data, the Young's modulus of the damping polymer was assumed 15.4 kpsi and the normal loss factor was assumed to be negligible (0.016). Parametric studies have indicated strong insensitivity of modal damping and frequency to the dilatational properties of the damping polymer. The nominal thicknesses of the Graphite/Epoxy tape and damping layers were 0.006 in (0.15 mm) and 0.005 in (0.13 mm), respectively. The plate was laid up by hand, co-cured at 350° F (175° C) and 50 psi (345 KPa), and finally cut to size. Frequency response functions for the composite plate were obtained from impulse tests. The signals from the hammer and the accelerometer were recorded with a high speed digital data acquisition system, and was then processed using FFT software to obtain the frequency response functions of the plate.

The measured and predicted response of a  $[0_2/90_2/i/90_2/0_2]_s$  plate (synthesized from the calculated modal damping and natural frequencies using a modal superposition technique) is shown in Fig. 6. Contrary to other cases, frequency effects on the properties of the viscoelastic layer have been included. With the exception of the first mode, the predicted response reproduces sufficiently the measured one. Both predicted and measured results fall within the range of uncertainty predicted from the upper and lower bounds of scatter in the manufacturer's data for this polymer film damping.

The predicted dynamic characteristics of two symmetric angle-ply plates with compliant damping layers are also shown in Figs. 7 and 8. The laminate configurations were  $[45_2/-45_2/i/45_2/-45_2]_s$  and  $[22.5_2/-22.5_2/i/22.5_2/-22.5_2]_s$  respectively. In-house measured [22] damping values and natural frequencies for these plates at a "free-hanging" configuration are also shown in these figures. In both cases, the correlation between measured and predicted modal damping and corresponding natural frequencies appears very good, especially in the low frequency regime. Predicted and measured results for composite plates of identical laminations but without damping layers are also shown in Figs. 7 and 8. It is pointed out, that the sole purpose of plotting these results is to compare and



Accelerance at point  $(x/\alpha, y/\beta) = (1/4, 3/4)$ .

**Figure 6** Frequency response of a  $[0_2/90_2/i/90_2/0_2]_s$  T300/934 simply-supported plate with ISD110 damping layers

demonstrate the obtained improvements in the damping characteristics of the various plates, rather than comparing the accuracy of the method, since damping data for the composite system were not available at the time of this paper.

#### Damping Enhancement in Angle-Ply Laminates.

The objective of this study is to explore and quantify unique advantages in improving the vibroacoustic characteristics of composite structures by embedding compliant layers between plies with strong interlaminar inhomogeneity. The applications demonstrate the potential to engineer/tailor such specialty composite laminates for high dynamic performance.

The predicted loss factors and corresponding natural frequencies for two modes are shown in Figs. 9 and 10 for plates with laminations  $[\theta_2/-\theta_2/i/\theta_2/-\theta_2]_s$  and  $[\theta_2/-\theta_2/i/-\theta_2/+ \theta_2]_s$  respectively. At  $\theta=0^\circ$  these modes correspond to the (1,1) and (2,2) modal shapes. The modal loss factors and natural frequencies of plates with identical geometrical and laminate configurations, but without damping layers (undamped), that is  $[\theta_2/-\theta_2/\theta_2/-\theta_2]_s$  and  $[\theta_2/-\theta_2/\theta_2/+ \theta_2]_s$  respectively, are also plotted in the same Figures. Clearly, the addition of the damping layers drastically improved the damping capacity of the composite plates as the mode order is increased. But most importantly, the predicted

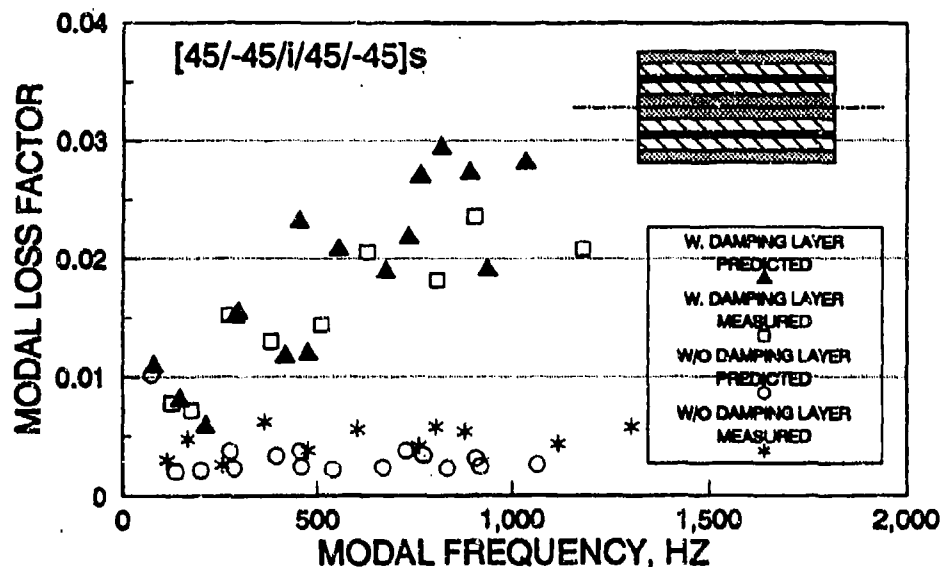


Fig. 7 Modal characteristics of a  $[45_2/-45_2/i/45_2/-45_2]$ , T300/934 simply supported plate with ISD110 damping layers.

results demonstrate that increased through-the-thickness inhomogeneity and anisotropy in the composite sublaminate may significantly improve the damping of the composite structure. This damping enhancement is further signified by the observation that the predicted damping of the composite plates without damping layers is typically reduced for ply angles between 0 and 90°. Finally, the damped plates exhibit similar or higher natural frequencies than the undamped plates between 0 and 90 degs, hence, this enhancement of damping does not seem to reduce the natural frequencies and stiffness.

#### 4. Conclusions and Ongoing Work

The development of generalized damping mechanics for the accurate analysis of composites structures was summarized. The capability of the mechanics to represent a broad spectrum of composite structures including thin and thick composite sections, as well as, "engineered" composite structures with embedded interlaminar damping layers. An exact semi-analytical solution for composite plates was described. Finally, a finite element based method for the prediction of damping in composite structures of general lamination, boundary conditions and geometry was developed also presented.

Numerous applications and evaluations of the mechanics illustrated their merit and

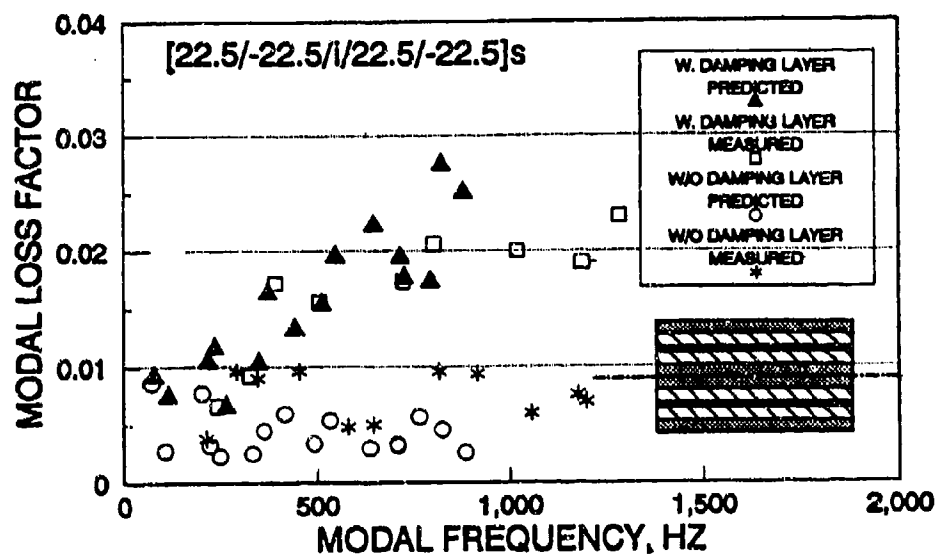


Fig. 8 Modal characteristics of a  $[22.5_2/-22.5_2/1/22.5_2/-22.5_2]_s$  T300/934 simply supported plate with ISD110 damping layers.

unique advantages in the case of composite structures with either high thicknesses, or high interlaminar inhomogeneity, or composite structures with damping layers. Ongoing work is focused on the development of a three-dimensional damping theory incorporating a variable through-the-thickness displacement field.

#### References

1. Hashin, Z., "Complex Moduli of Viscoelastic Composites - II. Fiber Reinforced Composite Materials," *Int. J. of Solids and Structures*, Vol. 6, 1970, pp. 797-807.
2. Schultz, A. B., and Tsai, S. W., "Measurements of Complex Dynamic Moduli for Laminated Fiber-Reinforced Composites," *J. of Composite Materials*, Vol. 3, 1969, pp. 434-443.
3. Adams, R. D., Fox, M. A. O., Flood, R. J. L., Friend R. J., and Hewitt R. L., "The Dynamic Properties of Unidirectional Carbon and Glass Fiber-Reinforced Plastics in Torsion and Flexure," *J. of Composite Materials*, Vol. 3, 1969, pp. 594-603.
4. Siu, C. C., and Bert, C. W., "Sinusoidal Response of Composite-Material Plates with Material Damping," *ASME J. of Engineering for Industry*, May 1974, pp.

15

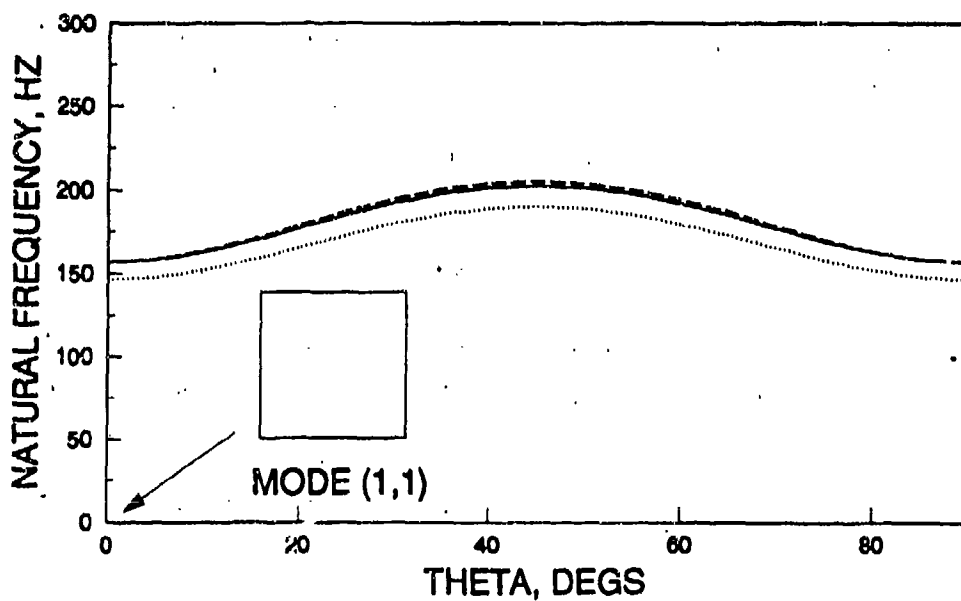
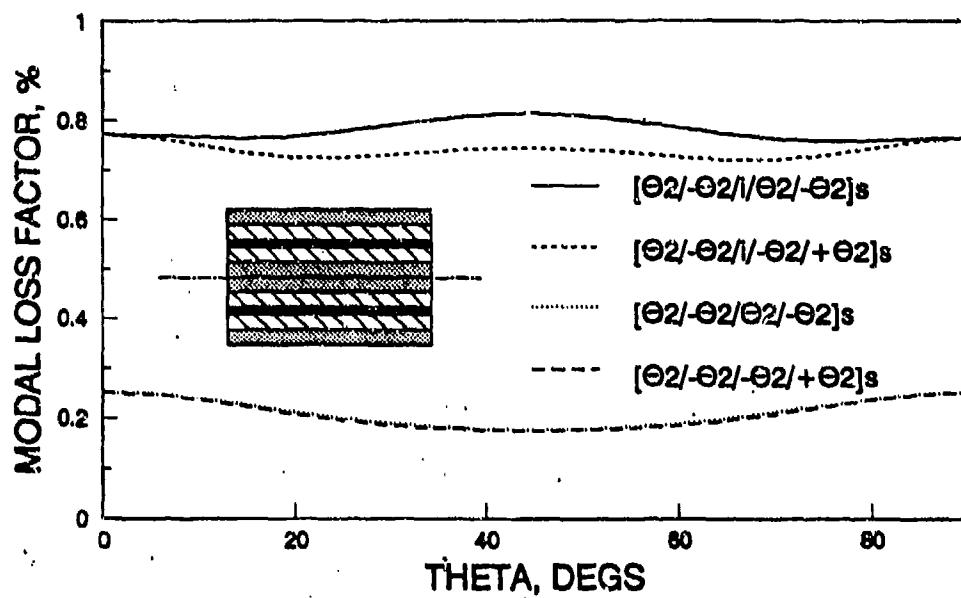


Fig. 9 Modal loss factor and natural frequency of angle-ply T300/934 simply supported plates; mode 1.

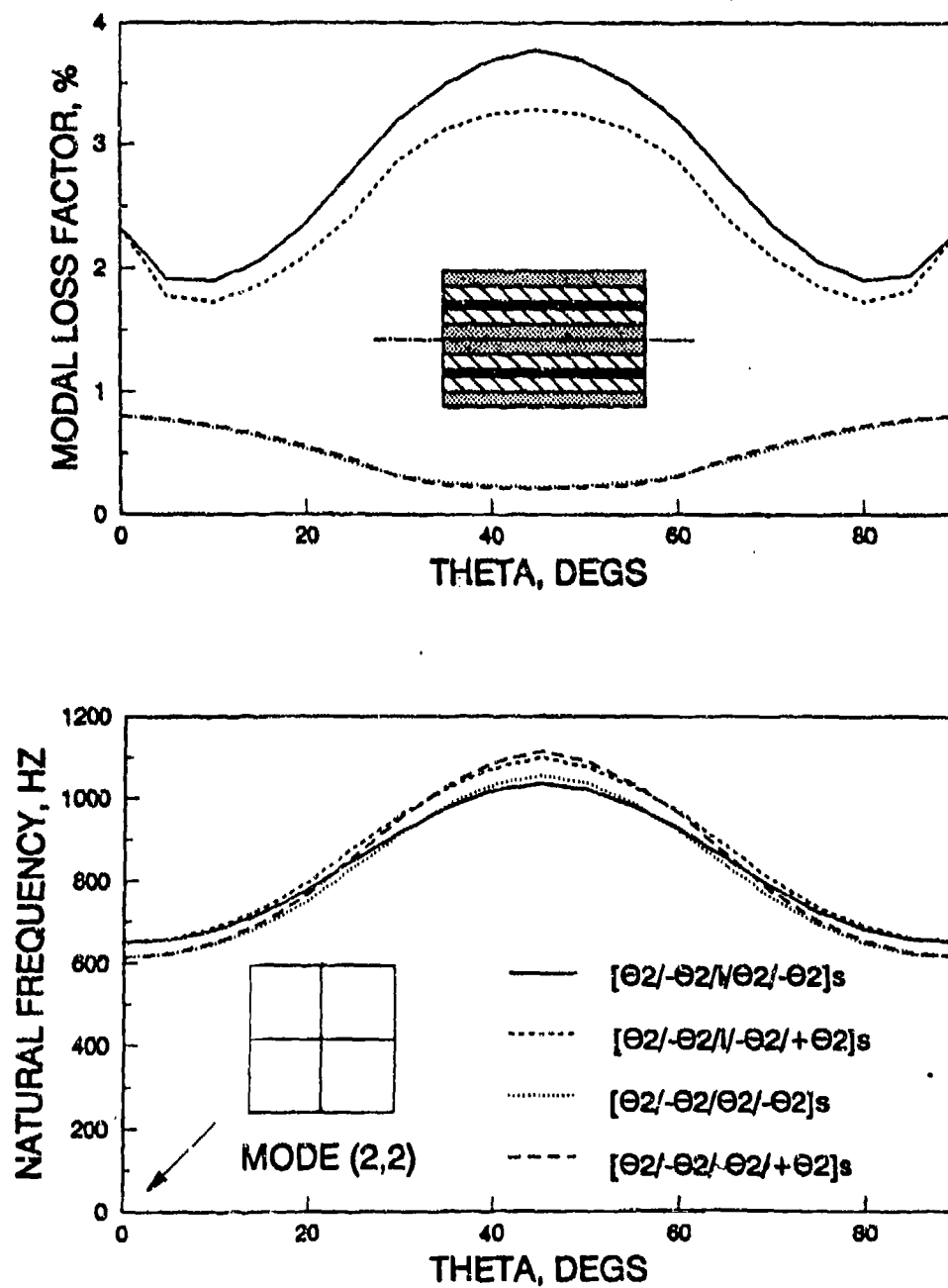


Fig. 10 Modal loss factor and natural frequency of angle-ply T300/934 simply supported plates; mode 5.



5. Sun, C. T., Chaturvedi, S. K., and Gibson, R. F., "Internal Damping of Short-Fiber Reinforced Polymer Matrix Composites," *Computers and Structures*, Vol. 20, No. 1-3, 1985, pp. 391-400.
6. Suarez, S. A., Gibson, R. F., Sun, C. T., and Chaturvedi, S. K., "The Influence of Fiber Length and Fiber Orientation on Damping and Stiffness of Polymer Composite Materials," *Experimental Mechanics*, Vol. 26, No. 2, 1986, pp. 175-184.
7. Saravanos, D. A. and Chamis, C. C. "Unified Micromechanics of Damping for Unidirectional and Off-Axis Fiber Composites," *J. of Composites Technology and Research*, Vol. 12, No. 1, 1990, pp. 31-40.
8. Saravanos, D. A. and Chamis, C. C. "Mechanics of Damping for Fiber Composite Laminates Including Hygro-Thermal Effects," *ALAA J.*, Vol. 28, No. 10, 1990, pp. 1813-1819.
9. Ni, R. G., and Adams, R. D., "The Damping and Dynamic Moduli of Symmetric Laminated Composite Beams -- Theoretical and Experimental Results," *J. of Composite Materials*, Vol. 18, 1984, pp. 104-121.
10. Bicos, A. S. and Springer, G. S. "Vibrational Characteristics of Composite Panels with Cutouts," *AIAA Journal*, Vol. 27, Aug. 1989, pp. 1116-1122.
11. Saravanos, D. A. and Chamis, C. C. "Computational Simulation of Damping in Composite Structures," *J. of Reinforced Plastics and Composites*, Vol. 10, 1991, pp. 256-278.
12. Alam, N. and Asnani, N. T. "Vibration and Damping Analysis of Fibre Reinforced Composite Material Plates," *J. of Composite Materials*, Vol. 20, 1986, pp. 2-18.
13. Chen G. S. and Wada B. K., "Passive Damping for Space Truss Structures," *29th Structures, Structural Dynamics and Materials Conference, 29th, Pt. 3, AIAA*, 1988, pp. 1742-1749.
14. Bronowicki A. J. and Diaz H. P., "Analysis, Optimization, Fabrication and Test of Composite Shells with Embedded Viscoelastic Layers," *Proceedings of Damping '89*, Wright-Paterson AFB, OH, Report WRDC-TR-89-3116-Vol-1, 1989, Sec. GC, paper GCA.
15. Mantena R. P., Gibson R. F. and Shwilong H. J., "Optimal Constrained Viscoelas-

tic Tape Lengths for Maximizing Damping in Laminated Composites," *Proceedings of Damping '89*, Wright-Paterson AFB, OH, Report WRDC-TR-89-3116-Vol-1, 1989, Sec. IA, paper IAB.

16. Rao V. S., Sun C. T. and Sankar B. V., "Damping and Vibration Control of Some Laminated Composite Beams Using Add-On Viscoelastic Materials," *Proceedings of Damping '89*, Wright-Paterson AFB, OH, Report WRDC-TR-89-3116-Vol-2, 1989, Sec. VA, paper VAA.
17. Barrett D. J., "An Anisotropic Laminated Damped Plate Theory," Naval Air Development Center, Warminster, PA, *Report No. NADC-90066-60*, July, 1990.
18. Saravanos, D. A. and Pereira J. M. "The Effects of Interlaminar Damping Layers on the Dynamic Response of Composite Structures," *AIAA Journal*, Vol. 30, No. 12, Nov. 1992, pp. 2906-2913.
19. Barbero, E. J., Reddy, J. N. and Teply, J., "An Accurate Determination of Stresses in Thick Composite Laminates Using a Generalized Plate Theory," *Int. J. for Numerical Methods in Engineering*, Vol. 29, 1990, pp. 1-14.
20. Saravanos D. A., "Analysis of Passive Damping in Thick Composite Structures," *AIAA Journal*, in press.
21. Saravanos D. A. and Chamis C. C., "Damped Dynamic Characteristics of Specialty Composite Materials and Structures," *Proceedings, Symposium on Vibroacoustic Characterization of Materials and Structures*, NCA-Vol. 14, ASME Winter Annual Meeting, Anaheim, California, Nov. 8-13, 1992, pp. 31-38.
22. Pereira M. J., "Dynamic Response of Composite Plates with Interlaminar Damping Layers," *Proceedings, Symposium on Vibroacoustic Characterization of Materials and Structures*, ASME Winter Annual Meeting, Anaheim, California, Nov. 8-13, 1992

#### APPENDIX: Fundamental Composite Mechanics

Off-axis ply stiffness matrix  $[Q_c]$ :

$$\{\sigma_c\} = [Q_c]\{e_c\}$$

$$[Q_c] = [R]^{-1}[Q_l][R]^{-T}$$

where  $[Q_l]$  is the stiffness matrix in the material axes. The transformation matrices are:

$$[R] = \begin{bmatrix} m^2 & n^2 & 0 & 0 & 0 & 2mn \\ n^2 & m^2 & 0 & 0 & 0 & -2mn \\ 0 & 0 & 1 & 0 & 0 & 0 \\ 0 & 0 & 0 & m & -n & 0 \\ 0 & 0 & 0 & n & m & 0 \\ -mn & mn & 0 & 0 & 0 & m^2 - n^2 \end{bmatrix}, \quad m = \cos\theta, \quad n = \sin\theta$$

$$[R]^{-1} = [R(-\theta)]$$

On-axis damping matrix:

$$[\eta_l] = \text{diag} [ \eta_{l11}, \eta_{l22}, \eta_{l33}, \eta_{l44}, \eta_{l55}, \eta_{l66} ]$$

The off-axis ply damping matrix is:

$$[\eta_c] = [R]^T[\eta_l][R]^{-T}$$

$$[\eta_c] = \begin{bmatrix} \eta_{c11} & \eta_{c12} & 0 & 0 & 0 & \eta_{c16} \\ \eta_{c21} & \eta_{c22} & 0 & 0 & 0 & \eta_{c26} \\ 0 & 0 & \eta_{c33} & 0 & 0 & 0 \\ 0 & 0 & 0 & \eta_{c44} & \eta_{c45} & 0 \\ 0 & 0 & 0 & \eta_{c54} & \eta_{c55} & 0 \\ \eta_{c61} & \eta_{c62} & 0 & 0 & 0 & \eta_{c66} \end{bmatrix}$$

VIBRATION RESPONSES OF A COMPOSITE SHELL MADE OF A  
METALLIC MATERIAL WITH DAMPING TREATMENTS

BY

Y. P. Lu, A. J. Roscoe and H. C. Neilson

Carderock Division

Naval Surface Warfare Center

Annapolis, Maryland 21402

(Formerly David Taylor Research Center)

**ABSTRACT**

Vibration responses of a damped composite shell structure are presented, evaluated and discussed. The composite shell structure analyzed is made of a metallic material with damping treatments. The damped composite structure is a configuration which has a number of axial beams adhered to the cylindrical shell surface by a viscoelastic material layer. The attached longitudinal beams are assumed identical, closely spaced and distributed around the full circumference of the shell. The driving point mechanical impedances are used as criteria for the evaluation of titanium material which is used here as an example for illustration purposes. Parametric analytical studies of vibration characteristics of shell composites on damping layer thicknesses, beam thicknesses, other physical, geometrical and material parameters were made. The issue of weight penalty versus performance payoffs of the titanium shell system is also discussed.

## I. INTRODUCTION

For years, it is known that noise and vibration can be reduced by the dissipation of energy within the vibrating members themselves by utilizing layers of viscoelastic shear damping materials. Much significant research work on damped beam, plate, and shell structures has been reported, see for instance, references [1-5]. In a previous paper [5], an analysis for the forced vibratory responses of damped cylindrical shells carrying discontinuously constrained beam elements was presented, in which a number of longitudinal beams were attached to the shell surface by a viscoelastic material layer. The attached beams were identical, closely spaced and distributed around the full circumference of the shell. The excitation was a concentrated vibratory force acting radially at the mid-section on the surface of the shell structure (Figure 1). Good correlations between the experimental data and analytical solutions of mechanical impedances for a given damped shell system were obtained over a wide range of frequencies.

This paper extends further the analysis on the physical problem defined in the cited reference and the associated numerical solutions for the geometrical and material parameters of the given system. Parameters such as beam thickness, damping layer thickness, and structural damping of the shell are studied for the evaluation of titanium material which is used here as an example for illustration purposes. These studies provide information on how the damping effectiveness of a given system can be controlled. In addition to the conclusion made in reference [5] that the damping effects caused by the use of constrained layer viscoelastic damping materials are significant, a comparison between analytical solutions including the structural damping of the shell material and of the beam material is also presented.

## II. ANALYSIS SUMMARY

From Reference [5], a set of reduced linear algebraic equations of motion of the shell for each value of  $m$  and  $n$ , can be written as

$$\begin{bmatrix} K_{11} - M & K_{12} & K_{13} \\ K_{12} & K_{22} - M & K_{23} \\ K_{13} & K_{23} & K_{33} - M \end{bmatrix} \begin{bmatrix} u_{mn} \\ v_{mn} \\ w_{mn} \end{bmatrix} = \begin{bmatrix} \frac{a}{D} p_{mn}^s \\ \frac{a}{D} p_{mn}^o \\ \frac{a}{D} p_{mn}^r + F_r \end{bmatrix}, \quad (1)$$

neglected. The damped shell response curve given in this figure is the same one (driving point impedance) used in the cited reference to compare with the experimental data. The greater detail shown here is a result of smaller frequency incrementing. The number pairs in this figure denote the dominant mode at each of the corresponding resonances, where the first and second numbers indicate the longitudinal half wave number and the circumferential mode number, respectively. It can be readily observed that the damping treatment significantly reduced the response of the shell structure. The reduction is not as great as for the fundamental longitudinal modes ( $m = 1$ ) of the shell for which the  $x$  dependence is  $\sin(\pi x/l)$ . In these first order bending modes, the viscoelastic layer is undergoing less shear deformation and therefore less damping is achieved. The first resonance (1,1 mode) occurs below the frequency range shown in this figure at 16 Hz, and 22 Hz for the damped and undamped shells, respectively. The static bending stiffnesses determined from the stiffness line of the impedance below these frequencies are  $3.5 \times 10^3$  lb/in ( $6.1 \times 10^5$  N/m) for the undamped shell and  $8.0 \times 10^3$  lb/in ( $1.4 \times 10^6$  N/m) for the shell with attached beam elements.

Figure 3 illustrates the effect on system response from the inclusion of structural damping of the shell material. Here, the response of the damped shell of Figure 2 is replotted together with that for an identical shell having structural damping of 0.03 (both for shell and for beam materials). The primary change resulting from inclusion of the structural damping is, as expected, the increased impedance at the first order bending resonances where the damping treatment alone provides little damping. Comparison of these levels and those measured experimentally suggests that a value for structural damping of somewhat less than 0.03, but of the same order, would more accurately model the experimental system.

#### IV. ANALYTICAL PARAMETRIC STUDIES OF TITANIUM SHELL

Based on the excellent correlations between analytical results and experimental data presented in the cited reference, the analysis can be used in practical applications to predict the general trend of the dynamic responses of the damped systems. The analysis is simple, practical, and requires little computation time; yet it is able to provide relatively accurate and critical information. As an example, a composite structural system made of titanium shell and beams is selected for illustration purpose of investigation.

In dealing with a composite damped system, various pieces of vibration information may be determined and used for evaluation purposes. Because of large numbers of parameters involved, it is very easy to have many possible combinations of data to evaluate. Therefore, we chose to use the driving point mechanical impedances for the full coverage damping configuration on which to conduct the parametric studies. In the following, the shell material is assumed titanium with negligible material loss factor, and the

environmental temperature is 70° F, in the frequency range from 20 to 2000 Hz, unless otherwise stated.

#### **EFFECT OF SUBSTITUTING TITANIUM FOR STEEL HAVING THE SAME PIPE WALL THICKNESS**

Figure 4 presents the driving point mechanical impedances of a 12-inch schedule 40S titanium pipe (shell) as compared with a 12-inch steel pipe (also schedule 40S) with the same wall thickness 0.375 inch (0.95 cm). The shell is assumed 100.0 inches (254 cm) long, each titanium or steel beam element (constraining layer) is 0.1875 inch (0.48 cm) thick and 0.375 inch (0.95 cm) wide, and the viscoelastic material layer is 0.010 inch (0.0254 cm) thick. The damping properties of the viscoelastic material are given in reference [6]. The stiffness line for the damped titanium pipe in the impedance plot is lower than that of the damped steel pipe. This is because of the smaller Young's modulus of titanium (14.9 million psi for titanium as compared with 30 million psi for steel). Resonance frequencies for damped titanium pipe are slightly lower than those of damped steel pipe because of its lower stiffness to density ratio. In general, impedance levels for damped steel pipe are higher than those of damped titanium pipe. The general features of the two response curves are similar, which implies that the titanium material is not much different from steel when the pipe wall thicknesses are the same. Figure 4 simply indicates that the damped titanium pipe under consideration will have similar vibrational behaviors, and much desirable weight savings (346.5 lb, or 157.2 kg for damped titanium structure, 601.6 lb, or 272.9 kg for damped steel structure for this geometrical configuration).

#### **EFFECT OF TITANIUM STRUCTURAL DAMPING**

The titanium material's damping properties are probably not much different from those of steel. If enough damping is provided from the damping material (it is, in this case), the effect of the titanium's structural damping should be less important. The driving point impedances will show that resonances are slightly less pronounced when small structural damping of titanium material is used. The overall value for the driving point impedance, however, will remain about the same.

#### **EFFECT OF OPERATIONAL AND ENVIRONMENTAL TEMPERATURE**

Environmental temperature is no doubt one of the very important factors in dealing with damping material. Figure 5 compares the mechanical impedances at temperatures of 20°F (-7°C), 45°F (7°C) and 70°F (21°C). These temperatures were chosen because at these temperatures the properties of the viscoelastic material used are known [6]. Other than the temperature, all geometrical dimensions of the damped titanium pipe are identical to those given in Figure 4. The properties of the viscoelastic material used indicate that the material is approximately ten times stiffer at 20°F than at 70°F. The loss factors are greater at the higher temperature (see

Table 1). Based on the calculations, the performance is worse at higher temperatures and better at lower temperatures. The overall performance is satisfactory over the operating temperature range.

**TABLE 1 - VISCOELASTIC MATERIAL PROPERTIES [6]**

Frequency, Hz .	Shear Modulus, G, psi .			Loss Factor, $\beta$		
	20°F	45°F	70°F	20°F	45°F	70°F
100	. 2675	707	225	. 0.92	1.16	1.05
1000	. 6681	2102	649	. 0.60	0.99	1.16
2000	. 8428	2862	905	. 0.52	0.90	1.15

#### **EFFECT OF BEAM THICKNESS**

Shown in Figure 6 are the driving point mechanical impedances of a damped titanium pipe. The titanium pipe is 100.0 inches (254 cm) long with an outside diameter of 12.75 inches (32.39 cm). The pipe wall thickness is 0.375 inch (0.95 cm). The viscoelastic material layer is 0.010 inch (0.0254 cm) thick at 70°F (21°C). The constraining beams, which are also made of titanium, are 0.375 inch (0.95 cm) wide and 0.1875 inch (0.48 cm) thick. The impedance for an additional titanium beam thickness of 0.375 inch (0.95 cm) is also calculated. The larger beam element thickness increases damping effectiveness only slightly. Performance of the various beam configurations is compared and discussed in relation to considerations of weight savings in a separate section given later in this paper.

#### **EFFECT OF BEAM WIDTH**

It has been demonstrated that the circumferential width of the beam segments, whether they are uniformly distributed or not, and the number of the beam segments to be attached are immaterial as long as they are small and closely spaced in full circumference [7].

#### **EFFECT OF VISCOELASTIC LAYER THICKNESS**

Figure 7 presents the driving point mechanical impedances of a damped titanium pipe with various thicknesses of the viscoelastic material layer. Impedances were calculated for three different thicknesses, i.e., 0.005 inch (0.0127 cm), 0.010 inch (0.0254 cm), and 0.020 inch (0.05 cm). For the particular geometric configuration experimentally tested in the past, the viscoelastic material's thickness seems not to be critical in the higher frequency region, but at the lower end of the frequency spectrum the thinner viscoelastic layer appears to be preferable.



## EFFECT OF BEAM MATERIAL

For the same titanium pipe configuration, driving point mechanical impedances were calculated for constraining beams made of different materials, such as steel, copper-nickel, and titanium. Figure 8 shows that the choice of beam material has significant effects in terms of vibration performance. Effects such as galvanic corrosion and other chemical reactions due to material incompatibility will not be considered in this paper.

## V. PERFORMANCE COMPARISON IN RELATION TO WEIGHT CONSIDERATIONS

Even though the titanium material is chosen here as an example for illustration purposes to demonstrate the vibration characteristics of a metallic material shell with damping treatments, it has however the potential as a possible replacement material for piping systems currently used. The titanium's potential advantages over other piping materials include lower weight due to lower density and greater flexibility (lower modulus of elasticity), possible lower reactions on attached equipment (due to a lower thermal expansion coefficient), more compact systems (due to greater flexibility possibly eliminating expansion loops), extension of service life and less maintenance (due to increased corrosion/erosion resistance), and the ability to weld directly to titanium condensers and heat exchangers in the latest ship designs, etc.

Weight considerations alone would be enough to warrant the use of titanium in piping systems. Comparing an undamped (or damped) 12-inch schedule 40S titanium pipe to an equivalent undamped (or damped) steel pipe, the weight savings from using titanium would be 42.5%. If the constraining beam elements on the titanium pipe cover 100% of the circumference, weight savings can be realized by using thinner beam elements. As shown in Figure 6, the thicker constraining beams do not necessarily improve damping effectiveness. If desired, partial circumferential damping coverages would provide more weight savings. Past experience strongly indicates that the damping effectiveness is essentially the same for some partial coverage treatments as it is for full coverage. Therefore, through partial damping coverage with thinner constraining beam elements, additional weight savings could be achieved without a significant loss in damping effectiveness.

Both titanium and steel materials are highly resonant when used in piping structures, as the calculated dynamic response for the undamped steel pipe in Figure 9 shows. Also shown is the effectiveness of the axial beam damping treatment in reducing these resonant vibrations for the titanium pipe. In comparing these two response curves, it can be concluded that the damped titanium pipe not only has a significantly better vibration performance than steel pipe, but also has a lighter weight even if the beam damping coverage is full.

## VI. CONCLUSIONS

This paper presents vibration evaluations of cylindrical shells (pipe) made of steel and titanium materials. From these evaluations and the accompanying analytical studies the following conclusions can be made. The dynamic responses of the titanium pipes are similar to pipes made of other conventional material such as steel. Resonant vibrations of titanium pipes, particularly in the higher frequency ranges, can be effectively and greatly suppressed or controlled by longitudinal beam element damping. The additional weight due to damping treatments can be minimized by reducing the percent coverage, by using thinner beam elements, or both. In any damped or undamped configuration, a titanium pipe system will be lighter than an undamped steel pipe system.

## REFERENCES

1. E. M. Kerwin, Jr. 1959 Journal of the Acoustical Society of America 31, 952-962. Damping of flexural waves by a constrained viscoelastic layer.
2. R. A. DiTaranto 1965 Journal of Applied Mechanics 32, 881-886. Theory of vibratory bending for elastic and viscoelastic layered finite-length beams.
3. D. J. Mead and S. Markus 1969 Journal of Sound and Vibration 10, 163-175. The forced vibration of a three-layer damped sandwich beam with arbitrary boundary conditions.
4. Y. V. K. Sadasiva Rao and B. C. Nakra 1974 Journal of Sound and Vibration 34, 309-326. Vibrations of unsymmetrical sandwich beams and plates with viscoelastic cores.
5. Y. P. Lu, A. J. Roscoe and B. E. Douglas 1991 Journal of Sound and Vibration 150, 395-403. Analysis of the response of damped cylindrical shells carrying discontinuously constrained beam elements.
6. M. L. Drake, 1989 AFWAL-TR-88-4248. Damping properties of various materials.
7. Y. P. Lu 1979 Journal of the Acoustical Society of America 65, 1329-1331. A note on the forced responses of damped rings.

## LIST OF FIGURES

- Figure 1. Geometry of a damped shell composite
- Figure 2. Computed driving point impedances of undamped and beam element damped shells
- Figure 3. Computed driving point impedances of a beam element damped shell with and without structural damping
- Figure 4. Vibration responses of damped titanium piping versus damped steel piping with same pipe wall thickness
- Figure 5. Effect of temperature on vibration responses of damped titanium pipe
- Figure 6. Effect of beam element thickness on vibration responses of damped titanium pipe
- Figure 7. Effect of viscoelastic layer thickness on vibration responses of damped titanium pipe
- Figure 8. Effect of beam element material on vibration responses of damped titanium pipe
- Figure 9. Vibration responses of damped titanium pipe versus undamped steel pipe

## LIST OF TABLES

- Table 1. Viscoelastic material properties

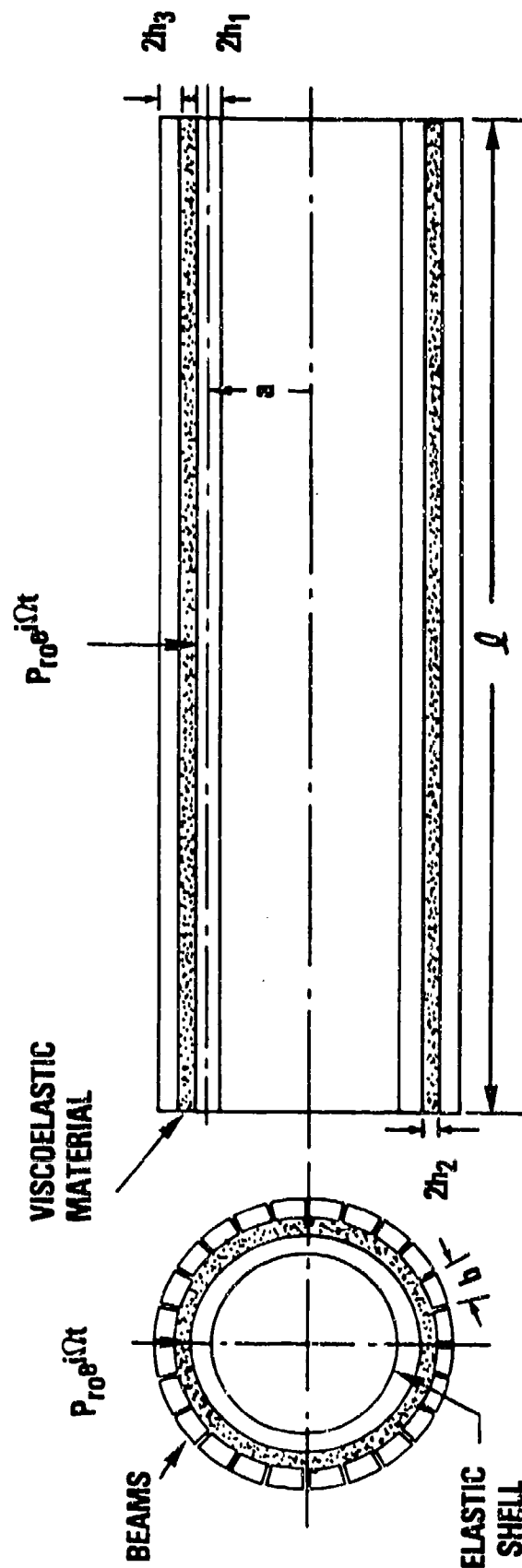


Figure 1: Geometry of a damped shell composite

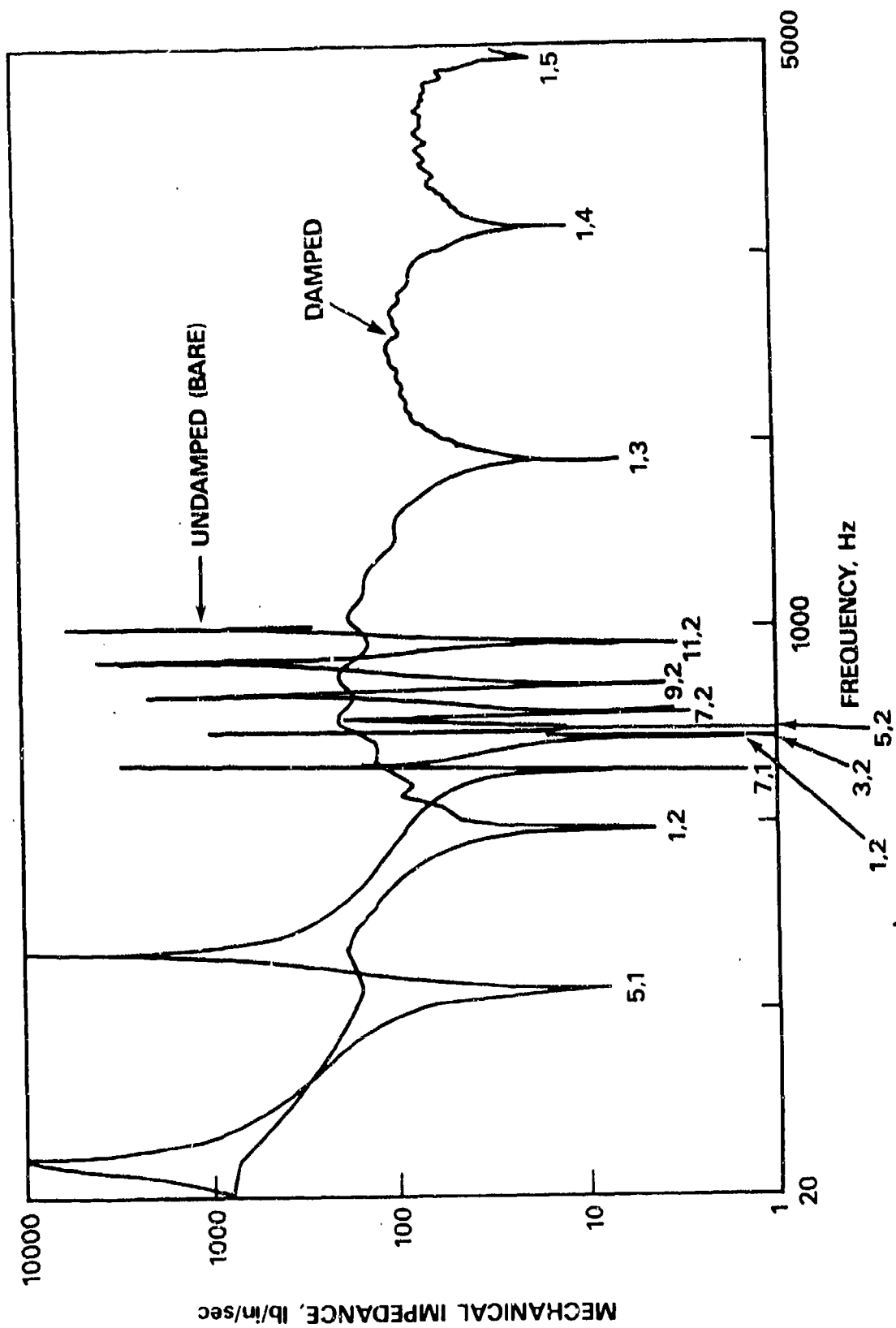


Figure 2: Computed driving point impedances of undamped and beam element damped shells

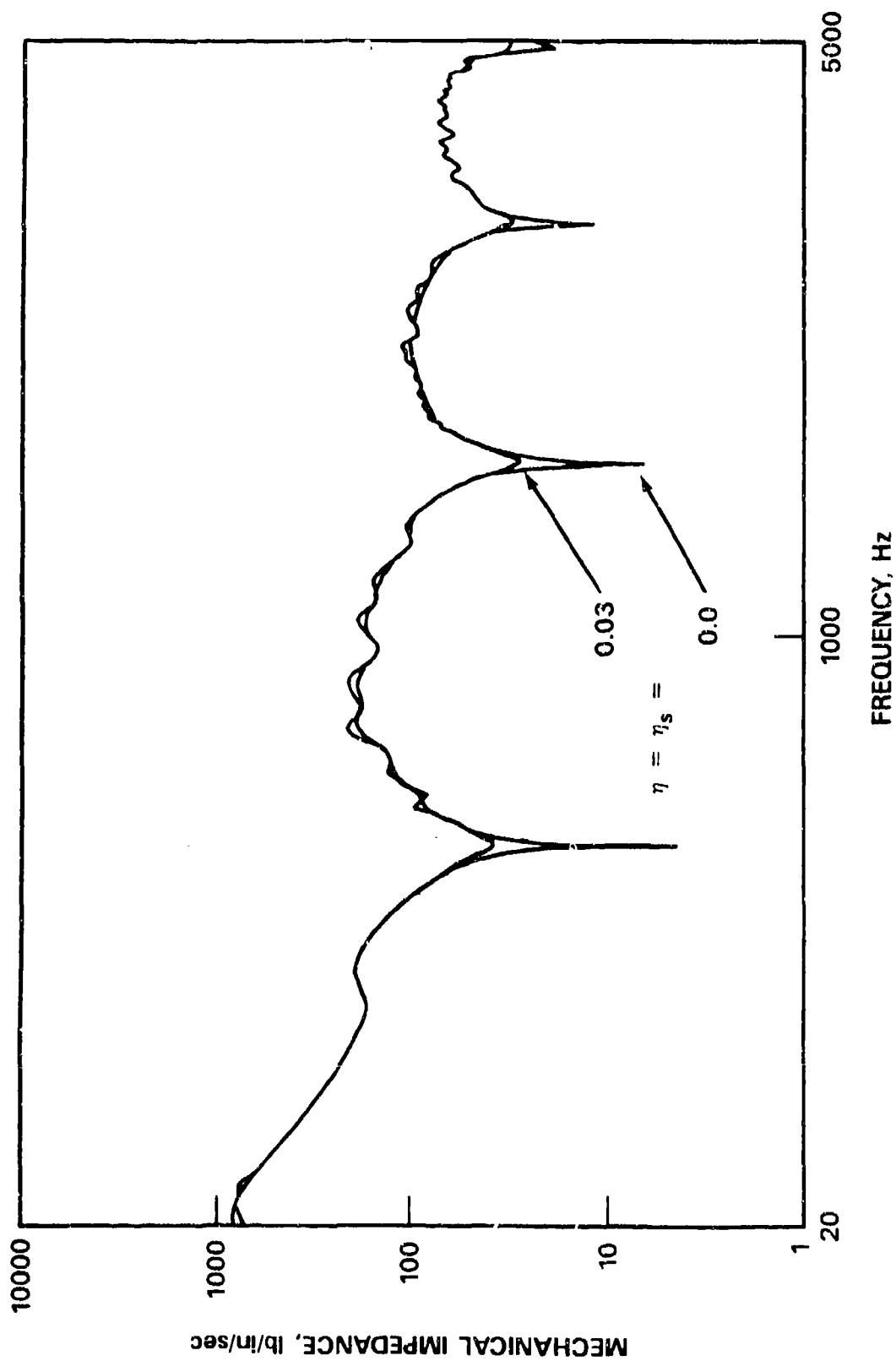


Figure 3: Computed driving point impedances of a beam element damped shell with and without structural damping

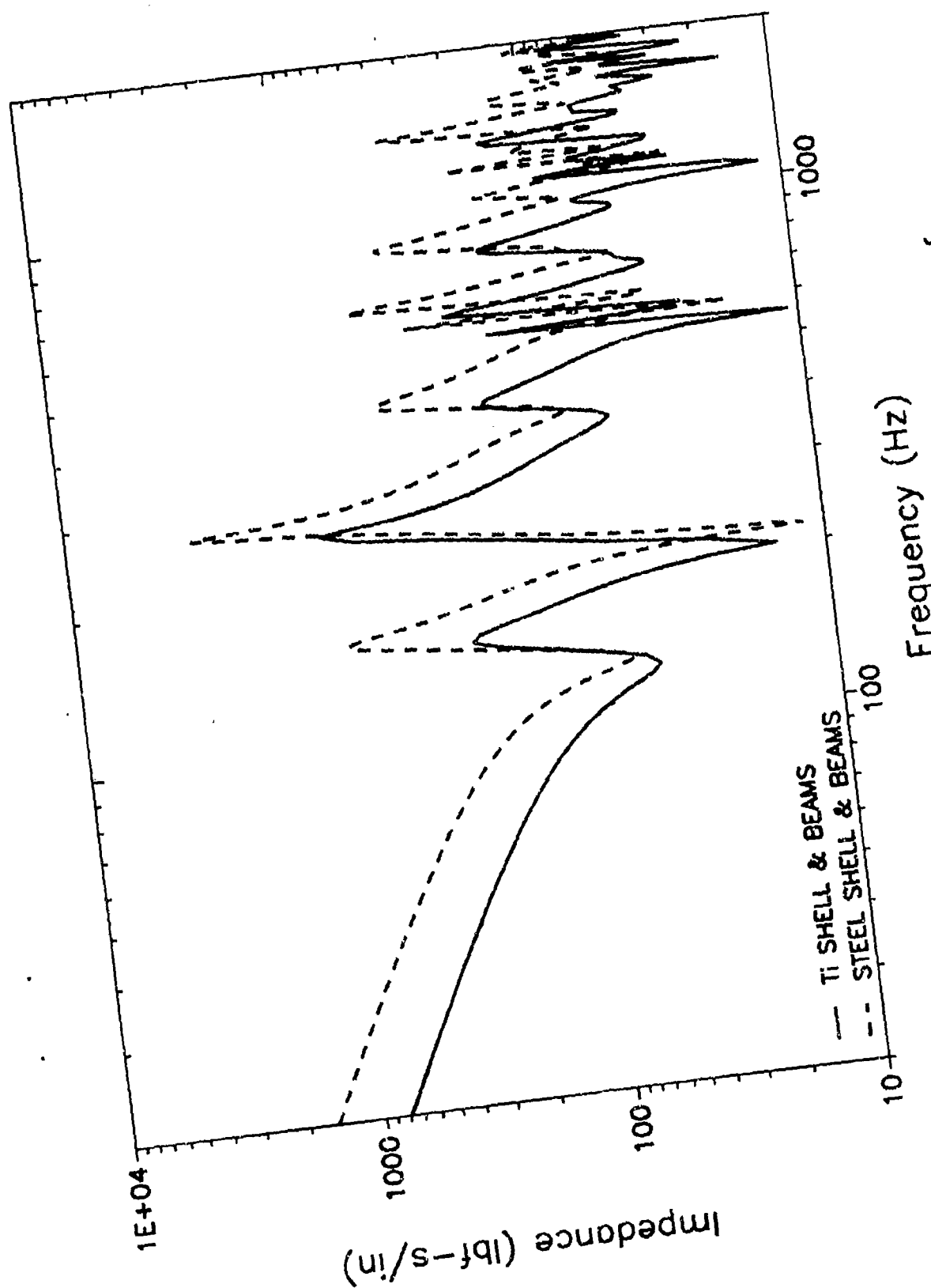


Figure 4: Vibration responses of  
damped titanium piping vs. damped steel piping  
with same pipe wall thickness



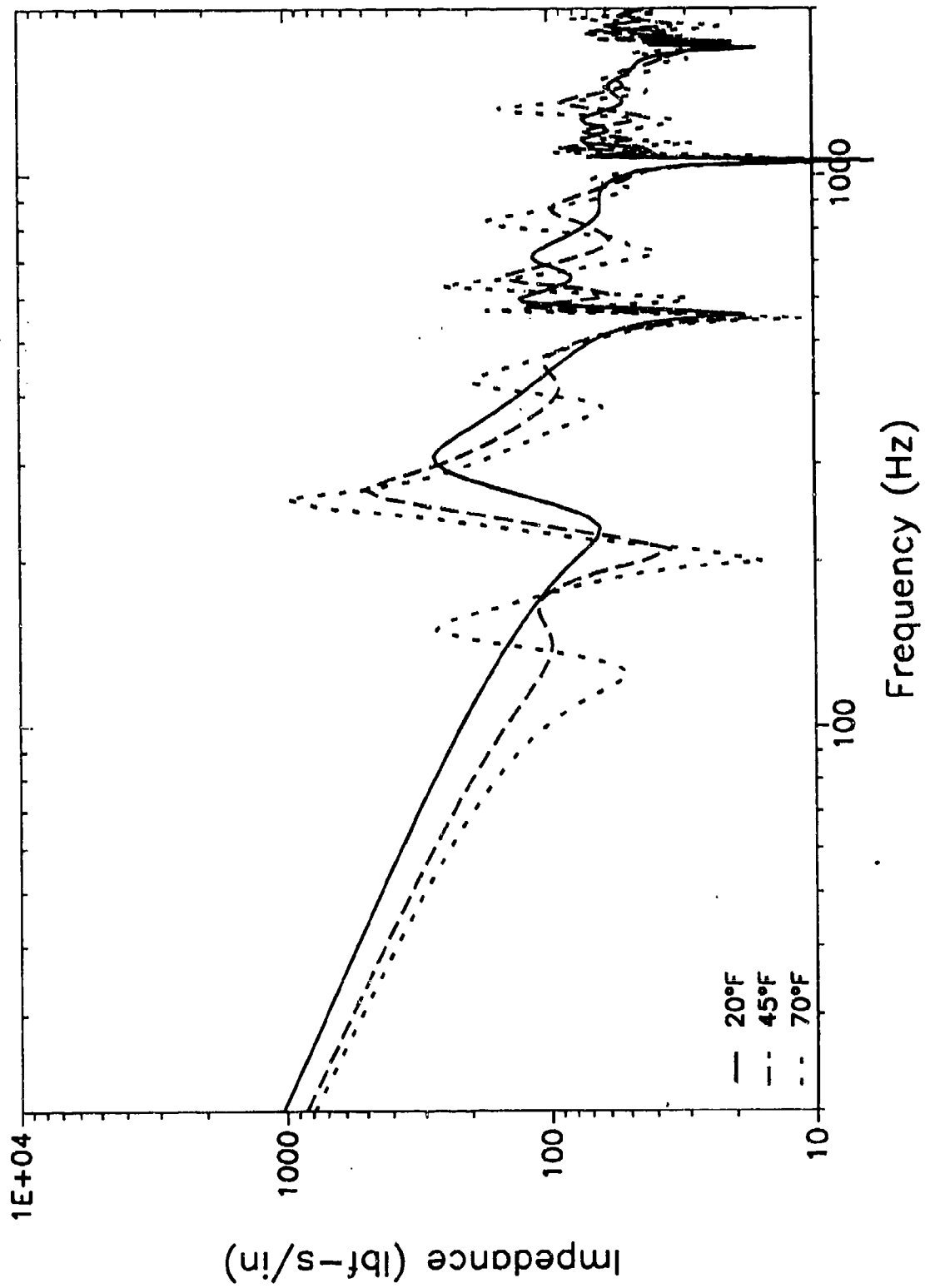


Figure 5: Effect of temperature on vibration responses of damped titanium pipe

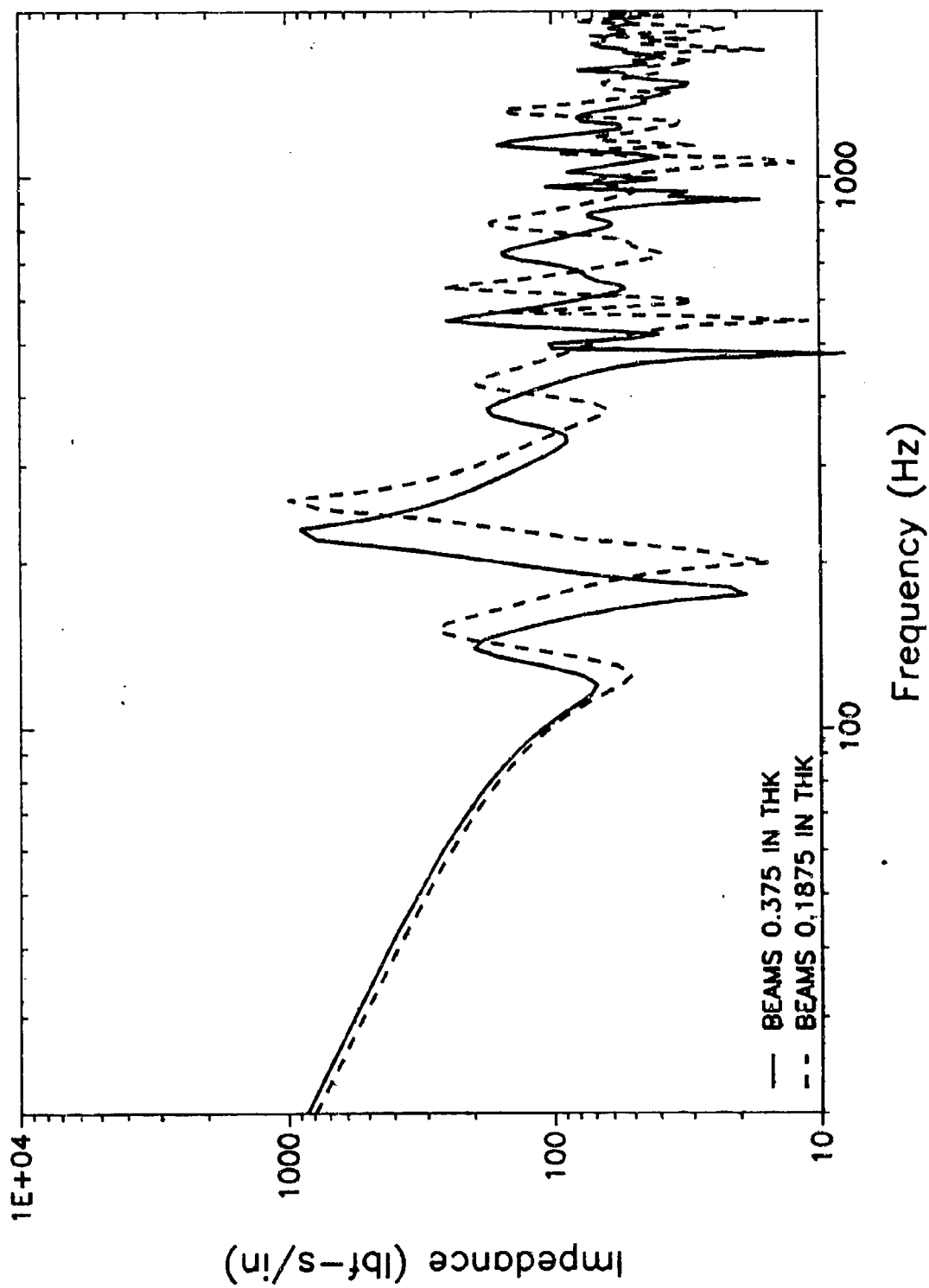


Figure 6: Effect of beam element thickness on vibration responses of damped titanium pipe

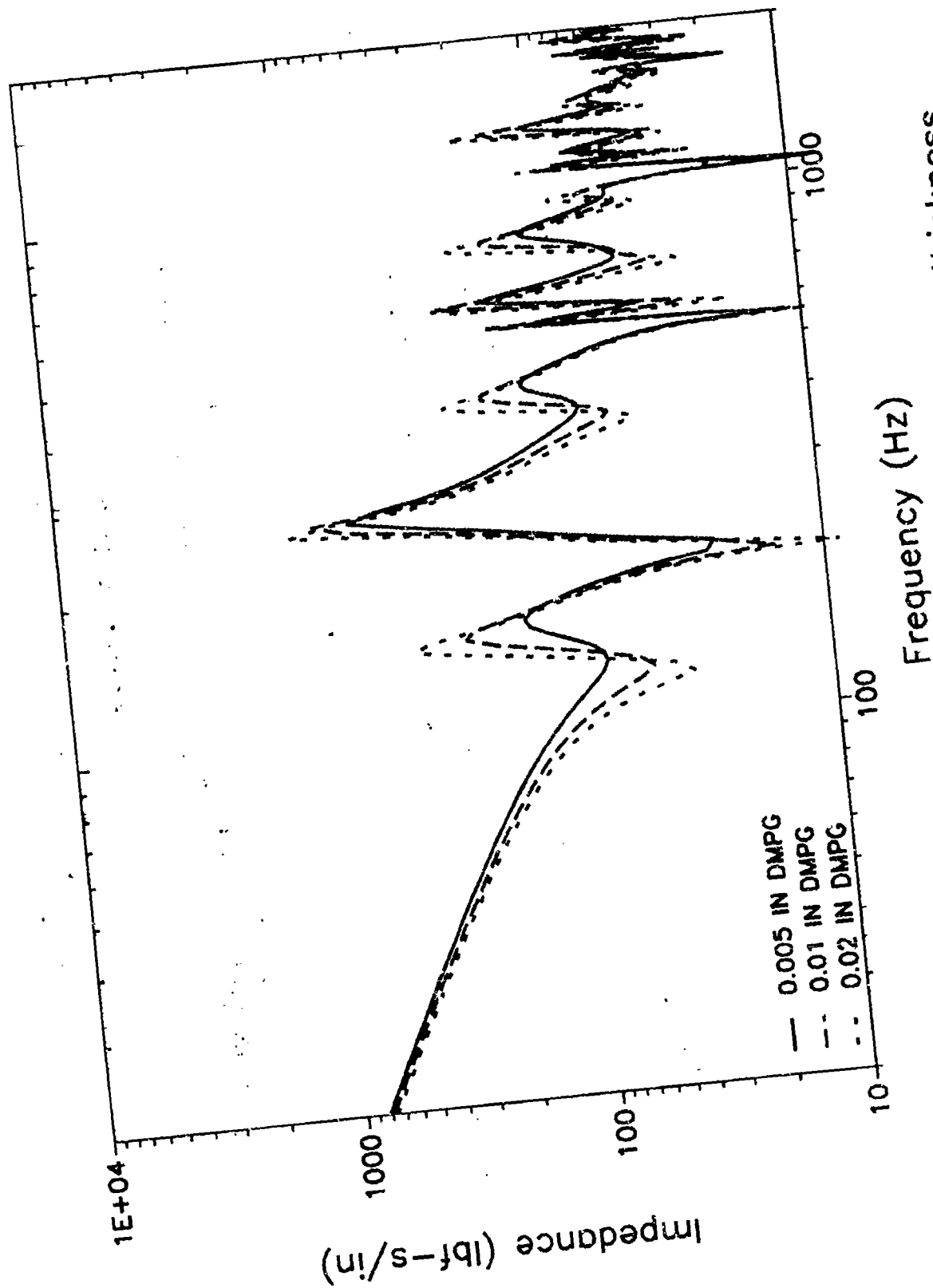


Figure 7: Effect of viscoelastic layer thickness on vibration responses of damped titanium pipe

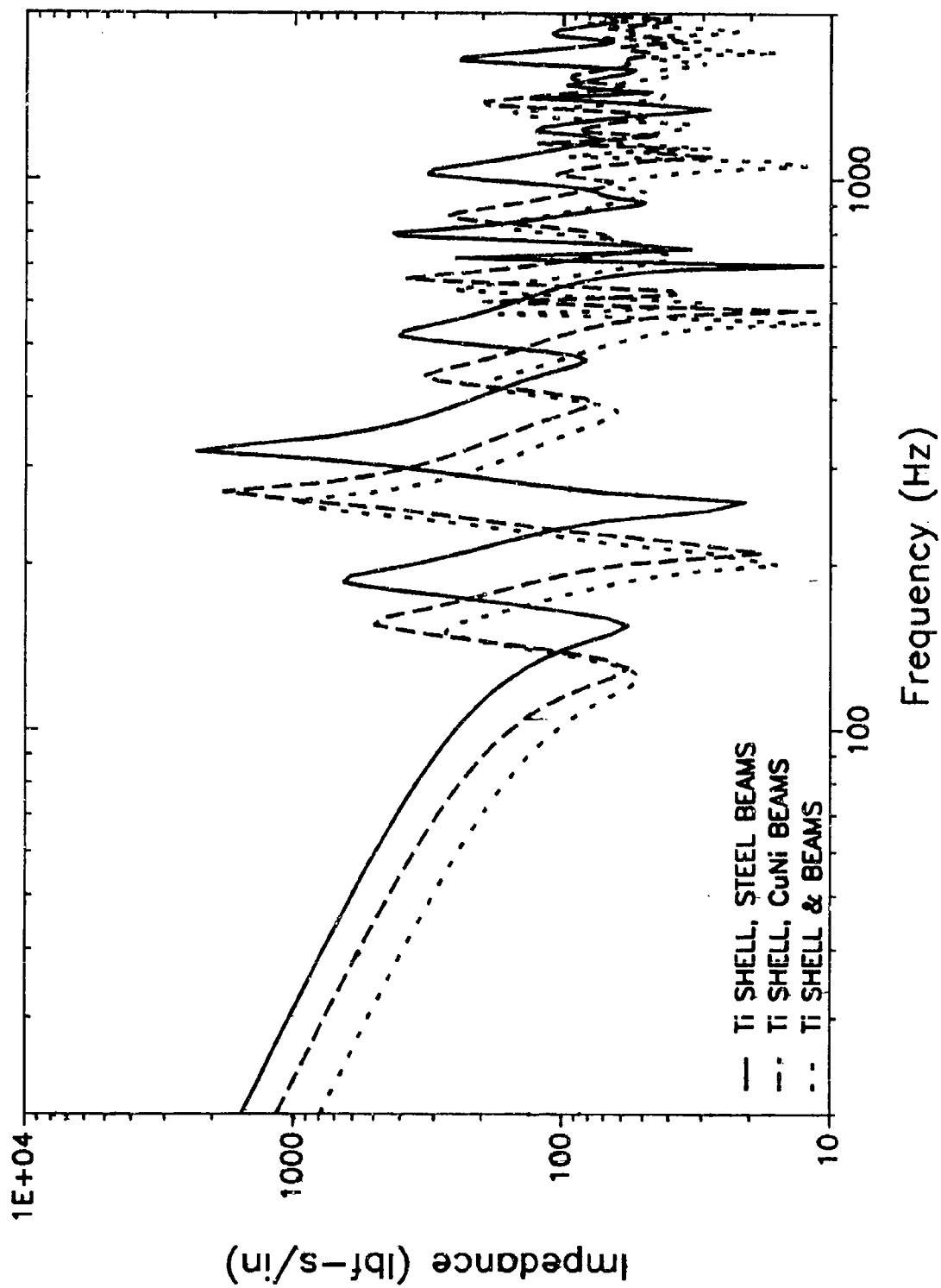


Figure 8: Effect of beam element material on vibration responses of damped titanium pipe

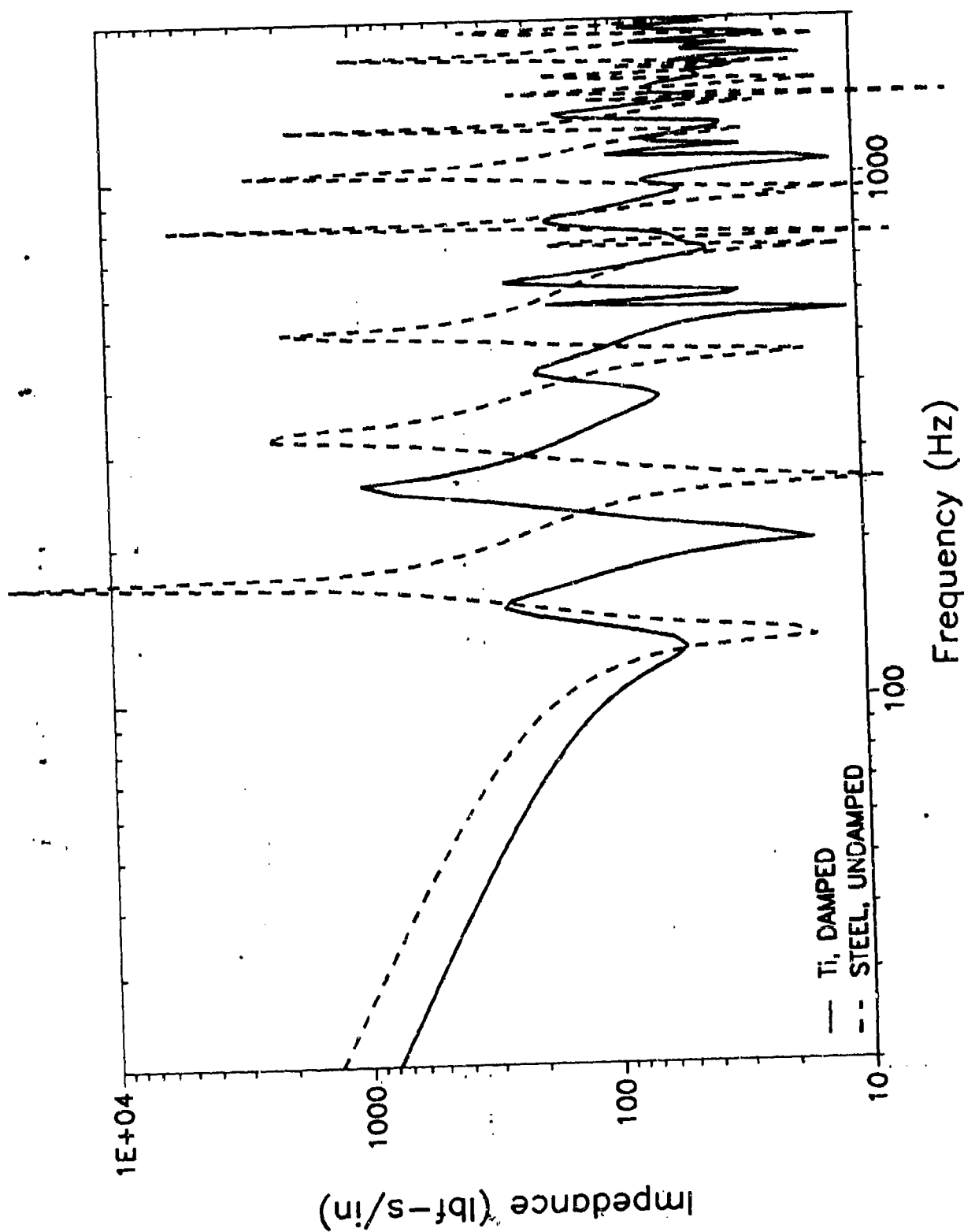


Figure 9: Vibration responses of damped titanium pipe vs. undamped steel pipe

**DAMPING THIN-WALLED COMPOSITE STRUCTURES  
WITH EMBEDDED CONSTRAINING LAYERS**

S. S. Sattinger  
Z. N. Sanjana

Westinghouse Science and Technology Center\*

ABSTRACT

Add-on damping treatments have been used successfully on many types of structures, but there are a number of factors that have tended to limit their use. Some of these factors relate to installation access or the obstructions and mechanical hazards that can be created by the treatments themselves. The treatments may also cause toxicity, flammability, or other environmental problems due to outgassing and combustibility of the damping materials. Conversely, exposed areas of these materials may be susceptible to the effects of moisture, lubricants, oxygen, vacuum conditions. The limited static and creep strength properties of many of these materials may also pose obstacles, as in attempts to apply damping treatments to rotating components that have high centrifugal acceleration levels. Embedding damping materials inside the walls of organic-matrix composite beam or shell structures during fabrication provides a way to overcome these limitations. Described is a Westinghouse-patented construction featuring embedded, fully encapsulated, constrained damping layers that provide high damping of all vibration modes, including those which tend to be difficult to damp. The latter modes include the long-wavelength, global beam-bending and torsional modes that occur at low frequencies and the in-plane axial and circumferential modes that are observed at higher frequencies. This paper discusses attained and projected damping and structural performance, various advantages of the construction, and some candidate product applications.

---

\*1310 Beulah Road  
Pittsburgh, PA 15235  
(412) 256-1327

## Introduction

One of the main approaches to the control of structural vibration response is the addition of passive damping treatments, in which vibrational energy is consumed in the deformation of lossy viscoelastic material layers. Two major categories of passive damping treatments are the following:

- Free- or unconstrained-layer treatments, consisting of thick tiles of stiff viscoelastic material (VEM) bonded to the surfaces of the structure to be damped.
- Constrained-layer treatments, consisting of thin films of soft VEM damping polymer bonded between constraining layers of stiff structural material and the surfaces of the structure to be damped.

Constrained-layer treatments are particularly effective in reducing the amplitudes of resonant vibration response for a given amount of added weight. There are, however, a number of factors that have tended to limit the use of damping treatments. It may be difficult to gain access to interior regions of a structure that would otherwise be plausible locations for the installation of damping treatment. The treatment, once installed, may create obstructions or mechanical hazards to personnel. The treatment may also cause toxicity, flammability, or other environmental problems due to outgassing and combustibility of the damping material. Conversely, exposed areas of this material may be susceptible to the effects of moisture, lubricants, oxygen, or vacuum conditions. The limited static and creep strength properties of many of these materials may also pose obstacles to the use of these treatments, as in the case of rotating components having high centrifugal acceleration levels.

Embedding damping materials inside the walls of organic-matrix composite beam or shell structures during fabrication as shown in Figure 1 can overcome these limitations. Described is a particular Westinghouse-patented construction\* featuring embedded, fully encapsulated, constrained damping layers. The cross-section configuration of the structure need not be of concern, provided that it be thin-walled and amenable to composite fabrication. This construction can provide high damping of all vibration modes, including those which tend to be difficult to damp. The latter modes include the long-wavelength, global beam-bending and torsional modes that occur at low frequencies and the in-plane axial and circumferential modes that are observed at higher frequencies. This paper discusses design considerations, attained damping performance, advantages of the construction, and some candidate product applications.

---

\*U.S. Patent No. 5,108,802, dated April 28, 1992.

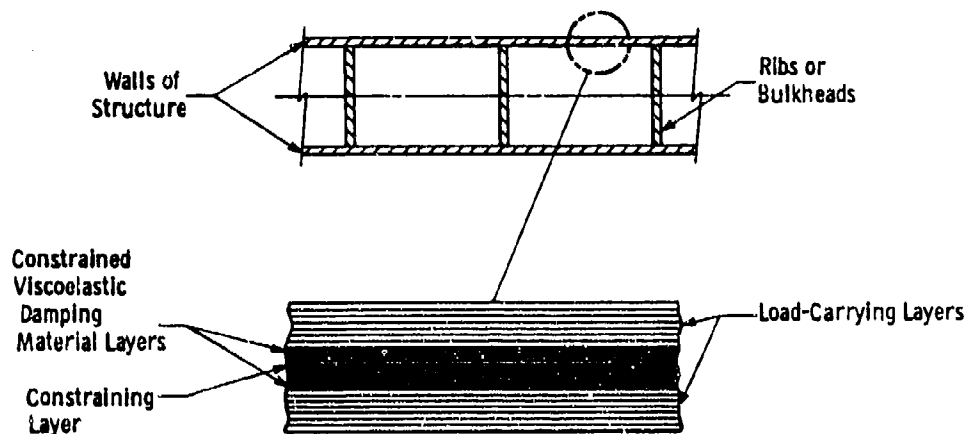


Fig. 1 - Concept for embedding constrained-layer damping within the walls of thin-walled composite structures

### The Embedded Constraining Layer Concept

Figure 2 contrasts the shapes of the global or long-wave-length bending modes, which normally are the lowest-frequency modes of a beam or extended shell structure, with the higher-frequency local bending modes, which are the kinds of modes that are more commonly damped with add-on passive treatments. The local bending modes may include either the plate-bending modes of the individual panels of a flat-sided tube or beam, or the shell-bending (lobal) modes of a cylindrical tube. Other types of modes that may need to be damped are the axial and circumferential modes, which include lower-frequency torsional modes but generally are associated with the higher frequencies. A state of in-plane extensional or shear strain which is nearly uniform through the thickness of the wall is associated with all of these vibration mode types except the local bending modes, in which the strain is linearly varying and undergoes a reversal in sign from the inside surface to the outside surface.

Although it is feasible to use add-on passive damping treatments to control the uniformly-stressed modes of tubes and other thin-walled structures (Torvik 1980; Sattinger 1990), most applications have been for purposes of controlling the local modes. Add-on constrained-layer damping of the uniformly-stressed modes requires deliberate axial segmentation of the constraining layer to induce energy-absorbing cyclic shear deformation of the damping polymer film, whereas the local bending modes can be damped either with or without this segmentation. If, instead of adding damping treatment externally, a properly sized layer of VEM damping polymer is embedded midway through the thickness of the wall, it can very effectively damp the local bending modes without the use of a



constraining layer, because the two equal-thickness wall portions will fulfill the mutual role of constraining layers for each other. Damping the uniformly-stressed modes internally, however, still requires the use of a segmented constraining layer, and it becomes necessary to place this internal constraining layer between two separate layers of VEM. Later discussion will point out the possible need for segmentation in both the axial and circumferential directions.

Restating the above reasoning as it applies to the embedding of damping materials:

- If only the local panel-bending or shell-bending modes of the thin-walled structure are of concern, their responses can be controlled by embedding a single layer of VEM midway through the thickness of the wall.
- If the vibration modes to be controlled are those having vibratory in-plane extensional or shear stresses that are uniform or nearly uniform through the wall, a segmented constraining layer is required. These uniformly-stressed modes include the global beam-bending and torsional modes that occur at low frequencies and the in-plane axial and circumferential modes that are observed at higher frequencies. This constraining layer may be placed midway through the wall thickness and sandwiched between two separate VEM layers as seen in Figure 1. The results shown later demonstrate that the local bending modes are also strongly damped by this arrangement.

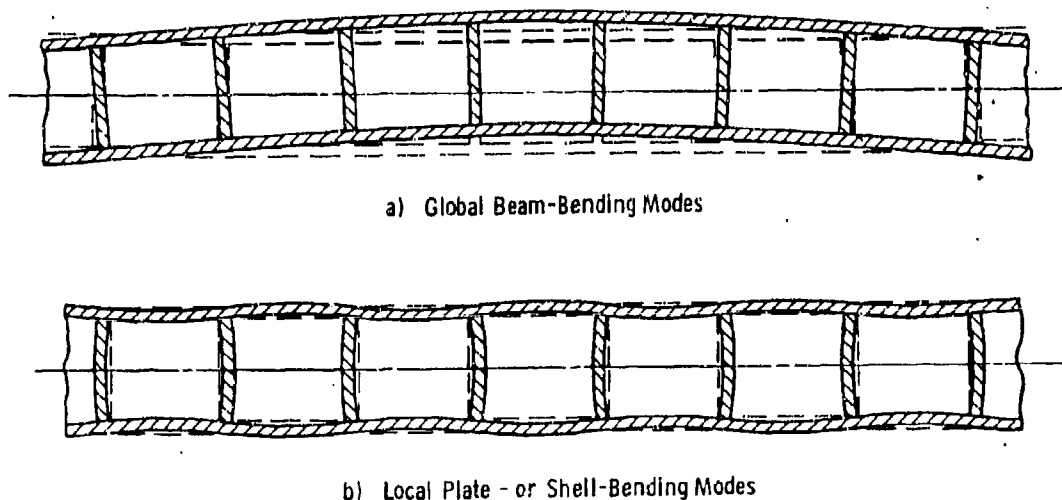


Fig. 2 - Global vs. local bending vibration mode shapes of thin-walled beam or shell structures

constraining-layer segments. In the free-free accelerance tests, global-bending-mode and column-mode strain energies in the end regions were assumed small, and the calculated loss factors were prorated downward by a 0.94 ratio of actual to nominal area per damping segment typical of the inboard regions. In the mass-loaded condition, the end regions were assumed to be stressed as highly as the inboard regions, and a 0.88 ratio of total damping segment area to total mid-plane area, including that occupied by the end closure segments, was used.

The good overall agreement between predictions and measurements seen in Figure 9 confirms that the damping of the extensionally stressed modes in segmented-layer constructions can be reasonably well predicted. There was a tendency for the damping to be overpredicted in the mass-loaded condition and underpredicted in the free-free condition, but we note that a shift of the prediction curves to the right by a factor of two on frequency would greatly improve the agreement. This shift would be well within typical variances in shear modulus data among differing material lots and differing properties test methods.

The peak loss factor of about 0.080 for the segmented-layer specimen represents strong damping of these hard-to-damp types of vibration modes. Not included among the damping data plotted in Figure 9 is a torsional-mode loss factor of 0.052 measured at a frequency of 137 Hz. The local shell-bending or lobar modes were observed to be strongly damped in both the segmented-layer and the continuous-layer specimens, with loss factors in the range from 0.1 to 0.4.

### **The Role of Segmentation**

This study demonstrates that the segmentation of the constraining layer is very important to the damping of the global beam-bending modes that occur at the lowest frequencies in thin-walled beam or shell structures. Because the wavelengths are very long, shear strain can be developed in the VEM for energy dissipation only by deliberately segmenting the constraining layer in the axial direction.

In some instances the circumferential or transverse segmentation of the constraining layer can also be important. Without circumferential segmentation in tubes, constraining layers having increasingly long axial lengths would be increasingly forced to conform to the bending curvature of the base structure. This conformance would result from the action of transverse normal forces. The VEM layers would sustain very little shear deformation as a result. Circumferential segmentation was the subject of an earlier analysis of damped, circular-cross-section tubes by the Russian authors Vinogradov and Chernoberevskii (1980). The conclusion of

their study was that the bending loss factors of tubes having axially-continuous constrained-layer treatments can be substantially increased by cutting lengthwise slits in the constraining layer, forming a number of arc-shaped segments.

### **Advantages and Likely Applications for the Construction**

Composite beam and shell structures damped by segmented, embedded constraining layers offer the following advantages over metal construction with add-on damping treatments:

- Barriers to VEM outgassing and combustion, and protection of the VEM from moisture and other deteriorating agents.
- Solutions to problems of access or obstruction.
- Improved ability of the damping layers to withstand centrifugal loading.
- Options for tailoring the material properties, e.g., imparting different stiffness and damping values in various directions. With fibers oriented as in the tubular specimens described in this paper, all vibration modes, including the uniform circumferential or "breathing" mode, are damped.
- Higher damping performance in local panel or shell bending modes than is attainable with add-on treatments.

The merging together and bonding of the load-carrying inner and outer portions of the walls at the ends and/or edges totally encapsulates the VEM and provides structural rigidity at the locations where the beam or shell would interconnect with other structural components. These features give decided advantages over damped composite tube constructions which rely on relative motions of the inner and outer wall portions to produce shear deformation in the interleaved VEM layers (Barrett 1989; Belknap and Kosmatka 1991). Damping is obtained without sacrifice to either the static or the dynamic axial stiffness or strength, and the dynamic stiffness is actually increased by the addition of the damping layers. We avoid placing the viscoelastic materials directly in the load path as is done, for example, in the alternating ply concept (Bronowicki and Diaz 1989).

Potential military applications of this construction include propulsion shafting, machinery components, and structures for naval ships and equipment; other possibilities include tracking system components and structures for spacecraft and helicopters. Robotic devices, turbomachinery structures, optical equipment, and sporting goods could be among the commercial applications. The shapes that could be produced include closed tubes of almost any desired cross-section, plus open sections such as channels, angles, or any other

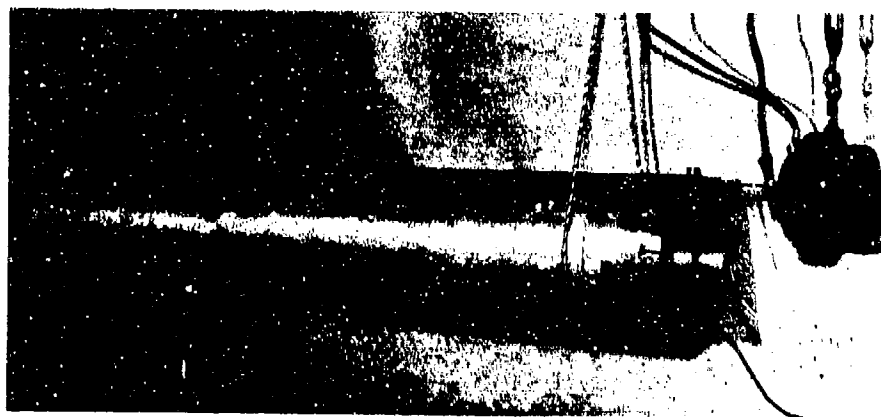


Fig. 4 - Internally damped specimen undergoing axially directed frequency-response measurements to provide data on damping and response attenuation.

Figure 7 reinforces these findings by showing similar results obtained in other, radially directed frequency-response tests. The segmented embedded constraining layer is highly effective in damping the shell-bending modes, and again the global beam-bending modes are well damped.

### Damping Values

Damping values for the segmented-layer specimen were inferred from drive-point accelerance magnitude peaks using the half-power bandwidth method:

$$\eta = \Delta f / f_n,$$

where  $\Delta f$  denotes the frequency difference between half-power points (points on the accelerance curve that are 3 dB down from the peak), and  $f_n$  denotes the damped natural frequency, which is taken as the frequency of the accelerance peak.

The frequency-response tests covered a range of frequencies which was quite high in relation to some possible applications for the embedded-constraining-layer construction. To supplement the high-frequency damping data from these tests with lower-frequency damping measurements, we mounted the segmented-layer specimen between solid steel discs as shown in Figure 8 using a thin layer of epoxy structural adhesive at each end. The discs added mass and inertia loadings and simulated reactions that would be present in a longer structure. The test assembly was freely suspended and sinusoidally driven at several different drive points in the axial and tangential

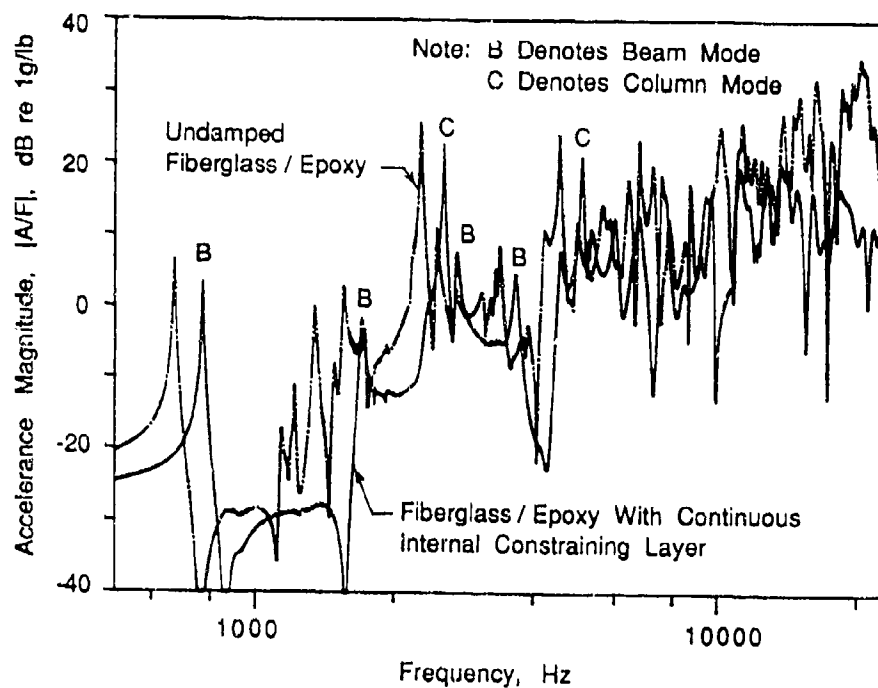


Fig. 5 - Axially directed transfer accelerance for specimen with continuous embedded constraining layer versus that of undamped fiberglass/epoxy.

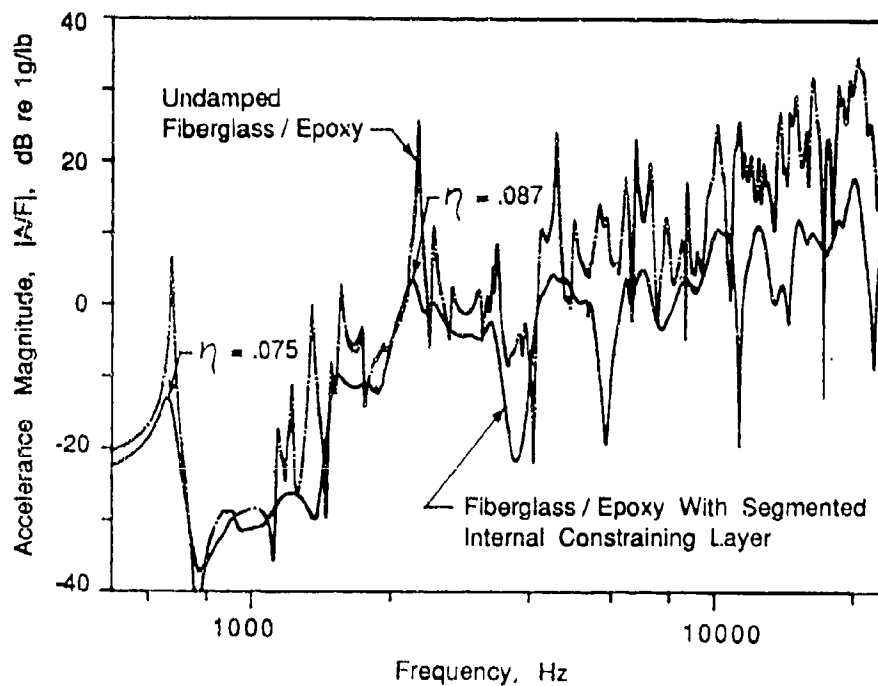


Fig. 6 - Axially directed transfer accelerance for specimen with segmented embedded constraining layer versus that of undamped fiberglass/epoxy.

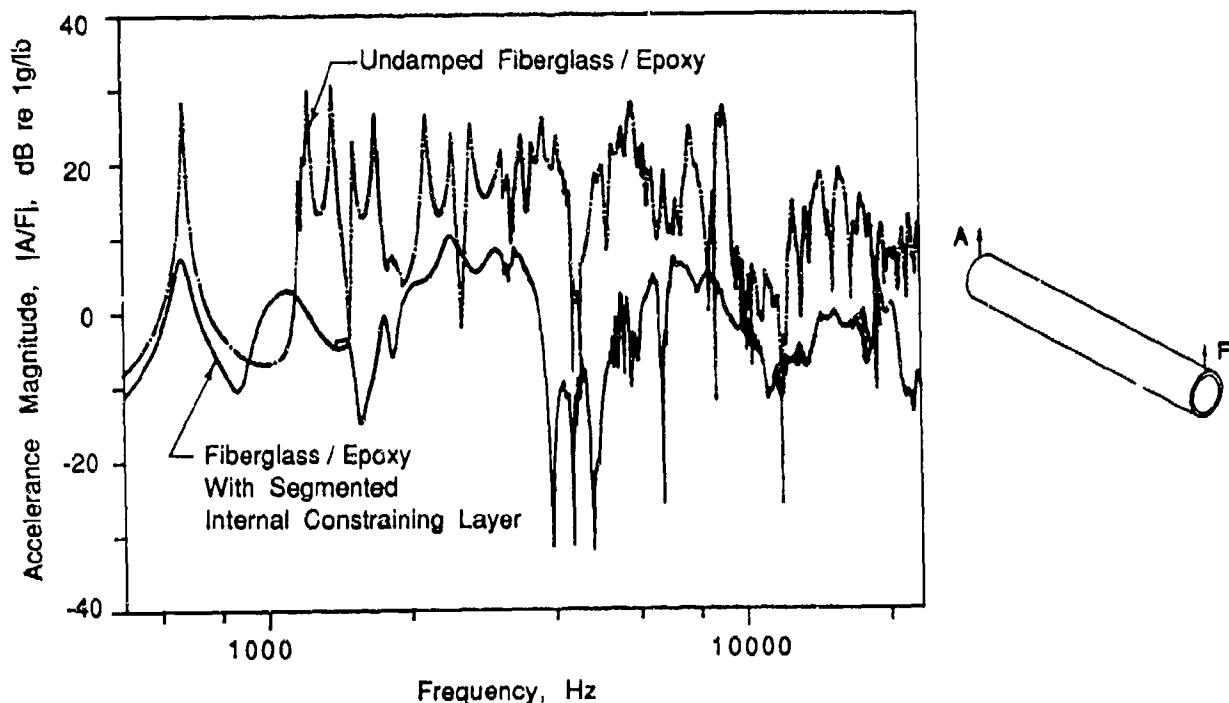


Fig. 7 - Radially directed transfer accelerance for specimen with segmented embedded constraining layer versus that of undamped fiberglass/epoxy.

directions to produce decays from beam-bending, extensional, and torsional mode resonances. The low-frequency damping values were obtained from the decay tests using the formula

$$\eta = [\ln(a_0/a_n)]/[\pi n],$$

where  $a_0$  is the acceleration amplitude at an arbitrarily chosen peak of a decay curve, and  $a_n$  is the acceleration amplitude of a peak occurring  $n$  cycles later.

Figure 9 compares predicted and measured room-temperature damping values for the vibration modes having in-plane, axially-directed extensional stresses that were uniform or nearly uniform through the thickness of the wall of the segmented-layer specimen. All predictions were generated using a previously described method for calculating the extensional damping performance of constrained-layer treatments (Torvik 1980; Sattinger 1991). This method applies to quasi-static conditions, i.e. in instances where the wavelength of the vibration mode is appreciably greater than the length of one damping treatment segment. The mismatch in the predicted-damping curves for the two test configurations is the result of different corrections for the incomplete coverage of the wall mid-plane area by the

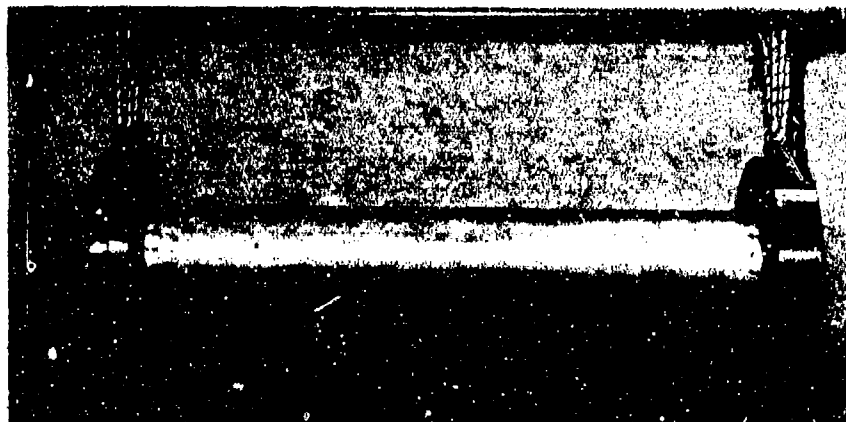


Fig. 8 - Segmented-constraining-layer specimen undergoing vibration decay tests with added mass loading to provide low-frequency damping data.

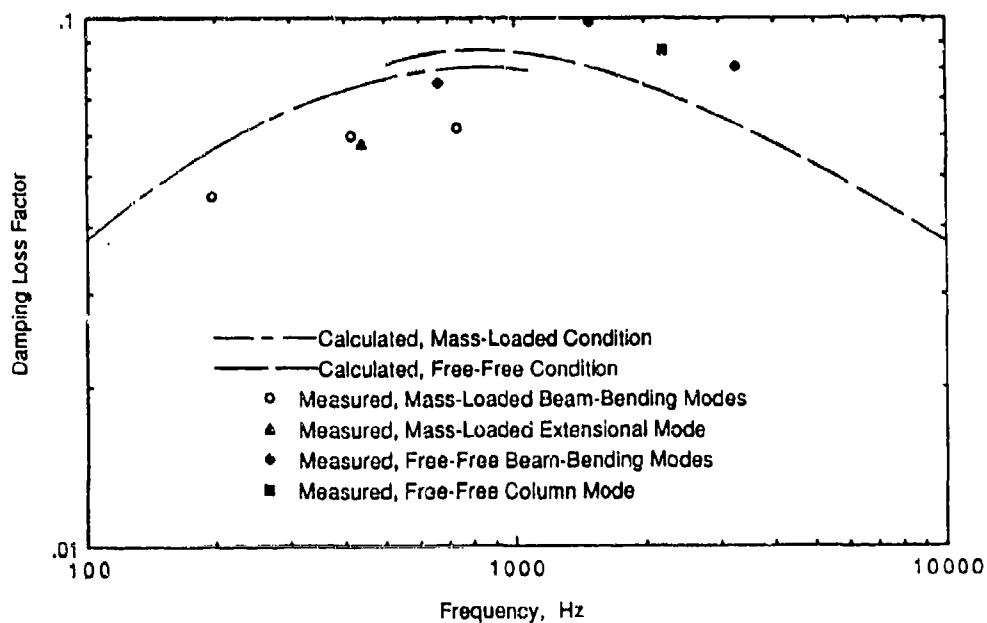


Fig. 9 - Predicted vs. measured damping performance for extensionally stressed vibration modes of the segmented-constraining-layer specimen.

constraining-layer segments. In the free-free accelerance tests, global-bending-mode and column-mode strain energies in the end regions were assumed small, and the calculated loss factors were prorated downward by a 0.94 ratio of actual to nominal area per damping segment typical of the inboard regions. In the mass-loaded condition, the end regions were assumed to be stressed as highly as the inboard regions, and a 0.88 ratio of total damping segment area to total mid-plane area, including that occupied by the end closure segments, was used.

The good overall agreement between predictions and measurements seen in Figure 9 confirms that the damping of the extensionally stressed modes in segmented-layer constructions can be reasonably well predicted. There was a tendency for the damping to be overpredicted in the mass-loaded condition and underpredicted in the free-free condition, but we note that a shift of the prediction curves to the right by a factor of two on frequency would greatly improve the agreement. This shift would be well within typical variances in shear modulus data among differing material lots and differing properties test methods.

The peak loss factor of about 0.080 for the segmented-layer specimen represents strong damping of these hard-to-damp types of vibration modes. Not included among the damping data plotted in Figure 9 is a torsional-mode loss factor of 0.052 measured at a frequency of 137 Hz. The local shell-bending or lobar modes were observed to be strongly damped in both the segmented-layer and the continuous-layer specimens, with loss factors in the range from 0.1 to 0.4.

### **The Role of Segmentation**

This study demonstrates that the segmentation of the constraining layer is very important to the damping of the global beam-bending modes that occur at the lowest frequencies in thin-walled beam or shell structures. Because the wavelengths are very long, shear strain can be developed in the VEM for energy dissipation only by deliberately segmenting the constraining layer in the axial direction.

In some instances the circumferential or transverse segmentation of the constraining layer can also be important. Without circumferential segmentation in tubes, constraining layers having increasingly long axial lengths would be increasingly forced to conform to the bending curvature of the base structure. This conformance would result from the action of transverse normal forces. The VEM layers would sustain very little shear deformation as a result. Circumferential segmentation was the subject of an earlier analysis of damped, circular-cross-section tubes by the Russian authors Vinogradov and Chernoberevskii (1980). The conclusion of



their study was that the bending loss factors of tubes having axially-continuous constrained-layer treatments can be substantially increased by cutting lengthwise slits in the constraining layer, forming a number of arc-shaped segments.

### **Advantages and Likely Applications for the Construction**

Composite beam and shell structures damped by segmented, embedded constraining layers offer the following advantages over metal construction with add-on damping treatments:

- Barriers to VEM outgassing and combustion, and protection of the VEM from moisture and other deteriorating agents.
- Solutions to problems of access or obstruction.
- Improved ability of the damping layers to withstand centrifugal loading.
- Options for tailoring the material properties, e.g., imparting different stiffness and damping values in various directions. With fibers oriented as in the tubular specimens described in this paper, all vibration modes, including the uniform circumferential or "breathing" mode, are damped.
- Higher damping performance in local panel or shell bending modes than is attainable with add-on treatments.

The merging together and bonding of the load-carrying inner and outer portions of the walls at the ends and/or edges totally encapsulates the VEM and provides structural rigidity at the locations where the beam or shell would interconnect with other structural components. These features give decided advantages over damped composite tube constructions which rely on relative motions of the inner and outer wall portions to produce shear deformation in the interleaved VEM layers (Barrett 1989; Belknap and Kosmatka 1991). Damping is obtained without sacrifice to either the static or the dynamic axial stiffness or strength, and the dynamic stiffness is actually increased by the addition of the damping layers. We avoid placing the viscoelastic materials directly in the load path as is done, for example, in the alternating ply concept (Bronowicki and Diaz 1989).

Potential military applications of this construction include propulsion shafting, machinery components, and structures for naval ships and equipment; other possibilities include tracking system components and structures for spacecraft and helicopters. Robotic devices, turbomachinery structures, optical equipment, and sporting goods could be among the commercial applications. The shapes that could be produced include closed tubes of almost any desired cross-section, plus open sections such as channels, angles, or any other

shapes that are amenable to composite fabrication, whether by fiber-winding, pultrusion, braiding, or other technique.

## Conclusions

In addition to surmounting application obstacles associated with access, strength, and environmental factors, the light-weight construction described in this paper can combine high vibration damping performance with high structural stiffness and strength. Peak measurements of damping loss factors in the vicinity of 0.08 for the global beam-bending and axial vibration modes of a tubular specimen with segmented constraining layer were reasonably well predicted and represent high damping of these hard-to-damp modes. A torsional-mode loss factor in the vicinity of 0.05 was also measured, and with the fiber orientations chosen, all vibration modes, including the uniform circumferential or "breathing" mode, were damped. In addition, composite structures damped by embedded constraining layers offer much higher local-mode damping performance than is attainable with add-on treatments of comparable thickness.

Advantages of this construction over other viscoelastically damped composite constructions include total encapsulation and restraint of the VEM and more efficient load transfer at interconnections with other components. Likely applications of this construction include structural components for marine, aerospace, and other military and commercial uses.

## References

1. Barrett, D. J., "A Design for Improving the Structural Damping Properties of Axial Members," Proceedings of Damping '89, U. S. Air Force Wright Aeronautical Laboratories, Flight Dynamics Laboratory, WRDC-TR-89-3116, Paper HCB, November 1989.
2. Belknap, F. M. and Kosmatka, J. B., "Vibration Suppression of Thin-Walled Composite Tubes Using Embedded Viscoelastic Layers," Proceedings of Damping '91, U. S. Air Force Wright Laboratory, Flight Dynamics Directorate, WL-TR-91-3078, Paper HAC, August 1991.
3. Bronowicki, A. J. and Diaz, H. P., "Analysis, Optimization, Fabrication, and Test of Composite Shells with Embedded Viscoelastic Layers," Proceedings of Damping '89, U. S. Air Force Wright Aeronautical Laboratories, Flight Dynamics Laboratory, WRDC-TR-89-3116, Paper GCA, November 1989.

4. Sattinger, S. S., "Constrained-Layer Damping of Global Bending Vibration Modes of Thin-Walled Beams," Vibration Control of Mechanical, Structural, and Fluid-Structural Systems, American Society of Mechanical Engineers, PVP Vol. 202, pp. 45-53, November 1990.
5. Sattinger, S. S., "Directional Damping of the Global Vibration Modes of Tubular Structures by Constrained-Layer Treatments," Proceedings of Damping '91, U. S. Air Force Wright Laboratory, Flight Dynamics Directorate, WL-TR-91-3078, Paper HBA, August 1991.
6. Torvik, P. J., "The Analysis and Design of Constrained Layer Damping Treatments," Damping Applications for Vibration Control, American Society of Mechanical Engineers, AMD Vol. 38, pp. 85-112, 1980.
7. Vinogradov, B. D. and Chernoberevskii, V. V., "Damping of Tubes by a Constrained Coating," Soviet Physics Acoustics, Vol. 26, No. 4, 1980, pp. 328-330.

# **ANALYTICAL AND EXPERIMENTAL STUDY OF A MASS DAMPER USING SHAPE MEMORY ALLOYS**

**Jose A. Inaudi\***

Earthquake Engineering Research Center, University of California at Berkeley

**James M. Kelly, Wendy Taniwangsa**

Earthquake Engineering Research Center, University of California at Berkeley

**Robert Krumme**

E\*Sorb Systems, Sunnyvale, California

## **Abstract**

The implementation of a tuned mass damper (TMD) using shape memory alloys (SMA) as a dissipating mechanism for the absorber is described in this paper. The TMD consists of a mass attached to a lightly damped structure with prestressed Nitinol (nickel-titanium) cables. The cables (or rods) are installed in the direction perpendicular to the motion of the points of attachment – both to the mass damper and to the structural system. This geometric configuration along with the prestress in the SMA rods introduces a resistance scheme which can be approximated by a bilinear relation between the force on the mass damper and the relative displacement between the mass damper and its support, leading to a triangular hysteresis loop. The goal of the TMD is to reduce the deformations in the main structural system under support or external forcing excitation. The efficacy of the TMD in reducing deformation response of the main system is investigated by subjecting an experimental model with and without the TMD, to a set of artificially generated support motions.

---

\* EERC, 1301 South 46th Street, Richmond, CA 94804; Tel.: (510) 231-9519.

## Shape memory alloys

Both passive and active damping applications of shape memory alloys (SMA) were first proposed by Krumme and Hodgson (Krumme, 1985). The investigation of the application of SMAs for seismic resistance design was initially conducted by Kelly and Nims at the Earthquake Engineering Research Center of the University of California (Aiken, Nims and Kelly, 1992). Work in passive damping applications of SMAs continues at the State University of New York at Buffalo, (Witting and Cozzarelli, 1992), the Earthquake Engineering Research Center of the University of California at Berkeley, and at E\*Sorb Systems (Sunnyvale, California). SMAs possess several features that make them suitable alternative material for vibration control. Among those features we can highlight the shape-memory effect, superelasticity and fatigue resistance.

These materials show hysteresis when cyclically loaded. Unlike plastically deforming metals – in which the dissipation of energy is due to a dislocation glide mechanism – SMAs exhibit a reversible phase transformation induced by stress (Duerig et al., 1990). The hysteresis loops of a prestressed rod of nickel-titanium subjected to cyclic deformation and a simplified mathematical model of the constitutive relationship of the material are shown in Fig. 1. At low stress levels superelastic SMAs show elastic behavior. When loaded above a certain stress level,  $\sigma_1$ , the tangent stiffness of the material reduces significantly because of a phase transformation from a body centered cubic austenitic crystal structure to a body centered tetragonal martensitic crystal structure. When unloaded, the reverse phase transformation takes place when the stress level is below  $\sigma_2$ , a lower stress level than  $\sigma_1$ . The material behaves elastically once the material is unloaded and no residual strain is shown. If the strain  $\epsilon$  exceeds  $\epsilon_2$  the material hardens.

### A nonlinear TMD using shape memory alloys

Let us consider a TMD consisting of prestressed shape memory alloy cables of length  $L$  and cross-sectional area  $A$  connecting the mass damper to the main structural system. The configuration of the system under analysis is shown in Fig. 2. The tension of the rod,  $T$ , is a function of the strain of the rods,  $\epsilon$ , through the constitutive relation of the shape memory alloy,  $\sigma(\epsilon, \dot{\epsilon}, z)$ , which for simplicity can be assumed piece-wise linear as described in Fig. 1. This constitutive relation shows memory. The memory of the element, represented by the element state variable  $z$ , is activated when the strain  $\epsilon$  exceeds  $\epsilon_1$ , the strain at which the phase-transformation starts.

The strain  $\epsilon$  is a function of the TMD deformation  $\Delta$  and the initial strain  $\epsilon_0$  according to the kinematic relation

$$\epsilon(t) = \epsilon_0 + \sqrt{1 - \frac{\Delta(t)^2}{L^2}} - 1 \quad (1)$$

where

$$\Delta(t) = y_2(t) - y_1(t) \quad (2)$$

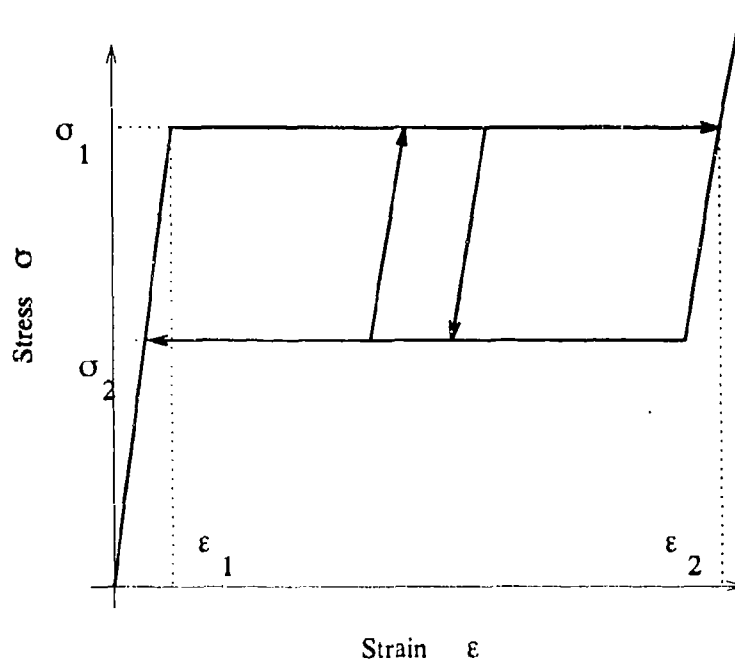
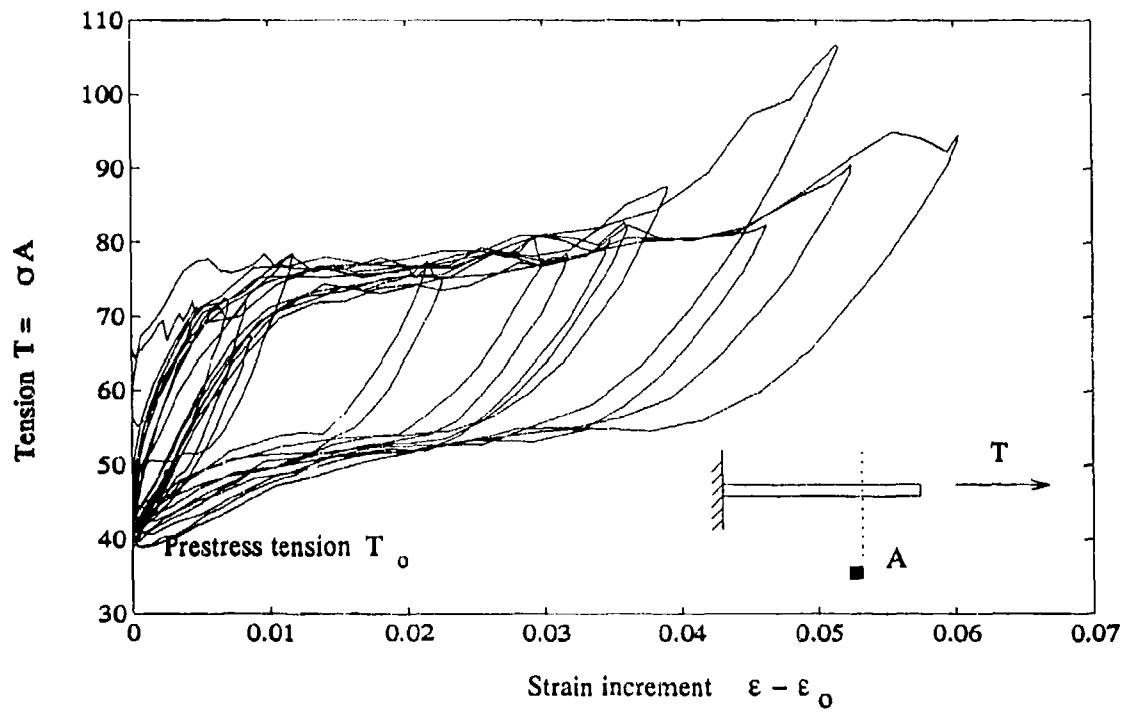


Figure 1. Constitutive relationship of shape-memory alloys.

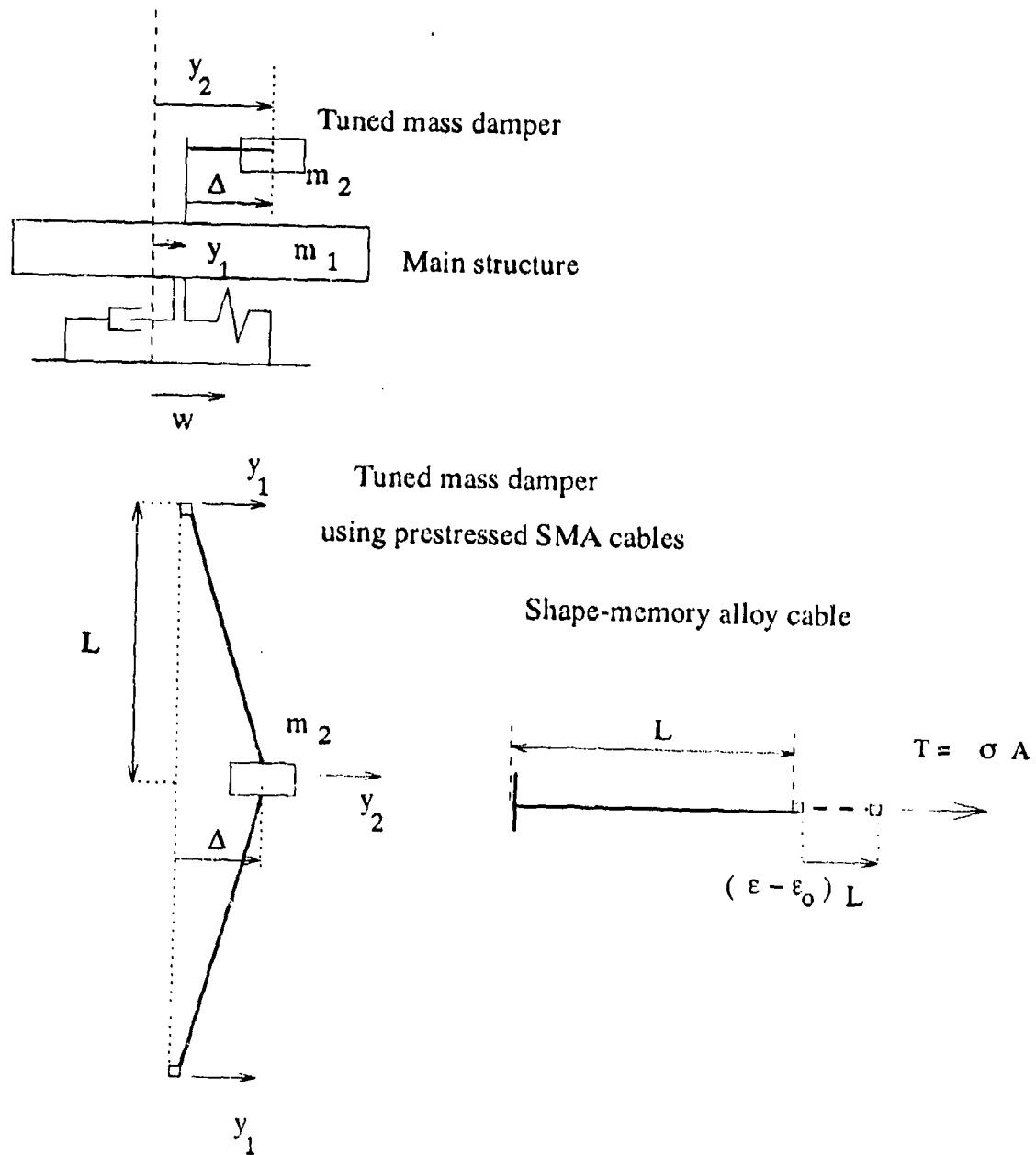


Figure 2. Schematic of a mass damper using prestressed shape-memory alloys rods.

and  $L$  is the length of the SMA rods in the undeformed configuration of the TMD (i.e., for  $\Delta = 0$ ). In Eq. (2)  $y_1$  represents the displacement of the main structure and  $y_2$  represents the displacement of the mass damper, as illustrated in Fig. 2.

The equations of motion of the main structural system with attached TMD subjected to support motion can be written as

$$\begin{aligned}\ddot{y}_1(t) &= -\omega^2 y_1(t) - 2\xi\omega \dot{y}_1(t) + \frac{2}{m_1} T(\Delta, \dot{\Delta}, z) \frac{\Delta(t)}{\sqrt{\Delta(t)^2 + L^2}} - w(t) \\ \ddot{y}_2(t) &= -\frac{2}{m_2} T(\Delta, \dot{\Delta}, z) \frac{\Delta(t)}{\sqrt{\Delta(t)^2 + L^2}} - w(t)\end{aligned}\quad (3)$$

where  $T(\dots)$  represents the tension in the SMA rods,  $\omega$  the natural frequency of the main structure,  $\xi$  the damping ration of the main structure, and  $w$  the support acceleration. It is convenient to define the following dimensionless parameters:

$$\mu = \frac{m_2}{m_1} \quad \eta_1 = \frac{T_1}{m_1 g} \quad \eta_2 = \frac{T_2}{m_1 g} \quad (4)$$

where  $T_1$  is the tension of the rod in the phase transformation of the loading path and  $T_2$  is the tension of the rod at the reverse transformation of the unloading path:

$$T_1 = A \sigma_1, \quad T_2 = A \sigma_2 \quad (5)$$

In Eq. (5)  $A$  represents the cross-sectional area of the rods,  $\sigma_1$  the stress at which the phase-transformation is induced, and  $\sigma_2$  the stress at the reverse transformation (Fig. 1). The mass ratio,  $\mu$ , rarely exceeds one tenth in typical applications of TMDs; the parameters  $\eta_1$  and  $\eta_2$  can be varied by selecting different cross-sectional areas for the SMA rods. The ratio  $\eta_1/\eta_2$  is constrained by the material properties of the SMA. For nickel-titanium alloys (the SMA used in this experimental investigation)  $0.30 < \eta_1/\eta_2 < 0.7$ .

### Numerical simulation of the response of a structure with a TMD

In order to illustrate the behavior of the TMD with SMA prestressed rods, numerical simulation of the response of a simple system under free vibration and under support excitation is developed. The main system under consideration is a lightly damped structure with the following natural frequency and damping ratio:

$$\omega = \pi \text{ rad/s} \quad \xi = 0.01 \quad (6)$$

Two mass ratios were considered in the simulations:  $\mu = 0.04$  and  $\mu = 0.10$ . For both cases the prestress in the Nitinol rods was assumed to be  $\sigma_o = \sigma_2$ .

For the case of  $\mu = 0.04$ , the parameters of the TMD system were assumed to be as follows:

$$\eta_1 = \frac{A \sigma_1}{m_1 g} = 0.01 \quad \eta_2 = \frac{A \sigma_2}{m_1 g} = 0.005 \quad \epsilon_1 = 0.01 \quad L = 50 \text{ cm} \quad (7)$$

For the case of  $\mu = 0.10$ , the parameters of the TMD system were assumed to be as follows:



$$\eta_1 = \frac{A \sigma_1}{m_1 g} = 0.03 \quad \eta_2 = \frac{A \sigma_2}{m_1 g} = 0.015 \quad \epsilon_1 = 0.01 \quad L = 50 \text{ cm} \quad (8)$$

For the free-vibration analysis the initial state of the system was assumed to be  $y_1(0) = 0$ ,  $\dot{y}_1(0) = 30 \text{ cm/s}$ ,  $y_2(0) = 0$ , and  $\dot{y}_2(0) = 0$ . The deformation histories of the structure are shown in Fig. 3 for the cases of no TMD,  $\mu = 0.04$ , and  $\mu = 0.10$ . Significant dissipation is achieved in the SMA rods as shown in the bottom figures of Fig. 3 where the TMD force-deformation relationship,  $f(\Delta, \dot{\Delta}, z)$ , is plotted against the TMD deformation,  $\Delta$ , to illustrate the hysteresis loops of the device. The TMD force,  $f(\Delta, \dot{\Delta}, z)$ , is the component of the tension of the rods in the direction of the deformation  $\Delta$  given by

$$f(\Delta, \dot{\Delta}, z) = 2 T(\Delta, \dot{\Delta}, z) \frac{\Delta}{\sqrt{\Delta^2 + L^2}} \quad (9)$$

For the forced-vibration problem the support acceleration,  $w(t)$ , was taken as filtered white noise, a zero-mean Gaussian random process obtained by filtering a white-noise signal through a second order filter:

$$\dot{\mathbf{x}}_f(t) = \begin{bmatrix} 0 & 1 \\ -\omega_f^2 & -2\xi_f\omega_f \end{bmatrix} \mathbf{x}_f(t) + \begin{bmatrix} 0 \\ 1 \end{bmatrix} v(t) \quad (10)$$

$$w(t) = -[\omega_f^2 \quad 2\xi_f\omega_f] \mathbf{x}_f(t)$$

where the white-noise,  $v(t)$ , was assumed to be a zero-mean Gaussian process with:

$$E[v(t)v(t+\tau)] = 100 \text{ cm}^2/\text{s}^3 \quad (11)$$

The filter frequency and damping ratio were assumed to be  $\omega_f = 4\pi \text{ rad/s}$  and  $\xi_f = 0.30$ , respectively.

The following table shows the results obtained in the simulation for both cases and compares them with the case of the structure without the TMD.

Table 1. Maximum responses obtained in numerical simulations.

	$\max  y_1 $ [cm]	$\max  \Delta $ [cm]
No TMD	11.5	-
TMD $\mu = 0.04$	10.6	28.8
TMD $\mu = 0.10$	7.8	17.6

Figure 4 shows the response of the main system,  $y_1(t)$ , for the system without the TMD, and for the system with the TMD ( $\mu = 0.04$  or  $\mu = 0.10$  and  $\sigma_o = \sigma_2$ ). The TMD improved the response of the main structural system. Significant energy dissipation occurs in the shape-memory alloy rods since large strain excursions are induced in the rods by the interaction (tuning in linear systems) between the TMD and the main structural system.

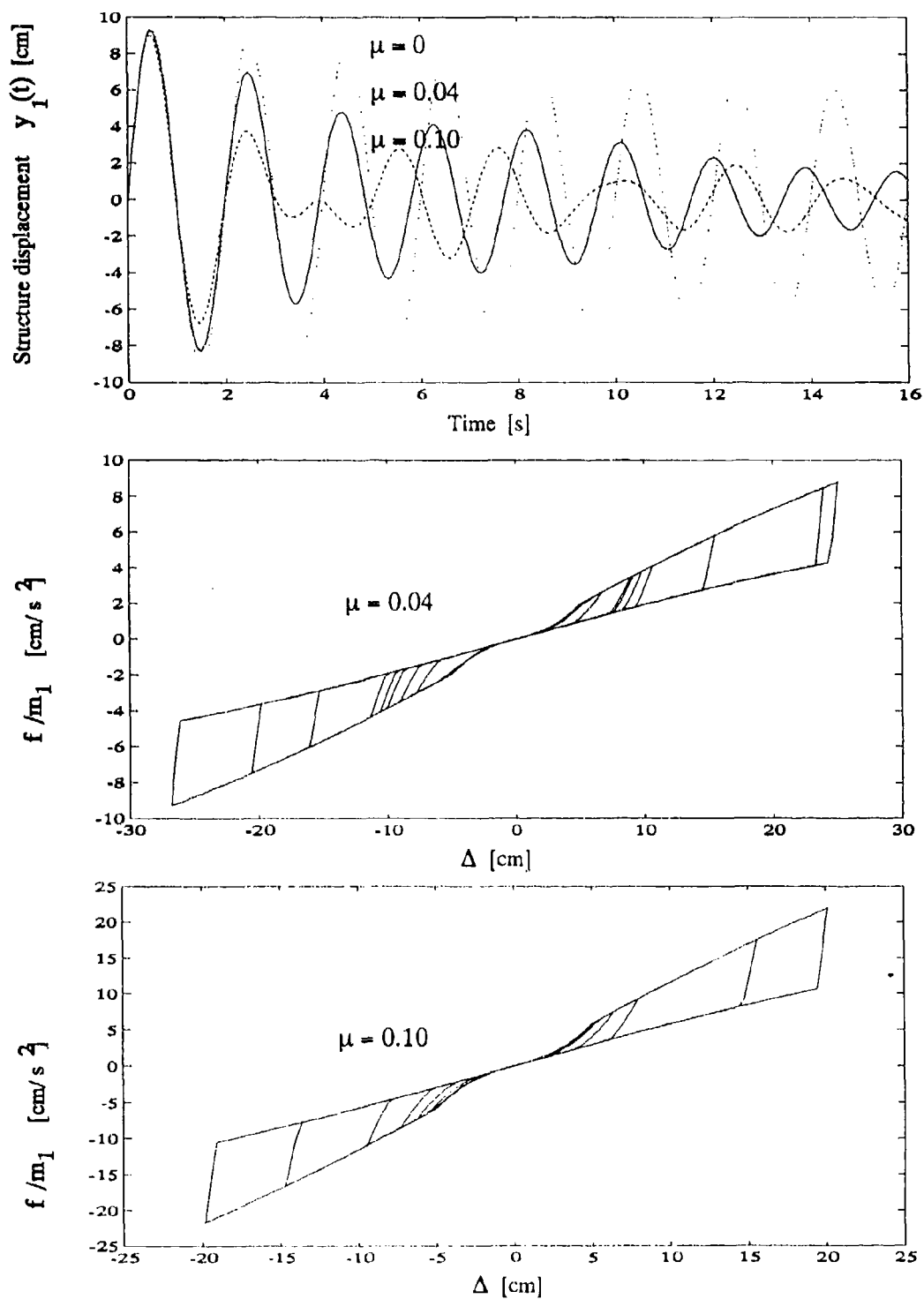


Figure 3. Structure displacement and hysteresis loops in free-vibration analyses.

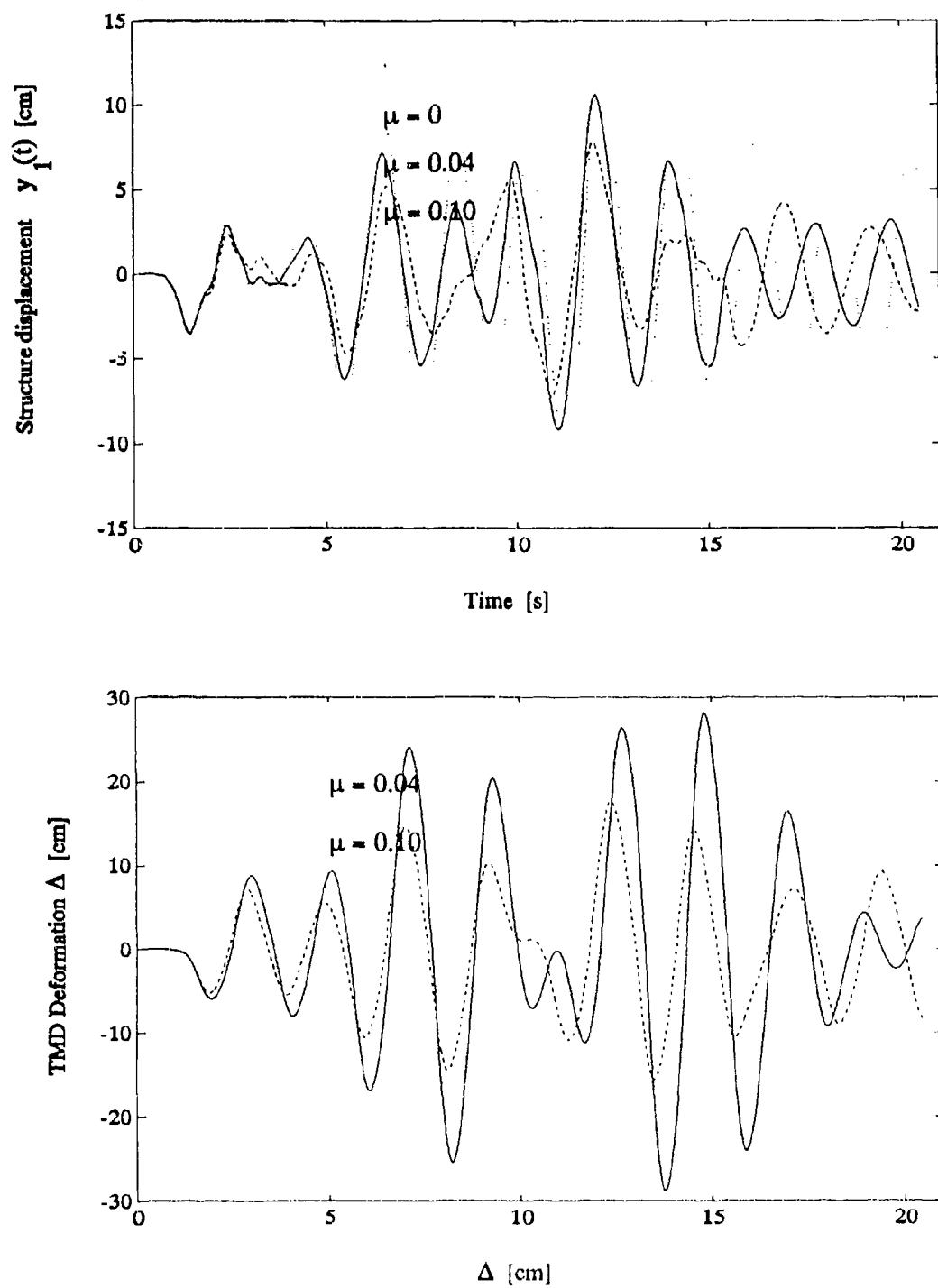


Figure 4. Structure displacement and TMD deformation under support excitation.

Owing to the prestress,  $\sigma_0 = \sigma_2$ , the force-deformation hysteresis loops  $f(\Delta, \dot{\Delta}, z)$  show a clearly defined equivalent stiffness  $K_e = (T_1 + T_2)/L$  which could be used as a tuning parameter. The energy dissipation capacity increases approximately with the square of the deformation amplitude since the hysteresis loop has approximately a triangular shape. A parameter,  $\omega_e$ , with units of frequency can be defined in this case by using the approximate tangent stiffness of the loading path of the TMD under tension,  $2T_1/L$ :

$$\omega_e = \sqrt{\frac{2T_1}{L\mu m_1}} = \sqrt{\frac{2g\eta_1}{L\mu}} \quad (12)$$

For the TMDs analyzed (defined by Eqs. (6)-(8)),  $\omega_e$  takes the following values:  $\omega_e = 3.13 \text{ rad/s}$  for  $\mu = 0.04$ , and  $\omega_e = 3.43 \text{ rad/s}$  for  $\mu = 0.10$ . These values of  $\omega_e$  are close to the natural frequency of the main structure ( $\omega = \pi \text{ rad/s}$ ), and this explains the significant interaction between the mass damper and the main structure.

## Experimental work

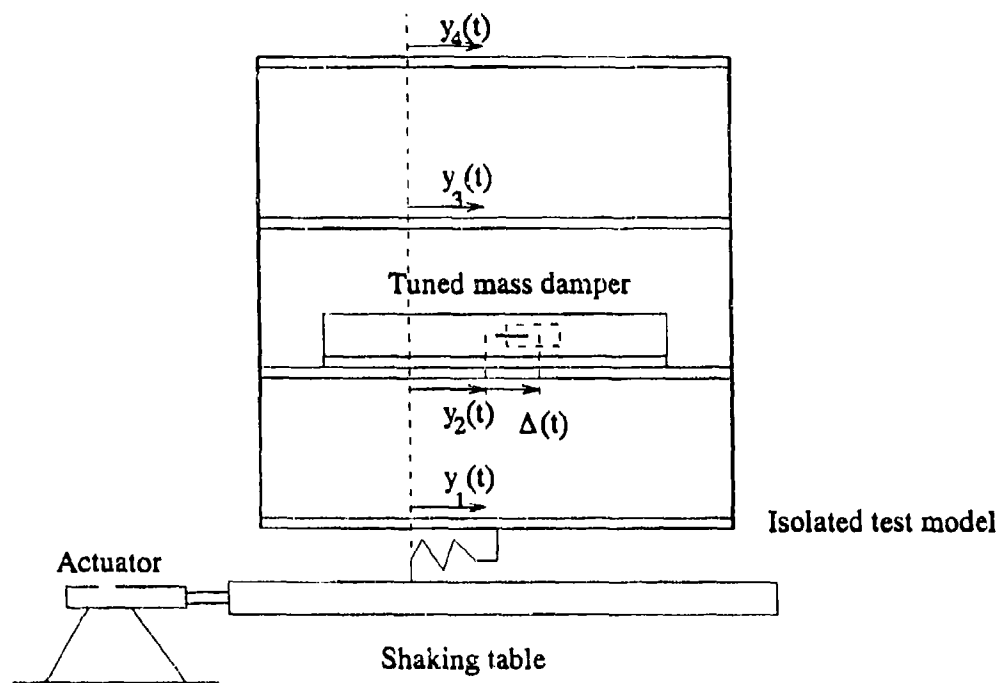
This section summarizes the main results of the experimental testing of a TMD with prestressed SMA wires for vibration reduction of structures subjected to ground excitation developed at the Earthquake Engineering Research Center of the University of California at Berkeley. A steel frame isolated with linear springs was the model used for the experiments. The TMD with prestressed SMA wires was installed on the test frame and the model was subjected to unidirectional support excitation using a shake table. More than forty tests were run using six different TMD configurations, and the performance of the main structural system with and without the TMD was evaluated. Significant improvement was obtained in the dynamic response of the structure when the prestress tension was set to tune the apparent frequency of the TMD to the first natural frequency of the isolated structure.

## Description of apparatus

### Frame

A four-story steel model was used for the experiments. The model was located on a shaking table which can produce unidirectional motion. The model was base isolated with linear springs in a single horizontal direction. An schematic of the test model, a moment-resisting frame, is shown in Fig. 5. The frame is three feet by four feet in plan and six feet high with story heights of two feet. Approximately one thousand pounds of lead weight were added to each floor.

The structural stiffness of the system was initially estimated from data obtained in a flexibility test of the model on fixed base (without base isolation). Selecting the horizontal displacement of each story of the test frame as the degrees of freedom, the condensed stiffness matrix which is shown in Appendix I, was computed by simple inversion of the flexibility obtained. Since the stiffness of the base isolators was known, the stiffness matrix for the complete model was obtained by expanding the fixed-base stiffness matrix. The



Plan view of the mass damper

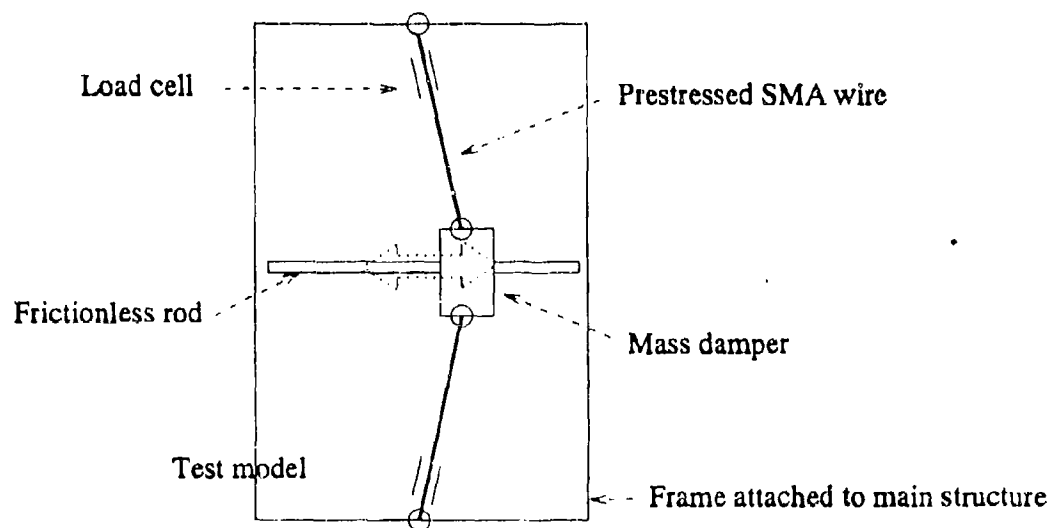


Figure 5. Schematic of the experimental setup.

computed stiffness matrix of the model is shown in Appendix I. The lumped mass model was adopted for the system and the diagonal mass matrix was estimated from weight tests. The mass matrix is shown in Appendix I. Frequencies and mode shapes were estimated by solving the eigenvalue problem and improved by means of a series of free vibration and impact tests on the model. The estimated structural properties of the model are shown in Appendix I.

#### *Tuned mass damper*

A mass damping device comprised of a mass sliding on a frictionless bearing oriented along the longitudinal horizontal axis was installed on the second floor of the frame. Wire loops, fabricated from a nickel-titanium shape-memory alloy and mounted transversely to the axis of the sliding mass, provided both damping and restoring forces for this mass damper system. The end connections of the wire loops – to the frame and to the sliding mass – were pinned, providing a tensile suspension with no bending or compressive capacity (Fig. 5). For the experiments the weight of the sliding mass, consisting of a set of lead plates, was fixed at approximately 4% (175 lb) of the weight of the frame in which it was embedded. The length of the wire loops was  $L = 25$  in.

#### **Instrumentation, data acquisition and control system**

Accelerometers and displacement transducers were attached to each floor of the test model and to the mass damper for data acquisition. Load cells were used to measure the tension of the shape-memory alloy cables. The transducers were powered by signal conditioners that provided the excitation voltage for the transducers, amplified the transducer output, and low-pass filtered the analog output. The cut-off frequency of the low-pass filter was 100 Hz for all channels. A software package (ATS-Automatic Testing System, 1992) was used for data acquisition and control of the servovalve which governed the actuator of the shake table.

#### **Input ground motions**

Since the aim of this research was to study the benefits of the TMD, passive isolation tests of the model without the TMD were initially carried out to allow comparison of the performances for both cases. Six artificially generated signals were used for this study. The simulated support motions were obtained by filtering a white-noise by second order filters of frequencies  $\omega_f = \pi, 2\pi, 3\pi, 4\pi, 5\pi, 6\pi$  rad/s and damping ratio  $\xi_f = 0.60$ . The signals lasted 20 sec and were scaled so that the maximum support displacement was 0.60 in. The command support displacement signals are shown in Fig. 6.

#### **Tests of the base-isolated structure without a TMD**

A series of 6 tests were done on the base isolated model without TMD. Table 4 summarizes the main results of each test in terms of maximum deformation in the isolation system of the main structural system. The analysis of the recorded data showed the expected result: the response of the model is dominated by the first mode of vibration of the model.

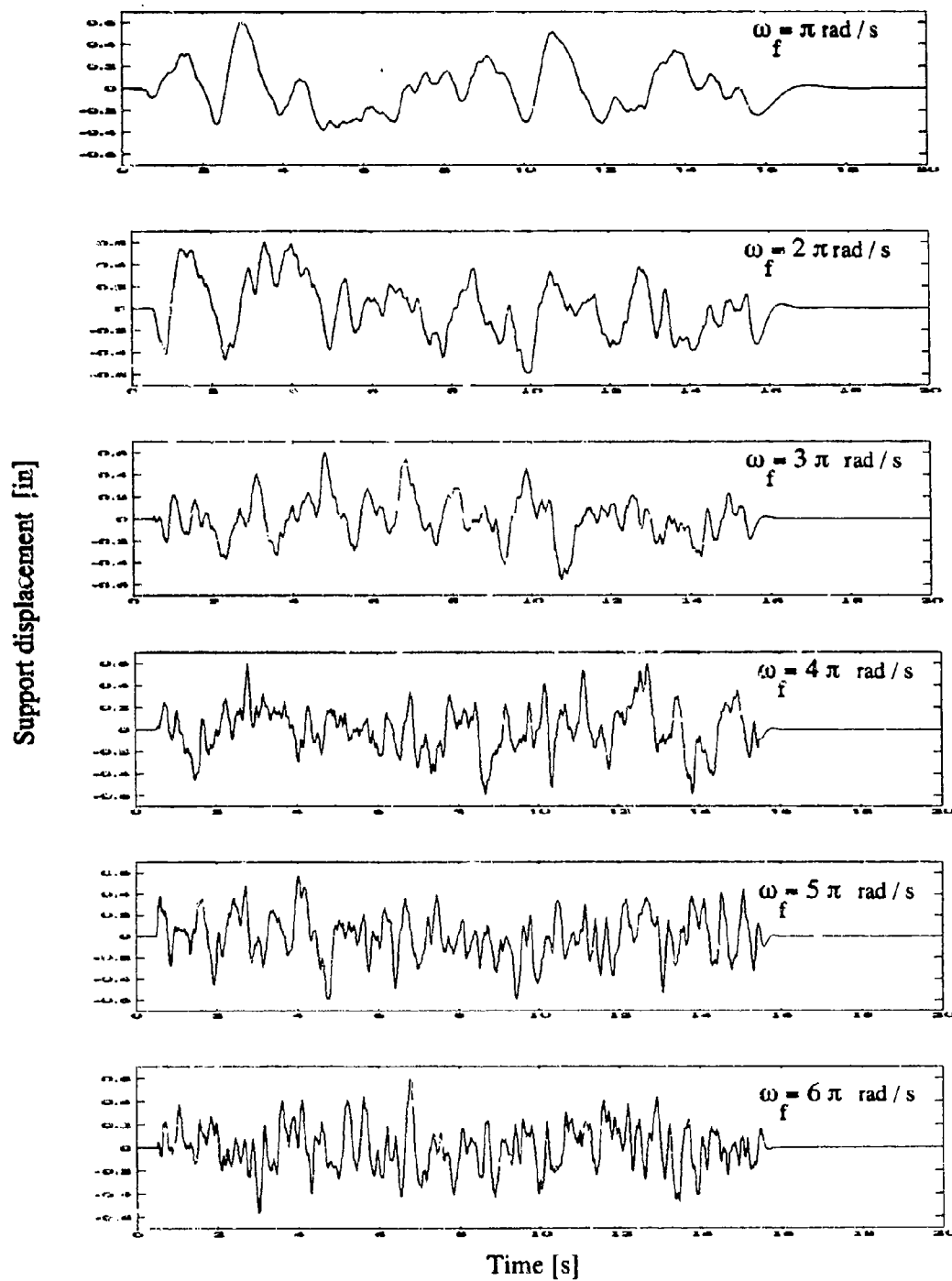


Figure 6. Support displacement command signals used for the experiments.

## Configurations of the TMD

Three configurations of the TMD were tested. The mass of the TMD was kept constant in all the experiments but the number of SMA wires and the prestress tension were changed in each configuration. Table 3 describes the main features of each configuration.

Table 3. Configurations of the TMD used in the test program

Config.	No. of wires	$T_o = A \sigma_o$ [lb]	$T_1 = A \sigma_1$ [lb]	$m_2 g$ [lb]	$\omega_e$ [rad/s]
I	1 loop	72	75	175	3.64
II	2 loops	117	150	175	4.64
III	2 loops	70	150	175	3.60

In configuration I  $\omega_e$  was close to the first natural frequency of the base-isolated model,  $\omega_1 = 3.77 \text{ rad/s}$ , and the energy dissipation capability was maximized since the prestress,  $\sigma_o$ , was very close to the yielding stress,  $\sigma_1$ . Configuration II showed no tuning for small deformations since  $\omega_e \gg \omega$  and the energy dissipating capability was significant since the prestress was close to the yielding tension of the wires. Configuration III showed good tuning but significant deformation had to be developed in the TMD system for energy dissipation to take place since the prestress was significantly lower than the yielding tension of the SMA wires.

Tables 4 and 5 summarize maximum values of deformation in the main structural system and maximum values of deformation in the TMD recorded during the tests for all configurations. In the second column of each table the results obtained without the TMD are shown for comparison.

Table 4. Tests results: Maximum deformation in the isolation system.

Signal filter freq. [rad/s]	No TMD $\max( y_1(t) )$ [in]	Config. I $\max( y_1(t) )$ [in]	Config. II $\max( y_1(t) )$ [in]	Config. III $\max( y_1(t) )$ [in]
$\pi$	1.69	1.21	1.16	1.44
$2\pi$	1.48	1.25	1.28	1.37
$3\pi$	1.37	0.99	1.33	1.44
$4\pi$	1.03	0.91	0.90	0.91
$5\pi$	1.18	0.89	0.80	0.88
$6\pi$	1.05	0.91	0.88	0.93



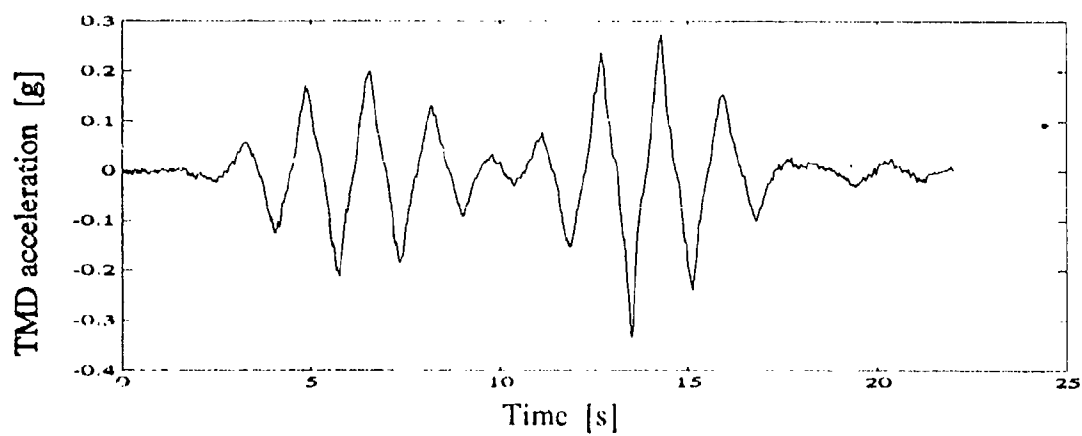
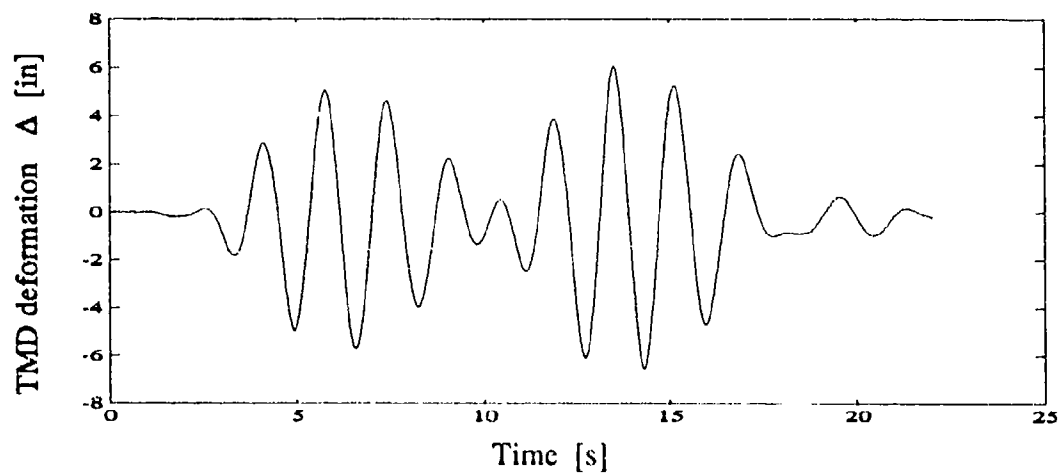
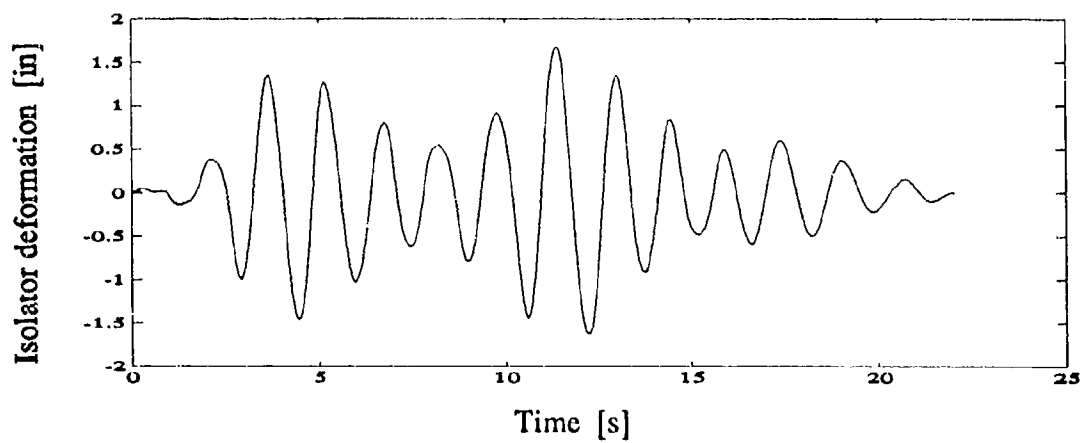


Figure 7. Responses obtained in the experiments (1 loop,  $T_O = 70$  lb, Signal  $\pi$  rad/s).

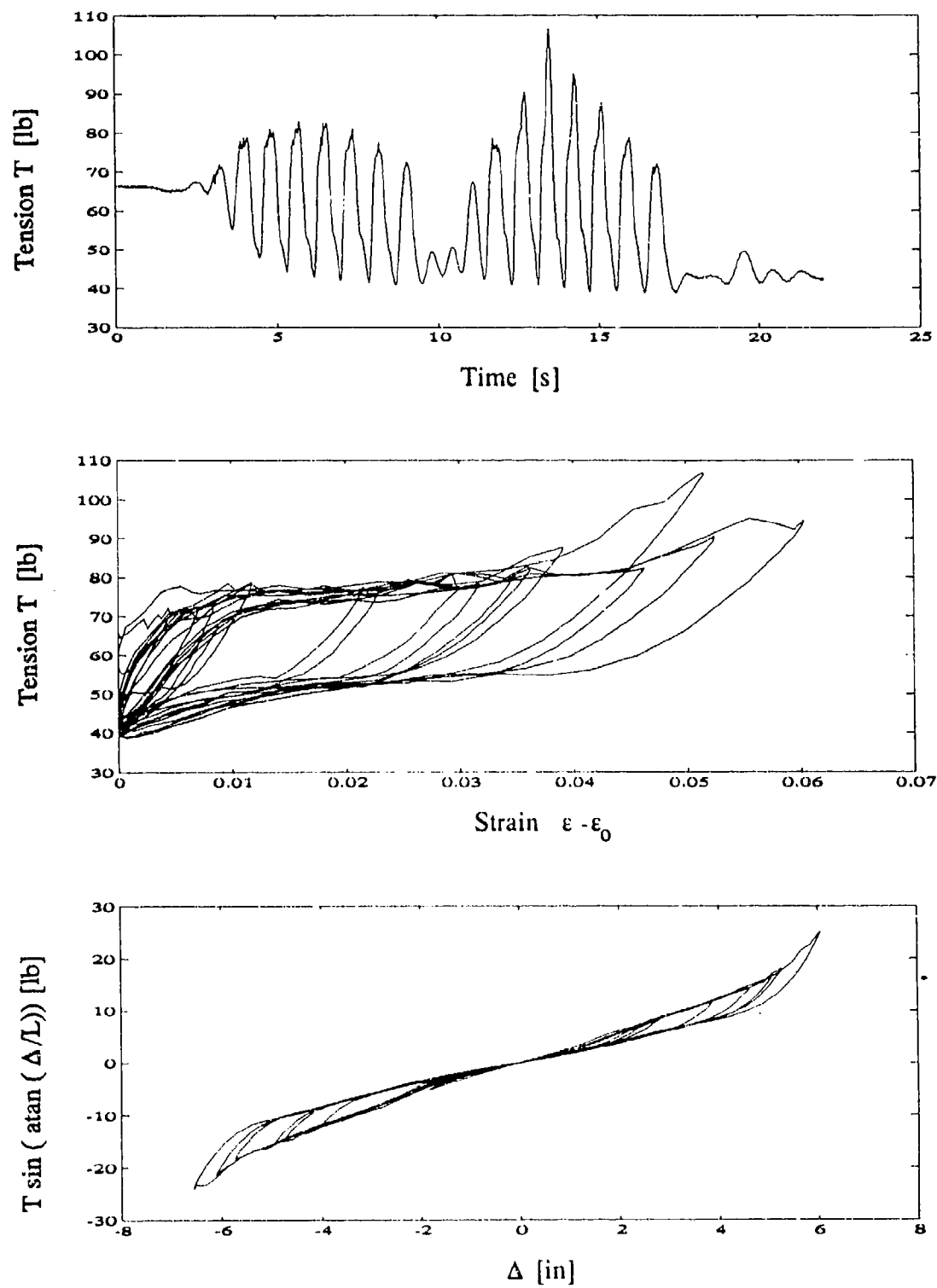


Figure 8. Tension of the rod and TMD force hysteresis loops ( $T_0 = 70$  lb, Signal  $\pi$  rad/s).

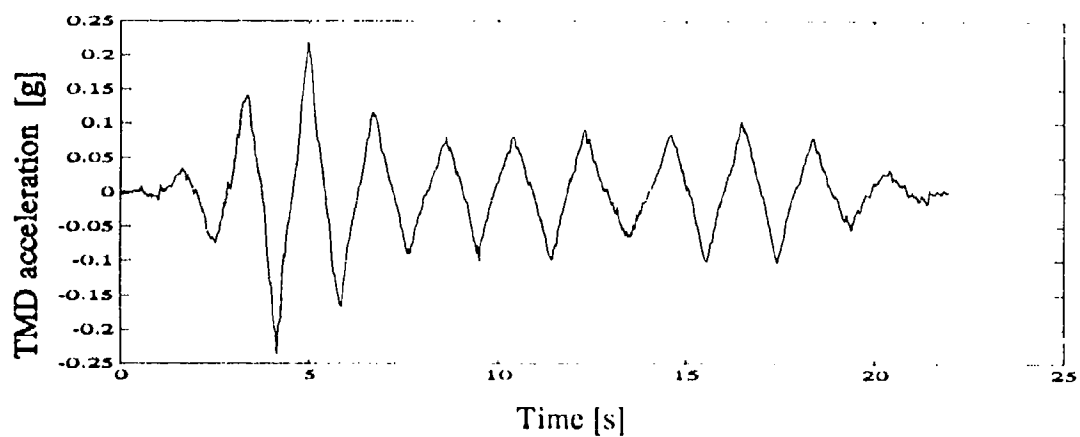
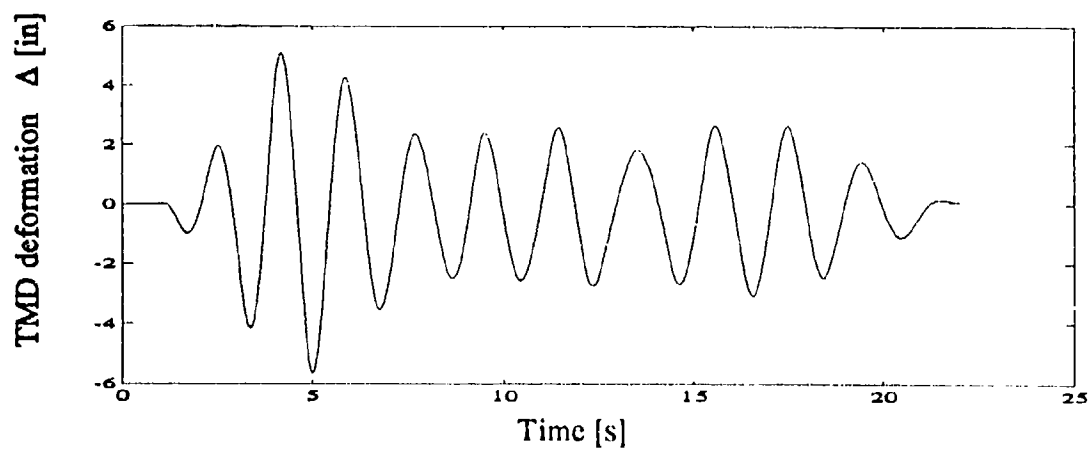
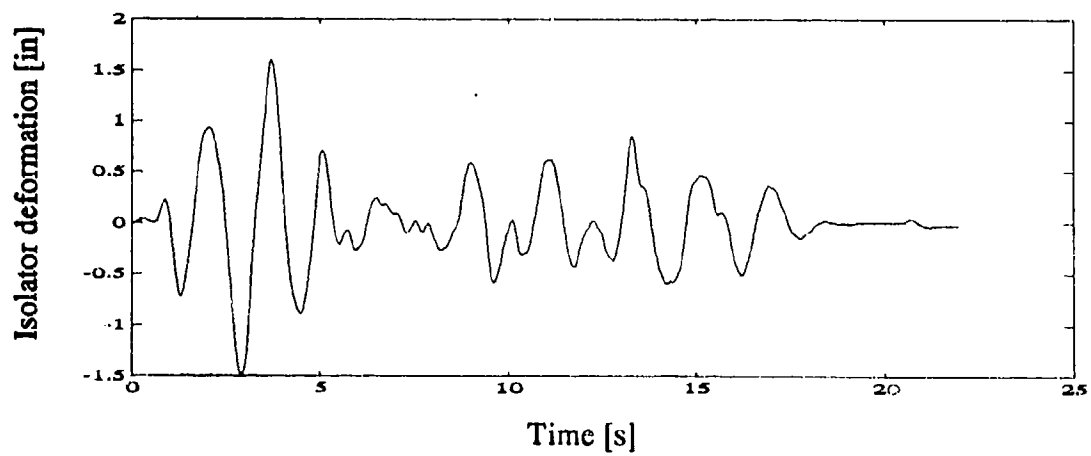


Figure 9. Responses obtained in the experiments ( 1 loop,  $T_0 = 70$  lb, Signal  $2\pi$  rad/s).

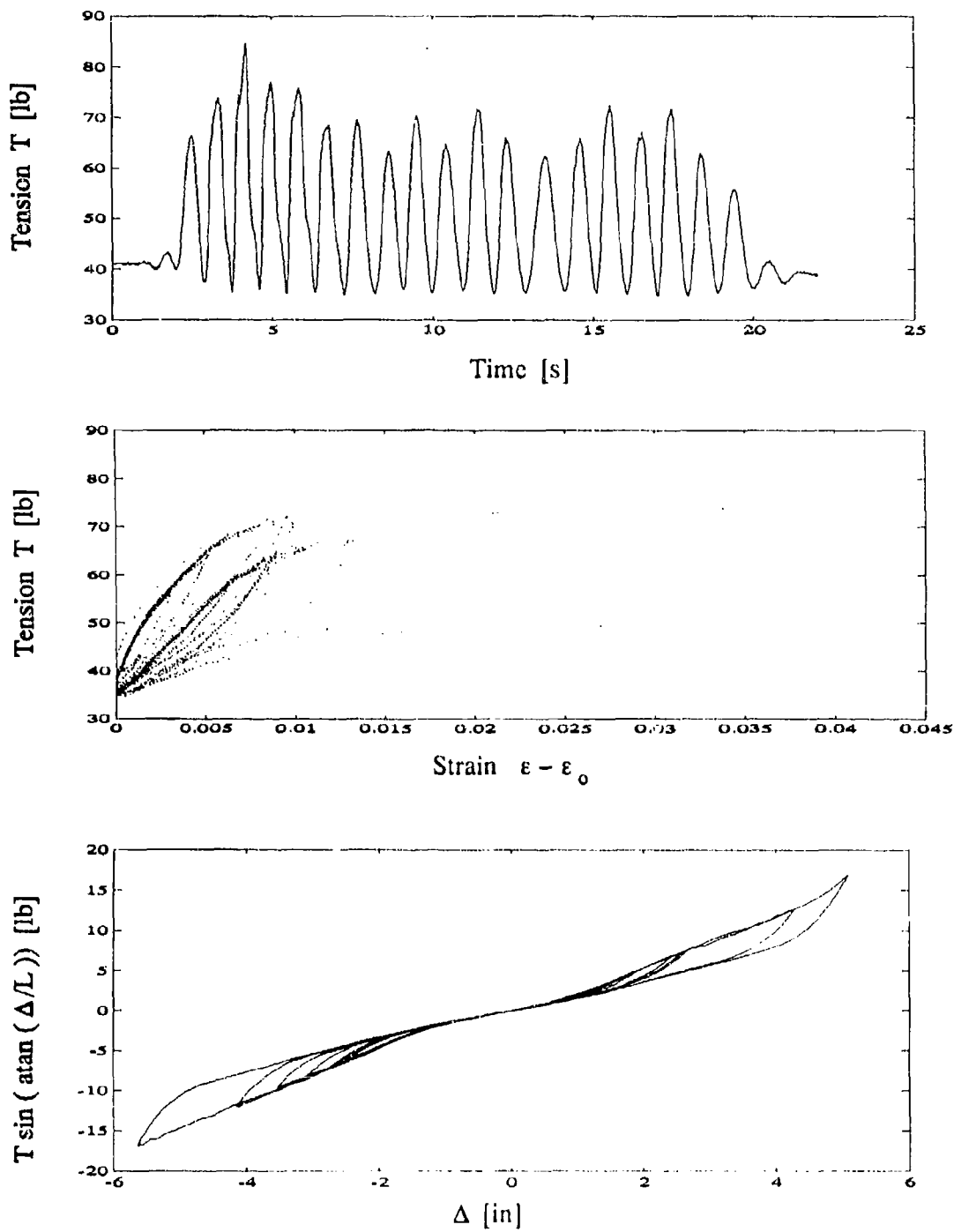


Figure 10. Tension of the rod and TMD force hysteresis loops ( $T = 70$  lb, Signal  $2\pi$  rad/s).

Table 5. Tests results: Maximum deformation in the TMD.

Signal filter freq. [rad/s]	Config. I $\max( \Delta(t) )$ [in]	Config. II $\max( \Delta(t) )$ [in]	Config. III $\max( \Delta(t) )$ [in]
$\pi$	4.18	2.68	1.95
$2\pi$	4.22	2.50	1.89
$3\pi$	3.78	2.38	2.04
$4\pi$	2.22	1.84	1.45
$5\pi$	2.05	1.89	1.60
$6\pi$	1.75	1.59	0.77

Figures 7 through 10 show typical force histories, deformation histories, accelerations histories, and hysteresis loops obtained in the experiments.

### Conclusions and directions for further research

The results given in Table 4 indicate that all the TMD schemes improved the dynamic performance of the system with regard to maximum deformations in the main structural system. A simple comparison of the performances of the different TMD configurations shows the improvement in dynamic response that this TMD scheme can provide in lightly damped flexible structures. Furthermore, the tuning and energy dissipating capability could be optimized to provide maximum reduction for a particular intensity and frequency content of the excitation. Optimization of the TMD parameters in this absorber scheme is an analytical study that would be interesting to pursue. This study could be done using a statistical representation of the excitation and by minimizing the mean square response of the main structure as a function of the parameters of the TMD. The statistical linearization technique can be used to estimate the mean square response of the structure with attached nonlinear TMD.

### References

- Aiken, I.D., Nims, D.K., and Kelly, J.M., 1992, "Comparative Study of Four Passive Energy Dissipation Systems", *Bull. N.Z. Nat. Soc. for Earthquake Eng.*, Vol. 25, No. 3, September.
- ATS-Automatic Testing System, 1990, Users Manual, *Digital Control Systems, Berkeley, California*.
- Inaudi, J.A., and Kelly, J.M., 1992, "A friction mass damper for vibration control", *Report No. UCB/EERC-92/15, Earthquake Engineering Research Center, University of California at Berkeley*.

Duerig, T.W., Melton, K.N., Stockel, D., and Wayman, C.M., 1990, "Engineering Aspects of Shape Memory Alloys", *Butterworth-Heinemann Publishers*, London.

Krumme, R.C., 1985, personal communication to Professor J.M. Kelly.

Nashif A.D., Jones D.I. and Henderson J.P., 1985, "Vibration Damping", *John Wiley & Sons*, New York.

Witting, P.R., and Cozzarelli, F.A., 1992, "Shape Memory Structural Dampers: Material Properties, Design and Seismic Testing", *Technical Report NCEER-92-0013, National Center for Earthquake Engineering Research*, State University of New York at Buffalo.

## Appendix I

### Estimated mechanical characteristics of the test frame

Mass matrix (lumped-mass model)

$$\mathbf{M} = \text{diag}( 3.263, 3.428, 3.474, 3.368 ) \text{ lb sec}^2 / \text{in}$$

Frequencies and mode shapes

Mode I (0.6 Hz)	Mode II (3.9 Hz)	Mode III (11.9 Hz)	Mode IV (24.0 Hz)
1.0	1.0	1.0	1.0
1.031	0.483	-0.789	-2.175
1.063	-0.304	-1.064	2.045
1.085	-1.074	0.9545	-0.7436

Solving for the stiffness matrix  $\mathbf{K}$  from mode shapes and frequencies

$$\mathbf{K} = \begin{bmatrix} 13289 & -20378 & 8370 & -1042 \\ -20378 & 42122 & -29070 & 7286 \\ 8370 & -29070 & 35266 & -14601 \\ -1042 & 7286 & -14601 & 8394 \end{bmatrix} \text{ lb / in}$$

Modal damping ratios from logarithmic decrement

$$\xi_1 = 0.02 \quad \xi_2 = 0.005 \quad \xi_3 = 0.004 \quad \xi_4 = 0.004$$

Solving for the damping matrix, we obtain

$$\mathbf{C} = \begin{bmatrix} 1.296 & -0.966 & 0.219 & 0.0029 \\ -0.966 & 2.431 & -1.218 & 0.163 \\ 0.219 & -1.218 & 2.529 & -0.921 \\ 0.0029 & 0.163 & -0.921 & 1.233 \end{bmatrix} \text{ lb s/in}$$

# HIGH DAMPING OF ANTIQUE WALLS

by Dr.-Ing. Juval Mantel,  
TEIC-TECHNION ENTREPRENEURIAL INCUBATOR CO. LTD.,  
Park Gutwirth, Technion City, Haifa 32000, Israel

## PREFACE

Several years ago there was a plan to make an opening of the wall of Old Jerusalem or to build a tunnel underneath the wall. To start with, the vibration of the wall had to be measured when certain impulse arousals (impact) took place.

The findings were surprising and lead to knowing the "building rules" of the walls, which are to be published elsewhere.

## 1. THE RESULTS

The vibration analysis was carried out by the impact of heavy (30 ton) trucks, moving slowly against the wall. The data recordings had been analysed at the laboratories of Dr. Mantel & Partners in Munich/Germany. Thus the resonance frequencies, damping and vibration magnitudes at the whole spectrum, in three axis, could be found.

- a) We found resonances between 6 and 24 Hz. These are not due to bending, but due to complex torsional vibration (with stiffing effect in ground and towers). Higher frequencies than 20 Hz are caused by pendulum modes or console vibration, and vertical vibration due to soft suspension.
- b) In extreme low frequencies the damping factor of the material of the walls shows surprising high damping factors. These values fall at high frequencies.

From the standpoint of security, this is most interesting, since the higher damping factors are at the strong self resonances, of the structure, and thus withstand horizontal impacts.

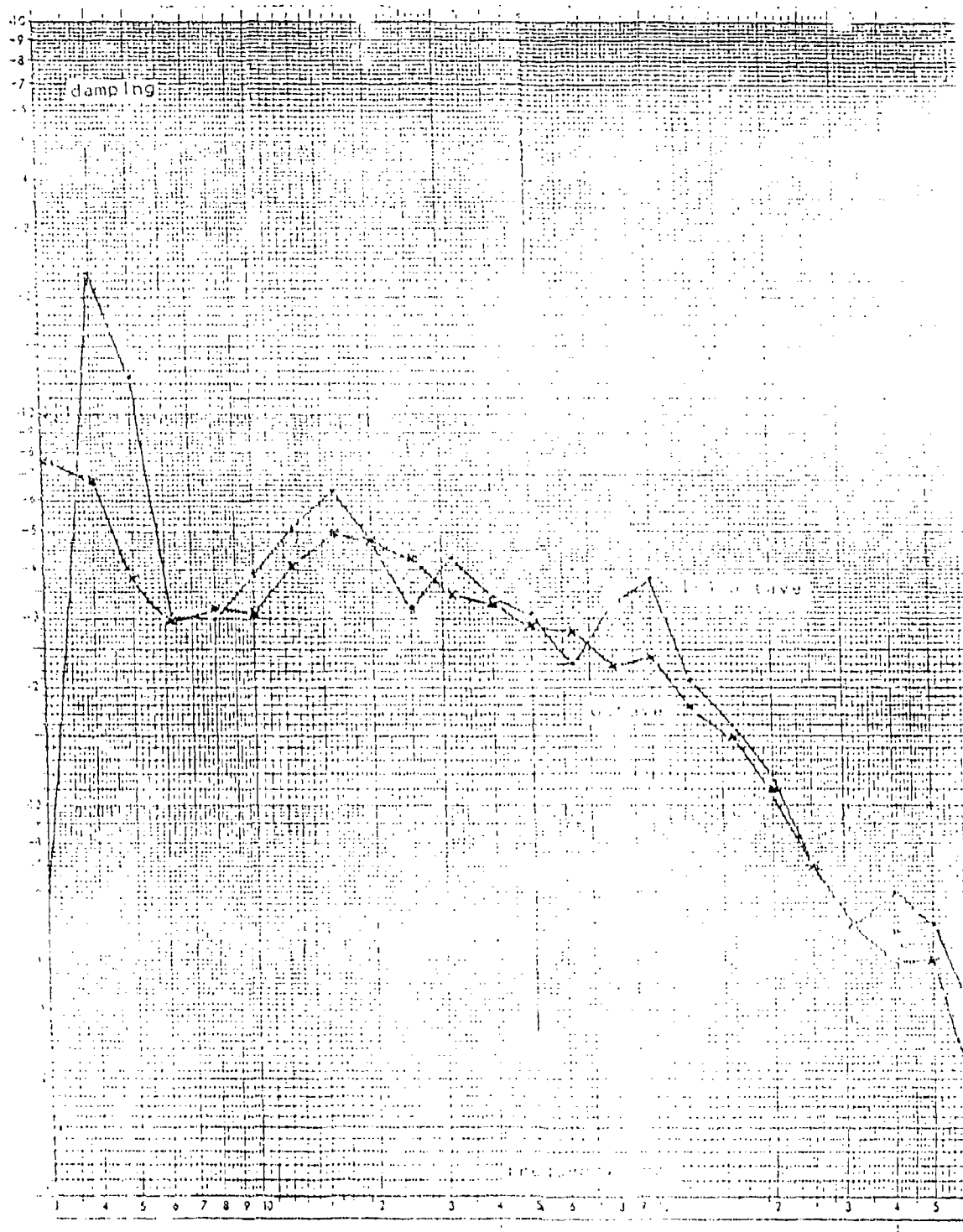
- c) The horizontal impact at the wall gave rise to a backward propagating wave, after 0.4 s, of 100 Hz and above. We assume that the reflection is due to connection of the wall to towers and gates in a distance of about 100 m. This leads to a propagation velocity of 500 m/s, which is not of a pressure wave but of a bending or probably of a torsional wave along the wall.

## 2. THE DAMPING FACTOR

The damping factor is shown in Fig. 1 in 1/3 octave and 1/1 octave bands, which were calculated from the reverberation times of body-borne sound in the wall.



Figure 1  
Damping Factor of a Vibrating Wall  
measured at the wall of Old Jerusalem/Israel

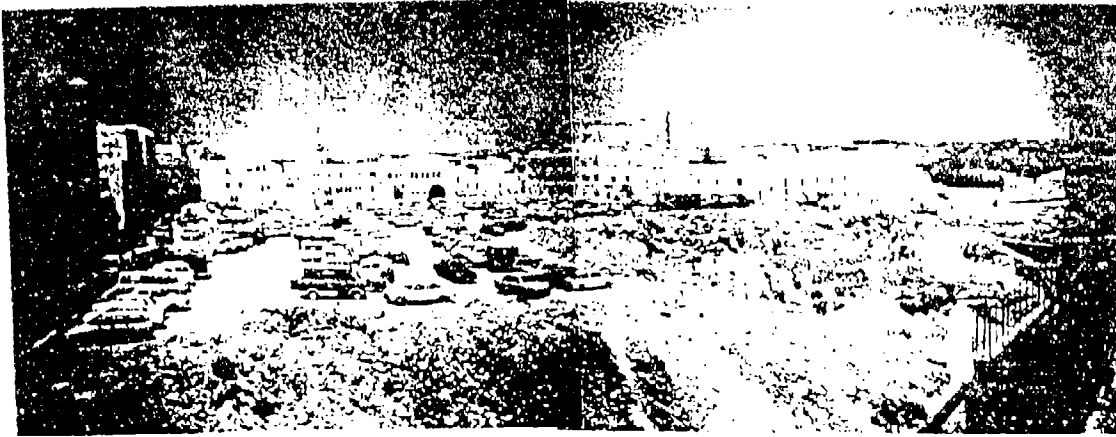


From the limited literature on damping factors of building materials at middle frequencies, we expect values of 0.01-0.10, mainly 0.03-0.05. Thus the value of 0.230 at an extreme low frequency is surprising. The explanation for the phenomena can be in the large spectrum of sizes of stones used in the wall as well as with the use of appropriate markers.

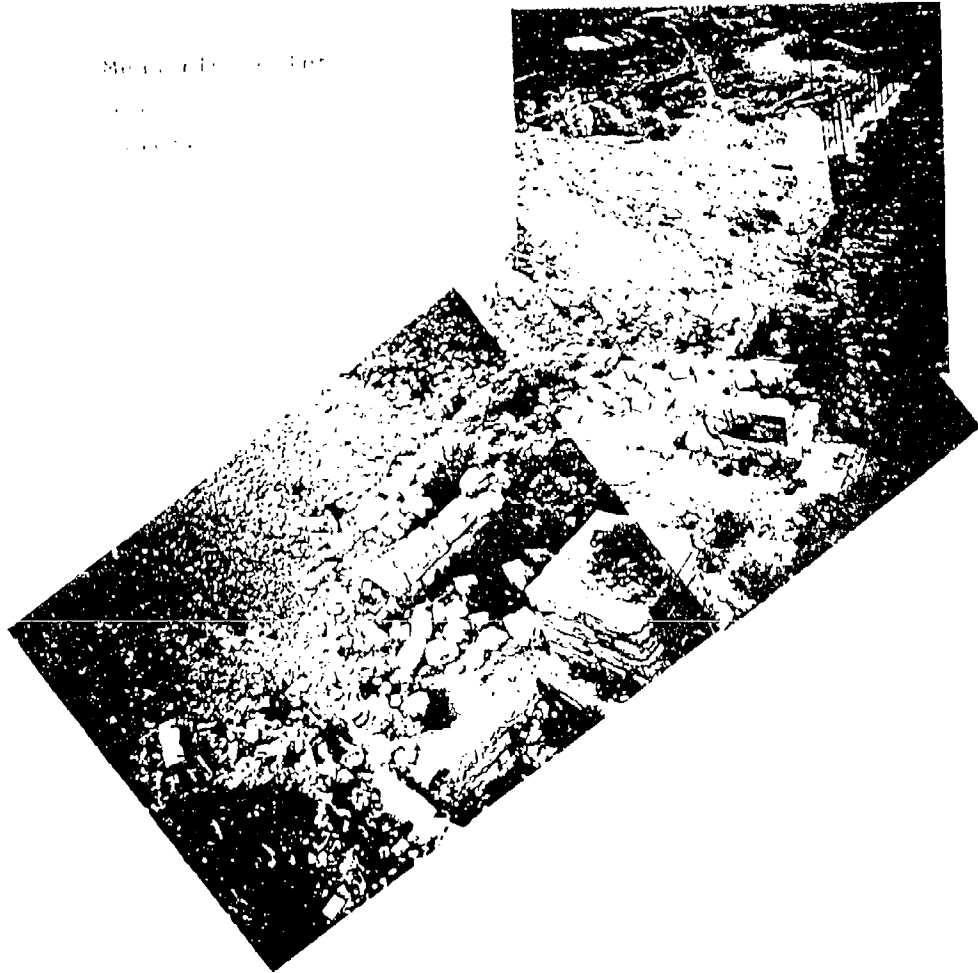
### 3. LITERATURE

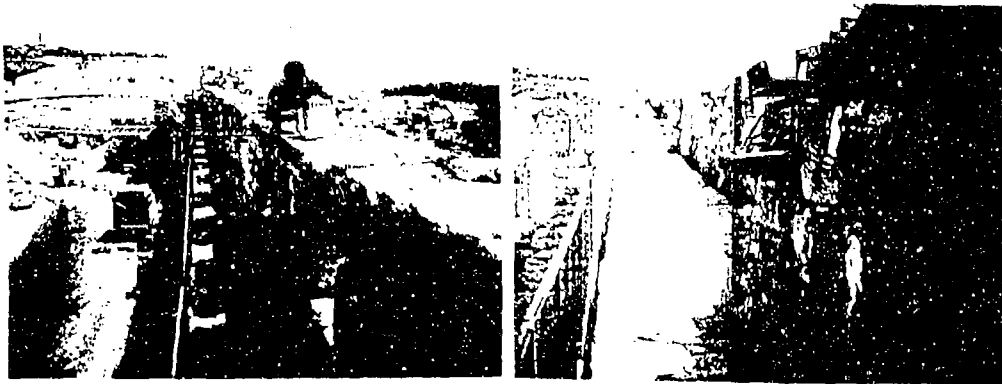
Acoustic Ltd. 10, 11, 12, 13, 14, 15, 16, 17, 18, 19, 20, 21, 22, 23, 24, 25, 26, 27, 28, 29, 30, 31, 32, 33, 34, 35, 36, 37, 38, 39, 40, 41, 42, 43, 44, 45, 46, 47, 48, 49, 50, 51, 52, 53, 54, 55, 56, 57, 58, 59, 60, 61, 62, 63, 64, 65, 66, 67, 68, 69, 70, 71, 72, 73, 74, 75, 76, 77, 78, 79, 80, 81, 82, 83, 84, 85, 86, 87, 88, 89, 90, 91, 92, 93, 94, 95, 96, 97, 98, 99, 100, 101, 102, 103, 104, 105, 106, 107, 108, 109, 110, 111, 112, 113, 114, 115, 116, 117, 118, 119, 120, 121, 122, 123, 124, 125, 126, 127, 128, 129, 130, 131, 132, 133, 134, 135, 136, 137, 138, 139, 140, 141, 142, 143, 144, 145, 146, 147, 148, 149, 150, 151, 152, 153, 154, 155, 156, 157, 158, 159, 160, 161, 162, 163, 164, 165, 166, 167, 168, 169, 170, 171, 172, 173, 174, 175, 176, 177, 178, 179, 180, 181, 182, 183, 184, 185, 186, 187, 188, 189, 190, 191, 192, 193, 194, 195, 196, 197, 198, 199, 200, 201, 202, 203, 204, 205, 206, 207, 208, 209, 210, 211, 212, 213, 214, 215, 216, 217, 218, 219, 220, 221, 222, 223, 224, 225, 226, 227, 228, 229, 230, 231, 232, 233, 234, 235, 236, 237, 238, 239, 240, 241, 242, 243, 244, 245, 246, 247, 248, 249, 250, 251, 252, 253, 254, 255, 256, 257, 258, 259, 260, 261, 262, 263, 264, 265, 266, 267, 268, 269, 270, 271, 272, 273, 274, 275, 276, 277, 278, 279, 280, 281, 282, 283, 284, 285, 286, 287, 288, 289, 290, 291, 292, 293, 294, 295, 296, 297, 298, 299, 300, 301, 302, 303, 304, 305, 306, 307, 308, 309, 310, 311, 312, 313, 314, 315, 316, 317, 318, 319, 320, 321, 322, 323, 324, 325, 326, 327, 328, 329, 330, 331, 332, 333, 334, 335, 336, 337, 338, 339, 340, 341, 342, 343, 344, 345, 346, 347, 348, 349, 350, 351, 352, 353, 354, 355, 356, 357, 358, 359, 360, 361, 362, 363, 364, 365, 366, 367, 368, 369, 370, 371, 372, 373, 374, 375, 376, 377, 378, 379, 380, 381, 382, 383, 384, 385, 386, 387, 388, 389, 390, 391, 392, 393, 394, 395, 396, 397, 398, 399, 400, 401, 402, 403, 404, 405, 406, 407, 408, 409, 410, 411, 412, 413, 414, 415, 416, 417, 418, 419, 420, 421, 422, 423, 424, 425, 426, 427, 428, 429, 430, 431, 432, 433, 434, 435, 436, 437, 438, 439, 440, 441, 442, 443, 444, 445, 446, 447, 448, 449, 450, 451, 452, 453, 454, 455, 456, 457, 458, 459, 460, 461, 462, 463, 464, 465, 466, 467, 468, 469, 470, 471, 472, 473, 474, 475, 476, 477, 478, 479, 480, 481, 482, 483, 484, 485, 486, 487, 488, 489, 490, 491, 492, 493, 494, 495, 496, 497, 498, 499, 500, 501, 502, 503, 504, 505, 506, 507, 508, 509, 510, 511, 512, 513, 514, 515, 516, 517, 518, 519, 520, 521, 522, 523, 524, 525, 526, 527, 528, 529, 530, 531, 532, 533, 534, 535, 536, 537, 538, 539, 540, 541, 542, 543, 544, 545, 546, 547, 548, 549, 550, 551, 552, 553, 554, 555, 556, 557, 558, 559, 560, 561, 562, 563, 564, 565, 566, 567, 568, 569, 570, 571, 572, 573, 574, 575, 576, 577, 578, 579, 580, 581, 582, 583, 584, 585, 586, 587, 588, 589, 590, 591, 592, 593, 594, 595, 596, 597, 598, 599, 600, 601, 602, 603, 604, 605, 606, 607, 608, 609, 610, 611, 612, 613, 614, 615, 616, 617, 618, 619, 620, 621, 622, 623, 624, 625, 626, 627, 628, 629, 630, 631, 632, 633, 634, 635, 636, 637, 638, 639, 640, 641, 642, 643, 644, 645, 646, 647, 648, 649, 650, 651, 652, 653, 654, 655, 656, 657, 658, 659, 660, 661, 662, 663, 664, 665, 666, 667, 668, 669, 670, 671, 672, 673, 674, 675, 676, 677, 678, 679, 680, 681, 682, 683, 684, 685, 686, 687, 688, 689, 690, 691, 692, 693, 694, 695, 696, 697, 698, 699, 700, 701, 702, 703, 704, 705, 706, 707, 708, 709, 710, 711, 712, 713, 714, 715, 716, 717, 718, 719, 720, 721, 722, 723, 724, 725, 726, 727, 728, 729, 730, 731, 732, 733, 734, 735, 736, 737, 738, 739, 740, 741, 742, 743, 744, 745, 746, 747, 748, 749, 750, 751, 752, 753, 754, 755, 756, 757, 758, 759, 760, 761, 762, 763, 764, 765, 766, 767, 768, 769, 770, 771, 772, 773, 774, 775, 776, 777, 778, 779, 780, 781, 782, 783, 784, 785, 786, 787, 788, 789, 790, 791, 792, 793, 794, 795, 796, 797, 798, 799, 800, 801, 802, 803, 804, 805, 806, 807, 808, 809, 810, 811, 812, 813, 814, 815, 816, 817, 818, 819, 820, 821, 822, 823, 824, 825, 826, 827, 828, 829, 830, 831, 832, 833, 834, 835, 836, 837, 838, 839, 840, 841, 842, 843, 844, 845,

23



More of the same



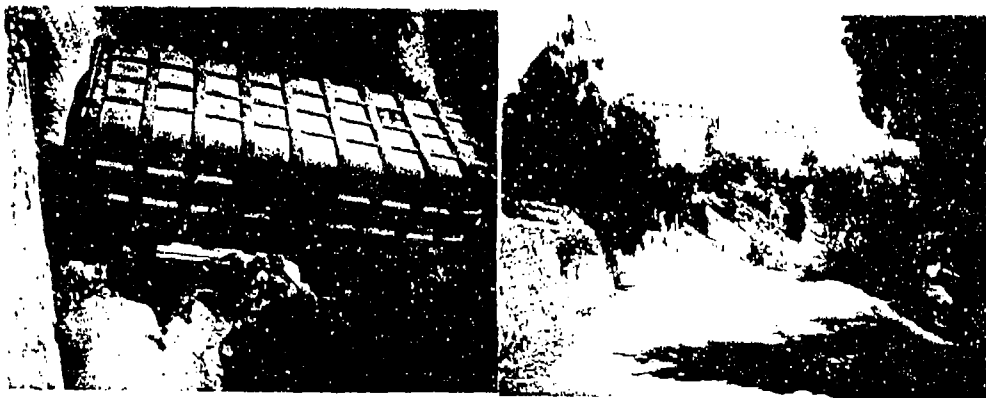


Measuring Place # 2

Measuring Place # 1

Lorry Touching the Wall

Light (Sulphur) Tower  
at the wall



## **Temperature Control in Viscoelastic Dampers for Buildings**

Warren C. Gibson  
Kevin L. Napolitano  
Bradley Allen

CSA Engineering, Inc.  
Palo Alto, CA

Roger E. Scholl

CounterQuake Corp.  
Redwood City, CA

*Damping 93*

San Francisco, CA  
February 25, 1993

## **Use of Viscoelastic Materials for Damping Motion in Buildings**

### **• Advantages**

- Effective for small to moderate motions (wind and small earthquakes)
- Passive - no power source needed
- Effective over moderately broad frequency ranges

### **• Disadvantage for severe earthquakes**

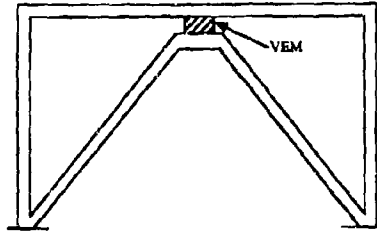
- Large blocks of material required to provide high damping forces
- Heat buildup in blocks may cause degradation of energy-dissipating characteristics

## **Use of Viscoelastic Materials for Damping Motion in Buildings**

Viscoelastic materials have been used successfully to reduce building deformations due to wind. Research has also indicated their suitability for counteracting small to moderate earthquake motions. Viscoelastic solutions are attractive in several ways. A completely passive solution is obviously desirable for earthquake dampers since power can't be relied on. Another advantage is that they work over moderately wide frequency ranges, unlike tuned devices.

The large motions and forces associated with severe earthquakes pose a serious problem. Large blocks of viscoelastic are needed to provide large forces. If the consequent heat isn't dissipated fast enough, the temperature may rise far enough that the material begins to lose stiffness and ceases to provide the required damping forces.

## Translating Earthquake Deformations into Shear in the Viscoelastic



- The chevron brace shown here converts "story drift" into shear deformations in the block of viscoelastic at the top.

## Translating Earthquake Deformations into Shear in the Viscoelastic

We need a mechanism to trigger large shear deformations in blocks of viscoelastic material when an earthquake occurs. The chevron brace shown here accomplishes that by concentrating the "story drift" at a block of material at the top of the brace. Viscoelastics can stand shear deformations of 50 to 100%.

## **Research Program**

- **Goals**
  - **Assess the heat buildup  
in a typical block of viscoelastic**
  - **Design ways to dissipate heat**
- **Approach**
  - **Thermoviscoelastic analysis procedure**
  - **Experimental program**

## **Research Program**

We undertook a research effort under NSF sponsorship. The goals were first to determine quantitatively whether heat buildup really is a problem as we suspected, and then to investigate various ways to dissipate heat.

We undertook both analytical and experimental investigations. The analysis was done using a thermoviscoelastic solution procedure which we developed. Tests were then performed on blocks of viscoelastic sized for application to medium-rise buildings.



### Characterization of Viscoelastic Materials

- Viscoelastics are typically characterized by their resistance to steady-state sinusoidal loads.
- The "storage modulus"  $G'$  indicates how much energy is stored.
- The "loss modulus"  $G''$  indicates how much energy is dissipated.
- Typically, the storage modulus is simply called the "modulus" and the "loss factor"  $\eta = G''/G'$  is used to indicate energy dissipation.

## Characterization of Viscoelastic Materials

Viscoelastic materials are typically represented by their resistance to steady-state sinusoidal loads. In the frequency domain, properties and responses are conveniently represented by complex numbers. The real part of the shear modulus is called the "storage modulus." This number indicates the degree to which energy is converted to recoverable strain energy. The "loss modulus" indicates the degree to which energy is stored is irrecoverable thermal energy.

For practical applications, the storage modulus is simply called the modulus and the ratio of the loss modulus to the storage modulus is called the "loss factor."

## Fully Coupled Analysis Problem

- Most viscoelastics soften markedly with rising temperature (shear modulus drops)
- Energy conversion capability also drops somewhat with temperature (loss factor)
- Temperature depends on energy input
- Energy input depends on shear modulus and loss factor

## Fully Coupled Analysis Problem

The modulus is highly sensitive to temperature and the loss factor is somewhat sensitive to temperature. Thus as the temperature builds up, a viscoelastic damper becomes less efficient. To determine the behavior of a damper, we need to solve the equations of motion and the thermodynamic equations simultaneously, updating the material properties "on the fly."

## Preliminary Study of the Thermodynamic Processes

- Material property changes ignored for this preliminary study
- Conversion of strain energy into stored thermal energy
  - Pure storage (conduction neglected)
  - Result for a typical block: one degree F per second
- Conduction of heat out of the viscoelastic
  - Steady state assumed (heat conducted out balances heat generation)
  - Result: nowhere near steady-state condition by the time the earthquake ends

## Preliminary Study of the Thermodynamic Processes

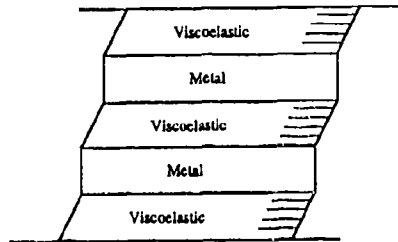
Before tackling the fully coupled problem, we decided to investigate two limiting cases, ignoring changes in material properties temporarily. In the first study, we did not allow any conduction out of the viscoelastic, but assumed all energy was contained as thermal energy. For a typical block of viscoelastic, we found a one degree F temperature rise per second. For a 90-second earthquake, this overly conservative analysis would indicate extreme temperatures.

We then looked at conduction and assumed a steady-state situation where the energy conducted out of the viscoelastic block into the adjoining steel took place at a rate that just balanced the generation of heat in the viscoelastic. We found that it took a half hour to reach steady state, much longer than the duration of any earthquake.

Conclusion: we cannot dissipate heat out of a large block of viscoelastic fast enough to do any good. We must penetrate the viscoelastic with metallic plates or rods to absorb heat locally.

## Solution Method

- Subdivide a block into a number of layers, each having uniform shear strain, temperature, and material properties



## Solution Method

We decided to represent a block of viscoelastic as a one-dimensional phenomenon with the block subdivided into a number of layers. In each layer, the shear strain, temperature, and material properties are assumed uniform. The equations of motion and the thermodynamic equations are then represented by tridiagonal matrix equations which are integrated forward in time.

### **Solution Method (cont.)**

- Assume steady-state sinusoidal imposed displacement
- Integrate equations forward in time, simultaneously.

At each time step, do the following:

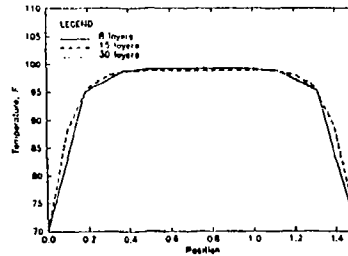
- Update shear strain using current material properties
- Compute current heat flux based on strain and strain rate
- Update temperature using current flux value
- Update material properties using current temperature

## **Solution Method (cont.)**

At each time step, we loop through all the layers and first update the shear strain using current material properties, then compute a current heat flux value based on the current shear strain and strain rate, next update temperatures using the current flux value, and finally update material properties by a table look-up based on the current temperature.

## First Analysis: Uniform Block of ISD110

- Block size: 8" long, 3" wide, 1.5" thick
- Imposed motion:
  - 0.6" zero-to-peak amplitude (40% shear strain)
  - 0.67 sec period (1.5 Hz)
- Results

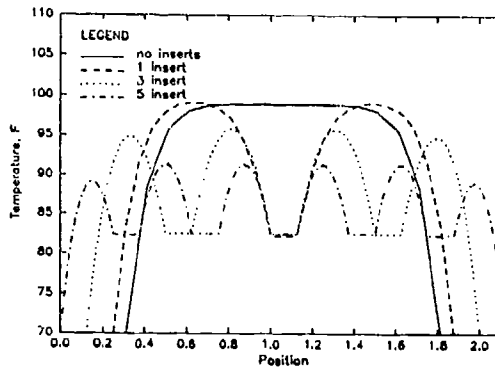


## First Analysis: Uniform Block of ISD110

For our first analysis, we looked at a uniform block of viscoelastic eight inches long (in the direction of motion), three inches wide, and 1.5 inches thick. We imposed an 0.6" shear displacement which amounts to 40% shear strain, with an 0.67 second period. For boundary conditions, we assumed no temperature rise at the interface with the steel framing members.

The graph shows that after 90 seconds the temperature in most of the material is approaching 100 degrees F. The various curves on the graph show different degrees of mesh refinement, just to make sure we have enough subdivisions.

## Analysis Experiments with Embedded Metallic Layers



## Analysis Experiments with Embedded Metallic Layers

We experimented with metallic inserts alternating with viscoelastic layers. As the graph shows, one layer helped very little, three layers somewhat more, and five layers reduced the average temperature considerably, although the peak was still above 90 degrees.

## Effect of Degraded Dampers in a Typical Building

- Two response spectra applied to a single-bay frame with a damper
  - "Soft soil record" (synthesized)
  - Llello, Chile 1985
- Reductions in spectral displacement and acceleration for "cool" and "hot" dampers:

Case	T (°F)	$S_D$	reduction	$S_A$	reduction
Soft soil	70	2.20 → 0.84	62%	0.90 → 0.54	40%
	110	2.20 → 1.45	34%	0.90 → 0.67	26%
Llello	70	3.37 → 1.31	61%	1.38 → 0.84	39%
	110	3.37 → 2.10	38%	1.38 → 0.97	30%

## Effect of Degraded Dampers in a Typical Building

We wanted to get a handle on how much the effectiveness of a damper would drop to to temperature rises. To do this, we ran response spectrum analyses on a representative single-bay building frame using two spectral inputs. The first, called the "soft soil record," is a synthesized record. The second is a record of the 1985 earthquake at Llello, Chile.

Both spectral accelerations and spectral displacements are important in assessing the damage an earthquake would cause. As the table indicates, a "hot" damper is only about half as effective in reducing spectral displacements as a "cool" damper. The loss of effectiveness is less pronounced with respect to spectral acceleration.



## Experimental Program

## Experimental Program

A heavy steel fixture was designed and built for testing viscoelastic blocks in double shear (right photo). A hydraulic shaker (left photo) was used to drive the center steel plate. Force and displacement sensors as well as thermocouples were connected to a Zonic System 7000, normally used for experimental modal analysis.

## First Experiment

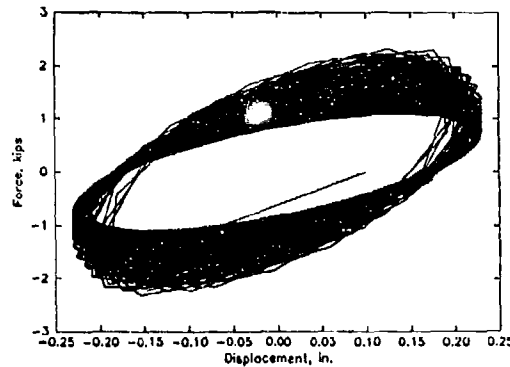
- Pure viscoelastic, 1.03" thick on each side (1/8" layers laid up)
- 0.3 in zero-to-peak displacement (29% shear strain)
- 0.67 sec period (1.5 Hz)
- Result: severe debonding. We did not use an epoxy and were relying on the adhesive properties of the viscoelastic

## First Experiment

Our first run was with pure viscoelastic, no metal inserts. We did not use an epoxy and unfortunately experienced severe debonding.

## Second Experiment

- 3M 1838 epoxy used for bonding
- 23% strain for 80 seconds



## Second Experiment

For our second run, we bonded the material to the steel with 3M 1838 epoxy. A 23% shear strain was run for 80 seconds. The hysteresis loop shows the drop in effectiveness as a decrease in the area of the loop as time goes on and the material heats up.

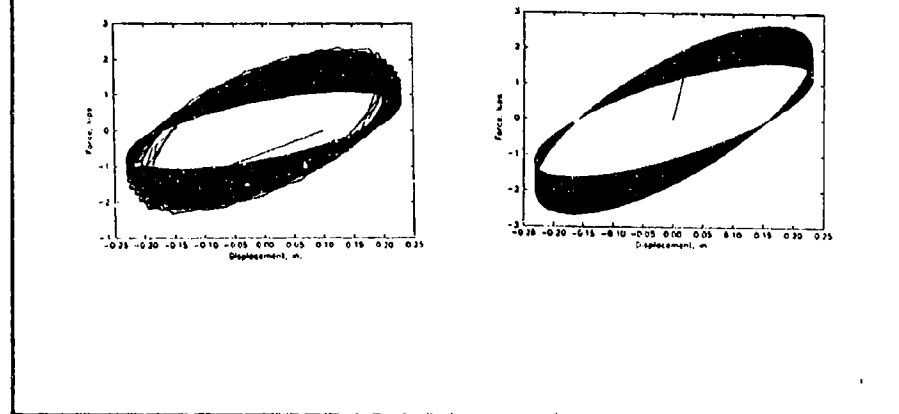
## Third Experiment

- Same configuration, strain increased to 45%
- Result: complete debonding of one layer.  
Friction at this interface continued to provide significant damping

## Third Experiment

Finally, we increased the shear to 45%. Although we completely debonded two layers of viscoelastic, the friction on this plane was considerable as shown in the hysteresis loop.

## Comparison of Test and Analysis



## Comparison of Test and Analysis

The graph shows a comparison between measured and predicted hysteresis loops. The comparison is quite favorable considering the uncertainties in material properties, boundary conditions, etc. Temperatures also compared well although there was considerable scatter in the temperature output.

## Thermoviscoelastic Analysis Procedure

- Equations of motion for block of material

$$K(T)U(t) + C(T)\dot{U}(t) + M\ddot{U}(t) = P(t)$$

- Heat flux equations

$$K_T(t) + \dot{C}_T(t) = F[U(t), \dot{U}(t)]$$

- where

$t$	time	$K$	stiffness matrix
$U$	displacement vector	$C$	damping matrix
$T$	temperature vector	$M$	mass matrix
$P$	applied force vector	$K_T$	conductance matrix
$F$	heat flux vector	$\dot{C}_T$	capacitance matrix

## Thermoviscoelastic Analysis Procedure

The equations of motion involve the material stiffness, loss factor, and mass density, as well as the dimensions of the block. The thermodynamic equations depend on the conductivity, specific heat, and mass density of the material.

**Response Study of Optimum  
Structural and Control Design**

**N. S. Khot\***  
**Structures Division**  
**Flight Dynamics Directorate**  
**Wright Laboratory, WL/FIBRA**  
**Wright-Patterson AFB OH 45433-7552**

**Abstract**

This paper studies the transient response of a minimum weight structure and robust control in the presence of uncertainties. The structure-control design problem is formulated as an optimization problem with the objective of reducing the weight of the structure, minimizing the control performance index, increasing the closed-loop damping and retaining the lowest structural frequency. The control design procedure is based on designing the LQG compensator with constraints on the  $H_{\infty}$  norm of the transfer function between the measured output and the disturbance.

---

\* Aerospace Engineer  
WL/FIBRA BLDG 45  
2130 EIGHTH ST STE 11  
WRIGHT PATTERSON AFB OH 45433-7552  
(513) 255-6992

## Introduction

Hale et.al<sup>(1)</sup> and Salama et.al<sup>(2)</sup> have minimized the sum of the mass of the structure and quadratic the control cost function with constraints on the structural and control design variables. The sensitivity of the control system to the structural modifications has been investigated by Haftka et.al<sup>(3)</sup>. The integrated approach, with the weight of the structure as the objective function and constraints on the damping parameters and frequency distribution of the closed-loop system, was presented by Khot<sup>(4)</sup>. The simultaneous optimization with constraints on the closed-loop eigenvalues and Frobenious norm was considered by Khot et.al<sup>(5)</sup>. The multiobjective problem, structure and control design, was discussed by Rao et.al<sup>(6)</sup>. Lust and Schmit<sup>(7)</sup> considered minimization of the structural mass and performance index with behavior constraints on displacements and frequencies. The robustness of the control system was not addressed in these publications. Lim and Junkins<sup>(8)</sup> considered the structural and control design by utilizing robustness parameters based on the solution of the Lyapunov equations. Rew et.al<sup>(9)</sup> presented pole placement techniques for obtaining robust eigenstructure assignment. Khot and Veley<sup>(10)</sup> used robustness parameters based on the spectral radius of the matrix in integrated structural control problems. These approaches primarily account for only structured uncertainties.

The control system must be robust in order to stabilize the system in the presence of uncertainties in the plant which defines the behavior of the structure. The uncertainties are characterized into two groups. Structured uncertainties are the variations in the parameters in the elements of the plant due to inaccuracies in the calculation of the frequencies, and structural damping. This is due to the approximations in the structural model, material properties, mass, etc. The unstructured uncertainties are due to the neglect of the unmodelled dynamics and not taking into account the dynamics of sensors and actuators, which sometimes is difficult to mathematically model.

This paper develops an algorithm to design the structure and control systems simultaneously, yielding a structure that is minimum weight and a controller that is robust under both structured and unstructured uncertainties. In the definition of the optimization problem, the weight of the structure is considered as the objective function and the constraints are imposed on the distribution of the structural frequencies, the upper bound on the linear quadratic gaussian (LQG) performance index, and the damping associated with the compensator. The control design procedure is based on designing the LQG compensator with a constraint on the  $H_\infty$  norm of the closed-loop system. The compensator satisfying these requirements was found by solving three Riccati equations and was based on the approach proposed in Ref. 11. The application of this integrated design approach was demonstrated on a three dimensional truss problem, and the transient response of the optimum design was investigated in the presence of uncertainties.

## Control Design Approach

The equations of motion of a flexible structure in state vector form can be written as

$$\dot{x} = \bar{A}x + \bar{B}f \quad (1)$$

where  $x(n_1 \times 1)$  is the state vector,  $f(p \times 1)$  is the control input vector,  $\bar{A}(n_1 \times n_1)$  is the plant matrix and  $\bar{B}(n_1 \times p)$  is the control input matrix. The plant and input matrices for a structural problem are given by

$$\bar{A} = \begin{bmatrix} 0 & I \\ -\omega^2 & -2\zeta\omega \end{bmatrix} \quad (2)$$

$$\bar{B} = \begin{bmatrix} 0 \\ \phi^T D \end{bmatrix} \quad (3)$$



where  $\omega^2$  is a diagonal matrix of the squares of the structural frequencies,  $\zeta$  is the vector of modal structural damping,  $-2\zeta\omega$  is a diagonal matrix and  $\mathbf{D}$  is the applied actuator load distribution matrix. Eq. 1 is written for a full order system or reference system. The number of state variables associated with this system is larger than the number of state variables used to design the control system. The number of state variables chosen for the control design is substantially smaller than  $n_1$ .

The control design approach used in this paper is based on the method proposed in Reference 11. This method utilizes the simultaneous linear quadratic gaussian (LQG) and  $H_\infty$  optimization. The dynamic equations of motion for an uncertain reduced order system can be written as

$$\dot{\underline{x}} = (\mathbf{A} + \Delta\mathbf{A}) \underline{x} + \mathbf{B} \underline{f} \quad (4)$$

$$\underline{y} = \mathbf{C} \underline{x} + \underline{w}_2 \quad (5)$$

$$\underline{z}_1 = \mathbf{C} \underline{x} \quad (6)$$

where  $\underline{x}$  is a  $n$ -dimensional state vector,  $\underline{f}$  is a  $p$ -dimensional input vector,  $\underline{y}$  is a  $q$ -dimensional output vector and  $\underline{z}_1$  is a  $q$ -dimensional measured output vector.  $\mathbf{A}(n \times n)$ ,  $\mathbf{B}(n \times p)$ , and  $\mathbf{C}(p \times n)$  are plant, input and output matrices of the reduced order model ( $n_1 > n$ ). In Eq. 5,  $\underline{w}_2$  is a  $p$  dimensional disturbance vector. The matrix  $\Delta\mathbf{A}$  is a real parameter variation matrix which is unknown but assumed to lie within some interval. Eqs. 4 and 5 with the fact that  $\mathbf{C} = \mathbf{B}^T$ , indicate that actuators and sensors are colocated. The  $n^{th}$  order compensator represented by the transfer function  $\mathbf{K}(s)$  can be written as

$$\dot{\underline{x}}_c = \mathbf{A}_c \underline{x}_c + \mathbf{B}_c \underline{y} \quad (9)$$

$$\underline{f} = \mathbf{C}_c \underline{x}_c \quad (8)$$

Using Eqs. 4 through 8, the closed-loop system equations can be written as

$$\dot{\underline{\underline{x}}} = (\underline{\mathbf{A}} + \Delta\underline{\mathbf{A}}) \underline{\underline{x}} + \underline{\mathbf{D}} \underline{w} \quad (9)$$

$$\underline{\underline{z}}_1 = \underline{\mathbf{C}} \underline{\underline{x}} \quad (10)$$

where

$$\underline{\underline{x}} = \begin{bmatrix} \underline{x} \\ \underline{x}_c \end{bmatrix} \quad \underline{w} = \begin{bmatrix} 0 \\ \underline{w}_2 \end{bmatrix} \quad (11)$$

$$\underline{\mathbf{A}} = \begin{bmatrix} \mathbf{A} & \mathbf{B}\mathbf{C}_c \\ \mathbf{B}_c\mathbf{C} & \mathbf{A}_c \end{bmatrix} \quad (12)$$

$$\Delta\underline{\mathbf{A}} = \begin{bmatrix} \Delta\mathbf{A} & 0 \\ 0 & 0 \end{bmatrix} \quad (13)$$

$$\underline{\mathbf{D}} = \begin{bmatrix} 0 & 0 \\ 0 & \mathbf{B}_c \end{bmatrix} \quad (14)$$

and

$$\underline{\mathbf{C}} = [\mathbf{C} \quad 0] \quad (15)$$

where  $\underline{\mathbf{A}}(2n \times 2n)$ ,  $\Delta\underline{\mathbf{A}}(2n \times 2n)$ ,  $\underline{\mathbf{D}}(2n \times 2n)$ , and  $\underline{\mathbf{C}}(p \times 2n)$  are closed-loop matrices. The transfer function between  $\underline{\underline{z}}_1$  and  $\underline{w}_2$  (See Fig. 1) can be written as

$$\mathbf{H}(s, \Delta\mathbf{A}) = \mathbf{G}(s, \Delta\mathbf{A}) \mathbf{K}(s) [\mathbf{I} + \mathbf{G}(s, \Delta\mathbf{A}) \mathbf{K}(s)]^{-1} \quad (16)$$

100

where

$$G(s, \Delta A) = C(sI - A - \Delta A)^{-1} B \quad (17)$$

$G(s, \Delta A)$  represents the transfer function of the uncertain plant and  $K(s)$  is the transfer function of the compensator given by

$$K(s) = C_c(sI - A_c)^{-1} B_c \quad (18)$$

The control design problem can be stated as follows:

For a given state space  $A, B, C$  and  $\Delta A$  matrices determine the controller state space matrices,  $A_c, B_c$ , and  $C_c$  such that the following conditions are specified.

1. The closed-loop system is asymptotically stable.
2. The  $H_\infty$  norm of Eq. 16.

$$\|H(s, \Delta A)\| \leq \gamma \quad (19)$$

where  $\gamma$  is a specified parameter.

3. The linear quadratic gaussian performance index satisfies the condition

$$J(\Delta A) = \lim E [x^T R_1 x + u^T R_2 u] \leq J_u \quad (20)$$

where  $J_u$  is the least upper bound on  $J$ .  $J_u$  depends on the weighting matrices  $R_1$  and  $R_2$  and the controller matrices  $A_c, B_c$ , and  $C_c$ . For specified  $\gamma$ , the controller matrices  $A_c, B_c$ , and  $C_c$  are calculated by solving three coupled Riccati matrices. Given a system with unmodelled dynamics  $L(s)$  modelled as multiplicative perturbations at the plant output, the  $H_\infty$  norm of Eq. 16 is inversely proportional to the level of the unmodelled dynamics  $L(s)$  that the controller can accommodate. Thus, the smaller the value of  $\gamma$  for which the controller can be designed, the higher the unmodelled dynamics that can be tolerated. However, for small value of  $\gamma$  it is numerically difficult to obtain the controller state space matrices satisfying all the Riccati equations.

### Numerical Procedure

The specified model parameter variation matrix  $\Delta A$  is first parameterized as

$$\Delta A = \sum_{i=1}^{p_2} D_i M N E_i \quad (21)$$

where  $D_i$  and  $E_i$  are the column and row vectors respectively of dimension  $n$  which describe the structure of the uncertainty.  $D_i$  contains only nonzero elements characterizing the  $i^{th}$  parameter variation and  $E_i$  is the nonzero element equal to unity at a location corresponding to the nonzero element in  $D_i$  (transpose). In Eq. 21,  $p_2$  is the number of terms to be parameterized and the product  $MN$  is a scalar matrix equal to the identity matrix. The iterative procedure for designing the controller consists of the following steps.

1. For specified values of  $M$  and  $N$  compute

$$V_1 = M \sum_{i=1}^{p_2} D_i D_i^T \quad V_2 = N \sum_{i=1}^{p_2} E_i^T E_i \quad (22)$$

2. Select the control weighting matrix  $\mathbf{R}_2$  and the parameter  $\gamma$  and compute

$$\mathbf{R}_{1\infty}^o = \mathbf{R}_1 = \mathbf{C}^T \mathbf{C} + \gamma^2 \mathbf{V}_2 \quad (23)$$

$$\mathbf{R}_{q1\infty} = \gamma^{-2} \mathbf{R}_1 \quad (24)$$

3. Solve for the symmetric positive definite Riccati matrix  $\mathbf{Q}$  from the equation

$$\mathbf{A}_q \mathbf{Q} + \mathbf{Q} \mathbf{A}_q^T + \mathbf{Q} \mathbf{R}_{q1\infty} \mathbf{Q} + \mathbf{V}_q = 0 \quad (25)$$

where

$$\mathbf{A}_q = \mathbf{A} \quad (26)$$

$$\mathbf{R}_q = \mathbf{R}_{q1\infty} - \mathbf{C}^T \mathbf{C} \quad (27)$$

$$\mathbf{V}_q = \mathbf{V}_1 \quad (28)$$

4. Compute

$$\mathbf{B}_c = \mathbf{B}_{co} = \mathbf{Q} \mathbf{C}^T \quad (29)$$

and initialize  $\mathbf{C}_c = \mathbf{C}_{co} = \mathbf{R}_2^{-1} \mathbf{B}^T$ .

5. Solve for a symmetric positive definite Riccati matrix  $\mathbf{Q}$  from the equation,

$$\mathbf{A}_{q1} \mathbf{Q} + \mathbf{Q} \mathbf{A}_{q1}^T + \mathbf{Q} \mathbf{R}_{q1\infty} \mathbf{Q} + \mathbf{V}_{q1} = 0 \quad (30)$$

where

$$\mathbf{A}_{q1} = \mathbf{A} + \mathbf{Q} \gamma^{-2} \mathbf{R}_{1\infty}^o + \mathbf{B} \mathbf{C}_c \quad (31)$$

$$\mathbf{V}_{q1} = \mathbf{B}_c \mathbf{B}_{co}^T \quad (32)$$

$\mathbf{R}_{q1\infty}$  is computed in step 2.

6. Solve for a symmetric positive definite Riccati matrix  $\mathbf{P}$  from the equation

$$\mathbf{A}_p^T \mathbf{P} + \mathbf{P} \mathbf{A}_p + \mathbf{P} \mathbf{R}_p \mathbf{P} + \mathbf{R}_1 = 0 \quad (33)$$

where

$$\mathbf{A}_p = \mathbf{A} + (\mathbf{Q} + \mathbf{Q}) \mathbf{R}_{q1\infty} \quad (34)$$

$$\mathbf{R}_p = -\mathbf{B} \mathbf{R}_2^{-1} \mathbf{B}^T \quad (35)$$

and  $\mathbf{R}_1$  is computed in step 2.

7. Compute

$$\varepsilon = \sigma_{\max}(\mathbf{C}_c - \mathbf{C}_{co} \mathbf{P}) \quad (36)$$

where  $\sigma_{\max}$  denotes the maximum singular value. Singular values are a measure of the size of the system matrix, and maximum singular values give an indication of how much amplification a particular transfer function under consideration will produce on a given signal of disturbance. If

$\varepsilon$  is smaller than the specified convergence criteria then go to step 8 otherwise set  $C_c = C_{co}P$  and repeat steps 5 through 7.

8. For the converged solution compute

$$A_c = A_{q1} - B_c C \quad (37)$$

$$B_c = Q C^T \quad (38)$$

$$C_c = C_{co} P \quad (39)$$

$$J_u = \text{tr} (Q + \underline{Q}) R_1 + \text{tr} (\underline{Q} C_c^T R_2 C_c) \quad (40)$$

and calculate  $\|H(s)\|_\infty$  norm of

$$H(s) = G(s) K(s) [I - G(s) K(s)]^{-1} \quad (41)$$

where

$$G(s) = C (sI - A)^{-1} B \quad (42)$$

and

$$K(s) = C_c (sI - A_c)^{-1} B_c \quad (43)$$

If the calculated norm is larger than the desired value, then reduce  $\gamma$  and repeat steps 2 through 8. This process may be continued until the converged solution can be obtained for the smallest  $\gamma$ . The limiting value of  $\gamma$  is one.

### Example

The three dimensional flexible truss shown in Fig. 1 was designed to achieve minimum weight and satisfy specified constraints on the structural and control response quantities. The coordinates of the node points are given in Table 1. For this structure the dimensions and the elastic properties are specified in consistent nondimensional units. The Young's modulus was equal to unity and the density of the material was assumed to be 0.1. The structure has twelve elements and twelve degrees of freedom. The colocated sensors and actuators are in the elements of bipods 7 through 12. The full order state space plant matrix in Eq. 1 is  $24 \times 24$  and since there are six colocated actuators and sensors, the input matrix  $\bar{B}$  and the output matrix  $\bar{C}$  are  $24 \times 6$  and  $6 \times 24$  respectively. Since the sensors and actuators are colocated  $\bar{C} = \bar{B}^T$ . The control design was based on using the reduced order plant model based on the two lowest structural frequencies. Therefore, in Eqs. 4 through 6, the matrices  $A$ ,  $B$  and  $C$  are  $4 \times 4$ ,  $4 \times 6$  and  $6 \times 4$  respectively. The cross-sectional areas of Design I, given in Table 2, were used for the initial design for optimization.

The value of the parameter  $\gamma$  in Eq. 23 was set equal to 3.0 and was assumed to be constant throughout the optimization procedure and the design of the compensator for the modified structure. The convergence criteria  $\varepsilon$  in Eq. 36 was set equal to 0.0001. The weighting matrices  $\bar{M}$  and  $\bar{N}$  in Eq. 22 were assumed to be scalar quantities and were set equal to 110 and 1/110 respectively. The control weighting matrix  $R_2$  in Eq. 20 was equal to  $\bar{\gamma}/I$ ;  $I$  being the identity matrix and  $\bar{\gamma}$  the control design variable. The modal structural damping  $\zeta$  in Eq. 2 for the two frequencies used in defining the matrix  $A$  was .05. The percentage of structured uncertainty in the reduced order plant matrix  $A$  was assumed to be  $\pm 5\%$  for calculating  $\Delta A$ . There were no uncertainties in matrices  $B$  or  $C$ .

The optimization problem was formulated with the weight of the structure being the objective function and constraints imposed on the square of the structural frequencies, performance index  $J_u$  in Eq. 40 and the damping associated with the compensator  $A_c$  in Eq. 37. The problem can be defined as

Minimize the weight

$$W = \sum_{i=1}^{\bar{n}} \rho_i A_i l_i \quad (44)$$

Subject to the structural constraints,

$$g_j(\omega_i^2) = \omega_i^2 - \bar{\omega}_i^2 \geq 0 \quad (45)$$

$$g_j(A_i) = A_i - \bar{A}_i \geq 0 \quad (46)$$

and the control design constraints,

$$g_j(J_u) = \bar{J}_u - J_u \geq 0 \quad (47)$$

$$g_j(\xi_i) = \xi_i - \bar{\xi}_i \geq 0 \quad (48)$$

In Eq. 44  $\rho_i$  denotes the density of the material,  $l_i$  is the length of the element and  $A_i$  is the cross-sectional area of the element. The number of structural design variables is equal to  $\bar{n}$ . Eq. 45 defines the constraint on the square of the structural frequency. The lower bound on the square of the structural frequencies is  $\bar{\omega}_i^2$ . In Eq. 46  $\bar{A}_i$  is the minimum value of the structural design variable. The constraint on the upper bound of the linear quadratic gaussian performance index (Eq. 40) is defined in Eq. 47.  $\bar{J}_u$  is the maximum allowable value of the upper bound on the performance index. The constraints on the compensator damping of  $A_c$  (Eq. 37) are defined in Eq. 48 where  $\bar{\xi}_i$  is the minimum acceptable value. The integrated optimization problem was solved by using the NEWSUMT-A<sup>(12)</sup> mathematical optimization program based on the extended interior penalty function method with Newton's method of unconstrained minimization.

The numerical optimization problem was set up with constraints on the square of the fundamental structural frequency  $\omega_1^2$ , the performance index  $J_u$  and the damping  $\xi_1$  associated with the lowest frequency of the compensator matrix  $A_c$ . The constraint values selected for  $\bar{\omega}_1^2 = 1.801$  and  $\bar{J}_u = 1.316$  were equal to the response quantities of the initial design, Design I. The constraint values for damping were  $\bar{\xi}_1 = 0.40$ . The objective was to obtain robust control, a minimum weight structure, decrease  $J_u$  and increase  $\xi_1$ . The cross-sectional areas of the optimum design are given in Table 2, designated as Design II. The convergence history is shown in Table 3. The square of the structural frequencies associated with the initial design in Table 4. The band width of the square of the structural frequencies for the optimum design has narrowed and the values associated with the first two modes are nearly equal. The initial and the final values of the constraints are given in Table 5.

The control analysis of the optimum structural/control design was performed by using the full order matrices in the definition of the closed-loop system. Thus in Eq. 12, the matrices  $A$ ,  $B$  and  $C$  were  $24 \times 24$ ,  $24 \times 6$  and  $6 \times 24$  respectively. They had the same order as the ones in Eq. 1. Thus, the controller designed on the basis of the first two frequencies was used to control the full order system. This would indicate the robustness of the controller to the unmodelled dynamics

and indicate whether there was any spillover effect leading to an unstable system. In order to investigate the robustness of the controller in the presence of structured uncertainties, responses of the two perturbed plant matrices were studied. The two perturbed systems were a +10% and -10% variation in  $\omega_1^2$  and  $\omega_2^2$  respectively, in the definition of the plant matrix A. This percentage was higher than the variation of  $\pm 5\%$  assumed in the calculation of  $\Delta A$  in Eq. 21. The modal structural damping parameter  $\zeta$  associated with the unmodelled higher modes 3 through 12 in Eq. 1 was set equal to 0.001. A lower value of  $\zeta$  was intentionally selected to evaluate whether the controller was robust against unmodelled dynamics to avoid the spillover effect.

Maximum singular values were computed for both the full order plant  $G(s)$  and the closed-loop system  $G(s)K(s)[I + G(s)K(s)]^{-1}$  at frequencies from 0.01 to 100 radians per second. Singular values are a measure of the size of the system matrix and maximum singular values give an overall indication of how much amplifications a particular transfer function under consideration would provide on a given signal of disturbance. Figs. 2 through 4 show full order plant and closed-loop maximum singular values for the optimum Design II and the perturbed design, Design II(+) and Design II(-). The plus and minus signs indicates positive and negative perturbations in the formulation of the plant matrices. For all the cases, the maximum singular value curves for the closed-loop system near the first two modes were above the open-loop curves, but remained below at higher unmodelled frequencies. This indicates that the controller would have higher attenuation for the disturbances associated with the higher unmodelled modes than for the two lower modes, which was the basis for the controller design.

The dynamic response of the closed-loop and open-loop systems for the optimum and perturbed cases was studied by calculating the displacement of node 1 in  $xy$ - plane due to an impulse force of unit magnitude applied to each of the actuators separately at time  $t = 0$ . Figs. 5 through 7 show the transient response for the three cases for an impulse at actuator No. 1. Since the response for the impulse forces at the remaining five actuators had a similar transient response and trend, these curves are not given in this paper. The controller designed on the basis of two structural modes was able to stabilize the system in the presence of unmodelled dynamics and structured uncertainties. As indicated by the singular value plots, when the controlled modes dominated initially, the magnitudes of displacement of the closed-loop system were slightly higher than those of the open-loop system. However, as time passes, the controller was able to stabilize the system and reduce the displacements. The difference in the response curves of the three cases is very small and requires careful comparison to note the variation. Thus in this design procedure, it was possible to design a minimum weight structure and design a controller which was stable in the presence of structured and unstructured uncertainties.

### Conclusions

This paper introduces a design procedure to obtain a minimum weight structure and synthesize a robust controller that accounts for structured parameter uncertainty in the state and unmodelled dynamics. The illustrative example consists of designing a controller based on a  $4 \times 4$  state matrix for a structure which has a  $24 \times 24$  full order state matrix. The transient response plots indicates the stability of the structural/control system in the presence of unmodelled dynamics and structured parameter uncertainty.

### References

1. Hale, A. L., "Integrated Structural/Control Synthesis Via Set - Theoretic Methods," AIAA/ASME/ASCE 26th SDM Conference, Orlando FL, 85-0806-CP, April, 1985.
2. Salama, M., Garba, J., and Demesetz, L., "Simultaneous Optimization of Contolled Structures," *Computational Mechanics*, Vol. 3, pp. 275-282, 1988.
3. Haftka, R. T., Martinovic, A. and Hallauer, Jr., W. L., "Enhanced Vibration Controllability by Minor Structural Modifications," *AIAA Journal*, Vol. 23, No. 8, August 1985, pp. 1260-1266.

4. Khot, N. S., "Structures/Control Optimization to Improve the Dynamic Response of Space Structures," *Computational Mechanics*, Vol. 3, 1988, pp. 179-186.
5. Khot, N. S. and Grandhi, R. V., "Structural and Control Optimization with Weight and Frobenius Norm as Performance Functions," *Structural Optimization*, (G. I. N. Rozvany and B. L. Karihaloo, eds.), Kluwer Academic Publishers, 1988, pp. 151-158.
6. Rao, S. S., "Combined Structural and Control Optimization of Flexible Structures," *Engineering Optimization*, Vol. 13, 1988, pp. 1-16.
7. Lust, R. V. and Schmit, L. A., "Control Augmented Structural Synthesis," *AIAA Journal*, Vol. 26, No. 1, 1988, pp 86-95.
8. Lim, K. B. and Junkins, J. L., "Robust Optimization of Structural and Controller Parameters," *J. Guidance*, Vol. 12, January 1989, pp. 89-96.
9. Rew, D. W., Junkins, J. L. and Juang, J. N., "Robust Eigenstructure Assignment by a Projection Method: Applications Using Multiple Optimization Criteria," *Proceedings of the AAS/AIAA Astrodynamics Conference*, Kalispell MT, August 1987.
10. Khot, N. S. and Veley, D. E., "Robustness Characteristics of Optimum Structural/Control Design," To be published in the *Journal of Guidance, Control and Dynamics*, 1991.
11. Banda, S. S., Yeh, H. H. and Heise, S. A., "A Surrogate System Approach to Robust Control Design," *Proceedings 1989 AIAA Guidance, Navigation and Control Conference*, Boston MA, 1989, pp. 576-582.
12. Grandhi, R. V., Thareja, R. and Haftka, R. T., "NEWSUMT-A: A General Purpose Program for Constrained Optimization Using Constraint Approximations," *ASME Journal of Mechanisms, Transmissions, and Automation in Design*, Vol. 107, 1985, pp. 94-99.

Table 1. Coordinates of Node Points

Node	X	Y	Z
1	0.0	0.0	10.165
2	-5.0	-2.887	2.0
3	5.0	-2.887	2.0
4	0.0	5.7735	2.0
5	-6.0	-1.1547	0.0
6	-4.0	-4.6188	0.0
7	4.0	-4.6188	0.0
8	6.0	-1.1547	0.0
9	-2.0	5.7735	0.0
10	2.0	5.7735	0.0

Table 2. Design Variables

Element Number	Design I	Design II
1 (1-2)	1000.0	210.84
2 (2-3)	1000.0	363.10
3 (1-3)	100.0	112.16
4 (1-4)	100.0	110.74
5 (2-4)	1000.0	322.97
6 (3-4)	1000.0	264.86
7 (2-5)	100.0	99.95
8 (2-6)	100.0	92.45
9 (3-7)	100.0	123.76
10 (3-8)	100.0	63.69
11 (4-9)	100.0	126.85
12 (4-10)	100.0	64.96
Weight	43.69	15.46
$\gamma$	1.0	0.0031



Table 3. Iteration History

Iteration No.	Weight
1	43.69
2	19.08
3	18.77
4	17.35
5	15.90
6	15.56
7	15.47
8	15.46

Table 4. Structural Frequencies ( $\omega_j^2$ )

Mode	Design I	Design II
1	1.801	1.801
2	2.771	1.801
3	8.356	6.324
4	8.746	7.891
5	11.55	8.608
6	17.68	14.77
7	21.73	19.46
8	22.61	24.40
9	72.92	28.74
10	85.57	35.39
11	105.8	37.17
12	166.5	53.18

Table 5. Constraint Values

Initial Values	Final Values
$\omega_1^2 = 1.801$	$\omega_1^2 = 1.801$
$J_u = 1.331$	$J_u = 0.998$
$\xi_1 = 0.0515$	$\xi_1 = 0.4650$
Weight = 43.69	Weight = 15.46

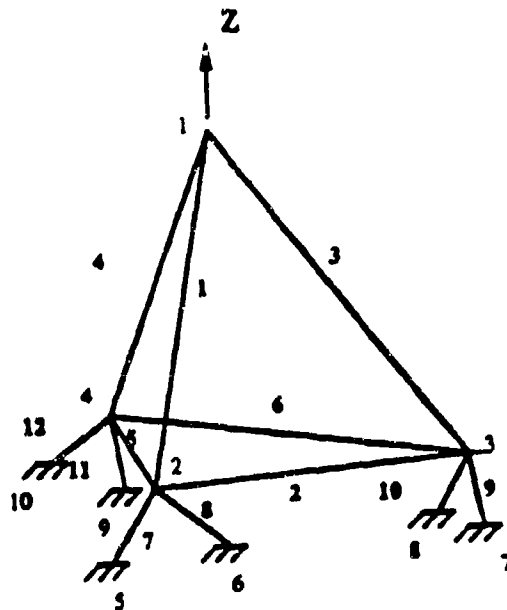


Fig. 1 Truss structure

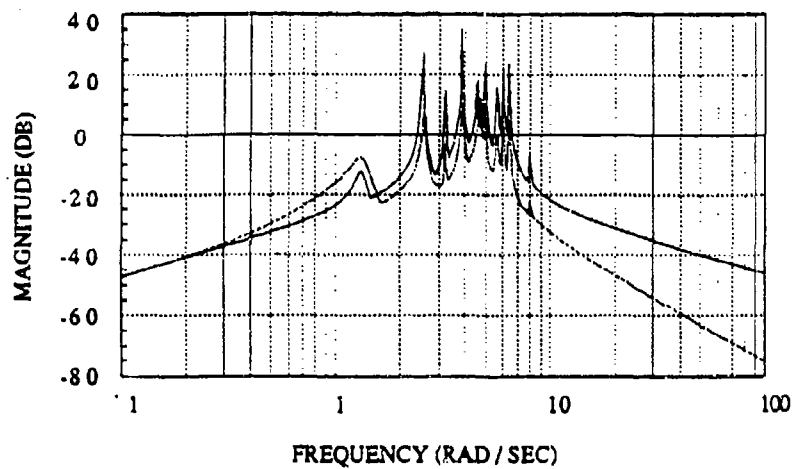


Fig. 2 Maximum Singular Values for Design II

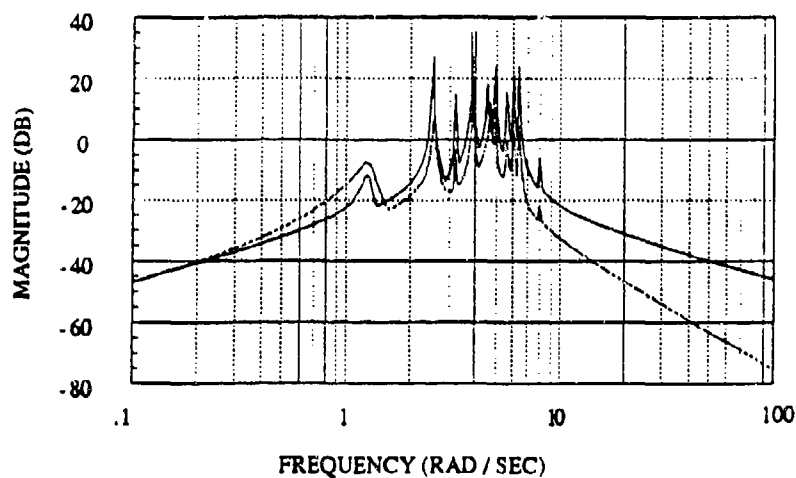


Fig. 3 Maximum Singular Values for Design II (+)

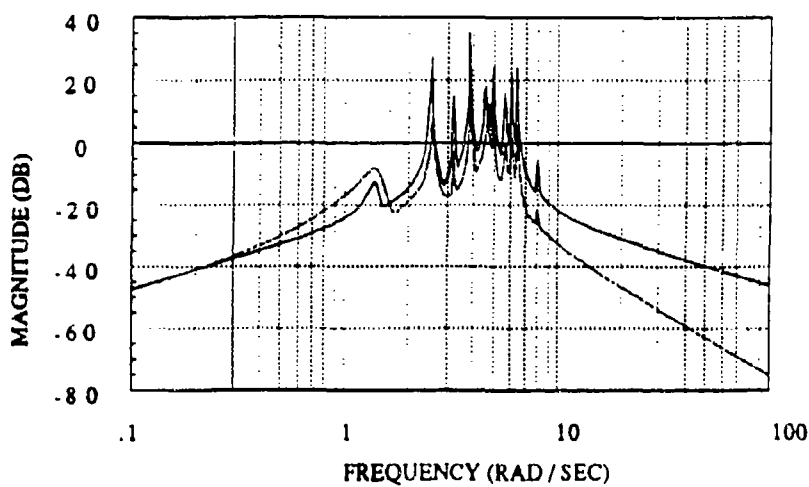


Fig. 4 Maximum Singular Values for Design II (-)

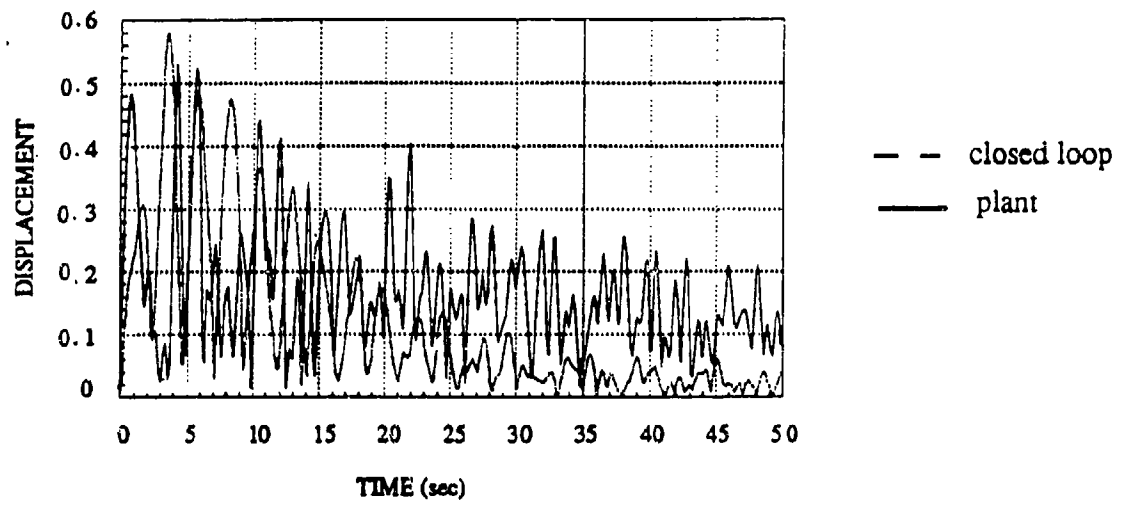


Fig. 5. Transient Response to Design II

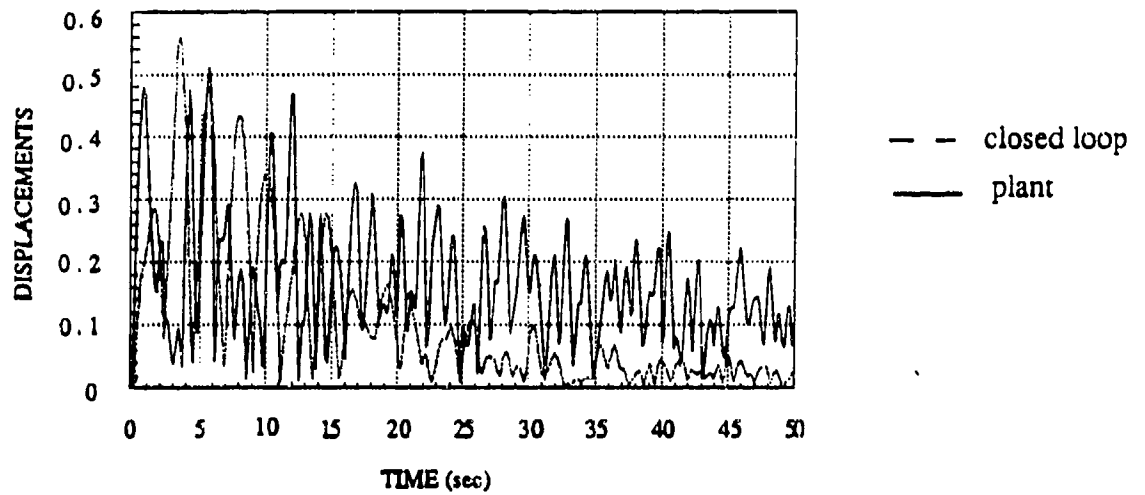


Fig. 6. Transient Response to Design II (+)

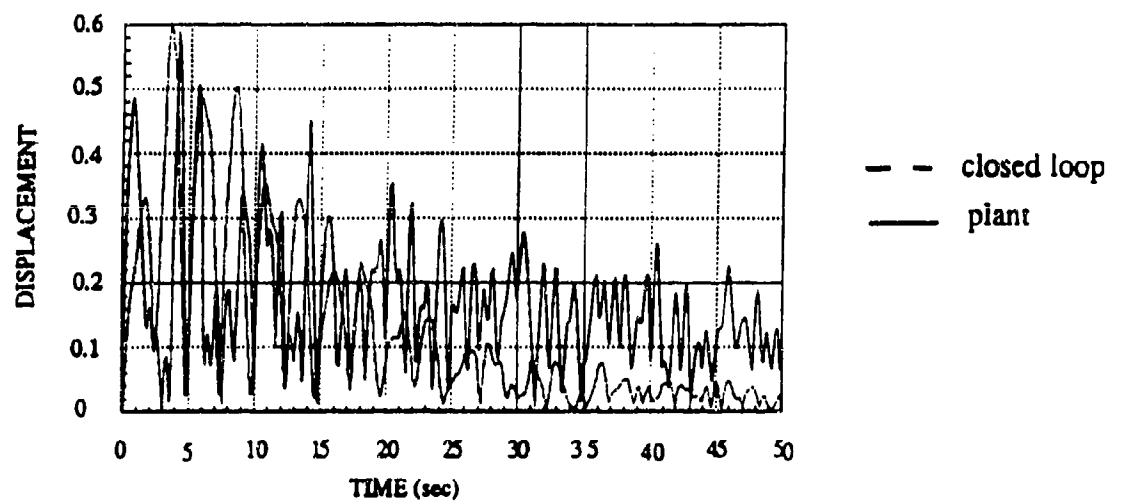


Fig. 7. Transient Response to Design II (-)

# Uniform Modal Damping of an Elastic Ring by the Natural Control Law

D. J. Rossetti, *Graduate Student*  
Department of Mechanical and Aerospace Engineering  
North Carolina State University  
Raleigh, North Carolina 27695

and

J. Q. Sun\*, *Engineering Specialist*  
Thomas Lord Research Center  
Lord Corporation  
405 Gregson Dr.  
Cary, North Carolina 27511

February, 1993

## Abstract

In some elastic ring applications the need arises to attenuate vibration in the lower order modes without substantially changing the natural frequencies and mode shapes of the uncontrolled ring. In this paper we study the uniform damping of the lower order modes of an elastic ring by using natural control. An extended form of the node control theorem due to Weaver and Silverberg is developed to determine the number and locations of the control forces. It is shown in this paper that by using velocity and position feedback of  $2M+2$  evenly spaced control forces the lowest  $2M+1$  modes of the ring can be uniformly damped. Further, when these are the only modes participating in the vibration, the control system is shown to preserve the natural frequencies and mode shapes of the uncontrolled modes of the ring. The control system is decentralized and simple to implement. Both transient and steady-state responses of a ring demonstrate the effectiveness of the control system design. Control spillover to higher-order modes of the ring is found to have a relatively small effect on the control performance.

## 1.0 Introduction

In principle, a control system can dampen any combination of the modes of a vibrating structure. In certain applications one wants to preserve the uncontrolled mode shapes and resonant frequencies of the lower order modes. When point control forces and sensors are used, the placement of the control forces and sensors on the structure plays an important role in achieving these objectives. Toward that end, the natural control theory, developed by Silverberg and Morton, provides a general strategy for designing a control system that preserves the resonant frequencies and mode shapes of the structure while uniformly damping the modes.[1, 2]. Weaver and Silverberg applied natural control to uniform beams and developed a control force and sensor placement strategy called node control [3]. The strategy is based on the node control theorem which states:

"If a uniform beam with homogeneous boundary conditions and with the lowest  $N$  modes participating in the system response is subject to  $N$  direct state

---

\* Phone: (919)469-2500 ext 317

feedback control forces placed at the  $N$  nodes of the  $(N+1)$ th mode, then the control gains can be selected such that the following properties apply to the controlled system: 1) Frequency Invariance; 2) Mode Invariance; 3) Uniform Damping." [3]

Further, the node control system is decentralized in that the control forces only use position and velocity information at their point of application. Such a control system is easier to implement than a centralized one.

This paper extends the node control theorem for uniform beams to uniform rings. In contrast with uniform beams, uniform rings possess no boundary conditions and they are degenerate in the sense that for each natural frequency there are two orthogonal mode shapes which can be described as a sine mode and a cosine mode. In the paper we develop a node control design for uniform damping of the lower order modes of uniform rings and show that  $2M+2$  control forces evenly spaced around the ring can provide uniform damping to the lowest  $2M+1$  modes and preserve the open-loop natural frequencies and mode shapes of these modes.

## 2.0 Elastic Ring Equations

The equations of motion for a uniform ring can be written as [4]

$$\begin{aligned} \rho A \ddot{v} - \left( \frac{EA}{R^2} + \frac{EI}{R^4} \right) \frac{\partial^2 v}{\partial \theta^2} - \frac{EA}{R^2} \frac{\partial w}{\partial \theta} + \frac{EI}{R^4} \frac{\partial^3 w}{\partial \theta^3} &= 0 \\ \rho A \ddot{w} + \frac{EA}{R^2} \frac{\partial v}{\partial \theta} - \frac{EI}{R^4} \frac{\partial^3 v}{\partial \theta^3} + \frac{EA}{R^2} w + \frac{EI}{R^4} \frac{\partial^4 w}{\partial \theta^4} &= r + u \end{aligned} \quad (2.1)$$

where  $\rho$  represents the mass density of the ring,  $E$  is Young's modulus,  $A$  is the cross sectional area, and  $R$  is the mean radius.  $w$  is the normal displacement of the ring and  $v$  is the in-plane motion. Both  $w$  and  $v$  are functions of location  $\theta$  and time  $t$ .  $r$  represents the excitation in the normal direction and  $u$  represents the normal control action. Both  $r$  and  $u$  are functions of  $\theta$  and  $t$ . It is assumed that there is no in-plane external force. Since the ring is uniform and continuous, the above equations are subject to no boundary conditions. Instead, we impose the conditions that  $w$ ,  $v$ ,  $r$  and  $u$  be periodic functions of  $\theta$ . The modal expansions of these quantities are given by

$$\begin{aligned} w(\theta, t) &= \sum_{n=-M}^M w_n(t) e^{jn\theta}, \quad v(\theta, t) = \sum_{n=-M}^M v_n(t) e^{jn\theta} \\ u(\theta, t) &= \sum_{n=-M}^M u_n(t) e^{jn\theta}, \quad r(\theta, t) = \sum_{n=-M}^M r_n(t) e^{jn\theta} \end{aligned} \quad (2.2)$$

where  $j^2 = -1$ ,  $w_n$  and  $v_n$  are modal displacements,  $r_n$  is a modal excitation and  $u_n$  is a modal control force. The expansions are truncated at  $n = \pm M$ . Note that in order for the expansions of (2.2) to be real valued, the coefficients must obey

$$\begin{aligned} w_n &= w_{-n}^*, & v_n &= v_{-n}^* \\ u_n &= u_{-n}^*, & r_n &= r_{-n}^* \end{aligned} \quad (2.3)$$

where \* denotes complex conjugate. Each term in the expansion of  $w(\theta, t)$  represents a wave traveling around the ring, and will be *loosely* referred to as a complex mode, or simply a mode of the ring. The sum of the  $\pm n$ th modes results in a real deformation pattern consisting of a sine mode and a cosine mode. The number of nodes of the real deformation pattern is equal to  $2n$ . The nodes are evenly spaced along the ring and may move around the ring as the phase of the sine and cosine modes changes. Several cosine modes of a uniform ring are shown in Figure 1.

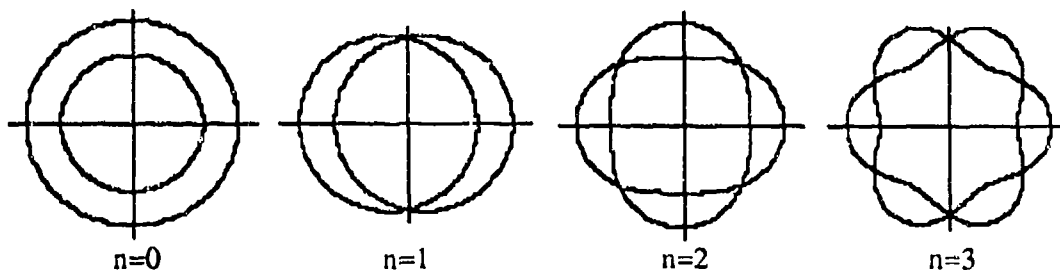


Figure 1. Cosine modes of a uniform ring.

Since there is no in-plane, external force the in-plane inertial term is assumed to be negligible, that is

$$\rho A \ddot{v} \approx 0 \quad (2.4)$$

This assumption will simplify the analysis since the system equation governing the deflection  $w(\theta, t)$  becomes second order in time instead of fourth order. Further, the assumption has little effect on the natural frequencies of the deflection  $w(\theta, t)$  of the ring.

Substituting the expansions of (2.2) in the equations of motion (2.1) leads to a set of decoupled equations for the coefficients  $w_n$  and  $v_n$ . The first equation of (2.1) yields an algebraic relationship between  $v_n$  and  $w_n$ .

$$v_n = \begin{cases} \frac{j}{n} \times \frac{\frac{EA}{R^2} + \frac{EI}{R^4} n^2}{\frac{EA}{R^2} + \frac{EI}{R^4}} w_n, & n \neq 0 \\ 0, & n = 0 \end{cases} \quad (2.5)$$

Eliminating  $v_n$  from the second equation of (2.1) by using equation (2.5) yields a set of second order ordinary differential modal equations:

$$\ddot{w}_n + \omega_n^2 w_n = \hat{r}_n + \hat{u}_n, \quad -M \leq n \leq M \quad (2.6)$$

where  $\omega_n$  is the open loop natural frequency of the  $n$ th mode, given by

$$\omega_n^2 = \begin{cases} \frac{E}{\rho R^2}, & n = 0 \\ \frac{1}{\rho A} \left[ \frac{EA}{R^2} + \frac{EI}{R^4} n^4 - \frac{\left( \frac{EA}{R^2} + \frac{EI}{R^4} n^2 \right)^2}{\frac{EA}{R^2} + \frac{EI}{R^4}} \right], & n \neq 0 \end{cases} \quad (2.7)$$

The normalized modal excitation  $\hat{r}_n$  and the normalized modal control force  $\hat{u}_n$  are

$$\hat{u}_n = \frac{u_n}{\rho A}, \quad \hat{r}_n = \frac{r_n}{\rho A} \quad (2.8)$$

### 3.0 Control System

#### Natural Control

Consider  $N$  discrete point control forces expressed as:

$$u(\theta, t) = \sum_{i=1}^N f_i(t) \delta(\theta - \theta_i) = \sum_{i=1}^N [h_i \dot{w}(\theta_i, t) + g_i w(\theta_i, t)] \delta(\theta - \theta_i) \quad (3.1)$$

where  $h_i$  is the velocity feedback gain and  $g_i$  is the position feedback gain of the  $i$ th control force  $f_i(t)$  located at  $\theta_i$ . The normalized modal control force in equation (2.8) becomes

$$\hat{u}_n = \sum_{m=-M}^M H_{nm} \dot{w}_m + \sum_{m=-M}^M G_{nm} w_m \quad (3.2)$$

where  $G_{nm}$  and  $H_{nm}$  are control gain matrices given by

$$H_{nm} = \frac{1}{2\pi\rho A} \sum_{i=1}^N h_i e^{j(m-n)\theta_i}, \quad G_{nm} = \frac{1}{2\pi\rho A} \sum_{i=1}^N g_i e^{j(m-n)\theta_i}. \quad (3.3)$$

Substituting equation (3.2) into equation (2.6), we obtain the modal equations of the closed-loop system

$$\ddot{w}_n + \omega_n^2 w_n = \sum_{m=-M}^M H_{nm} \dot{w}_m + \sum_{m=-M}^M G_{nm} w_m, \quad -M \leq n \leq M. \quad (3.4)$$

Note that the modal excitation  $\hat{r}_n$  is neglected in equation (3.4). Equation (3.4) represents a set of coupled differential equations. Assuming a solution to equation (3.4) in the form

$$w_n(t) = W_n e^{\lambda t} \quad (3.5)$$

we obtain the closed-loop eigenvalue problem



$$\sum_{m=-M}^M [(\lambda^2 + \omega_n^2) \delta_{nm} - \lambda H_{nm} - G_{nm}] W_m = 0, \quad -M \leq n \leq M \quad (3.6)$$

where  $\lambda$  is the closed-loop eigenvalue,  $W_n$  is the closed-loop eigenvector and  $\delta_{nm}$  is defined by:

$$\delta_{nm} = \begin{cases} 0, & n \neq m \\ 1, & n = m \end{cases} \quad (3.7)$$

As stated earlier, natural controls are developed to achieve three objectives:

1. To preserve the open-loop mode shapes.
2. To preserve the open-loop natural frequencies.
3. To dampen the modes at a uniform rate.

To meet Objective 1, the closed-loop system, like the open-loop system, has to be decoupled. This requires the matrices  $G_{nm}$  and  $H_{nm}$  to be diagonal,

$$H_{nm} \equiv G_{nm} \equiv 0, \quad n \neq m. \quad (3.8)$$

Substituting equation (3.8) into equation (3.6), we obtain the decoupled eigenvalue problem

$$[\lambda_n^2 + \omega_n^2 - \lambda_n H_{nn} - G_{nn}] W_n = 0, \quad -M \leq n \leq M. \quad (3.9)$$

where  $\lambda_n$  is a complex eigenvalue associated with the  $n$ th mode and can be written as:

$$\lambda_n = -\alpha_n \pm j\beta_n \quad (3.10)$$

where  $\alpha_n$  is the decay rate of the  $n$ th mode, and  $\beta_n$  is the associated closed-loop frequency. In order to preserve the open-loop frequencies (Objective 2), we require that

$$\omega_n = \beta_n. \quad (3.11)$$

Equations (3.9) and (3.11) lead to

$$H_{nn} = -2\alpha_n, \quad G_{nn} = -\alpha_n^2. \quad (3.12)$$

Objective 3 is readily satisfied by letting  $\alpha_n = \alpha$  for each  $n$ .

### Node Control

Next we determine feedback gains  $h_i$  and  $g_i$ , the locations  $\theta_i$  and the number of control forces  $N$ , that can accomplish the above natural control design, that is, that satisfy equations (3.8) to (3.12). We shall only consider a special subclass of the control design with equal gains for each control force:

$$h_i = h, \quad g_i = g, \quad i = 1, \dots, N \quad (3.13)$$

We turn to the node control theorem for uniform beams [3] and examine the nodes of elastic ring modes.

As discussed earlier, the nodes of the real deformation pattern resulting from the  $\pm n$ th modes are evenly spaced on the ring and may move along the ring. This suggests that if we want to control the lower order modes up to  $n=\pm M$ , we should first try to evenly place  $2(M+1)$  control forces on the ring. This is because the real deformation pattern resulting from the modes  $n=\pm(M+1)$  has  $2(M+1)$  nodes evenly spaced on the ring. The location of the control forces can be expressed as:

$$\theta_i = \frac{2\pi(i-1)}{N} + \gamma_0, \quad i=1,2,\dots,N \quad (3.14)$$

where  $N$  is equal to  $2M+2$ , and  $\gamma_0$  is an arbitrary reference angle. Note that  $\theta_i$  given in (3.14) is not necessarily at a node of the real deformation pattern resulting from the modes  $n=\pm(M+1)$ . For example, when  $M=1$ , we need four control forces evenly spaced around the ring. The matrices  $G$  and  $H$  become

$$H = \frac{3}{2\pi\rho A} \begin{bmatrix} h & 0 & 0 \\ 0 & h & 0 \\ 0 & 0 & h \end{bmatrix}, \quad G = \frac{3}{2\pi\rho A} \begin{bmatrix} g & 0 & 0 \\ 0 & g & 0 \\ 0 & 0 & g \end{bmatrix} \quad (3.15)$$

where

$$h_i = \frac{-4\pi\rho A\alpha}{N}, \quad g_i = \frac{-2\pi\rho A\alpha^2}{N} \quad (3.16)$$

In equation (3.16),  $N$  is equal to 4 ( $=2M+2$ ). More generally, the matrices  $G$  and  $H$  can be expressed as:

$$G_{nm} = -\alpha^2 F(n,m), \quad H_{nm} = -2\alpha F(n,m) \quad (3.17)$$

where  $F(n,m)$  is defined as:

$$F(n,m) = \begin{cases} 1, & n = m \\ 0, & n \neq m \text{ and } |n-m| \neq kN, \quad k=1,2,\dots \\ 1, & |n-m| = kN, \quad k=1,2,\dots \end{cases} \quad (3.18)$$

From equation (3.18), we can see that the matrices  $G$  and  $H$  are diagonal when  $n$  and  $m$  are within the range of the controlled modes, and are not diagonal when  $n$  and  $m$  are beyond the range of the controlled modes.

#### Control Spillover

We now examine the effect of the control forces on the higher order uncontrolled modes, i.e. the control spillover. As an example, we consider the case when  $M=1$  in which four evenly spaced control forces attempt to control the three modes  $n=-1, 0$ , and  $1$ .

Truncating the expansion of  $w(\theta,t)$  to  $n=\pm 3$ , we obtain the matrices  $G$  and  $H$

$$H = \begin{bmatrix} -2\alpha & 0 & 0 & 0 & -2\alpha & 0 & 0 \\ 0 & -2\alpha & 0 & 0 & 0 & -2\alpha & 0 \\ 0 & 0 & \begin{bmatrix} -2\alpha & 0 & 0 \\ 0 & -2\alpha & 0 \\ 0 & 0 & -2\alpha \end{bmatrix} & 0 & -2\alpha & 0 & 0 \\ 0 & 0 & 0 & -2\alpha & 0 & 0 & 0 \\ -2\alpha & 0 & 0 & 0 & -2\alpha & 0 & 0 \\ 0 & -2\alpha & 0 & 0 & 0 & -2\alpha & 0 \\ 0 & 0 & -2\alpha & 0 & 0 & 0 & -2\alpha \end{bmatrix}, G = \frac{\alpha}{2} H \quad (3.19)$$

The inner  $3 \times 3$  matrix corresponding to the controlled modes from  $n = -1$  to  $n = 1$  is diagonal as expected. Outside of this range, the above matrices are coupled indicating control spillover. The modes  $n = \pm 2$ , i.e. the ones above and below the controlled modes, are coupled to one another, but are not coupled to any of the lower order modes. Thus there is no control spillover to the  $n = \pm 2$  modes. Beyond  $n = \pm 2$  there is coupling of higher order modes to the controlled modes. In general only the odd order modes couple to the odd controlled modes, and likewise, the even modes couple to the even controlled modes.

#### 4.0 Numerical Results

In this section we simulate both transient and steady-state responses and examine the effect of control spillover. Table 1 shows the parameters of the ring used in the simulation. Table 2 gives the first 5 open-loop natural frequencies of the ring.

Table 1. Ring parameters.

Material	Aluminum
Mass Density, $\rho$	2800 kg/m <sup>3</sup>
Young's Modulus, E	7.2x10 <sup>10</sup> Pa
Cross Sectional Area, A	1.25x10 <sup>-3</sup> m <sup>2</sup>
Moment of Inertia, I	2.604x10 <sup>-7</sup> m <sup>4</sup>
Mean Radius, R	.6096 m

Table 2. Natural frequencies of the ring.

Mode, $n = \pm$	Natural Frequency, (Hz)
0	1324.8
1	0.0
2	94.1
3	250.9
4	470.4
5	752.6

#### Transient Solutions

Figure 2 shows the transient response of the modal displacement of modes  $n = 2$  and  $n = 3$  (i.e.  $w_2(t)$  and  $w_3(t)$ ) of the ring. Eight control forces are evenly placed on the ring. The modes from  $n = -3$  to  $n = 3$  are the controlled modes and also the modes included in the expansion of  $w(\theta, t)$ . In the simulation the cosine parts of modes  $n = 2$  and  $n = 3$  are given

an initial displacement of unity. The decay rate  $\alpha$  is chosen to be 40. Figure 2 clearly shows that the controlled modes decay within the envelope:

$$-e^{-\alpha t} \leq w_n(t) \leq e^{-\alpha t}. \quad (4.1)$$

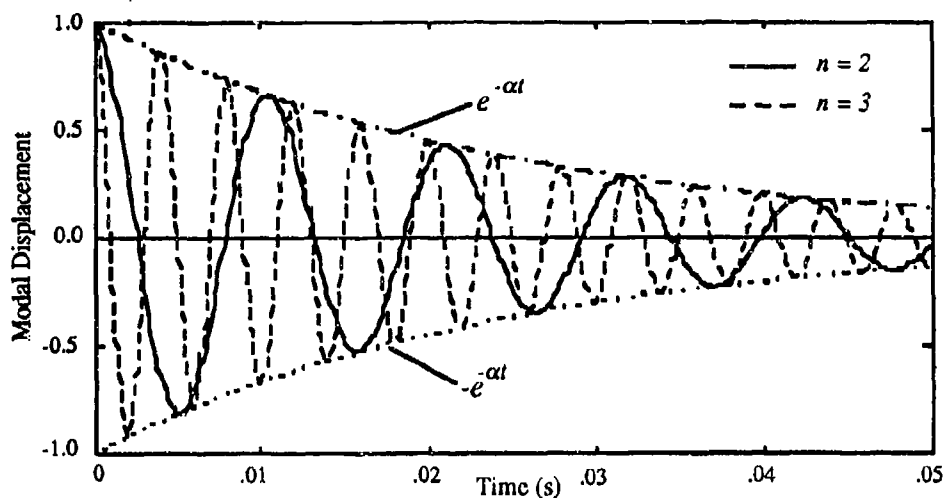


Figure 2. Transient response of modes  $n=2$  and  $n=3$ . ( $M=3$ ,  $-3 \leq n \leq 3$ ,  $\alpha=40$ ).

### Control Spillover

In this example we study the control spillover effect. We use six control forces to control the modes from  $n=-2$  to  $n=2$ . The modes from  $n=-4$  to  $n=4$  are included in the expansion. The decay rate is chosen to be  $\alpha=100$ . The cosine part of the mode  $n=2$  is given an initial displacement of unity. Figure 3 shows the coupling effect of the controlled modes on the higher order modes. It can be seen from Figure 3 that mode  $n=2$  begins with an initial displacement of unity and decays at a rate of  $\alpha=100$ . However, because this mode is coupled to mode  $n=4$ , mode  $n=4$  begins at rest and builds up some finite response. Like mode  $n=2$ , mode  $n=4$  is damped out quickly by the control system.

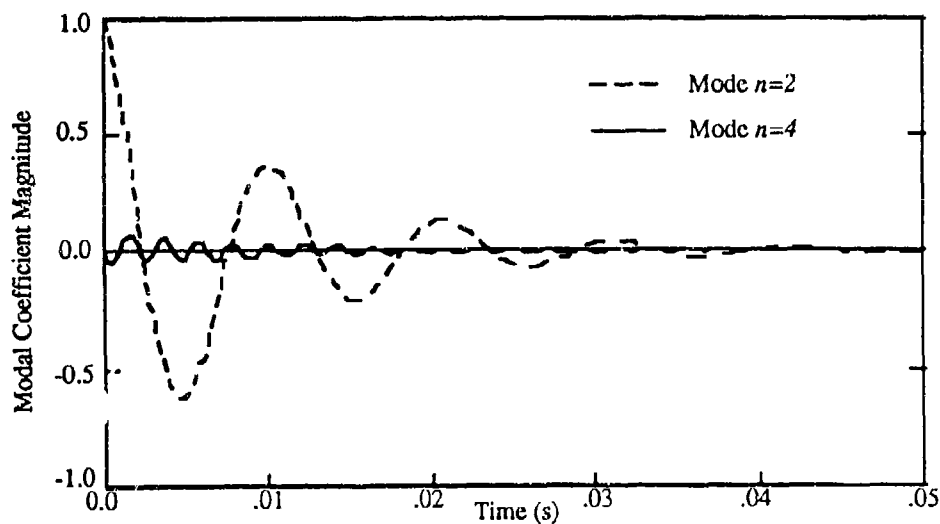


Figure 3. Transient response of modes  $n=2$  and  $n=4$ . ( $M=2$ ,  $-4 \leq n \leq 4$ ,  $\alpha=100$ ).

Figures 2 and 3 demonstrate two key properties of control spillover. 1) If the decay rate,  $\alpha$ , is reasonably low, the effect of the control spillover is small. 2) The modes which are excited by control spillover are dampened out along with the controlled modes.

Figure 4 shows the effect of the control system on the mode one order above the highest mode targeted by the control system. Once again, six control forces are used and the expansion of  $w(\theta, t)$  is truncated at  $n=\pm 4$ . The six control forces control the modes from  $n=-2$  to  $n=2$ . The control forces are evenly spaced beginning at an angle  $\gamma_0=\pi/4$ . Note that the real deformation pattern resulting from modes  $n=\pm 3$  has six evenly spaced nodes on the ring. Initially, the cosine part of mode  $n=3$  is excited. It then decays as the controller shifts some of its energy into the sine part. After about .015s, the magnitudes of the sine part and the cosine part are about the same and there is little change from that point on. What has happened is that the control system has shifted the nodes of the real deformation pattern resulting from modes  $n=\pm 3$  so that they lie very near the control forces. Hence, the control forces can no longer affect modes  $n=\pm 3$ . This phenomenon referred to as mode rotation is unique to elastic rings.

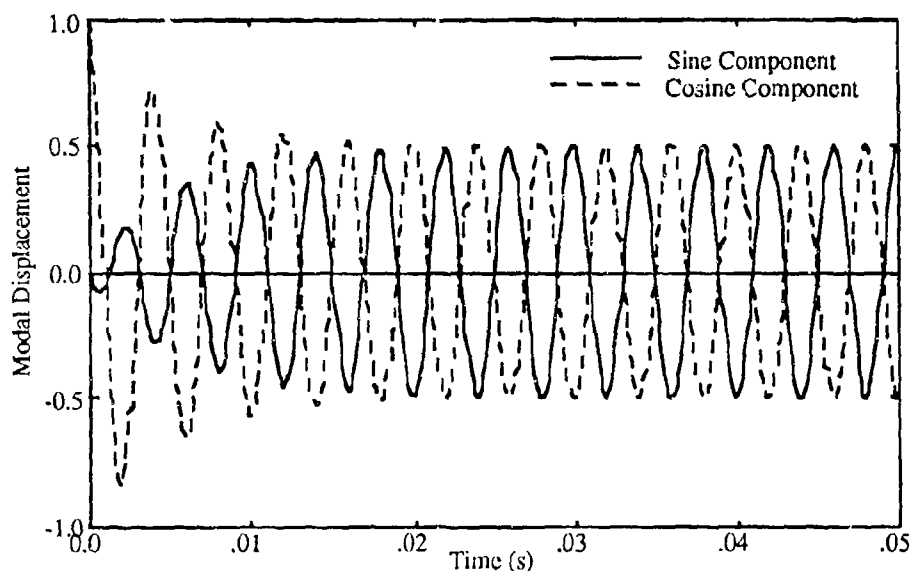


Figure 4. Transient response of modes  $n=-3$  and  $n=3$ . ( $M=2$ ,  $-4 \leq n \leq 4$ ,  $\alpha=100$ ).

#### Steady-State Solutions

As a final exercise, the steady-state response of the system is examined. A unit point force located at  $\theta=0$  with a harmonic time dependence is used as the excitation. Once again, six evenly spaced control forces starting at an angle  $\gamma_0=\pi/4$  are used. The response of the controlled and uncontrolled systems is calculated from 10hz to 1600hz as shown in Figure 5. A spatial average of the kinetic energy along the ring is used as a performance criterion. The results show that the effect of the control system is minimal when the system is off resonance. At resonant frequencies where the system is essentially damping controlled, the control system provides damping and is therefore very effective. Also note that the control has no effect on the modes  $n=\pm 3$  since the control forces are located at the nodes of the associated deformation pattern.

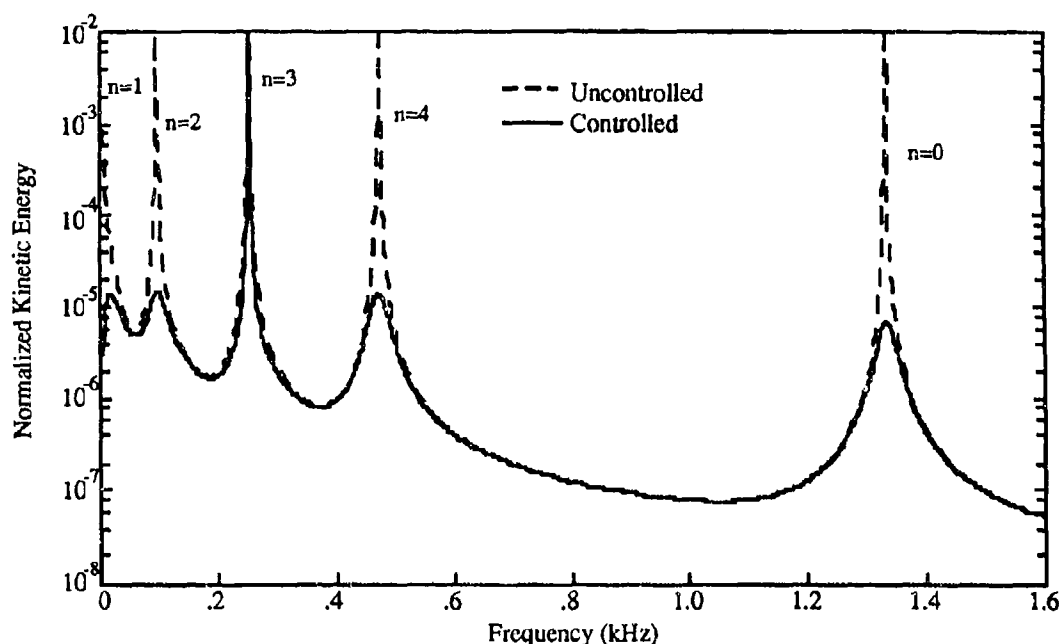


Figure 5. Steady-state response with and without control. ( $M=2$ ,  $-4 \leq n \leq 4$ ,  $\alpha=100$ ).

## Conclusions

We have presented a study of uniform modal damping of the  $2M+1$  lowest modes of elastic rings by using velocity and position feedback to  $2(M+1)$  control forces evenly spaced around the ring. The study makes use of the natural control theory and extends the node control theorem for uniform beams to uniform rings. The control system is shown to provide uniform damping to the controlled modes of the ring and preserve the mode shapes and natural frequencies of the controlled modes. Control spillover of the system has been found to have relatively little effect. Numerical simulations have demonstrated that the control system is effective in damping out transient vibrations of the ring and attenuates the resonant steady-state vibrations as well. The paper has also illustrated the elastic ring phenomenon of mode rotation.

## References

1. Silverberg, L., "Uniform damping control of spacecraft," *Journal of Guidance, Control and Dynamics*, **9**:2, 1986, 221-227.
2. Silverberg, L. and M. Morton, "On the nature of natural control," *Journal of Vibration, Stress, and Reliability in Design*, **111**:October, 1989, 412-422.
3. L. Weaver, . and L. Silverberg, "Node control of uniform beams subject to various boundary conditions," *Journal of Applied Mechanics*, **59**:December, 1992, 983-990.
4. Graff, K. F., Wave motion in elastic solids, Ohio State University Press, Columbus, Ohio, 1975.

**Two-DOF Small Structures-Optics-Controls-System  
A Parametric Study**

by

**Ernest B. Paxson, Jr**

**Technology Applications, Inc (TAI)  
Phillips Laboratory Supercomputer Center  
Kirtland AFB, NM**

**Paxson Engineering Services (1)  
MZA Associates, Inc  
Albuquerque, NM**

**ABSTRACT**

In order to study and understand the basic issues bearing on the behavior of three-discipline structures-optics-controls systems (SOCS), a small two-DOF SOCS was devised. It comprises two mirror masses (in piston motion) supported by their respective spring and viscous damper. One of the mirrors is a controlled mirror to which is also connected a voice coil actuator. The other mirror is excited by a disturbance (step function) force. A laser beam traverses these two mirrors by reflectance and enters a sensor, which detects translational excursion of the beam caused by movement of either of the two forementioned mirrors. An error signal from this sensor goes to the controller, which sends a correction signal to the voice coil actuator, thus using the controlled mirror to bring the laser beam back on target.

To develop a controller algorithm that completely zeroes out the beam translation error requires the controller to use not only displacement feedback but also velocity and acceleration feedback. In this way the controlled mirror can be made to exactly mimic the reverse of the effect of the disturbed mirror at the sensor thus zeroing out the beam translational error. One might suspect that the controller is always playing catch-up if only displacement feedback to a force actuator is used, since displacement lags acceleration by 180 degrees in a vibrating system. Response curves of the Two-DOF SOCS are included for (1) displacement feedback, (2) displacement and velocity feedback, and (3) displacement, velocity, and acceleration feedback in the control system.

(1) 4105 Shiloh Drive, NE; Albuquerque, NM 87111-4136; (505) 292-3841

## Two-DOF Small Structures-Optics-Controls System (SOCS) A Parametric Study

### I. Introduction

In order to study and understand the basic issues bearing on the behavior of a three-discipline structures-optics-controls system (SOCS), a small two-DOF SOCS was devised. It comprises two mirror masses (in piston motion) supported by their respective spring and viscous damper. One of the mirrors is a controlled mirror to which is also connected a voice coil actuator. The other mirror is excited by a disturbance (step function) force. A laser beam traverses these two mirrors by reflectance and enters a sensor, which detects translational excursion of the beam caused by movement of either of the two forementioned mirrors. An error signal from this sensor goes to the controller, which sends a correction signal to the voice coil actuator, thus using the controlled mirror to bring the laser beam back on target.

### II. Dynamic Equilibrium Equations

Illustrated in Figure 1 is a sketch of the Two-DOF SOCS.

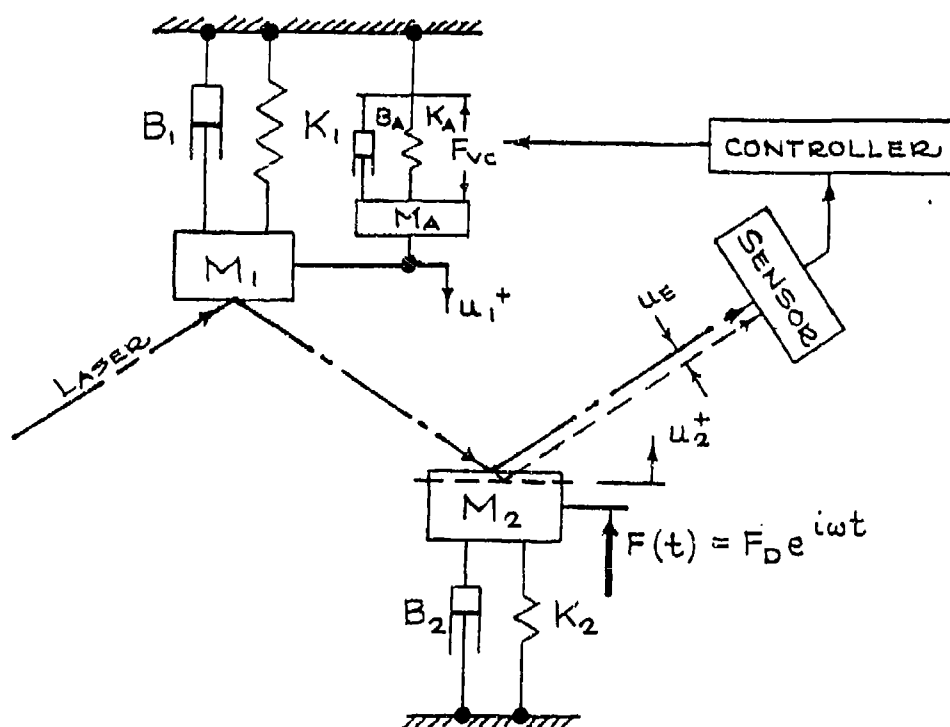


Figure 1 - Sketch of Two-DOF Structures-Optics-Controls-System (SOCS)



The  $M_1$  mass represents the controlled mirror and  $M_2$  is the mass of the disturbed mirror. Each mirror has a single degree-of-freedom (DOF) translation normal to the reflective surface (sometimes called piston motion) -  $u_1$  for  $M_1$  and  $u_2$  for  $M_2$ . Structural support for  $M_1$  and  $M_2$  is provided by springs  $K_1$  and  $K_2$ , respectively, and dampers  $B_1$  and  $B_2$ , respectively. The voice coil actuator, attached rigidly to  $M_1$ , has effector end mass  $M_A$  along with actuator spring  $K_A$  and damper  $B_A$ . It exerts a voice coil force,  $F_{vc}$  on mass  $M_A$  when commanded. The external disturbance force,  $F(t)$ , is applied to mass  $M_2$ . For this study the disturbance was a unit step force ( $F_D = 1$ ) applied for the first 0.2 sec of a 0.6 sec time window after which the disturbed mirror was in free vibration.

$$(M_1 + M_A)\ddot{u}_1 + (B_1 + B_A)\dot{u}_1 + (K_1 + K_A)u_1 = F_{vc} \quad (1)$$

$$M_2\ddot{u}_2 + B_2\dot{u}_2 + K_2u_2 = F_D e^{i\omega t} \quad (2)$$

for which the following structural parameter values were chosen

$K_1 = 160 \text{ lb/in}$	$K_A = 40 \text{ lb/in}$	$K_2 = 400 \text{ lb/in}$
$B_1 = 0.40 \text{ lb-sec/in}$	$B_A = 0.20 \text{ lb-sec/in}$	$B_2 = 0.10 \text{ lb-sec/in}$
$M_1 = 0.0253 \text{ lb-sec}^2/\text{in}$	$M_A = 0.0100 \text{ lb-sec}^2/\text{in}$	$M_2 = 0.0253 \text{ lb-sec}^2/\text{in}$

These values give a natural frequency for  $M_1$  of  $f_1 = 10.0 \text{ Hz}$  and for  $M_2$ ,  $f_2 = 20.0 \text{ Hz}$

### III. Sensor/Corrector Equations

The sensor in Figure 1 picks up the translational movement or LOS error of the laser beam, which is  $u_E$ . For mirror 1

$$u_{E1} = A_1 u_1 \quad \dot{u}_{E1} = A_1 \dot{u}_1 \quad \ddot{u}_{E1} = A_1 \ddot{u}_1 \quad (3)$$

where  $u_{E1}$  is the LOS error caused by movement of mirror 1 by itself. In addition,  $du_{E1}/dt$  and  $d^2u_{E1}/dt^2$  are the error velocity and error acceleration, respectively, due to the movement of mirror 1.  $A_1$  is the optical sensitivity coefficient of mirror 1. It is the ratio of (the movement of the laser beam as it impinges the sensor) to (the movement of mirror 1). For small displacements of plane mirrors the optical sensitivity coefficients are constant. For a particular arrangement of  $M_1$  and  $M_2$  (which was not as shown in Figure 1)  $A_1$  was calculated to be 1.732 in of beam error/in of  $M_1$  displacement. For mirror 2,  $A_2$  was computed to be 1.000 in of beam error/in of  $M_2$  displacement. Hence,

$$u_{E2} = A_2 u_2 \quad \dot{u}_{E2} = A_2 \dot{u}_2 \quad \ddot{u}_{E2} = A_2 \ddot{u}_2 \quad (4)$$

where  $u_{E2}$  is the LOS error caused by the movement of mirror 2 by itself. The total LOS beam error, then, would be

$$u_E(t) = u_{E1}(t) + u_{E2}(t) \quad \text{or} \quad u_E(t) = A_1 u_1(t) + A_2 u_2(t) \quad (5)$$

The correction necessary to zero out  $u_{E1}$  and  $u_{E2}$  will be exactly the negative of these two quantities. Hence,

$$u_{cor1} = -u_{E1} \quad \dot{u}_{cor1} = -\dot{u}_{E1} \quad \ddot{u}_{cor1} = -\ddot{u}_{E1} \quad (6)$$

$$u_{cor2} = -u_{E2} \quad \dot{u}_{cor2} = -\dot{u}_{E2} \quad \ddot{u}_{cor2} = -\ddot{u}_{E2} \quad (7)$$

Since mirror 1 is being used to correct the LOS beam error, we call its correction displacement  $u_{1c}$ . At the sensor  $u_{1c}$  will appear as  $A_1 u_{1c}$ , therefore the  $M_1$  correction displacements for the error contributions of each mirror movement will be

$$u_{1c1} = \frac{u_{cor1}}{A_1} \quad \dot{u}_{1c1} = \frac{\dot{u}_{cor1}}{A_1} \quad \ddot{u}_{1c1} = \frac{\ddot{u}_{cor1}}{A_1} \quad (8)$$

$$u_{1c2} = \frac{u_{cor2}}{A_1} \quad \dot{u}_{1c2} = \frac{\dot{u}_{cor2}}{A_1} \quad \ddot{u}_{1c2} = \frac{\ddot{u}_{cor2}}{A_1} \quad (9)$$

#### IV. Controller Equations

After some thought and inspiration from a greater Source than the author, the following error correction equation formulated:

$$S_e = a_1 u_{1c1} + b_1 \dot{u}_{1c1} + c_1 \ddot{u}_{1c1} + a_2 u_{1c2} + b_2 \dot{u}_{1c2} + c_2 \ddot{u}_{1c2} \quad (10)$$

where  $a_1$ ,  $b_1$ ,  $c_1$ , and  $a_2$ ,  $b_2$ ,  $c_2$  are yet-to-be-determined coefficients. Plugging Eqns (3),(4) and (6),(7) for  $u_{1c1}$  and  $u_{1c2}$  respectively, one will obtain Eqn (10) in terms of  $u_1$  and  $u_2$ .

$$S_e = -(a_1 u_1 + b_1 \dot{u}_1 + c_1 \ddot{u}_1) - \frac{A_2}{A_1} (a_2 u_2 + b_2 \dot{u}_2 + c_2 \ddot{u}_2) \quad (11)$$

At this point in the paper the reader needs to be cautioned. If we assume that we have perfect sensor, corrector, and controller components; then, the  $u_1$  and  $u_2$  displacement signals (as well as  $du_1$ ,  $du_2$  and  $d^2u_1$ ,  $d^2u_2$  w.r.t. time) in Eqn (11) above as they have gone through these components will have no amplitude variation, signal distortion, or phase lag. Such is not the case with real world components, even though the mathematics describing our ideal two-DOF SOCS implies this; hence, the reader needs to keep this in mind as he examines the following results.

Next, we assume that the voltage output of the controller is proportional to the error correction signal, i.e.,

$$E_e = G_e S_e \quad \text{where } G_e \text{ is a gain factor} \quad (12)$$

## V. Actuator Equation

Since  $K_A$ ,  $M_A$ , and  $B_A$  became part of the controlled mirror ( $M_1$ ) dynamic equilibrium equation, we need to add a force vs voltage relation.

$$F_{vc} = C_v E_u \quad (13)$$

In an actual voice coil actuator the force is proportional to the current rather than the voltage as indicated in Eqn (13). Also neglected were the electromagnetic effects, which in an actual physical system must be included. In future studies as the SOCS becomes more complicated, the author wishes to consider how the feedback signals are modified as they pass through more realistic sensor/controller/actuator subsystems.

## VI. System Equations

Pictured in Figure 2 is an equation block diagram for the two-DOF SOCS. One might note that the 2nd order Eqns (1) and (2) for each mirror have been broken down into two first order integrator blocks with the component spring and damper force blocks included. Putting the equations in this format allowed pulling off the velocity and acceleration signals for feedback purposes. Having the system equations displayed in block format allows for easy input to MATRIXx for time domain simulation.

During the early time domain simulations of the two-DOF SOCS a Kutta-Merson time integration technique was used. An examination of the results revealed that a time-step error was getting into the beam error response. As one studies Figure 2, he or she may see that the new acceleration for  $M_1$  is based on an  $F_{vc}$  that is computed from a feedback acceleration generated during the previous time step. Of course, decreasing the integration time step decreased the calculated beam error. MATRIXx also has what it calls a "stiff equation solver", which corrected the time step error, but one has to be careful when it is used to simulate real control systems.

Gathering Eqns (11) and (12) one may write  $F_{vc}$  from Eqn (13) in terms of  $u_1$  and  $u_2$  as

$$F_{vc} = -C_v G_u [(a_1 u_1 + b_1 \dot{u}_1 + c_1 \ddot{u}_1) + \frac{A_2}{A_1} (a_2 u_2 + b_2 \dot{u}_2 + c_2 \ddot{u}_2)] \quad (14)$$

Substituting Eqn (14) into Eqn (1) for  $F_{vc}$  results in

$$(M_1 + M_A + C_v G_u c_1) \ddot{u}_1 + (B_1 + B_A + C_v G_u b_1) \dot{u}_1 + (K_1 + K_A + C_v G_u a_1) u_1 = -C_v G_u \frac{A_2}{A_1} (a_2 u_2 + b_2 \dot{u}_2 + c_2 \ddot{u}_2) \quad (15)$$

for the controlled mirror,  $M_1$ . Having the feedback displacement, velocity, and acceleration terms on the LHS of Eqn (15) is another way of eliminating the time step error mentioned in the previous paragraph; however, it must be reiterated that Equation (15) does not permit any modification of the feedback signals as they pass through the sensor/controller/actuator subsystem, except algebraic gain factors. Recalling Eqn (2) for the disturbed mirror 2 gives

$$M_2 \ddot{u}_2 + B_2 \dot{u}_2 + K_2 u_2 = F_D e^{i\omega t} \quad (16)$$

The two-DOF SOCS equations have been reduced to two Eqns (15) and (16) and two unknowns  $u_1$  and  $u_2$ .

HBC-6

Examination of control parameters  $a_1, b_1, c_1, a_2, b_2, c_2$  (which are yet undetermined) in Eqn (15) will give us some insight as to their effect on system behavior. The parameters  $C_v, G_w, a_1, b_1, c_1$  give one the capability of actually modifying the mass, damping, and stiffness of the controlled mirror ( $M_1$ ) and thus change its dynamic characteristics. In addition,  $C_v, G_w, a_2, b_2, c_2$  allow one to tailor the response of the disturbed mirror ( $M_2$ ) in controlling the actuator force applied to  $M_1$ . With these ideas mind, one can study the effect of varying these parameters.

For the controls-OFF situation ( $a_1 = a_2 = b_1 = b_2 = c_1 = c_2 = 0$ ) the response of  $M_2$  and the beam error as calculated in MATRIXx are presented in Figures 3 and 4. Since the optical sensitivity coefficient of  $M_2$  is  $A_2 = 1.000$ , the beam error  $u_E$  will have the same value as the displacement of  $M_2$ . The maximum uncontrolled beam error was about  $u_E = 0.005$ , and this gives an error value with which to compare the controlled beam error using various strategies.

#### VII. Selection of Values for Control Parameters $a_1$ and $a_2$

In this situation we are trying to control a force (i.e., acceleration) input to  $M_1$  via a displacement signal, which, in a vibrating system, is already 180 degrees behind acceleration. Therefore, under these conditions our control system is always trying to play "catch-up." As one goes through the subsequent equations, he or she will notice that we can play "catch-up" faster and reduce the beam error but never quite fast enough to zero it out.

Starting with Eqn (15) and considering only  $a_1$  and  $a_2$ , we have

$$M_{T1}\ddot{u}_1 + B_{T1}\dot{u}_1 + (K_{T1} + C_v G_w a_1)u_1 = -C_v G_w \frac{A_2}{A_1} a_2 u_2 \quad (17)$$

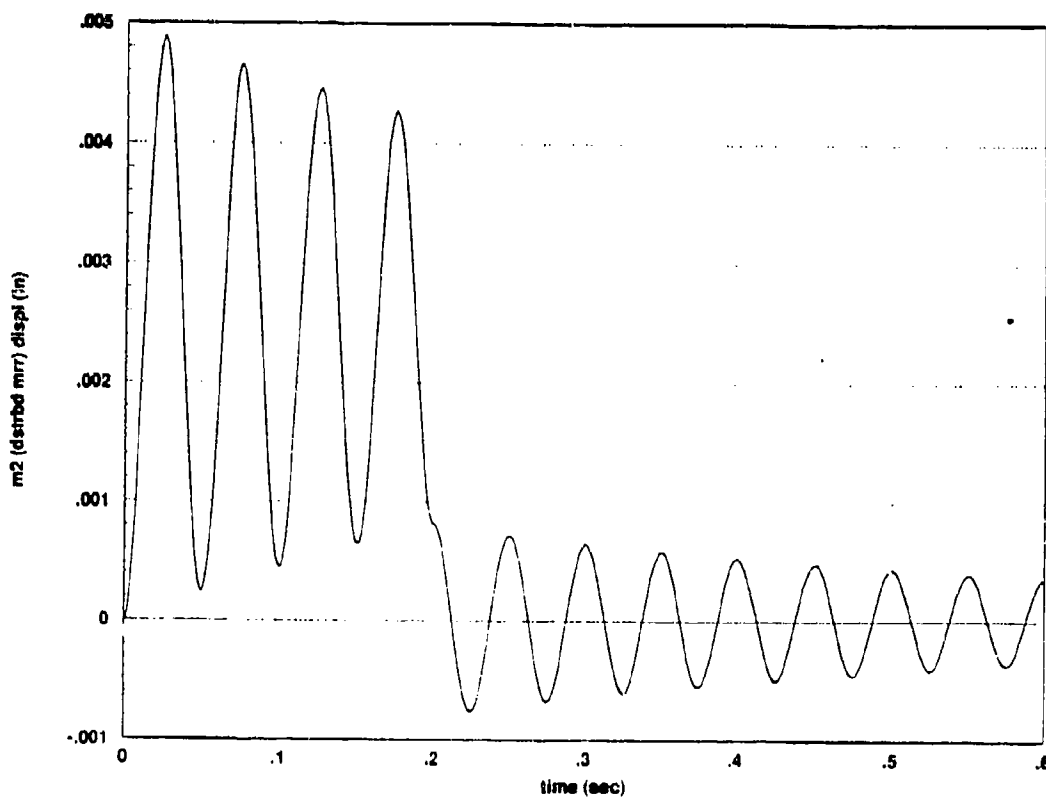
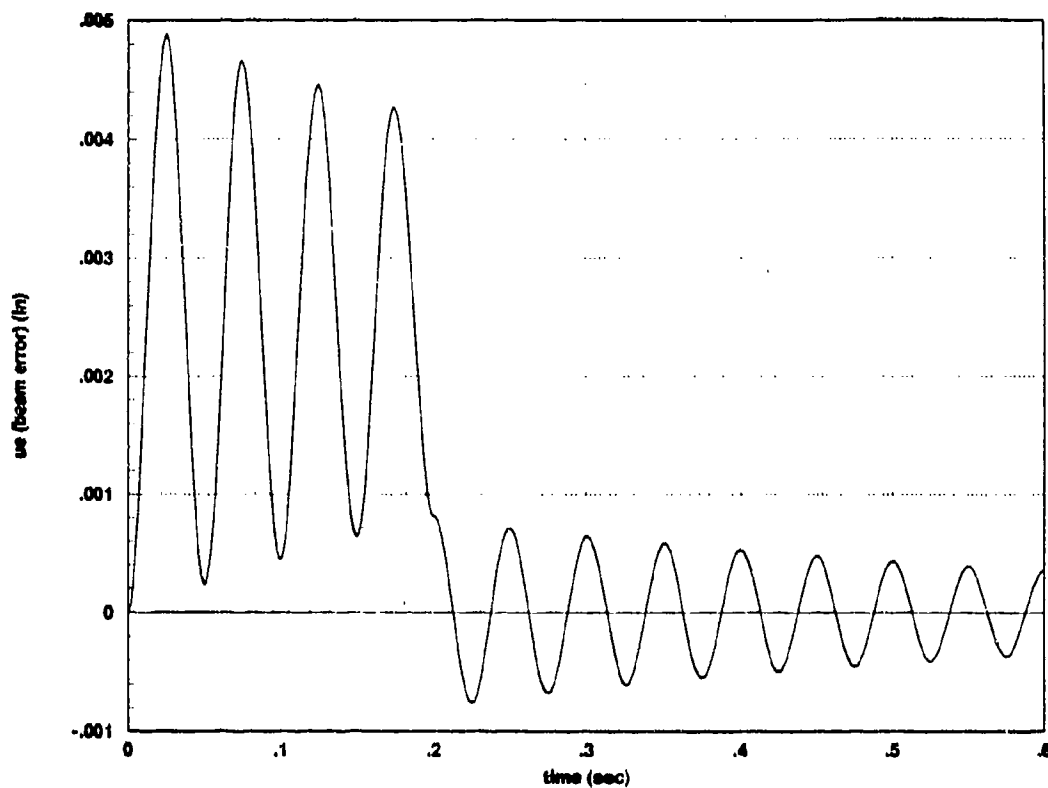
where  $M_{T1} = M_1 + M_A$ ;  $B_{T1} = B_1 + B_A$ ;  $K_{T1} = K_1 + K_A$   
The solution of Eqn (16) for  $M_2$  will be

$$u_2(t) = F_D T_2(\omega) e^{i(\omega t - \varphi_2)} \quad (18)$$

where

$$T_2(\omega) = \frac{1}{\sqrt{(K_2 - M_2 \omega^2)^2 + B_2^2 \omega^2}} \quad (19)$$

$$\tan \varphi_2(\omega) = \frac{B_2 \omega}{K_2 - M_2 \omega^2} \quad (20)$$



Substitution of Eqn (18) into Eqn (17) will yield

$$M_{T1}\ddot{u}_1 + B_{T1}\dot{u}_1 + (K_{T1} + C_v G_u a_1)u_1 = -C_v G_u \frac{A_2}{A_1} a_2 F_D T_2 e^{j(\omega - \varphi_2)} \quad (21)$$

the solution of which will be

$$u_1(t) = -C_v G_u \frac{A_2}{A_1} a_2 T_2 T_1 F_D e^{j(\omega - \varphi_1 - \varphi_2)} \quad (22)$$

where

$$T_1(\omega) = \frac{1}{\sqrt{(K_{T1} + C_v G_u a_1 - M_{T1}\omega^2)^2 + (B_{T1}\omega)^2}} \quad (23)$$

$$\tan \varphi_1(\omega) = \frac{B_{T1}\omega}{K_{T1} + C_v G_u a_1 - M_{T1}\omega^2} \quad (24)$$

Recalling Eqn (5), the beam LOS error, we have

$$u_E = A_1 u_1 + A_2 u_2 \quad (25)$$

Plugging Eqns (18) and (22) into the beam error equation results in

$$u_E = [-C_v G_u a_2 T_1 e^{-j\varphi_1} + 1] A_2 T_2 F_D e^{j(\omega - \varphi_2)} = 0 \quad (26)$$

when set equal to zero yields

$$C_v G_u a_2 = \frac{1}{T_1} e^{j\varphi_1} \quad (27)$$

for which the magnitude of  $C_v G_u a_1$  is  $1/T_1$  or

$$|C_v G_u a_2| = \sqrt{(K_{T1} + C_v G_u a_1 - M_{T1}\omega^2)^2 + (B_{T1}\omega)^2} \quad (28)$$

Eqn (28) tells us that  $a_2$  is dependent on frequency. Since most disturbances have many frequencies, not to mention the natural frequencies of the system, it would be difficult to settle on the best value of  $a_2$ . One can make  $a_2$  somewhat independent of frequency by recalling Eqn (24) for the phase angle of mirror 1. If we choose

$$C_v G_u a_2 > K_{T1} - M_{T1}\omega^2 \text{ and } B_{T1}\omega \text{ then } \varphi_1 \rightarrow 0 \quad (29)$$

Applying this condition to Eqn (27) or (28) gives the following result:

$$C_v G_u a_2 \approx C_v G_u a_1 \quad (30)$$

For the control parameters set at  $a_1 \approx a_2 = 1.0$ ,  $C_v = 1.0$ , and  $G_u = 30000$ , the time domain response curves for  $M_1$ ,  $M_2$ , beam error, and  $F_{wc}$  are presented in Figures 5, 6, 7, 8, respectively. One should note that the maximum beam error in Figure 7 was close to  $u_B = 0.00015$ , which was 1/33 of the uncontrolled beam error. The maximum actuator force, shown in Figure 8, was about  $F_{wc} = 2.5$  lbs. This will decrease as the control algorithm improves. While values of  $G_u$  higher than 30000 are possible, the integration time step of 0.0001 sec will have trouble resolving the higher frequency response of Mirror 1 (the controlled mirror) caused by the augmented "spring stiffness" due to the feedback displacement control signal.

#### VIII. Selection of Values for Control Parameters $a_1$ , $a_2$ , $b_1$ , $b_2$

In trying to control  $M_1$  with a velocity signal, which is only 90 degrees behind acceleration, one would expect that we should do better in correcting the beam error. With  $a_1$ ,  $b_1$ ,  $a_2$ , and  $b_2$  not zero, we rewrite Eqn (15) as

$$M_{T1} \ddot{u}_1 + (B_{T1} + C_v G_u b_1) \dot{u}_1 + (K_{T1} + C_v G_u a_1) u_1 = -C_v G_u \frac{A_2}{A_1} (a_2 u_2 + b_2 \dot{u}_2) \quad (31)$$

where  $M_{T1} = M_1 + M_A$ ;  $B_{T1} = B_1 + B_A$ ;  $K_{T1} = K_1 + K_A$   
Recalling the solution for Eqn (16) for  $M_2$ , we have

$$u_2(t) = F_D T_2(\omega) e^{i(\omega t - \phi_2)} \quad (32)$$

For velocity we obtain

$$\dot{u}_2(t) = i\omega F_D T_2(\omega) e^{i(\omega t - \phi_2)} \quad (33)$$

Plugging Eqns (32) and (33) into Eqn (31) gives

$$M_{T1} \ddot{u}_1 + (B_{T1} + C_v G_u b_1) \dot{u}_1 + (K_{T1} + C_v G_u a_1) u_1 = -C_v G_u \frac{A_2}{A_1} T_2 F_D (a_2 + i\omega b_2) e^{i(\omega t - \phi_2)} \quad (34)$$

the solution of which will be

$$u_1(t) = -C_v G_u \frac{A_1}{A_2} T_2 F_D T_1^{(1)} (a_2 + i\omega b_2) e^{i(\omega t - \phi_2 - \phi_1)} \quad (35)$$

where

$$T_1^{(1)}(\omega) = \frac{1}{\sqrt{(K_{T1} + C_v G_u a_1 - M_{T1} \omega^2)^2 + (B_{T1} + C_v G_u b_1)^2 \omega^2}} \quad (36)$$



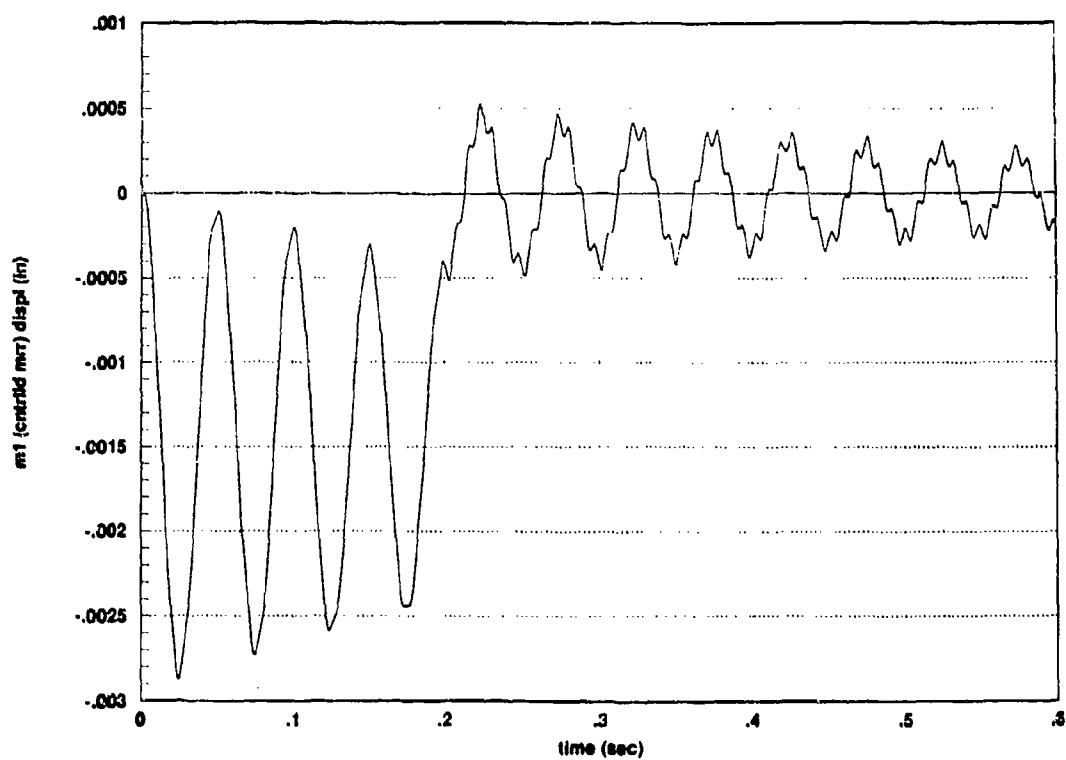


Figure 5 - Two-DOF Struts-Optics-Centris System ( $a_1=a_2=1.0$ ,  $G_u=30000$ )

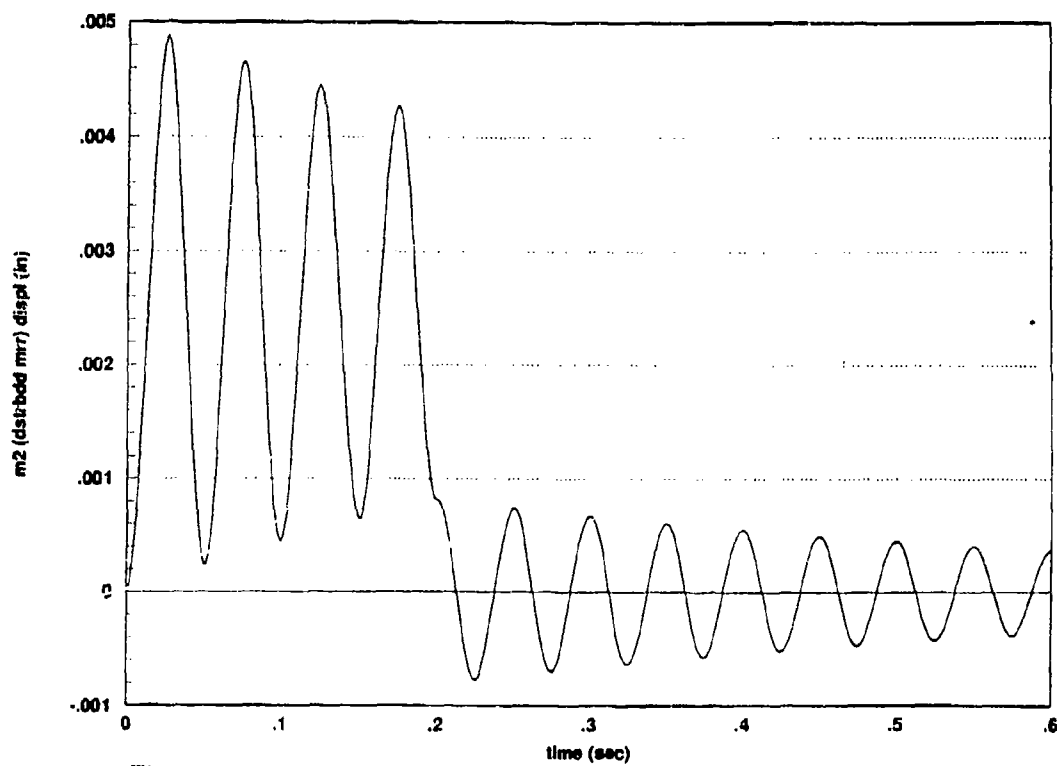


Figure 6 - Two-DOF Struts-Optics-Centris System ( $a_1=a_2=1.0$ ,  $G_u=30000$ )

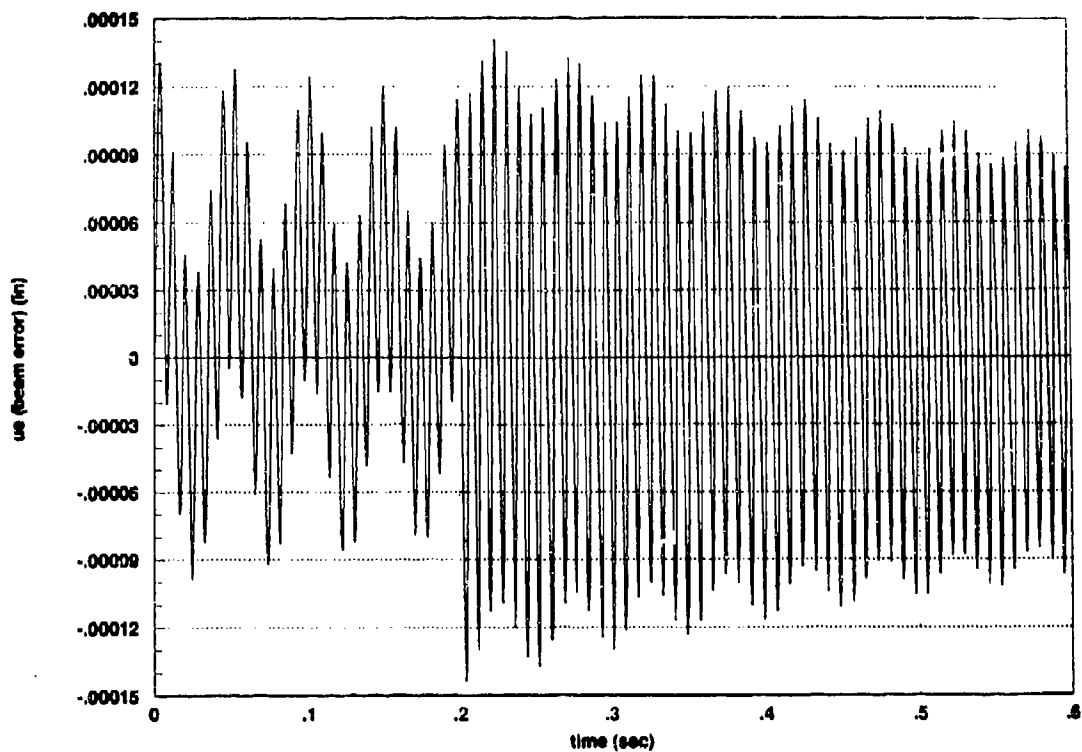


Figure 7 - Two-DOF Strain-Optics-Controls System ( $a_1=a_2=1.0$ ,  $G_u=30000$ )

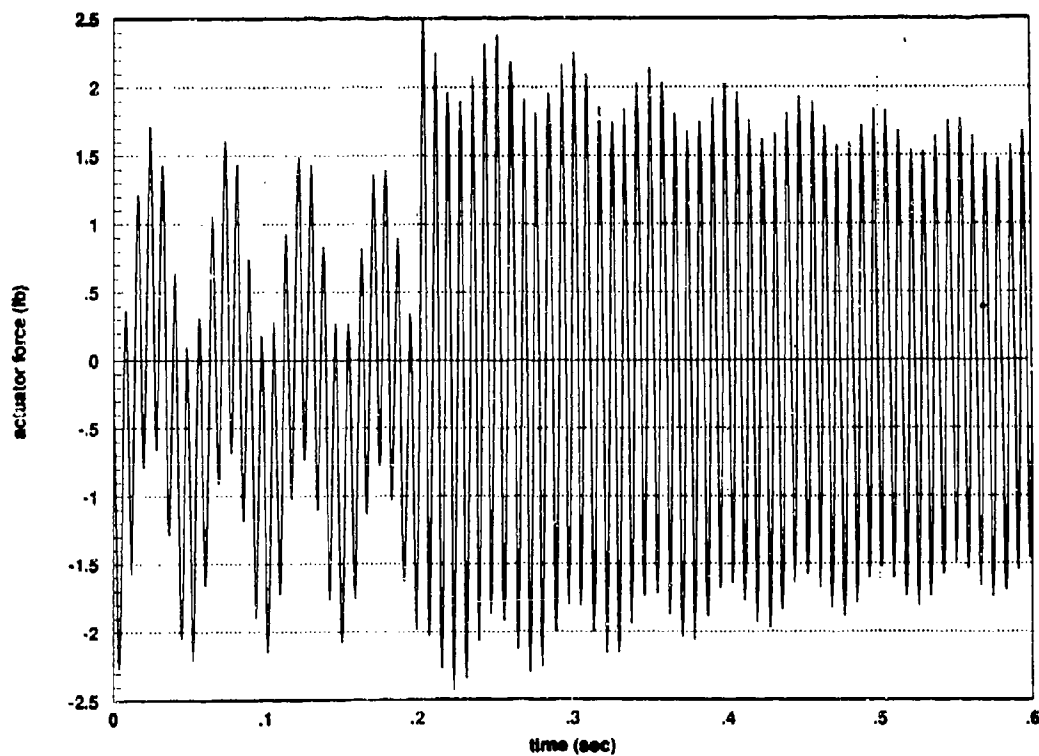


Figure 8 - Two-DOF Strain-Optics-Controls System ( $a_1=a_2=1.0$ ,  $G_u=30000$ )

$$\tan \varphi_1^{(1)} = \frac{(B_{T1} + C_v G_u b_1) \omega}{K_{T1} + C_v G_u a_1 - M_{T1} \omega^2} \quad (37)$$

Substituting for  $u_1$  and  $u_2$  in the beam error Eqn (25), we obtain

$$u_2 = [-C_v G_u T_1^{(1)} (a_2 + i \omega b_2) e^{-i \varphi_1} + 1] A_2 F_D T_2 e^{i(\omega - \varphi_2)} = 0 \quad (38)$$

Solving Eqn (38) for  $a_2$  and  $b_2$  on the LHS, we arrive at

$$C_v G_u \sqrt{a_2^2 + \omega^2 b_2^2} = \frac{1}{T_1^{(1)}} e^{i(\varphi_1 - \varphi_2)} \quad (39)$$

where

$$\tan \varphi_c = \frac{\omega b_2}{a_2} \quad (40)$$

for which the magnitude

$$|C_v G_u \sqrt{a_2^2 + \omega^2 b_2^2}| = \sqrt{(K_{T1} + C_v G_u a_1 - M_{T1} \omega^2)^2 + (B_{T1} + C_v G_u b_1)^2 \omega^2} \quad (41)$$

Eqn (41) tells us the  $a_2$  and  $b_2$  are frequency dependent, but there are some things we can do to make  $a_2$  and  $b_2$  somewhat independent of frequency. First we calculate

$$\tan (\varphi_1 - \varphi_c) = \frac{\frac{(B_{T1} + C_v G_u b_1) \omega}{K_{T1} + C_v G_u a_1 - M_{T1} \omega^2} - \frac{\omega b_2}{a_2}}{1 + \frac{(B_{T1} + C_v G_u b_1) b_2 \omega^2}{(K_{T1} + C_v G_u a_1 - M_{T1} \omega^2) a_2}} \quad (42)$$

$$\text{If we choose } \frac{b_2}{a_2} = \frac{B_{T1} + C_v G_u b_1}{K_{T1} + C_v G_u a_1 - M_{T1} \omega^2} \text{ then } \varphi_1 - \varphi_c = 0 \quad (43)$$

$$\text{Next, we select } C_v G_u a_1 > K_{T1} - M_{T1} \omega^2 \text{ and } B_{T1} \omega \quad (44)$$

With this selection and for  $a_1 = 1$ , we arrive at the approximate relation (since  $C_v G_m$  is large) from Eqn (43) of

$$\frac{b_2}{a_2} \approx \frac{b_1}{a_1} \quad (45)$$

If  $a_2 = a_1 = 1$ , then  $b_2 = b_1$ . The first trial values for  $b_1$  and  $b_2$  can be ascertained by calculating the critical damping limit for the controlled mirror,  $M_1$ , considering that stiffness for  $M_1$  has been augmented by  $C_v G_m a_1$ . Thus, one could compute what the augmented critical damping should be by

$$B_{1c} = 2\sqrt{(K_{T1} + C_v G_m a_1)M_{T1}} \quad (46)$$

The control parameters selected for the displacement and velocity feedback case were  $a_1 = a_2 = 1.0$ ;  $b_1 = b_2 = 0.015$ ;  $C_v = 1.0$  and  $G_m = 40000$ . The response curves for the two-DOF SOCS calculated in MATRIXx for the above conditions are shown in Figures 9 through 12. One might note that adding the damping control allowed the gain to be cranked up to  $G_m = 40000$ . Examining the beam error curve in Figure 11 reveals its maximum value to be about  $u_B \approx 0.00003$  in which is  $1/5$  of the beam error in the displacement-feedback-only case and  $1/167$  of the uncontrolled beam error. Also, the maximum actuator force in Figure 12 has been reduced to nearly 1.2 lbs, about  $1/2$  of that in the displacement-feedback only case.

#### IX. Selection of Balanced Values for Control Parameters

If we choose  $c_2 = M_2$ ,  $b_2 = B_2$ ,  $a_2 = K_2$  and  $c_1$ ,  $b_1$ ,  $a_1$  such that  $M_1 + M_A + C_v G_m c_1 = M_2$ ,  $B_1 + B_A + C_v G_m b_1 = B_2$ , and  $K_1 + K_A + C_v G_m a_1 = K_2$ ; then Eqn (15) becomes

$$M_2 \ddot{u}_1 + B_2 \dot{u}_1 + K_2 u_1 = -C_v G_m \frac{A_2}{A_1} (M_2 \ddot{u}_2 + B_2 \dot{u}_2 + K_2 u_2) \quad (47)$$

The reader should note that mirror 1 ( $M_1$ ) has mirror 2's mass, stiffness, and damping parameters. Since the RHS of Eqn (47) has imbedded in it the LHS of the dynamic equilibrium Eqn (2), we can write Eqn (47) as

$$M_2 \ddot{u}_1 + B_2 \dot{u}_1 + K_2 u_1 = -C_v G_m \frac{A_2}{A_1} F_D e^{i\omega} \quad (48)$$

Recalling the solution to Eqn (16) or Eqn (2) for mirror 2, which are Eqns (18), (19), (20), we have

$$u_2(t) = F_D T_2(\omega) e^{i(\omega t - \phi_2)} \quad (49)$$

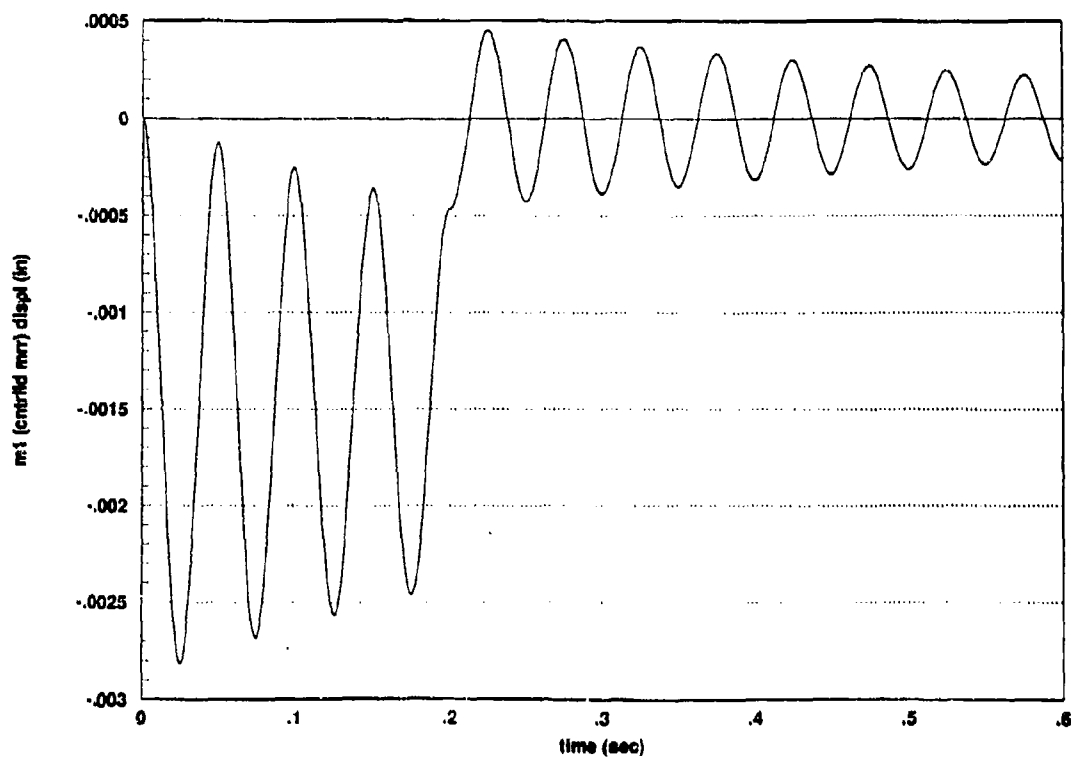


Figure 9 - Two-DOF Stretch-Optics-Cntrl System ( $a_1=a_2=1.0$ ,  $b_1=b_2=0.015$ ,  $G_u=40000$ )

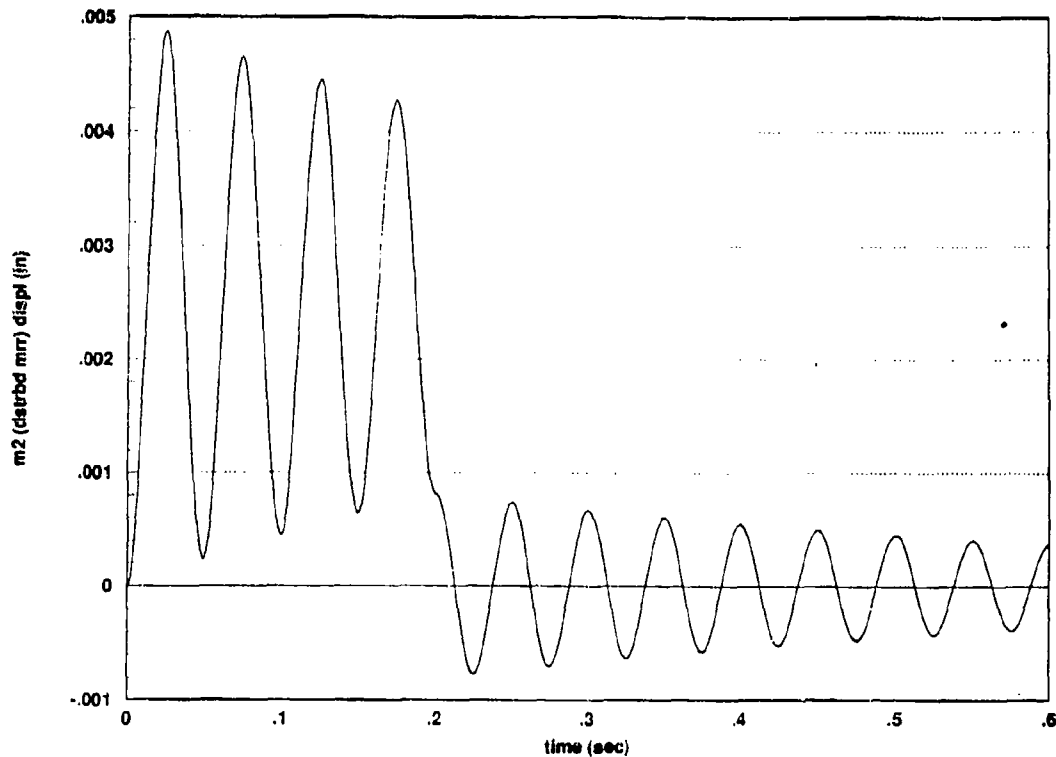


Figure 10 - Two-DOF Stretch-Optics-Cntrl System ( $a_1=a_2=1.0$ ,  $b_1=b_2=0.015$ ,  $G_u=40000$ )

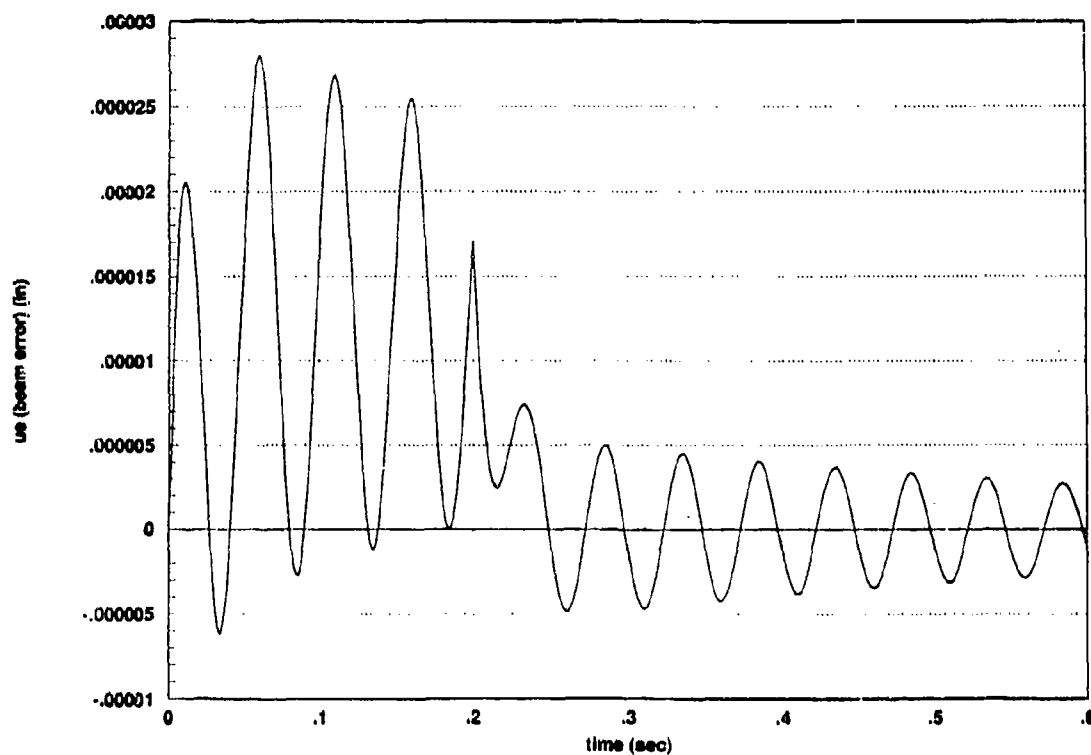


Figure 11 - Two-DOF Struts-Optics-Cntrlr Systm ( $a_1=a_2=1.0$ ,  $b_1=b_2=0.015$ ,  $G_u=40000$ )

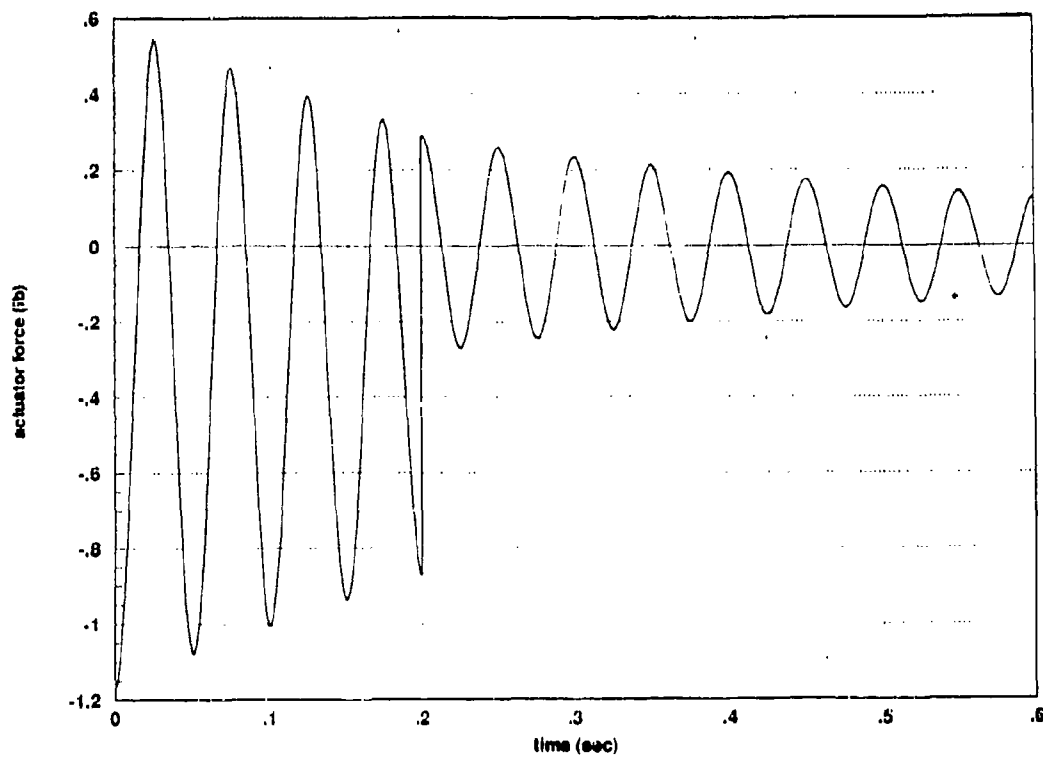


Figure 12 - Two-DOF Struts-Optics-Cntrlr Systm ( $a_1=a_2=1.0$ ,  $b_1=b_2=0.015$ ,  $G_u=40000$ )

The solution for Eqn (48) will be similar (since it has mirror 2's coefficients) except for the  $-A_2/A_1$  factor..

$$u_1(t) = -C_v G_u \frac{A_2}{A_1} F_D T_2(\omega) e^{j(\omega t - \tau_2)} \quad (50)$$

Inserting Eqns (49) and (50) for  $u_1$  and  $u_2$  in the error Eqn (5) or (25) will give

$$u_E = (-C_v G_u + 1) A_2 F_D T_2 e^{j(\omega t - \tau_2)} = 0 \quad (51)$$

For zero beam error it is required that  $C_v G_u = 1$ . For the previously chosen values of  $M_1, M_2, M_A, B_1, B_2$ , etc., the calculated values of the balanced control parameters will be

$$a_1 = 200 \text{ lb/in } b_1 = -0.50 \text{ lb-sec/in } c_1 = -0.0254 \text{ lb-sec}^2/\text{in}$$

$$a_2 = 400 \text{ lb/in } b_2 = 0.10 \text{ lb-sec/in } c_2 = 0.0253 \text{ lb-sec}^2/\text{in}$$

The system response curves for balanced parameters as computed by MATRIXx are included as Figures 13 through 16. In Figure 15 the maximum beam error comes out as machine numerical error.

#### X. Conclusions

On the basis of the results in this paper, it appears that control systems using acceleration feedback should achieve the best performance in correcting beam LOS error. It would be interesting to conduct experiments using the concepts contained herein in order to see how much actual performance of SOCS would be affected by the pass-through of the feedback signals in the sensor/controller/actuator components.

In general, the controller component has to "know" the SOCS well enough to control system response to the desired tolerances. The controller should have at its disposal sufficient DOF in the corrective optics to zero out the LOS beam displacement error coming from the DOF possessed by the disturbed optical components.

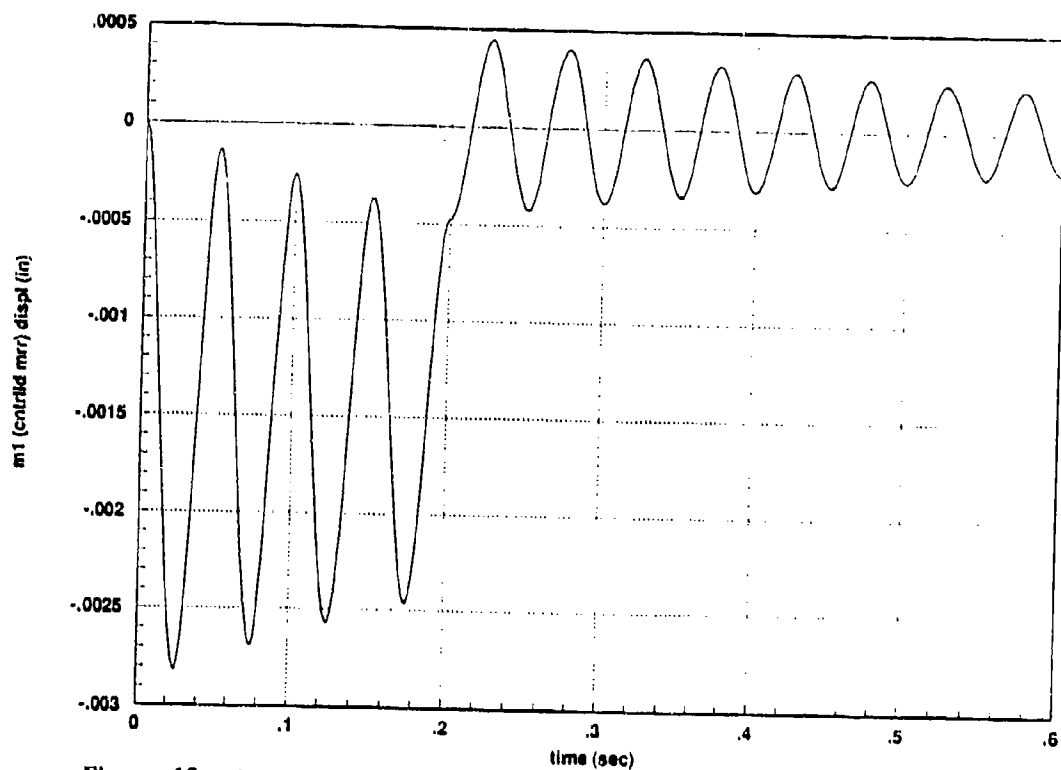


Figure 13 - Two-DOF Strctrs-Optics-Cntrl System (Balanced Cntrl Prmters,  $G_u=1.0$ )

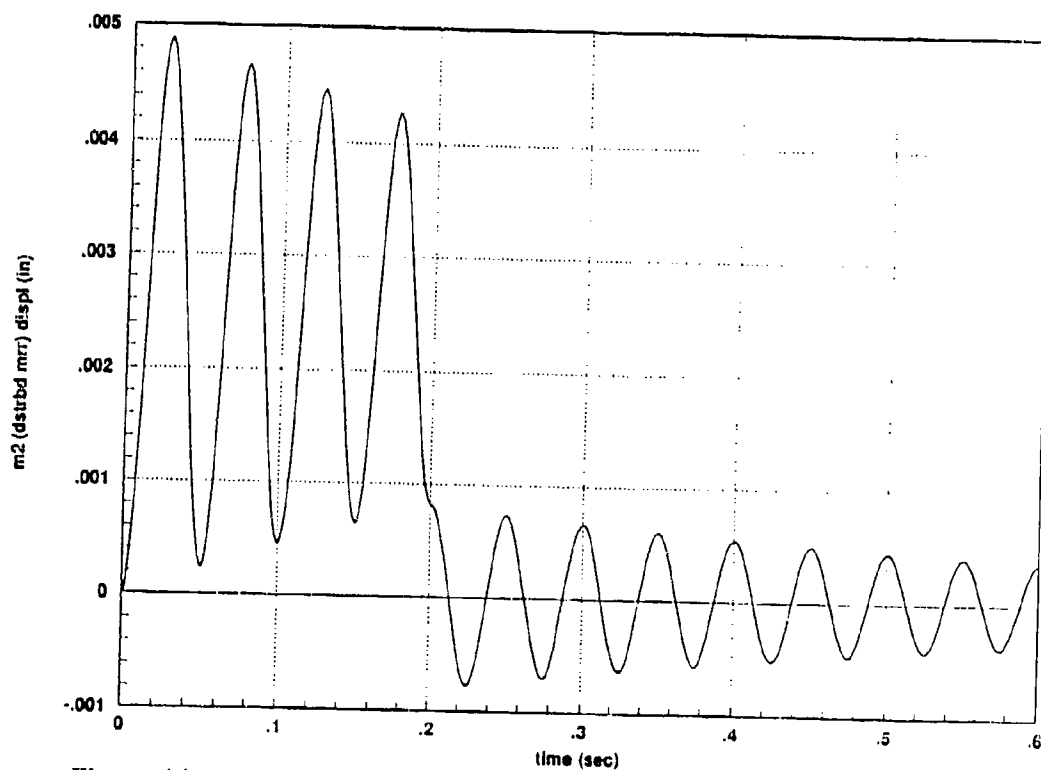


Figure 14 - Two-DOF Strctrs-Optics-Cntrl System (Balanced Cntrl Prmters,  $G_u=1.0$ )



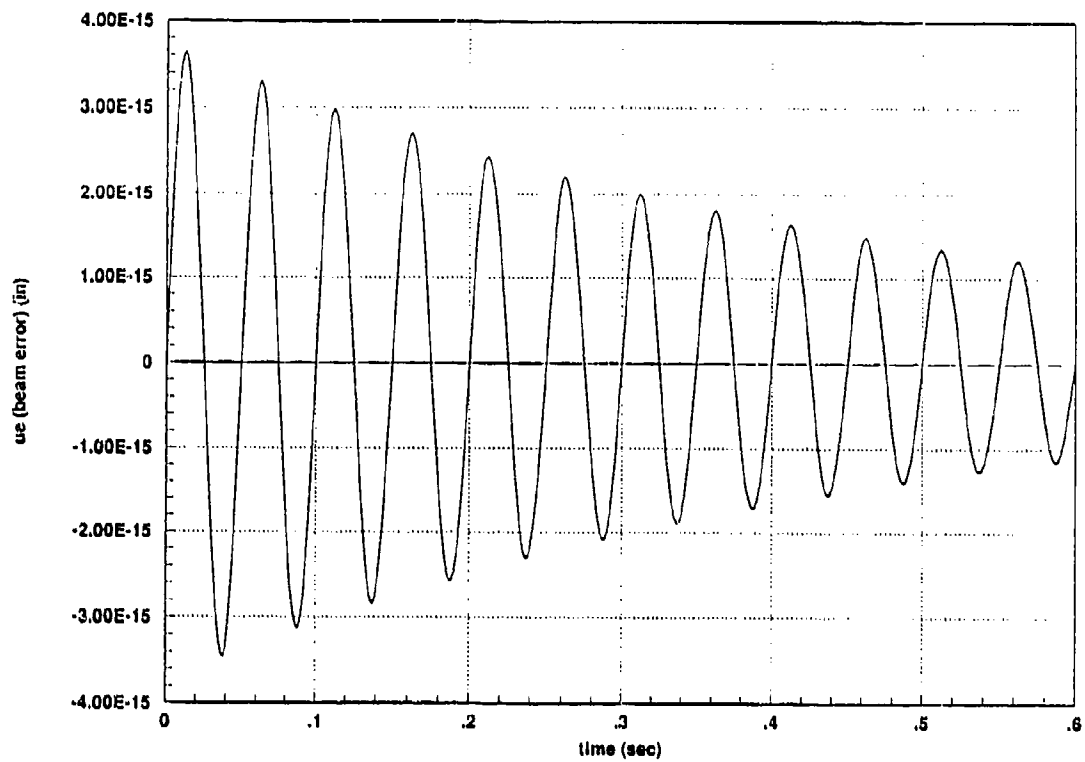


Figure 15 - Two-DOF Struts-Optics-Control System (Balanced Control Parameters,  $G_u=1.0$ )

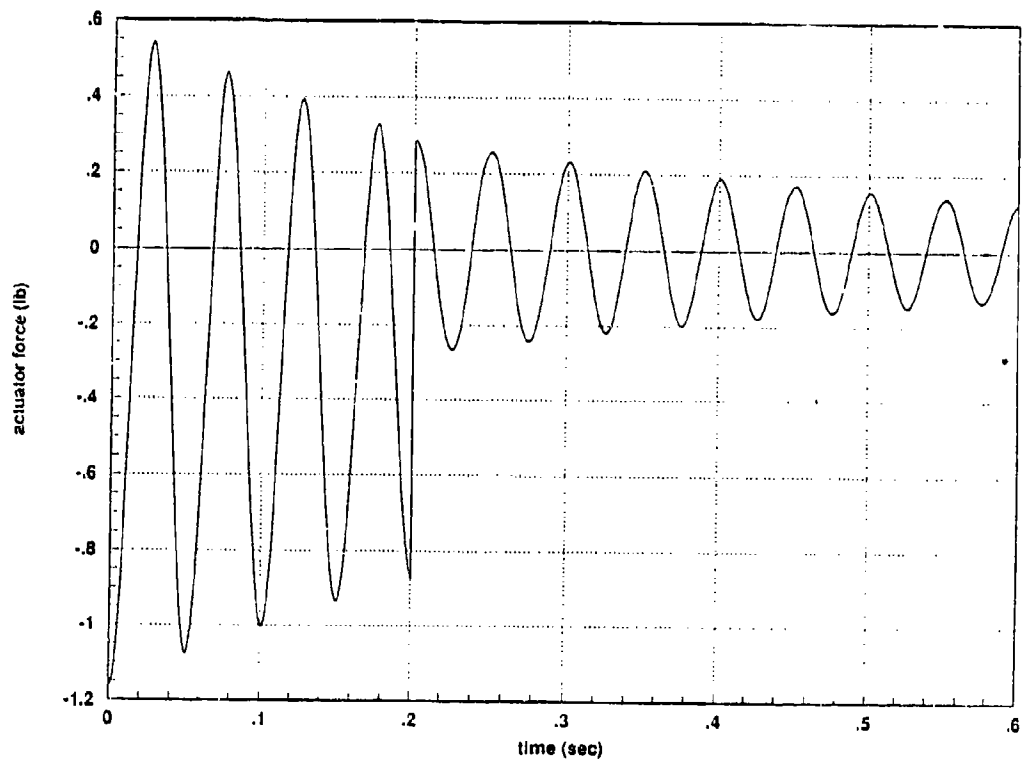


Figure 16 - Two-DOF Struts-Optics-Control System (Balanced Control Parameters,  $G_u=1.0$ )

# DAMPING BEHAVIOR OF 6061 Al/SiC/Gr METAL MATRIX COMPOSITES

R.J. Perez, J. Zhang, M.N. Gungor<sup>1</sup>, E.J. Lavernia  
Materials Science and Engineering  
Department of Mechanical and Aerospace Engineering  
University of California, Irvine, CA 92717

<sup>1</sup>Westinghouse Science and Technology Center  
1310 Beulah Road, Pittsburgh, PA 15235

The damping behavior of a hybrid MMC composed of a 6061 Al matrix with SiC and graphite reinforcement is evaluated. The MMC is processed using spray atomization and co-deposition and the volume fractions of graphite and SiC are each 0.05. The respective contributions to damping of the SiC and graphite reinforcements are evaluated through study of 6061/SiC and 6061/Gr MMCs with volume fractions of 0.05 and 0.10. The damping capacity, measured between 0.1 Hz and 10 Hz at temperatures ranging from 30 to 250°C, is shown to increase with increasing graphite volume fraction. An increase in SiC volume fraction from 0.05 to 0.10, however, is shown to provide damping increases only at high temperature ( $T > 125^{\circ}\text{C}$ ). The elastic modulus is reduced by the addition of graphite but increased by the addition of SiC. The slightly improved damping capacity of the hybrid MMC at room temperature is attributed primarily to dislocations and high intrinsic damping of graphite. At temperatures above approximately 200°C, the relatively large gain in damping capacity is attributed to matrix/reinforcement interfaces, preferred graphite orientation and dislocations.

## I. INTRODUCTION

Structural materials exhibiting high damping characteristics prove useful in the passive attenuation of noise and vibration in structures. This has driven investigators towards the development of materials possessing high damping capacity, along with high stiffness and low density. Due to the demonstrated ability of Al alloys to satisfy the latter two requirements, they have emerged as prime candidates to serve as the basis of such a material.

Although investigators have attempted to improve the damping capacity of Al through the addition of alloying elements<sup>[1]</sup> and heat treatment,<sup>[2,3]</sup> more dramatic gains are believed to be possible through the use of metal matrix composite (MMC) technology. This class of materials, which incorporates a non-equilibrium reinforcing phase into the matrix alloy, may affect damping through the addition of reinforcing phases which exhibit high intrinsic damping or which dramatically modify the matrix microstructure in such a way as to increase damping.

Some of the work on MMCs has proceeded in the direction of continuous fiber reinforcement of Al alloys. Such reinforcement, however, has been shown to increase stiffness with limited or no gain in damping capacity.<sup>[4]</sup> On the other hand, particulate reinforcement has been investigated by several researchers as a means of more directly increasing the damping capacity.<sup>[5,6]</sup> Among the materials which have been used as particulate reinforcements, one of the most widely used is SiC. This ceramic material, when added to the Al matrix, has been shown to provide substantial gains in specific stiffness and strength. Again, however, the increase in damping capacity with the addition of SiC has been reported to be small or nonexistent.<sup>[7,8]</sup>

Another reinforcing material which has been added to Al alloys is graphite. Graphite, unlike SiC, is found to exhibit a relatively high damping capacity when measured in its bulk form.<sup>[9,10]</sup> This is believed to be related to its unique anisotropic crystal structure which allows basal planes to slide easily over one another. Evidence of the efficiency of graphite in providing damping to a matrix metal was provided by Millet et al. in work performed on gray cast iron.<sup>[11]</sup> This showed that the characteristic damping spectrum of gray cast iron matched very closely with that of bulk graphite.

The addition of graphite particulates of various size and crystal structure to Al has been investigated by Zhang et al. and Perez et al.<sup>[12,13]</sup> This work has shown that the graphite particulates may produce a substantial increase in the damping capacity. The elastic modulus, however, was found to decrease with increasing additions of graphite.<sup>[13]</sup>

In light of the very different effects of SiC and graphite on the properties of an aluminum alloy, it seems logical to attempt to combine them. More specifically, the graphite may provide high damping, while SiC can maintain high stiffness. This is the driving force for the study of a hybrid Al/SiC/graphite MMC in the present work.

One consideration in the addition of ceramic reinforcement to an Al matrix is the possibility of reaction between the two when they are combined at high temperature. This, for example, can lead to the formation of carbides at an Al/graphite interface which may, in turn, lead to reduced strength.<sup>[14,15]</sup> In order to avoid such reactions, researchers have used coatings on the reinforcing particulates or relatively low temperature processing techniques, such as powder metallurgy. These processes, however, add significantly to the complexity (and cost) of the resultant material.

One technique which has demonstrated the ability to incorporate ceramic particulates in Al alloys with minimal interfacial reaction is spray atomization and co-deposition.<sup>[16]</sup> This technique, as used by Zhang et. al and Perez et al. in the previously mentioned Al/graphite work, involves the atomization and subsequent deposition of fine droplets of Al alloy.<sup>[12,13]</sup> The ceramic particulates are injected into the metal droplet stream in mid-flight. This rapid solidification technique minimizes the time and temperature under which the matrix and reinforcement must remain in contact.

By allowing the semi-solid droplets to directly collect into a solid form, the handling of fine reactive particulates requisite in powder metallurgical processes is eliminated. Instead, the solid material may be extruded to eliminate porosity present in the as-sprayed condition.<sup>[17]</sup> Thus, the process shows promise of being relatively cost effective.

In this study, a 6061/Gr/SiC hybrid MMC is fabricated and an effort is made to explain the contributions of each of its constituents to the overall damping. This is approached by first evaluating the damping behavior of the matrix and each of the reinforcements in their bulk form. Next, 6061/Gr and 6061/SiC MMCs will be presented to give the effect of each individual reinforcement. Finally, the three components are combined to form the hybrid MMC. The sources of any damping improvement are then evaluated in terms of known damping mechanisms.

## II. EXPERIMENTAL

### A. Materials Synthesis

In order to carry out the study as originally planned, five types of raw material were required. First, an Al matrix alloy was required to form the matrix of the composites. Next, SiC and graphite in particulate form were required to act as reinforcing phases. Finally, bulk SiC and graphite were desired to quantify the intrinsic damping capacity of those materials. These were selected as follows.

The Al matrix selected was 6061 Al alloy of commercial grade nominally composed of 1.0% Mg, 0.6% Si, 0.28% Cu, 0.2% Cr and balance in Al (wt.%). The particulate graphite was phase 2935 crystalline flake graphite powder with a mean particulate size of 7  $\mu\text{m}$ . The SiC particulates used were  $\alpha$ 1200, with an average size of 3  $\mu\text{m}$ . The bulk graphite material was in the form of pressed bars. Bulk SiC, however, was not measured directly in this study, instead, data was taken from the available literature.

A spray atomization and co-deposition technique was used to synthesize the MMCs. The experimental apparatus, depicted in Figure 1, utilized high velocity jets of nitrogen gas to energetically disintegrate molten 6061 Al into micrometer-sized droplets. The graphite (or SiC) particulates, carried by a separate flow of nitrogen, were co-injected via nozzles directed normal to the outline of the atomization cone. For the hybrid material, the graphite and SiC particulates were mixed in a 1:1 ratio by volume and were injected in similar fashion. The partially solidified droplets and entrained ceramic particulates then continued to travel under the combined effects of gravity and drag forces to impact and collect on a water-cooled copper substrate. An inert atmosphere was maintained in the environmental chamber during the entire process in order to minimize oxidation of the Al melt. A more detailed description of this synthesis methodology may

be found elsewhere.<sup>[14,18-20]</sup> A total of five spray deposition experiments were used to provide the material for the study. The compositions of these materials are summarized in Table I.

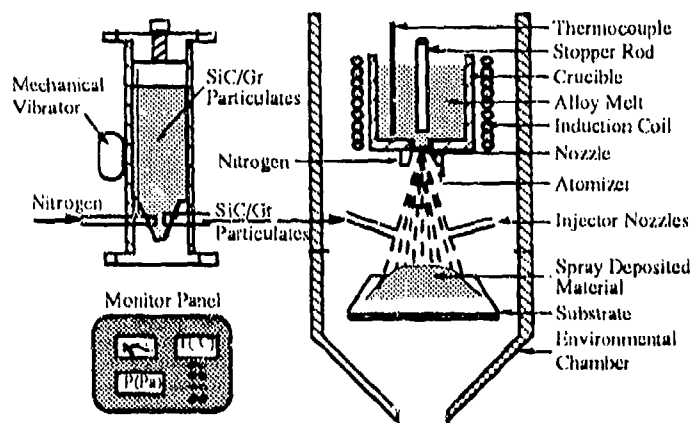


Fig. 1. Spray Atomization and Co-deposition facility.

Table I. Spray Deposited Material Compositions

Expt. #	Matrix	Reinforcement %	
		SiC	graphite
1	6061 Al	0	5
2	6061 Al	0	10
3	6061 Al	5	0
4	6061 Al	10	0
5	6061 Al	5	5

### B. Hot Extrusion

A 2.54 cm diameter extrusion billet was removed from each of the five spray deposited materials and was subsequently extruded at 400°C. In the case of the 6061/Gr materials, the extrusion ratio (area) was 4:1. For the 6061/SiC and 6061/Gr/SiC materials, the ratio was 16:1. This procedure was used to close the micrometer-sized porosity that is normally present in spray deposited materials.<sup>[18,21,22]</sup>

The quality of the MMC extrusions was found to degrade with increasing ceramic volume fraction. The 6061 Al/0.05Gr MMC yielded an extrusion with a severely "scaled" outside appearance. In the 6061 Al/0.10Gr MMC this effect was so large as to cause the extrusion to break up as it left the die. Although the 6061 Al/0.10Gr damping specimens used in this study were taken from the best section of the resultant segmented extrusion, their performance may have been affected by these imperfections. Future efforts may utilize a canning process of surrounding the billet with an unreinforced 6061 Al can before passing it through the die. This technique has shown promise in providing improved extrusion quality.

### C. Microstructural Characterization

Microstructural characterization of the MMCs was conducted on polished and etched samples utilizing standard metallographic techniques. Microstructural samples in both the radial and axial directions were taken from areas immediately adjacent to the damping specimens. The abundance of alloying elements in 6061 Al made grain morphology difficult to observe. The formula chosen to etch the 6061/0.05Gr as-spray deposited sample consisted of 2 parts Poulton's reagent,<sup>[23]</sup> 1 part HNO<sub>3</sub> and 2 parts H<sub>2</sub>O. Grain morphology of the extruded MMC specimens was not successfully discerned.

### D. Ceramic Volume Fraction

Chemical dissolution was used to determine the volume fraction of graphite and/or SiC particulates present in the spray deposited MMCs. Dissolution samples were taken from various areas within each deposit and were weighed to obtain the mass in air and apparent mass in ethylene glycol. The samples were then completely dissolved in a solution of 36% HCl, followed by filtering to separate the particulates. In the case of the hybrid MMC, the SiC/graphite mixture was heated in air to 800°C, thereby oxidizing the graphite and allowing the SiC/graphite ratio to be determined. The resultant dry reinforcement mass combined with the dry and submerged MMC weights and densities of Al, graphite and SiC were sufficient to calculate the volume fractions and porosity using Archimedes' principle.

### E. Damping Measurements

The intrinsic damping and the elastic modulus were determined using a Polymer Laboratories dynamic mechanical thermal analyzer (DMTA). Representative sections from the materials were removed and machined into 1 x 5 x 35 mm rectangular beam damping specimens. Each specimen, in turn, was clamped into the DMTA, one end being fixed to a rigid frame and the other end being driven by an electromagnetic vibrator via a composite drive shaft. This arrangement caused the specimen to deflect in a fixed-guided cantilever configuration. During operation, the electromagnetic vibrator maintained a sinusoidal time-varying force to the driven end of the sample with the corresponding displacement being measured using a non-contact eddy current transducer. The specimen and adjacent hardware were positioned within the hot zone of a resistance furnace capable of temperatures up to 800°C. The resulting sinusoidal force and displacement curves were compared to determine the phase shift between them,  $\phi$ . Taking the tangent of this loss angle yields the loss tangent,  $\tan\phi$ , which is measured by the DMTA with a resolution on the order of 0.0017. In addition, the storage modulus, which corresponds to Young's modulus for the non-dynamic case, is reported.

In the present study, samples were displaced 64  $\mu\text{m}$  peak to peak at the drive clamp, corresponding to a maximum strain of  $2.6 \times 10^{-4}$ . The furnace temperature was increased at a rate of 2°C per minute from 30 to 250°C and was monitored through a platinum resistor adjacent to the test specimen. During the temperature cycle, the sample was oscillated at three discrete frequencies of 0.1, 1, and 10 Hz in sequence. Elastic modulus readings were compensated for clamping length error with an end correction equation provided by Read *et al.*<sup>[24]</sup> Similarly, damping values were corrected in order to compensate for air friction effects on the driven components.

### III. RESULTS

#### A. Microstructure

Although the materials used for the damping experiments were all in the as-extruded condition, it is helpful to first observe the microstructure in the as-sprayed condition. As a typical example, Figure 2 shows the microstructure of the as-spray deposited 6061/0.05Gr MMC. This micrograph reveals the presence of an equiaxed grain morphology, with an average grain size of  $15\text{ }\mu\text{m}$ . The grain morphology of this specimen is representative of most spray atomized and deposited materials as reported by other investigators.<sup>[14,18,25]</sup> Micro-pores were observed in the as-sprayed specimens with average sizes ranging from 6 to  $10\text{ }\mu\text{m}$ . This agrees with previous work in which unreinforced spray deposited Al was found to contain non-interconnected porosity of a size comparable to the grain size.<sup>[22]</sup>

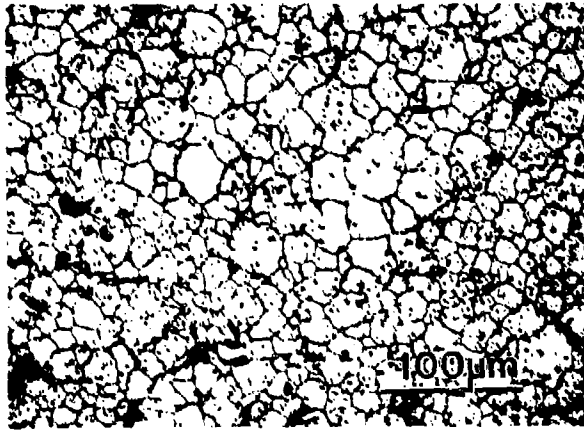


Fig. 2. Optical micrograph of as-spray deposited 6061/0.05Gr MMC.

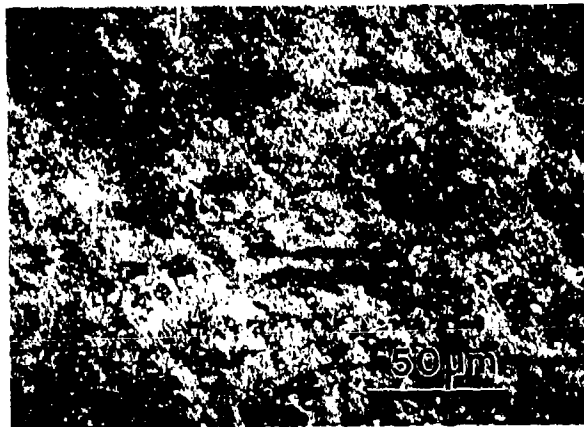


Fig. 3. Optical micrographs of as-extruded 6061/0.05Gr/0.05SiC hybrid MMC in longitudinal orientation.

Figure 3 shows the microstructure of the sprayed and extruded 6061/0.05Gr/0.05SiC hybrid MMC. Inspection of the specimen shows that the micro-pores were closed during hot extrusion. In addition, the graphite particulates were stretched into chain-like series while the distribution of SiC particulates remained relatively homogeneous. The lack of success in etching the extruded specimens precluded the measurement of grain size in those materials. However, from the results reported by Gupta *et al.*,<sup>[26]</sup> it may be inferred that the grain size of the as-spray deposited MMC was further refined during hot extrusion.

## B. Ceramic Volume Fraction

The graphite and SiC volume fraction data for the five spray deposited materials are given in Table I. Previous work on 6061/Gr material has demonstrated that the region in the middle of the spray deposit offers the highest density and most consistent reinforcement volume fraction. The extrusion billets were taken from this area in order to provide the best damping data.

## C. Damping Capacity

Damping capacity and elastic modulus data were collected by the DMTA for each material. A typical set of data corresponding to commercially available 6061 T6 Al alloy is given in Figure 4. In the figure, six curves are plotted over the 30 to 250°C temperature range; the darkened symbols denoting elastic modulus for each of the three frequencies used and the light symbols denoting damping capacity for the same.

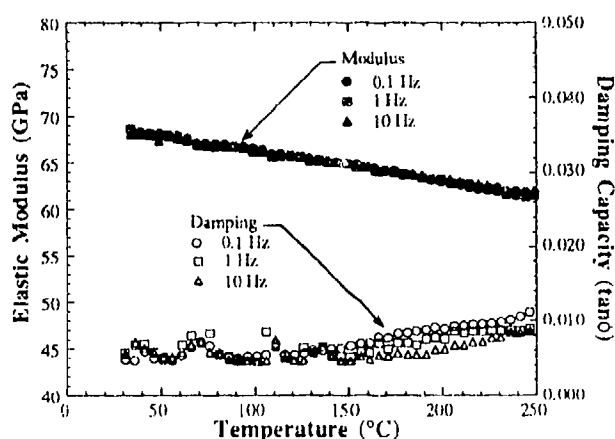


Fig. 4. Damping capacity and elastic modulus of 6061 T6

Several interesting trends may be noted from Figure 4 which are found to be characteristic of all of the sprayed and extruded MMCs. First, the elastic modulus is seen to decrease in a linear fashion with increasing temperature and exhibit little or no frequency dependence below 200°C (i.e., the 0.1, 1 and 10 Hz curves do not diverge). Next, the damping capacity is observed to be essentially frequency independent as well as temperature independent (i.e., near-zero slope) at temperatures below approximately 125°C. The damping capacity is then found to rapidly increase with increasing temperature and decreasing frequency above 150°C, but never exceeds a  $\tan\phi$  of 0.012.



The damping capacity data for the bulk graphite over the 0 to 250°C temperature range is presented in Figure 5. From the figure, it is evident that the damping behavior is relatively temperature independent in this range and is relatively high compared to 6061 T6 (Fig. 4).

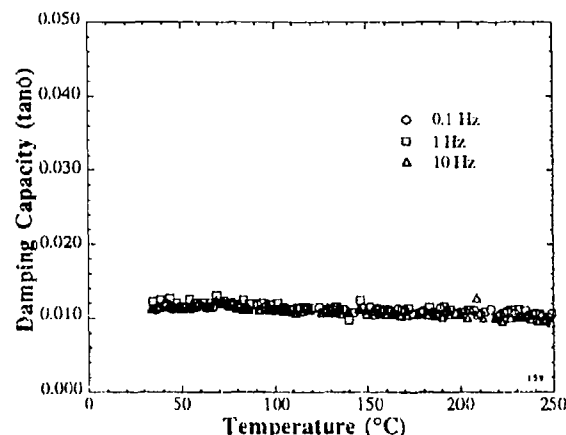


Fig. 5. Damping capacity of bulk graphite.

The effect of increasing graphite volume fraction on the 6061/Gr MMCs at 1 Hz is given in Figure 6. This figure demonstrates that large increases are made in damping capacity by raising the graphite volume fraction from 0.05 to 0.10. An associated reduction in modulus is also noted. Similarly, a comparison of damping data at 1 Hz for the 6061/SiC MMC at volume fractions of 0.05 and 0.10 is presented in Figure 7. This, unlike in the case of graphite, indicates that the damping capacity is relatively insensitive to an increase in SiC volume fraction from 0.05 to 0.10.

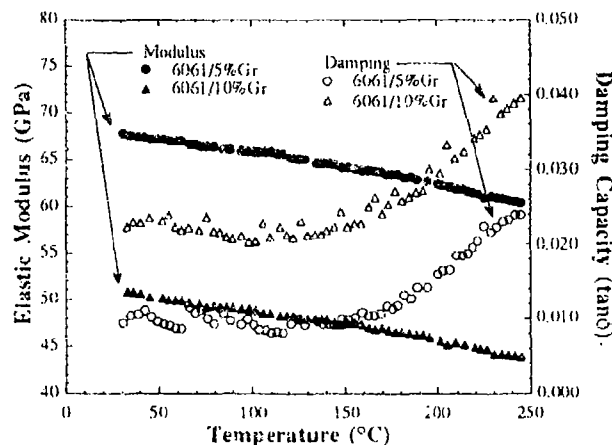


Fig. 6. Damping capacity and elastic modulus of 6061/0.05Gr and 6061/0.10Gr at 1 Hz.

In Figure 8, the damping capacity of the 6061/0.05Gr/0.05SiC hybrid MMC at 1 Hz is presented relative to that of 6061/0.10Gr and 6061/0.10SiC MMCs. It is evident that the damping capacity of the hybrid material very nearly matches that of the SiC reinforced MMC. The full set of damping capacity and modulus data for the 6061/0.05Gr/0.05SiC MMC is given in Figure 9.

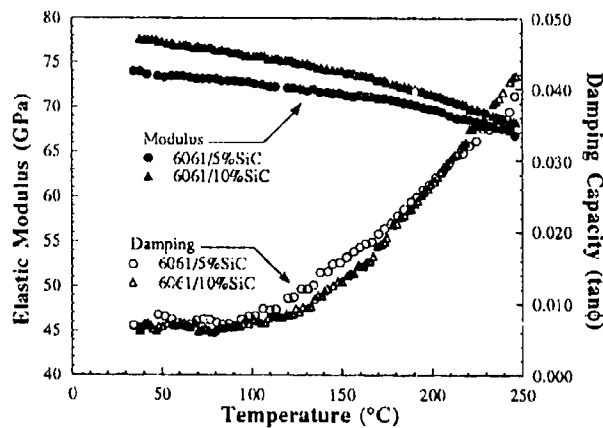


Fig. 7. Damping capacity and elastic modulus of 6061/0.05SiC and 6061/0.10SiC at 1 Hz.

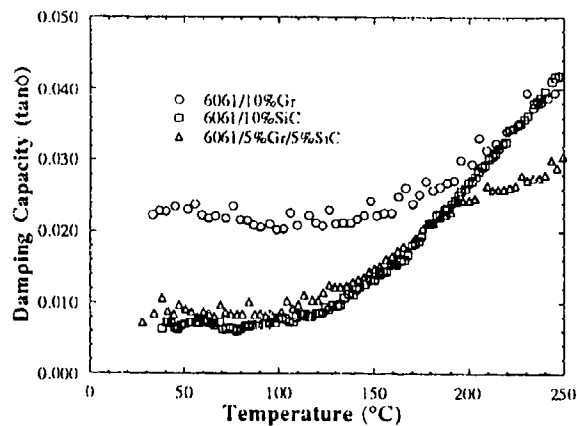


Fig. 8. Comparison of the damping capacity of graphite, SiC and hybrid reinforced MMCs at 1 Hz

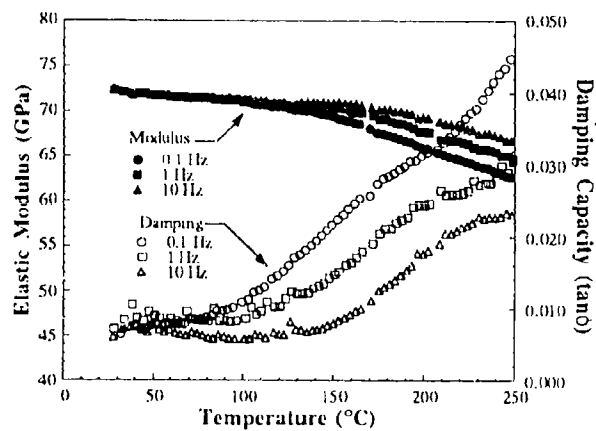


Fig. 9. Damping capacity and elastic modulus of 6061/0.05Gr/0.05SiC hybrid MMC.

## IV. DISCUSSION

A variety of mechanisms may contribute to the overall damping behavior of metals and alloys. These may include effects due to thermoelasticity, crystallographic defects, eddy currents, Snoeck effects, stress induced ordering and others.<sup>[27-29]</sup> As a reinforcing phase is added to the matrix, many of these factors may be augmented while additional new mechanisms may appear. The following discussion will address the factors which are thought to have been active in the MMCs studied herein.

### A. Intrinsic Damping

One potentially simple means of explaining the increase of damping capacity with increasing volume fraction of graphite is on the basis of the rule of mixtures (ROM). Accordingly, the overall damping capacity,  $\eta_{MMC}$ , would be proportional to the individual damping capacities of the matrix,  $\eta_m$ , and the reinforcements,  $\eta_{SiC}$  or  $\eta_{Gr}$ , multiplied by their respective volume fractions,  $Vf_m$ ,  $Vf_{Gr}$  and  $Vf_{SiC}$  as given by

$$\eta_{MMC} = \eta_m Vf_m + \eta_{Gr} Vf_{Gr} + \eta_{SiC} Vf_{SiC} \quad [1]$$

In considering the intrinsic damping capacities of the constituents of interest here, it may be inferred from Figure 4 that 6061-T6 is a relatively low damping material at room temperature. Conversely, from Figure 5 and the work of others,<sup>[30]</sup> graphite is a relatively high damping material with a value of  $\tan\phi$  in the range of  $1.0 \times 10^{-2}$  to  $1.5 \times 10^{-2}$  at room temperature. This characteristic is believed to result from the anisotropic crystal structure found in graphite. The structure consists of parallel hexagonal net planes in an ABABA stacking sequence. The strong in-plane covalent bonding and weak Van Der Waals through-plane forces allow the basal planes to be easily displaced in the in-plane direction when subjected to shear forces. Under cyclic loading, this sliding induces friction losses attributed largely to the dislocation mechanism proposed by Granato and Lücke.<sup>[31,32]</sup> This mechanism, based upon the sweeping motion of dislocations from pinning points, is believed to occur in the high concentration of glissile basal plane dislocations found in graphite. SiC, on the other hand, is a relatively low damping material with a reported loss factor of 0.005.<sup>[33]</sup>

In a recent study by the present authors,<sup>[13]</sup> in order to estimate the applicability of the rule of mixtures to the 6061/Gr system, Eq. [1] was used to predict damping values for extruded 6061 Al/0.05Gr and 6061 Al/0.10Gr MMCs. A comparison of the resultant theoretical data with the corresponding results from the DMTA revealed the ROM predictions to be lower than the experimental measurements. This agrees with the basic premise that the rule of mixtures should account for only the intrinsic damping mechanisms existent in the matrix and reinforcement, thereby neglecting additional damping mechanisms produced as a result of interfaces and interactions between the two. Thus, it was evident that in the case of particulate reinforced MMCs, the model must be supplemented by other mechanisms, several of which are discussed below.

### B. Thermal Expansion Mismatch

One consideration which is thought to be of great importance in the 6061/Gr material is the thermal expansion mismatch between the ceramic particulates and the Al matrix. Numerous studies have shown that although the dislocation concentration found in as-quenched, age-hardenable Al alloy is low, typically less than  $10^{12} m^{-2}$ ,<sup>[34]</sup> the dislocation concentration in Al

matrices of ceramic particulate reinforced MMCs is on the order of  $10^{12}$  to  $10^{14} \text{m}^{-2}$ .<sup>[35,36]</sup> These dislocations, generated to accommodate the residual strain associated with the difference in coefficient of thermal expansion (CTE, or  $\alpha$ ) between the matrix and the reinforcement, are located primarily near the reinforcement-matrix interface and decrease in concentration with increasing distance from the interface.<sup>[35]</sup> The residual thermal mismatch strain,  $\epsilon$ , is a function of the difference between the coefficients of thermal expansion of the reinforcement and matrix,  $\Delta\alpha$ , according to the expression  $\epsilon = \Delta\alpha\Delta T$ , where  $\Delta T$  is the temperature change. It is reported that the CTE of graphite ranges from  $-1.4 \times 10^{-6} \text{ }^\circ\text{C}^{-1}$  parallel to the basal planes to  $27 \times 10^{-6} \text{ }^\circ\text{C}^{-1}$  perpendicular to them.<sup>[9]</sup> The CTE of SiC is  $5.4 \times 10^{-6} \text{ }^\circ\text{C}^{-1}$  while that of Al is  $23 \times 10^{-6} \text{ }^\circ\text{C}^{-1}$ .<sup>[14]</sup>

The mechanism by which the dislocations are generally considered to affect damping behavior is through the theory offered by Granato and Lücke.<sup>[31,32]</sup> This mechanism, as previously mentioned in the discussion of intrinsic damping in graphite, assumes losses occur due to dislocations breaking away from weak pinning points under cyclic loading. This breakaway and sweeping motion dissipates energy in proportion to the area traversed and is represented by an equation which implies that a plot of  $\log \epsilon_0 \phi_h$  versus  $1/\epsilon_0$  should yield a straight line whose slope is inversely proportional to the minor pinning length,  $L_C$ , and whose intercept is proportional to  $\Lambda L_N^3/L_C$ . Here,  $\phi_h$  represents the hysteretic damping (the overall damping less the strain independent value),  $\epsilon_0$  represents the strain amplitude,  $\Lambda$  is the dislocation density,  $L_N$  is the major pinning length, and  $L_C$  is the minor pinning length. Previous work by the present authors<sup>[37]</sup> has shown the extruded 6061/Gr MMCs to obey the linear relationship of  $\log \epsilon_0 \phi_h$  versus  $1/\epsilon_0$  at room temperature.

Although the CTE mechanism is undoubtedly important in the creation of dislocations, additional dislocations may have been created in the extrusion process, thereby augmenting the damping effect. In addition, the contribution of dislocations to damping may be expected to fall with increasing temperature as their concentration is decreased as demonstrated by Arsenault and Shi<sup>[34]</sup> in Al/SiC MMCs. Thus, the damping provided by dislocations (incurred through CTE and extrusion) may be expected to provide a large percentage of the overall damping at room temperature but decrease in importance with increasing temperature.

### C. Grain Boundaries

One factor which is greatly altered by the spray atomization process (as well as the extrusion process) is the grain size. A fine-grained microstructure is a characteristic of materials processed using the spray atomization and co-deposition technique. Discussions on grain boundary viscosity, relaxation and anelasticity in polycrystalline metals by Kê,<sup>[38]</sup> Lazan,<sup>[27]</sup> Nowick and Berry<sup>[28]</sup> and Zener<sup>[29]</sup> have indicated that viscous flow at grain boundaries will serve as a source of internal friction. The energy absorbed in grain boundaries is dependent upon the temperature, the shear stress and the anelastic shear strain. In addition, early experiments on pure Al showed a grain boundary damping peak occurring at approximately  $300^\circ\text{C}$  to be shifted to lower temperatures by decreasing the grain size.<sup>[38]</sup> In view of this, the fine grained microstructure of the spray atomized and deposited material may play a role in the dissipation of elastic strain energy in the upper region of the  $30^\circ\text{C}$  to  $250^\circ\text{C}$  temperature regime considered here.

The experimental data provided by the DMTA allow an observation to be made regarding the effect of grain boundaries on damping. It is that the large gains made above  $150^\circ\text{C}$  are only evident when reinforcing particulates are present. This indicates that these large gains may not be attributed to grain boundary damping. Thus, it appears that although grain boundary damping is

expected to increase with temperature, it is not large enough to dominate the damping behavior of the extruded MMCs below 250°C.

#### **D. Particulate/Matrix Interface**

It has been suggested that the interface between reinforcement and matrix may play an important role in the damping behavior of composite materials although few studies have been conducted to clarify the mechanisms involved. In addition to the presence of dislocations resulting from the previously mentioned CTE effect, the particulate/matrix interface may also be characterized by its bonding strength as well as the existence of reaction products, voids and impurities. The work of Updike *et al.*<sup>[39]</sup> on graphite fiber reinforced MMCs showed that the presence of graphite fibers enhanced the damping behavior of Al matrix composites, particularly when there were no interfacial reactions at the Al/Gr interface. Bhagat *et al.*<sup>[40-42]</sup> and Rawal *et al.*<sup>[43]</sup> also commented on the contribution of the interface to damping in their respective studies of graphite fiber reinforced MMCs.

A theory regarding the contribution of precipitate/matrix interfaces to damping has been offered by Schoeck.<sup>[44,45]</sup> In this theory, precipitates are treated as ellipsoid inclusions in the matrix and the interaction energy between the precipitates and the applied stress is determined on the basis of the Eshelby inclusion theory.<sup>[46,47]</sup> Extension of the theory to encompass graphite particulates in the Al matrix was used to estimate the contribution of the Al/Gr interface to be estimated.<sup>[13]</sup> Although considerable uncertainties were introduced by the approximations used, it was suggested that the Al/Gr interface may produce a significant percentage of the overall high temperature damping.<sup>[13]</sup>

#### **E. Orientation**

In a study on the damping behavior of gray cast iron, Millet *et al.*<sup>[48]</sup> found that oriented lamellar graphite in a pearlitic matrix exhibited higher damping capacity than that of spheroidal graphite in a ferritic matrix. The damping spectra of these materials were found to resemble those of extruded (pencil) and nuclear graphite, respectively. Additionally, the nature of the matrix (pearlitic or ferritic) was found to have little effect on damping. This suggested that the orientation of the graphite precipitates was of great importance. Examination of the microstructure of the hybrid material in Figure 3 shows that the graphite particulates assumed a preferred orientation during extrusion while the SiC particulates did not. It has been suggested that the preferred orientation of graphite following extrusion may be related to damping gains incurred in the process.<sup>[13]</sup>

#### **F. Thermoelastic Damping**

The concept of thermoelastic damping, pioneered by Zener,<sup>[29]</sup> applies to materials subjected to an inhomogeneous state of deformation. In the case of bending loads, such as those produced in the DMTA specimens, thermoelasticity is characterized by losses incurred in the flow of heat across the neutral axis due to the heating (and cooling) produced by the compressive (and tensile) stresses. Thermoelastic damping may also be enhanced by stress inhomogeneities created by defects such as particulate reinforcement.

Thermoelastic theory, however, indicates that the contribution will be proportional to the frequency. It has been reported that thermoelastic contributions in particulate reinforced Al MMCs

becomes significant only at frequencies greater than 100Hz.<sup>[49]</sup> Thus, at frequencies below 10 Hz, the contribution of thermoelastic damping is believed to be minimal.

## V. CONCLUDING REMARKS

The addition of graphite particulates to 6061 Al alloy using spray atomization and co-deposition was shown to provide increased damping capacity in the 0.1 to 10 Hz frequency range. The damping capacity was found to increase with increasing graphite volume fraction although this was accompanied by a decrease in elastic modulus. The addition of SiC particulates was shown to produce less dramatic damping increases at low temperature but nearly identical increases at temperatures approaching 250°C. Also, unlike graphite, the elastic modulus is increased with increasing SiC volume fraction.

The damping capacity of the 6061/0.05Gr/0.05SiC hybrid material at 1Hz was compared to 6061/0.10Gr and 6061/0.10SiC. This indicated that the hybrid material offers a slight improvement over the MMC reinforced only by SiC at low temperature but did maintain a relatively high elastic modulus.

Although the close relationships among mechanisms make it difficult to clearly identify their relative significance, the following suggestions may be made. At low temperatures, dislocations, the intrinsic damping of graphite and the preferred orientation of graphite (induced through extrusion) appear to be mechanisms by which the damping may be improved. At high temperatures, Al/Gr interfaces, preferred graphite orientation, dislocations and grain boundaries appear to be significant.

## ACKNOWLEDGMENTS

The authors wish to acknowledge the Office of Naval Research (Grant No.: N00014-90-J-1923) for financial support. In addition, the authors would also like to express their gratitude to Catherine Wong of David Taylor Research and Development Center, and L.T. Kabacoff of the Office of Naval Research for their able technical assistance and valuable discussions; to Dr. R. W. Stewart of Superior Graphite Co. for providing quality graphite powders, to I. Sauer of the University of California at Irvine for his assistance with the experimental part of this study.

## REFERENCES

1. D.W. James: *Materials Science and Engineering*, 1969, vol. 4, p. 1.
2. J.H. Armstrong, S.P. Rawal and M.S. Misra: in *Proceedings of the American Society for Composites*, East Lansing, MI, 1990, p. 47.
3. I.G. Ritchie and Z.L. Pan: in *Proceedings of Damping '91*, J. Pearson and L. Rogers, eds., 1991, WL-TR-91-3078, Wright-Patterson AFB, OH, p. ICA-1.
4. J.E. Schoutens: in *Proceedings of Damping '91*, J. Pearson and L. Rogers, eds., 1991, WL-TR-91-3078, Wright-Patterson AFB, OH, p. HAB-1

5. C. Wong and S. Holcomb: *Damping Studies of Ceramic Reinforced Aluminum*, Report # DTRC-SME-91/15, David Taylor Research Center, Annapolis, MD, March 1991.
6. P.K. Rohatgi, R. Asthana and A. Kumar: in *Cast Reinforced Metal Composites*, S.G. Fishman and A.K. Dhingra, eds., ASM International, Materials Park, OH, 1988, p. 375.
7. J. Zhang, R.J. Perez, Y. Wu, M.N. Gungor and E.J. Lavernia: in *Damping of Multiphase Inorganic Materials*, R.B. Bhagat, ed., 1992, ASM Intl., Materials Park, OH, p. 1.
8. S. Umekawa, K. Nishiyama and E. Yamane: in *Proceedings of the Fourth Japan-U.S. Conference on Composite Materials*, Washington, D.C., 1988, p. 138.
9. B.T. Kelly: *Physics of Graphite*, Applied Sciences Publishers, London, 1981, p. 108.
10. A. Munier, J-M. Zhu, T.E. Sutto, B.A. Averill and B.S. Shivaram: in *Damping of Multiphase Inorganic Materials*, R.B. Bhagat, ed., 1992, ASM International, Materials Park, OH, p. 9.
11. P. Millet, R. Schaller and W. Benoit: *Journal Phys. Colloq.*, 1983, vol. 44 (C9), p. 511.
12. J. Zhang, R.J. Perez, M.N. Gungor and E.J. Lavernia: in *Developments in Ceramic and Metal-Matrix Composites*, K. Upadhyaya, ed., TMS 1992 Annual Meeting, TMS, 1992.
13. R.J. Perez, J. Zhang, M.N. Gungor and E.J. Lavernia: *Metall. Trans. A*, vol. 24A, 1993, in press.
14. I.A. Ibrahim, F.A. Mohamed and E.J. Lavernia: *J. Mater. Sci.*, vol. 26, 1991, p. 1137.
15. G.J.C. Carpenter and S.H.J. Lo: *J. Mater. Sci.*, 1992, vol. 27, p. 1827.
16. M. Gupta, I.A. Ibrahim, F.A. Mohamed and E.J. Lavernia: *J. Mater. Sci.*, vol. 26, 1991, p. 6673.
17. R.J. Perez, J. Zhang and E.J. Lavernia: in *ISTFA '91*, ASM International, Materials Park, OH, 1991, p. 445.
18. M. Gupta, F.A. Mohamed and E.J. Lavernia: *Int. J. Rapid Solidif.*, 1991, vol. 6, p. 247.
19. M. Gupta, F. Mohamed and E. Lavernia: *Metall. Trans. A*, 1992, vol. 23A, p. 831.
20. M. Gupta, F. Mohamed and E. Lavernia: *Metall. Trans. A*, 1992, vol. 23A, p. 845.
21. E.J. Lavernia, J.A. Ayers and T.S. Srivatsan: *Int. Mater. Rev.*, 1992, vol. 37, p. 1.
22. J. Zhang, M.N. Gungor and E.J. Lavernia: in *Proc. Damping '91*, J. Pearson and L. Rogers, eds., 1991, WL-TR-91-3078, Wright-Patterson AFB, OH, p. GDE-1.
23. P.R. Sperry and M.H. Bankard: *ASM Metals Handbook*, 8th Ed., vol. 8, p. 120.
24. B.E. Read, G.D. Dean and J.C. Duncan: *Physical Methods of Chemistry*, B.W. Rossiter and R.C. Baetzold, eds., 2nd Ed., John Wiley & Sons, Inc., New York, 1986, p. 1.
25. X. Liang, J.C. Earthman and E.J. Lavernia: *Acta Metall.*, 1992, vol. 40, p. 3003.
26. M. Gupta, C. Lane and E.J. Lavernia: *Scri. Metall.*, 1992, vol. 26, p. 825.
27. B.J. Lazan: *Damping of Materials and Members in Structural Mechanics*, Pergamon Press, Oxford, 1968, p. 38.
28. A.S. Nowick and B.S. Berry: *Anelastic Relaxation in Crystalline Solids*, Academic Press, New York, 1972, p. 248.
29. C. Zener: *Elasticity and Anelasticity of Metals*, The University of Chicago Press, Chicago, IL., 1948, p. 69.
30. B.T. Kelly: *Physics of Graphite*, Applied Sciences Publishers, London, 1981, p. 108.
31. A. Granato and K. Lücke: *J. Appl. Phys.*, 1956, vol. 27, p. 583.
32. A. Granato and K. Lücke: *J. Appl. Phys.*, 1956, vol. 27, p. 789.
33. N. Nishiyama, M. Yamanaka, M. Omori and S. Umekawa: *J. Mat. Sci. Lett.*, 1990, vol. 9, p. 526.
34. R.J. Arsenault and N. Shi: *Mater. Sci. Eng.*, 1986, vol. 81, p. 175.
35. I. Dutta and D.L. Bourell: *Mater. Sci. Eng. A*, 1989, vol. 112, p. 67.
36. I. Dutta and D.L. Bourell: *Acta Metall.*, 1990, vol. 38, p. 2041.
37. R.J. Perez, J. Zhang, E.J. Lavernia: *Scri. Metall.*, 1992, vol. 27, p. 1111.

38. T.S. Kê: *Phys. Rev.*, 1947, vol. 72, p. 41.
39. C. A. Updike, R.B. Bhagat, M.J. Pechersky and M.F. Amateau: *J. Met.*, 1990, vol. 40 (3), p. 42.
40. R.B. Bhagat, M.F. Amateau and E.C. Smith: *J. Compos. Technol. Res.*, 1989, vol. 11, p. 113.
41. R.B. Bhagat, M.F. Amateau, J.C. Conway, J.M. Paulick, J.M. Chrisholm, J.M. Parnell and D.G. Seidensticker: *J. Compos. Mater.*, 1989, vol. 23, p. 961.
42. R.B. Bhagat, M.F. Amateau and E. C. Smith: in *Cast Reinforced Metal Composite*, S.G. Fishman and A.K. Dhingra, eds., ASM Int., Materials Park, OH, 1988, p. 399.
43. S.P. Rawal, J.H. Armstrong and M.S. Misra: in *Damping Characteristics of Metal Matrix Composites*, AD-A213 712, May 1989.
44. G. Schoeck: *Phys. Status Solidi*, 1969, vol. 32, p. 651.
45. G. Schoeck and E. Bisogni: *Phys. Status Solidi*, 1969, vol. 32, p. 31.
46. J.D. Eshelby: *Proc. Roy. Soc.*, 1957, vol. A241, p. 376.
47. J.D. Eshelby: *Solid State Phys.*, 1956, vol. 3, p. 79.
48. P. Millet, R. Schaller and W. Benoit: *J. Phys. Colloq.*, 1981, vol. 43 (C5), p. 929.
49. J.E. Bishop and V.K. Kinra: *A Second Law Analysis of Thermoelastic Damping in Elementary Metal-Matrix Composites*, CMC Report No. 91-15, Texas A&M University, 1991.



# A SIMPLE APPROACH TO DESIGN, INSTALLATION, AND TESTING OF PASSIVE DAMPING FOR AN OPTICAL SYSTEM

Eric M. Austin and James C. Goodding  
CSA Engineering, Inc., Palo Alto, CA

Passive damping hardware has been fabricated, installed, and tested on a large optical system required to meet a stringent RMS specification for closed-loop residual jitter due to ground and coolant flow excitations. Over the course of the study, constrained layer treatments, tuned-mass dampers, and link dampers were analyzed. It was shown through analysis that one type of treatment alone was not sufficient to solve the problem due to the number of harmful modes spread over a relatively wide frequency range. The final solution incorporated constrained layer damping treatments on an interface component between the mirrors and their mounts, link dampers between selected locations on the optical bench, and constrained layer treatments on some mirror support plates. Tests were performed before and after the application of the damping hardware to demonstrate its effectiveness and applicability to this class of problem. The primary focus of this paper is the dynamic testing of the optical system and design, fabrication, installation, and qualification of the passive damping hardware.

## INTRODUCTION AND GOALS

A proposed modification to a high power optical system requires the addition of an bench with its associated optics and their mounts. Some of these optics require coolant flows to maintain proper mirror figure, and these flows generate substantial optical jitter that degrades the quality of the propagated laser beam. The primary goal of this work is to minimize the optical jitter introduced as beam passes through the optics on this bench. This paper discusses the analysis, design, fabrication, installation, and testing of damping hardware for the optical bench. Discussion of the work from the earlier phases of this five-phase, four-year effort will be limited to only what is needed to support conclusions made during this final phase.

Possible jitter-reduction techniques for this optical bench can be placed in three categories: 1) reduction of the disturbance energy input, primarily from the coolant flows, 2) improvement of the structural design to enhance its rigidity greatly, and 3) provide a passive damping design

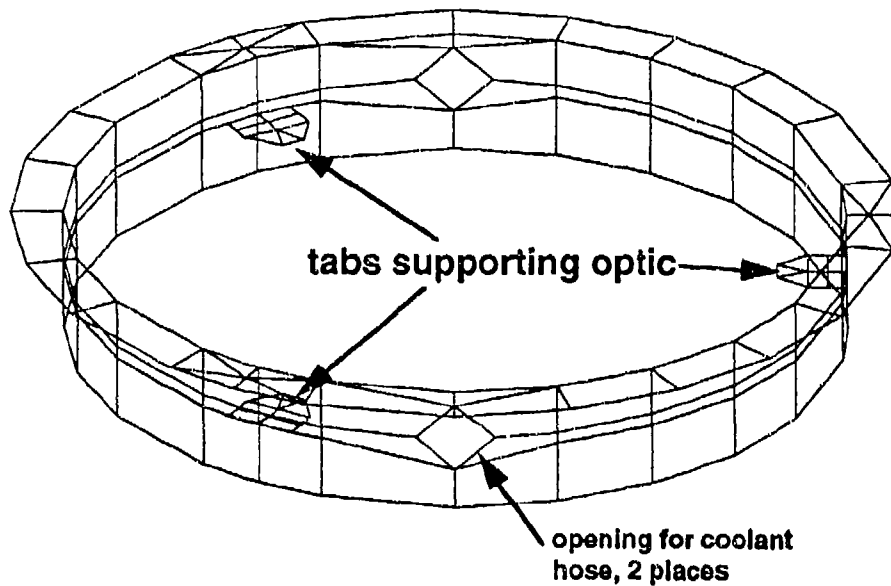


Figure 1: Finite element model of tangent flange.

to minimize mirror vibration response. The coolant flows were driven by cooling requirements of the optics. No-load fittings and flexible couplings were implemented in the coolant lines to help diminish excitations, but their effect was not enough to alleviate the problem. In the end, it was not clear how much of the jitter was caused by modal activity of the bench and how much was due to the excitations themselves. It was shown in the early phases of the work that the major source of damaging compliance had to be there for thermal reasons, thus ruling out stiffening. Passive damping was chosen as the only candidate solution that would fit the needs, time schedule, and budget of the program. The damping treatments had to be add-on due to the maturity of the structure's design.

Six optics are in the primary beam path of the optical bench, though only the three cooled optics were used to assess jitter. Each of the cooled mirrors is mounted on a relatively compliant tangent flange, which were originally designed to protect the polished surfaces from distortions from thermal or other static perturbations (see Figure 1). The tangent flange is attached to a massive, stiff mount with spherical washers and bolts. These mounts are bolted on thick steel supporting plates that span the width of the bench. The bench is designed as a three-dimensional space frame. The main frame members are steel rectangular tubes, and the diagonal bracings are steel I-beams.

## ANALYSIS AND PROBLEM IDENTIFICATION

The finite element model of the system changed considerably over the course of the many phases, evolving from a crude model used primarily to size frame members to a model with enough detail to predict local modes of optics accurately. The analytical measure of the system's residual jitter was a combination of rotations of the five primary optics — three cooled and two uncooled — via a ray-trace equation. Excitations came from coolant flows and floor vibration. The coolant flow

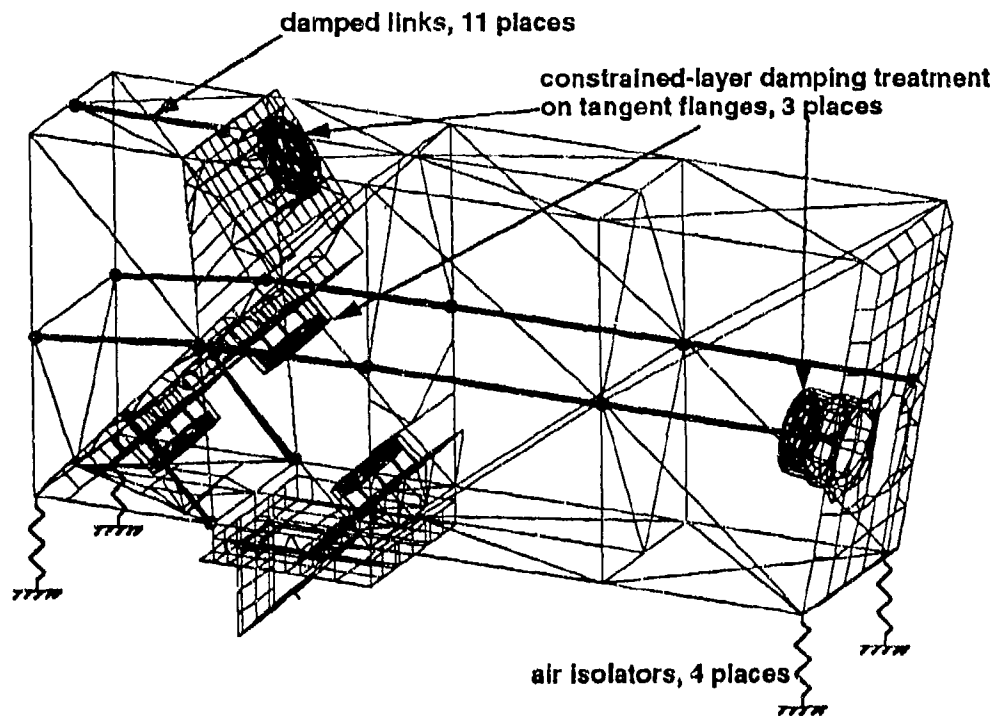


Figure 2: Finite element model of bench showing location of damping hardware.

excitations came from experience on earlier programs, and the floor excitations came from actual measurements in the bench's facility. The floor excitations were applied through the soft (nominally 3 Hz) air isolation system supporting the bench at the four corners, whereas the flow excitations were applied directly to the high-power mirrors. As one might expect, analysis showed that the coolant flows were the primary contributor to residual jitter.

Figure 3 shows finite element predictions of PSDs (power spectral density function) of the residual jitter ( $\theta_x$  and  $\theta_y$ ) of the baseline system. The forward sum of the PSDs gives a convenient visual check for which modes are contributing the most to the RMS, which is the quantity that we seek to reduce. Analysis predicted that over half of the modal strain energy (MSE) in the jitter-critical modes to be in the tangent flanges. The MSE in the thick steel plates supporting the mirrors and miscellaneous frame members each totaled roughly between 10% and 20% in these modes. Several candidate damping approaches were studied throughout the first three phases of the program:

1. tuned-mass dampers for local mirror/support resonances,
2. constrained-layer damping on frame members,
3. constrained-layer damping on tangent flanges, and
4. link dampers between selected frame locations.

Based on the MSE distribution predicted by the finite element model, the tangent flanges were chosen to be the primary focus of the damping design, with link dampers placing second. The feeling was that damping the tangent flanges would help reduce the largest spikes and that damping the frame would bring the overall levels down, since the frame participates at least some in all modes. Neither TMDs nor constrained-layer damping on frame members proved to be effective solutions in the final analysis.

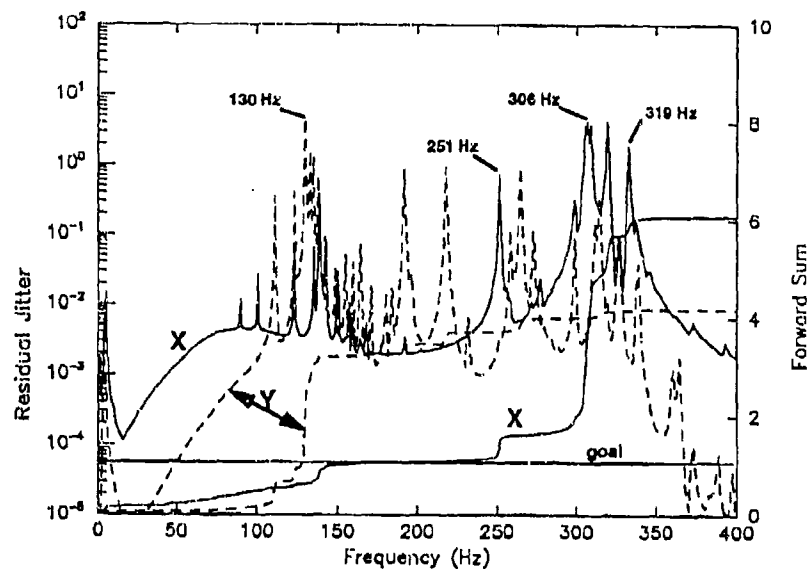


Figure 3: Baseline residual jitter predicted by finite element model.

The only practical way to attack the tangent flanges was with a constrained-layer treatment. Due to clearance problems, the thickness of the constraining layer was restricted to approximately 50 mils (0.050 inches). This limited the effectiveness of the treatment, but physical limitations like this are common in most problems. After trade studies on the VEM thickness and modulus and the constraining layer thickness and break locations, the treatment was set as a 10-mil-thick layer of 3M's ISD 110 with a three-piece, 40-mil stainless steel constraining layer. The constraining layer had to be split into three pieces both for application and to clear necked-down locations where the tangent flanges attach to the surrounding mounts. Analysis predicted between  $\frac{1}{2}\%$  and  $2\frac{1}{2}\%$  viscous damping for local tilt and plunger modes of the optics.

The damped links were placed between frame locations having relatively large relative displacements in the modes of most interest. Thirteen locations were chosen (see Figure 2), and the stiffness of the links was varied to seek maximum effectiveness. Trade studies showed that the optimum stiffness was about 130,000 lb/in. Since none of the links was replacing a load-carrying member, there was no need to provide an elastic load path through the link. Thus, the design strategy is to get as much of the compliance as possible from the viscoelastic material and as little as possible from the link itself. The design presented in the next section reflects this strategy. The VEM used was two layers (0.020 inches total) of 3M's Y-9473 due to good loss and stiffness characteristics. Analysis predicted between  $\frac{1}{4}\%$  and 5% viscous damping for modes not local to the optics.

### DESIGN, FABRICATION, AND INSTALLATION OF THE DAMPING HARDWARE

The design of the constraining layers for the tangent flanges was straightforward. It merely involved machining cutouts in 40-mil-thick sheet stock and rolling it to the correct curvature. The optics had to be removed in order to apply the constrained layer treatments to the tangent flanges. Since the ISD 110 is not self-adhesive at room temperature, heat guns were used to apply the VEM to the constraining pieces, and then band heaters were used to heat the VEM and constraining layer while clamping them to the tangent flanges.

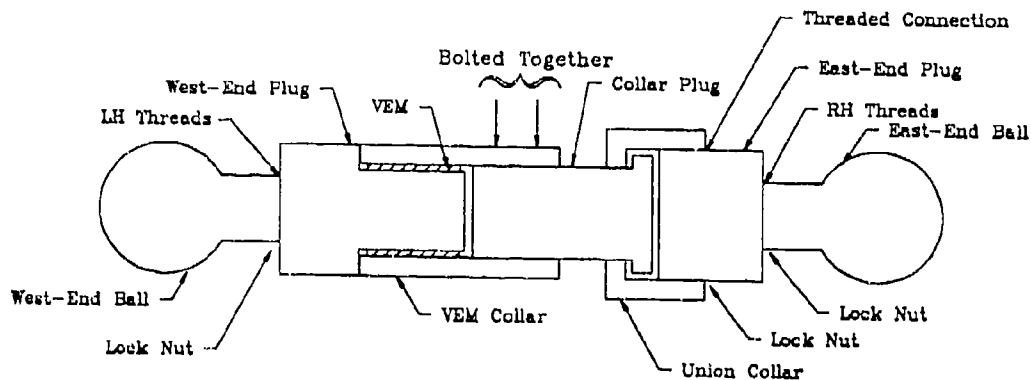


Figure 4: Schematic assembly view of the damped link.

Due to normal dimensional tolerances in such a large welded structure, the damped links had to be adjustable both in length and in orientation, i.e., there was no guarantee that the links' end locations would be parallel to one another. In addition, some of the links block access to the interior of the bench, so they needed to be removable with minimal effort. Figure 4 shows a schematic assembly view of the link. The rough length of each link was known to within  $\sim 1"$ , and this was accounted for by varying the length of the part labeled "Collar Plug." The length was fine-tuned with turnbuckle action of the middle assembly between the left-hand threads on the West-End Ball and the right-hand threads on the East-End Ball.

We established earlier that the link components had to be very stiff compared to the VEM, so the most weight-efficient solution would be to use a composite material. However, weight was not a factor, so all of the links' components were machined from 1018 steel (the heaviest weighed about 30 pounds). The assembled links are pictured in Figure 5. The links were installed in a manner that assured no preload in the VEM. After application of the damped links and tangent flange treatments, the optics were reinstalled and realigned before the second set of testing.

## TESTING

The underlying goal of the program was to demonstrate the effectiveness of the damping treatments designed during earlier phases. There were three approaches to this: 1) characterize modes of the mirrors in which the damping treatments participate strongly, 2) measure key responses on the bench, optics, and optics support structures under operating conditions, and 3) measure the "bottom line" jitter with a laser reflected off of the mirrors under flow conditions. Each of these tests were performed before and after application of the damping treatments.

### Modal Testing

The primary task of the modal tests was to characterize the dynamics of the bench to aid in interpretation of the results from the operational tests. A tight time schedule led to the following modest goals:

- Identify "tilt signatures" (frequencies and mode shapes) of the key high-power optics.
- Establish baseline damping in certain easily identified modes for comparison after installation of the damping hardware.

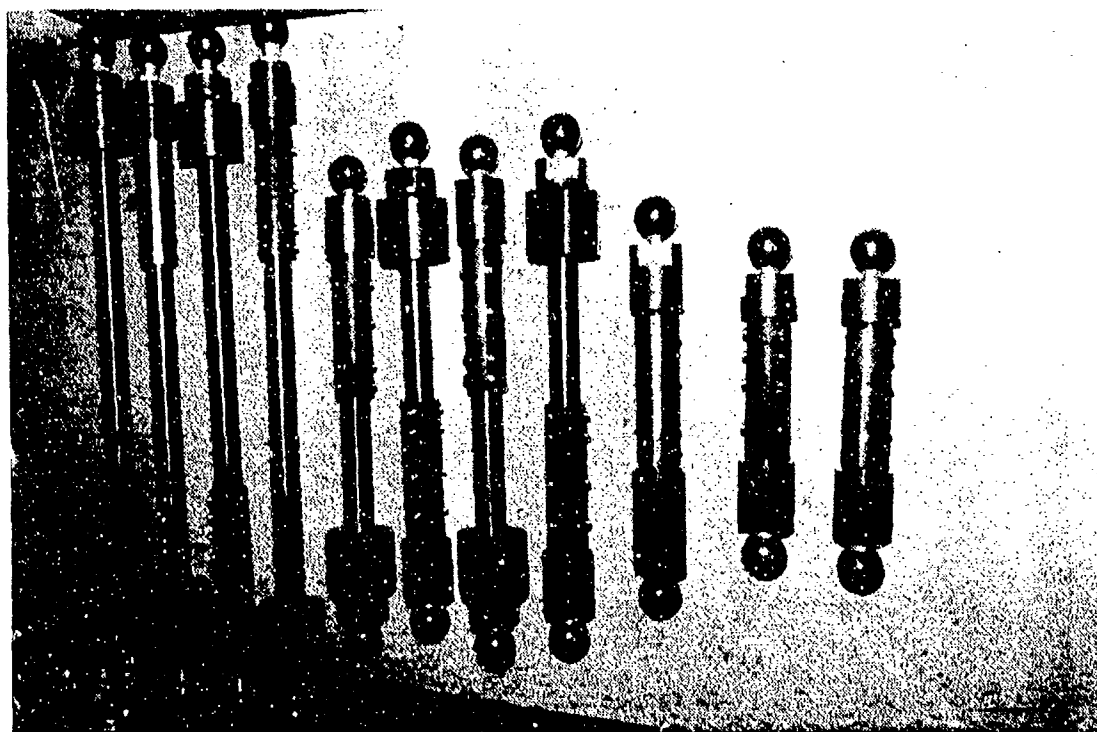


Figure 5: Photograph of assembled damped links.

- Gather information for assessing the accuracy of the finite element model, though tuning the model was not part of the task.

Analysis predicted that there would be several fairly local modes of each of the optics on their supporting structures below 400 Hz, and intuitively these are the most detrimental to jitter. Thus, a "local" modal test was done on each optic to identify modes dominated by tilting motions. It was hoped that these frequencies would help in interpretation of the data from the operational tests. The ideal way to measure mirror tilts is to instrument the mirrors themselves, but this was not possible on either the polished front surface or the inaccessible rear surface. Fortunately, a damaged, but fully functional, high-power optic was available and inserted for this purpose. A detailed modal survey was done on this optic, and the results helped infer frequencies of the tilt modes for the other optics from accelerations measured on the adjacent tangent flanges. Consistent with the predictions, the tests found between  $\frac{1}{2}\%$  and 1.8% viscous damping in the local mirror modes after application of the damping hardware.

A brief modal test was done on the overall bench, the primary goal of which was to identify modes that had large relative motions across the locations of the soon-to-be-installed damped links. For the most part, the frequencies measured during the modal tests were predicted well by the finite element model — within ~5%, though, again, these were not too significant for jitter. Due to very limited test resolution, it was difficult to measure more than the first few bench modes, but the damping of the treated bench was close to that predicted (~1% viscous).

### Operational Testing

The change in beam jitter before and after installation of the damping hardware is the true test of the damping treatments' effectiveness, though it is also the most difficult to measure. There were two primary outputs from the operational testing:

1. displacements of a small diagnostic beam on an X-Y position detector (called UDT hereinafter) after bouncing off the three high-power optics, and
2. acceleration signals taken at key locations on the structure.

The UDT signal was by far the more important measure of jitter, and it is the change in its RMS that was considered the true test of the damping hardware's effectiveness. The before and after measurements, by nature, had to be taken several days apart. There was approximately two days of downtime to remove the optics, apply damping hardware, reinstall the optics, and align the system. The jitter due to the random flow excitations was certain to be different during the second round of testing; the challenge was to sort out effects of damping and other possible changes.

Analysis predicted that the dominant excitation would be the coolant flow to the high-power mirrors, but the effects of different flow rates were not fully understood. Thus, the operational tests consisted of three flows at each of three flow rates. This resulted in a large volume of data. Since it was not practical to record such a volume of data on the modal system's disk, the signals were recorded on 14-track tape. Two passes were made so that 28 signals could be recorded. Of these, two channels were devoted to the UDT (one each for X and Y), and the rest were placed at locations likely to have high response in jitter-sensitive modes.

It was difficult to see clearly the effect of the damping during the operational tests. Cumulative power functions of the UDT's displacement PSDs were used to identify the makeup of the RMS values. For instance, there was more jitter below the frequency of the first elastic mode of the bench after the installation of the damping hardware than before. To sort out the effects of the damping hardware, the rise in the cumulative power was noted over key frequency ranges, i.e., areas of known mirror tilt modes. This method showed a decent improvement in the jitter. The analytical predictions for improvement in jitter accounted for the dynamics of more mirrors, so it is difficult to make direct comparisons between test and analysis. Overall, the damping treatments improved the jitter in the areas of the local mirror modes, just as the analysis predicted.

## CONCLUSIONS

On the whole, the program was successful to the extent that the structure was understood prior to its construction. It is likely that another iteration on the damping hardware, after the initial modal testing, would produce a better, more efficient damping treatment. The correlation was reasonable in that the modes that needed to be damped were, as demonstrated through both modal and operational tests. Figure 6 shows two example frequency-response functions: one from a mirror location and one "looking down the end" of a damped link.

It was clear that many of the largest peaks in the operational PSDs were reduced with the addition of the damping treatment. Looking only at the RMS value of a typical PSD was misleading, since there was significant difference in the energy below the first elastic mode of the bench before and after the damping treatment; the better measure of the damping's effect was the change in cumulative power within the range of elastic modes. Based on this, the RMS was reduced by 4.2% in the UDT X direction and 30.9% in the Y. However, when frequency bands containing the targeted modes are isolated, the contributions to the overall RMS were reduced between 30% and 50%.

## 1.0 INTRODUCTION

Most problems in machine and structure dynamics have been considered in the frequency or speed domain. The information obtained has been hence mostly of the indirect type, giving, eg., the instability threshold or the critical speeds in comparison to the operating ones. In particular, it is not explicit how sensitive and to what, the critical and unstable speeds or resonance frequencies are, and hence additional analysis or experience is required in order to determine whether or not operation will be satisfactory.

A new approach in Machine or system Dynamics, has been developed by the authors [1,2,3], in terms of the system configuration parameters which overcomes this difficulty. The machine or other system configuration is described by a set of parameters, eg. bearing transverse positions ie. alignment of a rotor; joint positions of a truss or a frame etc., giving the relative positions of the sub systems. These parameters are selected so that they can be easily changed in design or assembly without changing the sub systems. They are also subject to manufacturing and assembly errors.

For non-linear elements, eg. fluid-film bearings, variation of the configuration parameters changes the dynamic characteristics of the system. For statically indeterminate systems, additional conditions are imposed, instead of fixing them, thus allowing for the selection (optimisation) of the system dynamics at working speeds. Tolerance selection and experimental correction becomes also possible in this approach, ensuring operation correspondingly close to the selected (optimal) response.

For multi-bearing rotor systems, allowing for both transverse shift and tilt of the bearings, the number of independent configuration parameters is four times the number of bearings minus four equilibrium conditions. If short bearings are assumed, what is usually the case, the tilts and bearing moments disappear. Only the shifts of the bearing centres are considered. This number is then twice the number of bearings minus four. Positions of the centres (now positions of the bearings) of any two bearings can be fixed, providing the reference axis. The remaining independent parameters are varied in the vibration attenuation or dynamic optimisation process. Equivalently, corresponding reactions or point of operation of the bearings can be taken as those parameters.

Fig.1 gives an example of a boiler water feed pump assembly, with the pump-gear rotor considered [4,5,6]. Out of the eight steady state bearing reaction components, the four perpendicular to the load, can be always eliminated if the points of operation (journal centres) are positioned on the equilibrium loci of the bearings, Fig.2, for all the bearing shifts. Only two independent bearing reactions remain in this case, eg. 2 and 3 in Fig.1 and can be used for the vibration attenuation process. The above applies equally well to the aircraft or rocket compressor, gas turbine etc. as well, as to over constrained structures and on the other hand to robots, with the extra mobility providing the independent parameters.



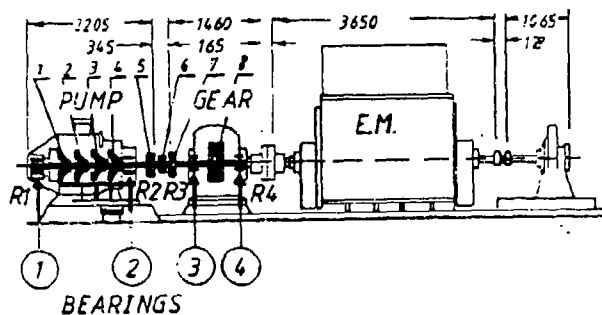


Fig. 1

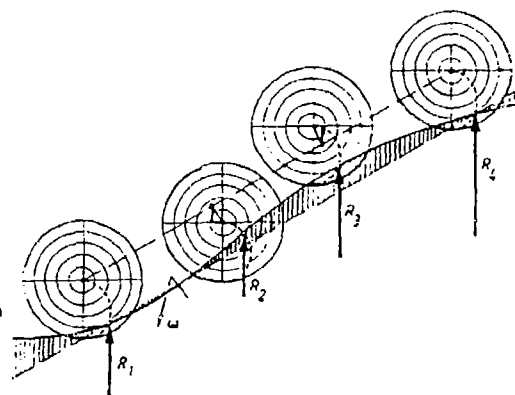
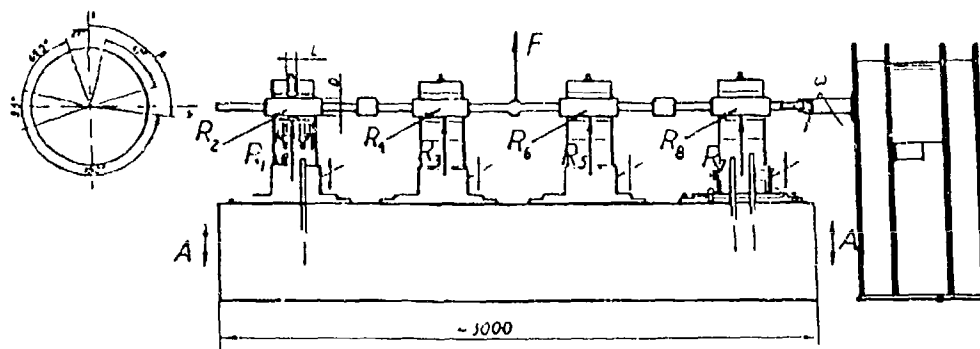


Fig. 2

## 1.1 NOTATIONS

[M]	mass matrix
[C]	damping matrix
[K]	stiffness matrix
[Φ]	eigenvector matrices
$\alpha$	natural circular frequency
$\{\xi\}$	vector of normal co-ordinates
$\Omega$	rotational speed
$c$	clearance ratio
$D$	bearing diameter
$e$	eccentricity
$r$	radial clearance

## 2.0 NON-LINEAR ANALYSIS



$$D = 50 \text{ mm} \quad L/D = 0.83 \quad c = 0.3 \quad \eta = 0.02 \text{ Ns/m}^2 \quad \omega = 300 \text{ rad/s} \quad G = 160 \text{ N}$$

Fig.3

A non-linear approach for rotor-bearing systems and a corresponding computer program system have been developed [7], for transient or post-stability analysis. The following shows their application to a post-stability (limit cycle) analysis of a laboratory installation, shown in Fig.3, [8, 9].

## 2.1 ROTOR MODELLING

With the finite element representation, the rotor is considered as a linear sub-system consisting of beam elements with discs (if existing) mounted at the ends of the elements. Four degrees of freedom i.e. the transverse deflection and cross-section rotation in two axial planes were introduced at each node. However two-level representation, reducing the system to span elements between applied forces, achieved significant reduction of the number of co-ordinates. The stiffness, damping and mass matrices of a span element are assembled from all elements in the span. Using the conditions of compatibility of displacement at the interface of the span elements, the system of second order differential equations (1) is obtained:

$$[M]\{\ddot{U}\} + [C]\{\dot{U}\} + [K]\{U\} = \{F(x, y, \dot{x}, \dot{y})\} + \{P(t)\} \quad (1)$$

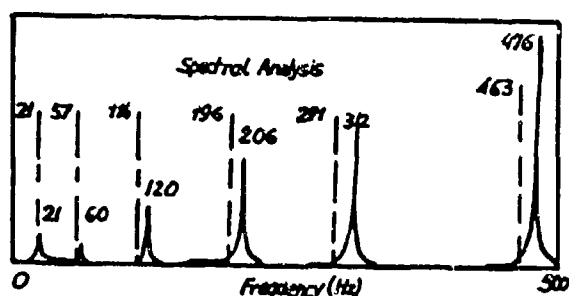


Fig. 4

The transformation into normal co-ordinates provides the natural frequencies and principal modes of the rotor free in space. In this way evaluation of the accuracy of the rotor modelling can be done, Fig. 4, before the system is assembled. The experimental values, also given in Fig. 4, were measured with the shaft suspended flexibly on a rope.

Introducing the normal co-ordinate system of the undamped rotor, equation (1) can be transformed into the second order differential equation system.

$$\{\ddot{\xi}\} + [\Delta]\{\dot{\xi}\} + [\alpha^2]\{\xi\} = [\Phi]^T (\{F\} + \{P\}); \quad [\Delta] = [\Phi]^T [C] [\Phi] \quad (2)$$

The eigenvalues and eigenvectors were computed for an undamped rotor and then damping was reintroduced in the modal (non-diagonal) form shown in (2). The system lower frequency response can be ensured with sufficient accuracy by retaining only a properly selected reduced number of constrained normal modes. Appropriate criteria ought to be applied to determine which modes may be truncated. Stability of the omitted modes should be assessed.

## 2.2 BEARING FORCES

The dimensionless fluid film forces, determined from Reynolds equation (3), are functions of four variables corresponding to the non-dimensional displacement and velocity of the journal centre [10]

$$\frac{\partial}{\partial x} \left( \frac{\rho h^3}{12\mu} \frac{\partial p}{\partial x} \right) + \frac{\partial}{\partial z} \left( \frac{\rho h^3}{12\mu} \frac{\partial p}{\partial z} \right) = \frac{\partial}{\partial x} (\rho h U) + \frac{\partial}{\partial z} (\rho h W) + \frac{\partial}{\partial t} (\rho h) \quad (3)$$

The bearing type used in the experimental installation and in this analysis is presented in Fig.5. The assumed ranges of the non-dimensional parameters are: eccentricity ratio 0.0 to 0.998, velocity ratio -0.6 to 0.6, attitude angle 0.0 to 360 deg. Components of the non-dimensional hydrodynamic forces were computed at the grid nodes and then stored for further use with any parameters of motion, by means of a shape function, specially developed [11]. Fig.6 plots the locus of the end points of the hydrodynamic force vectors. Each of the diagrams consists of several closed curves, corresponding to the eccentricity ratios and a given velocity ratio.

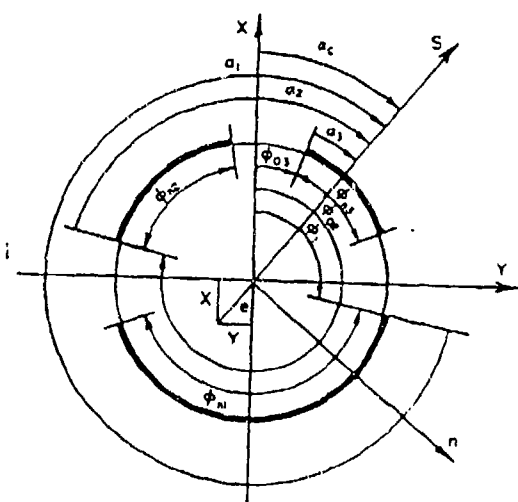


Fig. 5

$\phi_{01} = 97.7$   
 $\phi_{02} = 150$   
 $\phi_{03} = 282.5$   
 $\phi_{04} = 65.5$   
 $\phi_{05} = 18.5$   
 $\phi_{06} = 47$   
 $R = 25 \text{ mm}$   
 $L/2R = 0.83$   
 $r = 0.3 \text{ mm}$

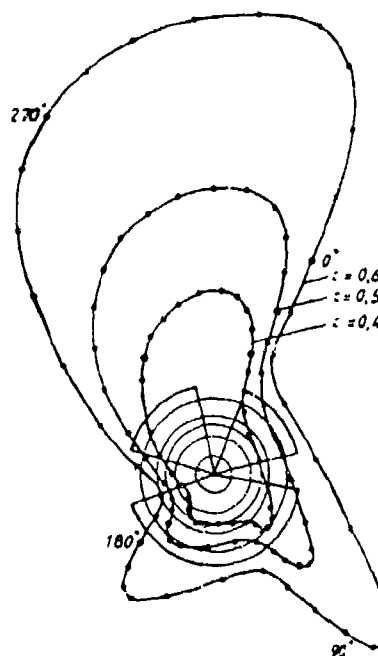


Fig. 6

## 2.3 TRANSIENT AND POST-STABILITY ANALYSIS

Computing the forces produced by a non-linear element (fluid film in the bearing) and applying conditions of force equilibrium along the connecting co-ordinates, the equations of motion are obtained. Their modal form for one of the linear substructures is (where delta is the modal damping matrix):

$$\{\ddot{\xi}\} + [\Delta]\{\dot{\xi}\} + [\alpha^2]\{\xi\} = [\Phi]^T(\{F(\xi)\} + \{P\}) \quad (4)$$

Modal acceleration (assumed constant in a time interval) and modal velocity in the time interval  $k+1$  are expressed by their values in time interval  $k$ , (5).

$$\begin{aligned} \{\ddot{\xi}_{k+1}\} &= D^2\{\xi_{k+1}\} - (D^2\{\xi_k\} + 2D\{\dot{\xi}_k\} + \{\ddot{\xi}_k\}) \\ \{\dot{\xi}_{k+1}\} &= D\{\xi_{k+1}\} - (D\{\xi_k\} + \{\dot{\xi}_k\}), \text{ where } D = 2/\delta t \end{aligned} \quad (5)$$

Substituting (5) into (4) the set of algebraic equations (6) is obtained.

$$\begin{aligned} F &= (\text{diag}[D^2 + \alpha^2] + [\Delta]D)\{\xi_{k+1}\} - [\Phi]^T\{f_{k+1}\} - \{g_k\} = 0 \\ \text{where} \\ \{g_k\} &= D^2\{\xi_k\} + 2D\{\dot{\xi}_k\}\{\ddot{\xi}_k\} \end{aligned} \quad (6)$$

Equation (6) can be solved by Newton-Raphson method for each time instant. For the  $j$ -th iteration the solution, [12], corresponding to the instant  $(k+1)$  is:

$$\begin{aligned} \{\xi_{k+1}^{j+1}\} &= \{\xi_{k+1}^j\} - J^{-1}F^j \\ F^j &= \text{diag}[D^2 + \alpha^2]\{\xi_{k+1}^j\} - [\Phi]^T\{f_{k+1}^j\} - \{g_k\} \end{aligned} \quad (7)$$

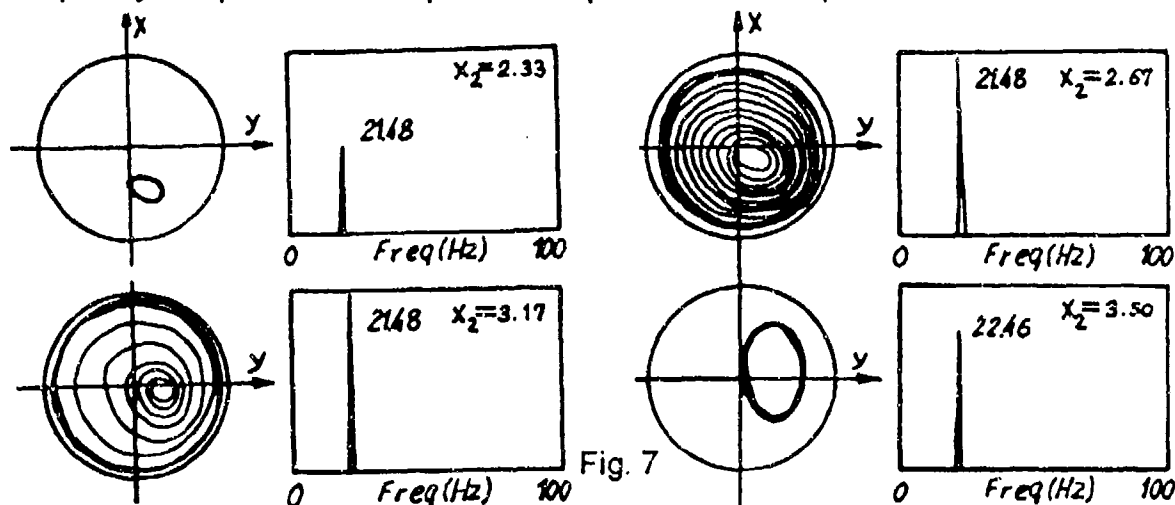
The Jacobian  $J$  is built using the shape function  $N$  presentation of oil pressure distribution.

$$J = \text{diag}[D^2 + \alpha^2] + [\Delta]D - [\Phi]^T \left[ \frac{\partial N(p)}{\partial p} \right] [\Phi]\{\xi_k^0\} \quad (8)$$

## 2.4 LIMIT CYCLE DEVELOPMENT

Some results are given for the four-bearing rotor system studied, Fig.3.

The diagrams, shown in Fig.7 present the journal centre limit cycle trajectories in the first bearing, followed by spectral analysis, revealing the frequency components. The operational speed was 3000 rpm.



The effect of vertical shifts of the second and third bearings on post-stability limit cycle development was studied. The bearing transverse shifts were measured from the straight line passing through the centres of the first and the last bearing. They were normalised by the radial clearance of the bearing. An example of the unbalance influence, at the onset of instability in bearing 2, is shown in Fig.8.

The presented non-linear analysis shows, that the self-excited vibration under unstable conditions attains a limit cycle (tends towards a cycling attractor) for all bearing alignments considered. As long as the limit cycle amplitude remains appropriately smaller than the bearing clearance (represented by the outer circles in Figures 7 and 8), post-stability operation is possible, as actually observed in practice

Bearing no.2  
Rotational speed: 6320 rpm  
2nd jour. br. x-pos. : 0.0  
2nd jour. br. y-pos. : 0.0  
3rd jour. br. x-pos. : 0.0  
3rd jour. br. y-pos. : 0.0

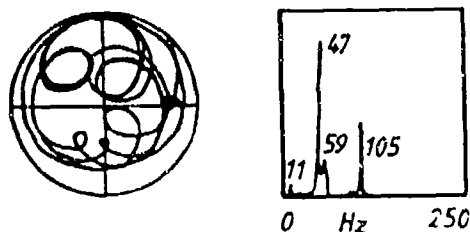


Fig. 8a

## 2.5 VIBRATION ATTENUATION -- SENSITIVITY TO ALIGNMENT

The results present a basis for a design for post-stability operation of rotor-bearing systems and their vibration (limit cycle amplitude) attenuation by the alignment variation. Diagrams like Fig. 8 present the frequency characteristics of a bearing and may be applied for bearing selection avoiding the main system frequencies, without even considering the background non-linear analysis.

To present the results in a better perspective, the system frequency and stability charts were obtained by solving the eigenvalue problem for the linearized system in the neighbourhood of its equilibrium positions (see next section). The contour maps, in Fig. 9 illustrate the changes of the real parts (damping factor), in

the upper diagrams and the imaginary parts (natural frequency) of the two first eigenvalues, at 3000 rpm, in terms of the bearings vertical shifts.

It is apparent by inspection, that the zero-aligned system is stable at 3000 rpm. Its eigenvalues have then their real parts negative. The instability threshold is about 6320 rpm, as shown in Fig. 8. The system stability margin can still be improved (at 3000 rpm), if required, by shifting the two bearings downward in the range of one radial clearance of the bearing ( of the order of 0.1 % of the bearing radius).

For vibration attenuation, the eigenvalue charts can be used (i) to recognise and eliminate frequencies transferred by the environment, or (ii), if these frequencies cannot be eliminated, to tune the system away from them. The plots show where the lowest two resonances are located. The zero-aligned system exhibits a tendency to amplify vibrations of frequencies close to 60 % of rotational speed. The system can be tuned up toward higher frequencies by moving the third bearing upward, in the range of one radial clearance. This, as was already mentioned, also increases the stability threshold.

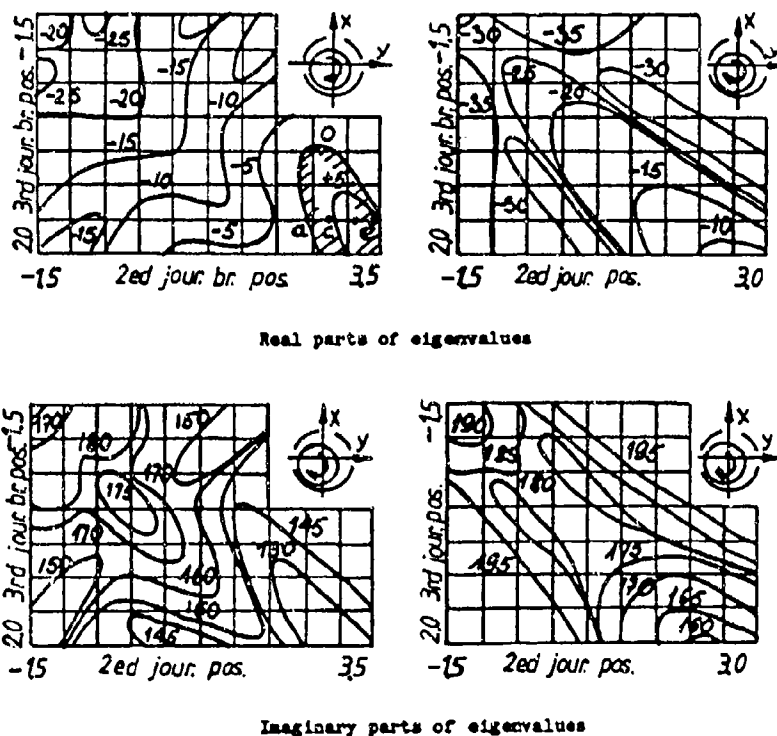


Fig.9

In order to estimate the level of self-excited vibration induced at operational conditions beyond the stability threshold (ie. the limit cycle), non-linear simulation, described before, was performed. Fig. 7 presents the computed limit cycles, at the first bearing, in the post-stability regime, for several positions of the second bearing and constant position of the third one (see Fig.9, points a,c,e). An experimental example of the combined self-excitation and unbalance response, as always existing, is given in Fig.8.

Fig. 10 gives the limit cycle amplitudes at 3000 rpm, for all the bearings, as functions of the second bearing shifts, corresponding to the straight line a-c-e in the unstable area shown in Fig. 9. Vibration attenuation possibilities are obvious, and stability limits are confirmed. Spectral analysis, Figs 7 and 8, revealed the frequencies of self-excited vibration, which remained in constant ratio close to 47% of the rotational speed.

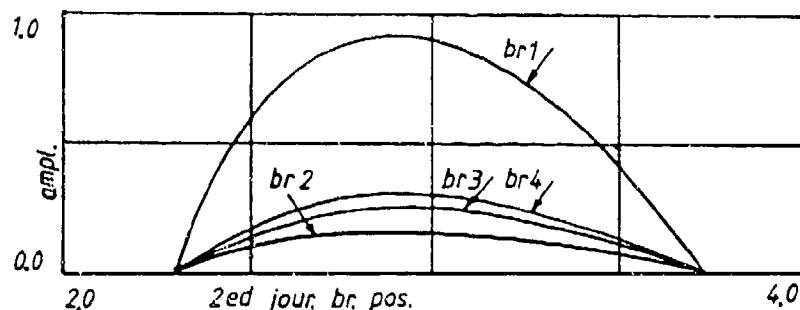


Fig.10

## 2.6 EXPERIMENTAL VERIFICATION

Vibrations were measured for various alignments of the laboratory installation, Fig.3, in the instability region at 3000 rpm, as well as at other speeds in the other region, Fig.9. The experiments confirmed well the computed results. An example of the measured limit cycle, including also unbalance forcing, in the second bearing at the onset of instability at 6320 rpm, at zero-alignment, is given in Fig. 8. At 3000 rpm, the system was only marginally stable with the shifts of 2.5 and 1.5 of the bearings 2 and 3 (the left computed stability boundary in Fig 9), was unstable (Fig. 8b) at 3.0 and 1.5, inside the computed unstable region (self-excited component of 23 Hz is present) and stable again at 3.5 and 1.5 (Fig. 8c) at the outer boundary.

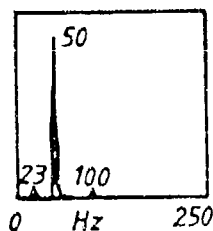
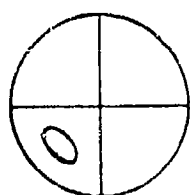


Fig. 8b

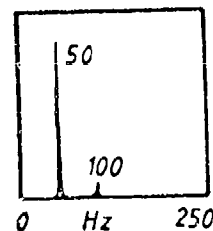
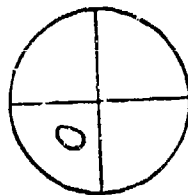


Fig. 8c

### 3.0 STABLE OPERATION -- LINEARIZED APPROACH

In the stability limits, as described by the conditions corresponding to the negative real parts of the eigenvalues, Fig.9, the system has a steady state and a corresponding equilibrium position (of the journals in the bearings). It is sufficient then to consider small vibration in the vicinity of that position. These positions, for a given load direction, say  $y$ , are given by equation (9) and the load condition (10).

$$F_x(x_0, y_0, 0, 0) = 0 \quad (9)$$

$$F_y(x_0, y_0, 0, 0) = P \quad (10)$$

The results are given in Fig.11 a,b, for the non-dimensional load, Sommerfeld number  $S$ . Developing, the previously obtained hydrodynamic force, at any point  $c$  of the equilibrium locus, and retaining only the linear terms, the stiffness and

damping coefficients of the bearing, are obtained, eg.:  $k_{xx} = \left( \frac{\partial F_x}{\partial x} \right)_0$ , Fig.11 c,d.

The linearized characteristics of the bearing takes hence the form presented in Fig.11 and is depending on the eccentricity ratio  $c=e/r$  at the equilibrium position.

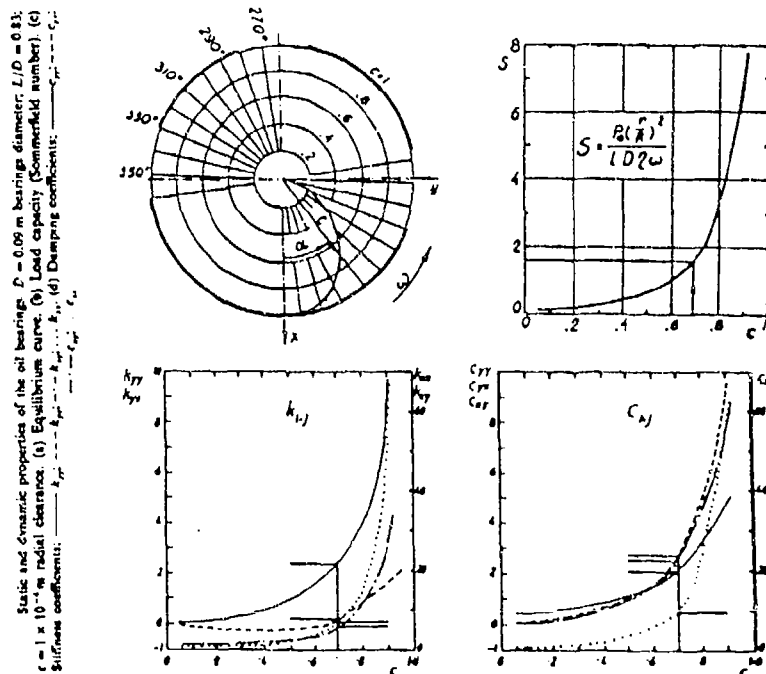


Fig.11

The system's response to a force excitation  $F$  or environment motion  $x_j$  excitation  $E(x_j)$  as well as the stability boundaries (for  $F=E=0$ ), in terms of the bearings independent reactions, are given by the receptance equation (11).

$$[\alpha_s(R_2, R_3, \dots)]^{-1} \{x_1 \quad x_2 \quad \dots \quad x_j \quad x_{j+1} \quad \dots \quad x_i\}^T = \begin{bmatrix} [\alpha_s]^{-1} \{x_1 \quad x_2 \quad \dots \quad x_j\}^T \\ 0 \end{bmatrix} + \{F\} \quad (11)$$



### 3.1 WATER PUMP APPLICATION

The boiler water feed pump, Fig.1 is considered, that presented some vibration problems in the past. These were resonance related and were eliminated by the replacement of the elastic coupling by a lighter one. Here the vibration attenuation, by the dynamically optimal alignment, is considered. The rotor of the pump-gearbox system is supported on four bearings, that dynamic properties depend on the journal steady state equilibrium positions, defined by the bearing reactions  $R$ , (S in non-dimensional form). The matrix of the system dynamic stiffness is a function of frequency  $\beta$  and two independent reactions  $R_2, R_3$ .

$$[\gamma(\beta, R_2, R_3)]\{x\} = \{P(\beta)\} \quad (12)$$

The rotor was modelled by FEM, and the bearings as three lob ones, Fig.11. The response to unit unbalance on the coupling was computed. Fig. 12 presents the square root of the mean square of the shaft amplitudes as a function of two reaction ratios  $R_2, R_3$  (ie. reactions divided by the rotor weight).

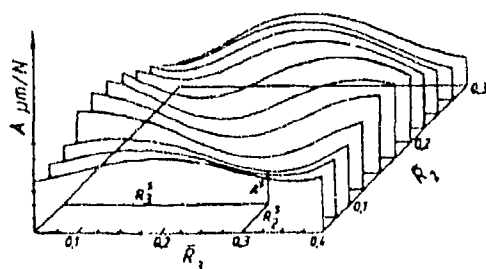


Fig. 12

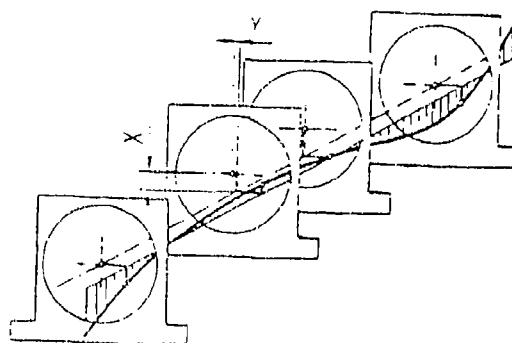


Fig. 13

Optimal reaction ratios are hence selected. Then, rotor elastic line is computed and the journal centre positions in the bearings are found, from Fig. 11, giving eventually an optimal configuration of the pump-gearbox rotor-bearing system, of the form shown in Fig.13.

### 3.2 DYNAMIC OPTIMISATION

The linearized approach, for steady state vibration response, was combined with the "Copes" constrained optimisation program, [12] to produce dynamically optimal configuration of any system, described by the program ANALIZ. This gives the formulation of the vibration response of the system considered in terms of the selected configuration parameters (here, the journals eccentricities in the bearings).  $n-2$  eccentricities may be assumed independently and the remaining two calculated from the equilibrium conditions. The IBM PC-AT, FORTRAN77 version of the mainframe based optimisation program Copes was compiled and applied. Fig. 14 shows the interface of the goal function (vibration level) calculations (the Analiz part) with Copes.

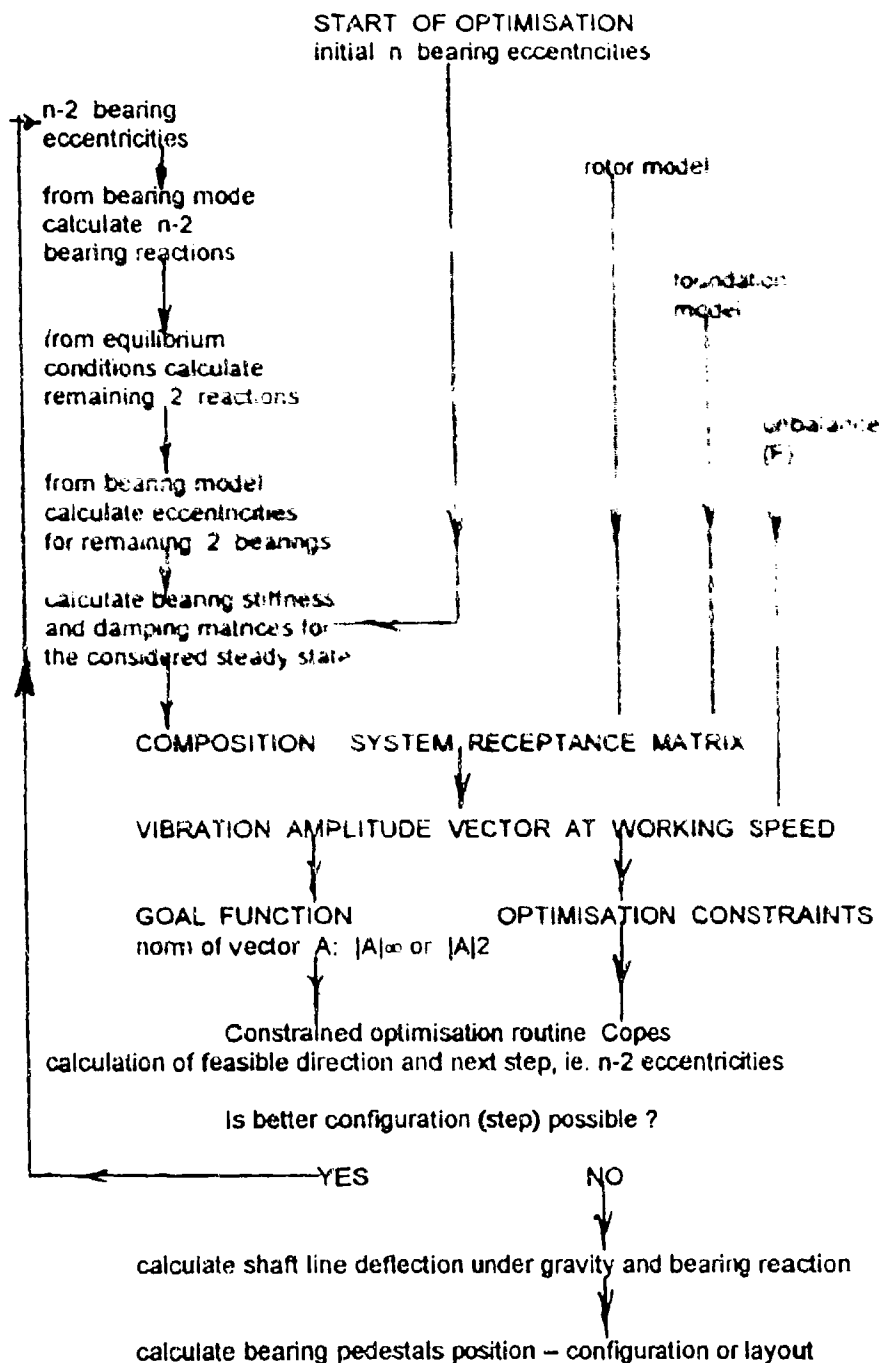


Fig. 14

### 3.4 TURBOGENERATOR APPLICATION

The turbogenerator considered was of 200 MW rating, operated in Latrobe Valley. The main dimensions of its shaft line and the type of all its six bearings are given in Fig. 15, together with the rundown test (for the bearing number 6 pedestal). The data are courtesy of the State Electricity Commission of Victoria

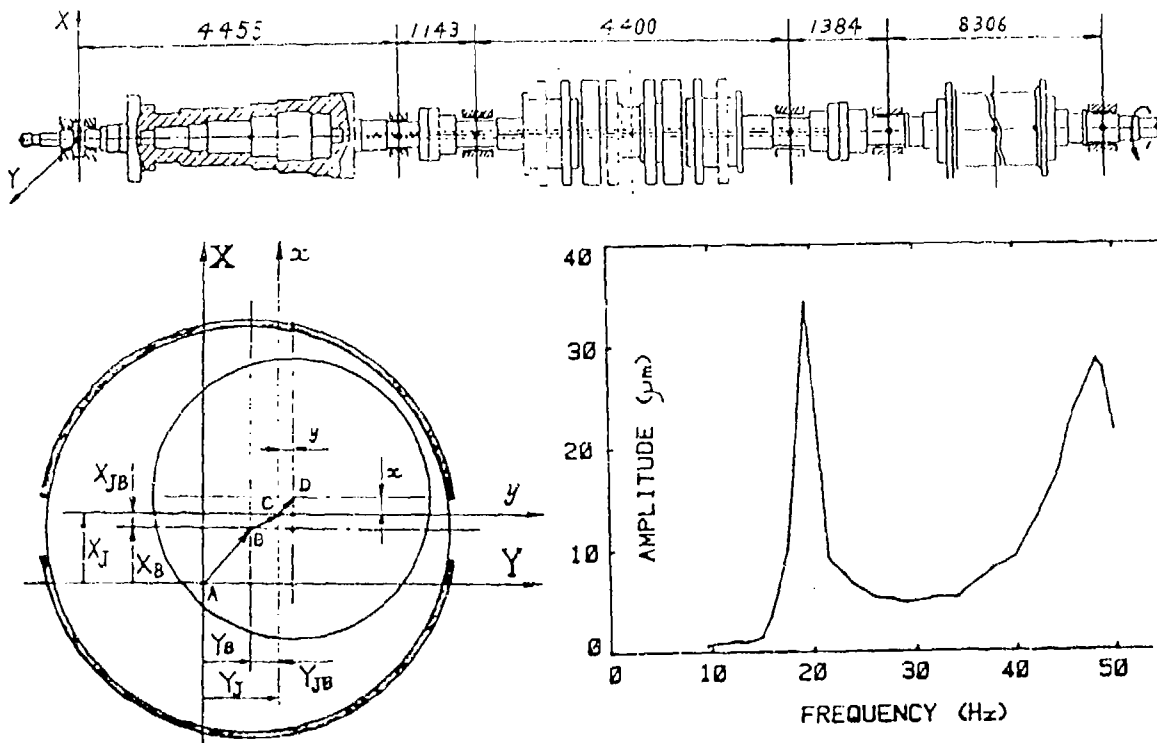


Fig. 15

Table 1 gives the amplitude (goal) function ratios (two lowest rows) of the optimal alignment to the initial one, as well as corresponding eccentricities and reactions in all the bearings.

Table 1	bearing number	initial alignment	optimal alignment
	1	.448	.498
journal	2	.506	.453
eccentricity	3	.310	.386
ratios	4	.367	.208
c	5	.419	.417
	6	.390	.431
bearing	1	.108	.133
reactions	2	.160	.128
	3	.171	.231
MN	4	.173	.083
	5	.212	.210
	6	.203	.238
$ A _{\infty} /  A _0$		1	.607
$ A _2 /  A _0$		1	.848

Computed maximum amplitude dropped nearly 40%, whereas the square average amplitude for the whole shaft line dropped by 15%.

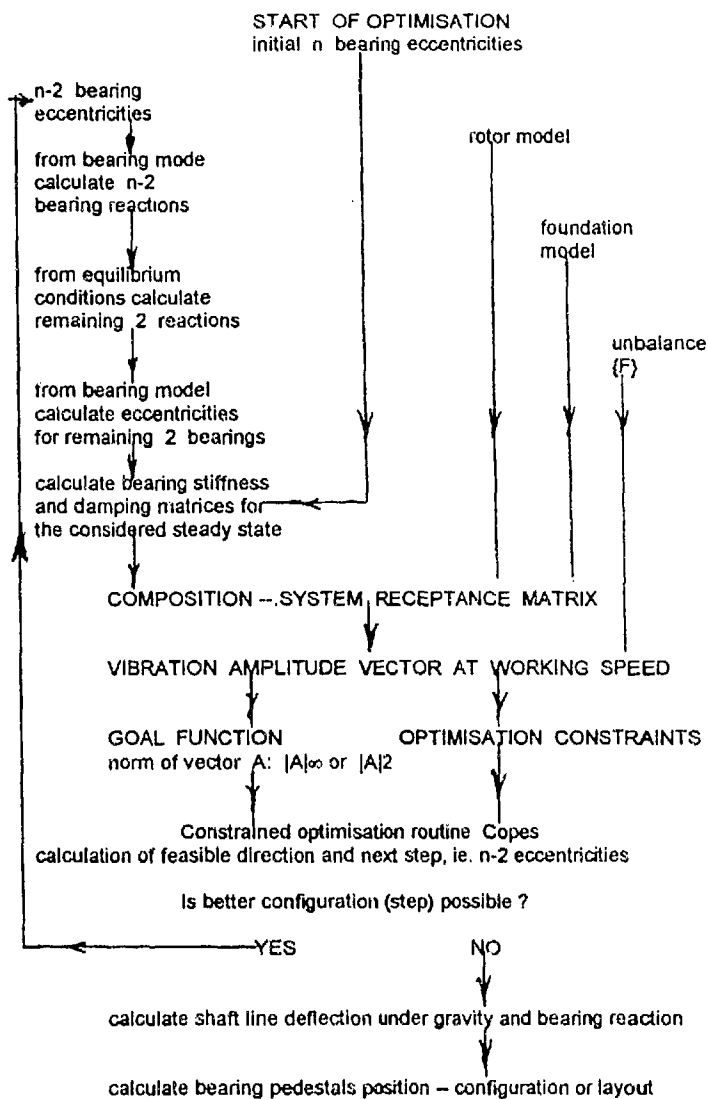


Fig. 14

### 3.4 TURBOGENERATOR APPLICATION

The turbogenerator considered was of 200 MW rating, operated in Latrobe Valley. The main dimensions of its shaft line and the type of all its six bearings are given in Fig. 15, together with the rundown test (for the bearing number 6 pedestal). The data are courtesy of the State Electricity Commission of Victoria

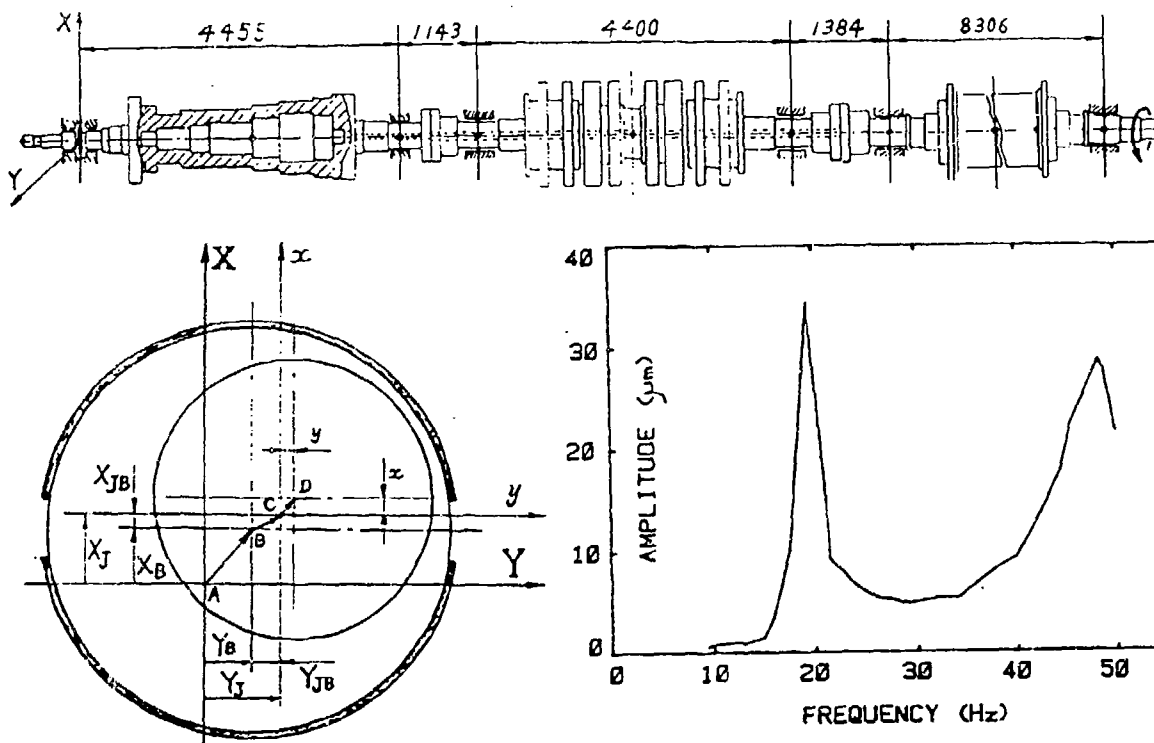


Fig. 15

Table 1 gives the amplitude (goal) function ratios (two lowest rows) of the optimal alignment to the initial one, as well as corresponding eccentricities and reactions in all the bearings.

Table 1	bearing number	initial alignment	optimal alignment
	1	.448	.498
journal	2	.506	.453
eccentricity	3	.310	.386
ratios	4	.367	.208
c	5	.419	.417
	6	.390	.431
bearing	1	.108	.133
reactions	2	.160	.128
	3	.171	.231
MN	4	.173	.083
	5	.212	.210
	6	.203	.238
$ A _{\infty} /  A _{\infty}$		1	.607
$ A _{20} /  A _2$		1	.848

Computed maximum amplitude dropped nearly 40%, whereas the square average amplitude for the whole shaft line dropped by 15%.

#### 4.0 REFERENCES

- 1 Parszewski Z.A., Krodkiwski J.M., "Machine Dynamics in Terms of the System Configuration Parameters", Proceedings of JSME-IFTOMM International Conference on Rotor dynamics, pp 234-244, Tokyo 1986.
- 2 Parszewski Z.A., "Dynamics in terms of the System Configuration Parameters", The Theory of Machines and Mechanisms, Vol.1 pp 327-330, Pergamon Press 1987.
- 3 Parszewski Z.A., "System Configuration and its Vibration Response", Rotating Machinery Dynamics Vol.1, pp 71-78, ASME 1988.
- 4 Parszewski Z.A., Krodkiwski J.M., Skoraczynski J., "Rigid FEM in a Case History of Boiler Water Feed Pump Vibration", Journal of Computers and Structures, Vol.31, No.1, pp 103-110, 1989.
- 5 Parszewski Z.A., "Vibrations and Dynamics of Machines", 422 pages- Polish, WNT, Warsaw 1982.
- 6 Parszewski Z.A., "Effect of Supporting Structure on Rotor Dynamics", Dynamics of Rotors, pp 251-281, Springer Verlag 1984.
- 7 Parszewski Z.A., Krynicki K., "Post-stability (Limit Cycle) Operation in Terms of Bearings Alignment", Rotating Machinery Dynamics, Vol.18, No.1, pp 199-203, ASME 1989.
- 8 Parszewski Z.A., Krodkiwski J.M., Skoraczynski J., "Computer-Experiment Interface in Rotor-Support Dynamics", Computers in Engineering, Vol.1, pp 563-569, ASME 1984.
- 9 Parszewski Z.A., Krynicki K., Kirby E.D., "Effect of Bearing Alignment on Stability Threshold and Post-stability Behaviour of Rotor-Bearing Systems", IMechE Publ. Vol. C263, No. 88, pp 311-316, 1988.
- 10 Parszewski Z.A., Nan X., Li D.X., "FEM for Thermo-Fluid Bearing Dynamic Characteristics", Journal of Computers and Structures, Vol.31, No.1, pp 93-102, 1989.
- 11 Krynicki K., Lewis W.P., Parszewski Z.A., "Shape Function Characteristics of Journal Bearing", Proceedings of the 5th International Conference in Australia on Finite Element Methods, pp 336-339, Melbourne 1987.
- 12 Parszewski Z.A., Krynicki K., "Configuration Sensitivity of Rotor-Bearing System Stability", Noise & Vibration'89, pp C72-C83, Nanyang Technological Institute, Singapore 1989.

- 13 Vandenplaats G.N., Copes - A Fortran Program for Engineering Synthesis, Conmin User's Manual Addendum, May 1979.
- 14 Parszewski Z. A., Li D.X., Multi-Bearing Rotor Response Presentation for the System Optimisation", Proceedings of International Conference on Mechanical Dynamics, Shenyang 1987.
- 15 Parszewski Z.A., Chalko T.J., Li D.X., "Turbogenerator Layout for Optimal Dynamic Response - A Study and A Case History", IMechE publ. Vol.C250, No.80, pp 427-434, 1988.

# Active Vibration Control using Parallel Processing Techniques

Gurvinder S Virk  
University of Bradford

## Abstract

This paper presents some preliminary results of research being done in collaboration with British Aerospace to develop active vibration suppression techniques for use in aircraft systems structures. The work reported here concentrates on a cantilever beam system rig interfaced to a transputer network. Theoretical and rig results are presented. These are based on a parallel processing approach where the overall computing task is partitioned into sub-tasks which are mapped onto suitably configured architectures for achieving real-time performance.

---

<sup>1</sup>Department of Electronic & Electrical Engineering, University of Bradford, Bradford, West Yorkshire BD7 1DP, UK. Tel (274) 384140.



# 1 Introduction

Increasing attention is being paid to acoustic noise and vibration problems in many application areas due to the severe problems which can result; tighter legislation and performance specifications compound the already complex and demanding situation. Vibration problems in particular can cause tremendous damage if adequate precautions are not undertaken in the analysis and design of mechanical structures systems. Most people are aware of the problems due to vibration in vehicles such as cars, aircraft and spacecraft; even large building structures can oscillate due to climatic disturbances. What is not common knowledge to the lay person is that the problem is much more widespread – in fact vibrations arise, to a greater or lesser degree, when *any* mechanical structure is moved. Although in most cases rigid motion is assumed, the actual behaviour is that for a flexible body, that is, the structure “wobbles” as it is shifted from one point to another. These oscillations are usually unwanted and degrade the performance of the system, and so for optimised performance, the oscillatory behaviour needs to be included in the design and analysis. Common methods for dealing with the unwanted oscillations are to

- (i) introduce passive damping elements such as springs and/or dampers – these absorb the unwanted energies which is then dissipated as heat and/or as lower level oscillations;
- (ii) use active control techniques to provide the damping when required – here instead of passive energy absorption, extra “anti-phase” energy is inserted into the structure to cancel the unwanted oscillations; or to
- (iii) use a combination of the two techniques.

This paper concentrates upon some of the vibration problems which arises in fixed wing military aircraft. Here the aircraft structure and avionics systems are subject to considerable aerodynamic and self-induced disturbances such as gun firing. These vibrational problems are getting worse in the lighter designs which are emerging because of the demands for more responsive aircraft. Passive methods on their own cannot easily handle the increased vibrational problems because the weight penalty can cause the aircraft to become sluggish, thus defeating the original design objective to produce an advanced vehicle. The active method, which is much more weight conscious represents a more viable option and is investigated here.

Although the theoretical concept of active control is simple, namely that additional energy is introduced to cancel with the unwanted vibrational energy, the practical implementation problems are much more complex. Determining the correct cancellation signals are extremely difficult because distributed parameter systems are being considered and these possess an infinite number of modes which require handling for good control.

It is clear that in computer control implementations the on-line processing demands for analysing the vibration signals, computing the active control strategy and applying the corrective forces requires significant computing resources. The situation is made worse when complex structures subject to wideband disturbances are studied. Active computer control is so demanding in processing terms that conventional computer systems cannot easily provide sufficient capacity to execute the control algorithms in real-time, and therefore parallel processing techniques as considered here offer a viable alternative. The paper will discuss some aspects of the active vibration control research being done at Bradford University in

collaboration with British Aerospace. The driving motivation for the research is to reduce the levels of vibrations in the aircraft structures upon which the flight avionics are mounted. These structures are essentially racks connected to the aircraft fuselage via anti-vibration (AV) mounts and the avionics are bolted onto these shelf-like structures. Considerable damage to the electronic and mechanical systems can result from the vibrations caused by aerodynamic and sub-system induced shocks. The AV mounts which support the avionics are mechanical shock absorbing devices much like automobile shock absorbers, and they normally have a resonance in the  $\approx 0-100$  Hz range. Disturbances above this frequency are adequately attenuated by the AV mounts, but those below 100 Hz need handling in some other way – one suitable option is to introduce active damping in the 0–100 Hz band; this together with the passive AV mounts could provide sufficient damping so that excessive vibrations over the whole frequency range of interest can be avoided.

As part of developing a solution for the aircraft application, we have been investigating the feasibility of active control by considering vibration control in simple structures. In particular, significant research to suppress one dimensional vibrations in a cantilevered beam system is being carried out. The main results of this work are described next.

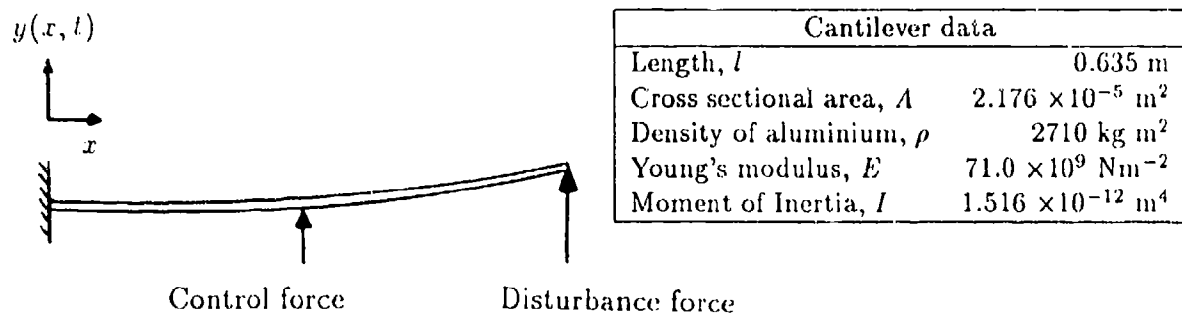


Figure 1: Cantilever beam in transverse vibration

## 2 Cantilever (1D) Vibration Control

The cantilever beam system under study is shown in Figure 1. It is well known that the transverse oscillations are described by the fourth order partial differential equation (PDE)

$$\mu^2 \frac{\partial^4 y(x, t)}{\partial x^4} + \frac{\partial^2 y(x, t)}{\partial t^2} = f_d(x, t) + f_c(x, t) \quad (1)$$

where  $y(x, t)$  is the deflection at a distance  $x$  from the fixed end at time  $t$ ,  $\mu = \frac{EI}{\rho A}$  and  $f_c(x, t)$  and  $f_d(x, t)$  are the control and disturbance forces acting on the beam respectively.

It is well known, see for example Meirovitch [1], that the resonant frequencies for a fixed-free beam are given by

$$\cosh(\beta_i l) \cos(\beta_i l) = -1 \quad \text{for } i = 1, 2, 3, \dots \quad (2)$$

where  $\beta_i^4 = \frac{\omega_i^2}{\mu^2}$ , and  $\omega_i$  are the resonant frequencies. For an aluminium beam of the dimensions shown, it is straightforward to deduce that the first five modes are 11.781,

73.832, 206.732, 405.113 and 669.680 rad s<sup>-1</sup>, or 1.875, 11.751, 32.902, 64.476 and 106.583 Hz.

The dynamic behaviour of such a structure has been studied extensively and is well documented (see for example Meirovitch [1]) and achieving good control using point sensors and actuators is notoriously difficult. Research via simulation and actual rig control is being

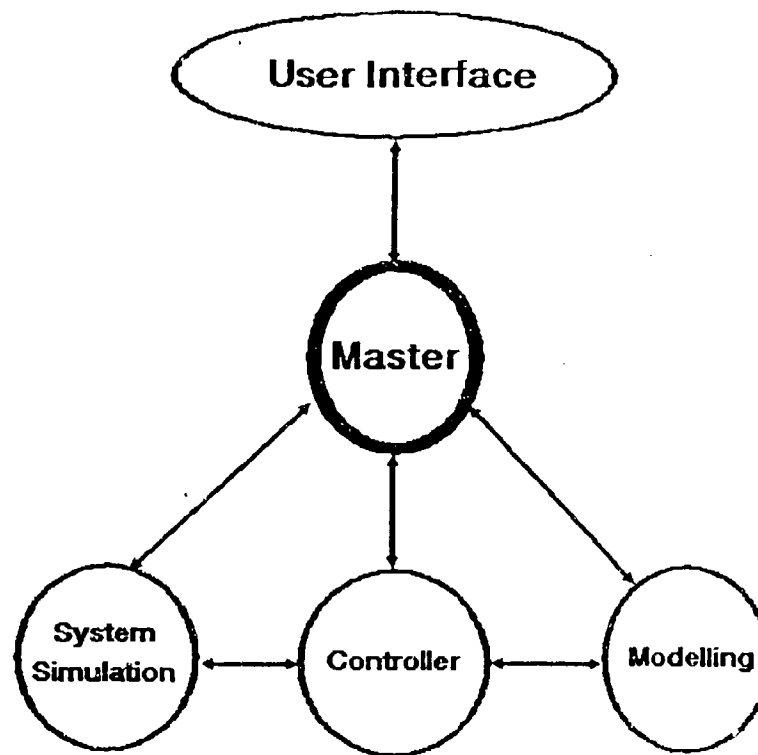


Figure 2: Functional decomposition block diagram

conducted to assess the merits of different control designs in introducing active damping to the structure. In both approaches the overall computing task is decomposed into smaller sub-tasks which are solved on suitably configured transputer networks. A block diagram of the decomposition for the simulation research is shown in Figure 2, where the main processing tasks and how they interact with each other can be seen. This simulation work has been described fully elsewhere (Kourmoulis [2], Virk and Kourmoulis [3]), but for convenience a summary is given here.

### 3 Simulation Research

The simulation work can be carried out in real-time by mapping the partitioned sub-tasks onto suitably configured transputer networks. The overall system synchronization is carried out by the "Master" process which also provides a user interface in the form of a graphics display. The main worker subtasks are:

**System Simulation:** The cantilever system has been simulated using first-order central finite difference approximations to replace the derivatives in equation (1). Using

standard notation, it can be shown that by using a first-order central finite difference method we have

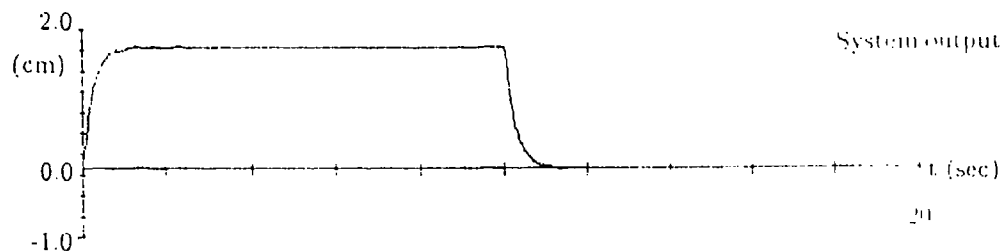
$$\frac{\partial^2 y(x, t)}{\partial t^2} = \frac{y_{j,k+1} - 2y_{j,k} + y_{j,k-1}}{(\Delta t)^2} \quad (3)$$

and

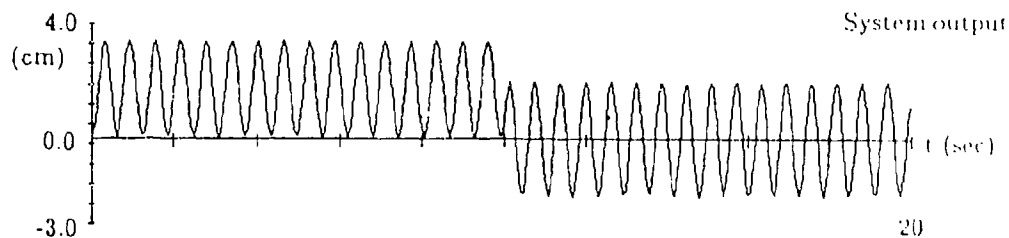
$$\frac{\partial^4 y(x, t)}{\partial x^4} = \frac{1}{(\Delta x)^4} \{y_{j+2,k} + 4y_{j+1,k} + 6y_{j,k} - 4y_{j-1,k} + y_{j-2,k}\} \quad (4)$$

where  $\Delta x$  and  $\Delta t$  are the step sizes along the beam and in time respectively,  $y_{j,k}$  represents the deflection of the beam at point  $j$  along the beam at the  $k^{\text{th}}$  time interval, etc. These formulae can be substituted into equation (1) and numerically solved to yield the beam's deflection under the influence of various disturbance and control forces.

Many parallel implementations for partitioning the overall processing can be carried out, but a straightforward mapping of sections of the beam onto transputers connected in a pipeline configuration appear to be the most appropriate. When the beam is partitioned into 20 sections and a time step size of 0.3 ms is used, it is possible to achieve real-time processing by using 5 T800 transputers.



(a) With state-feedback control



(b) Without compensation

Figure 3: Step sequence response of the beam (free end)

**Modelling:** Using a state-space approach, the beam can be represented by a  $10^{\text{th}}$  order model

$$x(k+1) = Ax(k) + Bu_c(k) + Du_d(k) \quad (5)$$

$$y(k) = Cx(k) \quad (6)$$

where  $A$  is a  $10 \times 10$  system matrix and so the first 5 modes are taken into consideration, and  $u_c$  is the control input and  $u_d$  is the disturbance force; the state for this

model can be estimated using standard observer techniques so that effective control can be attempted.

**Controller Design:** Many controller designs can be considered, such as state feedback and optimal control.

It has been demonstrated that the computing task can be partitioned in a natural way so that efficient parallel solutions are achieved. For effective control "spillover" effects of the unmodelled modes need to be taken into account in the controller design – see for example Balas [4]; essentially such effects dictate that unmodelled modes are prevented from becoming unstable. A step-response when a state feedback controller is utilised on the system simulation is shown in Figure 3(a). Here the controller is designed to introduce critical damping to the 5 modes considered – without the controller the response would show continual oscillation as shown in Figure 3(b) because the beam is assumed to possess no natural damping. The simulation work is continuing to develop further control solutions; in addition the use of the finite element method for simulation purposes is being assessed.

## 4 Cantilever Rig Control

To assess the practical viability of active vibration control the simulation work is being extended to the stage where a real cantilever rig is being used to demonstrate the technique. The practical set-up is shown in Figure 4. There are two rigs developed as part of our

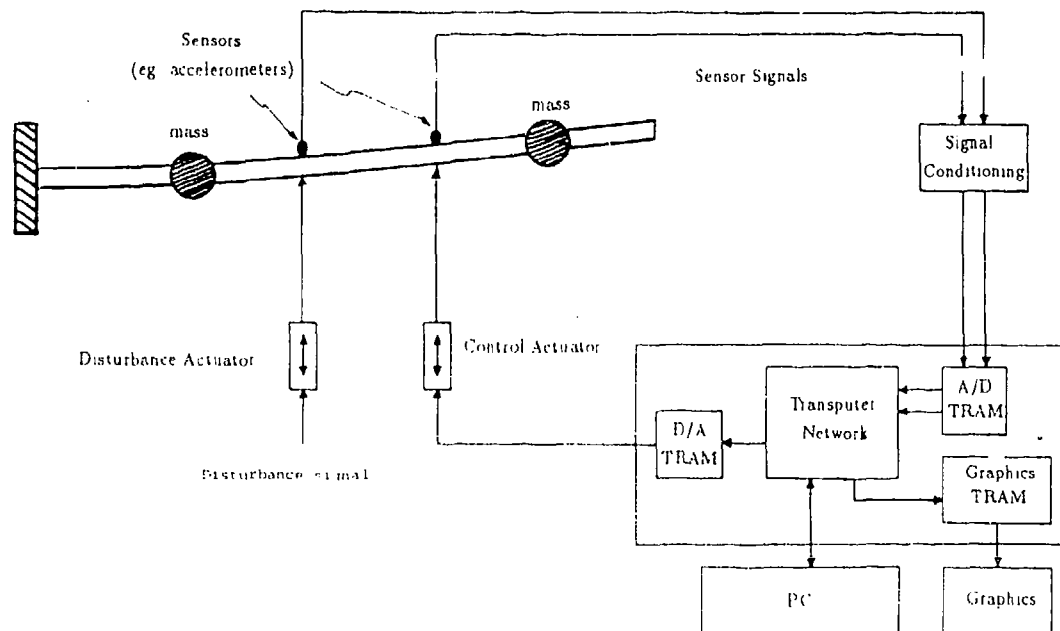


Figure 4: Active vibration control of cantilever rig

research; the first uses Hall effect position sensors to measure beam deflection, whereas the second uses accelerometers. Most of the work to date has concentrated on the position sensor rig, but the accelerometer sensors need to be assessed because the final aircraft solution is expected to utilize such devices.

As in any simulation work and actual practical implementation, there are several differences which need to be addressed before the theory can be applied in practice. The main differences in the rig work and the simulation work presented in the previous subsection are itemised next.

- (i) A Kalman filter is found to be necessary due to the stochastic nature of the signals present in a real rig. In the simulation work an ordinary deterministic state observer was sufficient.
- (ii) There is significant cross-coupling between the different modes; in a purely theoretical analysis such coupling is largely ignored.
- (iii) For ideal vibration control, the sensor and control actuator needs to be co-located (see Leipholz and Abdel-Rohman [5]). This was not possible due to various hardware limitations.

These differences/difficulties are being addressed at present and only preliminary results are available. On the positive side, it has been found that Kalman filtering gives excellent state estimation. A 10<sup>th</sup> order state-space model can predict the beam deflection quite accurately under practical conditions. In addition the concept of modal control has been demonstrated on the rig and the next stage is to consider the situation for wideband disturbances which occur in practice. Several difficulties still remain to be solved before active control becomes widely accepted; one such problem is due to non co-location of the sensor and actuator pairs. It is rapidly becoming clear that for optimum results it is necessary to incorporate distributed sensors and actuators in the design so that the "infinite" dimension of the application can be handled. Although this may seem far fetched, considerable work in the areas of "smart skins" and "smart structures" has been carried out to develop distributed sensors and actuators. Some limited success using piezoelectric type skin structures has already been reported -- see for example the Proceedings of a recent European Conference on Smart Structures [6]. Our future research is likely to be based on such sensors/actuators.

## 5 Conclusions

The use of parallel processing techniques in obtaining active vibration suppression in flexible structures has been discussed. The overall task is partitioned into sub-tasks which are then solved in real-time on suitably configured transputer networks. In this way on-line computer control is possible and the technique has been demonstrated for simple disturbances on a real cantilever rig system. More realistic disturbances need to be studied to establish whether the control strategies under these conditions can be executed in real-time; in principle it should be possible to introduce further transputers to enhance the processing capabilities, but practical demonstration is obviously required.

The next stage from the cantilever studies to make the problem formulation more akin to the true aircraft situation is to consider vibration suppression in thin plates so that the avionic shelf is approximated more closely. Here the vibrations are in 2 directions and the analysis is more complicated than the 1D case, and the processing requirements even more demanding. It is our intention to look into such 2D vibrational problems in the near future, and possibly use more appropriate hardware such as a digital signal processing and parallel processing techniques (DSP<sup>3</sup>), see Tokhi *et al* [7].

## Acknowledgements

The author would like to express his gratitude to Dr P K Kourmoulis who performed most of the detailed programming necessary for this research, and to British Aerospace (Brough) who funded the rig vibration control studies.

## References

- [1] Meirovitch L, Elements of vibration analysis, McGraw-Hill, NY, 1986.
- [2] Kourmoulis P K, Parallel processing in the simulation and control of flexible beam structures, PhD Thesis, University of Sheffield, 1990.
- [3] Virk G S and Kourmoulis P K, Real-Time Vibration Suppression, IEE Colloquium on Parallel Processing: Industrial and Scientific Applications, Digest No 1990/122, 3/1-3/6, 1990.
- [4] Balas M J, Feedback control of flexible systems, IEEE Transactions on Automatic Control, Vol. AC-23, no. 4, pp. 673-679, 1978.
- [5] Leipholz H H E and Adel-Rohman M, Control of Structures, Martinus Nijhoff Publishers, Boston, 1986.
- [6] Proceeding of the First European Conference on Smart Structures and Materials, IOPP/SPIE, Vol 1777, 1992.
- [7] Tokhi M O, Virk G S and Hossain M A; Integrated DSP<sup>3</sup> systems for Adaptive Active Control, IEE Colloquium on Active Techniques for Vibration Control - Sources, Isolation and Damping, Digest No 1992/185, pp 6/1-6/4, 1992.

# ACTIVE CONSTRAINED LAYER DAMPING

A. Baz

Mechanical Engineering Department  
The Catholic University of America  
Washington, DC 20064

## ABSTRACT

This paper presents a new class of Actively-controlled Constrained Layer Damping (ACLD) treatment which can be an effective means for damping out the vibrations of large flexible structures. The proposed ACLD consists of a visco-elastic damping layer which is sandwiched between two piezo-electric layers. The three-layer composite ACLD when bonded to a vibrating surface acts as a SMART constraining layer damping treatment with built-in sensing and actuation capabilities. The sensing is provided by the piezo-electric layer directly bonded to the vibrating surface whereas the actuation is generated by the other piezo-electric layer which acts as an active constraining layer. In this manner, the SMART ACLD consists of a conventional passive constrained layer damping which is augmented with efficient active control means to control the strain of the constrained layer, in response to the structural vibrations. With appropriate strain control, the shear deformation of the visco-elastic damping layer can be increased, the energy dissipation mechanism can be enhanced and the vibration can be damped out.

Therefore, the proposed ACLD relies in its operation on an optimized blend between the attractive attributes of both the active and passive controls. In other words, the simplicity and reliability of passive damping are combined with the low weight and high efficiency of active controls to achieve high damping characteristics over broad frequency bands. Such characteristics are essential to the optimal vibration damping. The fundamentals and the underlying principles that govern the operation of this new class of SMART ACLD are presented. A mathematical model is introduced to describe the interaction between the vibrating structure, piezo-electric sensor/actuator and visco-elastic damping layer. The model provides means for predicting the damping characteristics of the ACLD as a function of its design parameters. Comparisons with the performance of conventional passive constrained layer damping are presented. The results obtained emphasize the excellent merits of the SMART Actively-controlled Constrained Layer Damping and suggest its suitability for numerous critical applications such as aircraft cabins and interior of passenger cars.



## 1. INTRODUCTION

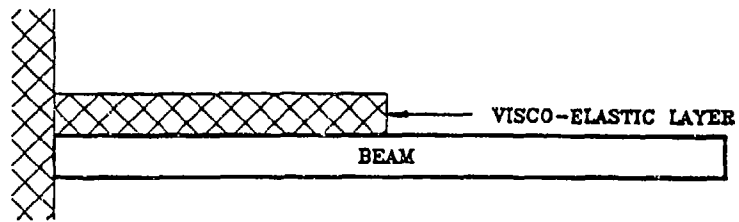
Passive surface treatments have been extensively utilized, as a simple and reliable means, for damping out the vibration of a wide variety of flexible structures (Cremer, Heckl and Ungar 1988). Such surface treatments rely in their operation on the use of visco-elastic damping layers which are bonded to the vibrating structures either in an unconstrained or constrained configuration as shown in Figures (1-a) and (1-b) respectively. Under cyclic loading, constrained damping layers experience shear strains which are much larger than those encountered in unconstrained damping layers (Nashif, A., D. Jones and J. Henderson 1985). Accordingly, the constrained damping layers are capable of dissipating higher vibrational energies and, in turn, achieving higher damping ratios than their counter-parts: the unconstrained damping layers. Higher damping ratios can also be attained, over a broad range of temperatures and frequencies, through the use of multi-damping layers (Asnani and Nakra 1976). However, these high damping ratios are obtained at the expense of adding considerable weight to the vibrating base structures. This poses serious limitation to their use for many applications where the weight is of critical importance.

It is therefore the purpose of this paper to introduce a new class of Actively-controlled Constrained Layer Damping (ACLD) treatment which has high energy dissipation-to-weight ratio as compared to conventional constrained or unconstrained damping layer configurations.

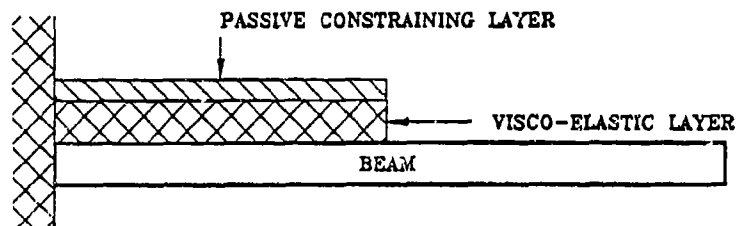
The proposed ACLD consists of a conventional **passive** constrained layer damping which is augmented with efficient **active** control means to control the strain of the constrained layer, in response to the structural vibrations as shown in Figure (1-c). The visco-elastic damping layer is sandwiched between two piezo-electric layers. The three-layer composite ACLD when bonded to a vibrating surface acts as a SMART constraining layer damping treatment with built-in sensing and actuation capabilities. The sensing, as indicated by the sensor voltage  $V_s$ , is provided by the piezo-electric layer which is directly bonded to the vibrating surface. The actuation is generated by the other piezo-electric layer which acts as an active constraining layer that is activated by the control voltage  $V_c$ . With appropriate strain control, through proper manipulation of  $V_s$ , the shear deformation of the visco-elastic damping layer can be increased, the energy dissipation mechanism can be enhanced and the structural vibration can be damped out.

In this manner, the ACLD provides a viable means for damping out the vibration as it combines the attractive attributes of passive and active controls. This makes the ACLD particularly suitable for critical applications where damping-to-weight ratio is important as in aircrafts and automobiles

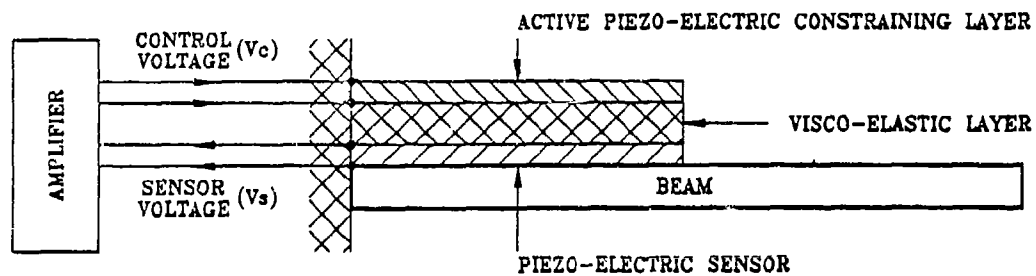
This paper is organized in five sections and an appendix. In section 1 a brief introduction is given. The concept of the active constrained layer damping is presented in section 2. The theory governing the operation of the ACLD is developed in section 3. In section 4 the performance of the ACLD is presented and compared with those of conventional constrained layer damping and classical active control strategies. Section 5 gives a brief summary of the conclusions and the appendix presents the dynamics of plain and actively controlled beams.



(a)



(b)



(c)

Figure (1) - Passive and active layer damping  
 (a) - passive: unconstrained,  
 (b) - passive: constrained,  
 (c) - active : constrained.

## 2. THE CONCEPT OF THE ACTIVE CONSTRAINED LAYER DAMPING

The proposed ACLD consists of a visco-elastic damping layer which is placed in between two piezo-electric layers as shown in Figure (2). The three-layer composite ACLD is bonded to a vibrating beam to act as a SMART constraining layer damping treatment with built-in sensing and actuation capabilities. The sensing is provided by the piezo-electric layer directly bonded to the vibrating surface whereas the actuation is generated by the other piezo-electric layer which acts as an active constraining layer. The effect of interaction between the sensor and the actuator on the operation of the ACLD can best be understood by considering the motion experienced by the beam during a typical vibration cycle. In Figure (2-a), as the beam moves downward away from its horizontal equilibrium position, the sensor which is bonded to the outer fibers of the beam will be subjected to tensile stresses generating accordingly a positive voltage  $V_s$  by the direct piezo-electric effect. If the sensor voltage is amplified, its polarity is reversed and the resulting voltage  $V_c$  is fed back to activate the piezo-electric constraining layer; the constraining layer will shrink by virtue of the reverse piezo-electric effect. The shrinkage of the active constraining layer results in a shear deformation angle  $\gamma_p$  in the visco-elastic layer, which is larger than the angle  $\gamma_c$  developed by a conventional passive constraining layer as indicated in Figure (2-a).

Similarly, Figure (2-b) describes the operation of the ACLD during the upward motion of the beam. During this part of the vibration cycle, the top fibers of the beam as well as the piezo-electric sensor experience compressive stresses and a negative voltage is generated by the sensor. Direct feedback of the sensor signal to the active constraining layer makes it extend and increases accordingly the shear deformation angle to  $\gamma_p$  as compared to  $\gamma_c$  for the conventional constraining layer.

The increase of the shear deformation of the visco-elastic layer, during the entire vibration cycle, is accompanied with an increase in the energy dissipated. Furthermore, the shrinkage (or expansion) of the piezo-electric layer during the upward motion (or during the downward motion) produces a bending moment on the beam which tends to bring the beam back to its equilibrium position. Therefore, the dual effect of the enhanced energy dissipation and the additional restoring bending moment will quickly damp out the vibration of the flexible beam. This dual effect, which does not exist in conventional constrained damping layers, significantly contributes to the damping effectiveness of the SMART ACLD. In this manner, the SMART ACLD consists of a conventional **passive** constrained layer damping which is augmented with the described dual effect to actively control the strain of the constrained layer, in response to the structural vibrations. With appropriate strain control strategy, the shear deformation of the visco-elastic damping layer can be increased, the energy dissipation mechanism can be enhanced and the vibration can be damped out. One possible strategy is the direct feedback of the sensor voltage to power the active constraining layer. Other strategies will rely on feeding back both the sensor voltage and its derivative to obtain proportional and derivative control action. With such a strategy additional damping can be imparted to the vibrating beam system and the versatility of active controls can be utilized to considerably improve the damping characteristics of the ACLD.

Therefore, the proposed ACLD relies in its operation on a blend between

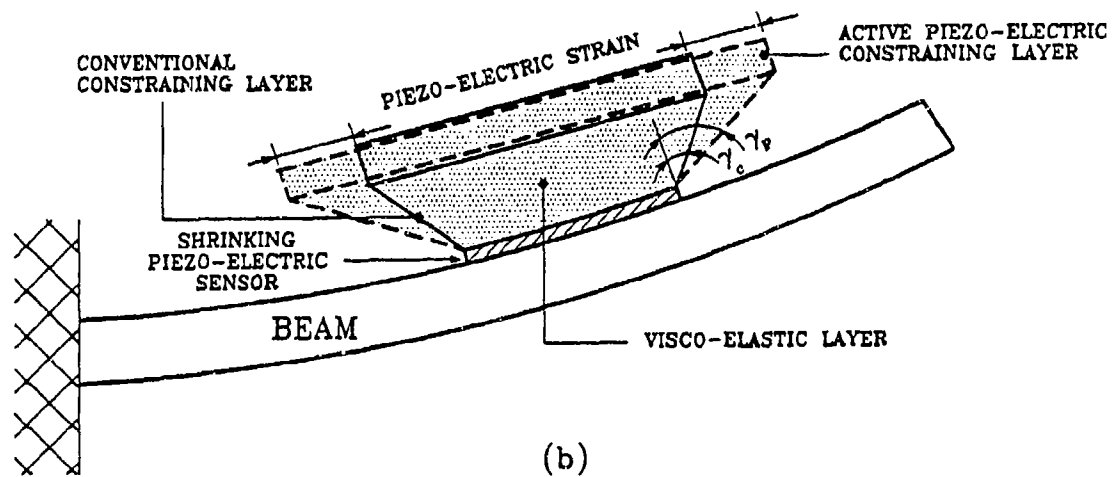
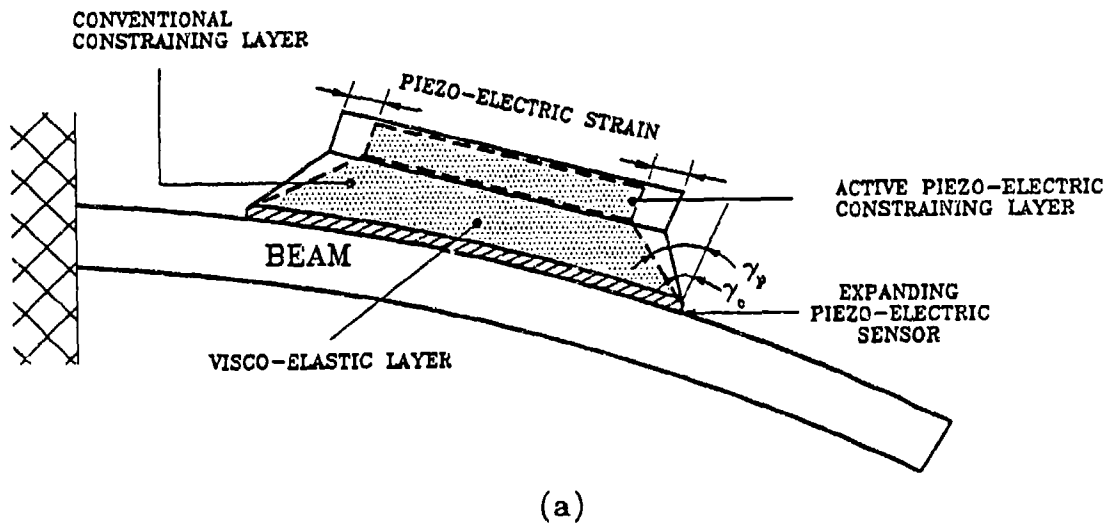


Figure (2) - Operating principle of the active constrained layer damping

the attractive attributes of both the active and passive controls. In other words, the simplicity and reliability of passive damping are combined with the low weight and high efficiency of active controls to achieve high damping characteristics over broad frequency bands. Such characteristics are essential to the optimal damping of vibration.

Also, it is critical here to mention that the ACLD provides an excellent and practical means for controlling the vibration of massive structures with the currently available piezo-electric actuators without the need for excessively large actuation voltages. This is due to the fact that the ACLD properly utilizes the piezo-electric actuator to control the shear in the soft visco-elastic core which is a task compatible with the low control authority capabilities of the currently available piezo-electric materials.

It is important to note that the ACLD configuration described in Figure (2) is only one of many other possible configurations. For example, the ACLD can be arranged in multi-layer configuration or in discrete patches that are distributed at optimal locations over the vibrating structure. Other possible configurations are only limited by our imagination.

### 3. THEORETICAL MODELING OF THE ACTIVE CONSTRAINED LAYER DAMPING

#### 3.1. Overview

A mathematical model is developed, in this section, to investigate the fundamentals and underlying principles governing the operation of the ACLD treatments. The model is based on the well-known shear damping model of Mead and Markus (1969 and 1970) which has been extensively used to analyze the dynamics of passive constrained layer damping (Lu and Douglas 1974 and Douglas and Yang 1978). The shear damping model is integrated with the models describing the behavior of the distributed piezo-electric sensor (Miller and Hubbard 1986) and the distributed piezo-electric actuator (Crawley and de Luis 1987) to generate the ACLD model. Appropriate control laws are considered to control the interaction between the piezo-sensor and actuator in order to achieve enhanced vibration control characteristics.

The emphasis of the present study is placed on the development of an analytical model for Bernoulli-Euler beams which are fully-treated with a single layer of ACLD in order to demonstrate the feasibility and merits of the ACLD concept. Analytical solutions and finite element analyses of fully or partially-treated Timoshenko beams, plates and shells with single or multi-ACLD are natural extensions of the present study.

#### 3.2. The model

Figure (3-a) shows a schematic drawing of the ACLD treatment of a sandwiched beam. It is assumed that the shear strains in the piezo-electric sensor/actuator layers and in the base beam are negligible. It is also assumed that the longitudinal stresses in the visco-elastic core are negligible. The transverse displacements  $w$  of all points on any cross section of the sandwiched beam are considered to be equal. Furthermore, the piezo-electric sensor/actuator layers and the base beam are assumed to be elastic and dissipate no energy whereas the core is assumed to be linearly visco-elastic. In addition, the piezo-electric sensor and the base beam are considered to be perfectly bonded together such that they can be reduced to a single equivalent layer. Accordingly, the original four-layer sandwiched

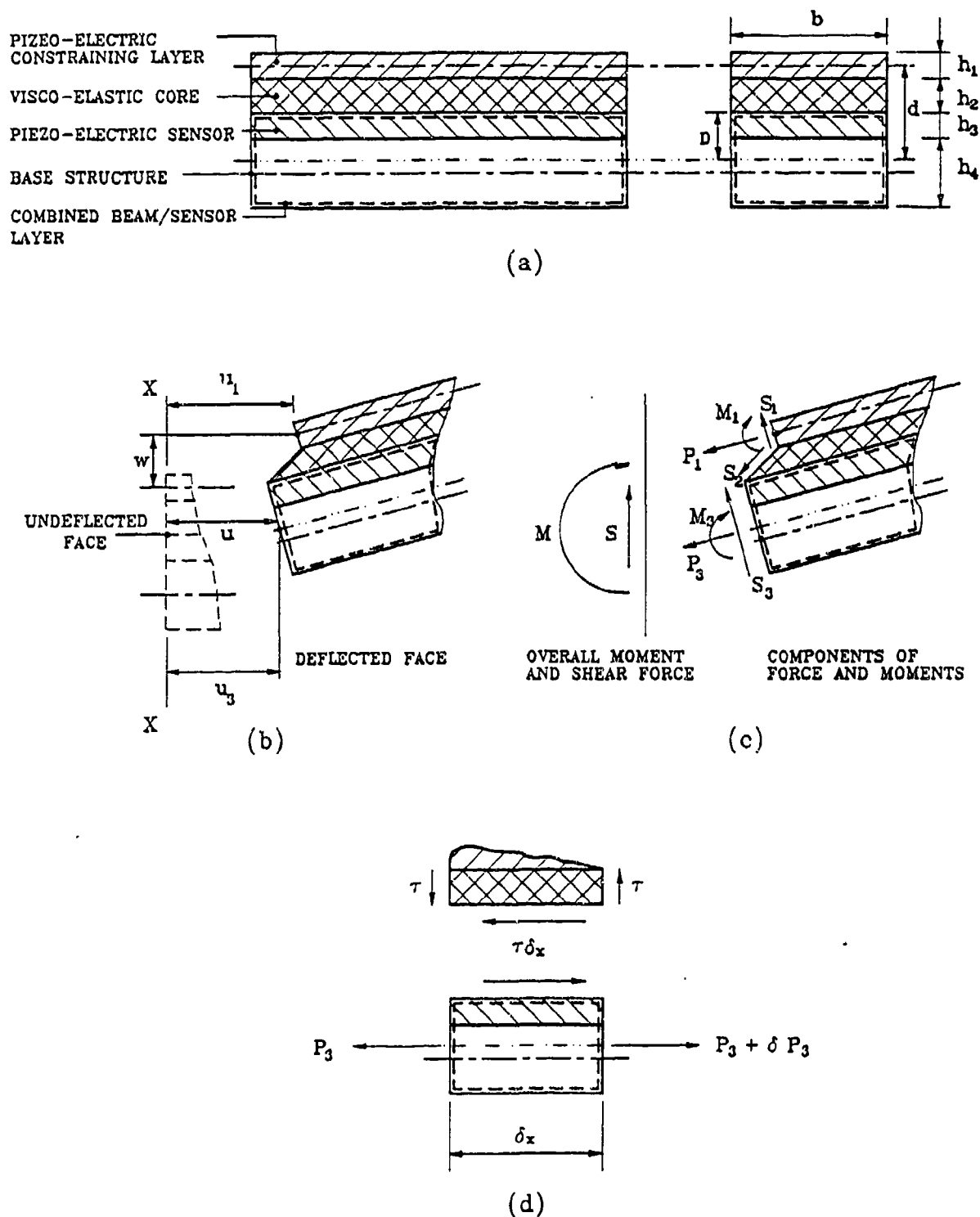


Figure (3) - Schematic drawing of the active constrained layer damping

(a) - structure and geometry

(b) - deflections, (c) - loads,

(d) - sensor/beam layer.

beam reduces to an equivalent three-layer beam.

From the geometry of Figure (3-b), it can be seen that the shear strain  $\gamma$  in the core is given by:

$$\gamma = d/h_2 \partial w/\partial x + (u_1 - u_3)/h_2 \quad (1)$$

where  $d = h_2 + h_1/2 + D$  (2)

with  $D$  denoting the distance from the neutral axis of the beam/sensor layer to the interface with the visco-elastic layer. It is given by:

$$D = (E_3 h_3^2 + 2E_4 h_3 h_4 + E_4 h_4^2) / [2(E_3 h_3 + E_4 h_4)] \quad (3)$$

where  $h_1$ ,  $h_2$ ,  $h_3$  and  $h_4$  denote the thicknesses of the piezo-actuator, the visco-elastic layer, the piezo-sensor and the base beam respectively. Also,  $E_3$  and  $E_4$  define Young's moduli of the piezo-sensor and beam respectively.

Considering Figure (3-c), then the shear forces  $S_1$ ,  $S_2$  and  $S_3$  acting on the piezo-actuator, visco-elastic layer and the sensor/beam layer are given by:

$$S_1 = E_1 I_1 \partial^3 w / \partial x^3, \quad S_2 = -G \gamma d b \quad \text{and} \quad S_3 = E_e I_e \partial^3 w / \partial x^3 \quad (4)$$

where  $E_1 I_1$  is flexural rigidity of piezo-actuator,  $E_e I_e$  is flexural rigidity of sensor/beam layer ( $= E_3 I_3 + E_4 I_4$ ),  $G$  is the complex shear modulus of the visco-elastic layer and  $b$  is the beam width.

Therefore, the total shear force  $S$  acting on the sandwiched beam cross section is:

$$S = S_1 + S_2 + S_3 \quad (5)$$

and the transverse loading  $p$  acting on a unit beam width is given by:

$$p = \partial S / \partial x = D_t \partial^4 w / \partial x^4 - G d^2 / h_2 \partial^2 w / \partial x^2 - G d / h_2 (\partial u_1 / \partial x - \partial u_3 / \partial x) \quad (6)$$

where  $D_t$  is given by:

$$D_t = (E_1 I_1 + E_e I_e) / b \quad (7)$$

Let the net longitudinal forces/unit width which are acting on the piezo-actuator layer and the sensor/beam equivalent layer be  $P_1$  and  $P_3$  respectively. Then, these forces are given by:

$$P_1 = E_1 h_1 (\partial u_1 / \partial x - \epsilon_p) \quad \text{and} \quad P_3 = E_e h_e \partial u_3 / \partial x \quad (8)$$

where  $E_e h_e = E_3 h_3 + E_4 h_4$  and  $\epsilon_p$  is the strain induced into the piezo-electric actuator layer described in section 3.4.

The equilibrium of the forces in the longitudinal direction requires that:

$$P_1 + P_3 = 0 \quad (9)$$

giving:  $E_1 h_1 (\partial u_1 / \partial x - \epsilon_p) = -E_e h_e \partial u_3 / \partial x$  (10)

Combining equations (6) and (10) gives:

$$\partial^4 w / \partial x^4 - (gY) \partial^2 w / \partial x^2 + (g E_e h_e d / D_t) \partial u_3 / \partial x - (gY/d) \epsilon_p = p / D_t \quad (11)$$

where

$$g = G/h_2 [(E_1 h_1 + E_e h_e) / E_1 h_1 E_e h_e] \text{ and } Y = d^2 / D_t [E_1 h_1 E_e h_e / (E_1 h_1 + E_e h_e)] \quad (12)$$

Considering the longitudinal equilibrium of the sensor/beam element shown in Figure (3-d) gives:

$$\partial P_3 / \partial x = - G \gamma \quad (13)$$

Combining equations (1), (8), (10) and (13) gives:

$$\partial^2 u_3 / \partial x^2 - g u_3 = - (gY D_t / E_e h_e d) \partial w / \partial x - (G / E_e h_e h_2) \times \epsilon_p \quad (14)$$

Eliminating  $u_3$  between equations (11) and (14) yields the following equation:

$$\partial^6 w / \partial x^6 - g(1+Y) \partial^4 w / \partial x^4 = 1/D_t (\partial^2 p / \partial x^2 - gp) \quad (15)$$

which is the same differential equation as that of the passive constrained layer damping treatment.

When the sandwiched beam is subject to time-dependent external transverse loading  $q(x, t)$ , then the total transverse loading  $p$  including the linear inertia is given by:

$$p = - m \partial^2 w / \partial t^2 + q \quad (16)$$

where  $m$  is the mass/unit width and unit length of the sandwiched beam.

From equations (15) and (16), we have:

$$\partial^6 w / \partial x^6 - g(1+Y) \partial^4 w / \partial x^4 + m/D_t (\partial^4 w / \partial x^2 \partial t^2 - g \partial^2 w / \partial t^2) = 1/D_t (\partial^2 q / \partial x^2 - gq) \quad (17)$$

Using the classical separation of variables approach, the transverse deflection  $w$  can be expressed by the following equation:

$$w = W(x) T(t) \quad (18)$$

where  $W(x)$  is a spatial function in  $x$  and  $T(t)$  is a temporal function of the time  $t$ . Substituting equation (18) into equation (17) and setting  $\ddot{T}/T = -\omega^2$  yields the following characteristic equation:

$$[\lambda^6 - g(1+Y) \lambda^4 - \omega^2 m / D_t \lambda^2 + \omega^2 m / D_t g] W = 0 \quad (19)$$

where  $\lambda$  is the differential operator with respect to  $x$ . The roots  $\pm \delta_1$  of the above characteristic equation are given by:

$$\delta_1 = [(\gamma_1 + \gamma_2) + g/3 (1+Y)]^{1/2} \quad (20)$$

$$\delta_2 = [-(\gamma_1 + \gamma_2)/2 + 1 (\gamma_1 - \gamma_2) \sqrt{3}/2 + g/3 (1+Y)]^{1/2} \quad (21)$$



$$\delta_3 = [-(\gamma_1 + \gamma_2)/2 - 1 (\gamma_1 - \gamma_2)\sqrt{3}/2 + g/3 (1+Y)]^{1/2} \quad (22)$$

where  $\gamma_1 = [-\zeta_2/2 + (\zeta_2^2/4 + \zeta_1^3/27)^{1/2}]^{1/3} \quad (23)$

$$\gamma_2 = [-\zeta_2/2 - (\zeta_2^2/4 + \zeta_1^3/27)^{1/2}]^{1/3} \quad (24)$$

with  $\zeta_1 = - (m \omega^2/D_t) - 1/3 g^2 (1+Y)^2 \quad (25)$

$$\zeta_2 = g(m \omega^2/D_t) - 1/3 g(1+Y)(m \omega^2/D_t) - 2/27 g^3 (1+Y)^3 \quad (26)$$

These roots can be used to generate the spatial function  $W(x)$  as follows:

$$W(x) = C_1 e^{\delta_1 x} + C_2 e^{-\delta_1 x} + C_3 e^{\delta_2 x} + C_4 e^{-\delta_2 x} + C_5 e^{\delta_3 x} + C_6 e^{-\delta_3 x} \quad (27)$$

where the coefficients  $C_i$ 's can be determined from the boundary conditions of the sandwiched beam.

### 3.3. The boundary conditions

The computation of the six coefficients requires the specification of six boundary conditions. For a cantilevered sandwiched beam subject to sinusoidal transverse load  $P_0$  at its free end, these boundary conditions are:

a. at the free end ( $x = 0$ )

i. **moment  $M(x=0)$  is zero** This yields the following equation:

$$M = D_t/g [-\partial^4 W/\partial x^4 + g(1+Y) \partial^2 W/\partial x^2 + m\omega^2/D_t W + (gY/d) \epsilon_p] = 0 \quad (28)$$

ii. **shear force equals applied load** Differentiating the above moment equation with respect to  $x$  gives the shear force  $S$  which yields the following expression:

$$S = D_t/g [-\partial^5 W/\partial x^5 + g(1+Y) \partial^3 W/\partial x^3 + m\omega^2/D_t \partial W/\partial x] = P_0 e^{i\omega t} \quad (29)$$

iii. **Longitudinal displacement is unrestrained** This gives the following expression:

$$P_3 = - D_t/g [-\partial^4 W/\partial x^4 + (gY) \partial^2 W/\partial x^2 + m\omega^2/D_t W + (gY/d) \epsilon_p] = 0 \quad (30)$$

It can be easily shown that the above equations reduce to the following three boundary conditions at the free end of the beam:

$$[ \partial^4 W/\partial x^4 - m\omega^2/D_t W - (gY/d) \epsilon_p ]_{x=0} = 0, \quad (31)$$

$$[ \partial^3 W/\partial x^3 ]_{x=0} = P_0/D_t e^{i\omega t}, \quad (32)$$

and  $[ \partial^2 W/\partial x^2 ]_{x=0} = 0. \quad (33)$

b. at the fixed end ( $x = L$ )

i. transverse deflection is zero

$$[W]_{x=L} = 0, \quad (34)$$

ii. slope is zero

$$[\partial W / \partial x]_{x=L} = 0, \quad (35)$$

iii. shear of visco-elastic layer is zero This gives :

$$[\partial^5 W / \partial x^5 - Y_g \partial^3 W / \partial x^3 - (m\omega^2 / D_t) \partial W / \partial x]_{x=L} = 0 \quad (36)$$

Equation (31) indicates the dependence of the boundary conditions on the piezo-actuator strain  $\epsilon_p$  which in turn depends on the piezo-sensor output voltage  $V_s$  and the control law that governs the interaction between the sensor and the actuator. Computations of  $\epsilon_p$ ,  $V_s$  and the appropriate control laws are given in sections 3.4, 3.5 and 3.6 respectively.

It is important to note that the development of the ACLD model is presented in the same manner and using the same nomenclature as the Passive Constrained Layer Damping (PCLD) model of Mead and Markus (1969 and 1970). Also, development of the boundary conditions for the ACLD is carried out using the same approach and the same coordinate system used by Douglas and Yang (1978). In this way, it would be easy and convenient to follow the extension of the well-known PCLD models to the ACLD model.

### 3.4. The piezo-actuator

The strain  $\epsilon_p$  induced in the piezo-electric actuator is given by (Crawley and de Luis 1987):

$$\epsilon_p = (d_{31} / h_1) V_c \quad (37)$$

where  $d_{31}$  is the piezo-electric strain constant resulting from the application of the voltage  $V_c$  across the piezo-actuator layer. In equation (37),  $V_c$  is assumed constant over the entire length of the beam, i.e.  $\partial \epsilon_p / \partial x = 0$ . The voltage  $V_c$  is generated from the proper manipulation of the piezo-sensor voltage  $V_s$  as will be described in section 3.5.

### 3.5. The piezo-sensor

The strain  $\epsilon_s$  induced in the piezo-sensor is proportional to the beam curvature ( $\partial^2 w / \partial x^2$ ) and is given by:

$$\epsilon_s = - D_d \partial^2 w / \partial x^2 \quad (38)$$

where  $D_d$  is the distance from the beam neutral axis to the sensor surface.

Integrating the induced strain  $\epsilon_p$  over the entire length of the sensor, due to its distributed nature, generates an output voltage  $V_s$  given by

(Miller and Hubbard 1987):

$$V_s = - [k_{31}^2 D_d b / g_{31} C] \int_0^L \partial^2 W / \partial x^2 dx \quad (39)$$

where  $k_{31}$  is the electro-mechanical coupling factor,  $g_{31}$  is the piezo-electric voltage constant and  $C$  is the capacitance of the sensor which is given by:

$$C = 8.854 (10^{-12}) A k_{3t} / h_3 \quad (40)$$

where  $A$  is the sensor surface area and  $k_{3t}$  is the dielectric constant.

### 3.6 The control law

The manipulation of the piezo-sensor voltage  $V_s$  to generate the actuator voltage  $V_c$  is governed by the following proportional and derivative control law:

$$V_c = - K_p V_s - K_d dV_s/dt \quad (41)$$

where  $K_p$  and  $K_d$  are the proportional and derivative control gains respectively. The implementation of the above control law is extremely simple and straight forward due to the particular nature of the piezo-sensor. First, the proportional control action is directly generated by amplifying the sensor voltage  $V_s$ . Second, the derivative control action is developed by amplifying the sensor current  $i_s$  because the time derivative of the sensor voltage ( $dV_s/dt$ ) is given by:

$$dV_s/dt = i_s / C \quad (42)$$

Such linear dependence of the control law on readily accessible measurements significantly contributes to the practicality of the ACLD treatment. Only simple analog amplifiers are needed to achieve broad band vibration attenuation as compared to the more sophisticated digital signal processing and controllers required in most active control systems.

### 3.7 The compliance of the ACLD

The ACLD model is integrated with the boundary conditions, the piezo-actuator equations, the piezo-sensor model and the control law to predict the response of beams treated with ACLD treatments. In the present study, the response is quantified by computing the compliance  $\mathcal{C}$  of the beam, due to a sinusoidal transverse load applied to its free end, from:

$$\mathcal{C}(x, \omega) = W(x) T(t) / P_o e^{i\omega t} = W(x) / P_o \quad (43)$$

Therefore, predicting the compliance  $\mathcal{C}$  requires the computation of the coefficients  $C_1$ 's defining the spatial deflection  $W(x)$  which is given by equation (27). Such computation can be carried out after putting the boundary conditions of section 3.3 in the following matrix forms:

$$\begin{bmatrix}
 R_1 & R_2 & R_3 & R_4 & R_5 & R_6 \\
 \delta_1^3 & -\delta_1^3 & \delta_2^3 & -\delta_2^3 & \delta_3^3 & -\delta_3^3 \\
 \delta_1^2 & \delta_1^2 & \delta_2^2 & \delta_2^2 & \delta_3^2 & \delta_3^2 \\
 e^{\delta_1 L} & e^{-\delta_1 L} & e^{\delta_2 L} & e^{-\delta_2 L} & e^{\delta_3 L} & e^{-\delta_3 L} \\
 \delta_1 e^{\delta_1 L} & -\delta_1 e^{-\delta_1 L} & \delta_2 e^{\delta_2 L} & -\delta_2 e^{-\delta_2 L} & \delta_3 e^{\delta_3 L} & -\delta_3 e^{-\delta_3 L} \\
 U_1 e^{\delta_1 L} & U_2 e^{-\delta_1 L} & U_3 e^{\delta_2 L} & U_4 e^{-\delta_2 L} & U_5 e^{\delta_3 L} & U_6 e^{-\delta_3 L}
 \end{bmatrix}
 \begin{bmatrix}
 C_1 \\
 C_2 \\
 C_3 \\
 C_4 \\
 C_5 \\
 C_6
 \end{bmatrix}
 =
 \begin{bmatrix}
 0 \\
 \bar{P} \\
 0 \\
 0 \\
 0 \\
 0
 \end{bmatrix}
 \quad (44)$$

where

$$\begin{aligned}
 R_1 &= \delta_1^4 - (m\omega^2/D_t) + K_o \delta_1, \\
 R_2 &= \delta_1^4 - (m\omega^2/D_t) - K_o \delta_1, \\
 R_3 &= \delta_2^4 - (m\omega^2/D_t) + K_o \delta_2, \\
 R_4 &= \delta_2^4 - (m\omega^2/D_t) - K_o \delta_2, \\
 R_5 &= \delta_3^4 - (m\omega^2/D_t) + K_o \delta_3, \\
 R_6 &= \delta_3^4 - (m\omega^2/D_t) - K_o \delta_3.
 \end{aligned}
 \quad (45)$$

with  $K_o = (gY/d) (K_1 + i \omega K_2)$  (46)

where  $K_1 = K_p [k_{31}^2 D_d b / g_{31} C] [d_{31}/h_1]$  (47)

$$K_2 = K_d [k_{31}^2 D_d b / g_{31}] [d_{31}/h_1] \quad (48)$$

also

$$\begin{aligned}
 U_1 &= \delta_1^5 - Y g \delta_1^3, & U_2 &= -[\delta_1^5 - Y g \delta_1^3], \\
 U_3 &= \delta_2^5 - Y g \delta_2^3, & U_4 &= -[\delta_2^5 - Y g \delta_2^3], \\
 U_5 &= \delta_3^5 - Y g \delta_3^3, & \text{and} & & U_6 &= -[\delta_3^5 - Y g \delta_3^3].
 \end{aligned}
 \quad (49)$$

with  $\bar{P} = P_o / D_t$  (50)

Equation (44) is used to compute the coefficients  $C_i$ 's of the ACLD at different frequencies and control gains. These coefficients are then used to compute the compliance  $\mathcal{C}$  of beams with ACLD and PCLD treatments. For the case of the PCLD treatments, the gain parameter  $K_o$  set equal to zero. Comparisons are made with the compliances of plain beams and beams which are actively controlled with piezo-sensors and actuators without the use of any visco-elastic treatments. Expressions for the compliances of plain and actively controlled beams are given in the appendix for the sake of completion.

#### 4. PERFORMANCE OF BEAMS WITH ACLD and PCLD TREATMENTS

##### 4.1 Materials

The effectiveness of the ACLD treatment is demonstrated using a cantilevered steel beam which is 0.5 m long, 1.25 cm thick and 5 cm wide. The beam is treated with an acrylic base visco-elastic material which is .75

cm thick and has the following complex shear modulus (Douglas and Yang 1978):

$$G = 0.142 e^{0.494 \ln(\omega/2\pi)} (1 + 1.46 i), \quad \text{MN/m}^2 \quad (51)$$

The visco-elastic core is sandwiched between two ceramic piezo-electric films (PTS-1195, Piezo-electric Products, Meutchen, NJ) whose physical and geometrical characteristics are given in Table 1.

Table 1 - The main physical and geometrical properties of the piezo-sensor and actuator layers

$d_{31}$ (m/V)	$k_{31}$	$g_{31}$ (Vm/N)	$k_{3t}$	$E_1$ (N/m <sup>2</sup> )	$h_1$ (cm)
$18.6 \times 10^{-11}$	.34	$11.6 \times 10^{-3}$	1950	$63 \times 10^9$	.25

#### 4.2 Plain and passively treated beams

The compliance of the free end of the plain untreated steel beam is shown in Figure (4) when it is subjected to sinusoidally varying end load. The figure shows also the compliance of the beam when it is passively treated with the sandwiched visco-elastic damping treatment. In that case, the control loop that regulates the interaction between the piezo-sensor and the piezo-actuator is maintained open. It is evident that the conventional Passive Constrained Layer Damping (PCLD) treatment has effectively attenuated the vibration of the beam over the frequency band under consideration.

The characteristics with the PCLD treatment will be used as a datum for measuring the effectiveness of the ACLD treatment with its various configurations and control strategies.

#### 4.3 Beams with ACLD treatment

The effect of using the ACLD on the compliance of the steel beam is shown in Figure (5-a) when a proportional control law is employed. The figure indicates that the vibration is significantly attenuated as compared to PCLD treatment, particularly at the first three modes of vibration of the beam, when the proportional control gain  $K_p$  is set at 2000. Further increase of the control gain to 4000 produces insignificant improvement at the low frequencies. However such insignificant improvement is accompanied with a slight increase in the actuator voltages are shown in Figure (5-b). It is evident that the control voltage is maintained below 100 volts when the control gain is set at 2000 but higher values are obtained when the gain is increased to 4000 particularly at the fifth and seventh modes of vibration.

The performance is improved by augmenting the proportional control law with a derivative component as can be seen in Figure (6). The excessively high compliance and actuator voltage are eliminated when the derivative control gain  $K_d$  is set at 1E9. Figure (6-a) indicates that the ACLD has produced compliances that are significantly lower than the PCLD treatment for all the vibration modes considered. Figure (6-b) shows also that the control voltage has also been decreased particularly at the fifth mode of vibration.

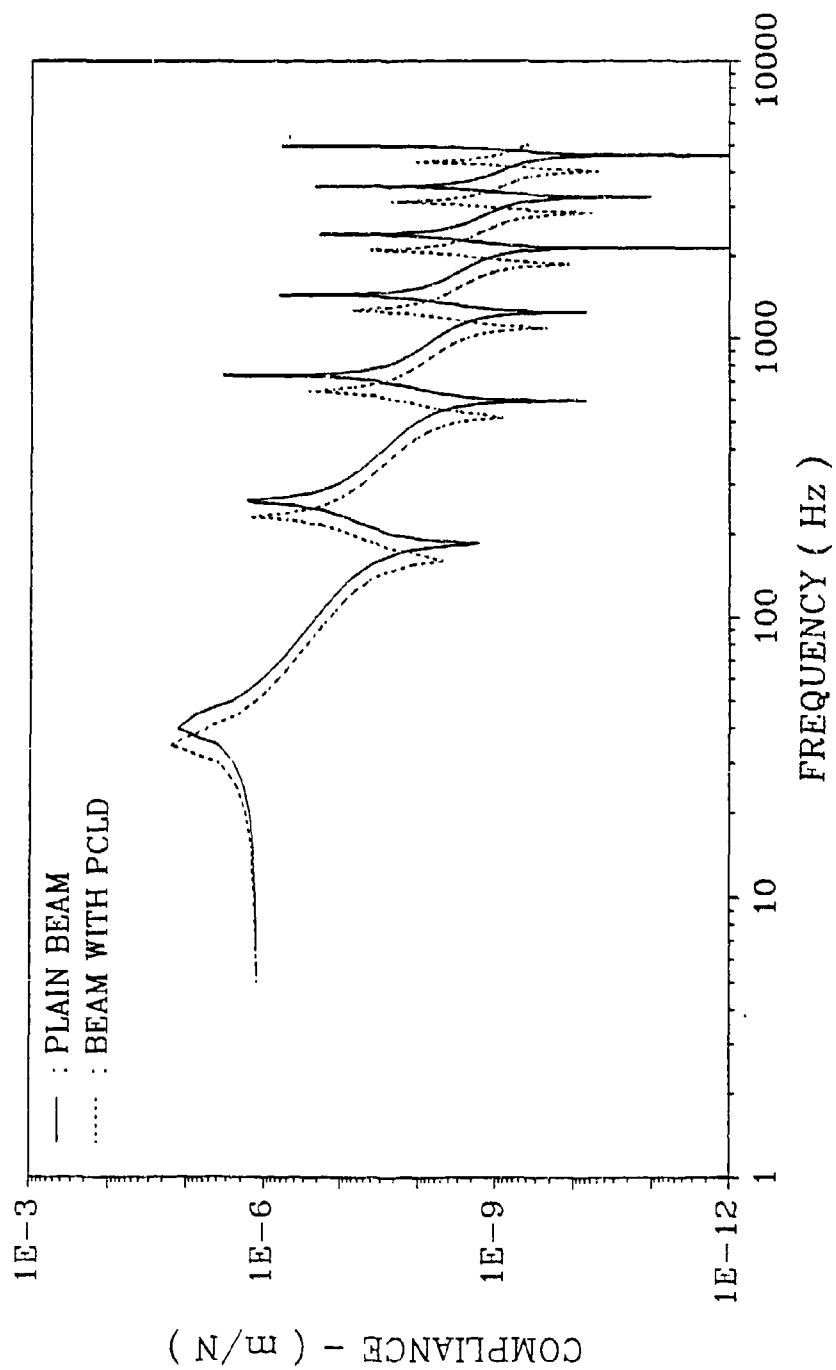


Figure (4) - Compliance of the free end of plain and passively treated steel beams

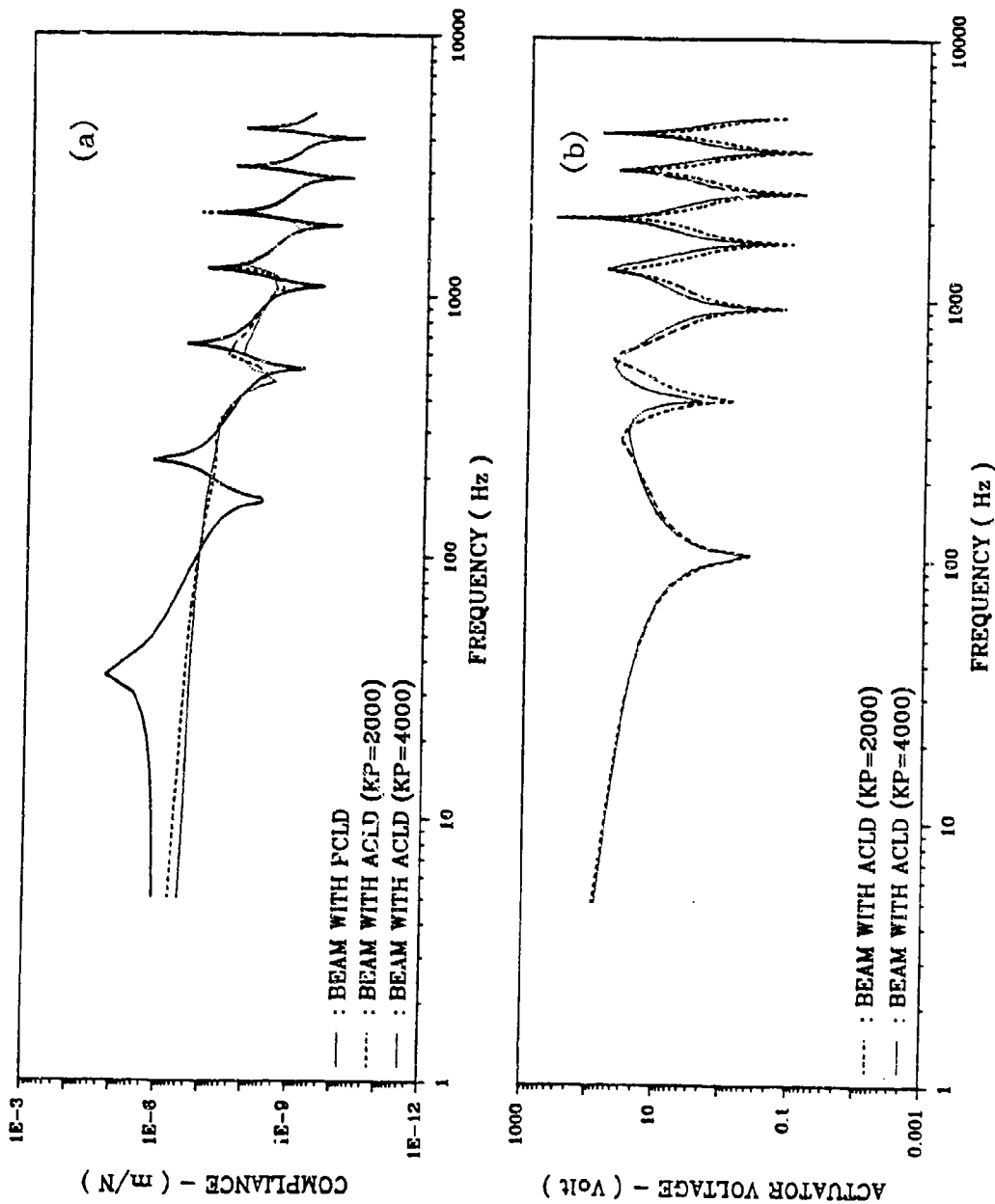


Figure (5) - Comparison between beam with PCLD and beam with ACLD treatment and Proportional controller  
(a) - Compliance and (b) - Actuator voltage

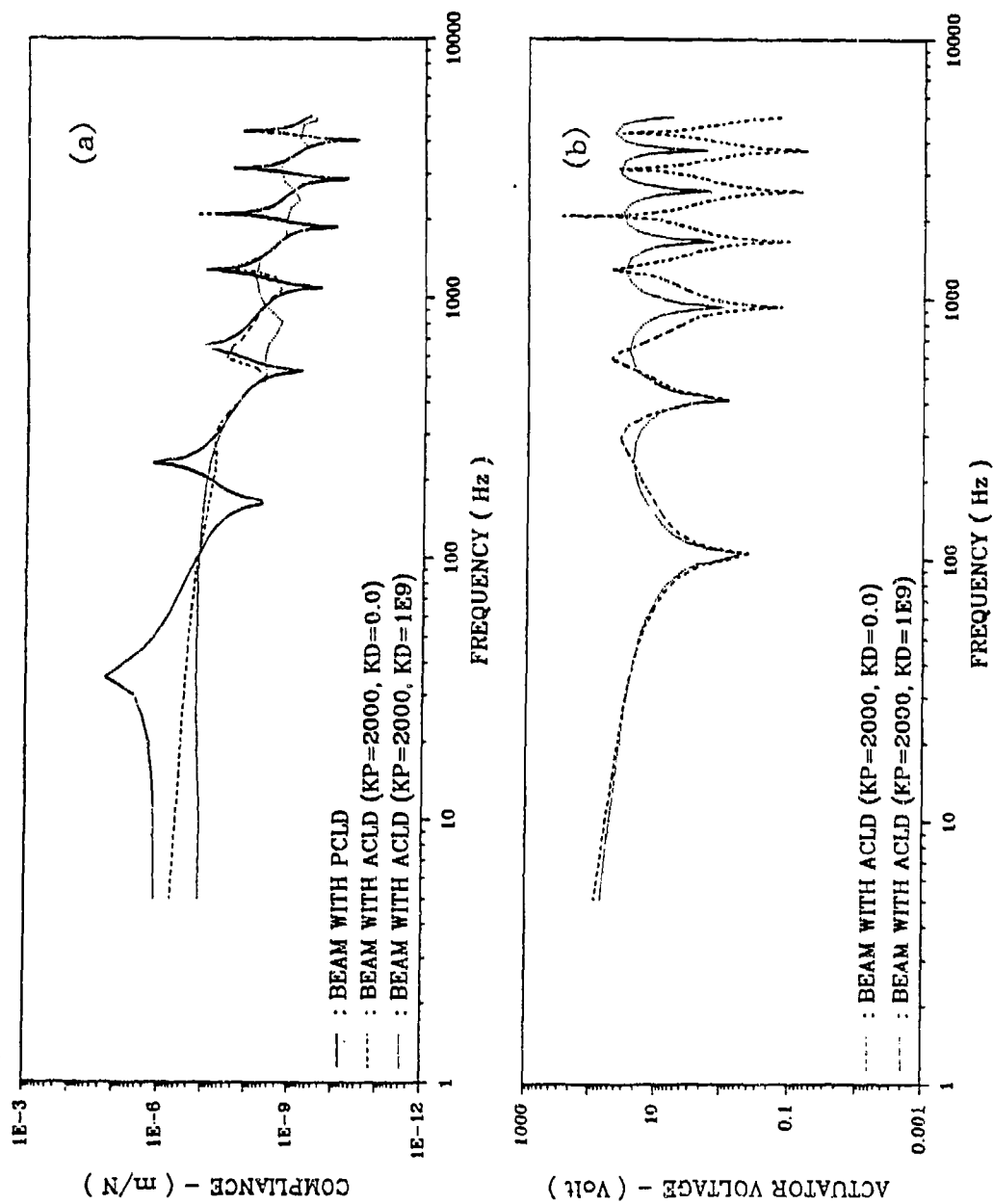


Figure (6) - Comparison between beam with PCLD and beam with ACLD treatment and Proportional and Derivative controller  
 (a) - Compliance and (b) - Actuator voltage



#### 4.4 Untreated beams with conventional active control

The performance of beams with PCLD and ACLD treatments is compared with the performance of an untreated steel beam which is controlled only by a piezo-sensor/actuator pair using conventional active control laws. The compliance equation of this actively controlled beam is given in the appendix.

Figure (7) shows such a comparison and indicates that the ACLD treatment is superior not only to PCLD treatment but also to conventional active control damping. Such superiority stems from its ability to produce lower amplitudes of vibration with lower control voltages as can be seen from Figures (7-a) and (7-b) respectively. In the figures, a proportional and derivative control law is used as a basis for comparison between the ACLD and PCLD with  $K_p=2000$  and  $K_d=1E9$ .

#### 5. CONCLUSIONS

This paper has presented a new class of active constrained layer damping treatment which consists of conventional visco-elastic core augmented with built-in sensing and actuation capabilities. The equations governing the performance of this class of surface treatment are presented using a distributed-parameter formulation and the concept of mechanical compliance. Numerical examples are presented to demonstrate the merits of the ACLD treatment as compared to PCLD treatments and conventional active control methods. The results obtained indicate the ACLD treatment is superior not only to PCLD treatment but also to conventional active control damping. Such superiority stems from its ability to combine the attractive attributes of both the passive and active controls to produce lower amplitudes of vibration with lower control voltages. Also, it is found that the performance of the ACLD with a proportional controller is very effective at low frequencies. However, augmenting the control law with a derivative component is found to extend the effectiveness of the ACLD over wide frequency band.

It is important here to note that although the emphasis of the present study has been placed on the development of an analytical model for Bernoulli-Euler beams which are fully-treated with a single layer of ACLD, our main goal is to demonstrate the feasibility and merits of the ACLD concept. Therefore, analytical solutions and finite element analyses of fully or partially-treated Timoshenko beams, plates and shells with single or multi-ACLD are nothing but a natural extensions of the present study. Also, the selection of the optimal control gains, robust control strategies and shaping of the piezo-sensor/actuator pairs are among the other issues that are currently under consideration to enhance the effectiveness of the ACLD treatment.

#### ACKNOWLEDGEMENTS

Special thanks are due to the Army Research Office (ARO) for sponsoring this study and for Dr. Gary L. Anderson, the technical monitor, for his invaluable technical inputs.

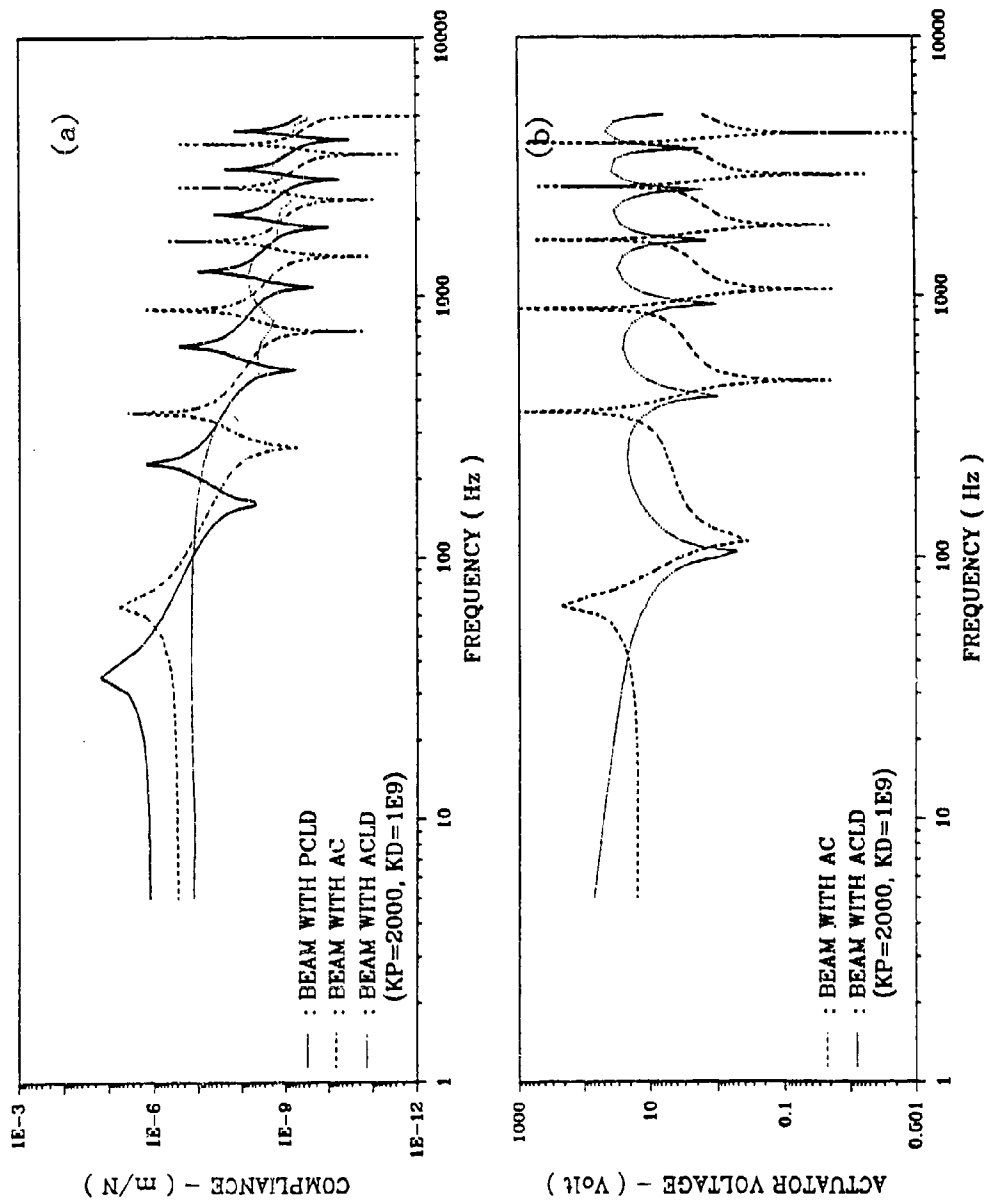


Figure (7) - Comparison between beam with PCLD, beam with AC and beam with ACLD treatment  
 (a) - Compliance and (b) - Actuator voltage

## REFERENCES

- Asnani, N. T. & Nakra, B. C.**, "Vibration Damping Characteristics of Multi layered Beams with Constrained Viscoelastic Layers", *ASME Trans. Journal of Engineering for Industry*, pp. 895-901, 1976.
- Bailey, T. and J. Hubbard**, "Distributed Piezo-electric Polymer Active Vibration Control of A Cantilever Beam", *Journal of Guidance and Control*, Vol. 8, pp.606-611, 1985.
- Baz, A.**, "Active Constrained Layer Damping", U.S.Patent application, 1992.
- Baz, A.**, "Active Constrained Layer Damping", *DAMPING'93 Conference*, San Francisco, CA , February 1993.
- Baz, A. and J. Ro**, "Partial Treatment of Flexible Beams with Active Constrained Layer Damping", *Conference of Engineering Sciences Society*, Charlottesville, VA, June 1993.
- Baz, A. and J. Ro**, "Control of Active Constrained Layer Damping", *Ninth Conference on Dynamics & Control of Large Structures*, VPI & SU, Blacksburg, VA, May 1993.
- Crawley, E. and J. De Luis**, "Use of Piezoelectric Actuators as Elements in Intelligent Structures" *Journal of AIAA*, Vol. 25, No.10, pp. 1373-1385, 1987.
- Cremer, L., M. Heckel and E. Ungar**, *Structure-Borne Sound: Structural Vibrations and Sound Radiation at Audio Frequencies*, Second edition, Springer-Verlag, Berlin, 1988.
- Douglas, B. E. and J. Yang**, "Transverse Compressional Damping in the Vibratory Response of Elastic-Viscoelastic-Elastic Beams", *AIAA Journal*, Vol. 16, No. 9, pp. 925-930, 1978.
- Lu, Y. P. & Douglas, B. E.**, "On the Forced Vibrations of Three-Layer Damped Sandwich Beams", *Journal of Sound and Vibration*, Vol. 32, No. 4, pp. 513-516, 1974.
- Mead, D. J. & Markus, S.**, "The Forced Vibration of a Three-Layer, Damped Sandwich Beam with Arbitrary Boundary Conditions", *Journal of Sound and Vibration*, Vol. 10, No. 1, pp. 163-175, 1969.
- Mead, D. J.**, "Loss Factors and Resonant Frequencies of Encastred Damped Sandwich Beams", *Journal of Sound and Vibration*, Vol. 12, No. 1, pp. 99-112, (1970).
- Miller, S. and J. Hubbard, Jr.**, "Observability of a Bernoulli-Euler Beam using PVF<sub>2</sub> as a Distributed Sensor", *Seventh Conference on Dynamics & Control of Large Structures*, VPI & SU, Blacksburg, VA, pp. 375-930, May 1987.
- Nashif, A., D. Jones and J. Henderson**, *Vibration Damping*, John Wiley & Sons, New York, 1985.
- Piezo-Electric Products, Inc.**, "Piezo-Design Aid: Program Manual", Vol.I, Metuchen, New Jersey, 1985.

## APPENDIX

### COMPLIANCE OF PLAIN AND ACTIVELY CONTROLLED BEAMS

The dynamics of a beam which is subject to sinusoidal end load and controlled with piezo-electric actuator and sensors can be written as follows:

$$EI \partial^4 w / \partial x^4 + \bar{m} \partial^2 w / \partial t^2 = 0 \quad (A-1)$$

where  $EI$  is the flexural rigidity of the beam/sensor/actuator system and  $\bar{m}$  is its mass per unit length.

Equation (A-1) has solution  $w$  given by:

$$w = W(x) T(t) \quad (A-2)$$

such that  $\ddot{T}/T = -\omega^2$  and the spatial function  $W(x)$  is given by:

$$W(x) = D_1 e^{\alpha x} + D_2 e^{-\alpha x} + D_3 e^{i\alpha x} + D_4 e^{-i\alpha x} \quad (A-3)$$

where  $\alpha = (\bar{m} \omega^2 / EI)^{1/4}$

The four coefficients  $D_1$  through  $D_4$  are determined from the following boundary conditions:

$$[w]_{x=L} = [\partial w / \partial x]_{x=L} = 0, \quad (A-2)$$

$$EI [\partial^2 w / \partial x^2]_{x=0} = -c V_c, \quad (A-3)$$

$$\text{and} \quad EI [\partial^3 w / \partial x^3]_{x=0} = b P_o e^{i\omega t}. \quad (A-4)$$

$$\text{where} \quad c = 1/2 d_{31}(h_1 + h_e)(E_1 E_e h_e b) / (E_1 h_1 + E_e h_e) \quad (A-5)$$

$$\text{and} \quad V_c = - (K_p + i \omega K_d) [k_{31}^2 D_d b / g_{31} C] \int_0^L \partial^2 w / \partial x^2 dx \quad (A-6)$$

The above boundary conditions can be written in the following matrix form:

$$\begin{bmatrix} \alpha^3 & -\alpha^3 & -i\alpha^3 & i\alpha^3 \\ \alpha^2 + \alpha V_c & \alpha^2 - \alpha V_c & -\alpha^2 + i\alpha V_c & -\alpha^2 - i\alpha V_c \\ \alpha e^{\alpha L} & -\alpha e^{-\alpha L} & i\alpha e^{i\alpha L} & -i\alpha e^{-i\alpha L} \\ e^{\alpha L} & e^{-\alpha L} & e^{i\alpha L} & e^{-i\alpha L} \end{bmatrix} \begin{bmatrix} D_1 \\ D_2 \\ D_3 \\ D_4 \end{bmatrix} = \begin{bmatrix} \bar{P} \\ 0 \\ 0 \\ 0 \end{bmatrix} \quad (A-7)$$

Equation (A-7) is used to compute the coefficients  $D_i$ 's which are then used to compute the spatial transverse deflection function  $W(x)$  from equation (A-3). The compliance  $\mathcal{C}$  of the beam can then be calculated from:

$$\mathcal{C}(x, \omega) = W(x) / P_o \quad (A-8)$$

For plain beams, the compliance is obtained by setting  $V_c = 0$ .

# NOMENCLATURE

## Latin symbols

A	surface area of piezo-sensor
b	beam width
C	sensor capacitance
$\mathcal{C}$	compliance
$C_1$	coefficients of the spatial deflection given by equation (27)
d	distance given by equation (2)
$d_{31}$	piezo-electric strain constant of piezo-actuator
D	distance between neutral axis of beam/sensor layer to sensor interface with visco-elastic layer
$D_1$	coefficients of the spatial deflection given by equation (A-3)
$D_d$	distance between neutral axis of entire sandwiched beam and sensor interface with visco-elastic layer
$D_t$	combined flexural rigidity of sandwiched beam/unit width
E	modulus of elasticity of plain or actively controlled beam
$E_{1,3,4}$	moduli of elasticity of piezo-actuator, piezo-sensor and beam respectively.
$E_e$	equivalent modulus of elasticity of combined sensor/beam layer
g	parameter given by equation (12)
$g_{31}$	piezo-electric voltage constant of piezo-sensor
G	complex shear modulus of the visco-elastic core
$h_{1,2,3,4}$	thicknesses of piezo-actuator, visco-elastic core, piezo-sensor, and beam respectively.
$\sqrt{-1}$	
$I_s$	current of piezo-sensor
I	area moment of inertia of plain or actively controlled beam
$I_{1,3,4}$	area moment of inertia of piezo-actuator, piezo-sensor and beam respectively
$I_e$	area moment of inertia of combined sensor/beam layer
$k_{31}$	electro-mechanical coupling factor of piezo-sensor
$k_{3t}$	dielectric constant of piezo-sensor
$K_{d,p}$	derivative and proportional control gains
$K_{o,1,2}$	parameters given by equations (46), (47) and (48) respectively
L	beam length
$\bar{m}$	mass of sandwiched beam/unit length and unit width
$\underline{m}$	mass of beam/unit length
M	moment
p	total transverse loading
P	parameter given by equation (50)
$P_o$	transverse load applied to free end of beam
$P_{1,3}$	longitudinal loads acting on piezo-actuator and sensor/beam layer
q	external transverse loading on beam
$R_1$	parameters given by equation (45)
S	total shear force
$S_{1,2,,3}$	shear forces acting on piezo-actuator, visco-elastic core and piezo-sensor/beam layer respectively
t	time
T	temporal function of equation (18)
$u_{1,3}$	longitudinal deflection of neutral axes of piezo-actuator and piezo-sensor/beam layer
$U_1$	parameter given by equation (49).

$V_{c,s}$	piezo-actuator and sensor voltages respectively
$w$	transverse deflection of sandwiched beam
$W$	spatial transverse deflection of sandwiched beam
$x$	position along beam
$Y$	parameter given by equation (12)

#### Greek symbols

$\alpha$	$(\bar{m} \omega^2/EI)^{1/4}$
$\gamma$	shear strain of visco-elastic core
$\gamma_{1,2}$	parameters given by equations (23) and (24)
$\delta_i$	roots of characteristic equation (19)
$\epsilon_{p,s}$	strains of piezo-actuator and piezo-sensor respectively
$\lambda$	differential operator
$\omega$	frequency
$\zeta_{1,2}$	parameters given by equations (25) and (26)

# **COMPARING PASSIVE DAMPING AND ACTIVE CONTROL ON FLEXIBLE STRUCTURES WITH EITHER CLOSELY SPACED OR COINCIDENT MODES**

**Major Steven G. Webb\***  
Department of Engineering Mechanics  
US Air Force Academy

**2Lt Dean Cibotti**  
Department of Engineering Mechanics  
US Air Force Academy

## **ABSTRACT**

Passive damping and active control schemes are implemented on a single reaction mass actuator to control the vibrations of a flexible structure. In one case, the structure is lightly damped and possesses closely spaced low frequency resonant modes. In a second situation, the structure possesses a pair of lightly damped low frequency coincident modes. For the structure with closely spaced modes, there is little variation in the amount of control authority exhibited with passive damping, local velocity feedback (LVF) or linear quadratic regulator (LQR) control overlaid on passively damped actuators, and LVF or LQR control only. The vibrations of the entire structure were eliminated using a single actuator. On the other hand, implementing control on the structure with coincident modes produced significantly different results. Vibration suppression was accomplished at the point where the actuator was attached to the structure, but at other points on the structure vibration suppression was greatly diminished. Further, for the structure with coincident modes, using only LVF control proved to be much more effective than the other passive damping or active control schemes in eliminating the structure's vibrations at the point where the actuator was located.

\*DFEM, USAF Academy, CO 80840

This paper is declared a work of the U. S. Government and is not subject to copyright protection in the United States.

## INTRODUCTION

The control of large flexible structures has been a topic of intense research. Both active control and passive damping schemes have been examined as means of suppressing the vibrations associated with all of the structure's significant resonant modes, some of which may be closely spaced or even coincident. Effective control schemes must be sufficiently robust to account for the effects of these modes.

Passive vibration absorption, or passive damping, is probably the simplest way to suppress a flexible structure's vibrations. Various ways of introducing passive damping to a structure have been extensively examined<sup>1</sup>. Further, many analytical studies on active control have been based on linear quadratic (LQ) control techniques<sup>2</sup>. Fundamental to these control strategies is the linear quadratic regulator (LQR), which requires the full states of the structure, as well as the actuators, to be available to each of the controllers<sup>3</sup>. Since it is difficult to design and implement a controller that is of the same order as a finite element model of a large space structure, control systems are usually designed based on a reduced order model of the structure.

Even with a reduced model of the structure, LQ control schemes may be difficult to implement due to the possible introduction of instabilities in higher order modes<sup>3</sup>. Hence, many experimental studies have addressed simpler control laws to suppress a flexible structure's vibrations<sup>2,4,5</sup>. One such control system uses local velocity feedback (LVF) to generate control signals to the actuators. Coupling either LQR or LVF controllers with a passively damped actuator can result in a very effective control system<sup>6</sup>.

This paper compares the effectiveness of using either passive damping only, active control overlaid on a passive damper, or active control only to suppress a flexible structure's vibrations. Two structures will be examined: one with low frequency closely spaced modes and one with low frequency coincident modes.

## EXPERIMENTAL SET-UP

An experimental test bed located at the U. S. Air Force Academy was used to examine the effectiveness of passive damping and active control schemes on suppressing a flexible structure's vibrations. This structure, known as the MRT (Mass Reactive 'T') structure, was designed to possess low-order coupling. That is, there were to be two dominant low-frequency bending and torsional structural modes, and the higher modes were to be well separated from the first two<sup>7,8</sup>. The MRT structure, shown in Figure 1, is described in more detail in reference 8.



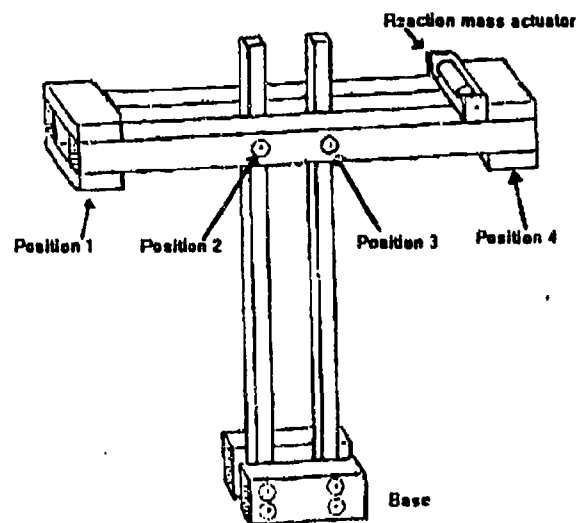


FIGURE 1 Experimental Structure

The structure's first two resonance's could be altered simply by moving the RMA brackets and four mounted lead weights to various symmetric inboard positions. For this study, two configurations were examined: one which generated closely space modes, and the other which generated coincident modes.

A 144 degree of freedom finite element model (FEM) of the MRT structure was generated using MSC/NASTRAN. Employing a modal reduction technique outlined by Hallauer and Barthelemy<sup>9</sup>, a fourth order model was selected such that the first two structural modes were as accurate as possible. This FEM was verified by comparing the open loop, or baseline, structure's resonant frequencies to those obtained experimentally. The baseline configuration was defined to consist of no moving parts; hence, all moving components of the reaction mass actuator used in the experiment were removed. Table 1 compares the FEM and experimental resonant frequencies obtained for the first two modes for both configurations.

#### CLOSELY SPACED

Analytical (HZ)	Experimental (HZ)	Percent Error (%)
4.6417	4.618	0.5
5.1904	5.113	1.5

#### COINCIDENT

Analytical (HZ)	Experimental (HZ)	Percent Error (%)
5.1691	5.075	1.8
5.1708	5.075	1.9

**TABLE 1. FINITE ELEMENT MODEL AND EXPERIMENTAL STRUCTURAL  
RESONANT FREQUENCIES**

The third resonant frequency was above 90 Hz; thus, it was indeed well separated from the first two modes in both structural configurations.

For the structure with the closely spaced modes, the first structural resonant frequency corresponded to a torsional, or twisting motion about the vertical axis. The second frequency was a bending motion about the horizontal axis parallel to the structure's horizontal beams (refer to Figure 1). By moving the lead weights located at either end of the horizontal beams (again see Figure 1) towards the center of the structure, the torsional frequency would increase while the bending frequency would remain approximately the same. With the weights located at a certain symmetric distance inboard on the structure, both the torsion and bending modes became coincident.

For this study, the structure's settling time was the criteria to compare the effectiveness of the various control schemes implemented on MRT. Note, in Figure 1, that the RMA was located at one end of the structure, at Position 4. The structure was deflected a set distance of 0.25 inches at Position 1 and then released. The settling time was defined to be the amount of time it took for the structure to settle to within two percent of its maximum displacements at each of the four positions on the structure, as shown in Figure 1. The settling times, as well as the maximum displacement, were recorded at each of the four positions and are summarized in Table 2 for both structural configurations.

**CLOSELY SPACED**

	Position 1	Position 2	Position 3	Position 4
Settling Time	141.984	144.972	146.268	143.280
Displacement	0.2500	0.1316	0.1297	0.2380

**COINCIDENT**

	Position 1	Position 2	Position 3	Position 4
Settling Time	242.913	150.784	280.000	319.936
Displacement	0.2728	0.1316	0.0811	0.1049

**TABLE 2.  
FINITE ELEMENT MODEL STRUCTURAL SETTLING TIMES (SECONDS) AND  
MAXIMUM DISPLACEMENTS (INCHES) - BASELINE STRUCTURE**

Note that there is a significant difference between the settling times shown in the table. Apparently, the coincident modes significantly decreased the structural damping. Even though the structure with coincident modes was disturbed 0.25 inches at Position 1, the maximum displacement at that position was larger than the initial displacement. The interaction between the two modes caused a beating at Positions 1 and 4; when the displacement was maximized at Position 1 it was minimized at Position 4, and vice versa. Energy was exchanged between the two end positions of the structure. Because the structure was so lightly damped, this energy exchange actually created a larger displacement at Position 1 than the initial disturbance.

Experimentally, for the structure with closely spaced modes, the settling time at Position 1 was 143 seconds, which equates to a 0.78 percent error from the FEM value of 141.984 seconds. The other experimental settling times were similarly close to their corresponding FEM values.

With the analytical model validated, a reaction mass actuator was added to one end of the MRT structure. A close-up view of this actuator is shown in Figure 2.

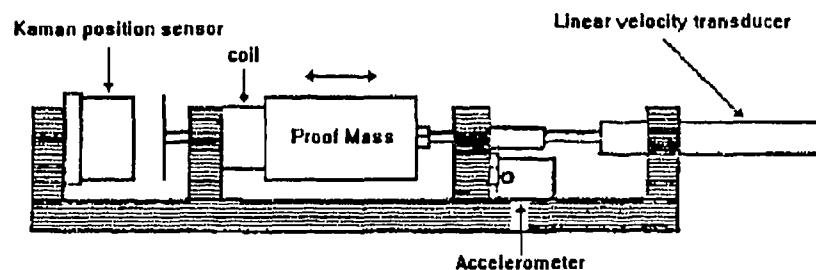


FIGURE 2 Reaction Mass Actuator

A moving mass core was built around a series of rare earth magnets which encircled the actuator's coil. In addition, a magnetic shaft, connected to this core, passed through the center of the stationary coil of a linear velocity transducer and sensed the velocity of the reaction mass relative to the structure. The actuator assembly also included a non-contacting transducer which sensed the relative position of the reaction mass. Each of the resulting signals from the two transducers was multiplied by an appropriate gain constant and fed via a power amplifier, to adjust the stiffness and viscous damping parameters. The natural frequency and viscous damping factor of the reaction mass actuator (RMA) could then be varied by adjusting the two gain constants. These constants were varied either by a pair of input resistance potentiometers or by changing the input values on a digital controller. There was a small amount of uncontrollable rolling friction in the motion of the actuator's shaft through two linear bearings; hence, the total damping of the actuator was a combination of this small, but uncontrollable, friction plus the controllable and much larger linear viscous damping.<sup>8,10</sup>

## SYSTEM DYNAMICS

In developing the passive damping and active control schemes for the MRT structure, the dynamics of the structure and the actuator were first modeled.<sup>10</sup> Once this was accomplished, both the RMA and the structure could be modeled using second order dynamics.<sup>11</sup> The following model combined the dynamics of the baseline structure with the dynamics of the reaction mass actuator so that

$$M\ddot{x} + D\dot{x} + Kx = B_f f_s \quad (1)$$

where  $x$  was a five element vector with the first element being the absolute position of the RMA and the other four elements representing the first four modal positions of the MRT structure. In addition,

$$M = \begin{bmatrix} m_a & 0 & 0 & 0 & 0 \\ 0 & & & & \\ 0 & M_s & & & \\ 0 & & & & \\ 0 & & & & \end{bmatrix} \quad D = \begin{bmatrix} d_a & -d_a & 0 & 0 & 0 \\ -d_a & & & & \\ 0 & D_s + D_r & & & \\ 0 & & & & \\ 0 & & & & \end{bmatrix} \quad (2)$$

$$K = \begin{bmatrix} k_a & -k_a & 0 & 0 & 0 \\ -k_a & & & & \\ 0 & K_s + K_r & & & \\ 0 & & & & \\ 0 & & & & \end{bmatrix} \quad B_f^T = [1 \ 0 \ -1 \ 0 \ 0 \ 0]$$

$M_s$  and  $K_s$  were the reduced order matrices from the NASTRAN model. The terms  $m_a$ ,  $d_a$ , and  $k_a$  were mass, damping, and stiffness values associated with the RMA. The matrices  $K_R$  and  $D_R$  were defined to be

$$D_r = \begin{bmatrix} d_a & 0 & 0 & 0 \\ 0 & 0 & 0 & 0 \\ 0 & 0 & 0 & 0 \\ 0 & 0 & 0 & 0 \end{bmatrix} \quad K_r = \begin{bmatrix} k_a & 0 & 0 & 0 \\ 0 & 0 & 0 & 0 \\ 0 & 0 & 0 & 0 \\ 0 & 0 & 0 & 0 \end{bmatrix} \quad (3)$$

The structural damping matrix,  $D_s$ , was constructed such that

$$D_s = S_m \text{DIAG}[2\xi_1\omega_1, \dots, 2\xi_4\omega_4] S_m^T \quad (4)$$

where  $\xi_1\omega_1$  was the product of the damping ratio and natural frequency of each of the first four resonant frequencies and the matrix  $S_m$  represented the normalized mass weighted eigenfunctions of the FEM model.<sup>10</sup>

The input matrix,  $B_p$ , reveals the interaction effects of an inertial actuator in that, as the actuator's reaction mass moves, an equal and opposite force reacts on the structure. The control force,  $f_g$ , is a function of the force/voltage constant of the RMA and the voltage command signal.

### PASSIVE DAMPING

The vibrations of both structural configurations on MRT were first suppressed using classical passive damping techniques.<sup>7,8,12,13</sup> Two cases for each configuration were examined; the RMA was tuned to each structure's first resonant frequency. In the first case, values for the RMA's stiffness and damping were obtained using the equations derived by Den Hartog<sup>7,13</sup>:

$$\omega_a = \frac{\omega_1}{1 + \mu} \quad (5)$$

$$\zeta_a = \left[ \frac{3\mu}{8(1 + \mu)^3} \right]^{\frac{1}{2}} \quad (6)$$

where  $\omega_a$  was the frequency to tune the RMA,  $\mu$  was the ratio of the RMA mass to the modal mass of the structure's first resonant frequency, and  $\zeta_a$  was the damping ratio to tune the RMA.

For the second set of passive damping parameters, the values calculated in Eqns-(5) and (6) were adjusted until the best settling time was obtained. Specifically, one parameter--either the stiffness or the damping ratio--was held constant while the other was varied until the settling time was minimized. That parameter was then set to the value yielding the best settling time, and the first parameter was varied until the settling time was further minimized. This iteration continued until the smallest possible settling time was obtained.

Table 3 summarizes the FEM simulation results for the above cases of passive damping as applied to the MRT structure in both configurations of closely spaced and coincident modes.

### PASSIVE DAMPING

#### CLOSELY SPACED

DEN HARTOG  $\omega_a = 4.549 \text{ HZ}$   $\zeta_a = 0.0821$

	Position 1	Position 2	Position 3	Position 4	Stroke
Settling Time	9.210	8.570	8.448	9.978	N/A
Displacement	0.2500	0.1316	0.0842	0.1091	0.5023

#### CLOSELY SPACED

MAX DAMPING  $\omega_d = 4.581\text{HZ}$   $\zeta_d = 0.1675$

	Position 1	Position 2	Position 3	Position 4	Stroke
Settling Time	2.982	3.254	3.554	3.994	N/A
Displacement	0.2500	0.1316	0.0887	0.1239	0.3526

#### COINCIDENT

DEN HARTOG  $\omega_d = 5.075\text{HZ}$   $\zeta_d = 0.0811$

	Position 1	Position 2	Position 3	Position 4	Stroke
Settling Time	68.390	69.454	69.454	32.220	N/A
Displacement	0.2830	0.1316	0.0855	0.0339	0.0659

#### COINCIDENT

MAX DAMPING  $\omega_d = 5.623\text{HZ}$   $\zeta_d = 0.2190$

	Position 1	Position 2	Position 3	Position 4	Stroke
Settling Time	67.914	68.880	69.748	21.504	N/A
Displacement	0.2826	0.1316	0.0825	0.0332	0.0406

TABLE 3

#### FINITE ELEMENT MODEL STRUCTURAL SETTLING TIMES (SECONDS) AND MAXIMUM DISPLACEMENTS (INCHES)

As with the baseline structure, an initial disturbance of 0.25 inches was applied at Position 1, and the settling time and maximum displacements for each of the four structural positions were recorded (refer to Table 3). In addition, the maximum stroke length required by the RMA to effect vibration suppression is listed for each case examined. The FEM simulation responses were again validated experimentally. For the RMA tuned to the Den Hartog stiffness and damping values, the settling time was experimentally determined to be 9.02 seconds, a 2.1 percent error from the FEM value of 9.21 seconds. As for the situation with the RMA tuned to the maximum passive damping values, the experimental settling time was 3.02 seconds, which was a 1.3 percent error from the FEM settling time of 2.982 seconds.

For the MRT structure with closely spaced modes, both passive damping techniques proved to be quite effective in suppressing the structure's vibrations, not only at the position where the RMA was located, but throughout the entire structure. It is interesting to note that, for both cases, the maximum settling time occurred at Position 4 even though the RMA was located at that point. Tuning the RMA to the Den Hartog passive parameters reduced the MRT structure's settling time from around 144 seconds to less than 10 seconds, or an 93 percent reduction in the settling time. With the maximum passive damping parameters tuned, the settling time was reduced to less than 4 seconds, a 97 percent reduction.

Clearly, the Den Hartog solution does not yield values for a passive actuator's stiffness and damping which result in the best settling time for the structure. The Den Hartog parameters were derived based on the structure's frequency response; hence, a settling time criteria is not optimized.<sup>13</sup> Further, note that the stroke length required by the RMA tuned to the Den Hartog parameters is much larger than that required when the RMA was tuned to the parameters yielding maximum passive damping. In this situation, the Den Hartog solution yielded a damping ratio about one-half that required for maximum passive damping; a more lightly damped actuator requires a larger stroke length to effect vibration suppression.<sup>13</sup>

The results for the MRT structure configured to possess two coincident modes differ from those summarized above. Although both damping techniques significantly reduced the settling times of MRT when a 0.25 inch disturbance was imparted to it at Position 1, the resulting settling times were not as good as in the closely spaced mode configuration. Still, when the RMA was tuned to the Den Hartog parameters, there was a 90 percent reduction in the settling time at Position 4 and between 54 and 75 percent reductions at the other positions. As for the RMA tuned to the maximum passive damping parameters, Position 4 experienced a 93 percent reduction in the settling time while the other positions still had between 54 and 75 percent reductions. So, even though the settling times at Position 4 were not as small as the corresponding times in the closely spaced mode case, the percent reductions in settling time were only slightly less. Unfortunately, the RMA was not able to suppress the structure's vibrations as well at points other than where the RMA was located.

An earlier study stated that, in attempting to control a structure possessing a pair of coincident modes with a single actuator, one mode was uncontrollable.<sup>14</sup> At first glance, it appears that the above results contradict the study summarized in Reference 14. However, by examining the experimental responses of the structure with coincident modes, it was observed that the RMA stopped the vibrations at the end of the structure where it was located. This end then acted like a cantilevered beam for the rest of the structure and "increased" the structural damping of MRT. This damping--not the RMA itself--caused the rest of the structure to stop vibrating in a time that was shorter than the baseline case. One mode of the structure was still uncontrollable; hence, the results summarized in Reference 14 were verified.

Another interesting comparison can be made concerning the results of damping the two structural configurations. For the configuration possessing closely spaced modes, the stroke lengths required to effect vibration suppression were larger than the initial disturbance. However, the stroke lengths required by the RMA to suppress the vibrations of the structure with coincident

modes were significantly smaller than the initial disturbance. it would seem that, for the second structural configuration, the settling time could be reduced if the stroke length were larger. However, this was not the case; the settling time actually increased if the stroke length was increased. The explanation for the small stroke lengths required by the RMA lies in the fact that the maximum displacements at Position 4 (where the RMA was located) are much smaller than the corresponding displacements for the structural configuration possessing closely coupled modes. Hence, a smaller structural disturbance at the location of the RMA requires a smaller stroke length to effect vibration suppression.

### LOCAL VELOCITY FEEDBACK

After passive damping was successfully implemented on the MRT structure, the next step in this study was to construct a simple control strategy involving local velocity feedback (LVF). This LVF control scheme possessed characteristics typical of low authority controllers; that is, the actuator applied a control force which was governed only by a sensor physically collocated with the RMA assembly. The control force,  $f_g$ , in Eqn (1) was set equal to a gain constant,  $k_g$ , multiplied by the local velocity of the structure at the RMA,  $\dot{x}_4$ , or

$$f_g = k_g \dot{x}_4 \quad (7)$$

This type of sensor feedback control is not truly collocated in a mathematical sense. The philosophy behind this controller is that the vibration suppression system is self-contained, requiring only power and control circuitry.<sup>10</sup> The control law was implemented on a digital controller.

To implement LVF control, the RMA was first passively tuned to the two sets of stiffness and damping parameters calculated in the first part of this study. For two situations, LVF control was overlaid on the passively damped RMA tuned to the two sets of parameters previously mentioned, and the gain constant  $k_g$  was adjusted until the settling time was minimized. In addition, the actuator's passive stiffness and damping parameters were set equal to zero, and  $k_g$  was adjusted to obtain the best settling time. Hence, three cases of LVF control were examined: two combining passive damping and active control, and one using active control only. Table 4 summarizes the FEM simulation results obtained for each case for both structural configurations.

### LOCAL VELOCITY FEEDBACK CONTROL

#### CLOSELY SPACED

DEN HARTOG  $k_g = 20.82$

	Position 1	Position 2	Position 3	Position 4	Stroke
Settling Time	8.212	8.208	8.302	8.824	N/A



Displacement	0.2500	0.1316	0.0869	0.1010	0.4970
--------------	--------	--------	--------	--------	--------

#### CLOSELY SPACED

MAX DAMPING  $k_p = 0.345$

	Position 1	Position 2	Position 3	Position 4	Stroke
Settling Time	2.994	3.264	3.656	3.348	N/A
Displacement	0.2500	0.1316	0.0888	0.1238	0.4001

#### CLOSELY SPACED

$\omega_n = 0$   $\zeta_n = 0$   $k_p = 163.92$

	Position 1	Position 2	Position 3	Position 4	Stroke
Settling Time	2.916	3.956	4.454	4.772	N/A
Displacement	0.2500	0.1316	0.0820	0.1025	Drifts

#### COINCIDENT

Den Hartog  $k_p = 21.653$

	Position 1	Position 2	Position 3	Position 4	Stroke
Settling Time	68.488	69.454	68.880	12.884	N/A
Displacement	0.2825	0.1316	0.0874	0.0330	0.0646

#### COINCIDENT

Max Damping  $k_p = 44.814$

	Position 1	Position 2	Position 3	Position 4	Stroke
Settling Time	68.488	69.454	69.552	16.972	N/A
Displacement	0.2818	0.1316	0.0869	0.0318	0.0453

#### COINCIDENT

$\omega_n = 0$ ,  $\zeta_n = 0$   $k_p = 803.067$

	Position 1	Position 2	Position 3	Position 4	Stroke
Settling Time	68.880	68.978	69.454	0.592	N/A
Displacement	0.2772	0.1335	0.0874	0.0283	Drifts

TABLE 4.  
FINITE ELEMENT MODEL STRUCTURAL SETTling TIMES (SECONDS)

## AND MAXIMUM DISPLACEMENTS (INCHES)

Once again, the FEM simulation results verified. However, the two cases where  $\omega_a = \zeta_a = 0$  were not experimentally implemented on the MRT structure as the RMA required a certain amount of stiffness and damping. An accelerometer was collocated with the RMA assembly, and the signal from this sensor was fed to a digital controller. The controller then used a low pass filter to integrate the signal to provide the local velocity of the structure, and multiplied it by a gain constant before sending it back to the RMA.

A comparison of the results summarized in Tables 3 and 4 indicate that there is no advantage in overlaying LVF control on a passively tuned actuator for this structural configuration. When the structure possessed closely coupled modes and both passive damping and active control were implemented on the RMA, the settling times were almost identical to those obtained when the RMA was passively tuned only. The stroke lengths required for passive damping and active control were slightly smaller than those required for passive damping, but the difference was not significant. Notice the difference in the gain constants in the first two cases of Table 4. The small value of  $k_g$  required when LVF control was overlaid on an actuator passively tuned to the maximum damping parameters indicates that LVF control really does not add much control authority.

On the other hand, there was a difference in the results obtained when the MRT structure possessed coincident modes. The required stroke lengths listed for cases 4 and 5 in Table 4 are slightly smaller than their corresponding values in Table 3; however, the smaller maximum displacement at Position 4 accounts for the difference in stroke lengths for the case where LVF control is overlaid on RMA tuned to the Den Hartog parameters. The fact that the stroke length for the fifth case in Table 4 is larger than the situation where the RMA is tuned to the maximum passive damping parameters only indicates that LVF control requires a larger stroke length. Interestingly, this observation is confirmed by examining the corresponding results for the structural configuration with closely coupled modes.

Overlaying LVF control on a passively tuned RMA significantly decreased the MRT structure's settling time at the location of the RMA; there is almost no change in the settling times at the other locations. For the MRT with coincident modes a control scheme coupling LVF control with an actuator passively tuned to the Den Hartog parameters suppresses structural vibrations at Position 4 faster than either using LVF control coupled with an actuator passively tuned to the maximum damping parameters or using passive damping only. This observation directly contradicts the results obtained when the MRT structure was configured to possess closely coupled modes.

As for the situation where active control only was used to suppress the vibrations of the MRT structure, the results again depended upon the structural configuration. For the closely spaced mode structural configuration, the settling times at all four positions on MRT were about the same as the situation where vibration suppression was implemented with either passive damping only or passive damping and active control. However, since there was nothing to center

the RMA mass the RMA drifted off after the structure's vibrations were suppressed. Unless the reaction mass was physically constrained, it would continue drifting without limit. For this reason, the RMA requires a measure of passive stiffness and damping to keep the reaction mass centered.

This same phenomena was observed when LVF control only was used to suppress the vibrations of the structure with coincident modes. However, for this case, LVF control only suppressed the MRT structure's vibrations at the location of the RMA in less than one second. The settling times at the other three positions were still the same as when control was applied either by passive damping or passive damping coupled with LVF control.

Thus, it appears that the effectiveness of LVF control depends on the structural configuration. If the structure possesses closely spaced modes, using a passively damped actuator to effect vibration suppression yields results almost identical to the situations when control is implemented using LVF control, either by itself or overlaid on a passively damped actuator. There is no advantage in increasing the complexity of the controller by adding LVF control if a passively damped actuator performs just as well.

If the structure possesses a pair of coincident modes, LVF control is much more effective in suppressing structural vibrations than using a passively damped actuator only. Excluding the problem of RMA drift, using LVF control only yields significantly shorter settling times at the place where the RMA is located than using a passively damped actuator or combining passive damping with LVF control. Unfortunately, a single RMA cannot suppress the vibrations along the entire length of the structure since one mode is uncontrollable.

### LINEAR QUADRATIC REGULATOR CONTROL

The final control strategy examined in this study involved linear quadratic control. The system in Eqn (1) was cast in the following state space representation.<sup>15</sup>

$$\dot{x} = ax + bu \quad (7)$$

with the output given by

$$y = Cx \quad (8)$$

where the matrix C specified the relationship between the coordinates of the vector x and the measurements. The standard linear quadratic regulator had a performance index of the form

$$J = \int_0^{\infty} [x'Qx + u'Ru]dt \quad (9)$$

where Q and R were weighting matrices. The optimum value of the performance index with a

vector of initial conditions  $x_0$  was

$$J_{opt} = x_0^T s x_0 \quad (10)$$

where  $s$  was found by solving an algebraic matrix Riccati equation.<sup>11</sup>

Various methods exist for choosing suitable weighting matrices. For this study, the  $10 \times 10$   $Q$  matrix was defined to be

$$Q = \begin{bmatrix} Q_p & 0 \\ 0 & Q_v \end{bmatrix} \quad (11)$$

where the sub-matrices  $Q_p$  and  $Q_v$  were

$$Q_p = \begin{bmatrix} w1 & 0 & 0 & 0 & 0 \\ 0 & w2 & 0 & 0 & 0 \\ 0 & 0 & w2 & 0 & 0 \\ 0 & 0 & 0 & w2 & 0 \\ 0 & 0 & 0 & 0 & w2 \end{bmatrix} \quad Q_v = \begin{bmatrix} w3 & 0 & 0 & 0 & 0 \\ 0 & w2 & 0 & 0 & 0 \\ 0 & 0 & w2 & 0 & 0 \\ 0 & 0 & 0 & w2 & 0 \\ 0 & 0 & 0 & 0 & w2 \end{bmatrix} \quad (12)$$

where the weighting coefficients  $w1$ ,  $w2$ , and  $w3$  determined the penalties on the displacement of the reaction mass, the structural displacement and velocity, and the velocity of the reaction mass, respectively. For this study,  $w1$  was set to one and  $w3$  was set to zero. In effect, these weighting values minimized the penalty on the reaction mass and increased the control system's performance. The penalty on the controller,  $R$ , and  $w2$  were varied to obtain the best settling time using LQR control. With  $Q$  and  $R$  determined, the control equation was

$$u = -Fx \quad (13)$$

where the feedback gain matrix was  $F = B^T S R^{-1}$ .

As with LVF control, three control schemes were examined using LQR control: LQR control was overlaid on the RMA passively tuned to both the Den Hartog and the maximum passive damping parameters, and LQR control, with  $\omega_o = \zeta_o = 0$ . The results of suppressing the MRT structure using these controllers are summarized in Table 5.

## LINEAR QUADRATIC REGULATOR CONTROL

### CLOSELY SPACED

Den Hartog  $w_2 = 95.601$   $R = 9.7 \times 10^{-6}$

	Position 1	Position 2	Position 3	Position 4	Stroke
Settling Time	2.804	3.004	4.468	2.920	N/A
Displacement	0.2500	0.1316	0.0812	0.1412	0.3684

CLOSELY SPACED

Max Damping  $w_2 = 84.940$   $R = 6.2 \times 10^{-6}$

	Position 1	Position 2	Position 3	Position 4	Stroke
Settling Time	2.808	3.028	4.456	3.024	N/A
Displacement	0.2500	0.1316	0.0812	0.1417	0.3925

CLOSELY SPACED

$\omega_n = 0, \zeta_n = 0$   $w_2 = 83.565$   $R = 4.4 \times 10^{-6}$

	Position 1	Position 2	Position 3	Position 4	Stroke
Settling Time	2.808	3.028	4.458	3.024	N/A
Displacement	0.2500	0.1316	0.0812	0.1417	0.4004

COINCIDENT

Den Hartog  $w_2 = 27570$   $R = 2.0 \times 10^{-15}$

	Position 1	Position 2	Position 3	Position 4	Stroke
Settling Time	68.490	68.685	69.165	41.220	N/A
Displacement	0.2655	0.1341	0.0847	0.0167	0.0383

COINCIDENT

Max Damping  $w_2 = 29507$   $R = 2.0 \times 10^{-15}$

	Position 1	Position 2	Position 3	Position 4	Stroke
Settling Time	68.490	68.490	69.165	43.548	N/A
Displacement	0.2656	0.1340	0.0846	0.0168	0.0381

COINCIDENT

$\omega_n = 0, \zeta_n = 0$   $w_2 = 21906.8$   $R = 4.5 \times 10^{-16}$

	Position 1	Position 2	Position 3	Position 4	Stroke
Settling Time	68.970	69.360	70.905	27.600	N/A
Displacement	0.2772	0.1335	0.0874	0.0283	0.0350

TABLE 5.  
FINITE ELEMENT MODEL STRUCTURAL SETTLING TIMES (SECONDS)  
AND MAXIMUM DISPLACEMENTS (INCHES)

The same digital controller used to implement experimental LVF control on the MRT structure was used to implement experimental LQR control, and the results shown in the figures, as well as in Table 5, were verified.

When compared to using either passive damping or LVF control to suppress vibrations of the MRT structure with closely spaced modes, LQR control was slightly better. For the two cases where LQR control was overlaid on a passively damped RMA, the stroke lengths were comparable to the values obtained previously. The settling times obtained with LQR control overlaid on the RMA tuned to the maximum passive damping parameters were similar to those obtained in the previous two cases involving maximum passive damping. However, with LQR control overlaid on the RMA passively tuned to the Den Hartog parameters, the settling times at each of the four positions on the MRT structure were significantly smaller than the two previous cases involving the Den Hartog values.

In fact, the case where LQR control was overlaid on the RMA tuned to the Den Hartog parameters yielded the best settling times for the structural configuration with closely coupled modes. The results of using LQR control only were slightly worse, indicating that some form of passive damping coupled with LQR control is the best control scheme to implement. It is possible to further optimize this settling time by varying the actuator's passive stiffness and damping, as well as by adjusting the weighting on the LQR controller. Notice, in Table 5 that implementing LQR control without any passive damping still results in the RMA returning to a center position after the structure's vibrations are suppressed. This differs from the results obtained in the LVF control only situation due to the fact that there is weighting on the actuator's position, which has the effect of centering the RMA.

For the structural configuration with coincident modes, LQR control generated the largest settling times of all cases examined in this study. Table 5 shows a tremendous amount of weighting on the structure, and, hence, the maximum displacement at the location of the RMA is quite small. Since the structural displacement is so small, the resulting stroke length is also small, and LQR control authority is minimal. However, the stroke length is sensitive to variations in the weighting on the structure, and decreasing the weight increases the structure's settling time. Hence, the settling times recorded in Table 5 are the optimum times obtained in this study. Notice that, as previously mentioned, the settling times at Positions 1, 2, and 3 result from the structure's uncontrollable mode.

### CONCLUSIONS

Based on the results of this study, the type of control scheme used to suppress a structure's vibrations depends on the configuration of that structure. Using a settling time criteria,

three types of control schemes were examined: attaching a passive damped actuator to the structure, overlaying either LVF or LQR control on a passively damped actuator, and implementing either LVF or LQR control on an actuator without any passive damping.

For a structure with two closely spaced modes, the most effective type of control occurred when LQR control was overlaid on a passively damped actuator. The structure's settling time could be minimized by varying the actuator's stiffness and damping, as well as the weighting matrices associated with the LQR controllers. However, using passive damping only to suppress the structure's vibrations yields settling times almost as small as those obtained with an active controller. Finally, a single RMA was able to suppress the vibrations of the entire structure.

As for a structure possessing a pair of coincident modes, the best control strategy utilized LVF control implemented on a single actuator that had no stiffness or damping. Physically, an RMA requires some stiffness and damping, or the reaction mass drifts off after the structure's vibrations are suppressed. Because a single actuator controlled only one mode, the other structural mode was uncontrollable, and control was effective only at the location of the RMA. The structure's settling times at other positions were smaller than the times obtained without any control because the actuator stopped the vibrations of one part of the structure, and effectively increased the structure's inherent damping.

#### REFERENCES

1. Webb, S. G. and Turcotte, J. S., "Experimental Analysis of a Passively Tuned Actuator on a Low Order Structure," AIAA Journal of Guidance, Control and Dynamics, Vol. 14, No. 6, November-December 1991, pp. 1110-1114.
2. Martinovic, Z. N., Schamel, G. C. II, Haftka, R. T., and Hallauer, W. L., Jr., "Analytical Investigation of the Output Feedback vs Linear Quadratic Regulator," AIAA Journal of Guidance, Control and Dynamics, Vol. 13, No. 1, January-February 1990, pp. 160-167.
3. Meirovitch, L., Dynamics and Control of Structures, John Wiley & Sons, New York, 1990.
4. Skidmore, G. R. and Hallauer, W. L., Jr., "Experimental-Theoretical Study of Active Damping with Dual Sensors and Actuators," Proceedings of the AIAA/ASME/AHS 27th Structures, Structural Dynamics and Materials Conference, Pt. 2, AIAA, New York, 1986, pp. 613-620.
5. Zimmerman, D. C. and Inman, D. J., "On the Nature of the Interaction Between Structures and Proof-Mass Actuators," AIAA Journal of Guidance, Control and Dynamics, Vol. 13, No. 1, January-February 1990, pp. 82-88.
6. Lynch, P. J. and Banda, S. S., "Active Control for Vibration Damping," Large Space Structures: Dynamics and Control, Springer-Verlag, Berlin, 1988.

7. Webb, S. G. and Turcotte, J. S. , "Analysis of a Passively Tuned Actuator on a Low-order Structure," 1990 AIAA Guidance, Navigation and Control Conference, AIAA Paper 90-3500, August 1990.
8. Webb, S. G. and Fisher, C. A., "Using Passively-Tuned Reaction Mass Actuators to Alter a Structure's Characteristics," Proceedings of the First Joint US/Japan Conference on Adaptive Structures, Maui, Hawaii, November 1990.
9. Hallauer, W. L., Jr., and Barthelemy, J.-F. M., "Active Damping of Modal Vibrations by Force Apportioning," 21st AIAA Structures, Structural Dynamics and Materials Conference, Paper 80-0806 in AIAA CP804, Part 2, 1980, pp. 863-873.
10. Webb, S. G. I Smith, J. C. , Turcotte, J. S. , and Garcia, E. , "A Sensitivity Analysis of Closed Loop Control Systems on Flexible Structures," 1991 AIAA Guidance, Navigation, and Control Conference, AIAA Paper 91-2654, August 1991.
11. Phillips, C. L. and Harbor, R. D. , Feedback Control Systems, Prentice-Hall, Englewood Cliffs, New Jersey, 1988.
12. Duke, J. P. , Webb, S. G. , and Vu, H. , "Optimal Passive Control of Multi-Degree of Freedom Systems Using a Vibration Absorber," 1990 AIAA Guidance, Navigation and Control Conference, AIAA Paper 90-3499, August 1990.
13. Webb, S. G. , Stech, D. J. , and Trimboli, M. S. , "Design Trade-Offs for Reaction Mass Actuators, Of 33rd AIAA Structures, Structural Dynamics, and Materials Conference, Dallas, Texas, AIAA Paper 92-2569, April 1992.
14. Webb, S. G. , Stech, D. J. , Turcotte, J. S. , and Trimboli, M.S. , "Modification of Damping in a Structure with Coincident Modes," Proceedings of the ADPA/AIAA/ASME/SPIE Conference on Active Materials and Adaptive Structures, Alexandria, Virginia, November, 1991.
15. Inman, D. J., Vibration with Control, Measurement, and Stability, Prentice-Hall, Englewood Cliffs, New Jersey, 1989.



# Damping of Structural Vibration with Piezoelectric Materials and Parameters Optimization

Tang Yongjie, Hu Xuanli, Zhang Shenbi, Huang Xieqing  
Institute of Vibration and Noise  
Department of Mechanical Engineering  
Xi'an Jiaotong University  
Xi'an, Shannxi Province, 710049  
P. R. China

## Abstract

In this paper, two strain models for a beam surface-bonded with finite-length spatially distributed piezoactuators is formulated. The control moment is derived for these models. A method for optimization the parameters of piezoactuators is presented. In this process, the maximum bending moment induced by the actuators is selected as objective function. According to the analysis, some criterions for selecting piezoactuator is obtained.

## Introduction

Intelligent structures are the structures which integrated with distributed sensors and actuators and electronic networks. They have lead to a great deal of interest in the area of vibration and noise control in recent years. Distributed sensors and actuators, such as poly-vinylidene fluoride (PVDF), piezoceramic materials (PZT) and shape memory alloy (SMA), have been widely used to active vibration control (Baliy and Hubbard, 1985; Crawley and de Luis, 1987; Wilson D.G. and Dr. R. Ikegami etc, 1989) and structural acoustics control (Dimitriadis and Fuller, 1989; Wang and Fuller, 1991).

Intelligent structures are of coupled systems. In order to describe the mechanical coupling between the piezoelectric materials and substructures, many research have studied this problem. Some models have been presented to formulate the interaction between piezoactuators and substructures.

Crawley and de Luis (1987) presented a rigorous study of strain-stress-voltage for a one-dimensional cantilever beam that surface-bonded and embedded piezoelectric patches. They showed that the shear stresses at the bonding layer and beam interface become uniform within the actuators boundaries when the piezoactuators are ideally bonded. The control moment induced by piezoactuators is concentrated at the two ends of the

piezoelectric patches and increased by using stiffer piezoelectric material.

Dimitriadis, Fuller and Roger (1989) presented a two-dimensional model for piezoceramic patches perfectly bonded to the top and bottom surfaces of a rectangular plate. They showed that the bending control moment induced by the piezoceramic patches were along the four edges of the piezoceramic patches. The geometry of the piezoactuators shape affects the modal distribution of plate and the location of the piezoceramic affects the vibration response dramatically.

Tzou and Tseng (1990) presented a finite element formulation for the application of distributed actuator to the shells.

In this paper, we present two strain models and determine the moment induced by the distributed piezoactuators. To maximize the control moment, the parameters of the piezoactuator is studied. The optimal thickness of the piezoactuator is estimated for a beam under constant field.

### The Coupling Analysis for Piezoactuator and Beam

A beam with two actuators bonded to the top and bottom of its surface symmetrically is represented in Fig.1. The voltage applied to the actuators is  $180^\circ$  out of phase. A bending

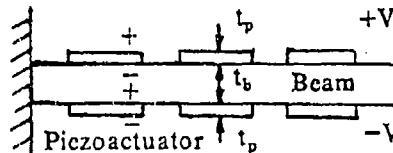


Fig.1 Beam Bounded with Piezoactuator Patches

moment produced by one pair of piezoactuator can be obtained. In order to simplify the analysis, the basic assumptions are as follow:

1. Ideal bonding between beam and actuator.
2. The same width for piezoactuator and beam ( $b_p = b_b = b$ ).
3. Euler-Bernoulli beam theory being used.

According to these assumptions, two strain models can be obtained and represented in Fig.2 and Fig.3. The first model assumes only uniform extensional strain in the actuators.

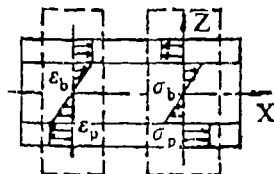


Fig.2 Uniform Strain Model

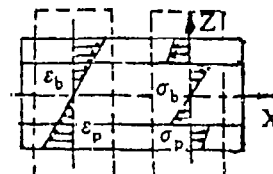


Fig.3 Consistent Strain Model

This model is valid for the relatively thin actuator ( $t_p < t_b$ ). It is named Uniform Strain Model. It is not appropriate for the thicker piezoactuator in comparison to the beam. The second model is the Consistent Strain Model that assumes extension and bending strains included in the actuator.

#### Uniform Strain Model

The result of uniform strain model is presented by Crawley and de Luis (1987). For the case of induced bending, the strain in the actuator and the upper surface of the beam is identical.

$$\varepsilon_p = \varepsilon_b^{surf} = \frac{6\Delta}{6 + \Psi} \quad (1)$$

$$\Delta = \frac{d_{31} V}{t_p} \quad (2)$$

where  $\Delta$  is the piezoelectric free strain.  $V$  is the control voltage.  $\Psi$  is the stiffness parameter. For a general cross-section is written as:

$$\Psi = \frac{12(EI)_b}{t_b^2(EA)_p} \quad (3)$$

For a rectangular beam,  $\Psi$  is expressed as:

$$\Psi = \frac{(EA)_b}{(EA)_p} = \frac{2}{\alpha\beta} \quad (4)$$

$$\text{where } \alpha = \frac{E_p}{E_b}, \quad \beta = \frac{t_p}{h}, \quad h = \frac{t_b}{2} \quad (5)$$

The two equivalent concentrated control moments acting at the edges of an piezoactuator can be expressed as:

$$m = \frac{t_b^2 E_b}{6 + \Delta} \Delta b = \frac{2\beta}{3\alpha\beta + 1} h^2 E_p b \Delta \quad (6)$$

#### Consistent Strain Model

The strain distribution is a linear function of  $z$  across the coupled structure. The strain can be represented as:

$$\varepsilon(Z) = \varepsilon_p(Z) = \varepsilon_b(Z) = \lambda Z \quad (7)$$

where  $\lambda$  is the strain slope. The strains for the actuators and beam at the interface is identical. A discontinuity stress distribution at the interface occurs. The stress distribution in the beam can be expressed as:

$$\sigma_b = \frac{\sigma_s Z}{h} \quad (8)$$

where  $\sigma_s$  is the stress of the upper surface of beam.

Based upon Hook's law, we can also obtained:

$$\sigma_b = E_b \varepsilon_b = E_b \lambda Z \quad (9)$$

From Eq.(8) and Eq.(9), the strain slope is:

$$\lambda = \frac{\sigma_s}{E_b h} \quad (10)$$

The stress distribution in the piezoactuator is represented as:

$$\sigma_p = E_p(\varepsilon_p - \Delta) = \alpha \left( \frac{\sigma_s}{h} \right) Z - E_p \Delta \quad (11)$$

According to force equilibrium condition, the interface stress  $\sigma_s$  can be determined by the force equilibrium condition about the neutral axis.

$$\int_0^h \sigma_b Z dZ + \int_h^{h+t_p} \sigma_p Z dZ \quad (12)$$

From Eq.(12),  $\sigma_s$  can be expressed as:

$$\sigma_s = \frac{E_p t_p h (2h + t_p)}{2 \left[ h^3 + \alpha t_p (3 + h_2 + t_p^2 + 3ht_p) \right]} \Delta \quad (13)$$

The induced control moment is written as:

$$m = \int_{-h}^h \sigma_b b Z dZ = \frac{2\beta + \beta^2}{1 + \alpha\beta(3 + 3\beta + \beta^2)} h^2 E_p b \Delta \quad (14)$$

## Parameters Optimization

The expression for induced control moment is a function of thickness and material properties of the actuator and beam. The control moment is proportion to the free piezoelectric strain  $\Delta$ . That is, it is proportion to the electric field ( $V/t_p$ ). To simplify, we assume the electric field is constant. Under this assumption, the piezoactuator which posses a high piezoelectric strain constant is desirable.

From Eq.(6) and Eq.(14), we can also see larger control moment can be obtained by using stiffer piezoelectric material. If the type of the piezoelectric material and beam is specified, the piezoelectric strain constant  $d_{31}$  and stiffness of the material and beam are specified

Tab.1 Physical Properties of Piezoactuators and Beam

$E_p = 64.5 \text{ Gpa}$	$E_b = 70 \text{ Gpa}$
$E = 100 \text{ V / mm}$	$t = 2 \text{ mm}$
$d_{31} = 190 \times 10^{-12} \text{ m / V}$	

also. The control moment is only dependent upon the thickness ratio  $\alpha$ . They are reperesented in Fig.4 and Fig.5 for these two models. The physical properties of piezoactuator and beam are tabulated in Tab.1.

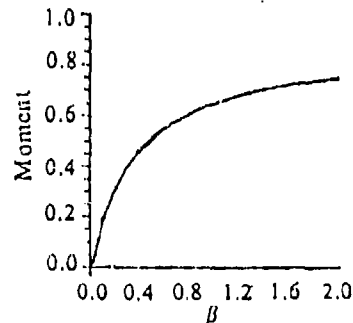


Fig.4 Induced Moment by a Pair of piezoactuators for Uniform Strain Model

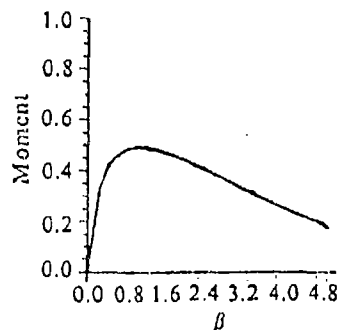


Fig.5 Induced Moment by a Pair of piezoactuators for Consistent Strain Model

Fig.4 shows that the bending moment, for the uniform strain model, goes to zero when the thickness of piezoactuators close to zero and it increases when using thicker piezoactuators. The moment increment becomes small when  $\beta > 1.0$ . Therefore, the half-beam thickness of piezoactuator is desirable.

Fig.5 shows that the bending moment goes to zero when the piezoactuator thickness approaches to zero. The bending moment decreases as  $\beta$  increasing. There is a optimal thickness for that case the bending moment is maximum. It is also about half-beam thickness ( $\beta = 1.0$ ) for this aluminum beam.

According to the analysis, some criterions for selection piezoactuators can be obtained:

- (1) High piezoelectric constant and stiffer material is desirable.
- (2) Half-beam thickness piezoactuator is desirable for the aluminum beam. Choosing slightly thicker material, if the optimal thickness can not get.

### Conclusion

Two strain models are presented. The interaction between piezoactuators and beam are analyzed. The control moment induced by the piezoactuators is derived. The parameters of the piezoactuator are studied. For an aluminum beam, the optimal thickness of piezoactuators is about half-beam.

### References

- Bailey, T. and J.E. Hubbard. 1985, " Distributed Piezoelectric Ploymer Active Vibration Control of a Cantilever Beam", J. Guidance, Control and Dynamics, 8(5):605-611.
- Crawley, E.F. and de Luis J. 1987, " The Use of Piezoelectric Actuators as Elements of Intelligent Structures", AIAA J., 25(10):1373-1385.
- Dimitriadis, E.K. and C.R. Fuller. 1989, " Investigation on Active Control of Sound Transmission Through Elastic Plate Using Piezoelectric Actuators", AIAA Paper. 89-1602.
- Tzou, H.S. and C.I. Tseng. 1990, " Distributed Dynamic Identification and Control of Flexible Shells", AIAA Paper. 90-1089.
- Wang B.T., C.R. Fuller and E.K. Dimitriadis. 1991, " Active Control of Structurally Radiated Noise Using Multiple Piezoelectric Actuators", AIAA J. 29(11):1802-1809.
- Wilson D.G., Dr. R. Ikegami, J.R. Anderson and G.J. Julien. 1989, "Active Vibration suppression Using NiTiNOL Sensors and Actuators", Damping'89, ICB1-ICB9.

## DAMPING PROPERTIES OF PTMG/PPG BLENDS

Mr. Gilbert F. Lee<sup>a</sup>, Mr. John D. Lee, Dr. Bruce Hartmann, and  
Dr. Dasara Rathnamma\*

Naval Surface Warfare Center  
Dahlgren Division, White Oak Laboratory  
\*Carderock Division, Annapolis Laboratory

### ABSTRACT

Hard segment crystallinity strongly influences the dynamic mechanical properties of polyurethanes. Usually the systems studied are either highly crystalline or completely amorphous. The present work considers systems that have intermediate degrees of crystallinity. To achieve the variation of crystallinity, blends of a highly crystalline PTMG system with a low degree of crystallinity PPG system were studied. It was found that the rubbery modulus of the blends varied from 4 to 18 MPa. The damping peak height varied from 0.3 to 0.9, while the location of the peak varied from 0.2 to 10 kHz. Along with this variation of peak height, the width of the peak varied from 4 to 8 decades of frequency. This relation between height and width agrees with our earlier findings.

<sup>a</sup>Principal author: Gilbert F. Lee, Code R31, Naval Surface Warfare Center, 10901 New Hampshire Avenue, Silver Spring, Maryland 20903-5640, phone 301-394-1199, FAX 301-394-2414

## INTRODUCTION

The molecular structure of polyurethanes governs their damping properties of polyurethanes. These polymers are molecular composites composed of soft segments and hard segments alternating along the polymer chain. The soft segments consist of flexible, straight chains of carbon atoms connected by single chemical bonds. The hard segments contain rigid rings of carbon atoms connected by double bonds.

Hard segment crystallinity strongly influences the dynamic mechanical properties of polyurethanes (Lee et al., 1991; Hartmann et al., 1991; Duffy et al., 1990). Usually the systems studied are the extremes of either highly crystalline or completely amorphous. Crystalline polymers have higher rubbery modulus and lower, broader damping peaks than amorphous polymers. In particular, polymer systems based on poly(tetramethylene ether) glycol are highly crystalline. For systems made from poly(propylene ether) glycol, the degree of crystallinity is low. The present work considers systems that have intermediate degrees of crystallinity. To achieve the variation of crystallinity, polymers were synthesized from blends of poly(tetramethylene ether) glycol and poly(propylene ether) glycol.

In general, polyurethanes are synthesized by first reacting a polyol with a diisocyanate to form a prepolymer. The prepolymer is then reacted with a chain extender to form the final polymer. For this work, five different prepolymers were synthesized. The nominal molecular weight of these polyols was 1000. The hard segment concentration was 50 percent.

Damping properties were measured with a resonance apparatus. Master curves were obtained using the time-temperature superposition principle. Degree of crystallinity was estimated from the heat of fusion measured in a differential scanning calorimeter.

## EXPERIMENTAL

### POLYMER SYNTHESIS

Prepolymers were synthesized from mixtures of poly(tetramethylene ether) glycol (PTMG) and poly(propylene ether) glycol (PPG) and a



polycarbodiimide-modified diphenylmethane diisocyanate (MDI). Five different polyol blends were prepared using various molar ratios of PTMG and PPG. Nominal molecular weight of both PTMG and PPG was 1000.

To synthesize a prepolymer, three moles of MDI were reacted with one mole of a polyol blend at 50°C. The exotherm from the reaction raised the temperature of the mixture to 80°C. The mixture was held between 75 and 80°C for about 2 hours under vacuum. Under these reaction conditions, a prepolymer was formed. The prepolymer was then cooled to room temperature and sealed under a nitrogen blanket. The next step was to measure the percent of free isocyanate in the prepolymer. A chain extender, 1,4-butanediol, was then added. Knowing the percent of free isocyanate, the stoichiometry of the chain extender was adjusted to result in a 5 percent excess of isocyanate. With this formulation, a lightly crosslinked polymer is produced.

All samples were cured at 100°C for 16 hours and postcured at room temperature for one week. After postcuring the samples, calorimetry and dynamic mechanical measurements were made. The room temperature densities were measured by an immersion technique.

As an abbreviated form of reference, the above polymers will be identified by the ratio of the two polyols used. For example, PTMG/PPG 50/50 is a mixture of 50 percent PTMG and 50 percent PPG.

## CALORIMETRY TECHNIQUE

A differential scanning calorimeter (DSC) was used to determine the heat of fusion of these polymers, and their transition temperatures. The instrument was a Seiko Instruments Model SSC5200 with a DSC 220 module. Measurements were made in an argon purge at a scanning rate of 10°C/min. Sample sizes were 5-20 mg.

A glass transition temperature,  $T_g$ , is seen as a reversed s-shaped portion of the curve. A melting temperature,  $T_m$ , appears as a v-shaped portion of the curve. Heat of fusion,  $E_a$ , is calculated from the area under the v-shaped curve. This calculation yields the heat of fusion per gram of polymer. The percent hard segment was calculated from the idealized structure of the linear polymer. This value was used to calculate the heat of fusion per gram of hard segment. Since all these polymers are 50

percent hard segment, the heat of fusion per gram of hard segment is exactly twice the heat of fusion per gram of polymer.

## DYNAMIC MECHANICAL TECHNIQUE

Measurements of dynamic mechanical properties were made using a resonance device (Madigosky and Lee, 1983), shown in Figure 1. A sample in the shape of a bar is excited into resonance at various harmonics. Typically, four or five resonant peaks can be determined in a range of 1.5 decades centered at about 1 kHz. The real ( $G'$ ) and imaginary ( $G''$ ) parts of the complex shear modulus ( $G^*$ ) are calculated at these resonant frequencies. The measurements are repeated as a function of temperature.

An overall summary presentation of this data can be displayed in a log-log plot of loss factor ( $G''/G'$ ) versus  $G'$ , sometimes called a wicket plot from its shape. The plot combines the temperature and frequency dependencies onto one curve. From this plot, a qualitative feel for the consistency of the experimental data is determined.

Data at the different temperatures can be superimposed to form a master curve of modulus and loss factor over a wide frequency range at a given reference temperature. To present the data on a common basis, master curves will be presented at a reference temperature of 25°C. The process used to generate master curves is called time-temperature superposition. The basis of the time-temperature superposition principle is that the effect of a temperature change on modulus and loss factor is equivalent to a change in frequency. At a melting point, however, a change in temperature produces major changes in modulus and loss factor that are not equivalent to a frequency change.

The amount of shift along the log frequency axis to overlap two sets of data at different temperatures is called the shift factor,  $a_T$ . The shift factor data is fitted to the VLF equation (Ferry, 1980)

$$\log a_T = -c_{10} (T-T_0)/(c_{20}+T-T_0) \quad (1)$$

where  $c_1$  and  $c_2$  are constants for a given polymer. The subscript 0 indicates the reference temperature  $T_0$  at which the equation is evaluated. To present the shift factor data on a common basis, the glass transition

temperature ( $T_g$ ) of each polymer is used to form a reduced temperature,  $T-T_g$ , for plotting each polymer.

## ANALYTICAL MODEL

The best analytical model of the glass transition is due to Havriliak and Negami (1966). This model represents the complex modulus data as a function of frequency to within the accuracy of the measurements. The Havriliak-Negami (HN) equation is

$$(G^* - G_\infty)/(G_0 - G_\infty) = (1 + (i\omega\tau)^\alpha)^{-\beta} \quad (2)$$

where  $G_\infty$  is the limiting high frequency modulus,  $G_0$  is the limiting low frequency modulus,  $\omega = 2\pi f$  is the circular frequency of the measurement,  $\tau$  is the average relaxation time,  $\alpha$  is a parameter governing the width of the transition, and  $\beta$  is a parameter governing the asymmetry of the transition. Both  $\alpha$  and  $\beta$  are dimensionless parameters with values between zero and one. The relaxation time,  $\tau$ , is a measure of the location of the glass transition.

A non-linear least-square algorithm was used to fit the HN model to the experimental data. The fitting routine used in this algorithm was obtained from the International Mathematical and Statistical Libraries Inc. (IMSL) software library under the name DUNLSF. The algorithm was written in FORTRAN for a PC.

A detailed description of the loss factor peak can be calculated using the HN equation. The specific properties desired are the location, height, width, and asymmetry of the peak. The location of the peak is given in terms of a frequency,  $f_0$ , in Hz. The height,  $H$ , is the maximum value of the loss factor and is dimensionless. The width,  $W$ , is expressed as decades between the two frequencies at half height ( $H/2$ ). These two frequencies are designated  $f_+$  and  $f_-$  for the values above and below  $f_0$  respectively. A measure of asymmetry,  $A$ , is the fraction of  $W$  from  $f_0$  to  $f_+$  minus the fraction from  $f_-$  to  $f_0$  and is expressed in decades of frequency.

## RESULTS

### CALORIMETRY

A composite thermogram for the five polymers is shown in Figure 2. All five polymers have a glass transition and a melting point. The glass transition occurs in the soft segments of the polymers. The glass transition curve is narrow for the PTMG/PPG 0/100 polymer and broad for the PTMG/PPG 100/0 polymer. For the blends, the curves are intermediate between the two extremes.

Melting occurs in the hard segments of the polymer. The melting curve is narrow for the PTMG/PPG 0/100 polymer, indicating a narrow distribution of crystalline sizes. The melting curve is broad for the PTMG/PPG 100/0 indicating a broad distribution of crystalline sizes. Not only is the melting curve broad, there are two overlapping melting peaks. For the blends, the curves are generally intermediate between the two extremes. Only the PTMG/PPG 75/25 blend show two overlapping peaks.

Two independent measurements were made on each polymer. Average glass transition and melting point temperatures and heats of fusion are presented in Table 1. The  $T_g$  decreases as the concentration of PTMG increases. This decrease in  $T_g$  is a result of an decrease in phase mixing of the hard and soft segments with increasing PTMG concentration. This result was already noted in our earlier work (Lee et al. 1992 and Hartmann et al. 1991).

These differences in glass transition temperatures provide an explanation for the variations in density listed in Table 1. In general, the higher the measurement temperature is above  $T_g$  the lower the density will be. Since all of the densities were measured at room temperature, the PTMG/PPG 100/0 polymer has the lowest density because it is furthest from its  $T_g$ .

In Table 1,  $T_m$  values for all the polymers are about the same, with an average value of 160°C. This result is based on the first melting peak temperature only.

In general, the degree of crystallinity is proportional to the heat of

fusion. As shown in Table 1, the degree of crystallinity generally increases with increasing concentration of PTMG. There is some scatter in the results, but an overall trend is apparent. The difference in the chemical structure between PTMG and PPG is that PPG has a methyl pendant group while PTMG is a straight chain. This pendant group in the soft segments of PPG prevents the crystallization of the hard segments.

## DYNAMIC MECHANICAL

Typical wicket plots of  $\log G''/G'$  vs  $\log G'$  are shown in Figure 3 for PTMG/PPG 100/0 polymer and Figure 4 for PTMG/PPG 0/100. Each data point represents a different temperature-frequency combination. The data is reasonably consistent. However, the data shows more scatter for PTMG/PPG 100/0 polymer than PTMG/PPG 0/100 polymer.

Shift factor versus reduced temperature is shown in Figure 5. Each data point for a given polymer represents a different temperature. The data was fitted to the WLF equation (eq. 1) using  $T_g$  as the reference temperature. Results are listed in Table 2. As seen in Figure 5, the data fits the WLF equation very well over almost the entire temperature range. The five curves are similar in shape. The WLF constants are comparable to those for the series with varying hard segment concentration and hard segment length (Lee et al. 1992 and Duffy et al. 1990).

A typical master curve is shown in Figure 6 for the PTMG/PPG 0/100 polymer. The data covers 16 decades of frequency at a reference temperature of 25°C. The solid lines representing the fit of the experimental data to the HN model are also shown. As can be seen, the HN model fits the data within the accuracy of the measurements. In the remainder of this paper, only the HN fits will be shown.

Figure 7 shows the shear modulus master curves for the five polymers. Loss factor data is shown in Figure 8. To analyze these results, the HN fitting parameters listed in Table 3 will be compared. A linear correlation between the natural log of  $\tau$  and the reciprocal of the glass transition temperature (in degrees Kelvin) was shown by Hartmann and Lee, 1991 and Hartmann et al., 1992. Except for PTMG/PPG 0/100, the data obtained here is in excellent agreement with that correlation.

The low frequency limiting modulus,  $G_0$ , (Table 3) is correlated with

the heat of fusion,  $E_a$ , (Table 1). Values of  $G_0$  increase with increasing values of  $E_a$ . Since  $E_a$  is proportional to the degree of crystallinity, the crystalline hard segments are acting like a reinforcing filler in a soft segment matrix.

The high frequency limiting modulus,  $G_{\infty}$ , is about the same for all the polymers as listed in Table 3. This result is similar to that found with polyurethanes in general.

In Table 3, as the degree of crystallinity increases,  $\alpha$  decreases. This trend results in a broadening of the loss factor peak as shown in Figure 8. Even though there is some scatter in values,  $\beta$  increases as the degree of crystallinity increases. The interpretation of this result is that the loss factor peak is becoming more asymmetrical as the degree of crystallinity increases. The trends seen in both  $\alpha$  and  $\beta$  are typical of polyurethanes.

A detailed description of the loss factor peak location, height, width, and asymmetry will now be presented. In Table 4, the location of the loss factor peak,  $f_0$ , varies by a factor of 50 (from 200 Hz to 10 kHz) as the degree of crystallinity varies. Recall that these values are calculated at a reference temperature of 25°C. At some other reference temperature, the values of  $f_0$  would be different.

The loss factor peak heights,  $H$ , in Table 4 decrease with increasing degree of crystallinity. As a rule of thumb,  $H$  is correlated with the value of  $G_0$ : the higher the rubbery modulus, the lower the peak height.

The width,  $W$ , increases as the degree of crystallinity increases. Values of  $W$  vary from 4 to 8 decades. The results also follow our observations (Hartmann et al., 1992) that height and width are not independent. A low loss material inevitably has a broad peak while a high loss material has a narrow peak.

Finally, the values of asymmetry,  $A$ , demonstrate that the transition is becoming more asymmetrical as the degree of crystallinity increases. Values of  $A$  for a low loss materials are usually large.

## CONCLUSIONS

A series of five polyurethanes were synthesized with varying degrees of hard segment crystallinity. To achieve the variation of crystallinity, polymers were made from blends of poly(tetramethylene ether) glycol and poly(propylene ether) glycol. The concentration of diisocyanate and chain extender were kept constant. The thermal and dynamic mechanical damping properties of these polymers were measured.

Based on these measurements, the following conclusions were reached. As the degree of hard segment crystallinity increases:

- The soft segment glass transition temperature decreases.
- $G_0$  increases from 4 to 18 MPa.
- The height of the loss peak decreases from 0.9 to 0.3.
- The width of the loss peak varies from 4 to 8 decades.

## ACKNOWLEDGEMENT

This work was sponsored by the Independent Research Program at the Naval Surface Warfare Center, White Oak Detachment and the Materials Block Program at the Annapolis Detachment.

## REFERENCES

Duffy, J. V., Lee, G. F., Lee, J. D., and Hartmann, B., in Sound and Vibration Damping with Polymers, R. D. Corsaro and L. H. Sperling, eds., ACS Symposium Series 424, 1990, pp 281-300.

Lee, J. D., G. F. Lee, and B. Hartmann, 1992, Proceedings of Vibro-Acoustic Characterization of Materials and Structures, NCA-Vol 14, American Society of Mechanical Engineers, pp 155-166.

Lee, J. D., G. F. Lee, and B. Hartmann, Proceedings of Damping '91, Vol. III, pp GDF-1 to GDF-12, 1991.

Ferry, J. D., 1980, Viscoelastic Properties of Polymers, John Wiley & Sons, Inc., 3rd ed., pp 264-320.

Hartmann, B. and Lee, G. F., 1991, "Dynamic mechanical relaxation in some polyurethanes," Journal of Non-Crystalline Solids, Vol 131-133, pp 887-890.

Hartmann, B., Lee, G. F., and Lee, J. D., 1992, Proceedings of Vibro-Acoustic Characterization of Materials and Structures, NCA-Vol 14, American Society of Mechanical Engineers, pp 21-25.

Havriliak, S. and Negami, S., 1966, "A Complex Plane Analysis of  $\alpha$ -

Dispersions in Some Polymer Systems," Journal of Polymer Science: Part C, No. 14, pp 99-117.

Madigosky, W. M. and Lee, G. F., 1983, "Improved resonance technique for materials characterization," Journal of the Acoustical Society of America, Vol. 73, pp 1374-1377.

Table 1: Transition Temperatures, Heat of Fusion, and Density

PTMG/PPG	$\rho$ , g/cm <sup>3</sup>	$T_g$ , °C	$T_m$ , °C	$E_a$ , J/g
0/100	1.187	-6	163	10
25/75	1.174	-8	159	8
50/50	1.166	-21	165	22
75/25	1.155	-28	158	20
100/0	1.145	-34	154	28

Table 2: WLF Shift Constants

PTMG/PPG	$T_g$ , °C	$c_{1g}$	$c_{2g}$ , °C
0/100	-6	13.6	85.0
25/75	-8	15.8	72.7
50/50	-21	21.7	134
75/25	-28	23.0	125
100/0	-34	27.1	144

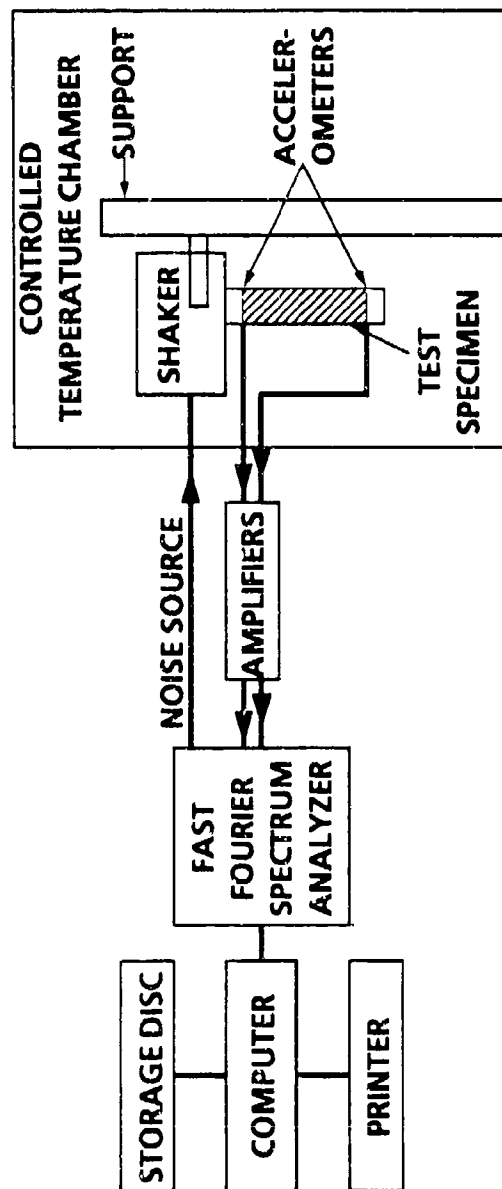


Table 3. HN Fitting Parameters

PTMG/PPG	$\tau, \mu\text{sec}$	$G_0, \text{MPa}$	$G_{\infty}, \text{GPa}$	$\alpha$	$\beta$
0/100	3.81	6.43	1.95	.507	.135
25/75	93.2	4.36	2.20	.572	.056
50/50	2.92	10.4	1.12	.451	.194
75/25	5.76	7.80	1.60	.418	.101
100/0	0.29	18.1	1.28	.271	.238

Table 4. Loss Peak Characteristics

PTMG/PPG	$f_0, \text{kHz}$	H	W, dec	A, dec
0/100	2.04	.752	4.40	.397
25/75	0.177	.856	3.75	.423
50/50	3.79	.572	4.69	.458
75/25	1.79	.530	5.31	.639
100/0	9.56	.305	7.94	.770



**FIGURE 1. SCHEMATIC DRAWING OF RESONANCE APPARATUS FOR MEASURING COMPLEX MODULUS.**

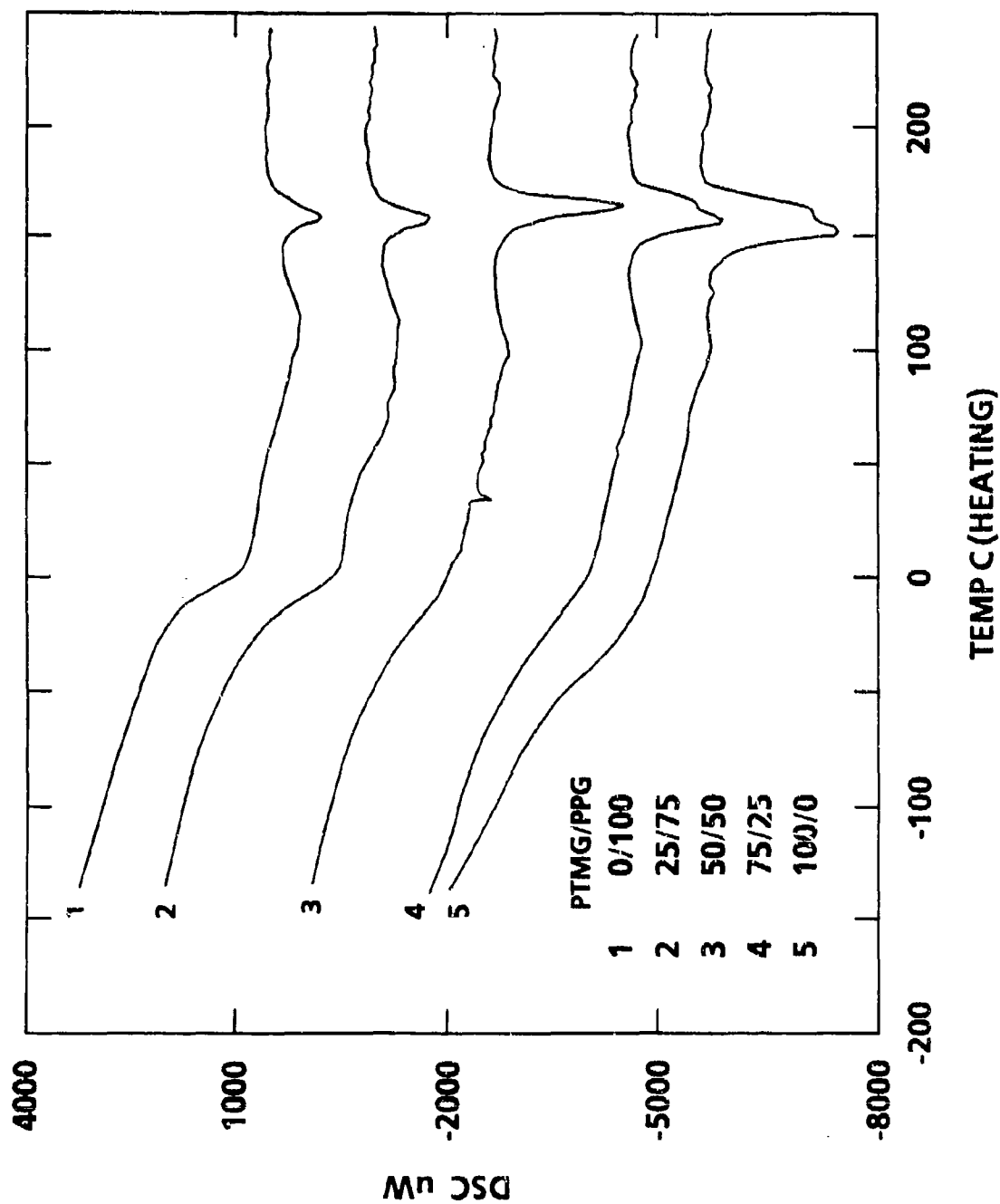


FIGURE 2. DIFFERENTIAL SCANNING CALORIMETER THERMOGRAMS FOR POLYURETHANES SYNTHESIZED WITH GLYCOL BLENDS OF PTMG/PPG 0/100, 25/75, 50/50, 75/25, AND 100/0.

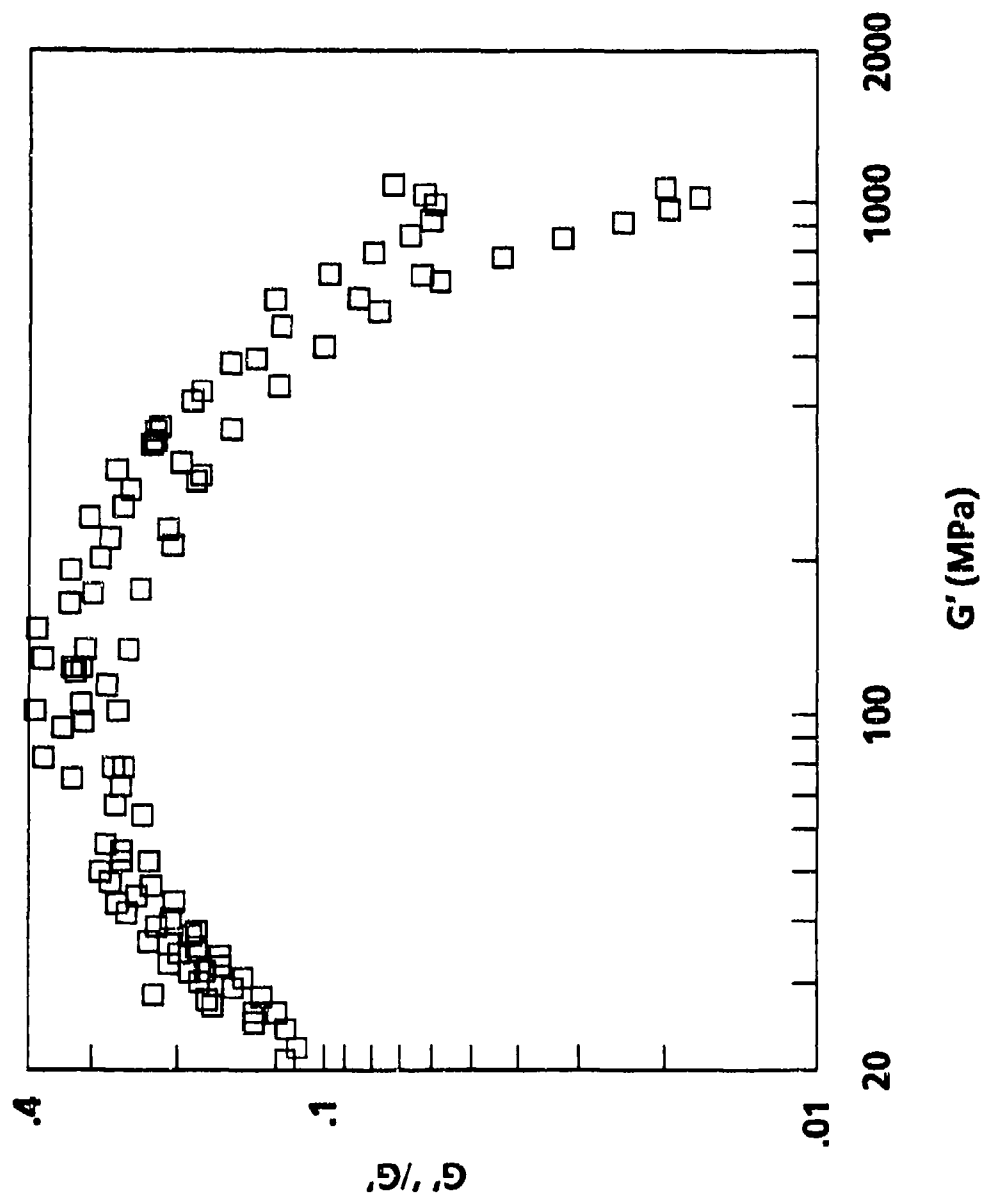


FIGURE 3. WICKET PLOT FOR POLYURETHANE SYNTHESIZED WITH PTMG/PPG 100/0 WITH A LOW LOSS FACTOR PEAK.

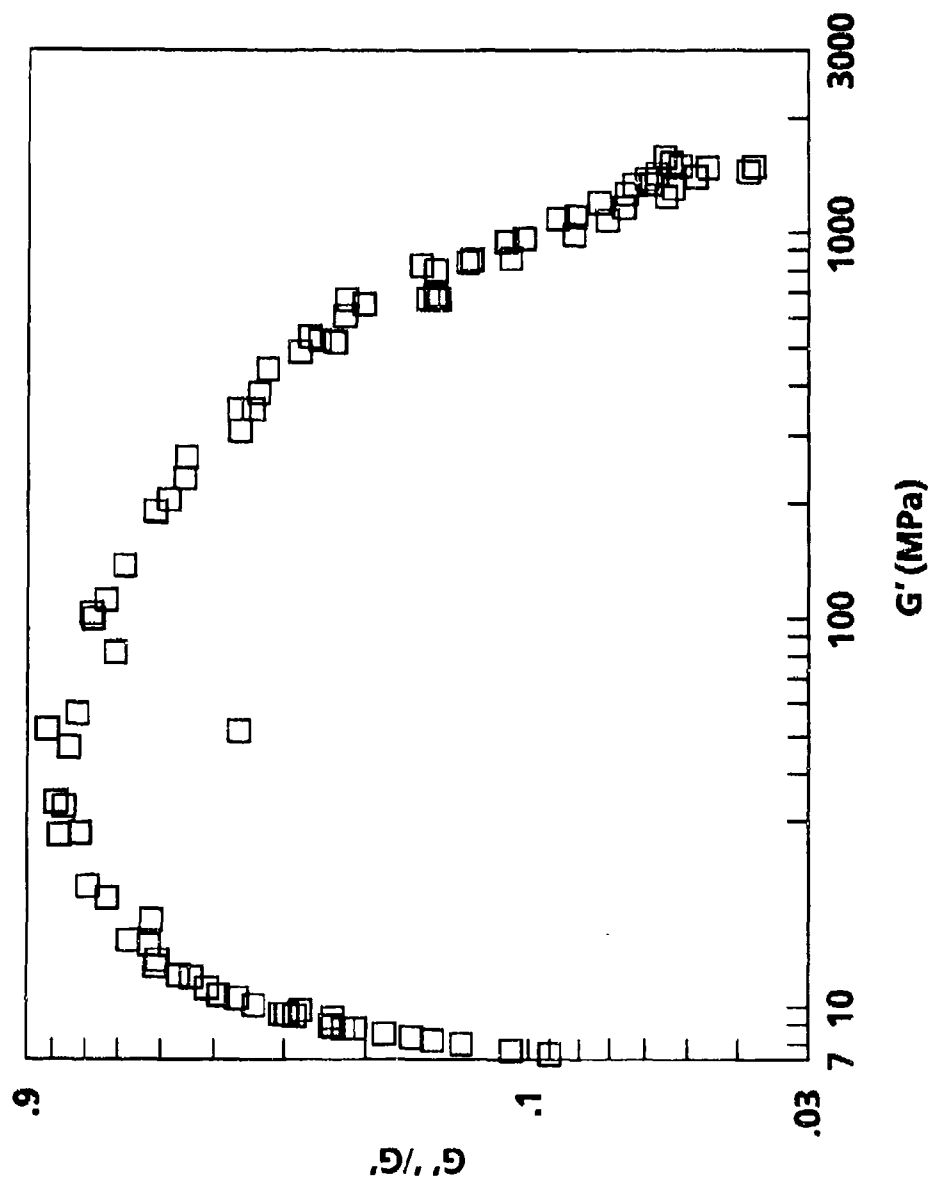


FIGURE 4. WICKET PLOT FOR POLYURETHANE SYNTHESIZED WITH PTMG/PPG 0/100 WITH A HIGH LOSS FACTOR PEAK.

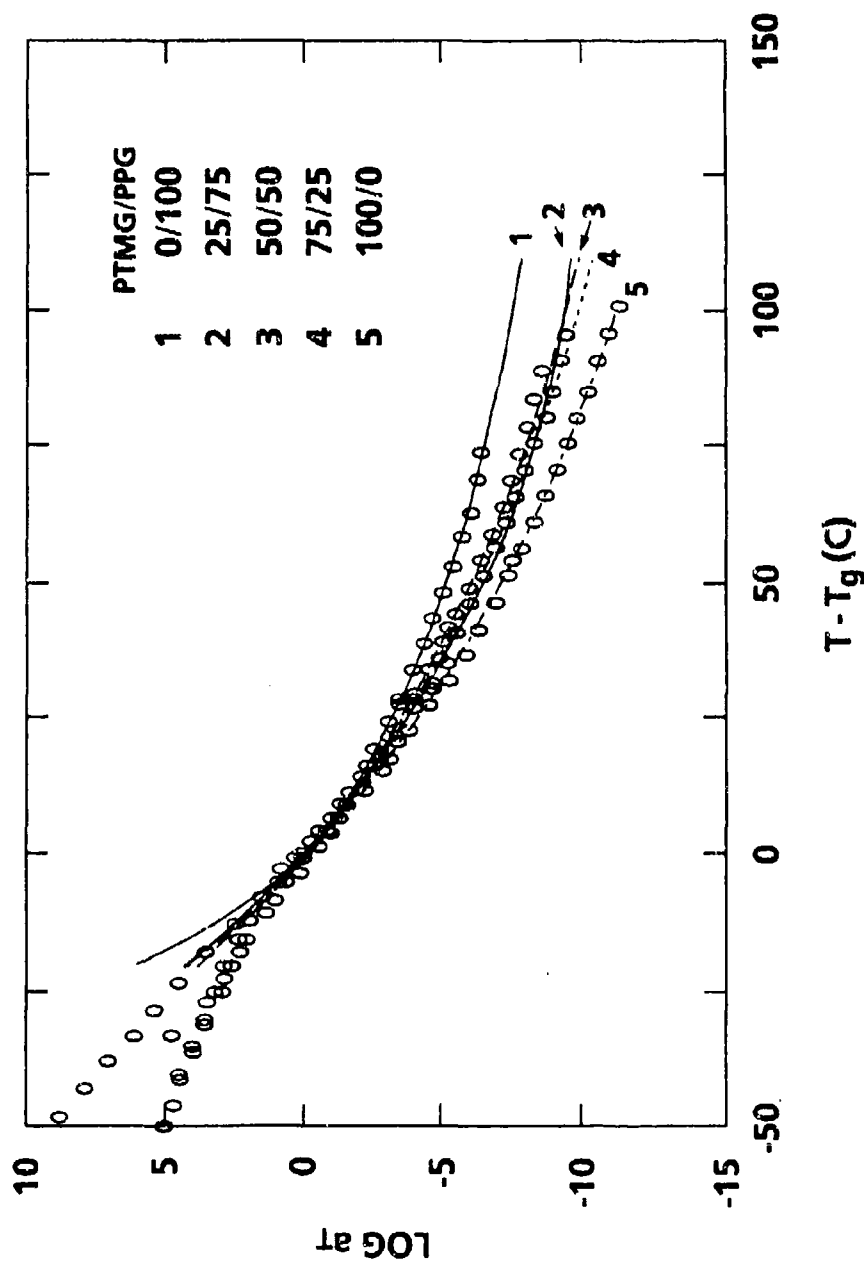


FIGURE 5. SHIFT FACTOR AS A FUNCTION OF REDUCED TEMPERATURE  $T - T_g$  FOR POLYURETHANES SYNTHESIZED WITH PTMG/PPG 0/100, 25/75, 50/50, 75/25, AND 100/0. THE OPEN SYMBOLS ARE EXPERIMENTAL DATA. THE LINES ARE FITTED TO THE WLF EQUATION.

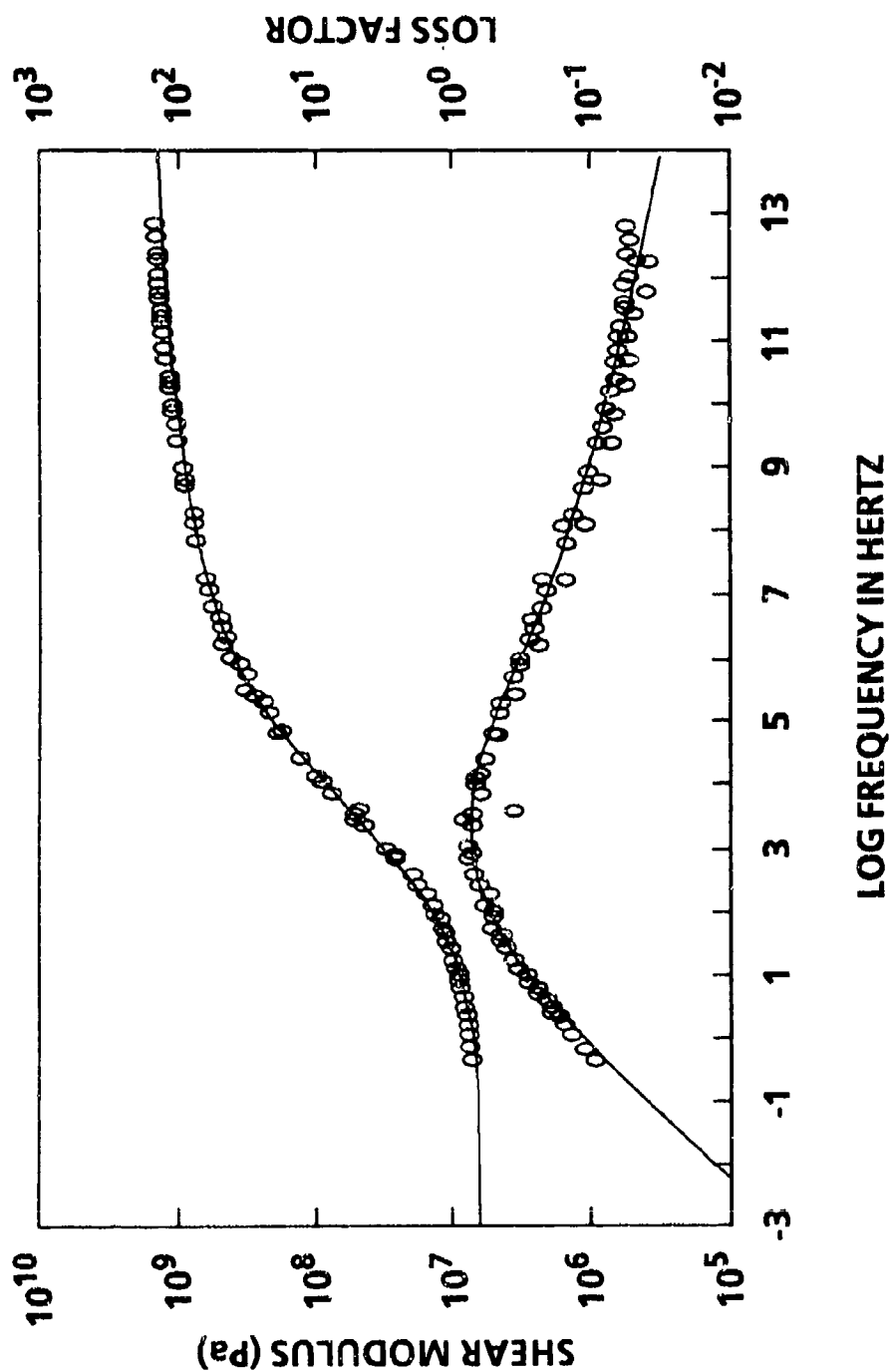


FIGURE 6. SHEAR MODULUS AND LOSS FACTOR FOR POLYURETHANE SYNTHESIZED WITH PTMG/PPG 0/100. SHIFTED EXPERIMENTAL DATA IS SHOWN BY OPEN SYMBOLS. THE SOLID LINES ARE THE FITTED HAVRILIAK-NEGAMI EQUATION.

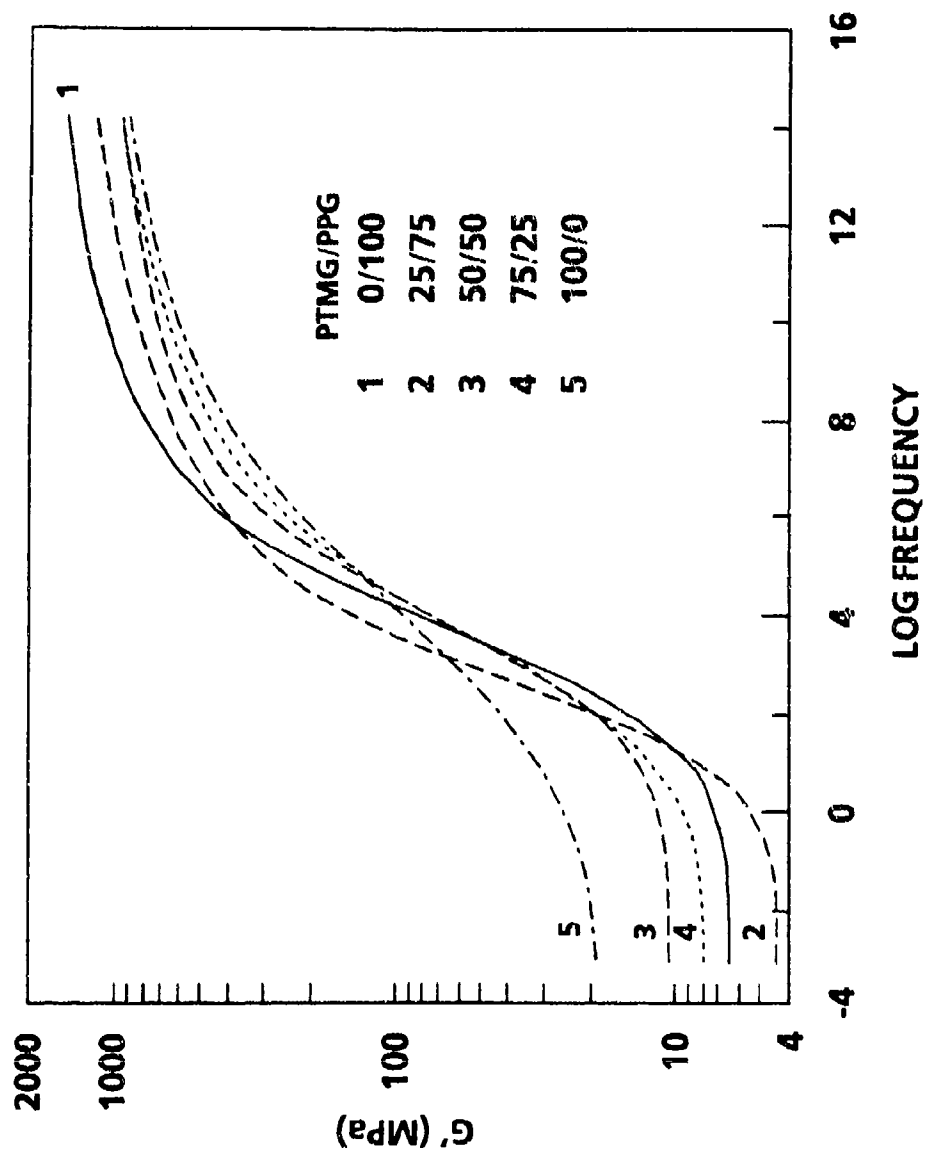


FIGURE 7. SHEAR MODULUS MASTER CURVES FOR POLYURETHANES SYNTHESIZED WITH PTMG/PPG 0/100, 25/75, 50/50, 75/25, AND 100/0.



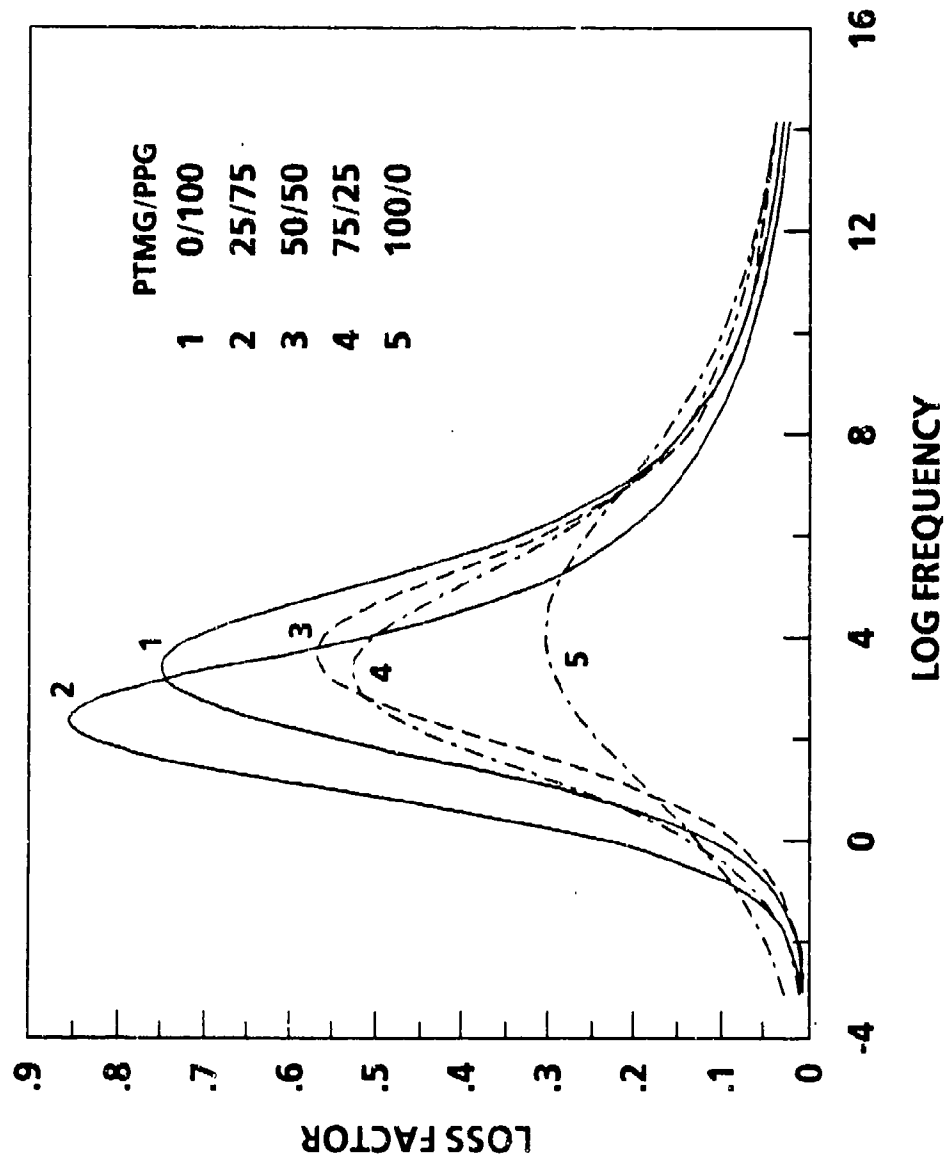


FIGURE 8. LOSS FACTOR MASTER CURVES FOR POLYURETHANES SYNTHESIZED WITH PTMG/PPG 0/100, 25/75, 50/50, 75/25, AND 100/0.

# INVESTIGATION OF DAMPING PROPERTIES FOR THE FIBER ENHANCED VISCOELASTIC DAMPING POLYMERS

Thomas E. Alberts and Houchun Xia

*Department of Mechanical Engineering and Mechanics*

*Old Dominion University\**

## ABSTRACT

A new composite damping material is proposed, which consists of a viscoelastic matrix and fiber inclusions. This fiber enhanced viscoelastic damping polymer is intended to be applied to flexible structures as surface treatment for passive vibration control. A micromechanical model for this composite material is established, and closed form expressions for its effective complex moduli are derived. Based on the model, an optimal relation between the design parameters, such as length, diameter, spacing and Young's modulus of fibers and shear modulus of viscoelastic matrix, is obtained for achieving a maximum damping capability. The theoretical development is validated by a NASTRAN finite element analysis. Upon comparison of the enhanced viscoelastic damping polymer with conventional metallicly constrained viscoelastic layer treatment, it is found that the enhanced polymer provides a significant improvement in damping performance.

---

\* Norfolk, Virginia 23529-0247. Telephone: (804) 683-3720; Fax: (804) 683-5344.

## INTRODUCTION

As science and technology be rapidly moving ahead, equipment and structures with lightweight and high performance are in great demand. The inherent flexibility of such structures has led to the need for serious consideration of vibrational and acoustic noise control problems. Among many possible solutions to these problems, viscoelastic passive damping technology has proven to be one of the most effective methods in many circumstances. Based on energy dissipation mechanism, the viscoelastic damping scheme offers many desirable characteristics, such as being simple, reliable, inexpensive, unobtrusive and lightweight. Numerous useful design techniques and successful applications have been reported since the early 1950's [1-2]. Several of the key developments are briefly reviewed here.

In 1952, Oberst proposed to apply a thin layer of viscoelastic material to the surface of flexible structures for passive vibration control [3]. Unfortunately, this free layer treatment works on extensional deformation mechanism and thus yields a very small amount of damping. Kerwin [4], in 1959, introduced the constrained viscoelastic damping treatment, in which the viscoelastic layer is covered in turn by a high tensile stiffness metallic constraining layer. The constraining layer induces shear strains in the viscoelastic layer, and thus greater damping are produced. After this full coverage constrained single layer treatment was introduced, many efforts have been made to modify it. Ungar and Ross [5 (1959)] suggested a multiple constrained layer treatment with a intention to increase the damping. Parfitt [6 (1962)] reported that by choosing a proper section length for the constraining layer, the damping can be significantly increased. Indeed, Plunkett and Lee [7 (1970)] later derived a method to calculate the optimal section length of the constraining layer that provides maximum damping for a prescribed frequency.

Examination of the previous work suggests that an effective viscoelastic damping treatment should have the following features:

- 1) Maximum loss modulus for viscoelastic damping materials;
- 2) High extensional stiffness for constraining layers;
- 3) Multiple layer treatment with large number of layers;
- 4) Optimal section length for constraining layers.

Due to the high elastic modulus, usually twice and six times as much as that of steel and aluminum, respectively, high elastic modulus fibrous materials, for example Kevlar or graphite fiber, is a desirable candidate for the material used for constraint to the viscoelastic materials. By embedding fiber into viscoelastic polymers to make a single composite damping product, all the features mentioned above can be readily achieved. The optimal section length of the fibers can be controlled in fabricating processes, and the effective number of damping layers can be increased to a great extent without difficulty. Furthermore, the proposed fiber enhanced viscoelastic damping polymer can be conveniently installed onto structural surfaces as a free layer treatment, and the light weight of fibers will benefit the applications where the weight has to be considered.

In this paper, a micromechanical model for the fiber enhanced viscoelastic damping

polymer is established, and closed form expressions for the effective complex moduli are derived. Based on this model, the enhanced damping polymer is optimized for the maximum damping capability, which depends on an optimal relation between the design parameters, such as length, diameter, spacing and Young's modulus of the fibers and the shear modulus of the viscoelastic matrix. The theoretical development is validated by a NASTRAN finite element analysis. Using a flexible cantilever beam as an example, the effectiveness of the fiber enhanced viscoelastic damping polymer on passive vibration control is evaluated by comparison with the optimally sectioned metallic constrained viscoelastic layer treatment.

## EFFECTIVE COMPLEX MODULI

### PACKING GEOMETRY AND REPRESENTATIVE VOLUME ELEMENT

Based on the investigation of damping mechanism in constrained viscoelastic layer treatments, it is believed that the packing geometry as shown in Figure 1 makes the most effective use of the materials. In this figure, the rods with square cross section and finite length represent fibers which are embedded in a viscoelastic matrix. The diameter, length and spacing of fibers are denoted as  $d_f$ ,  $L_f$  and  $t_v$ , respectively. The fibers are designed to be staggered relative to each other so that one fiber end is at the middle of its neighboring fibers. The spacing between neighboring fibers is assumed to be the same and the gaps between fiber ends are neglected. Since the top view of the geometry is the same as the front view, only the latter, along with the side view, is illustrated in the figure.

Figure 1 also shows a selected representative volume element whose geometrical characteristics and stress-strain relations are the same for any of such elements, regardless of its position in the composite material. The average stress and strain of the representative

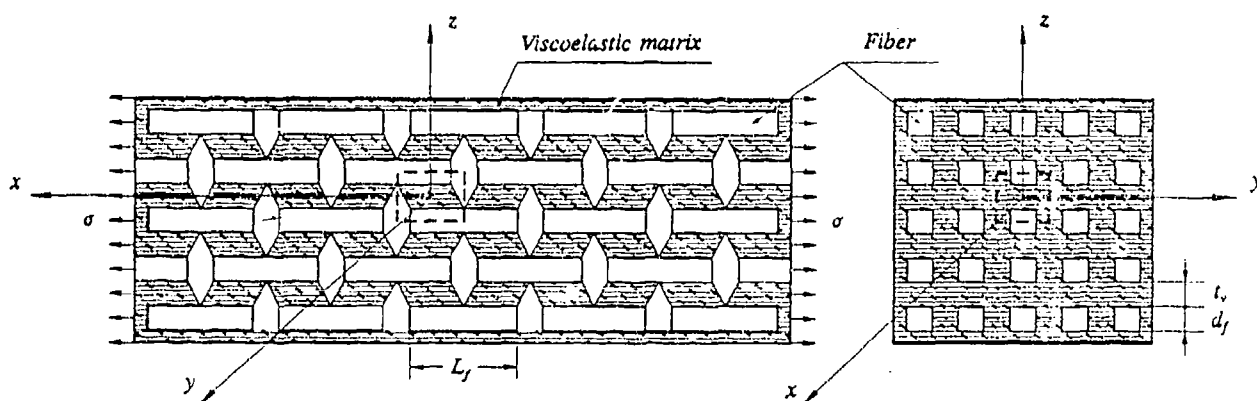


Figure 1 Schematic of the fiber enhanced viscoelastic polymer under stretching

volume element, therefore, are the same for any such elements and also the same as that of the entire composite material under a uniform loading. It should be pointed out that the configuration described here is only intended as the statistical ideal. It is not practical to manufacture a composite with such exact dimensions. It is believed however that the deviation of the configuration cannot change the overall properties of the composite material significantly when compared to other uncertainties, such as the material properties data available for the viscoelastic matrix and the adhesion between fibers and matrix. The huge number of the representative volume elements and the statistical characteristics of the composite should also be taken into account. It is believed that the square cross section of fibers in the model, used for convenience, instead of the more realistic round section, will not make a significant influence on the analytical results since the fiber diameter is so small.

## **DISPLACEMENT FIELD UNDER AXIAL LOADING**

After the fiber enhanced viscoelastic damping polymer is applied to the surface of a flexible structure, it will be subjected to a periodically axial loading when the base structure vibrates, as shown in Figure 1. In the development of the displacement field within the composite under this axial loading, the following assumptions are used:

1) Due to the much higher stiffness of the fibers, usually orders of magnitude higher than that of the viscoelastic matrix, it is assumed that the fiber sustains extensional stress only and the viscoelastic matrix transmits shear stress only.

2) Uniform normal stress field and uniform shear stress field are assumed through the cross sections of the fibers and the viscoelastic matrix, respectively, due to their very small dimensions.

3) Linear material properties are assumed for both fibers and viscoelastic matrix.

4) Poisson's ratio effects are negligible.

5) Fibers are elastic and dissipate no energy.

The free body diagram of the representative volume element is illustrated in Figure 2 (a). The front and back sides of the fibers are subjected to shear stresses due to the existence of the viscoelastic matrix. This part of the matrix, however, is not displayed in the figure since its deformation and effects are the same as that of the matrix shown. Due to the symmetric configuration of the composite, the solution of the displacement field can be reduced to a two dimensional problem.

The equilibrium condition of a fiber element with an infinitesimal length is shown in Figure 2 (b), from which one can get the following differential equation:

$$\frac{d_f}{2} \frac{\partial \sigma}{\partial x} = 2 \tau \quad (1)$$

Substituting the linear stress-strain relations of fibers and matrix into (1) gives

$$\frac{d_f E_f}{4} \frac{\partial^2 u}{\partial x^2} = G_v \gamma \quad (2)$$

where  $E_f$  is the tensile modulus of the fiber,  $G_v$  the shear modulus of the viscoelastic matrix,  $\gamma$  the shear strain in the matrix, and  $u$  the displacement in  $x$  direction.

From Assumption 2,  $\tau$  is invariant in  $z$  direction and so is  $\gamma$ . Therefore,  $u$  should be linear in  $z$  and can be written as

$$u(x, z) = z g_1(x) + g_2(x) \quad (3)$$

For the configuration and loading condition considered here, the axial displacement,  $u(x, z)$ , should be antisymmetric in  $x$  and  $z$  as shown in Figure 2 (a). This implies that  $g_1(x)$  must be symmetric and  $g_2(x)$  antisymmetric.

From the definition of shear strain and Equation (3) one can get

$$\gamma = \frac{\partial u}{\partial z} = g_1(x) \quad (4)$$

Substituting (3) and (4) into (2) yields

$$L_1 z \frac{d^2 g_1(x)}{dx^2} - g_1(x) = -L_1 \frac{d^2 g_2(x)}{dx^2} \quad (5)$$

where  $L_1 = E_f d_f / 4 G_v$ .

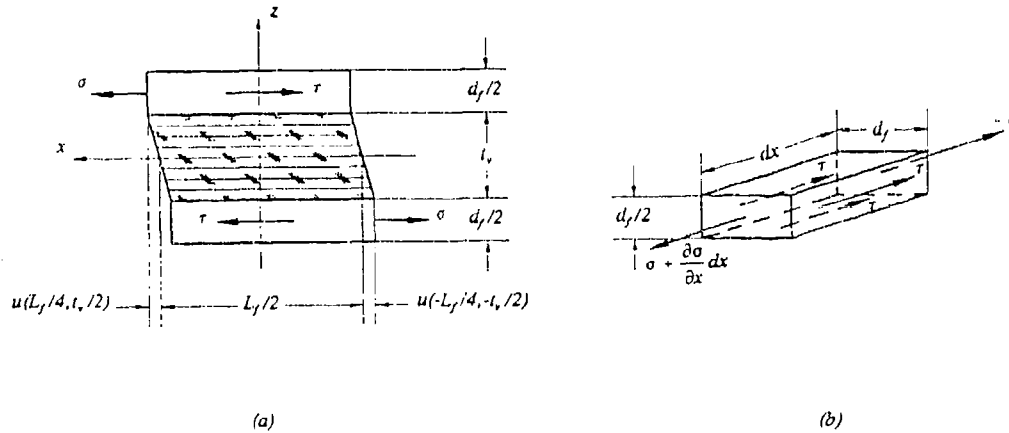


Figure 2 Free body diagram of the representative volume element

To ensure the symmetric and antisymmetric properties for  $g_1(x)$  and  $g_2(x)$ , respectively, both sides of (5) must vanish, i.e.,

$$L_1 z \frac{d^2 g_1(x)}{dx^2} - g_1(x) = 0 \quad (6)$$

and

$$\frac{d^2 g_2(x)}{dx^2} = 0 \quad (7)$$

Solving these two ordinary differential equations and substituting the results into (3) yields

$$u(x, z) = Bz \cosh \frac{x}{\sqrt{L_1 z}} + Cx \quad (8)$$

where  $B$  and  $C$  are the constants determined by the boundary conditions:

$$E_f \frac{\partial u}{\partial x} \bigg|_{\left(\frac{L_f}{4}, \frac{t_v}{2}\right)} = \sigma, \quad E_f \frac{\partial u}{\partial x} \bigg|_{\left(-\frac{L_f}{4}, \frac{t_v}{2}\right)} = 0 \quad (9)$$

From (8) and (9) one can get the final expression for the displacement field in the representative volume element as

$$u(x, z) = \frac{\sigma z \sqrt{d_f}}{2 \sqrt{2 E_f G_v t_v} \sinh \beta} \cosh \frac{x}{\sqrt{L_1 z}} + \frac{\sigma}{2 E_f} x \quad (10)$$

where  $\beta$  is defined as

$$\beta = \frac{\sqrt{2} L_f}{4 \sqrt{L_1 t_v}} = \frac{L_f \sqrt{G_v}}{\sqrt{2 t_v d_f E_f}} \quad (11)$$

## **EFFECTIVE COMPLEX MODULI**

It is well known that the complex modulus approach is an efficient method to describe the dynamic behavior of homogeneous viscoelastic materials [8]. It has been shown that it is also possible to define effective complex moduli for viscoelastic composites [9-11]. These effective complex moduli are related to the effective elastic moduli of composites by an

elastic-viscoelastic correspondence principle [12]. According to this principle, the effective complex moduli of a composite can be obtained as follows:

- 1) Evaluate effective elastic moduli for the composite;
- 2) Replace all the phase elastic moduli by the corresponding phase complex moduli in the expressions of the effective elastic moduli to form the effective complex moduli for the composite;
- 3) Separate the real and imaginary parts of the effective complex moduli to get the storage modulus, loss modulus and loss factor of the composite.

The effective elastic moduli of a statistically homogeneous composite are defined by the averages of stress and strain over a representative volume element as

$$\langle \sigma_{ij} \rangle = C_{ijkl} \langle \epsilon_{kl} \rangle \quad (12)$$

where  $C_{ijkl}$  are the effective elastic moduli of the composite,  $\langle \sigma_{ij} \rangle$  and  $\langle \epsilon_{kl} \rangle$  the volume averages of stress and strain over the representative volume element which are given by the following integration, respectively,

$$\langle \sigma_{ij} \rangle = \frac{1}{V} \int_V \sigma_{ij}(x_l) dv, \quad \langle \epsilon_{ij} \rangle = \frac{1}{V} \int_V \epsilon_{ij}(x_l) dv \quad (13)$$

The  $\sigma_{ij}(x_l)$  and  $\epsilon_{ij}(x_l)$  in the above equations are infinitesimal tensor and characterize the stress and strain fields in the representative volume element, respectively.

The average normal stress,  $\sigma_a$ , can be obtained as

$$\sigma_a = \frac{\sigma \frac{d_f^2}{2}}{(t_v + d_f)^2} = \frac{\sigma}{2} \frac{d_f^2}{(t_v + d_f)^2} \quad (14)$$

where the subscript,  $a$ , represents averages.

Because of symmetry, the average strain can be obtained by taking the mean displacement over half of the length of the representative volume element as

$$\epsilon_a = \frac{u(\frac{L_f}{4}, \frac{t_v}{2})}{\frac{L_f}{4}} = \frac{\sigma}{2E_f} (1 + \frac{1}{\beta} \coth \beta) \quad (15)$$

Therefore, the effective elastic modulus in the  $x$  direction,  $E_c$ , is given as



$$\begin{aligned}
E_c &= \frac{\sigma_a}{\epsilon_a} = E_f \frac{d_f^2}{(d_f + t_v)^2} \left(1 + \frac{1}{\beta} \coth \beta\right)^{-1} \\
&= E_f v_f \left(1 + \frac{1}{\beta} \coth \beta\right)^{-1}
\end{aligned} \tag{16}$$

where the subscript, c, represents composites, and the quantity,  $v_f = d_f^2/(d_f + t_v)^2$ , is the fiber volume fraction of the composite.

According to the elastic-viscoelastic correspondence principle and Assumption 5, the effective complex modulus can be derived from (16) as

$$E_c^* = E_f v_f \left(1 + \frac{1}{\beta^*} \coth \beta^*\right)^{-1} \tag{17}$$

where the superscript, \*, indicates complex variables, and the dimensionless quantity,  $\beta^*$ , is defined as

$$\beta^* = \frac{L_f \sqrt{G_v' (1 + i \eta_v)}}{\sqrt{2 t_v d_f E_f}} = \alpha (1 + i \eta_v)^{1/2} \tag{18}$$

In (18),  $G_v'$  is the storage shear modulus of the viscoelastic matrix,  $\eta_v$  the material loss factor of the matrix, and  $\alpha$  a dimensionless quantity which will be called the characteristic value of the composite and defined as

$$\alpha = \frac{L_f \sqrt{G_v'}}{\sqrt{2 t_v d_f E_f}} \tag{19}$$

In order to obtain the storage and loss moduli of the composite material, the complex modulus,  $E_c^*$ , has to be separated into real and imaginary parts. To do so, one has to separate the complex variable,  $\beta^*$ , first. Using Taylor series expansion,  $\beta^*$  can be approximated by the first two terms as

$$\beta^* = \alpha + \frac{i}{2} \alpha \eta_v \tag{20}$$

Based on the fundamental relations between trigonometric and hyperbolic functions,  $\coth \beta^*$  can then be written as:

$$\coth \beta^* = \frac{1 - i \coth \alpha \cot \frac{\alpha \eta_v}{2}}{\coth \alpha - i \cot \frac{\alpha \eta_v}{2}} \quad (21)$$

Substituting (20) and (21) into (17) and separating real and imaginary parts gives

$$E_c^* = E_f \nu_f \left( \frac{N_1 + i N_2}{D} \right) \quad (22)$$

where  $N_1$ ,  $N_2$  and  $D$  are real functions and defined as

$$N_1 = (\coth \alpha)^2 \left( 1 + \frac{\eta_v^2}{4} - \frac{\eta_v}{2\alpha} \cot \frac{\alpha \eta_v}{2} \right) + \left( \cot \frac{\alpha \eta_v}{2} \right)^2 \left( 1 + \frac{\eta_v^2}{4} + \frac{1}{\alpha} \coth \alpha \right) + \frac{\eta_v}{2} \cot \frac{\alpha \eta_v}{2} + \coth \alpha \quad (23)$$

$$N_2 = \cot \frac{\alpha \eta_v}{2} \left[ \frac{1}{\alpha} (\coth \alpha)^2 - 1 \right] + \frac{\eta_v}{2} \coth \alpha \left[ 1 + \frac{1}{\alpha} \left( \cot \frac{\alpha \eta_v}{2} \right)^2 \right] \quad (24)$$

$$D = (\coth \alpha)^2 \left[ 1 + \frac{\eta_v^2}{4} - \frac{\eta_v}{\alpha} \cot \frac{\alpha \eta_v}{2} + \frac{1}{\alpha^2} \left( \cot \frac{\alpha \eta_v}{2} \right)^2 \right] + \left[ \cot \frac{\alpha \eta_v}{2} \right]^2 \left[ 1 + \frac{\eta_v^2}{4} + \frac{2}{\alpha} \coth \alpha \right] + 2 \coth \alpha + \eta_v \cot \frac{\alpha \eta_v}{2} + 1 \quad (25)$$

The final expressions for the effective properties of the fiber enhanced viscoelastic damping polymers under uniaxial loading are given as:

1) Storage modulus:

$$E_c' = E_f \nu_f \frac{N_1}{D} \quad (26)$$

2) Loss modulus:

$$E_c'' = E_f \nu_f \frac{N_2}{D} \quad (27)$$

3) Loss factor:

$$\eta_E = \frac{N_2}{N_1} \quad (28)$$

It can be seen that all these effective properties are the functions of packing geometry of the composite and the material properties of the constituents. These properties will be employed to evaluate using numerical methods.

### OPTIMIZATION OF DAMPING PROPERTIES

The closed form expressions of the effective material properties developed above allow us to optimize the damping properties for the fiber enhanced viscoelastic polymers. To do so, the criterion for the optimization has to be established.

Intuitively, a large value of loss factor is a desired property for damping materials. However, practically this is not the only consideration. Consider the damping mechanism in a viscoelastic material. In order to dissipate energy, a damping material must store some energy first. The more energy it can store, the more energy it will dissipate. The ability to store energy is measured by the storage modulus of materials. It is clear that the best quantity reflecting the damping capability of a viscoelastic material is the loss modulus of the material, i.e., the product of the loss factor and the storage modulus. This observation has been verified by many analytical and experimental results, e.g., [13]. It may not always be desirable, though, to use a very high storage modulus to achieve a high loss modulus. The reason is that a high storage modulus of a damping material could significantly change the stiffness of the base structure on which it will be bonded. Therefore, a good design involves proper balance between loss factor and storage modulus.

The proposed strategy for the optimization of the fiber enhanced viscoelastic damping polymer is given below.

- 1) Examine the variation of the composite loss factor,  $\eta_E$ , with the characteristic value,  $\alpha$ , in a rather broad range using (28);
- 2) Based on the results of step one, select a narrowed range of  $\alpha$  to maximize the loss modulus,  $E_c''$ , using (27);
- 3) After all the parameters are determined, evaluate the storage modulus,  $E_c'$ , and loss factor,  $\eta_E$ , using (26) and (28), respectively.

The computed loss factors of the composite damping polymer,  $\eta_E$ , are illustrated in Figure 3, in which the x axis represents the characteristic value,  $\alpha$ , varying from 0.1 to 10 with the increment of 0.1. Three values of the matrix loss factor,  $\eta_m$ , have been considered. It can be seen from Figure 3 that the large value of  $\eta_E$  occurs in the range of  $\alpha$  less than unity for all three cases.

Next, the effect of the characteristic value,  $\alpha$ , on the loss modulus of the composite,  $E_c''$ , is examined. The results are plotted in Figure 4. Again, the x axis represents  $\alpha$ , but the searching range for the optimization is narrowed to 0.01 - 1.5. The increment of  $\alpha$  is

0.01 so that 150 numerical points have to be evaluated for each curve. The ratio of  $E_c''$  and  $E_f v_f$  is given by y axis. The variation of this ratio is essentially the same as that of  $E_c''$  providing that  $E_f$  and  $v_f$  are prescribed. The maximum value of  $E_c''$  occurs at the value of  $\alpha$  around 0.75, which varies slightly with different matrix loss factors,  $\eta_v$ . It can be concluded, therefore, that for maximum damping capability the characteristic value of the composite,  $\alpha$ , should be taken around 0.75. The exact optimum value of  $\alpha$  for different loss factors  $\eta_v$  can be determined from a chart like Figure 4. To satisfy this optimum condition, one can vary any quantity in (19) with other quantities fixed. For example, if  $E_f$ ,  $G_v'$ ,  $t_v$ , and  $d_f$  are prescribed by a specific design, satisfaction of this condition will yield an optimal section length,  $L_o$ , for the fibers. Furthermore, Equation (27) indicates that a large value for the fiber Young's modulus,  $E_f$ , is a desired property for the fiber enhanced viscoelastic damping polymer.

### COMPUTATIONAL VALIDATION USING FINITE ELEMENT ANALYSIS

Finite element analysis has proven to be a dependable technique for evaluating the damping properties of viscoelastically damped structures [14]. In this paper, the computer code NASTRAN is employed for this purpose. In addition, the finite element results are also used to validate the theoretical development described above. A schematic of the finite element model for the representative volume element is illustrated in Figure 5. The model has 27 quadrilateral elements (QUAD4) and 40 nodes. All of the nodes are allowed to move in  $x$  direction and rotate about  $z$  direction only, to prevent the stiffness matrix from singularity.

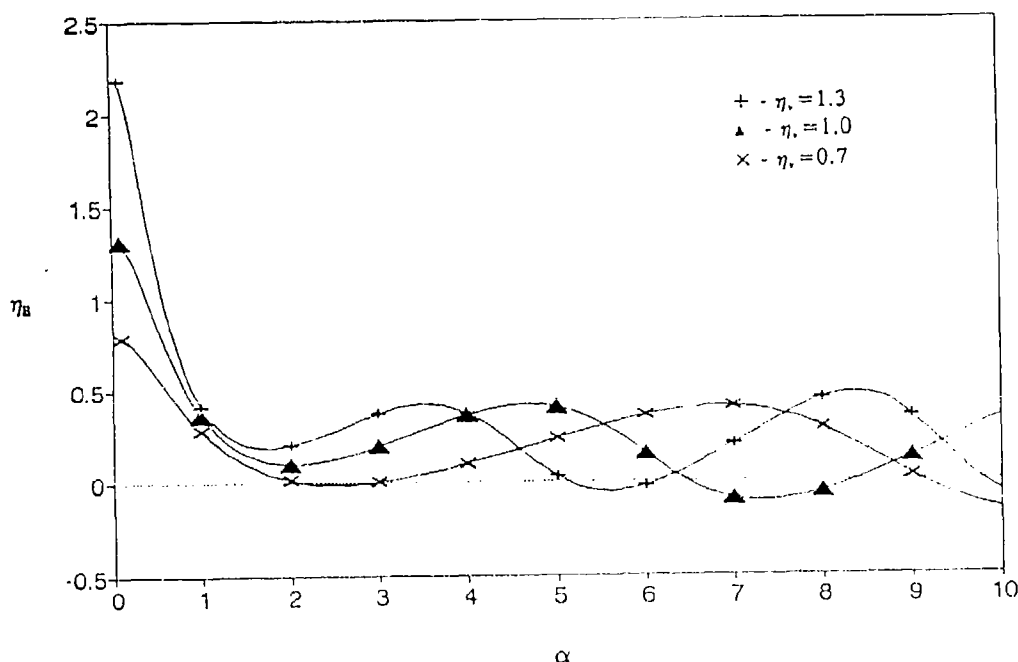


Figure 3 Effect of characteristic value,  $\alpha$ , on loss factor

Data used for this analysis are listed in Tables 1. Graphite fiber UHM from Hercules Advanced Materials & Systems Company is employed because of its high stiffness-to-weight ratio. The material designated for the viscoelastic matrix is 3M Scotchdamp ISD 110 polymer, whose shear modulus is arbitrarily chosen as 130 psi in the commonly used range. The finite element computation is conducted on a CDC CYBER 930 computer, and the displacement of each node in the model can be read out from NASTRAN output files. For example, the  $x$  direction displacement of point  $a$  (see Figure 1) is  $6.155 \times 10^{-4}$  inches. The corresponding analytical result from Equation (10) is  $6.566 \times 10^{-4}$  inches, which shows a difference of 6.26%. It is believed that the theoretical model gives results closer to the exact solution while the slightly lower value obtained from the finite element analysis is due to the extra constraints to the nodal motion since only two degrees of freedom are retained for each node.

Next, the finite element model is employed to calculate the material loss factor for the fiber enhanced viscoelastic damping polymers. There are several approaches to calculate loss

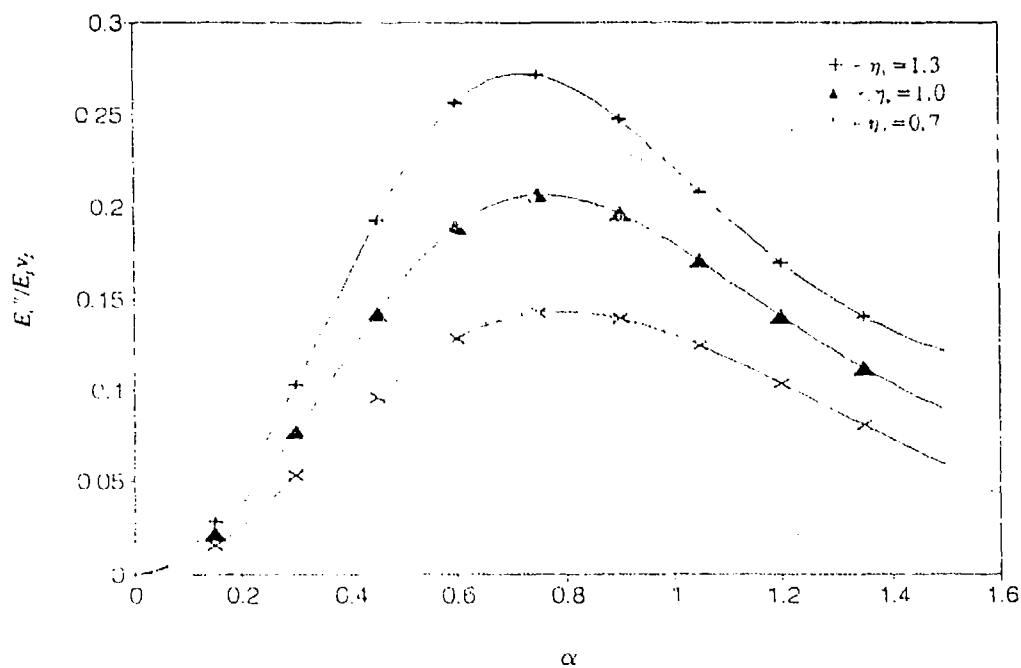


Figure 4 Effect of characteristic value,  $\alpha$ , on loss modulus

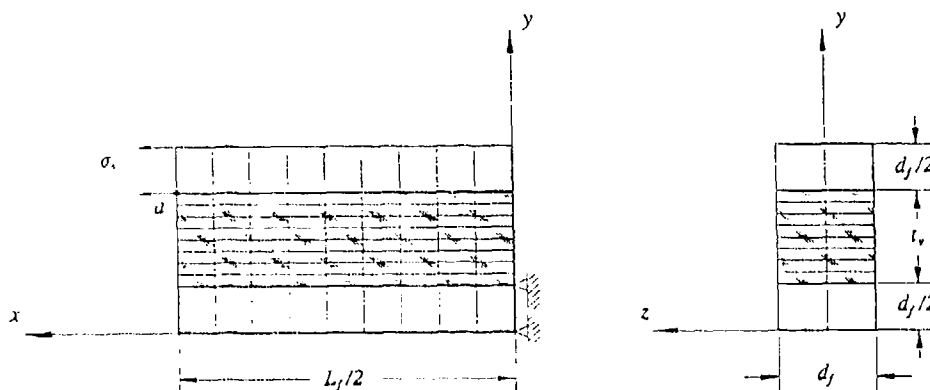


Figure 5 Schematic of finite element model for representative volume element

factors for viscoelastically damped structures using finite element methods. The most commonly used one is the modal strain energy method which is based on the following relation [15]:

$$\eta_s^r = \eta_v^r \frac{U_v^r}{U_s^r} \quad (29)$$

where  $\eta_s^r$  —  $r$ 'th modal loss factor of damped structures,  
 $U_s^r$  —  $r$ 'th modal strain energy of damped structures,  
 $\eta_v^r$  —  $r$ 'th modal loss factor of viscoelastic damping materials,  
 $U_v^r$  —  $r$ 'th modal strain energy of viscoelastic damping materials.

According to (29), the  $r$ 'th modal system loss factor of a damped structure can be obtained by computing the modal strain energy ratio of the damped structure and then multiplying it by the  $r$ 'th modal loss factor of the viscoelastic material used.

Many of commercial codes available feature a function for computing the modal strain energy. For example, NASTRAN has a function called Element Strain Energy (ESE). The calculation is based on the following equation

$$ESE = [\phi]_r^T [K] [\phi]_r \quad (30)$$

where  $[\phi]_r$  and  $[K]$  are the  $r$ 'th eigenvector and stiffness matrix of an element, respectively.

**Table 1 Model data for representative volume element**

Quantity	Symbol	Unit	Value
Distance between fibers	$l_v$	in	0.00021
Diameter of fibers	$d_f$	in	0.0005
Half length of fibers	$L_f/2$	in	0.05
Normal stress	$\sigma$	lb/in <sup>2</sup>	$1.44 \times 10^5$
Fiber volume fraction	$v_f$	-	0.5

The ESE function computes the modal strain energy of each element. By summing the energy of all the viscoelastic elements and the energy of all elements of the damped structure, separately, the energy ratio required for (29) can be obtained.

The computed strain energy ratio for the representative volume element model is equal to 0.945, and the resultant system loss factor,  $\eta_s$ , which is essentially the same as the effective loss factor of the composite polymer,  $\eta_E$ , are listed in Table 2, along with the theoretical results obtained from (28) and the relative error between the two predictions. Some observations can be reached as below:

1) The theoretical analysis presents a very good prediction for the effective loss factor of the fiber enhanced damping polymer when the loss factor of the viscoelastic matrix,  $\eta_v$ , is not very high. An error of 5.54% between theoretical and finite element results has been observed when  $\eta_v$  is equal to 0.7, which represents a good value of the loss factor of viscoelastic materials that can be achieved in practice.

2) The error of theoretical results increases as  $\eta_v$  goes up. The reason is that the Taylor series expansion is used to approximate the complex variable,  $\beta^*$ , as shown in (20).

**Table 2 Comparisons of the effective loss factor,  $\eta_E$** 

Loss factor of matrix, $\eta_v$	Theoretical results	Finite element results	Relative error (%)
0.7	0.704	0.665	5.54
1.0	1.117	0.945	15.40
1.3	1.695	1.229	27.49

When  $\eta_v$  becomes large, the omission of higher order terms of  $\eta_v$  will significantly reduce the value of  $\beta^*$  and thus  $\alpha$ . From Figure 3 it can be seen that lower values of  $\alpha$  correspond to a larger value for  $\eta_E$ . The error rises to 27.49% when  $\eta_v = 1.3$ . This may still be an acceptable result compared to other uncertainties in damping predictions.

3) Examination of Columns one and three in Table 2 indicates that the fiber enhanced viscoelastic polymer can produce very large amount of damping. The loss factor of the enhanced polymer is nearly equal to that of the pure viscoelastic materials.

4) The relative error listed in Table 2 can be used to correct the theoretical results. For example, if  $\eta_v = 0.7$ , the operation of  $0.704 \times (1-0.0554)$  will give the corrected results of 0.665.

### EVALUATION OF DAMPING EFFECTIVENESS

To evaluate the damping effectiveness of the fiber enhanced viscoelastic polymer on engineering structures, in this section, the enhanced damping polymer will be hypothetically bonded onto the surface of a flexible base structure. The system loss factor of the damped structure will be calculated and the results will be compared with that from a conventional metallic constrained viscoelastic layer damping treatment. The base structure to be used is an aluminum cantilever beam which is the arm of a single link flexible robot experiment.

As mentioned above, the fiber enhanced viscoelastic damping polymer can be considered as a statistically homogeneous material. Since the effective properties of this composite material have been worked out, it is not difficult to calculate the system loss factor of a sandwich beam consisting of an elastic beam core bonded on both sides with the same free layer treatment of the fiber enhanced viscoelastic damping polymers. In the following derivation, it is assumed that the dissipated energy in the damped beam is equal to the energy dissipated by the damping polymers. Therefore, the energy dissipated per cycle, when the beam vibrates periodically, will be

$$D = 2\pi\eta_E U_c \quad (31)$$

and the system loss factor of the damped beam

$$\eta_s = \frac{D}{2\pi U} = \frac{\eta_E U_c}{U_b + U_c} \quad (32)$$

where  $U$  is the total strain energy stored in the damped structure, and hereafter, the subscripts,  $b$  and  $c$ , represent the beam and the composite damping polymers, respectively.

The strain energy of an Euler beam can be expressed as

$$U = \int_0^L \frac{1}{2} EI \left( \frac{d^2 w}{dx^2} \right)^2 dx \quad (33)$$



where  $E$  is the Young's modulus,  $I$  the area moment of inertia,  $w$  the lateral deflection, and  $L$  the length of the beam.

Applying (33) to the undamped beam core and the composite polymer beam shell, respectively, to obtain  $U_b$  and  $U_c$  and then substituting the results into (32) yield

$$\begin{aligned}\eta_s &= \eta_E \frac{2E_c'(3t_b^2 t_c + 6t_b t_c^2 + 4t_c^3)}{2E_c'(3t_b^2 t_c + 6t_b t_c^2 + 4t_c^3) + E_b t_b^3} \\ &= \eta_E \frac{2eh(3+6h+4h^2)}{1+2eh(3+6h+4h^2)}\end{aligned}\quad (34)$$

where  $e = E_c'/E_b$  is the Young's modulus ratio and  $h = t_c/t_b$  is the thickness ratio.

Equation (34) provides the exact solution of system loss factor,  $\eta_s$ , for the sandwich beam. It can be seen that if  $eh \gg 1$ , the system loss factor,  $\eta_s$ , will tend to the material loss factor of the composite polymers,  $\eta_E$ .

Equation (34), along with (28), is used to evaluate the effect of fiber volume fraction,  $v_f$ , and thickness ratio,  $h$ , on the system loss factor,  $\eta_s$ . The results are shown in Figure 6. It has been shown that although  $\eta_s$  increases as  $v_f$  and  $h$  increase, there is no significant change in  $\eta_s$  when  $v_f$  and  $h$  are greater than 0.6 and 0.4, respectively. Moreover, there

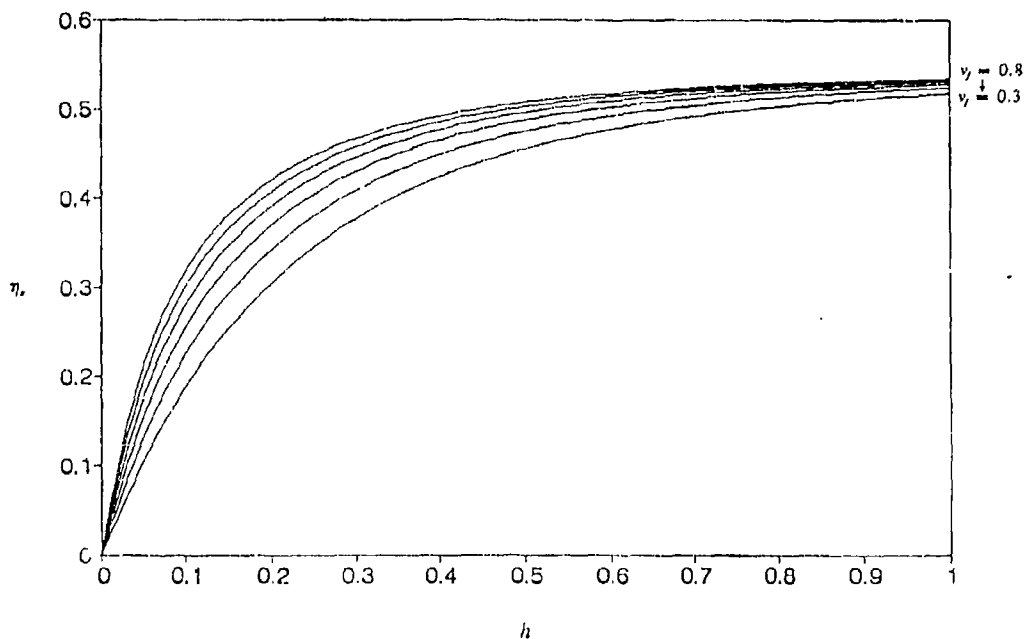


Figure 6 Effect of fiber volume fraction and thickness ratio

exists a trade-off between the fiber volume fraction and thickness ratio. For example, if  $\eta_f = 0.4$  is desired, one can choose either  $\lambda = 0.17$  and  $n = 0.3$  or  $\lambda = 0.3$  and  $n = 0.34$ . To do so, a horizontal line through  $\eta_f = 0.4$  has to be drawn. Then, the intersection of this line and the curve representing  $\lambda$  or  $n$  versus  $\eta_f$  can be found. The corresponding values can be obtained. It is clear that the data like that given in Table 3 can be used for passive damping design for the treatment of a fiber reinforced constrained beam.

The geometric data and the material properties of the beam are given in Table 3. The beam, which will be used to compare the fiber reinforced beam with the conventional beam, is the conventional metallic constrained viscoelastic layer treatment. The viscoelastic layer is properly chosen to give the maximum damping. The data are employed for the first two cases of the present study. The material properties of the viscoelastic layer are assumed to be the same as those of the fiber reinforced beam. The temperature of 75 F is assumed. Two options have been considered. In the first case, the frequency of controlling the fundamental mode of the cantilever beam is chosen to be equal to 2.658 Hz. In the second case, the natural frequency is taken as the upper modes with frequency of 44.603 Hz. Once the optimal fiber length is defined by the target frequency, using this relation,  $\lambda = 0.75$ , it will be a fixed design value. Hence, the effect of changing the values for other modes have to be evaluated from also and the results are given in the last two columns of Table 4.

The resultant system loss factors for the conventional metallic constrained viscoelastic layer treatments with optimal length sectioned constraining layer are obtained from previous

**Table 3 Geometric data and natural frequencies of undamped beam**

Quantity	Symbol	Unit	Value		
Length	$L_b$	in	47		
Width	$b_b$	in	0.75		
Thickness	$t_b$	in	0.1875		
Young's modulus	$E_b$	lb/in <sup>2</sup>	$1.0 \times 10^7$		
Poisson's ratio	$\nu_b$	-	0.33		
Mass density	$\rho_b$	lb-sec <sup>2</sup> /in <sup>4</sup>	$2.59 \times 10^{-4}$		
Natural frequencies	$f_b$	Hz	M O D E	1	2.658
				2	16.182
				3	44.603
				4	85.259
				5	127.306

**Table 4 Material data used for 3M ISD-110 polymer and the effective values of  $\alpha$** 

Mode	Shear modulus $G_v'$ (lb/in <sup>2</sup> )	Loss factor $\eta_v$	Effective value of $\alpha$	
			Case I	Case II
1	41	1.2	0.750	0.336
2	103	1.6	1.238	0.532
3	220	1.45	1.810	0.750
4	370	1.18	2.347	1.008
5	500	1.03	2.728	1.172

**Table 5 Comparisons of system loss factor**

Mode	Case I			Case II		
	$L_c=3.75"$	$L_o=0.304"$	PID (%)	$L_c=1.72"$	$L_o=0.131"$	PID (%)
1	0.16627	0.2087	25.5	0.08862	0.1471	66.0
2	0.12414	0.0947	-23.7	0.11934	0.2386	99.9
3	0.09116	0.0806	-11.6	0.12494	0.2055	64.5
4	0.07714	0.0795	3.1	0.10758	0.1540	43.1
5	0.06673	0.0747	11.9	0.10432	0.1177	12.8
Notes: 1) $L_c$ - Optimal section length of metallic constraining layers; 2) $L_o$ - Optimal section length of fibers; 3) PID - Percentage increase of damping; 4) " - Inches.						

experimental work [15] and reprinted here in Table 5. For the fiber enhanced viscoelastic damping treatment, Equation (34) is employed to evaluate the system loss factor of the damped cantilever beam. The results, after correction using the procedure discussed above, are given in Table 5 along with the damping percentage increases provided by the fiber enhanced viscoelastic treatment. Examinations of Tables 4 and 5 allow the following observations:

1) The fiber enhanced viscoelastic polymer provides more damping at the target modes than the conventional metallic constrained treatment when both treatments have the same thickness. The percentage increases of damping provided by the fiber enhanced treatment are 25.5% and 64.5% over the conventional one for Cases I and II, respectively.

2) The fiber enhanced viscoelastic polymer adds less weight to the damped structure than the metallic constrained treatment does. The weight percentage added by the fiber enhanced treatment is roughly 1/5 of that added by the metallic constrained treatment when they have the same thickness.

3) When the effective characteristic value,  $\alpha$ , is greater than 1.2, the damping performance of the fiber enhanced viscoelastic polymer will deteriorate. This situation occurs for Modes two through four in Case I.

4) The system loss factor of Mode two in Case II, provided by the fiber enhanced polymer, is higher than that of the target mode (Mode three). The reason is that at Mode two the material loss factor of the viscoelastic matrix,  $\eta$ , is equal to 1.6. Under this condition, the value of  $\alpha = 0.532$  (Mode two) will produce a larger loss modulus for the enhanced polymer, i.e.,  $E_c''$ , than the value of  $\alpha = 0.75$  at Mode three (refer to Figure 4).

### CONCLUSIONS

The damping properties of the proposed fiber enhanced viscoelastic damping polymer have been investigated, and an optimal relation between the design parameters, such as length, diameter, spacing and Young's modulus of fibers and shear modulus of viscoelastic matrix, has been established based on a micromechanical model and the derived effective complex moduli of the new damping materials. Good agreement between the theoretical development and a NASTRAN finite element analysis has been obtained. The fiber enhanced viscoelastic damping treatment provides a damping ratio of 0.11 for a damped cantilever beam at the target modes and adds 6.75% weight to it. These results represent an up to 64.5% increase in damping and 80% decrease in weight added when compared to a conventional constrained optimally sectioned viscoelastic damping layer treatment.

### REFERENCES

1. Nakra, B.C., "Vibration Control with Viscoelastic Materials," *Shock and Vibration Digest*, Vol.8, No.6, June, 1975, pp 3-12.
2. Nelson, F.C., "Techniques for The Design of Highly Damped Structures," *Shock and Vibration Digest*, Vol.9, No.7, July, 1977, pp. 3-11.
3. Oberst, H., "Über die Dämpfung der Biegeschwingungen dünner Bleche durch fest haftende Beläge," *Acustica*, Vol. 2, Beiheft 4, 1952, pp 181-194.
4. Kerwin, E.M., Jr., "Damping of Flexural Waves by A Constrained Viscoelastic Layer," *Journal of Acoustical Society of America*, Vol.31, No.7, 1959, pp. 952-962.
5. Ungar, E.E., Ross, D., "Damping of Flexural Vibrations by Alternate Viscoelastic and Elastic Layers," *Proceedings of the Fourth Conference on Solid Mechanics*, University of Texas, Austin, Tex., Sept., 1959.

6. Parfitt, G.G., "The effect of cuts in Damping Tapes," Int. Cong. Acoust., 4th, Copenhagen, Aug., 1962, pp. 21-28.
7. Plunkett, R. and Lee, C. T., "Length Optimization for Constrained Viscoelastic Layer Damping," *Journal of Acoustical Society of America*, Vol.48, No.1, 1970, pp. 150-161.
8. Nashif, A.D., Jones, D.I.G., and Henderson, J.P., *Vibration Damping*, John Wiley & Sons, Inc., 1985.
9. Hashin, Z., "Complex Moduli of Viscoelastic Composites - I. General Theory and Application to Particulate Composites," *Int. J. Solids Structures*, Vol.6, 1970, pp. 539-552.
10. Hashin, Z., "Complex Moduli of Viscoelastic Composites - II. Fiber Reinforced Materials," *Int. J. Solids and Structures*, Vol.6, 1970, pp. 797-807.
11. Christensen, R.M., *Mechanics of Composite Materials*, John Wiley & Sons, New York, 1979.
12. Hashin, Z., "Analysis of Composite Materials - A Survey," *Journal of Applied Mechanics*, Vol.50, 1983, pp. 481-505.
13. Kerwin, Jr., E.M., "Macromechanism of Damping in Composite Structures," in *Internal Friction, Damping and Cyclic Plasticity*, ASTM STP 378, 1965, pp. 125-149.
14. Alberts, T.E., Chen, Y., and Xia, H., "On the Effectiveness of Section Length Optimization for Constrained Viscoelastic Layer Damping Treatments," SPIE Technical Conference, Orlando, FL, Apr., 1990.
15. Johnson, C.D. and Kienholz, D.A., "Finite Element Prediction of Damping in Structures with Constrained Viscoelastic Layers," *AIAA Journal*, Vol.20, No.9, Sept., 1982, pp. 1284-1290.

# ON THE DYNAMIC PROPERTIES OF NATURAL RUBBER AND EPOXIDIZED NATURAL RUBBER

by

Keith N.G. Fuller\*, Hamid Ahmadi\* and Alan Muhr\*

Malaysian Rubber Producers' Research Association

## ABSTRACT

Dynamic property measurements are presented for natural rubber and two polymers derived from natural rubber by a chemical modification process - epoxidation - and possessing higher glass transition temperatures. The tests are carried out using the longitudinal vibration technique and forced non-resonance of a double-shear geometry testpiece. In the case of the former, data on the higher damping elastomers are obtained both at frequencies near resonance and at those off-resonance so that results at regular, narrowly spaced frequencies, can be obtained. Results from the forced non-resonance and longitudinal vibration tests are compared in the region where the test frequencies overlap. The loss factor data agree well, the moduli from the longitudinal vibration technique are up to nearly 20% higher.

The experiments are carried out over a range of test temperatures and the data empirically shifted to obtain master curves showing how the shear modulus and loss factor at room temperature vary over a wide frequency range. The high frequency data for the epoxidized vulcanizates obtained by shifting the forced non-resonance results is compared with direct measurements using the longitudinal vibration technique. The moduli from the latter are substantially higher by an approximately constant amount (about 30%). For the elastomer with a loss factor  $<1$  throughout the test range the agreement between the shifted and directly measured loss factors is within 25%. For the higher damping epoxidized natural rubber the discrepancy is larger, particularly at frequencies over 2000 Hz.

The comparison of the master curves obtained from the two techniques shows that the modulus curves are of similar shape, but that the 30% discrepancy persists over all frequencies. The loss factor results agree less well, particularly at values approaching unity. The higher losses obtained for ENR-50 from the longitudinal vibration tests at room temperature, are reflected in the ENR-25 data transformed to frequencies between  $10^4$  and  $10^5$  Hz.

\* MRPRA, Brickendonbury, Hertford SG13 7NL, UK. Tel: +44 992 584966

## INTRODUCTION

The dynamic properties of elastomers at frequencies above those commonly accessed by servohydraulic testing-machines are becoming more important to designers and engineers. Behaviour in the audio frequency range can be relevant to such applications as vibration isolation and noise reduction. High frequency data at normal ambient temperatures can be obtained by transforming measurements at low frequencies and low temperature using frequency-temperature equivalence<sup>1</sup>. The equivalence principle can be used to obtain master curves of dynamic properties at a particular temperature over a much wider range than it is possible to access directly by a particular technique. The reliability of this approach has been at least partially demonstrated<sup>2</sup> for an unfilled natural rubber (polyisoprene) vulcanizate by comparing room temperature results obtained directly at frequencies up to 1500Hz with transformed data from tests carried out for frequencies between 0.1 and 15Hz at temperatures down to -40°C. Other workers<sup>3</sup>, adopting a different strategy, have also demonstrated the applicability of the master curve approach to polyisoprene rubber. Despite the assurance offered by such studies, it would seem prudent to rely on frequency-temperature equivalence to transform data only through a limited frequency shift. There is thus an interest in extending the direct measurement of dynamic properties at frequencies over 1kHz to other elastomers.

The longitudinal vibration technique is suitable for high frequency tests but is generally used to obtain data only at certain discrete frequencies near the point of resonance<sup>2,4,5</sup>. The paper by Dlubac et al<sup>4</sup> compares the results obtained by this method with a forced oscillation technique using a torsion geometry and a bending cantilever beam apparatus; it concludes that reasonably consistent data is obtained. A comparison<sup>2</sup> between forced non-resonance using double-shear or compression geometries and the longitudinal vibration method showed discrepancies of up to nearly 20% in modulus and absolute discrepancies of up to 0.01 in loss factor; the reason for the differences were not clear. Results are here obtained for natural rubber at frequencies near resonance up to 8kHz and over temperatures from -50 to 35°C.

Some workers<sup>6</sup> have used the longitudinal vibration technique to obtain material properties at regular, narrowly spaced frequency intervals, i.e. off resonance. This approach is adopted in the present study for two polymers derived from natural rubber by a process of chemical modification -epoxidation - and possessing higher glass transition temperatures. The tests on the epoxidized natural rubber (ENR) have been carried out over frequencies up to 8kHz and at temperatures ranging from -50°C to 35°C.

In addition, dynamic properties for the three elastomers, along with a very low molecular weight uncrosslinked sample of one of the materials, have been obtained from forced non-resonance experiments using a high frequency servohydraulic testing-machine. These tests extended over frequencies from 0.5Hz to 500Hz and, in the case of the epoxidized natural rubbers, temperatures from -26 to 30°C. A direct comparison is made between the forced non-resonance and longitudinal vibration data for the natural rubber in the limited frequency range over which the methods overlap.

Master curves for room temperature are constructed from the forced non-resonance results and compared with the directly measured longitudinal vibration data. The latter measurements over

the complete temperature range are in turn transformed to give master curves showing how the dynamic properties at room temperature vary for frequencies up to 100kHz.

The range of application and sources of error of the longitudinal vibration and forced non-resonance techniques as used here are discussed.

## EXPERIMENTAL

### MATERIALS

The tests were performed on unfilled vulcanizates of natural rubber (NR) and epoxidized natural rubber (ENR-25 and ENR-50). The latter is a chemically modified variant of NR produced by replacing respectively 25% and 50% of the carbon-carbon double bonds by epoxide groups. The effect of the epoxidation on the glass transition temperature ( $T_g$ ) is indicated in Table 1. The detailed formulations and curing conditions are also given in that Table. Some forced non-resonance measurements were also made on a low molecular weight (weight average,  $M_w = 5.2 \times 10^4$ ) unvulcanized sample of 50% epoxidized NR (LENR-50)

TABLE I Formulations of elastomers			
Elastomer	Parts by weight per 100 parts elastomer		
NR (smoked sheet)	100		
ENR-25		100	
ENR-50			100
Sulphur	2.5	1.5	1.5
accelerator - TBBS <sup>a</sup>		1.5	1.5
- CBS <sup>b</sup>	0.8		
Calcium stearate		5	5
Zinc Oxide	5	5	5
Stearic Acid	2	2	2
Antioxidant <sup>c</sup>		1	1
Cure temperature, °C	140	130	130
Cure time, min	30	34	30 <sup>3</sup>

a tertiary butyl benzothiazole-2-sulphenamide

b N-cyclohexyl benzothiazole-2-sulphenamide

c N-(1,3-dimethylbutyl)-N-phenyl-p-phenylenediamine



## TEST PIECES

The longitudinal vibration experiments generally used samples of various lengths transfer moulded as cylinders of diameter 5mm. Some tests on NR used 5mm wide strips cut from 5mm thick sheet.

The testpieces for the force non-resonance experiments had a double-shear geometry. The vulcanized elastomer samples were in the form of cylinders of 2mm nominal length and 25.4mm diameter. They were produced by transfer moulding into a cavity containing the aluminium metal endpieces and central piece, and curing under the conditions given in Table 1. A hot bonding adhesive system (Chemlok 205/220) was used. The LENR-50 testpieces were produced by applying a toluene solution of the elastomer to the metal pieces and compressing these together to form a disc of thickness approximately 0.1mm; no adhesive was necessary.

## HIGH FREQUENCY TEST METHODS

### FORCED NON-RESONANCE METHOD

A servohydraulic machine, Schenck VHF7 was used to deform the double-shear testpieces sinusoidally. A schematic diagram of the machine (showing transducer location) and test pieces is given in Figure 1. The principle of this method is well documented<sup>7</sup>. The generator of a Solartron 1250 Frequency Response Analyser (FRA) provided the driving signal. The facilities of the FRA were utilized to analyze the signal from the piezo-electric force transducer and the displacement transducers. The transducer from which the displacement signal was taken switched from a linear variable differential transformer (LVDT) to a piezo-electric accelerometer at about 290Hz. The results were obtained in terms of the ratio of the peak force to peak displacement signal at the driving frequency and their relative phase angle. The shear modulus,  $G^*$ , and loss angle,  $\delta$ , of the material were calculated making correction for the compliance and loss angle associated with the grip connections. Thermal breaks machined from phenolic based cotton fabric laminate (Tufnol) rods were introduced on each side of the testpiece jig to speed the attainment of thermal equilibrium. The temperature of the testpiece was checked using a thermocouple.

The upper limit, taken here as 400Hz, for the frequency of testing with this method is generally set by one of the following factors:

1. Resonance of the sample. The speed of shear waves for most rubbers at room temperature is around 25 to 35ms<sup>-1</sup>, and for a 2mm thick sample the first resonant frequency is around 6 to 9kHz. As the driving frequency approaches sample resonance, the influence of the inertia of the sample can be observed as an increase in the apparent dynamic stiffness,  $K^*$  and a change in sign of the phase angle between the force and displacement signals.

The theory for the propagation of plane waves can be employed<sup>2</sup> to quantify the error in the measured  $G^*$  and  $\tan\delta$ . When the sample length is 5.5% of the wave length the error in the modulus is about 2%; the error rises to 7% when the length of the sample becomes 10% of the

wavelength. The first resonance occurs when the sample length is 50% of the wave length. For natural rubber at room temperature a sample of 2mm thickness gives 2% error at 800Hz and 7% error at 1450Hz. This compares to 265Hz and 483Hz for the 6mm long sample recommended by the British Standard for measurement of dynamic moduli<sup>8</sup>.

2. Resonance in the testing-machine or grip connection. The crosshead and column arrangement of the Schenck VHF7 resonates at frequencies over 1kHz. For example, when the crosshead is at its highest position the resonant frequency is about 1200Hz. As resonance is approached the base of the machine, the "seismic mass", moves in phase with the actuator, the amplitude depending upon the frequency. The error in the force signal from the load cell is proportional to the mass and amplitude of movement of the grip attached to it. For the Schenck VHF7 this is a significant artefact even though the load cell and grip are attached to a large seismic mass. The effect was minimised by using lightweight alloys in construction of the jig.

The frequency at which the resonance introduced significant error into the force signal was determined as follows. A sample was placed in the lower grip, but the upper grip was left unattached. The level of the force on the load cell was recorded for frequencies up to 1000Hz, the displacement amplitude of the actuator being 10µm. The upper grip was then connected, and the sample tested with the same amplitude. The percentage error in the force signal due to resonance depended on the stiffness of the test piece. For NR at room temperature it was found to reach 0.5% at a frequency between 450-600Hz.

#### **LONGITUDINAL VIBRATION TESTS**

In this technique the modulus and loss factor of linear viscoelastic materials are determined by applying an acceleration input at one end of a rod and measuring the amplitude and phase of the output. Norris and Young<sup>9</sup> have presented the equations describing longitudinal forced vibration of a viscoelastic rod with an added mass at the free end. The end mass, which may represent a detector (accelerometer), can influence the response significantly, and should not be neglected as some workers have done previously. The equations can be solved to give an expression for the complex parameter  $Q$ , the ratio of the peak acceleration at the free end to that at the driven end. Its reciprocal,  $1/Q$ , can be written in the form of real and imaginary parts:

$$\frac{1}{Q} = \text{Re} + i\text{Im}$$

which are functions of the frequency of excitation and the dynamic properties of the viscoelastic material.

In order to write expressions for  $\text{Re}$  and  $\text{Im}$  the following parameters need to be defined. The complex Young's modulus,  $E^*$ , of the viscoelastic rod is written as

$$E^* = E' + iE'' = Ee^{i\delta}$$

where  $E'$ , and  $E''$  are the in-phase and out-of-phase components of the modulus and

$$E = (E'^2 + E''^2)^{1/2}$$

and  $\delta$  is the loss angle. The phase velocity,  $c$ , of plane waves travelling down the rod is given by

$$c = (E/\rho)^{1/2} \sec (\delta/2)$$

where  $\rho$  is the density of the rod material. A parameter,  $\xi$ , the frequency ratio can be defined by

$$\xi = \omega L/c$$

where  $L$  is the length of the viscoelastic rod, and  $\omega$  is the exciting angular frequency. The mass ratio,  $R$  is defined as

$$R = m/M$$

where  $m$  is the end-mass, and  $M$  the mass of the viscoelastic rod. Finally a parameter  $\beta$  given by:

$$\beta = \xi \tan \delta/2$$

is introduced.

Expressions for the  $Re$  and  $Im$  can now be given in the form:

$$Re = \cosh \beta (\cos \xi - R \xi \sin \xi) + R \beta \cos \xi \sinh \beta \quad (1)$$

$$Im = \sinh \beta (\sin \xi + R \xi \cos \xi) + R \beta \sin \xi \cosh \beta \quad (2)$$

Often measurements of  $Q$  are only made at frequencies for which the phase angle between input and output is  $90^\circ$ , a point near but, for an imperfectly elastic material, not at resonance. Equations (1) and (2) are easier to solve at such frequencies since then  $Re = 0$  and  $Im = 1/Q$ . Also the material data obtained is less sensitive to errors in the measurement of  $Q$ ; this is particularly important in the case of tests on low damping materials<sup>10</sup>. Measurements on NR were carried out using this approach. In addition measurements on ENR-25 and ENR-50, elastomers exhibiting higher damping than NR over the test conditions, were made at closely spaced frequency intervals (off-resonance) in order to obtain a continuous record of the variation in the dynamic properties.

The elastomer rod specimen was driven by an electromagnetic shaker (Ling dynamics V201) as shown schematically in Figure 2. A Solartron 1250 frequency response analyser (FRA) was used to provide the driving signal for the shaker and to analyze the signals from the input and output accelerometers (Kistler 8086 A500; mass 0.5g). The rod was bonded to the housing of the shaker and to the end-mass by cyanoacrylate adhesive. The total end-mass was 1.5g. Typically, the length of the specimen was about 7cm. Longer specimens were used successfully, but for

specimens shorter than 5cm the larger mass ratio,  $R$ , increased the significance of any uncertainty in the contribution of the cable of the output accelerometer to the end-mass. The uncertainty could lead to significant errors in the case of the damping factor, particularly for high frequencies. The temperature of test was monitored by a thermocouple attached to the shaker.

As seen in Figure 2 the input accelerometer was not fixed to the outside of the housing where the rod was bonded. For the off-resonance tests (where the results are sensitive to signal error) a series of calibrations at all the temperatures of test and over the entire frequency range was carried out to determine the relationship between the signal given by the input accelerometer (the apparent input) and the excitation experienced by a second accelerometer fixed where the specimen rods were glued to the shaker housing (the true input). The second accelerometer used in the calibration was that used to monitor the output at the free end of the rods, so these calibration tests also served as a check on the relative sensitivity of the input and output accelerometers. The ratio between the apparent and true input accelerations was generally 0.95, but ranged from 0.94 to 1.05.

At each frequency of test, the equations (1) and (2) were solved for the observed ratio  $Q$  by an iteration routine based on the Newton-Raphson method to give values of the frequency ratio,  $\xi$ , and loss angle,  $\delta$ . From these the shear modulus,  $G^*$ , is obtained by assuming the elastomers are incompressible and hence  $G^* = E^*/3$ .

For the tests carried out at regular, narrowly spaced frequencies some difficulty was experienced in choosing a starting-point for the iteration that would always give convergence to the desired solution. More than one physically permitted solution existed, so care was needed to ensure that the desired one was obtained. The starting-point strategies suggested by Buchanan<sup>10</sup> did not always work. The scheme adopted here was to start the iteration at the solution for the nearest point where  $1/Q$  was purely imaginary. For subsequent test frequencies the previous solution was taken as the starting-point. Occasionally this strategy did not work; then a set of iterations were tried with starting-points closely spaced about the expected value of  $\xi$ . As mentioned previously, when  $1/Q$  is not purely imaginary the off-resonance technique gives large errors, particularly in  $\delta$ , for low damping elastomers ( $\tan \delta \leq 0.1$ ). Testing high damping elastomers ( $\tan \delta \geq 1$ ) can also lead to large errors because the high absorption results in low output accelerations. In the present tests no data was collected if  $|Q| < 10^3$ .

Another limit to the range of applicability of the longitudinal vibration technique arises from the requirement in the theory that  $d/\lambda \ll 1$  (where  $d$  is the diameter of the rod and  $\lambda$  the wavelength). In the tests reported here the criterion  $d > 6\lambda$  was chosen. Though Pochhammer and Chree<sup>11</sup> provide an analysis for perfectly elastic rods when transverse planes can no longer be assumed to remain plane, there appears to be no comparable analysis for viscoelastic media. The analysis for elastic rods suggests that when the wavelength is comparable to the lateral dimension of the sample the plane wave velocity  $c$  is no longer simply given by the "bar velocity",  $c_0 = \sqrt{E/\rho}$ . Instead it becomes a function of the ratio of the smallest lateral dimensions of the bar,  $d$ , to the wavelength,  $\lambda$ , the Poisson's ratio of the material,  $\nu$ , and the bar velocity,  $c_0$ . Applying the correction to the apparent modulus values obtained from previous longitudinal vibration tests on polybutadiene<sup>2</sup> did not give the expected lack of variation of modulus with frequency; the correction factor appeared to be too large. The loss factor data obtained<sup>2</sup> also

appeared to be affected when  $\lambda \sim d$ , and the elastic theory provides no means of correction in this case. Thus it appears necessary to confine measurements to  $d \ll \lambda$ .

## RESULTS AND DISCUSSION

The shear modulus and loss factor obtained for the epoxidized natural rubbers using forced non-resonance of a double shear testpiece is presented in Figures 3 and 4 in the form of master curves showing the variation with frequency at room temperature (23°C). Data only up to the frequencies of 100Hz were used to construct the master curves in order to avoid any possibility of significant heat build up within the testpieces. For each polymer, the shear modulus data at each test temperature,  $T^\circ\text{K}$ , was adjusted by the ratio  $296/T$ , and then shifted horizontally to produce a best fit to the single master curve. The same horizontal shift factor was applied to the loss factor results to produce master curves for this parameter.

For ENR-50 the actual data points are given on Figures 3 and 4 to demonstrate that the scatter in the data is small and that the data at each temperature after shifting tightly falls onto the appropriate master curve. The quality of the data and the goodness of fit to the master curves was similar for the ENR-25 and LENR-50. The variation of each empirically determined shift factor with test temperature was found to fit quite well to the shift factor,  $a_T$ , as given by the WLF transform<sup>12</sup>:

$$\log a_T = -8.86 (T - T_g) / (101.6 + T - T_g) \quad (3)$$

with an appropriate choice of the reference temperature,  $T_g$ . The values of  $T_g$  giving the best fit to the empirical shift factor curves are listed in Table 2; as expected<sup>12</sup> most are approximately  $T_g + 50$ . The reference temperature for LENR-50 did not correspond to expectations. The fact that its  $T_g$  (-18.5°C according to differential scanning calorimetry) was found to be higher rather than lower than that of the high molecular weight ENR-50 is somewhat surprising.

The master curves of ENR-50 and ENR-25 are broadly similar in shape but shifted horizontally by an amount expected from the difference in the glass transition temperatures. The LENR-50 behaves like a polymer with a molecular weight too low to produce a significant number of physical entanglements. Thus there is no constant modulus region at low frequency. Its modulus is well below that of the crosslinked, high molecular weight ENR-50 throughout the frequency range in Figure 3. At sufficiently high frequency, as  $T_g$  is approached, the two modulus curves would be expected to converge but there is no indication of this. Corresponding to the absence of a plateau in the modulus the loss factor for LENR-50 remains high down to low frequencies.

The longitudinal vibration test data obtained for natural rubber at room temperature is shown in Figures 5 and 6. This data was obtained only near resonance in order to minimise the errors. The shear modulus data (Figure 5) indicates a slight dependence upon testpiece length, at least for the shortest specimens, presumably due to end effects. There is no evidence of these influencing the loss factor (Figure 6).

Also included on Figures 5 and 6 are forced non-resonance results for natural rubber at room

temperature obtained using a double-shear testpiece. The agreement in  $\tan\delta$  between the two methods is quite good. It should be noted that the figures are linear-logarithmic plots. However the shear modulus determined from the longitudinal vibration tests is nearly 20% higher than that from the double-shear testpieces. The reason for the discrepancy is not clear. The quasistatic shear modulus of the rod was closer to the double-shear value.

The natural rubber near resonance longitudinal vibration data covering test temperatures from -50°C to 35°C in steps of 5°C are shown in the form of room temperature (23°C) master curves of shear modulus and loss factor in Figure 7. The shift factors were determined empirically to provide the best fit of the shear modulus data at each temperature to the master curve. In this case the vertical correction was not applied. The shift factors determined from the modulus data were used to produce the loss factor master curve. The value of  $T_g$  that provided the best fit of the WLF transform (equation 3) to the empirical shift function was -19.5°C.

The off-resonance longitudinal vibration data for ENR-50 and ENR-25 are presented in Figures 8 and 9. The variation of the shear modulus and loss factor with frequency at room temperature are given as master curves derived in the manner described for natural rubber. The data points are given as a guide to the scatter in the data and the degree of fit of the individual temperature data to the master curve. It is evident that the scatter is greater and the degree of fit to the master curve poorer than for the forced non-resonance data (Figures 3 and 4). The value of the reference temperature,  $T_r$ , for these polymers are given in Table 2.

TABLE 2 Glass transition and reference temperature				
	ENR-25	ENR-50	LENR-50	NR
$T_g$ °C forced non-resonance	2.5	24.5	8.5	
$T_g$ °C longitudinal vibration	-1	22.5		-19.5
$T_g$ °C Differential Scanning Calorimetry	-41.5	-24	-18.5	-68

Figures 10 and 11 show the master curves of shear modulus and loss factor respectively obtained for ENR-25 and ENR-50 by the forced non-resonance and off-resonance longitudinal method. The vertical lines on the curves for the latter technique indicate the limits of the frequency range over which data was recorded at room temperature, ie. the range of the untransformed data.

Comparing the longitudinal vibration and forced non-resonance results, it is apparent that the former produce a modulus about 30% higher. The discrepancy is similar to that found in the tests on natural rubber (Figure 5). The two techniques give modulus master curves of similar shape. In comparing data obtained from various techniques, Dlubac et al<sup>4</sup> found discrepancies

in modulus of a similar magnitude. Over the frequency range of the room temperature longitudinal vibration tests the two techniques give reasonably similar loss factors for ENR-25; the agreement is not quite as good as that obtained for NR (Figure 6). In contrast, the loss factor of ENR-50 observed in the longitudinal vibration tests diverges from the transformed forced non-resonance data as the frequency rises. The discrepancy widens at frequencies above the range of the direct longitudinal vibration measurements. At such frequencies a similar difference is seen for ENR-25. The reason for results from the two techniques to diverge at high loss angles is not clear, particularly as no corresponding effects are seen in the modulus data.

## CONCLUSIONS

Dynamic properties data for natural rubber and two epoxidized natural rubbers have been obtained using forced non-resonance of a double-shear testpiece and longitudinal vibration of a rod. The latter technique was successfully used at frequencies off-resonance so that results at regularly spaced frequency intervals were possible.

The longitudinal vibration technique gave shear modulus values consistently higher by 20-30% than the forced non-resonance method. For low loss factors the two techniques agree reasonably well, but comparison of forced non-resonance data and longitudinal vibration data at loss factors approaching unity indicate the latter to give significantly higher values. The discrepancy is seen in the results for ENR-50 in the frequency range where the longitudinal vibration data is directly measured, and for the ENR-25 at frequencies where data from both techniques have been transformed using time-temperature equivalence. The origin of the discrepancies in the modulus and loss factor results from the two techniques is not clear.

Dynamic properties data directly measured at high frequency show some differences from results produced by transforming low frequency data. The shape of shear modulus-frequency curves directly measured by the longitudinal vibration method are, however, similar to those given by the transformed forced non-resonance data. The differences in magnitude are seen when comparing data obtained at the same temperature. The comparisons of directly measured and transformed loss factor results conflict - in one case the data agree reasonably well and in the other diverge significantly. The lack of agreement appears to be associated with higher loss angles. Errors in the measurement techniques require further consideration.

## REFERENCES

1. Ferry, J.D. (1980) *Viscoelastic Properties of Polymers*. 3rd ed., Wiley, New York.
2. Ahmadi, H.R., Fuller, K.N.G. and Muhr, A.H. (1992) High Frequency Dynamic Properties of Natural Rubber. *J.Nat.Rubb.Res.*, 7, 181.
3. Oyadiji, S.O. and Tomlinson, G.R. (1991) Establishing the validity of the Master Curve Technique for Complex Modulus Reduction, Paper DBC, Proceedings of Damping '91, publ. by Airforce Command Systems, Wright-Patterson Airforce Base, Ohio.

4. Dlubac, J.J. et al. (1990) Comparison of the complex dynamic modulus as measured by three apparatus, Sound and Vibration Damping with Polymers by Corsaro, R.D. and Sperling, L.H., American Chemical Society Symposium Series 424.
5. Capps, R.N. (1983) Dynamic Young's Moduli of some commercially available Polyurethanes, *J. Acoust. Soc. Am.*, **73**, 2000.
6. Capps, R.N. and Beumel, L.L. Dynamic Mechanical Testing, ACS series 324; see reference 4.
7. Read, B.E. and Dean, G.D. (1978) The Determination of Dynamic Properties of Polymers and Composites, Adam Hilger, Bristol.
8. British Standards Institution (1976) Measurement of Dynamic Moduli. BS903: Part A24.
9. Norris, JR., D.M. and Young, W.C. (1970) Complex Modulus Measurement by Longitudinal Vibration Testing, *Expl Mech.*, **10**, 93.
10. Buchanan, J.L. (1987) Numerical Solution for the Dynamic Moduli of a Viscoelastic Bar. *J. Acoust. Soc. Am.*, **81**, 1775.
11. Love, A.E.H. (1927) The Mathematical Theory of Elasticity, p.287, 4th edition, Cambridge University Press.
12. Williams, M.L., Landel, R.F. and Ferry, J.D. (1955) The Temperature Dependence of Relaxation Mechanisms in Amorphous Polymers and Other Glass-forming Liquids, *J. Am. chem. Soc.*, **77**, 3701.



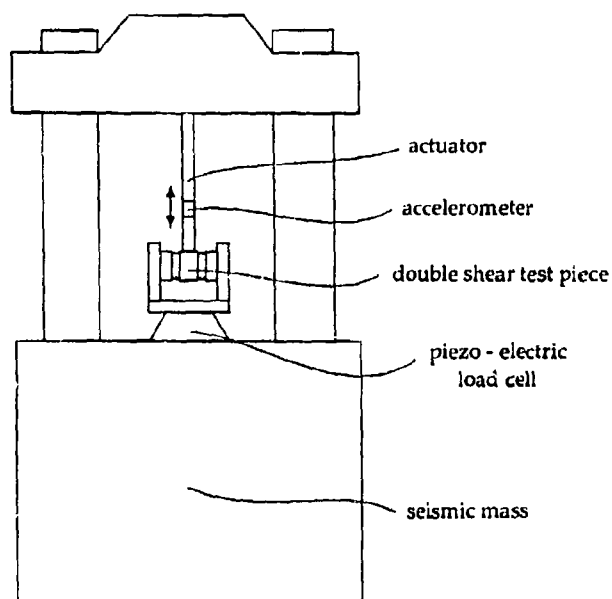


**Figure 1** Schematic diagram of servohydraulic machine and double shear testpiece used in the forced non-resonance method.

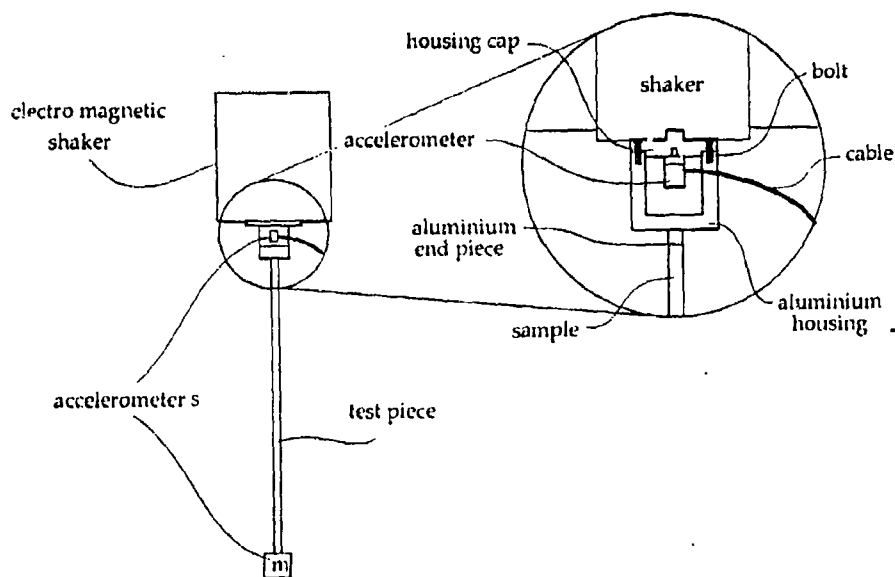


**Figure 2** Schematic diagram of longitudinal vibration apparatus showing the location of the input accelerometer within its housing, the testpiece and output accelerometer.

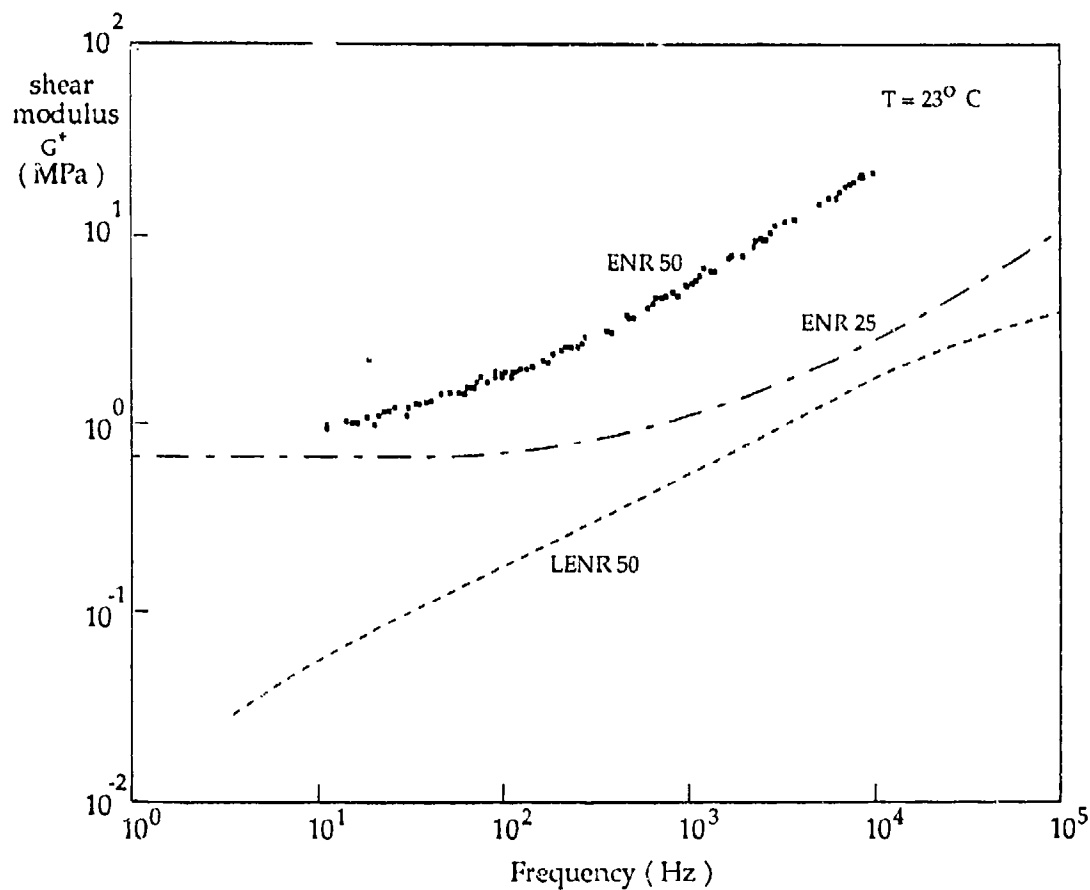


**Figure 3** Mastercurves showing the variation of dynamic shear modulus  $G^*$  with frequency for ENR-50, ENR-25 and LENR-50 at a temperature of  $23^\circ\text{C}$ . The data were obtained by forced non-resonance method at temperatures ranging from  $-26$  to  $30^\circ\text{C}$ . The individual data points are shown for ENR-50; the consistency of the data for ENR-25 and LENR-50 was similar.

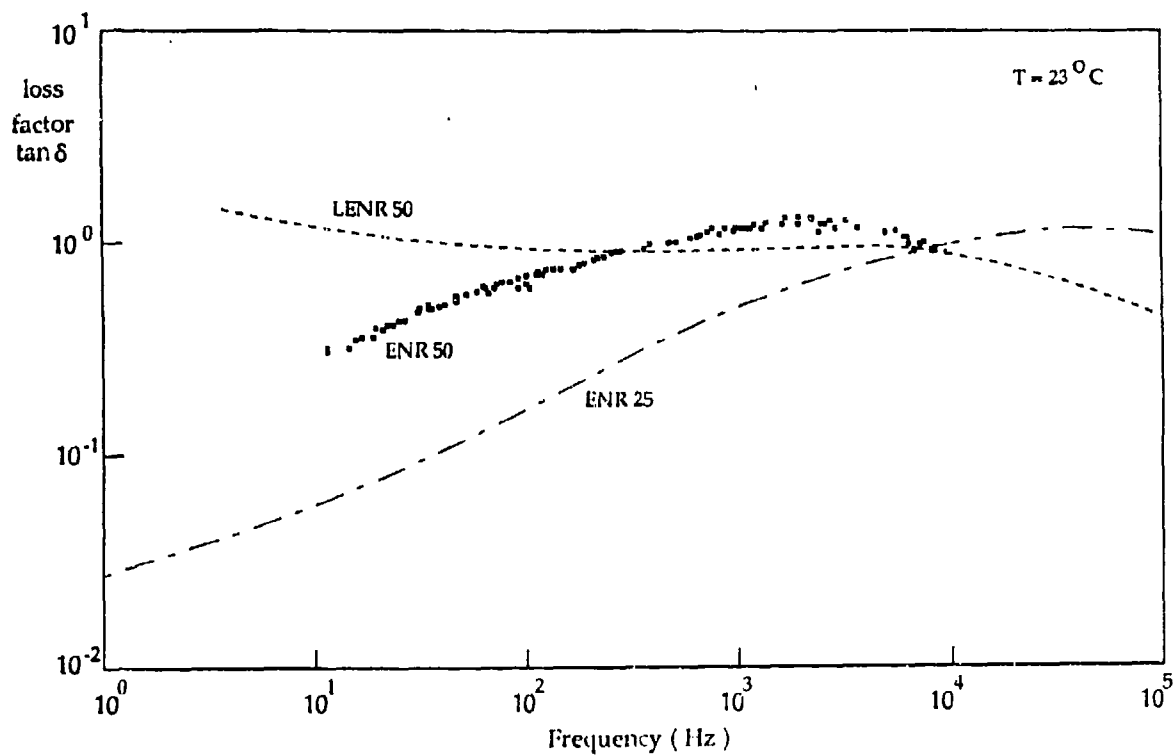


**Figure 4** Master curves showing the variation of loss factor  $\tan \delta$  with frequency for ENR-50, ENR-25 and LENR-50 at a temperature of  $23^\circ\text{C}$ . Details as for Figure 3.

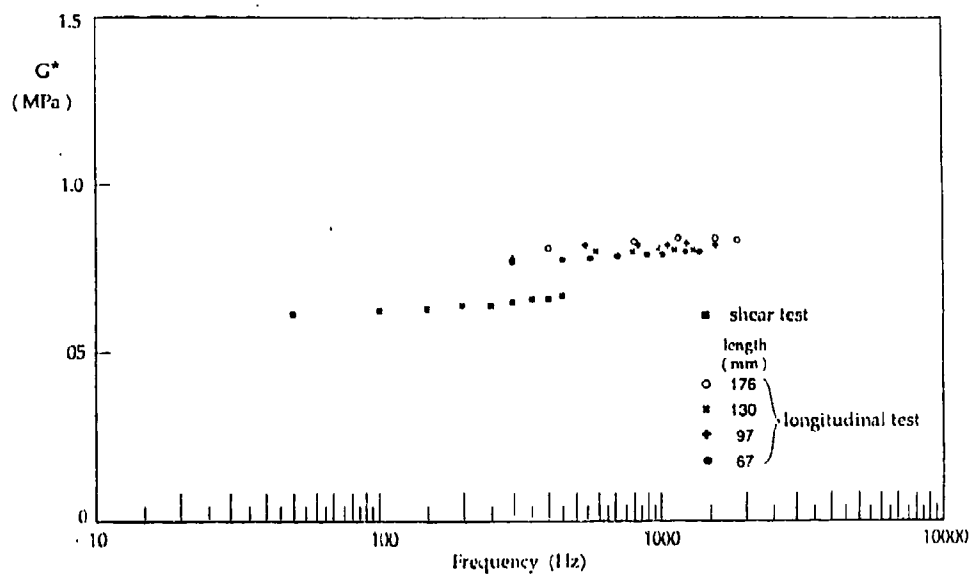


**Figure 5** Variation of the dynamic shear modulus  $G^*$  with frequency for a natural rubber vulcanizate measured directly at room temperature ( $23^\circ\text{C}$ ) by both the forced non-resonance method in simple shear and the near resonance, longitudinal vibration method.

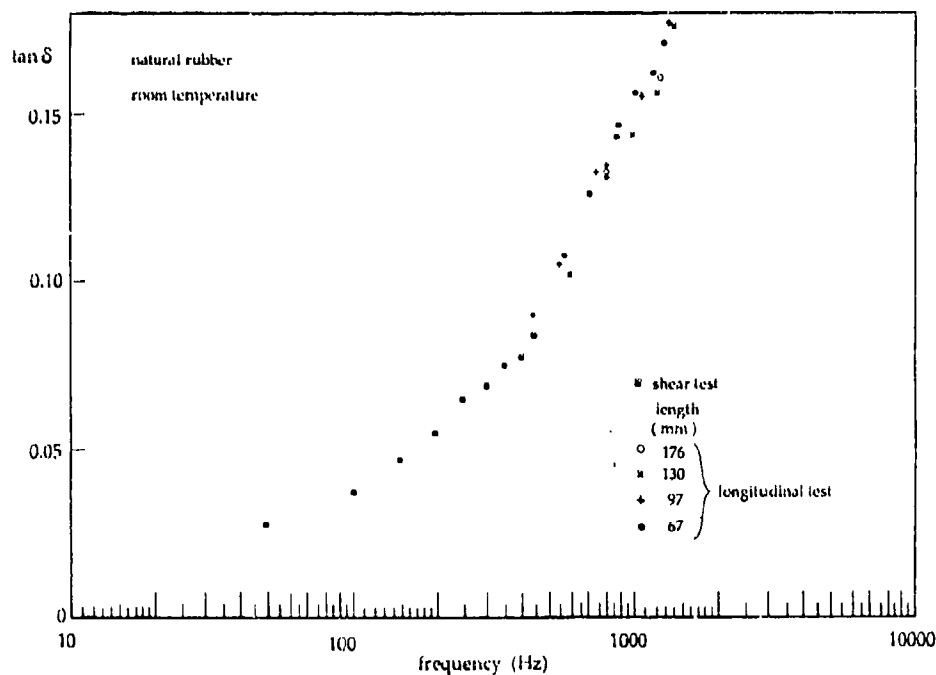


**Figure 6** Variation of the loss factor  $\tan \delta$  with frequency for natural rubber vulcanizate at room temperature ( $23^\circ\text{C}$ ). Details as in Figure 5.

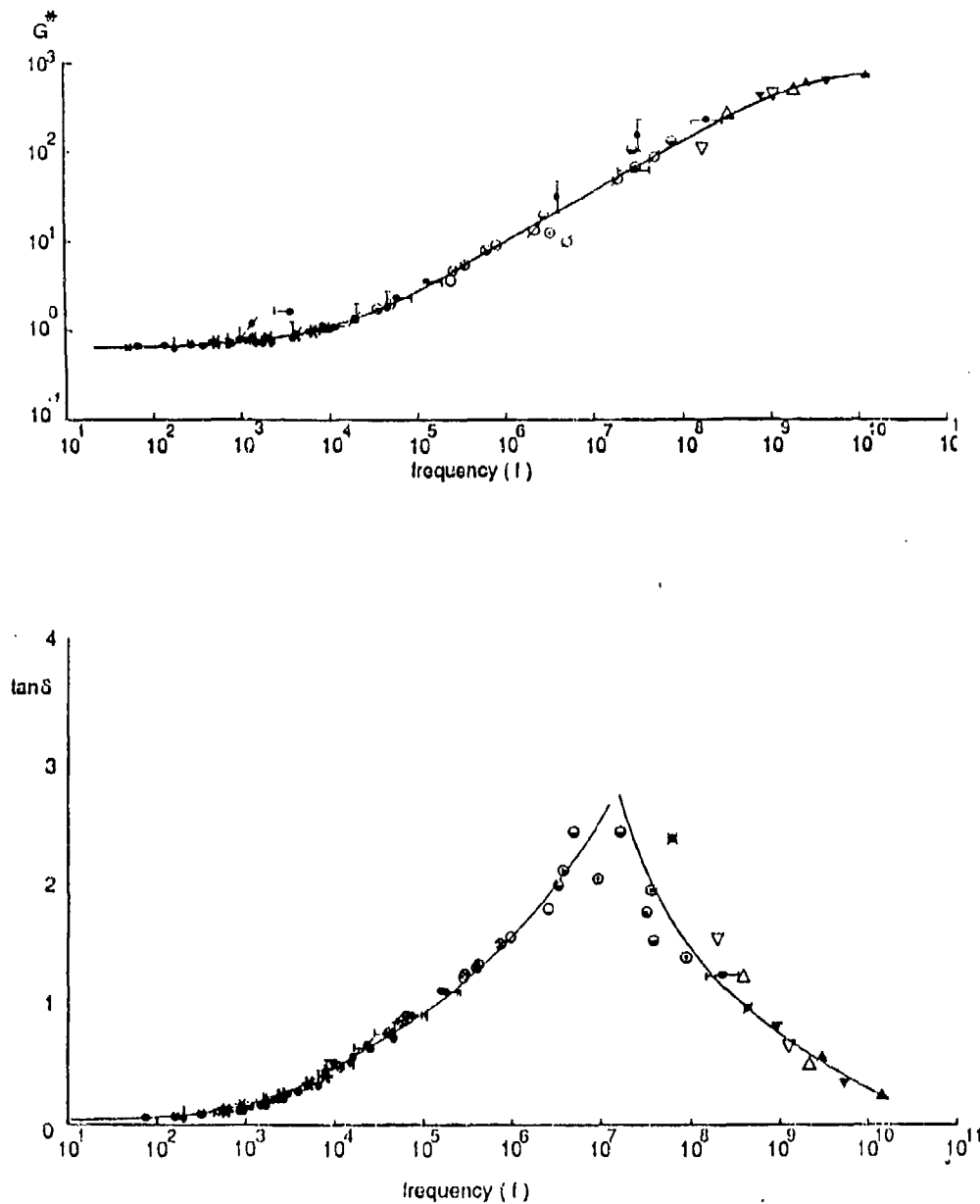


**Figure 7** Master curves showing the variation of (a) dynamic shear modulus  $G^*$  and (b) loss factor  $\tan\delta$  with frequency at  $23^\circ\text{C}$ . Data points obtained by near-resonance longitudinal vibration method at temperatures ranging from  $-50^\circ\text{C}$  to  $30^\circ\text{C}$  in steps of  $5^\circ\text{C}$ .

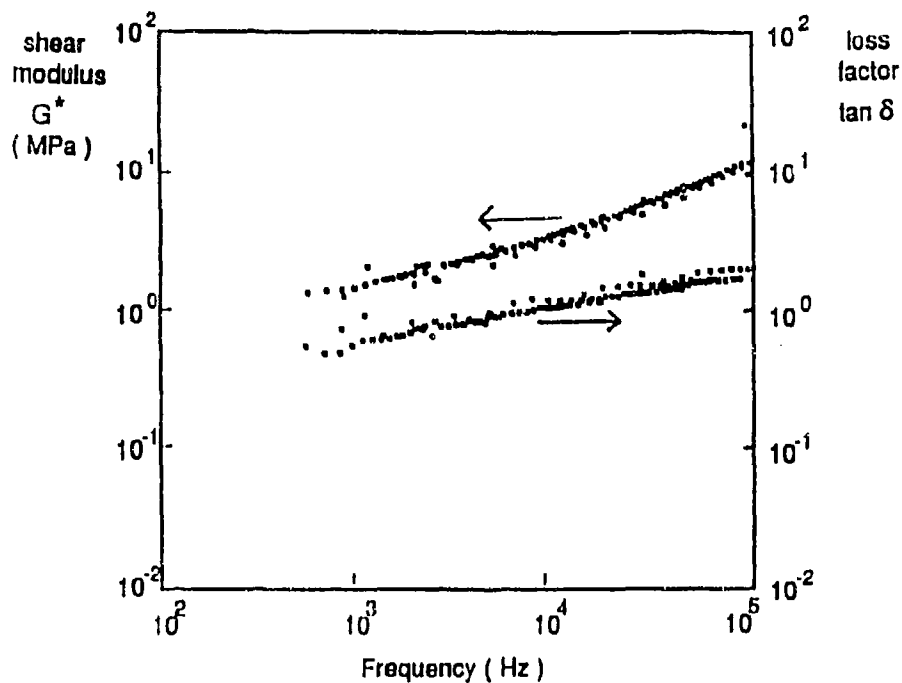


Figure 8 Master curves showing the variation of the dynamic shear modulus  $G^*$  and loss factor  $\tan \delta$  with frequency for ENR-25 at 23°C. Data points obtained by off-resonance longitudinal vibration method at temperatures ranging from 23°C to -10°C in steps of 5°C.

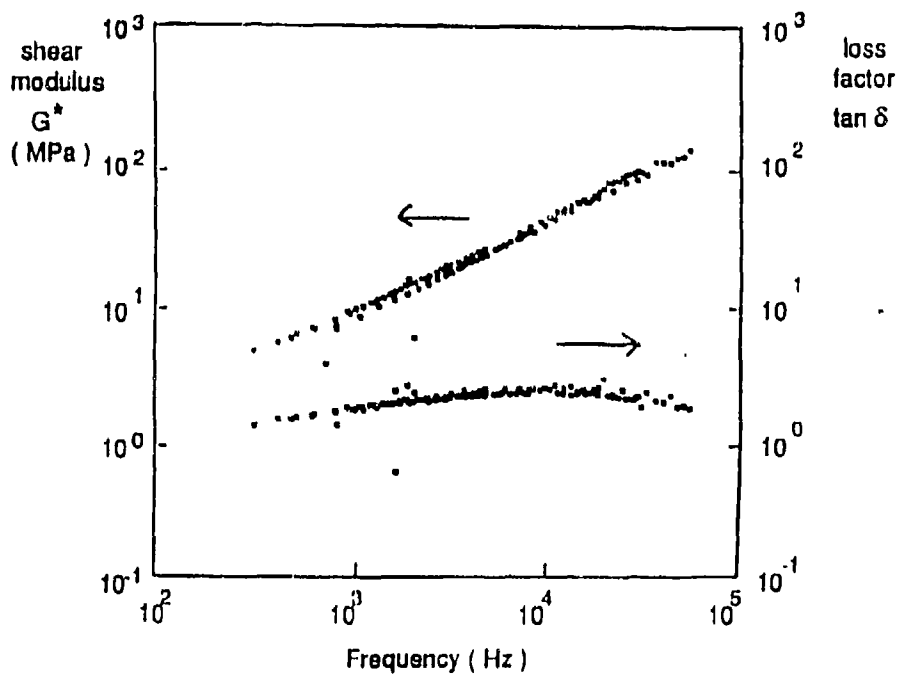
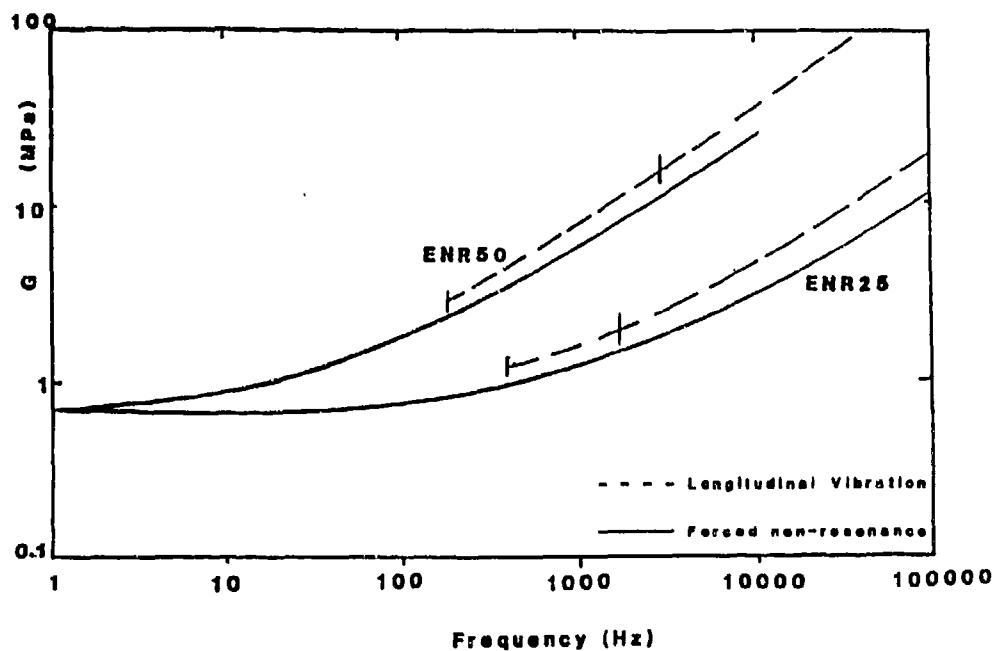
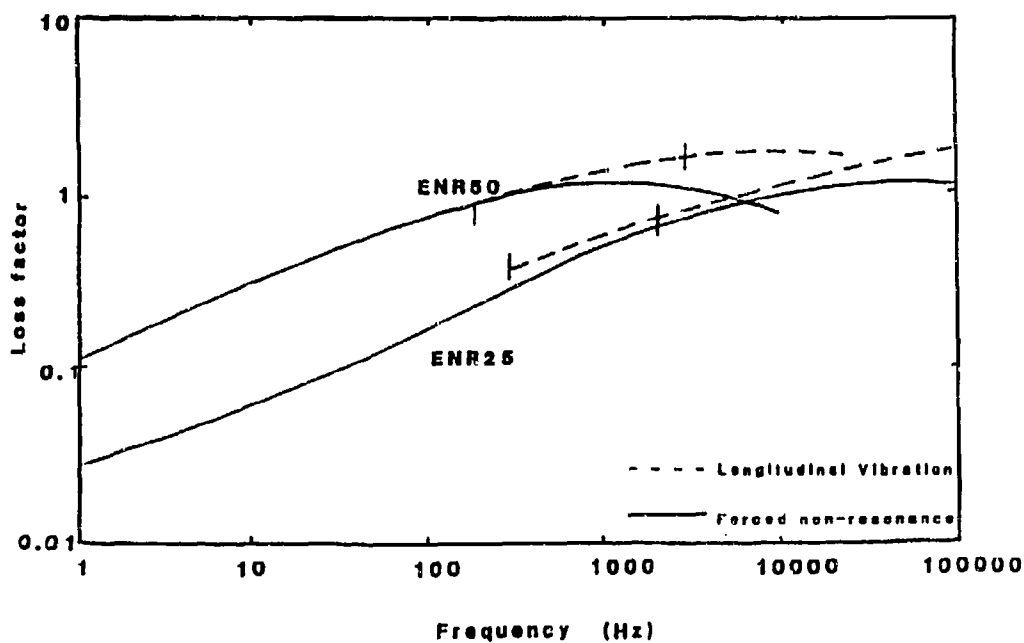


Figure 9 Master curves showing the variation of the dynamic shear modulus  $G^*$  and loss factor  $\tan \delta$  with frequency for ENR-50 at 23°. Data points obtained by off-resonance longitudinal vibration method at temperatures ranging from 23°C to -11°C in steps of 2°C.



**Figure 10** Master curves showing the variation of the dynamic shear modulus  $G'$  with frequency, transformed to 23°C as predicted by forced non-resonance method and longitudinal vibration method. The data in between the vertical lines was directly measured at 23°C using longitudinal vibration method.



**Figure 11** Master curves showing the comparison between the variation of the loss factor  $\tan \delta$  with frequency, transformed to 23°C, as predicted by forced non-resonance method and longitudinal vibration method. The data in between the vertical lines was directly measured data at 23°C by the longitudinal vibration method.

# EFFECT OF LONG SPACE EXPOSURE UPON PROPERTIES OF VISCOELASTIC MATERIALS

by

David I.G. Jones<sup>\*</sup>  
Wright Laboratory

and

John S. Kirby<sup>#</sup> and Donald Edberg<sup>@</sup>  
McDonnell Douglas Space Systems Company

## ABSTRACT

This paper reports work in progress toward characterizing the effect of long duration exposure in space on viscoelastic material behavior. As part of its experiments for NASA's Long Duration Exposure Facility (LDEF), McDonnell Douglas Space Systems Company (MDSSC), in collaboration with the Air Force's Wright Laboratory, constructed a series of advanced composite materials which employed viscoelastic damping. The samples were flown on the LDEF satellite, after being characterized with respect to their damping properties, while control samples were retained on the ground. The ground control samples of all materials were retained in a controlled environment, by MDSSC, for post flight evaluation. Preliminary post flight characterization of the recovered samples is now underway, and tentative evaluations of the effect of long term space exposure are reported herein. Data from these samples will ultimately provide information about potential changes in the properties of viscoelastic materials after extended space exposure. When post flight characterization is complete, MDSSC will use the information to determine the impact of the observed changes upon the performance of two space structures, namely Space Station Freedom and a large truss structure suitable for advanced Air Force weapons systems.

---

\* Senior Research Engineer, Flight Dynamics Directorate (WL/FIBG),  
Wright-Patterson AFB, OH 45433. Tel: (513) 255-5229 X 414.

# Manager, Advanced Materials and Survivability, 5301 Bolsa Avenue,  
Huntington Beach, CA 92647.

@ Senior Engineer/Scientist, Advanced Structures, 5301 Bolsa Avenue,  
Huntington Beach, CA 92647.



## INTRODUCTION

Many material and structural samples were exposed to low earth orbit (LEO) environment during the Long Duration Exposure Facility mission (LDEF)[1]. A number of composite beams with viscoelastic cores were included, and these were placed inside the satellite on the leading and trailing edge portions. Table 1 identifies some of the samples. The beam geometries are illustrated in Figure 1. The beams were about 3.5 inches (88.9 mm) long and about 0.5 inches (12.7 mm) wide, with various thicknesses of several viscoelastic materials sandwiched between the two-ply layers of co-cured T300 carbon fiber-5208 epoxy composite sheets. Some preflight dynamic response tests were conducted [2], and the same samples were again tested after the satellite was recovered. Control samples, kept in storage on the surface of the Earth, were also tested. Preliminary results are presented in this paper.

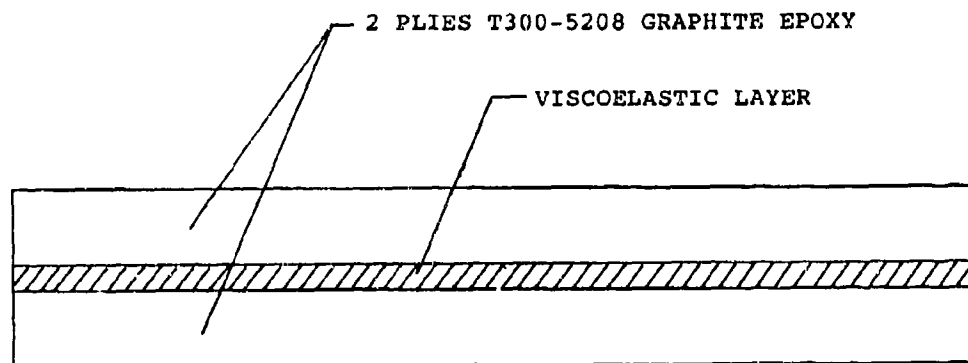


Figure 1. Test Sample Configuration

## TEST SYSTEM

The beams, illustrated in Figure 1, were extremely small and light. Ideally, a free-free test configuration would have been desired but early tests conducted before the LDEF mission [2] showed that the clamped-free configuration gave the most reliable results with the least scatter. The test setup used in this preliminary evaluation is illustrated in Figures 2 and 3. The magnetic transducers provided adequate excitation levels in the first two modes, up to about 1500 Hz. Transducer sensitivity dropoff was significant at higher frequencies, both with respect to excitation and pickup, and no higher order modes were observable. A fiber-optic probe, which measured the displacement amplitude, also failed to detect the higher order modes, partly because suitable signal conditioning amplifiers were not available and also, probably, because of dropoff experienced by the exciting transducer. Miniature accelerometers were not available, although acceleration would be the most appropriate parameter to measure at high frequencies. It was decided that the present setup was adequate for the preliminary measurements, but that more advanced excitation and pickup systems would be needed to complete the full evaluation.

TABLE 1. LDEF VISCOELASTIC COMPOSITE BEAM SPECIMENS

Aerospace Sample Number	MDSSC Sample Number	Location (Edge)	Material Obj	Description
EP17-1	LDEF-1-GE/112-2-6	Leading	Damping	2 plies of T300 carbon fiber - 5208 epoxy cocured on each side of 2 mils of 3M 112 viscoelastic materials
EP18-1	LDEF-1-GE/113-2-6	Trailing	Damping	2 plies of T300 carbon fiber - 5208 epoxy cocured on each side of 2 mils of 3M 113 viscoelastic materials
EP19-1	LDEF-1-GE/110-10-6	Trailing	Damping	2 plies of T300 carbon fiber - 5208 epoxy cocured on each side of 10 mils of 3M 110 viscoelastic materials
EP20-1	LDEF-1-GE/113-10-6	Trailing	Damping	2 plies of T300 carbon fiber - 5208 epoxy cocured on each side of 10 mils of 3M 113 viscoelastic materials
	LDEF-1-GE/112-2	Control		Control sample for EP17-1
	LDEF-1-GE/113-2	Control		Control sample for EP18-1
	LDEF-1-GE/110-10	Control		Control Sample for EP19-1
	LDEF-1-GE/113-10	Control		Control Sample for EP20-1
		Control		Control Sample - 4 plies of T300 carbon fiber with 5208 epoxy resin

### TEST RESULTS

The response of the first and second modes was measured many times and the temperature, resonant frequency and modal damping, determined by the "half-power bandwidth" method, recorded for each test. As in most beam tests, there was some scatter from test to test even under nominally identical conditions wherein the specimen was not disturbed in any evident way. By conducting a number of such tests, a statistically valid estimate of the average resonant frequency and modal loss factor could be obtained for each mode and test specimen. The results are summarized in Table 2. Figures 4 and 5 show plots of modal loss factor versus modal resonant frequency for the exposed and control samples of 3M ISD-110 adhesive laminated between two T300 carbon fiber/5208 epoxy sheets, respectively. Figure 6 shows the results of preflight experiments in the clamped-free configuration [2]. Apart from the high level of scatter in Figure 6, the results show relatively little significant change of behavior as a result of over six years' exposure to the low earth orbit environment. No effort was made, in this preliminary investigation, to calculate the complex modulus properties of the exposed and control samples of the viscoelastic layer from the modal resonant frequencies and loss factors. Figure 7 shows a similar plot for the exposed 3M ISD-112 adhesive sandwiched between the T300 carbon fiber/5208 epoxy composite sheets, and Figure 8 shows results for the preflight test [2]. Again, major changes are not evident. The control sample results for this case were not satisfactory, and the results are not reported here.

Other results also indicate that, for some viscoelastic materials, long duration exposure in space may not seriously degrade the damping properties [3].

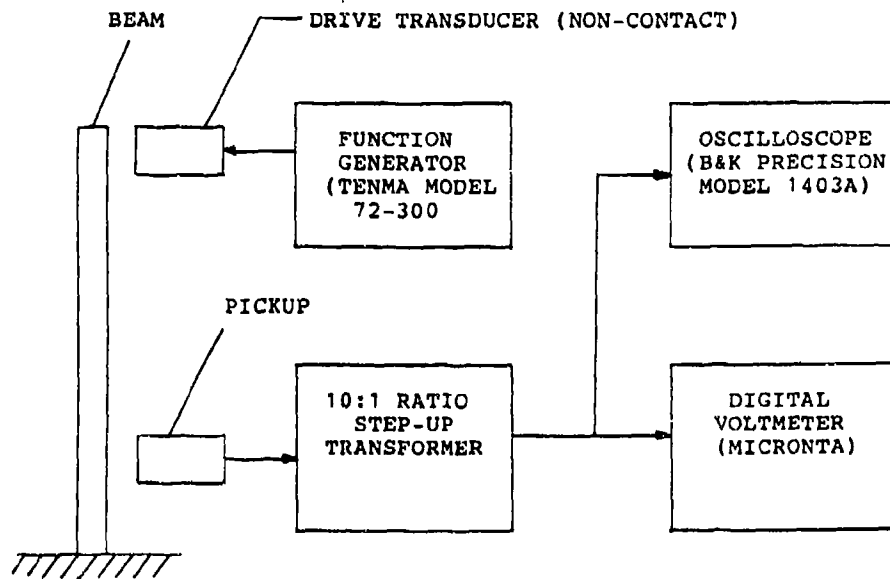


Figure 2. Test Setup

## CONCLUSIONS

Preliminary tests on exposed, control and preflight samples from the LDEF experiment indicate that long duration exposure to the Low Earth Orbit environment may not seriously degrade the damping properties of some viscoelastic materials, especially when they are partly confined in a sandwich configuration. This data, along with other physical tests to determine effects of LEO on other properties, will be useful for design of future space based systems. Further experiments will be conducted, when feasible, to confirm these results for more samples, at temperatures other than room temperature, and analyses will be conducted to determine the complex modulus properties from the modal frequency and loss factor values.

## REFERENCES

1. E.H. Phillips, "Long Duration Exposure Facility Teaches NASA About Effects of Low-Earth Orbits", Aviation Week and Space Technology, pp 178-183, 17 June 1991.
2. M.L. Drake et al, "Damping Materials, Finite Elements and Special Projects", AFWAL-TR-82-4167, pp 77-91, December 1982.
3. C.V. Stahle et al, "RELSAT Damped Satellite Equipment Panels - Dynamic Performance", Proc. DAMPING '89 Conference, WRDC-TR-89-3116, Vol. III, pp JBB-6, 7 and 16, November 1989.

TABLE 2. RESULTS OF RESPONSE TESTS ON LDEF BEAMS

SPECIMEN	TEMP	MODE 1		MODE 2	
	°C	$f_1$ , Hz	1	$f_2$ , Hz	2
T6111-10-EP-19-1 (ISD-110) (0.010 in.)	76	203	0.099	-	-
	76	203	0.099	1257	0.123
	74	203	0.118	1346	0.110
	74	198	0.126	1145	0.157
	74	200	0.125	-	-
	70	204	0.098	1174	0.140
	75	208	0.144	1496	0.290
	70	208	0.101	1287	0.117
	68	209	0.081	1289	0.141
	66	211	0.090	1276	0.073
	68	206	0.083	1330	0.104
	70	205	0.088	1227	0.134
	68	207	0.089	1222	0.082
	AVERAGE	71.5	205	0.102	1277
LDEF-1-GE/111-10 (CONTROL)	70	209.5	0.129	1301	0.196
	68	224	0.103	1381	0.123
	62	226	0.097	1403	0.096
	69	226	0.102	1391	0.116
	68	223.5	0.103	1389	0.131
	70	224	0.107	1393	0.128
	64	228	0.092	1415	0.148
	66	227	0.088	1409	0.158
	AVERAGE	67.1	223.5	0.103	1385
LDEF-1-GE/110-10 (Preflight [2])	70	218.4	0.0252	1394.8	0.0629
	70	210.8	0.0346	1360.1	0.0857
	70	227.9	0.1479	1429.8	0.0686
L6111-10-EP17-1 (ISD-112) (0.002 in.)	63	204.5	0.020	1322	0.019
	63	204.5	0.020	1322	0.018
	64	205	0.022	1321	0.018
	65	202.5	0.015	1318	0.019
	65	205	0.020	1320	0.018
	AVERAGE	64.0	204.3	0.019	1321
LDEF-1-GE/112-2 (Preflight [2])	70	191.0	0.0188	1240.1	0.0236
	70	195.3	0.0251	1237.5	0.0261
	70	189.6	0.0258	1200.1	0.0273
	70	201.0	0.0323	1242.7	0.0237
	70	184.2	0.0179	1226.8	0.0267

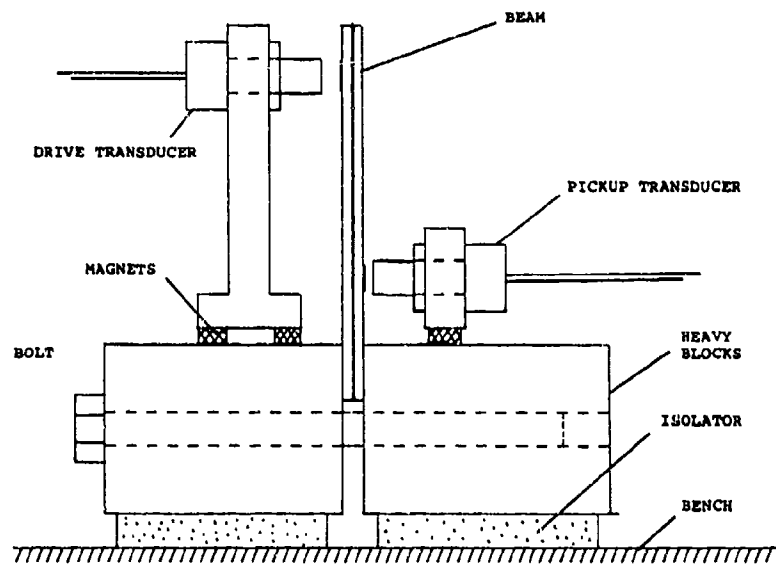


Figure 3. Vibration Test Configuration

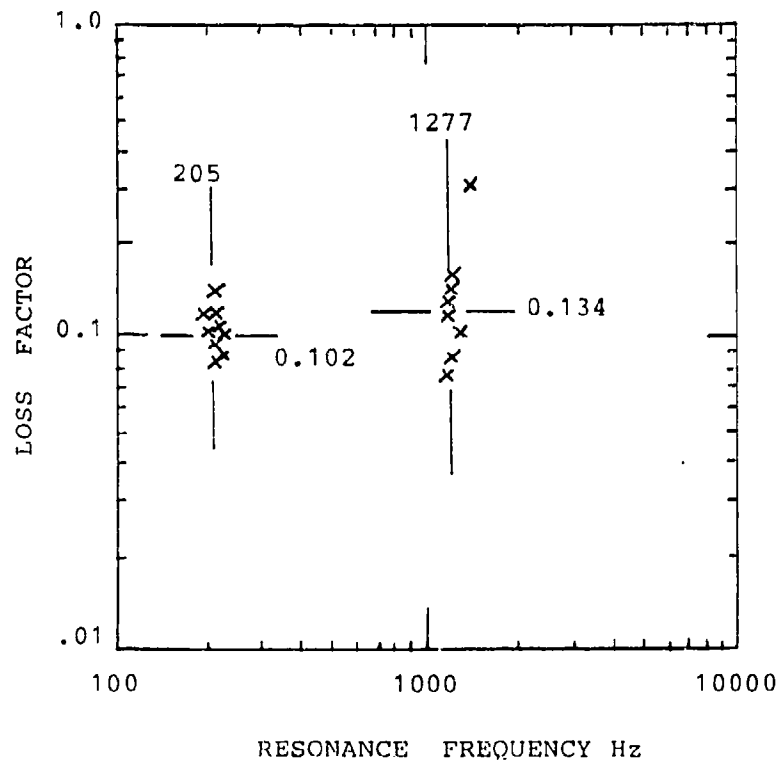


Figure 4. Plot of Modal Loss Factor Versus Resonance Frequency for ISD-110 Specimen After Exposure

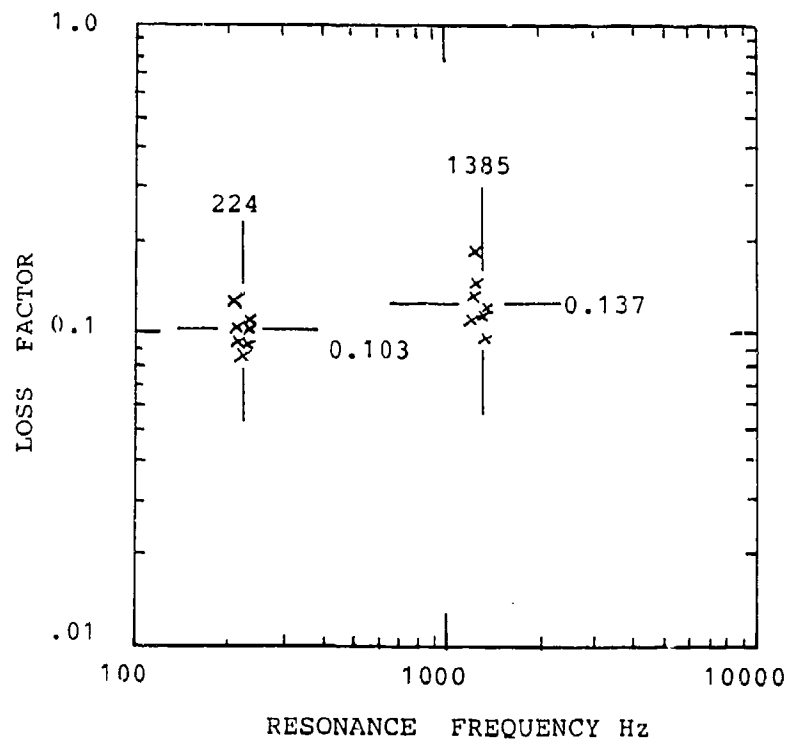


Figure 5. Plot of Modal Loss Factor Versus Resonance Frequency for ISD-110 Control Specimen

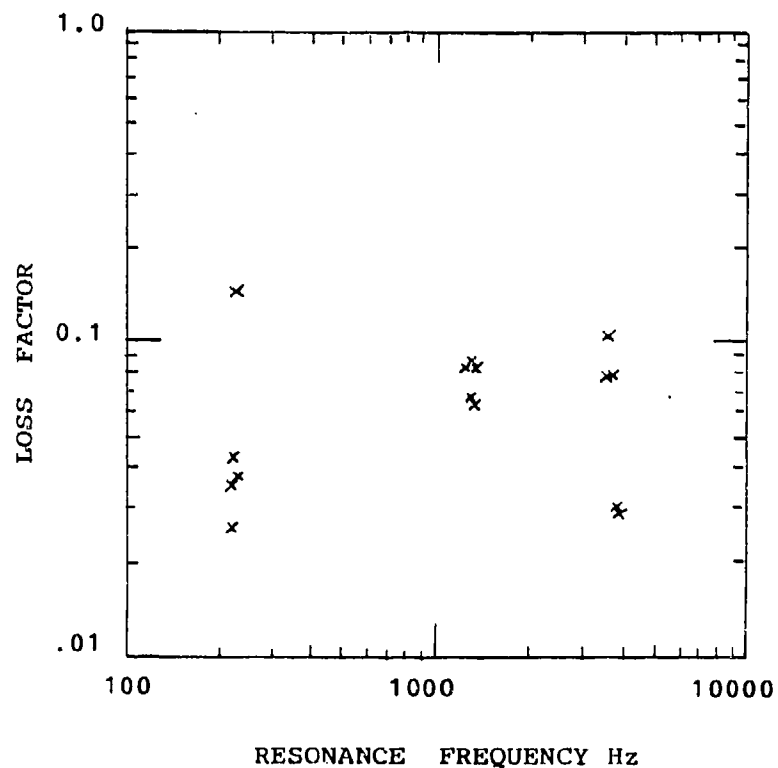


Figure 6. Plot of Modal Loss Factor Versus Resonance Frequency for ISD-110 Pre-Flight Specimen [2]

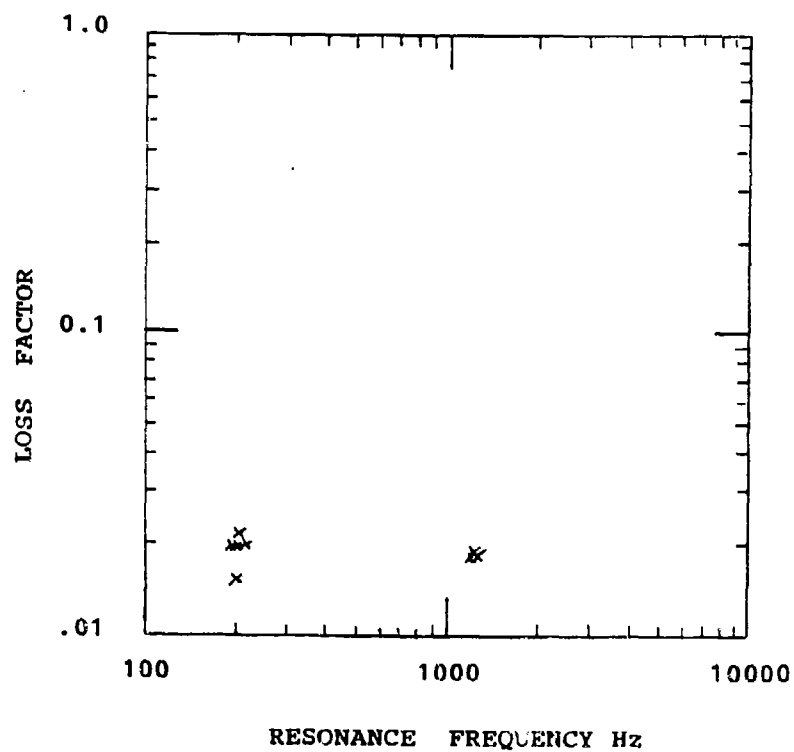


Figure 7. Plot of Modal Loss Factor Versus Resonance Frequency for ISD-112 Specimen After Exposure

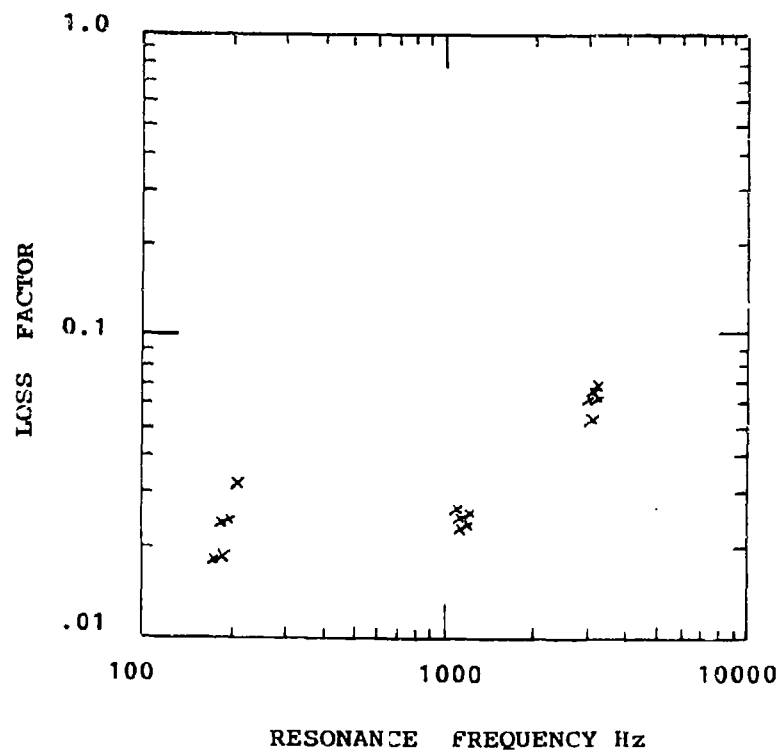


Figure 8. Plot of Modal Loss Factor Versus Resonance Frequency for ISD-112 Pre-Flight Specimen [2]

## **A MODAL STRAIN ENERGY APPROACH TO THE PREDICTION OF RESISTIVELY-SHUNTED PIEZOCERAMIC DAMPING**

**Christopher L. Davis<sup>†</sup>**  
The Pennsylvania State University

**George A. Lesieutre**  
The Pennsylvania State University

### **ABSTRACT**

The use of piezoceramic materials with resistive shunting circuits has been shown to increase passive vibration damping. An ability to tailor the frequency dependence of damping is especially attractive when active linear time-invariant control of uncertain structures is to be attempted. A method for predicting the damping performance of resistively-shunted piezoceramics based on a variation of the modal strain energy approach has been developed. The damping for a structural mode of vibration is found as the product of the fraction of modal strain energy stored in the piezoceramic material, an effective piezoceramic material loss factor, and a frequency shaping factor. A finite element model is used to determine the effective modal strain energy fraction. The effective material loss factor is related to the piezoceramic electromechanical coupling coefficient, while the frequency shaping factor is related to the dynamics of the shunting circuit. Design concerns include the effect of stiff piezoceramic material on mode shapes, the frequency dependence of piezoceramic elastic properties, and the effect of adhesive on load transfer from the structure to the piezoceramic. Analytical and experimental results are presented for a cantilevered beam with two resistively shunted piezoceramic plates. The results show good agreement between predicted and measured added damping.

---

<sup>†</sup> Department of Aerospace Engineering, 233 Hammond Building, State College, PA 16802, (814) 863-7502



## INTRODUCTION

Damping structural vibrations is a key factor in enhancing the performance of many engineering systems. With the advent of large flexible space structures comes the need for better methods of controlling structural dynamic response while not significantly increasing structural mass. This is especially important in precision space-based interferometers and earth-observing satellites. In order to assure broadband linear time-invariant (LTI) control of uncertain structural dynamic systems, a minimum level of passive damping is required within the control bandwidth [1].

Discrete damping devices, viscoelastic treatments, or active control have been used to damp unwanted structure vibrations. The performance of a discrete damping device (such as a mass on a viscoelastic spring) is sensitive to tuning to a specific frequency. Viscoelastic surface damping treatments offer high damping capability over a broad frequency range [2], but because of low stiffness, often do not participate significantly in terms of strain energy fraction. The use of piezoceramics combines tunability with high stiffness. In addition, piezoceramics also offer relative temperature insensitivity.

Piezoceramic materials generate electric fields in response to mechanical strains, or undergo mechanical strains when a field is applied across them. This facilitates use both as sensors and actuators. Small amounts of piezoceramic material may be distributed along a structure without significantly increasing mass or passive dynamic properties [3]. The piezoceramics can be used in conjunction with 'tuned' electrical circuits to increase damping in a structure. This involves converting mechanical strain energy to electrical energy via the piezoelectric effect, and dissipating it via joule heating through a passive electrical network (such as a resistor, in the simplest case). Thus, a possible solution to the above mentioned problem of requiring a minimum level of passive damping could involve the use of networks of resistively shunted piezoceramics.

The first to propose such an idea were Forward [4] and Edwards and Miyakawa [5]. Much of the modeling and analytical derivation for damping structural vibrations with piezoelectric materials and passive electrical networks has been done by Crawley, Hagood, and von Flotow et al [3, 6]. These works characterize the electro-mechanical interactions of a structure and a piezonetwork, and offer some experimental verification.

The focus of this research is to expand upon this previous work by creating a method which best utilizes this technique. Ideally, the incorporation of this technique into a mature method for predicting structural damping (i.e. the modal strain energy approach) would enhance its acceptance. Such a method for predicting the amount of added damping a resistively shunted piezoceramic network is described.

This work has addressed several steps. First, a relatively simple analytical model of the structure and attached piezoceramic element is created. Next, a computer code generates a 'map' of the fraction of strain energy found in the piezoceramic as a function of position on the structure. A more detailed finite element model of the structure and piezoceramic pieces is then created using these results as guides for piezoceramic placement. The FEM solution yields an approximation of the total strain energy of the system and each piezo element. The ratio of the strain energy in the piezoceramic element to the total system strain energy is then used to predict the amount of added damping possible for a given mode. Finally, two experiments are presented. The first characterizes the amount of added damping per mode per individual ceramic element, while the second shows the effect of combining sets of piezoceramic pairs for increased damping in several modes simultaneously.

## BACKGROUND

### ANELASTIC RELAXATION DAMPING

Real materials which exhibit both an instantaneous linear elastic response and a time dependent non-elastic response are considered anelastic. The magnitude of the time dependence is directly related to the relaxation strength,  $\Delta$ , and the relaxation time constant,  $\tau_e$ , of the material. The relaxation strength relates the apparent instantaneous (unrelaxed) modulus,  $M_U$ , and the long-term (relaxed) modulus,  $M_R$ , through the following:

$$M_U = M_R(1 + \Delta) \quad (1)$$

Such a material with a single relaxation exhibits a frequency-dependent complex modulus  $M(\omega) = M_1(\omega) + iM_2(\omega)$  as follows:

$$M_1(\omega) = M_R \left\{ 1 + \Delta \frac{\omega^2 \tau_e^2}{1 + \omega^2 \tau_e^2} \right\} \quad (2)$$

and

$$M_2(\omega) = M_R \Delta \frac{\omega \tau_e}{1 + \omega^2 \tau_e^2} \quad (3)$$

This frequency-dependent loss factor may also be expressed as:

$$\eta(\omega) = \frac{M_2(\omega)}{M_1(\omega)} = \frac{\Delta \omega \tau_e}{1 + (1 + \Delta) \omega^2 \tau_e^2} \quad (4)$$

It can be shown that this loss angle (or also sometimes called the "internal friction") of an anelastic material (which is actually a measure of how much the strain lags the stress) can be expressed as:

$$\eta(\omega) = \eta_{\max} F(\omega) \quad (5)$$

where

$$\eta_{\max} = \frac{\Delta}{2(1 + \Delta)^{1/2}} \quad (6)$$

$$F(\omega) = \frac{2\omega \tilde{\tau}}{1 + \omega^2 \tilde{\tau}^2} \quad (7)$$

$$\tilde{\tau} = \tau_e(1 + \Delta)^{1/2} \quad (8)$$

## PIEZOCERAMIC STRUCTURAL INTERACTION

For damping applications discussed herein, piezoelectric elements are bonded to the structure, allowing load transfer from the structure to the piezoceramic element. Piezoelectric strain energy is then converted to electrical energy and dissipated through a passive electrical network. The following is a brief description of the interaction between piezoceramic and structure.

First, a coordinate system is defined with respect to a thin piezoceramic plate (Figure 1).

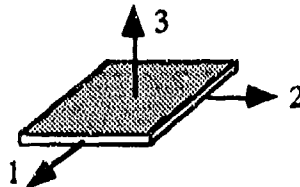


Figure 1. Coordinate Convention

By convention, the "3" direction corresponds to the poling direction of the material. With these coordinates, the different modes of the piezoelectric element can be defined. For the work described in this paper, the "3-1" or transverse mode of the piezoceramic is used. In terms of the mechanical coupling coefficient,  $k_{31}$ , mechanical strain in the 1-direction results in a potential difference between the electrodes in the 3-direction. The potential difference occurs in the 3-direction because the material is "poled" in that direction.

Figure 2 shows a simple schematic of two equally sized piezoceramic plates attached to a beam in bending.

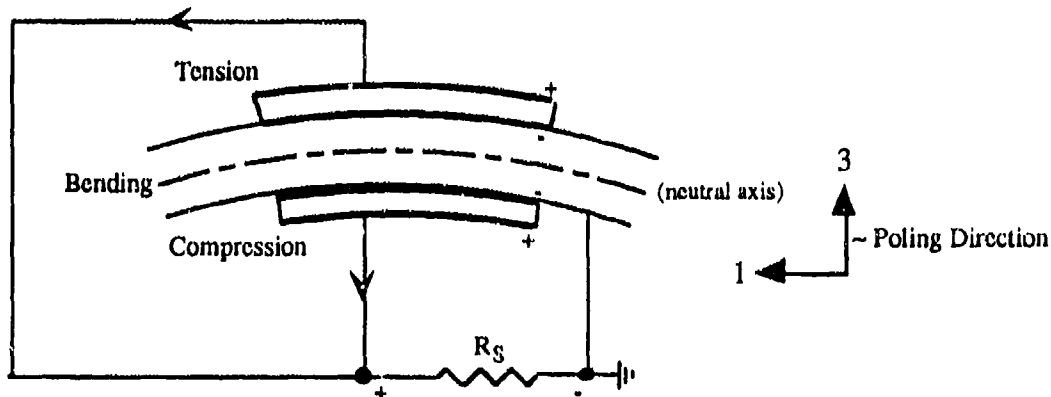


Figure 2. Piezoelectric Element and Structure Coupling

Note that both plates are poled in the same direction, but create opposite field directions due their relative locations (upper plate in tension, lower in compression). If the beam is considered ground and the piezoceramic plates are connected as show in figure 2 (i.e. in parallel), deflection in the negative "3" direction produces a current in the direction shown. For an oscillating beam, the current alternates direction and varies with the frequency of the structural vibration. The resistor coupled with the inherent capacitance of the piezoceramic provides the means for dissipation of the converted electrical energy. As will become evident later, the resistor effectively modifies the frequency dependent loss factor and stiffness of the piezoceramic to resemble that of a viscoelastic material. While not addressed in this paper, the shunt resistance,

$R_S$ , could be replaced by other passive electrical circuits such as an inductor and resistor in series thereby achieving an analogy to the mechanical vibration absorber [6].

## MODIFICATION OF RELAXATION TIME CONSTANT

The relaxation strength,  $\Delta$ , may be defined in terms of the appropriate piezoelectric electromechanical coupling coefficient,  $k_{ij}$ . The coupling coefficient is the ratio of the peak electrical energy stored by the inherent capacitance of the piezoceramic to the peak energy stored in the material as a mechanical strain under constant electrical displacement. For a uniaxial force in the  $j$  direction and electric field in the  $i$  direction:

$$k_{ij} = \frac{d_{ij}}{\sqrt{s_{jj}^E \epsilon_i^T}} \quad (9)$$

where  $d_{ij}$  is the piezoelectric constant,  $s_{jj}^E$  is the material compliance at constant field, and  $\epsilon_i^T$  is the dielectric constant at constant stress. Note that  $(k_{ij})^2$  represents the fraction of mechanical work that is converted to electrical energy. The relaxation strength can now be expressed in terms of  $k_{ij}$  as:

$$\Delta = \frac{k_{ij}^2}{1 + k_{ij}^2} \quad (10)$$

In the case considered here,  $k_{31}$  is of interest. Finally, the characteristic time constant for the system under constant strain,  $\tau_\epsilon$ , for the case of purely resistive shunting is equal to:

$$\tau_\epsilon = RC^S \quad (11)$$

where  $R$  is the shunt resistance, and  $C^S$  is the total capacitance measured at constant strain. For a rectangular piezoceramic plate,  $C^S$  is:

$$C^S = \frac{A\epsilon^S}{l} \quad (12)$$

where  $A$  is the area of the electrodes,  $l$  is the thickness of the piezoceramic plate, and  $\epsilon^S$  is the dielectric constant measured at constant strain.

## MODIFIED MODAL STRAIN ENERGY METHOD

### EFFECTIVE STRAIN ENERGY FRACTION

For a vibration mode of a composite structure, the total damping can be expressed as the sum of each constituent's damping scaled by the contribution of each constituent to the total strain energy of the mode [2]. When calculating this strain energy fraction for a piezoceramic element, it is necessary to take into account the effect of the poling direction of the piezoelectric (i.e. which way the field direction and resulting current are created). Take, for instance, a piezoelement centered directly on a strain node (half the plate compression, half in tension). The net effect would be little or no current generated thus rendering the shunt resistance useless.

Therefore it is necessary to introduce the "effective strain energy fraction of the piezoceramic",  $V^*$ , as follows:

$$V^* = \frac{V_p}{U_s + U_p} \quad (13)$$

where  $U_s$  is the total strain energy in the base structure,  $U_p$  is the strain energy in the piezoceramic, and  $V_p$  is the effective strain energy of the piezoceramic. The effective strain energy is found not by squaring the curvature of the beam, but rather by multiplying the absolute value of curvature of the beam by the curvature of the beam. This product is then integrated over the length of the piezoelement and assigned as a positive value via a second absolute value operation. The overall result is a volume integral of a non-positive semidefinite quantity. For a piezoceramic plate element bonded to a beam in transverse bending,  $V_p$  is given by:

$$V_p = \frac{1}{2} E_p J_p \int_0^L \left( \frac{\partial^2 w}{\partial x^2} \right) \left| \frac{\partial^2 w}{\partial x^2} \right| dx \quad (14)$$

For the specific case of a vibrating cantilevered beam, the transverse displacement,  $w(x)$ , is given by:

$$w(x) = (\sin \beta L - \sinh \beta L)(\sin \beta x - \sinh \beta x) + (\cos \beta L + \cosh \beta L)(\cos \beta x - \cosh \beta x) \quad (15)$$

where  $\beta L$  is an eigenvalue of the system characteristic equation for a given mode.

A computer program was created to calculate  $V^*$  as a function of mode number and location of the piezoceramic plate from the root of the beam. It assumes that such a plate is perfectly bonded to the beam, which experiences a pure vibrational mode shape. Table 1 shows the material properties and dimensions used in the example case. The results for the first three modes of a cantilevered beam with a pair of identical surface-bonded piezoceramic plates (one on either side of the beam) are shown in Figure 3.

Table 1. Material Specifications

Material	T-2024 Aluminum	Lead Zirconate Titanate PKI 550
Length (in)	16	1
Width (in)	1	1
Thickness (mils)	125	23
Young's Modulus ( $\times 10^6$ psi)	10.40	10.03
Coupling Coefficient, $k_{31}$	--	0.34
Dielectric Constant, $\epsilon^S$ (F/in)	--	$0.033 \times 10^{-8}$
Capacitance (clamped), $C^S$ (F)	--	$1.469 \times 10^{-8}$

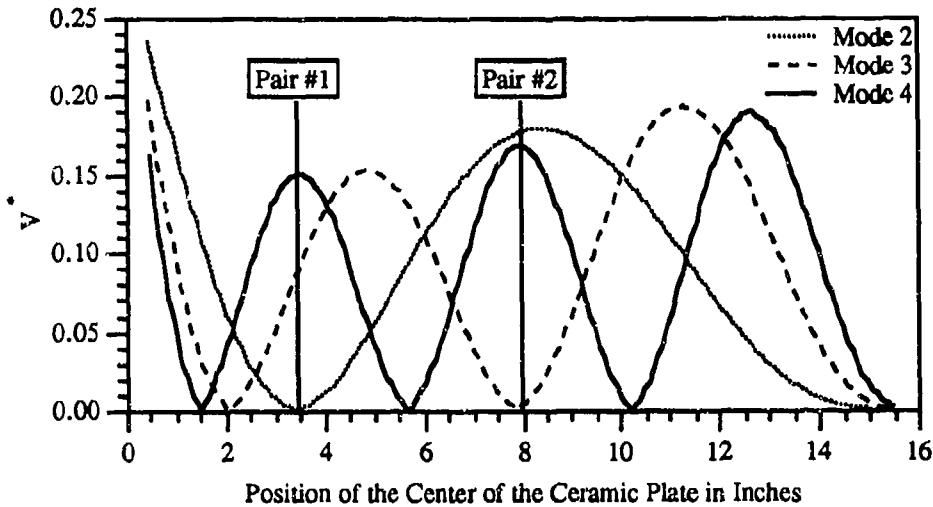


Figure 3. Strain Energy Map for Piezoelectric Element Placement

Mode 1 is excluded because it was not used in experimental work. As seen in Figure 3, there are some locations (strain nodes) at which  $V^*$  will be effectively zero. This is not possible with conventional damping treatments. These results provide insight into the key features that govern behavior, but are limited in that a "pure" mode shape was used. In reality, piezoelectric elements can significantly stiffen the structure locally and adversely affect the mode shape. For this reason, these initial results were only used as a first step to guide piezo placement in a more detailed calculation of the strain energy fraction.

### ADDED DAMPING AND FREQUENCY TUNING

As stated earlier, the total damping for a given mode can be expressed as the sum of each constituent's damping scaled by the contribution of each constituent to the total strain energy of the mode. This relates the purely material and structural parameters,  $\eta_{\max}$  and  $V^*$ , to the tuning ability of the piezoceramic-passive circuit element as follows:

$$\eta(\omega) = \underbrace{\eta_{\max}}_{\text{material}} \underbrace{V^*}_{\text{structural}} \underbrace{F(\omega)}_{\text{tuning}} \quad (16)$$

With this in mind, the piezoelectric damping added to a structural vibration mode "j" in terms of modal damping ratio  $\zeta$ , can be approximated (for small constituent damping) by:

$$\zeta_j(\omega) = \sum_{i \text{ piezos}} \frac{1}{2} \eta_{\max, i} V_{ij}^* \frac{2 \left( \omega_j / \omega_{0i} \right)}{1 + \left( \omega_j / \omega_{0i} \right)^2} \quad (17)$$

where  $\omega_{0j}$  is the inverse of the electrical relaxation time constant of the passive circuit formed by the inherent capacitance of the piezoelectric and the resistance of the passive circuit for a given mode. For the  $j^{\text{th}}$  structural vibration mode,  $\omega_0$  is formulated by combining equations (6), (10), and (11) into:

$$\omega_{oi} = R_o C^s (1 + \Delta)^{1/2} \quad (18)$$

Note that by substituting (17) into (16) and canceling the one-half and the two, the frequency ratio  $\omega/\omega_{oj}$  can be expressed as  $R_j/R_{oj}$  and equation (16) becomes:

$$\zeta_j(R_j) = \sum_{i \text{ piezos}} \frac{1}{2} \eta_{\max_i} V_{ji}^* \frac{2 \left( \frac{R_j}{R_{oi}} \right)}{1 + \left( \frac{R_j}{R_{oi}} \right)^2} \quad (19)$$

Therefore, in order to tailor the design of frequency dependent damping, the designer must choose the appropriate combination of material and structural materials. Material choices will define the maximum allowable added damping and structural choices will decide the participation of the maximum allowable. Once this is defined, the use of an external tuning variable (i.e. the resistance, R) will allow this damping to be effectively turned on or off for a given mode.

### PREDICTING THE EFFECTIVE STRAIN ENERGY FRACTION

Two locations (Pair #1 and Pair #2) were selected from Figure 3 for two pairs of surface bonded piezoceramic plates. These locations were chosen because they each have very near peak  $V^*$  values in some modes, and almost zero  $V^*$  values in other modes. This was exploited in later experimental work. A finite element model was then created using commercial finite element modeling software. In order to make the model more realistic, an adhesive layer was also included between the piezoceramic and beam elements. The F.E. code calculates the modal strain energy for each element ( $V_p$ ), an external program adds all elemental values and calculates  $V^*$  for each piezoceramic plate pair. Table 2 shows the F.E. results and the corresponding values as predicted using the pure mode shape method for modes 2, 3, and 4.

Table 2. Predicted  $V^*$  Values

Mode #	Plate Pair #1		Plate Pair #2	
	Pure Mode Shape $V^*$ Prediction (%)	F.E.M. $V^*$ Prediction (%)	Pure Mode Shape $V^*$ Prediction (%)	F.E.M. $V^*$ Prediction (%)
2	0.1832	0.0361	16.2341	3.2660
3	7.6474	1.8104	0.3515	0.0484
4	11.9499	3.3847	13.7625	3.8447

Clearly, there exists a large difference in these values. Close examination of the F.E. mode shapes show that the plates significantly stiffen the structure locally. This makes use of the pure mode shapes inappropriate for predicting  $V^*$  magnitudes but still fairly accurate for initial placement purposes. Figure 4 illustrates this by comparing the cantilever beam mode shape,  $w(x)$ , and F.E. transverse displacements.

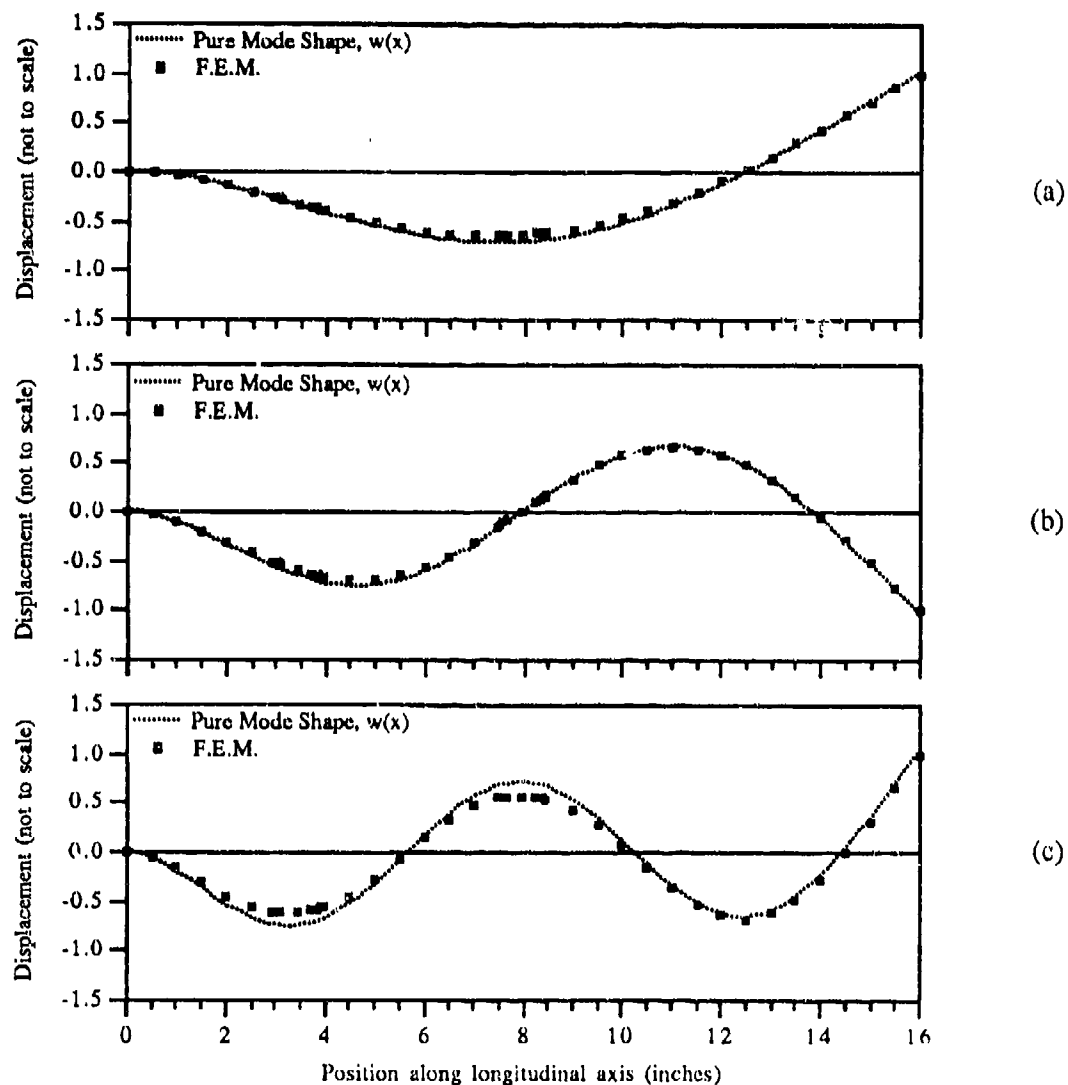


Figure 4. Change in Mode Shape Due to Addition of Surface Bonded Piezoceramic Material

As indicated by the plots, the deflection of the beam in areas with bonded piezoceramic materials exhibit decreased curvature and displacement. This can be thought of as experiencing a hinge condition at each edge of the piezoceramic plate with little curvature resulting between them.

## EXPERIMENTAL RESULTS

### FREQUENCY TUNING VERIFICATION

The ability to predict the amount of added damping with confidence is one of the main focuses of this paper. An experiment was developed based on the materials and structural



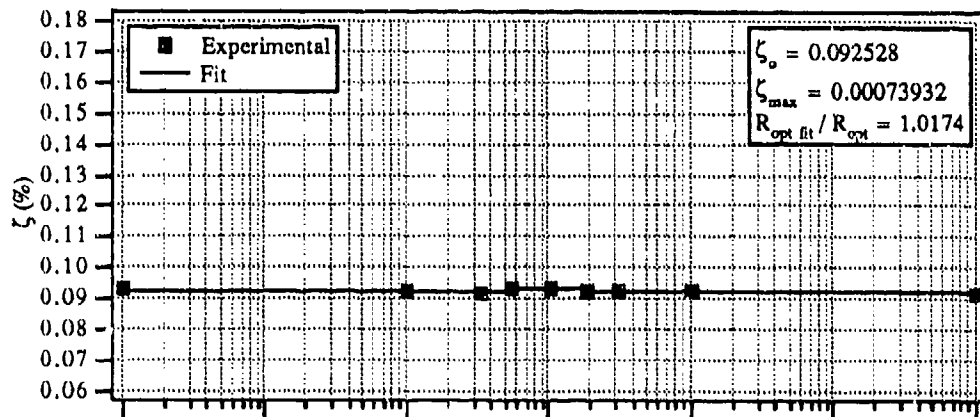
configurations used in the pure mode shape and F.E. prediction programs to test the predictability and "tunability" of the damping. Each plate pair was tested in each mode by varying the shunt resistance,  $R$ , from 1/10 to 10 times the optimal value calculated for that mode (including short circuit,  $R \approx 0$ , and open circuit,  $R \approx \infty$ ). For each value of shunt resistance,  $R$ , the modal damping ratio,  $\zeta$ , was calculated from poles curve fit to swept sine frequency response data. This resulting modal damping ratios were then curve fit with the following function:

$$\zeta_{curve\ fit} = \zeta_o + \zeta_{max} \left( \frac{2\Lambda}{1 + \Lambda^2} \right) \quad (20)$$

where

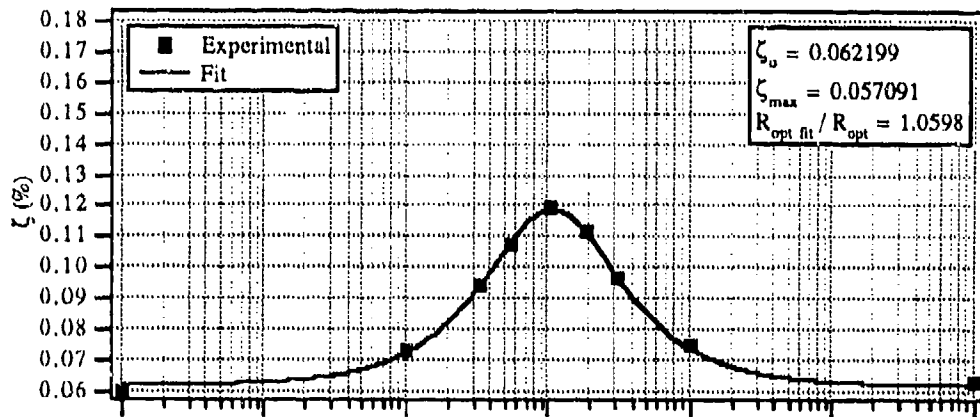
$$\Lambda = \frac{\left( \frac{R}{R_{opt}} \right)}{\left( \frac{R_{opt\ fit}}{R_{opt}} \right)} \quad (21)$$

$R_{opt\ fit}/R_{opt}$  is a measure of how well the optimal shunt resistance,  $R_{opt}$ , is predicted while  $\zeta_o$  and  $\zeta_{max}$  are the baseline and maximum added damping respectively. Figures 5 and 6 show these results for plate #1 and plate #2 respectively with (a), (b), and (c) representing modes 2, 3, and 4 respectively.



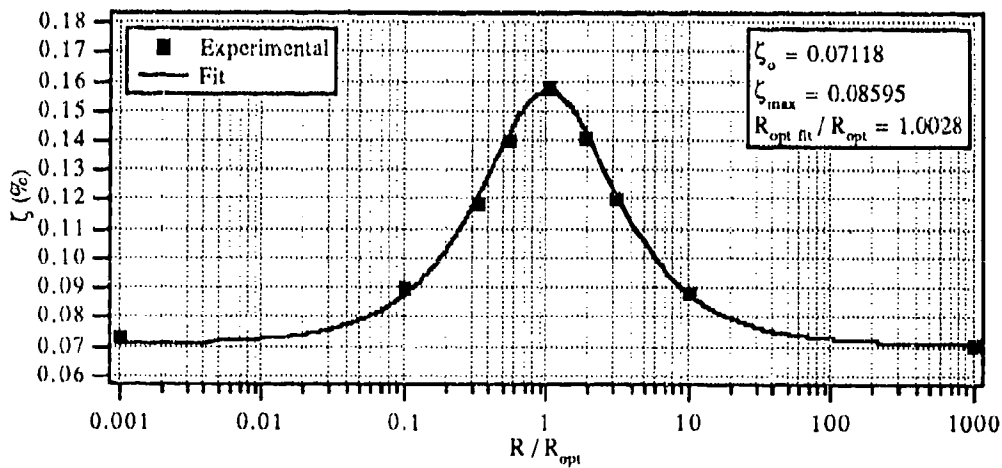
(a)

Mode 2  
(98 Hz)



(b)

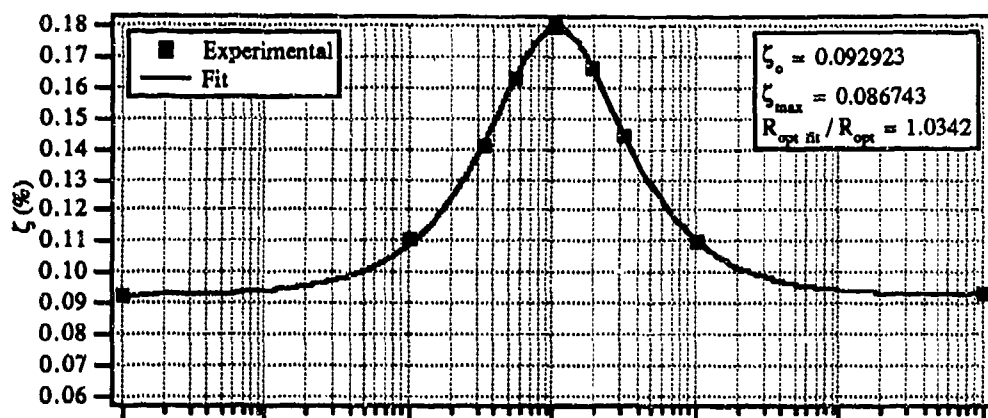
Mode 3  
(274 Hz)



(c)

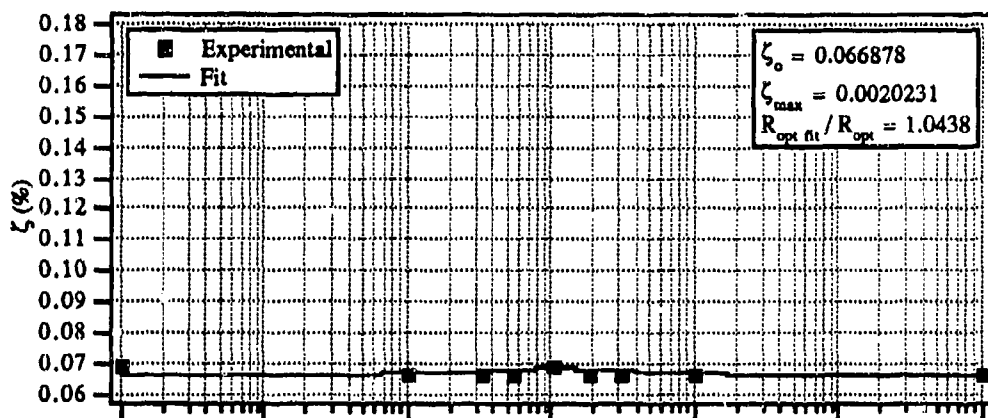
Mode 4  
(535 Hz)

Figure 5. Frequency Characterization Results for Plate Pair #1



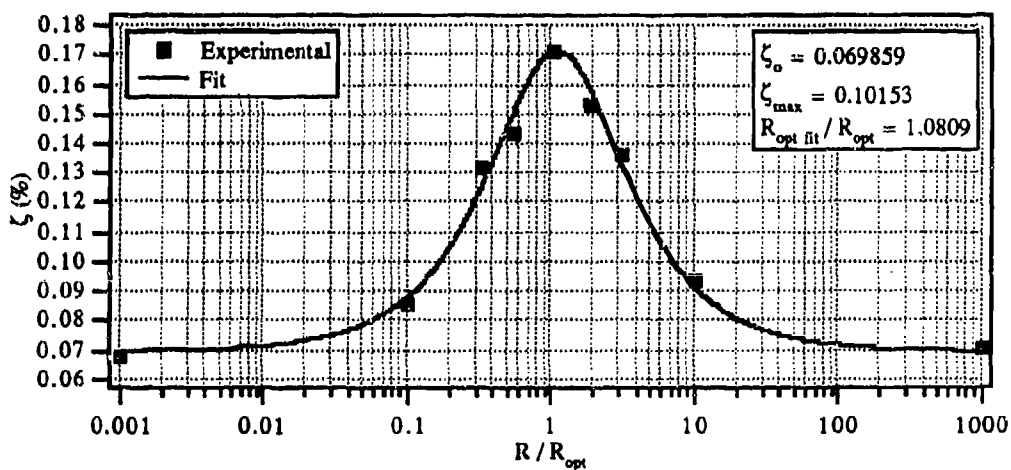
(a)

Mode 2  
(98 Hz)



(b)

Mode 3  
(274 Hz)



(c)

Mode 4  
(535 Hz)

Figure 6. Frequency Characterization Results for Plate Pair #2

These results clearly show what was predicted earlier, i.e. that plate #1 increases the damping of modes 3 and 4, but not of mode 2. Similarly, plate #2 increases the damping of modes 2 and 4, but not of mode 3. Overall, these results also agree well (generally within 5%) with the predicted values of optimal resistance. The magnitude of the added damping was also predicted fairly well, though not quite as accurately as the optimal resistance. Figures 7 and 8 illustrate the difference in added damping for each of the plates in modes 2, 3, and 4.

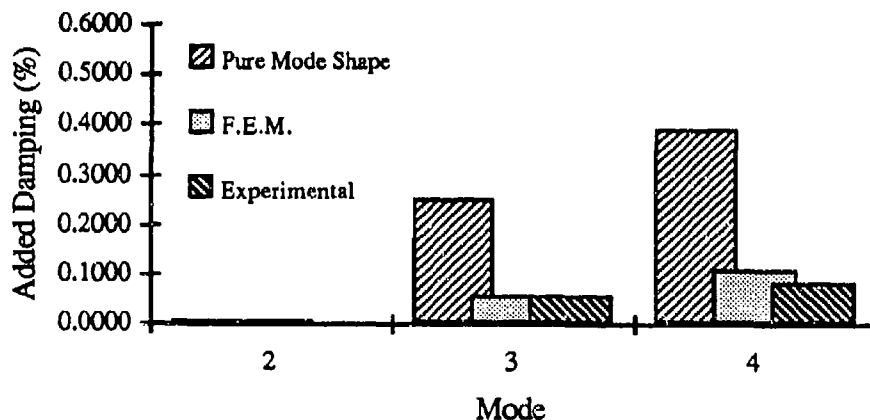


Figure 7. Added Damping by Mode for Plate #1

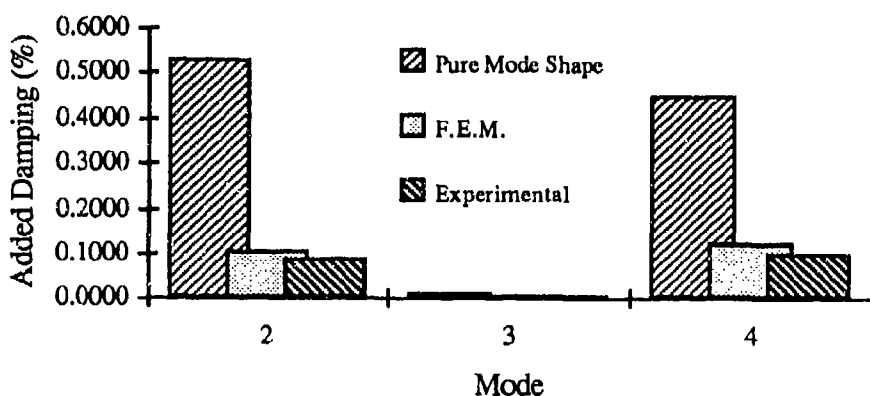


Figure 8. Added Damping by Mode for Plate #2

Clearly, the prediction of added damping using the "pure" mode shape for a cantilevered beam significantly overpredicts the amount of added modal damping. The F.E. predictions, while still higher, compare much better with experimental results.

## MULTIPLE PIEZOCERAMIC PAIR EXPERIMENTS

In addition to qualifying the tuning capability of the shunted piezoelectric network, two experiments were conducted to test the effect of shunting two plates at the same time with equal or distinct resistances. Recall that equation (18) sums the effect of "i" piezo pairs. For the first example, both plates are shunted with the optimal resistance for mode 4. For the case of two piezoceramic elements working together, the frequency tuning function becomes a function of two variables (resistance ratios). When  $R_1=R_2=10.20k\Omega$ , peak damping is achieved. Using the finite element predicted  $V^*$ 's,  $(\zeta_{\text{added}})_{\text{tot}}=0.236\%$ . Experimentally achieved added damping was

found to be 0.194% . Differences in these values for added damping can be attributed mostly to the local stiffening effect of the piezoceramic. In addition, incorrect modeling of the interface between the beam and piezoceramic plate add error to the F.E. predictions.

Another experiment addressed the addition of equal damping to two modes. This involves simultaneously solving the added damping equations for modes 2 and 3 for shunt resistances  $R_1$  and  $R_2$ . The set of resistances chosen for the experiment were  $R_1=21.67k\Omega$  and  $R_2=16.86k\Omega$ . The predicted level of added damping was 0.060% per mode. Experimentally, mode 2 damping increased by 0.047% and mode 3 by 0.061%. Difficulty in measuring such small levels of damping coupled with the before mentioned stiffening effects and modeling inaccuracies contribute to these values not being equal.

## SUMMARY AND CONCLUSIONS

A modified modal strain energy approach has been developed which allows frequency tuning of the added modal damping of a composite system. By choosing set combinations of material and structural parameters, a designer may achieve useful added damping in single or multiple structural vibrational modes. Two prediction methods were developed to determine the effective strain energy fraction of the piezoceramic additions. The first relies upon a "pure" known vibrational mode shape and offers insight into the minimum and maximum areas of effective strain energy but does not accurately predict magnitude of the effective strain energy. A finite element method uses predicted piezoceramic plate locations from the previous method to predict a more accurate level effective strain energy. Finally, the strain energy fraction and frequency shaping function are combined with classical methods for predicting the material damping loss factor to create an equation which yields total added damping for a selected vibrational mode. Experimental results confirm tunability of the damping treatment and show insight into the additive effects of multiple pair use.

## REFERENCES

1. von Flotow, A.H.; Vos, D.W., "The Need for Passive Damping in Feedback Controlled Flexible Structures," *1991 Proc. Conf. on Recent Advances in Active Control of Sound and Vibration*, Lancaster: Technomic, pp. 593-603.
2. Nashif, Ahid D.; Jones, David I. G.; Henderson, John P., *Vibration Damping*, John Wiley & Sons, New York, 1985.
3. Crawley, E.F.; de Luis, J.; Hagood, N.W.; Anderson, E.H., "Development of Piezoelectric Technology for Applications in Control of Intelligent Structures," Massachusetts Institute of Technology, Cambridge, MA.
4. Forward, Robert L., "Electronic Damping of Vibrations in Optical Structures," *Journal of Applied Optics*, Vol. 18, No.5, March 1979, pp. 690-697.
5. Edwards, R.H., Miyakawa, R.H., *Large Structure Damping Task Report*, Hughes Aircraft Co. Report No. 4132.22/1408, May 1980.
6. Hagood, N.W., von Flotow, A., "Damping of Structural Vibrations with Piezoelectric Materials and Passive Electrical Networks," *Journal of Sound and Vibration*, Vol. 146, No.1, April 1991.
7. Lesieutre, G.A., Davis, C.L., "Frequency-Shaped Passive Damping Using Resistively-Shunted Piezoceramics," proceedings of the Symposium on Active Materials and Adaptive Structures, November 1991, pp. 355-358.

# A REFINED THEORY OF FLEXURAL VIBRATION FOR VISCOELASTIC DAMPED SANDWICH BEAMS

J. M. Bai<sup>+</sup> and C. T. Sun<sup>+</sup>

Department of Aerospace Engineering,  
Mechanics and Engineering Science  
University of Florida

## ABSTRACT

The effects of more flexible core materials and interfacial bond on the dynamic response and damping of sandwich beams are studied by introducing a refined sandwich beam theory. The beam theory of the core is based on the elasticity solution of more accurate displacement assumptions, including nonlinear transverse deformation. The face layers are considered as ordinary beams with axial and bending resistance. Imperfect interface conditions between faces and core are defined as linear relations between interface displacements discontinuities and associated shear stresses. With the viscoelastic properties of the core material which is complex and is function of frequency for a given temperature, the linear equations of motion describing the vibration of the sandwich finite beam are derived based on the Hamilton principle. Consistent boundary conditions are accomplished by either prescribing the stress resultants or the corresponding time derivatives of the displacement components. Typical cases of a simply supported beam under the harmonic excitation are numerically investigated. The numerical results of a mechanical impedance example are well agreed with experimental data in the literature. The effect of core thickness and stiffness on resonance frequencies are studied parametrically. It is also shown that the imperfect bonding has a certain influence upon the loss factor of the beam.

---

<sup>+</sup> Address: Department of Aerospace Engineering, Mechanic and Engineering Science,  
University of Florida, Gainesville, FL 32611.  
Phone number: (904)392-8157

## 1. INTRODUCTION

Significant advances in the development of sandwich constructions have fostered its applications in various industry. Recent improvements in bonding techniques, face and core materials make the problem too complicated to solve by using some assumptions and simple theories. More accurate analysis is required to examine the effects of more flexible and damped core and bonding quality on the vibration damping of sandwich structures.

The beam theory of flexural vibrations for viscoelastic sandwich beams has long been interests since 1960's. In a very fundamental paper, Ross, Ungar and Kerwin[1] treated the problem by assuming the perfect bonding, the same amount of transverse displacement in each layer, the damping only from the shearing of the viscoelastic core and simply supported end conditions. DiTaranto[2] extended this analysis to freely vibrating beams having any end conditions. Based on DiTaranto's work the sixth-order differential equations of motion were derived in terms of transverse displacement by Mead and Markus[3], and this theory was correlated with experimental data by Lu and Douglas[4]. Yan and Dowell[5] used the principle of virtual work to obtain a set of five differential governing equations. A more accurate theory including the inertia effects of transverse, longitudinal and rotary motions was carried out by Rao and Nakra[6]. In recent years, various vibration theories of undamped sandwich beams have been developed by Vaswani et. al.[7], Ko[8] and Lu and Libove[9].

Existing theories of vibration damping of sandwich beams have invariably assumed perfect bonding between faces and core as well as constant transverse displacement through the thickness of the beam. Subsequently the plane of sections remains plane and the transverse normal(peeling) stresses are neglected. Nevertheless, the existence and influence of an interface layer between faces and core have been recognized during recent years[10,11]. Also it has been observed that the flexibility of the core may cause the beam to change its height and its plane of section to distort, especially for much thicker and softer core. The free vibration theory of undamped sandwich beams has been developed by Frostig and Baruch[13], considering the transverse deformation of the core.

In this paper, a refined beam theory of sandwich vibration damping is introduced to eliminate both perfect bonding and constant transverse deformation assumptions. The nonlinear displacement field of the core in both longitudinal and vertical directions through the thickness are assumed based on the elasticity solution. the face layers are considered as the ordinary beams, acting longitudinally only and interconnected with the core through equilibrium and compatibility at the interface layers. Imperfect bonding is quantitatively defined as the longitudinal displacements discontinuities at the interface layers being proportional to the associated shear stresses. The differential equations of motion are derived by using Hamilton principle in terms of five basic unknown functions. The boundary conditions are given at each face layers and core respectively, accomplished by either prescribing the stress resultants or the corresponding time derivatives of the displacement components. Numerical results of a simply



supported beam under a mechanical impedance are compared with experimental data and other theoretical analysis in the literature. The parametric studies are carried out to examine the effects of core thickness and stiffness on the resonance frequencies for a simply supported sandwich beam under the harmonic excitation. The effect of imperfect bonding on the damping of the beam is also examined and some conclusions are drawn briefly.

## 2. GOVERNING EQUATIONS OF MOTION

Consider a three layer sandwich beam of length  $\ell$  and unit width, subjected to a transverse dynamic load  $q(x,t)$ . It has face layers of thickness,  $h_1$  and  $h_2$ , and a core of thickness  $h$  shown in Figure 1. The face layers are the elastic material with high Young's moduli of  $E_1$  and  $E_3$ . The flexible core is linearly viscoelastic with a Young's modulus  $E$  and a shear modulus of  $G$  where  $E$  and  $G$  are expressed by complex numbers under the harmonic excitation.

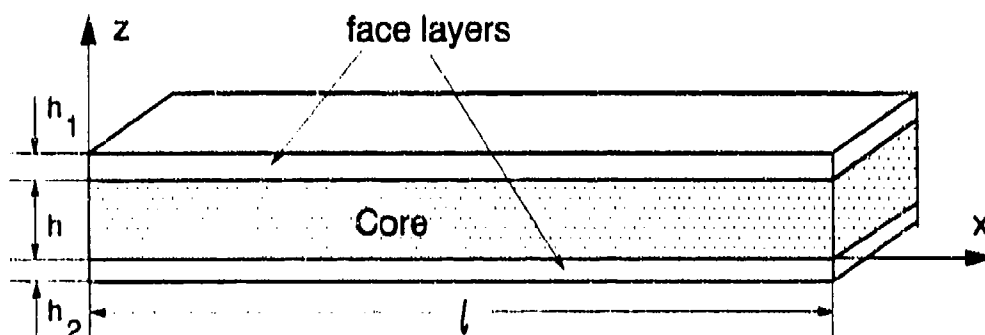


Figure 1. Sandwich beam construction

The following assumptions underline the present development

1. The elastic face layers are considered as ordinary beams with axial and bending resistance.
2. The viscoelastic core carries null longitudinal stresses, but takes nonlinear displacement fields in both  $x$  and  $z$  directions.
3. The longitudinal displacement discontinuity (slip) is proportional to the shear stress at the face-core interface.

Based on the assumption 1 and 2, the following displacement fields are given

For the top and bottom face layers:

$$\begin{aligned} u^i(x, z, t) &= u_1(x, t) - z_1 \frac{\partial w_1(x, t)}{\partial x} \\ w^i(x, z, t) &= w_1(x, t) \end{aligned} \quad (1)$$

$$u^b(x, z, t) = u_2(x, t) - z_2 \frac{\partial w_2(x, t)}{\partial x} \quad (2)$$

$$w^b(x, z, t) = w_2(x, t)$$

For the core:

$$u^c(x, z, t) = u_0(x, t) - z \frac{\partial w_0(x, t)}{\partial x} + e \psi(x, t) - \frac{z^2}{2} \frac{\partial \phi(x, t)}{\partial x} + \frac{z^3}{6} \frac{\partial^2 \psi(x, t)}{\partial x^2} \quad (3)$$

$$w^c(x, z, t) = w_0(x, t) + z \phi(x, t) - \frac{z^2}{2} \frac{\partial \psi(x, t)}{\partial x}$$

where superscripts t, b and c denote top, bottom face layers and the core,  $u_i(x, t)$  and  $w_i(x, t)$  ( $i=0, 1, 2$ ) are the longitudinal and vertical displacements of the centroid of the core and face layers and  $z_1 = z - h - h_1/2$ ,  $z_2 = z + h_2/2$  are measured from the centroid of the faces respectively, as shown in Figure 2. Deformation pattern and sign convention for stresses, resultants and displacements also appear in Figure 2.

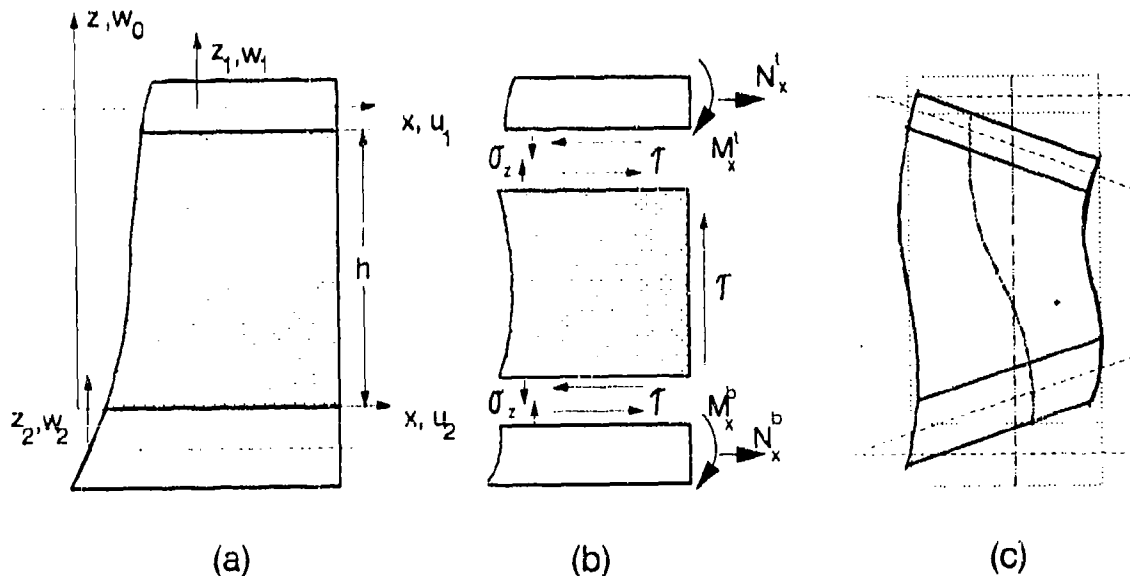


Figure 2. (a) Geometry (b) Sign convention (c) Deformation pattern

The Kinematic relations for the face layers, using small deformation theory, can be written as:

$$\epsilon_x^t = \frac{\partial u_1}{\partial x} - z_1 \frac{\partial^2 w_1}{\partial x^2} \quad (4)$$

$$\epsilon_x^b = \frac{\partial u_2}{\partial x} - z_2 \frac{\partial^2 w_2}{\partial x^2} \quad (5)$$

The Kinematic relation for the core is:

$$\begin{aligned} \epsilon_z^c &= \phi(x, t) - z \frac{\partial \psi(x, t)}{\partial x} \\ \gamma_{xz}^c &= e \psi(x, t) \end{aligned} \quad (6)$$

where  $e$  is a constant to be determined by Hamilton principle.

The Compatibility conditions of deformations between the faces and the core are described by imperfect interface conditions and the continuity conditions of transverse normal displacement at the interface.

At  $z=h$  (upper interface)

$$\tau^c = K(u^t - u^c) \quad (7)$$

$$w^c = w^t \quad (8)$$

At  $z=0$  (lower interface)

$$\tau^c = K(u^c - u^b) \quad (9)$$

$$w^c = w^b \quad (10)$$

where  $K$  is called adhesive bonding stiffness. Small values of  $K$  represent the weak bonding layer between the faces and the core. When  $K \rightarrow \infty$ , it approaches perfect bonding interface that is usually assumed in the sandwich theory.

Elimination of  $u_0(x,t)$ ,  $w_0(x,t)$ , and  $\phi(x,t)$  yields an independent compatibility equation:

$$K(u_1 - u_2 + \frac{h_1 + h}{2} \frac{\partial w_1}{\partial x} + \frac{h_2 + h}{2} \frac{\partial w_2}{\partial x}) - (Ke + 2E_c)\psi + K \frac{h^3}{12} \frac{\partial^2 \psi}{\partial x^2} = 0 \quad (11)$$

A set of force and moment resultants are defined for top and bottom faces separately:

$$N_x^i = \int_{-\frac{h_j}{2}}^{\frac{h_j}{2}} \sigma_x^i dz_j$$

$$M_x^i = \int_{-\frac{h_j}{2}}^{\frac{h_j}{2}} \sigma_x^i z_j dz_j \quad (12)$$

where  $i=t, b$  correspond to  $j=1, 2$  respectively.

Then the constitutive relations can be written as follows,  
For the elastic face layers:

$$N_x^t = E_1 A_1 \frac{\partial u_1}{\partial x}$$

$$N_x^b = E_2 A_2 \frac{\partial u_2}{\partial x}$$

$$M_x^t = -E_1 I_1 \frac{\partial^2 w_1}{\partial x^2}$$

$$M_x^b = -E_2 I_2 \frac{\partial^2 w_2}{\partial x^2} \quad (13)$$

where  $E_i A_i$  and  $E_i I_i$  are the axial and the flexural rigidities of the face layers.  
For the viscoelastic core:

$$\sigma_z^c = E_c \epsilon_z^c = E_c (\phi - z \frac{\partial \psi}{\partial x})$$

$$\tau_{xz}^c = \tau^c = G_c \gamma_{xz}^c = G_c e \psi \quad (14)$$

where  $G_c$ ,  $E_c$  and  $e$  are complex constants.

The governing equations of motion and the boundary conditions are derived via variational calculus, the Hamilton principle, which requires:

$$\delta \int_{t_1}^{t_2} [T - U] dt = 0 \quad (15)$$

where  $T$  is the kinetic energy;  $U$  is the internal potential energy;  $t_1, t_2$  define the time interval.

The total kinetic energy of the sandwich beam can be expressed as:

$$\begin{aligned} T = \frac{1}{2} \int_0^l & \left\{ \rho_1 h_1 [(\dot{u}_1)^2 + \frac{h_1^2}{12} (\frac{\partial \dot{w}_1}{\partial x})^2 + (\dot{w}_1)^2] \right. \\ & + \rho_2 h_2 [(\dot{u}_2)^2 + \frac{h_2^2}{12} (\frac{\partial \dot{w}_2}{\partial x})^2 + (\dot{w}_2)^2] \\ & \left. + \int_{-\frac{h}{2}}^{\frac{h}{2}} \rho [(\dot{u}^c)^2 + (\dot{w}^c)^2] dz \right\} dx \end{aligned} \quad (16)$$

The total potential energy,  $U$ , consists of the contributions from both face layers  $U_1$  and  $U_2$ , core shear strain  $U_3$ , core normal  $U_4$ , and potential terms  $V$ , due to applied loading. The effects of imperfect bonding,  $\varphi$  is considered by introducing a Lagrange multiplier  $\lambda$  with eqn(11) into the total potential energy contributions. Thus,

$$U = U_1 + U_2 + U_3 + U_4 + \varphi + V \quad (17)$$

$$\begin{aligned} U_1 &= \frac{1}{2} \int_0^l E_1 h_1 \left[ \left( \frac{\partial u_1}{\partial x} \right)^2 + \frac{h_1^2}{12} \left( \frac{\partial^2 w_1}{\partial x^2} \right)^2 \right] dx \\ U_2 &= \frac{1}{2} \int_0^l E_2 h_2 \left[ \left( \frac{\partial u_2}{\partial x} \right)^2 + \frac{h_2^2}{12} \left( \frac{\partial^2 w_2}{\partial x^2} \right)^2 \right] dx \\ U_3 &= \frac{1}{2} \int_0^l G_c h (e \psi)^2 dx \\ U_4 &= \frac{1}{2} \int_0^l E_c h \left[ \phi^2 + \frac{h^2}{12} \left( \frac{\partial \psi}{\partial x} \right)^2 \right] dx \end{aligned} \quad (18)$$

$$\begin{aligned}\varphi = \lambda \int_0^l & \left[ K(u_1 - u_2 + \frac{h_1 + h}{2} \frac{\partial w_1}{\partial x} + \frac{h_2 + h}{2} \frac{\partial w_2}{\partial x}) \right. \\ & \left. - (Ke + 2E_c)\psi + K \frac{h^3}{12} \frac{\partial^2 \psi}{\partial x^2} \right] dx \\ V = \int_0^l & q w_1 dx\end{aligned}\quad (19)$$

where  $(\dot{\phantom{x}})$  denotes a first derivative with respect to time and  $q = q(x, t)$  is transverse distributed dynamic loading at surface of top face layer.

It is noted that  $T$  and  $U$  can be further expressed by five basic unknown functions— $u_1(x, t)$ ,  $w_1(x, t)$ ,  $u_2(x, t)$ ,  $w_2(x, t)$  and  $\psi(x, t)$ . Taking variation in Hamilton's equation with respect to  $u_1$ ,  $w_1$ ,  $u_2$ ,  $w_2$ ,  $\psi$  and  $\lambda$ , six equations of motions and boundary conditions are obtained after integration by parts in  $x$  and  $t$ , and some algebraic manipulations and substitutions. It is noted that homogeneous conditions for the displacement and the velocity at  $t=t_1, t_2$  are assumed. The physical meaning of Lagrange multiplier  $\lambda$  is the face-core interface shear force. The number of governing equations is reduced from six to five by elimination the  $\lambda$ . The governing equations can be written in the matrix form:

$$[M]\{\ddot{U}\} + [K]\{U\} = \{F\} \quad (20)$$

where

$$\{U\} = \{u_1, w_1, u_2, w_2, \psi\}^T$$

$$\{F\} = \{0, q, 0, 0, 0\}^T$$

$[M]$  — the mass matrix differential operator

$[K]$  — the stiffness matrix differential operator

It is noted that  $[K]$ ,  $\{U\}$  and  $\{\ddot{U}\}$  are complex valued and  $e = E_c/G_c$ .

The boundary conditions, at the end of the beam, are given,

at the top face layer ( $x=0$  and  $x=l$ ):

$$N_x' = 0 \quad \text{or} \quad u_1 = 0 \quad (21)$$

$$M_x' = 0 \quad \text{or} \quad w_{1,x} = 0 \quad (22)$$

$$\begin{aligned}\frac{\partial M_x'}{\partial x} + G_c h \frac{h_1}{2} \psi - \rho \frac{h_1}{6} \ddot{u}_1 - \rho \frac{h_1}{12} \ddot{u}_2 + \rho \frac{h_1^2}{12} \frac{\partial \ddot{w}_1}{\partial x} - \rho h_1 \frac{h_2}{24} \frac{\partial \ddot{w}_2}{\partial x} &= 0 \\ \text{or} \quad w_1 &= 0\end{aligned}\quad (23)$$

at the bottom face layer (  $x=0$  and  $x=l$  ):

$$N_x^b = 0 \quad \text{or} \quad u_2 = 0 \quad (24)$$

$$M_x^b = 0 \quad \text{or} \quad w_{2,x} = 0 \quad (25)$$

$$\frac{\partial M_x^b}{\partial x} + G_c h \frac{h_2}{2} \psi + \rho \frac{h_2}{6} \ddot{u}_2 + \rho \frac{h_2}{12} \ddot{u}_1 + \rho \frac{h_2^2}{12} \frac{\partial \ddot{w}_2}{\partial x} - \rho h_1 \frac{h_2}{24} \frac{\partial \ddot{w}_1}{\partial x} = 0 \quad (26)$$

or  $w_2 = 0$

at the core (  $x=0$  and  $x=l$  ):

$$\psi = 0 \quad \text{or} \quad w_1 + w_2 - h^2/6 \psi_{,x} = 0 \quad (27)$$

where the subscript ,x denotes a first partial derivative with respect to x.

### 3. SOLUTION OF FORCED HARMONIC MOTION

Consider a sandwich beam under the harmonically varying loading,

$$q(x,t) = Q(x)e^{i\omega t}$$

where  $\omega$  is the forcing frequency. In general, as the frequency of  $q(x,t)$  varies, both the amplitude and mode of vibration vary. We assumed here that the response due to the applied force is harmonic and vibrating at the excitation frequency.

Let  $\{U\}$  be

$$\{U\} = \begin{Bmatrix} u_1(x) \\ u_2(x) \\ w_1(x) \\ w_2(x) \\ \psi(x) \end{Bmatrix} e^{i\omega t} \quad (28)$$

Thus the partial differential operators change to ordinary differential operators, and the governing equations, eqn(20) becomes:

$$(-\omega^2 [M] + [K]) \{U\} = \{f\} \quad (29)$$

where  $\{f(x)\} = \{0, Q(x), 0, 0, 0\}^T$ .

The set of simultaneous ordinary differential equations described by eqn(29) can be solved using known procedures from mathematics[14], in conjunction with the boundary conditions as indicated in eqns(21) to (27). Since the motion is now harmonic, it is legitimate to admit hysteretic damping into the core by putting  $G_c = G'(1 + i\eta_G)$  and  $E_c = G'(1 + i\eta_E)$ .

To determine the loss factor of the sandwich beam, we use so called the direct frequency response method. When a forced vibration over a range of frequencies is considered, a theoretical response spectrum is generated from which the overall damping of the system is calculated. Since the complex modulus approach is used, the eqn(29) are complex. For each frequency of excitation, the displacement per unit applied force is calculated by solving the system of complex-valued simultaneous equations, and the response function is thereby generated. Loss factor is calculated from the generated response spectrum by using the half-power-bandwidth technique, or from the real part of the spectrum as shown in Figure 3.

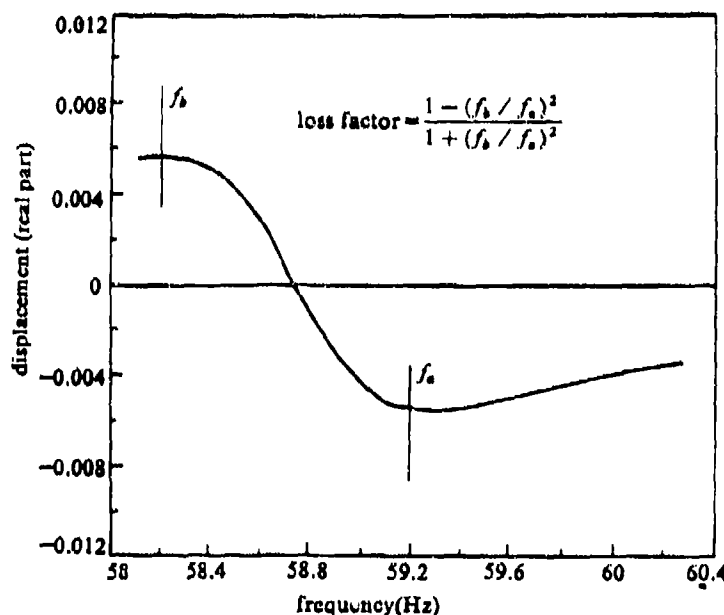


Figure 3. Real part of the response spectrum

Loss factor can also be calculated by using the energy ratio method. After the resonant frequency and the corresponding displaced shape at resonance have been calculated, the loss factor of the beam system can be calculated from

$$\eta_s = \frac{\{U^*\}^T [K''] \{U\}}{\{U^*\}^T [K'] \{U\}} \quad (30)$$

where  $\{U^*\}$  is the complex conjugate of  $\{U\}$  and

$$[K] = [K'] + i[K''] \quad (31)$$



#### 4. NUMERICAL RESULTS AND DISCUSSION

Vibration damping of simply supported sandwich beams is numerically studied. In this case, all boundary conditions are satisfied and the solution is analytical and may be expressed as:

$$\{U\} = \begin{Bmatrix} c_{u1} \cos \frac{n \pi x}{l} \\ c_{u2} \cos \frac{n \pi x}{l} \\ c_{w1} \sin \frac{n \pi x}{l} \\ c_{w2} \sin \frac{n \pi x}{l} \\ c_{\psi} \cos \frac{n \pi x}{l} \end{Bmatrix} e^{i \omega t}$$

where  $c_i$  ( $i=u1, u2, w1, w2, \psi$ ) are the amplitude coefficients and  $n$  is the wave number.

In the first example, the results corresponding to a three-layered symmetric sandwich beam used in Ref.[4] through both analytical and experimental methods are used here for comparison with the present analysis. The geometric and material properties are the same as the specimen 2 in Ref.[4]. The beam were excited by an electromechanical vibration generator which is modeled by a concentrated load applied at the mid-span of the beam. Figure 4 shows the comparison for the mechanical impedance versus frequency. It is noted that although Mead and Markus theory[3] is well agreed with the experiment data, the present theory improves the high mode results.

To examine the effects of transverse deformation and imperfect bonding, parametric studies are carried out for the variations of non-dimensional resonant frequency and loss factor of the beam system. The effect of the core thickness on the resonant frequency is presented in Figure 5. It can be seen that the resonant frequency decreases with increasing the core thickness, and Mead and Markus theory overestimates the resonant frequency especially for the thicker core. Figure 6 shows the effect of the modulus of elasticity of the core in the vertical direction on the resonant frequency. In the Mead and Markus theory,  $\epsilon_z^c=0$ , meaning that  $E_c=\infty$ , so that it overestimates the resonant frequency. Such discrepancy may be greater if the core material is getting softer. In the Figure 7, the loss factor of the beam is plotted against the adhesive bonding stiffness. It is shown that the adhesive bonding stiffness of the interface layer has a strong effect, up to a certain level, on the beam loss factor. Beyond this level, the usual assumption of perfect bonding used in classical theories is quite acceptable. This level to constitute "perfect" bonding is given in terms of the ratio of the adhesive stiffness to the core

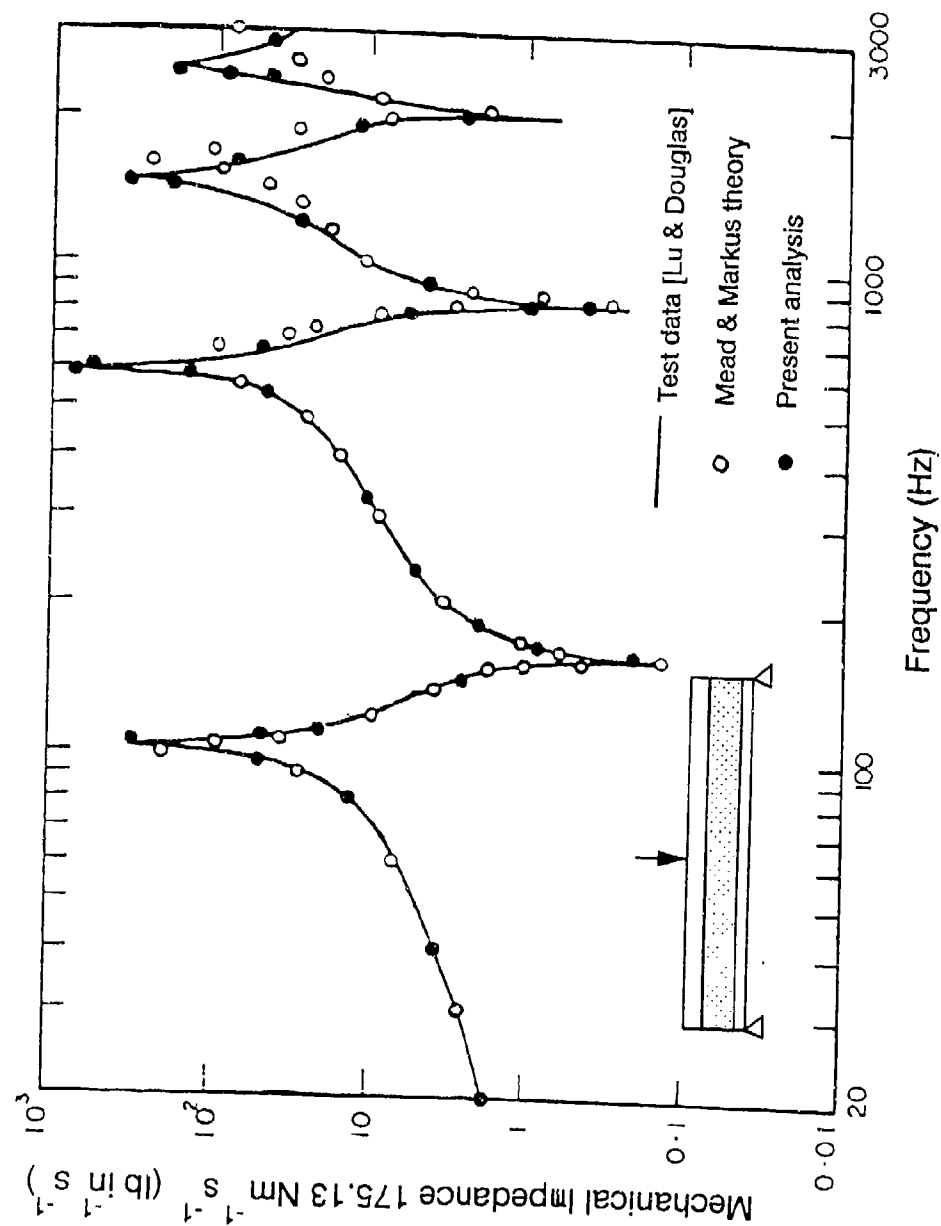


Figure 4. Driving point mechanical impedances of a damped sandwich beam

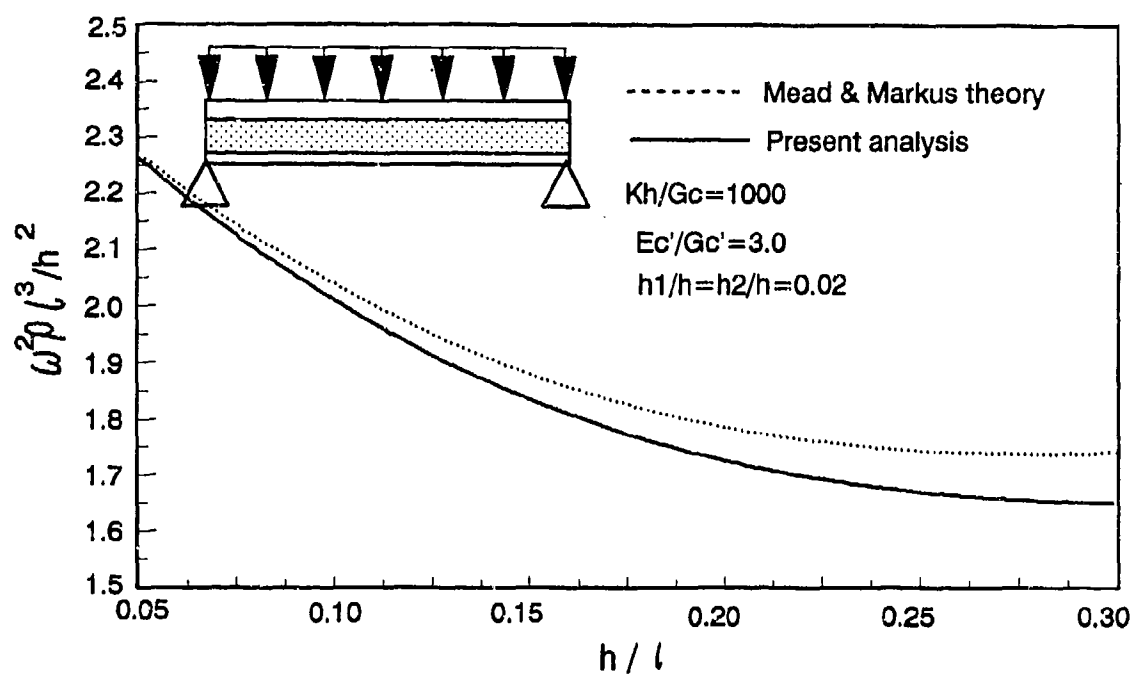


Figure 5. Variation of First Resonant Frequency with Core Thickness

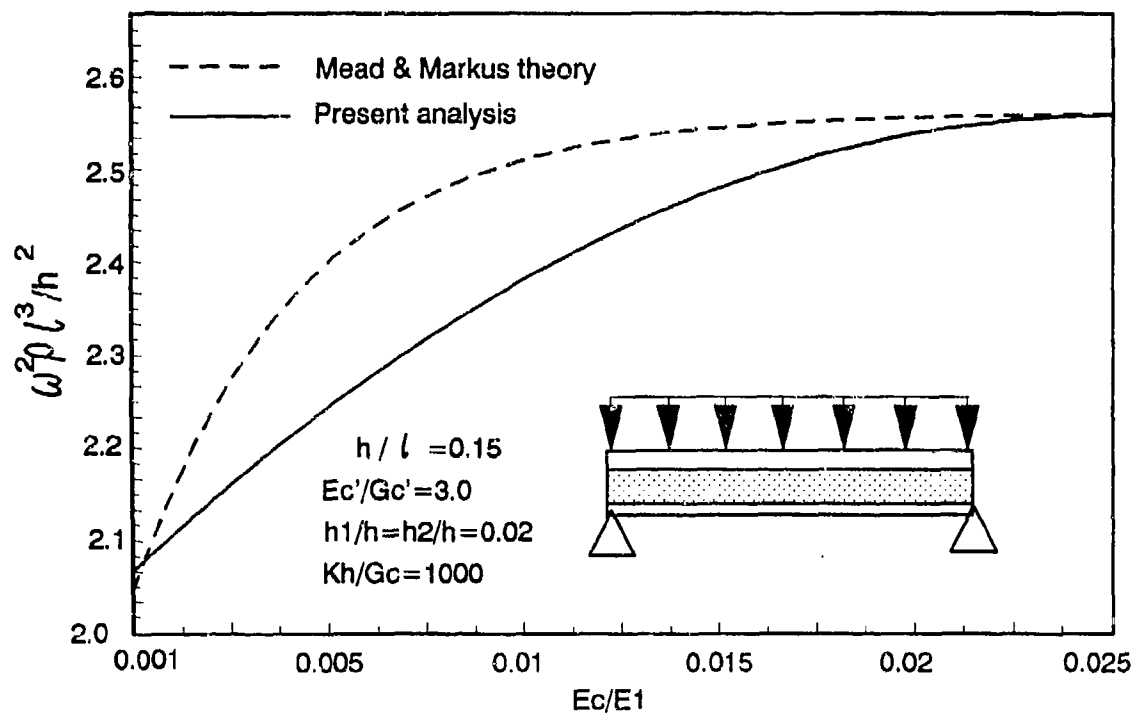


Figure 6. Effect of Core Modulus on The Resonant Frequency

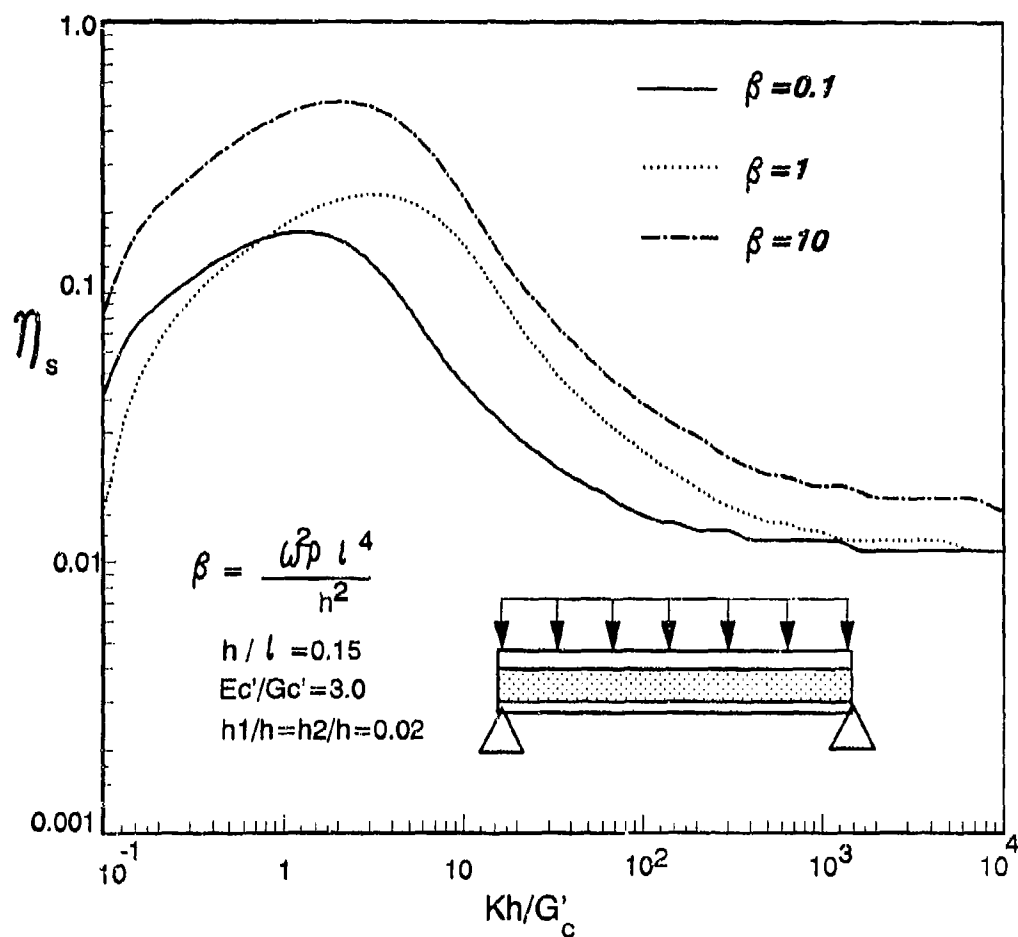


Figure 7. Effect of Adhesive Bonding stiffness  $K$  on System Loss Factors

stiffness. There may exist the difference of the level between the static response and dynamic response.

## 5. CONCLUDING REMARKS

A refined vibration theory of damped sandwich beams has been developed to consider the transverse deformation and interface effects. The proposed theory enhances the physical insight of the vibration damping behavior of sandwich beams consisting of more flexible cores. Results demonstrate that the present theory is more accurate for higher frequency modes. Effects of the core transverse deformation are important for more flexible core and thicker core. It is also shown that the adhesive bonding stiffness has a strong effect on the system damping (loss factor) up to a certain level which is given in terms of the ratio of adhesive stiffness to the core stiffness. This theory can be extended to the sandwich plate and is applicable to sandwich beams with any type of constructions and flexible core materials.

## REFERENCES

- [1] Ross, D., Ungar, E. E. and Kerwin, Jr., "Damping of Plate Flexural Vibrations by means of Viscoelastic Laminate", Structural Damping, ASME, New York, pp.49-88, 1959.
- [2] DiTaranto, R. A., "Theory of Vibratory Bending for Elastic and Viscoelastic Layered finite Length Beams", ASME J. Appl. Mech., Vol. 87, pp.881-886, 1965.
- [3] Mead, D. J. and Markus, S., "The Forced Vibration of a Three-Layer, Damped Sandwich Beam with Arbitrary Boundary Conditions", J. Sound & Vibration, Vol. 10, pp.163-175, 1969.
- [4] Lu, Y. P. and Douglas, B. E., "On the Forced Vibrations of Three-Layer Damped sandwich Beams", J. Sound & Vibration, Vol. 32, pp.513-516, 1974.
- [5] Yan, M. J. and Dowell, E. H., "Governing Equations for Vibrating Constrained-Layer damping of Sandwich Beams and Plates", ASME J. Appl. Mech., Vol. 94, pp.1041-1047, 1972.
- [6] Rao, Y. V. K. S. and Nakra, B. C., "Vibrations of Unsymmetrical Sandwich Beams and Plates with Viscoelastic Cores", J. Sound & Vibration, Vol. 34, pp.309-326, 1974.
- [7] Vaswani, J., Asnani, N. T. and Nakra, B. C., Composite Structures, Vol. 10, pp.231-245, 1988.
- [8] Ko, C. L., AIAA J., Vol. 27, pp.1425-1433, 1989.
- [9] Lu, C. and Libove, C., AIAA J. Vol. 29, pp.299-305, 1989.
- [10] Hussein, R., "Sandwich Plates with Interlayer Slip", J. Engng. Mech., ASCE, Vol. 110, pp.493-506, 1984.
- [11] Kim, C. G. and Hong, C. S., "Viscoelastic Sandwich Plates with Crossply Faces", J. Stru. Engng., ASCE, Vol. 114, pp.150-164, 1988.
- [12] Weissman-Berman, D., Pertrie, G. and Wang, M. W., "Flexural Response of Foam-Cored FRP Sandwich Panels", Transactions, Society of naval Archetects and Marine Engineering,

pp.73-95, 1988.

- [13] Frostig, Y. and Barush, M., "Free Vibrations of Sandwich Beams with a Transversely Flexible Core - A High Order Approach", 2nd International Conference on Sandwich Construction, University of Florida, March 9-12, 1992.
- [14] Dym, C. L. and Shames, I. H., *SOLID MECHANICS: A VARIATIONAL APPROACH*, McGraw-Hill, New York, 1973.

# A CONSTITUTIVE EQUATION FOR THERMOVISCOELASTIC BEHAVIOR OF POLYMERIC MATERIALS

Surendra N. Ganeriwala (Suri)\*  
Philip Morris Research Center

## ABSTRACT

With increasing uses of polymeric materials for providing viscoelastic damping in many mechanical systems and structures, it has become necessary to develop appropriate constitutive equations. Conventional constitutive theories and master curves do not provide a sufficient representation of the linear thermoviscoelastic properties needed for a sound engineering analysis and design. This paper presents a new scheme that yields a complete constitutive equation suitable for analysis of complex problems. The model is based on postulates of generally observed temperature and frequency (or time) dependent behavior of polymeric materials and our new model of the glass transition phenomenon. The model is internally consistent and makes remarkable predictions. The time-temperature principle is an integral part of this model. An initial test of the new approach was carried out with two different classes of polymers and results were excellent. It is adaptable to most computer systems.

\*Philip Morris USA, P. O. Box 26583, Richmond, VA 23261-6583, Tel: (804) 274-5694

## INTRODUCTION

Viscoelastic materials are valuable for isolation and control of sound and vibration because of their ability to dissipate energy. The damping ability of these materials is increasingly utilized to develop advanced composite materials such as high strength low weight aircraft structures and other engineering components. A distinguishing feature of viscoelastic materials is strong dependence of mechanical properties on temperature and frequency (or time). For an optimum design, dynamic analysis of viscoelastically damped structures must be performed at a design phase. Such engineering analyses requires a constitutive equation for the material viscoelastic behavior. Many dynamic mechanical property studies have been reported but appropriate constitutive equations defined over a wide ranges of temperature and frequency have been elusive [5,8,13,20].

The mechanical behavior of most polymers and the amorphous materials can be adequately represented by the theory of viscoelasticity. A broad classes of materials form a disordered solid structure when cooled from the molten state; polymers are just a one class from the list. But because of wide uses of polymers, viscoelasticity is generally associated with polymers only. In this paper, polymers and polymeric materials will be synonymously used to designate viscoelastic materials.

Recently, Bagley and co-workers [3,4] developed a fractional derivative model. This is probably the first constitutive equation for the representation of viscoelastic behavior of polymers and is a significant advancement in the field. The material viscoelasticity law is described by fractional powers of frequency (or time). The model does not represent material viscoelastic response at high frequencies well, although the authors have provided a theoretical basis of the model.

We developed a simple phenomenological model for polymeric materials based on basic physical postulates derived from observed material behavior. The foundation of our constitutive equation is our new model of the glass transition phenomenon [12]. In order to demonstrate the significance of the glass transition phenomenon, a brief description of the process is provided. The time-temperature principle is an integral part of this modeling scheme.

An initial test of the new approach was carried out with the data obtained by testing a nitrile butadiene rubber (NBR). A novel technique, the Fourier Transform Mechanical Analysis (FTMA) [13], was used to obtain dynamic mechanical properties. The primary feature of FTMA is that a complete isotherm for the complex modulus is obtained in just a few seconds with minimum heating and other structural changes normally associated with other techniques. Our modeling scheme was also applied to an another class of polymer, polyisobutylene, and results were excellent.



## OVERVIEW OF GLASS TRANSITION PHENOMENON

The glass transition is probably the most important property of polymeric materials. It is generally believed that glass transition is a failure of a material to crystallize and settle into a thermodynamically unstable amorphous state known as a glassy structure [1,8,12-16,20]. Reference 20 lists 8 classes of materials such as soda lime glasses, acids, alcohols, polymers, metallic alloys, etc. which have been found to display this type of behavior. When liquids of these materials are cooled, in a certain region of temperature their viscosity precipitously increases by several orders of magnitude to an approximate value of  $\sim 10^{13}$  Pa-sec, probably due to molecular asymmetry. This increase in viscosity is responsible for the energy dissipation due to internal friction or the damping property of polymeric materials. Blowing of glasses, molding polymers and the like are made possible by this phenomenon.

A typical temperature dependent stiffness of a polymer is illustrated in Figure 1. During a glass transition region, material stiffness changes by a several orders of magnitude. The material behavior changes from soft and ductile to hard and brittle. It has been demonstrated that there is an equivalence in a materials viscoelastic response with respect to temperature and frequency (or time) [8,21]. This equivalence is also illustrated in Figure 1. Figure 2 shows a typical plot of damping factor versus temperature at several frequencies. The peak of a damping curve shifts to a lower temperature with a decrease in frequency. The reason this shift is believed to be the inability of a material to maintain equilibrium with the external excitation during a transition. At lower frequencies a material is able to follow the stimulus down to lower temperatures and vice-versa. Note that the peak of a damping factor curve lies approximately half way between the transition region shown in figure 1 and is not the glass transition temperature, as sometimes used in the literature.

A comprehensive understanding of transition process requires a molecular interpretation [1,8,12-16,20,22]. At a given temperature, every molecule occupies a configuration in equilibrium with its thermal and vibrational energies. A deviation in temperature causes a change in the molecular equilibrium configuration. For liquids this variation happens instantaneously. However, for polymeric materials, at a certain temperature, molecular motion becomes sluggish due to increase in viscosity. Consequently, the time required for a molecule to occupy a configuration in equilibrium with the environment, generally referred to as the relaxation time, increases. On further lowering the temperature, relaxation time gets so large that the material system starts losing equilibrium with the external changes. At temperatures approaching  $T_g$  time scales become infinitely large making it practically impossible to maintain a complete thermodynamic equilibrium in any experimental study. Such long range processes are responsible for physical aging of glassy materials or the brittleness of plastics with time [1,12,16,20].

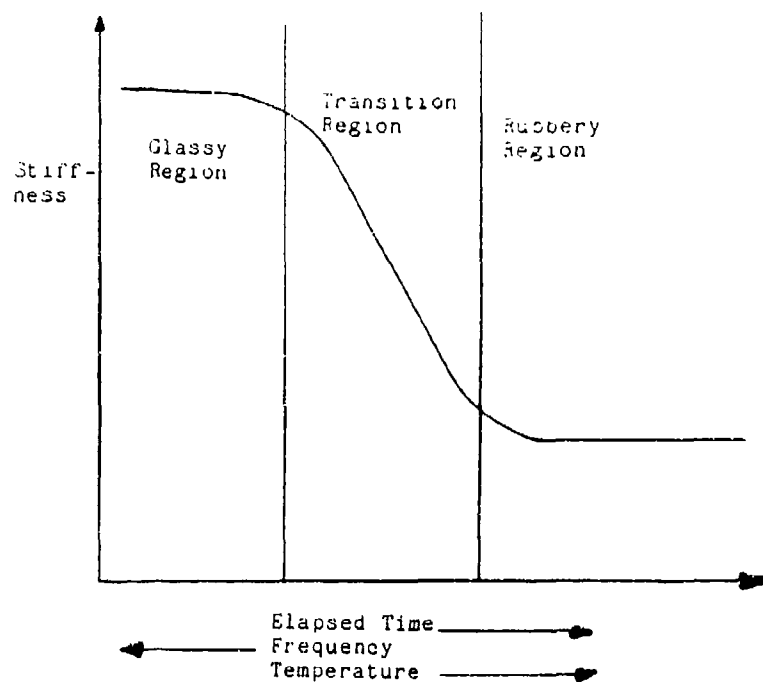
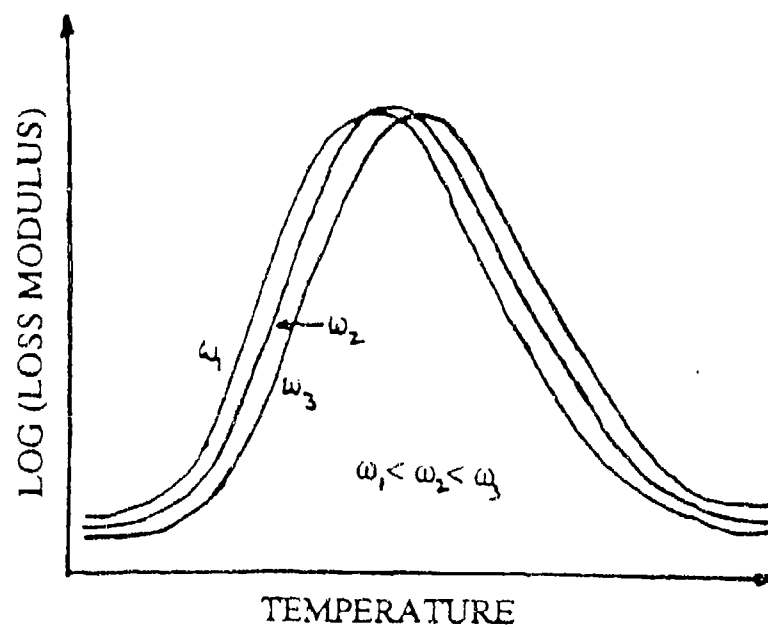


Figure 1,2 Typical behavior of viscoelastic materials as a function of time, temperature, or frequency.



Considering the importance of glass transition, it is intriguing that the fundamental principle governing the process is not fully understood. Complexities of the process can be illustrated by a typical thermal and volumetric behaviors of glass forming materials as shown in Figure 3. Observed glass transition is a rate dependent process with nonlinear kinetics. Material properties (heat capacity, expansion coefficient, etc.) versus temperature curves show asymmetry and hysteresis. The deviation of a material function from the nominal value can not be modeled by a first order process even very close to thermodynamic equilibrium. Also, this deviation cannot be predicted by any known theory.

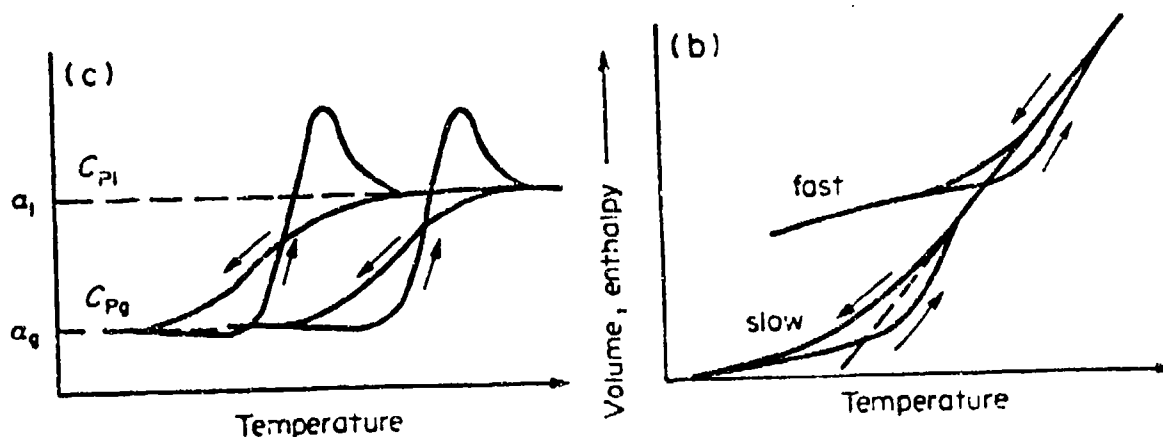


Figure 3. Temperature dependence of properties of glassy materials. Notice rate effect, asymmetry, nonlinearity, and hysteresis.

The foregoing results clearly illustrate the complexities of the glass transition phenomenon. However, it is important to note the following universal features of glass transition [1,12,16]: (1) viscosity of all glassy materials increases to  $\sim 10^{13}$  Pa-sec near their transition temperature. (2) The temperature rate of increase of the relaxation time is found to be the same in many different classes of amorphous materials. (3) Similar relaxation processes seems to be involved in different molecular motions associated with different types of experiments such as mechanical, thermal, dilatation, dielectric polarization, diffusion, etc. Viewing the universal nature of the process, one is curious to ask the question, what is the fundamental driving force governing the glass transition phenomenon?

Theoretically the problem is pursued along two lines of thought [2,12,15,16,20,22]. One school of thought says that the glass transition is a kinetic process and has nothing to do with thermodynamics whatsoever. While believers in thermodynamics claim that even though the observed behavior appears kinetic, the underlying fundamental principle governing the process is the second order thermodynamic transition. The second order transition designates a discontinuity in the second derivative of free energy with respect to intensive variables. In 1933 Ehrenfest [6,7] argued that the second order phase transitions are

thermodynamically admissible just as the first order transitions of metals, water and etc. Following his work, it has been postulated that glass transition phenomenon will mimic a second order transition in an infinitely slow approach to glass transition temperature. However, the second order transition has never been realized in any experiment. Our model suggests that the fundamental principle governing such a complex process is indeed a second order thermodynamic transition.

## CONSTITUTIVE EQUATION DEVELOPMENT

The foregoing description of glass transition clearly illustrates the complexities of modeling the thermoviscoelastic behavior of polymeric materials. A coupled theory of thermoviscoelasticity which includes the effects of both temperature as well as strain histories on the mechanical material functions is beyond the scope current theoretical development. In this work, we take a pragmatic approach to develop a phenomenological model that describes the observed material behavior and be consistent with the basic principles of thermodynamics. The development of the constitutive equation is provided for the case of a one dimensional shear deformation. However, the procedure can be easily generalized for a three dimensional case.

### Linear Viscoelastic Model

We begin with a general constitutive equation for a one dimensional deformation of isotropic, homogeneous, and hereditary (non-aging) linear viscoelastic materials. The equation at a temperature  $T$  is given by [5,6]:

$$\sigma(t, T) = \int_{-\infty}^{\infty} G(t, t-t', T) \dot{\gamma}(t', T) dt' \quad (1)$$

where the kernel  $G(t-t')$  is a monotonic nonincreasing function of time known as the stress relaxation modulus,  $\sigma(t)$  is current stress, and  $\dot{\gamma}(t')$  is the strain rate history.

For the case of sinusoidal strain history Equation 1 can be transformed to yield an expression for the complex modulus,  $G^*(j\omega)$ :

$$G^*(j\omega) = G'(\omega) + jG''(\omega) \quad (2)$$

where  $j = \sqrt{-1}$ ,  $\omega$  is the frequency, and  $G'(\omega)$  and  $G''(\omega)$  are the storage modulus and loss modulus, respectively.  $G'$  is related to the amount of energy stored and released in a cyclic oscillation and  $G''$  indicates the energy dissipated. In damping applications Equation 2 is expressed:

$$G^*(j\omega) = G'(1 + j\eta) \quad (3)$$

where  $\eta$  is designated as the material damping factor defined as the ratio of  $G''$  over  $G'$ . Since these material functions are explicitly related to each other [5,8] a model of only one of the material function is required to completely characterize the viscoelastic behavior of a material. Also, the temperature dependence must be the same for all of them. Thus, the objective of this research is to derive a constitutive equation of the storage modulus as a function of frequency and temperature.

### Thermodynamic Formulation

A most frequently discussed model of the glass transition phenomenon is Ehrenfest's second order transition [6,7,22]. Since the model has never been verified experimentally, it is often rejected. However, the fundamental idea of Ehrenfest's formulation is sound: during a "transition" certain thermodynamic quantity or its derivative passes through a discontinuity and quantitative relations between the magnitude of these quantities may or may not exist. Ehrenfest's generalization was more of a mathematical than a physical nature. Here, we extend his formulation to include the effect of mechanical deformation. We shall present relations that characterize the second order transition of a body subjected a simple shear steady state dynamic deformation.

The Gibbs free energy  $G$  can be defined in terms of state variables pressure  $p$ , temperature  $T$ , and deformation  $x$  as [22]:

$$G = H - TS + Fx = U + pV - TS + Fx \quad (4)$$

Where  $H$  is enthalpy,  $S$  entropy,  $T$  absolute temperature,  $U$  internal energy,  $p$  pressure,  $V$  volume,  $x$  deformation measure, and  $F$  the force.

Ehrenfest defined well known transitions like freezing, evaporation, boiling, etc. as first order transitions. It is known that during such transitions, the Gibbs free energy function is equal for the two phases.

$$G_{gl} = G_{liq} \quad (5)$$

where subscripts  $gl$  and  $liq$  denote the quantity is the glassy and liquid phases respectively. But the first derivative of  $G$  with respect to  $p$ ,  $T$ , and  $x$  are not continuous:

$$\left[ \frac{\partial G}{\partial T} \right]_{p,x} = -S \quad ; \quad \left[ \frac{\partial G}{\partial p} \right]_{T,x} = V$$

$$\text{and} \quad \left[ \frac{\partial G}{\partial x} \right]_{p,T} = F \quad (6)$$

The first order transition is characterized by:

$$G_{gl} = G_{liq} \quad (7a)$$

$$S_{liq} - S_{gl} = \Delta S > 0 \quad (7b)$$

$$V_{liq} - V_{gl} = \Delta V > 0 \quad (7c)$$

$$F_{gl} - F_{liq} = \Delta F > 0 \quad (7d)$$

Ehrenfest defined the second order transition in which both  $G$  and the quantities involving first derivatives of  $G$  are continuous, but the second derivative of  $G$  terms are discontinuous across the transition surface.

$$\begin{aligned} \left[ \frac{\partial^2 G}{\partial T^2} \right]_{p,x} &= - \left[ \frac{\partial S}{\partial T} \right]_{p,x} = - \frac{C_p}{T} \\ \left[ \frac{\partial^2 G}{\partial p^2} \right]_{T,x} &= \left[ \frac{\partial V}{\partial p} \right]_{T,x} = -\kappa V \\ \left[ \frac{\partial^2 G}{\partial p \partial T} \right]_x &= \left[ \frac{\partial V}{\partial T} \right]_x = - \left[ \frac{\partial S}{\partial p} \right]_x = \alpha V \\ \left[ \frac{\partial^2 G}{\partial x^2} \right]_{p,T} &= M \end{aligned} \quad (8)$$

where  $C_p$ ,  $\kappa$ ,  $\alpha$ , and  $M$  are heat capacity, coefficient of compressibility, coefficient of thermal expansion, and a measure of modulus, respectively. Thus, for second order transition we have

$$C_{p,liq} - C_{p,gl} = \Delta C_p > 0 \quad (9a)$$

$$\kappa_{liq} - \kappa_{gl} = \Delta \kappa > 0 \quad (9b)$$

$$\alpha_{liq} - \alpha_{gl} = \Delta \alpha > 0 \quad (9c)$$

$$M_{gl} - M_{liq} = \Delta M > 0 \quad (9d)$$

Equations 9a - 9d can be used to derive relations between the magnitudes of the jumps in various quantities along the transition line [2,12,15,16,20,22]. It is important to note that these relationships are valid for systems under equilibrium.

With respect to the glass transition, it not possible to determine the magnitudes of the jumps because of the relaxation process. The values have to be estimated using some appropriate model. It will be shown later that our model provides the value of the jump in  $M$ . For simple shear experiment  $F$  is shear stress  $\tau$ ,  $x = V\gamma$ , and  $M = V G$ , where  $G$  is shear modulus. Since the loss modulus approaches zero near transition temperature, the storage modulus equals the dynamic modulus.

The phase transition implies a change in the state of a material such as liquid to solid etc. The change can be brought about by two means [16]: (1) thermodynamics and (2) kinetics. The thermodynamic transitions are the transformation of a material from one equilibrium state to another equilibrium state. The transformation occurs spontaneously at a fixed temperature and/or pressure. It arises from the quantum mechanical discreteness of its energy levels. The kinetic transition, on the other hand, is freezing in of a certain configuration (or molecular degree of freedom) of a material state as a consequence of a deficiency in the experimental procedure. The original configuration can be recovered by allowing enough time before making an observation. The new state is not in equilibrium.

The amorphous materials are known to have some very long range processes. It has been argued that that an infinitely slow experiment is needed to observe a second order transition. For an mortal human being, such experiments cannot be performed. Nevertheless, a lack of experimental evidence is not sufficient to disprove the theory. In this research we present a glass transition model consistent with the second order transition. The central theme of our concept is illustrated in a generalized plot of the storage modulus versus temperature at two different frequencies as shown in Figure 4.

Consider the storage modulus at  $\omega_1$ . As a sample is cooled from a fairly high temperature, modulus increases with decrease in temperature. At a certain temperature, the relaxation time for molecular configuration changes become comparable with the frequency of excitation and system response begins to lag the input. The material storage modulus increases rapidly, indicated the vertical shift from the dotted line, due to the loss in a certain degree of freedom. The modulus increase accelerates with further reduction in temperature. A precaution must be taken to ensure a complete thermal equilibrium of the sample with its environment. Note that this requires increasingly longer time the temperature is lowered further. However, if the glass transformation is driven by a thermodynamic principle then the increase in storage modulus due to viscoelastic effects will cease at a temperature.

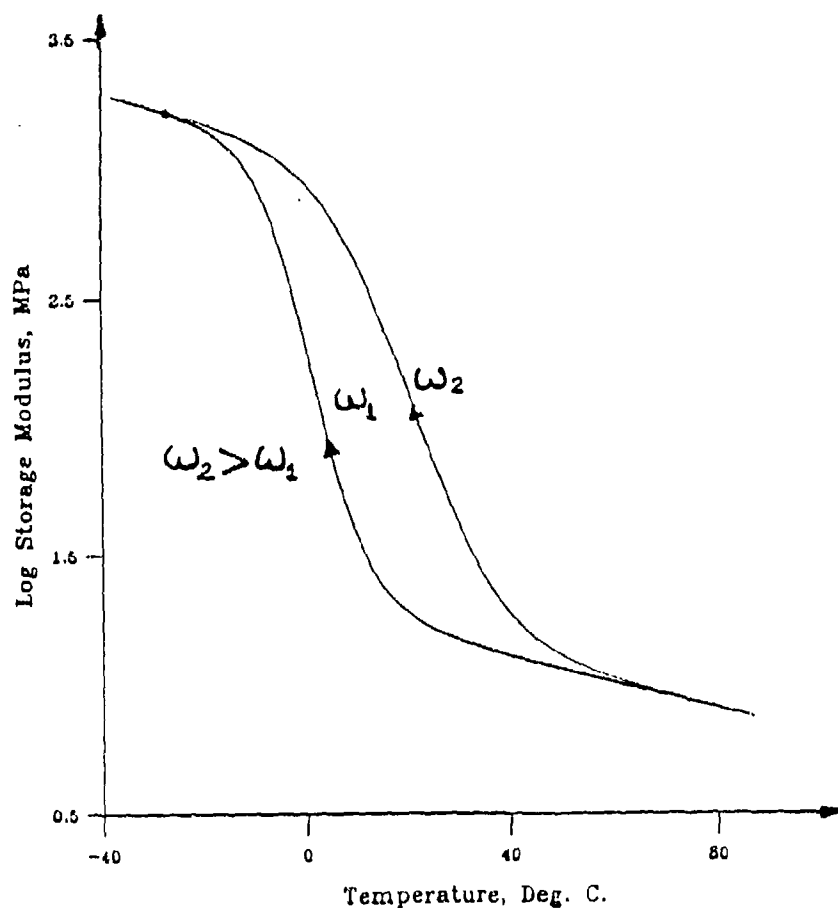


Figure 4. Temperature dependence of viscoelastic properties of polymeric materials.

The response at the higher frequency  $\omega_2$  will follow the similar trend, but the temperature for the onset of viscoelastic effect will be higher than before due to a decrease in the relaxation time at which the system begins to lag the stimulus. Again, due to the thermodynamics, if the transition is governed by the second order transition than the viscoelastic effect will disappear at a temperature which must be exactly the same as before. For a given material, this temperature must be independent of the frequency of excitation. This implies that the storage modulus isofrequency versus temperature curves, obtained at various frequencies, will converge at a certain temperature. The point of intersection is the second order glass transition temperature. It can be realized only in an infinitely low frequency experiment.

Since it is practically impossible to perform an infinitely slow experiment, a second order transition temperature cannot be measured experimentally. It has to be estimated by carefully extrapolating the storage modulus versus temperature curves at different frequencies and determining the point of intersection. This can be only achieved by using a representative model for temperature and frequency dependent viscoelastic behavior of polymeric materials.



### Phenomenological Model

We begin by examining a typical temperature dependent mechanical behavior of polymers. Figure 5 shows a typical plot of the storage modulus  $G'$  as a function of temperature at a given frequency. The entire response can be thought of as a sum of three distinct parts without the loss of any generality [12,14]:

- (1) All materials attain the highest modulus at the absolute zero temperature.
- (2) The modulus of all materials decreases with increase in temperature. We postulate that the log of  $G'$  decreases linearly with temperature.

(3) The glass transition region, which is unique to polymers (or amorphous materials in general). Experience has shown that the observed glass transition is a sigmoidal process. A complete characterization of the process requires three parameters: first, the height of transition; second, the width of transition; and third, the temperature of  $T_g$ . Krumhansl and Sheaffer [17] have shown that such phase transitions can be represented by a hyperbolic tangent function. We found that a modified form of the hyperbolic tangent modeled two different classes of materials very well.

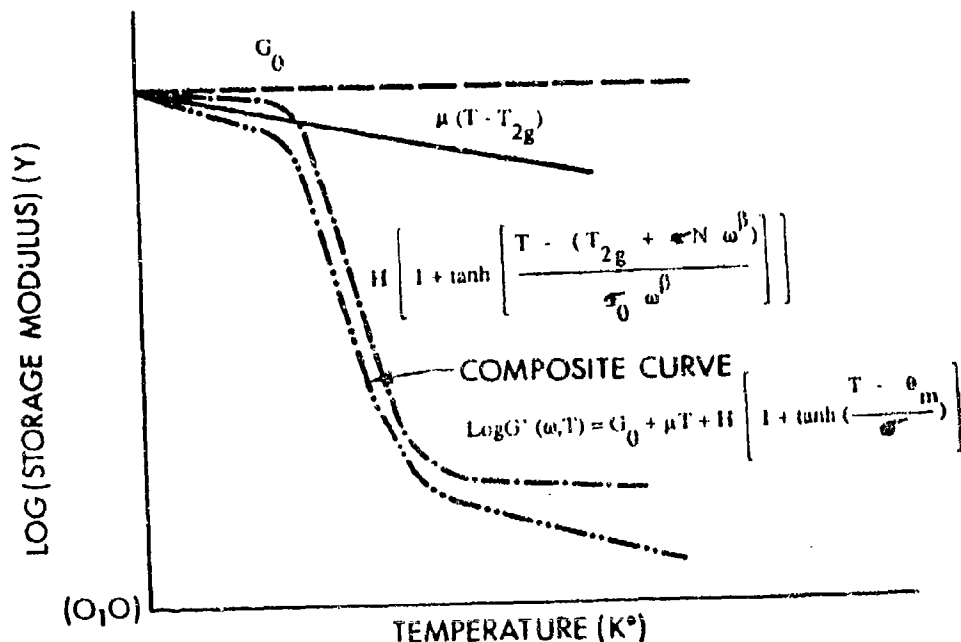


Figure 5. A phenomenological representation of polymer viscoelastic behavior.

Thus, a complete temperature dependent behavior of a viscoelastic material at a given frequency (or time) is characterized by five parameters: two common to all materials and the other three unique to amorphous materials. Each parameter has a definite physical meaning [4,5]. Mathematically the function is given as:

$$\text{Log} G'(\omega, T) = G_0 + \mu T + H \left[ 1 + \tanh \left( \frac{T - \theta_m}{\sigma} \right) \right] \quad (10)$$

where  $T$  = absolute temperature in Kelvin, and  $G_0$ ,  $\mu$ ,  $H$ ,  $\theta_m$ , and  $\sigma$  are the modulus at the absolute zero, temperature rate of change of modulus, transition height, mid-point of the transition, and the transition spread function. The model can be applied at many frequencies, and the five parameters can be studied as functions of frequency.

The kinetics (or relaxation) of glass transition is governed by the parameter  $\alpha$ . Since glass transition is a nonlinear process we postulated the spread to be a power law function of frequency. Also, the power law form of the spread function is consistent with generally observed nature of the glass transition kinetics. We tried several other functions, but power seems to provide the best results. Also, we found that the mid-point of transition was linearly related to the spread and  $T_{2g}$ . Thus:

$$\sigma = \sigma_0 \omega^\beta \quad (11)$$

and

$$\theta_m = T_{2g} + N \sigma \quad (12)$$

where  $N$  represents the distance of the mid-point from  $T_{2g}$ .

### Constitutive Equation

Since the material behavior is not known at temperatures below  $T_{2g}$ , the regression process was found to improve significantly by shifting the origin to the transition temperature. By combining equations 10, 11, and 12, we obtain a complete constitutive equation:

$$\begin{aligned} \text{Log} G'(\omega, T) = & G_0 + \mu (T - T_{2g}) \\ & + H \left[ 1 + \tanh \left[ \frac{T - (T_{2g} + \sigma N \omega^\beta)}{\sigma_0 \omega^\beta} \right] \right] \end{aligned} \quad (13)$$

The above equation can be used to obtain the temperature shift factor  $a_T$  with respect to a reference temperature  $T_{ref}$ . Since  $a_T$  is a frequency multiplication factor that gives the same modulus at two different temperatures, we obtain the expression for the shift

factor by equating the arguments of the hyperbolic tangent function at two different temperatures. Thus we get:

$$(14) \quad \frac{T_{ref} - (T_{2g} + \sigma N \omega_1^\beta)}{\sigma_0 \omega_1^\beta} = \frac{T - (T_{2g} + \sigma N \omega_2^\beta)}{\sigma_0 \omega_2^\beta}$$

simplification yields:

$$(15) \quad \log(a_T) = \log(\omega_1/\omega_2) = \frac{1}{\beta} \left[ \frac{(T_{ref} - T_{2g})}{(T - T_{2g})} \right]$$

Note that the shift factor according to the WLF (Williams, Landel, Ferry) equation is

$$(16) \quad \log(a_T) = \frac{-C_1 (T - T_g)}{C_2 + (T - T_g)}$$

Since WLF equation was first derived to represent the experimental data for polyisobutylene, it would be appropriate to apply our model to the polyisobutylene original data. It will be shown in the results section that the agreement between the two is excellent.

## DATA REDUCTION

The raw data was strings of storage modulus,  $G'$ , and frequency,  $\omega$ , obtained at various temperatures. Figure 6 shows  $G'$  versus frequency for NBR (nitrile butadiene rubber) at various temperatures. The data was determined using FTMA apparatus [5,6]. Data reduction was carried out with linear temperature,  $T$ ,  $Y = \log G'$ , and  $X = \log(\omega/100)$ . The reduced scale for  $X$  was used so that intercepts at  $X=0$  would correspond to 100 Hz frequency and fall within the experimental range. There was some noise in the modulus data attributable to mechanical and electrical perturbations. These small perturbations were removed by smoothing with simple linear and second order polynomial functions. From the original data, curves of  $G'$  versus absolute temperature were obtained at a various frequencies. Figure 7 shows NBR  $G'$  versus temperature at several frequencies.

Model equation (6) suggests that parameters  $G_0$  and  $\mu$  can be determined uniquely from the low and high temperature data and their first derivative. However, we used a multiple linear regression to estimate these values. The values were found to be essentially invariant of frequency. These values were than used in the model equation to represent the

entire temperature data at a one frequency. The procedure was repeated at several frequencies. Newton-Rhapson nonlinear least square technique was used for regression. The results are shown in Figure 7. As it can be seen from Figure 7, the model fit is not very good. But the procedure provided initial estimate of model parameters.

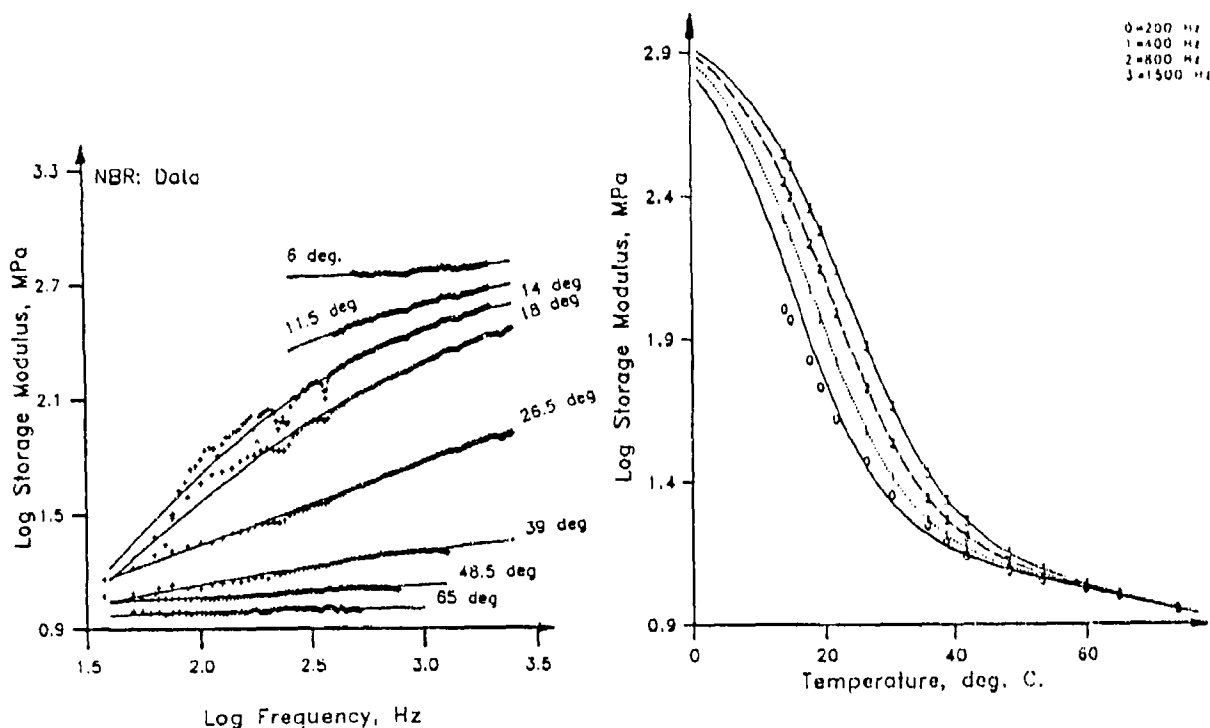


Fig. NBR Storage modulus vs frequency at various temp. Lines are smooth isotherms

Fig. NBR temperature dependent behavior. Lines are model contours. Points are FTMA data.

The initial values were then used to obtain the point of convergence of isofrequency  $G'$  versus temperature curves at various frequencies. The model parameters were allowed to seek the optimum values using the Newton-Rhapson non-linear least square method. Results are shown in Figure 8. The point of convergence is the thermodynamics second order transition temperature, designated by  $T_{2g}$ . To insure that the material data indeed converges at a low temperature, several attempts were made to avoid the convergence by using a limited data set of different frequency combinations. Every time isofrequency versus temperature curves converged to a point, although there was some variation in the temperature of convergence for each family of curves. The variation can be attributed to regression procedure.

The same procedure was used to model polyisobutylene. Again, the results were excellent. In all cases there were good linear correlations. (Statistical correlation coefficients,  $R > .99$ ). The temperature shift factor was determined by using equation 15.

## RESULTS

In order to verify the success of our modeling scheme, the previously published "classical" data on polyisobutylene were obtained from the literature [11,12]. The term classical is used to indicate that these data were originally used to derive the famous WLF equation. The procedure described above was used to model polyisobutylene. Figure 9 shows polyisobutylene storage modulus versus temperature at various frequencies. The lines are model contours and the point of convergence is the thermodynamic second order glass transition temperature. The spread of the transition region was consistent with a power law dependence on frequency. It was found that  $B_0$ ,  $\mu$  and  $H$  were essentially invariant over the range of frequencies.

Since the convergence of isofrequency versus temperature curves provided an excellent representation material data, the results were extrapolated over a very low and high frequencies. Figure 10 shows NBR storage modulus as a function of temperature over a very broad range of frequencies. At extremely low frequency transition becomes narrow and approaches a second order transition. Whereas at high frequency transition region gets broad due to decrease in the relaxation time for the onset of the viscoelastic effect. Figure 11 is a similar plot for polyisobutylene. Again, the material characteristics are identical to NBR.

The model was verified by comparing experimental data with predictions. Figure 12 shows polyisobutylene  $G'$  versus frequency data and model lines at various temperatures. Figure 13 illustrates a comparison of the storage modulus experimental data of NBR with the model predictions. It can be seen that in both cases, the model predictions agreed very well with measurements.

Gibbs and DiMarzio, in 1958 [15], developed a statistical mechanics theory to model the glass transition phenomenon of polymers. Probably, this is the only molecular theory to date derived from the first principles. The model predicts that the underlying principle of the glass transition is indeed a thermodynamics second order transition. It also predicts that the value of the second order transition would lie between 20 to 50 C. below the measured  $T_g$ . To compare the results of our model we obtained NBR  $T_g$  in our laboratory using Perkin Elmer DSC (Differential Scanning Calorimetry) instrument. Figure 14 shows the DSC scan of NBR material sample. Measured value was -5 C. and our model estimated second order transition temperature was -26 C. Also, the literature value of polyisobutylene is -70 C. and our model was -81 C. It can be seen that our model values for both materials are in very good agreement with Gibbs and DiMarzio theoretical predictions.

The model can also be used to compute the shift factor using equation 15. Figure 15 shows a plot of shift factor as a function of temperature for polyisobutylene. Also shown in the figure is the WLF equation shift factor. Note that initially the WLF equation was an empirical representation of material data. The theoretical basis of the equation was given

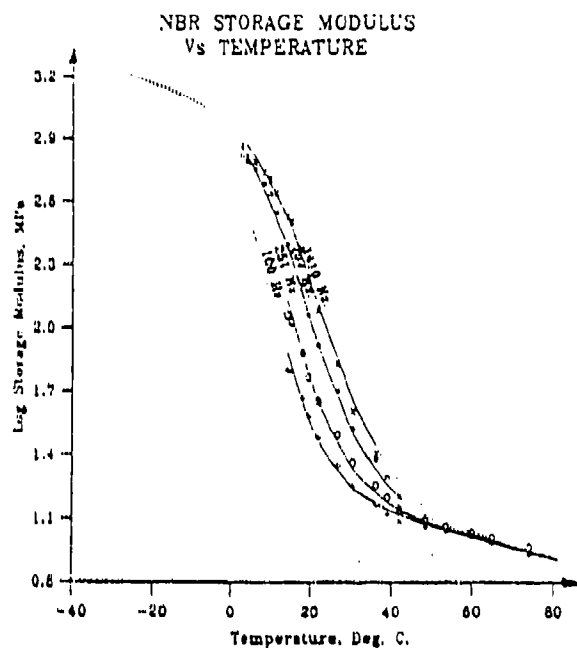


Figure 8. Convergence of NBR storage modulus versus temperature data at various frequencies.

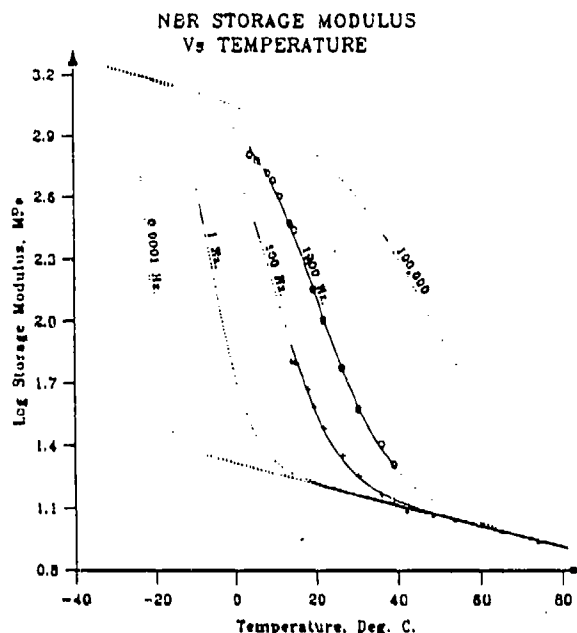


Figure 10. Extrapolation of NBR storage modulus data to a very low and high frequencies using our model.

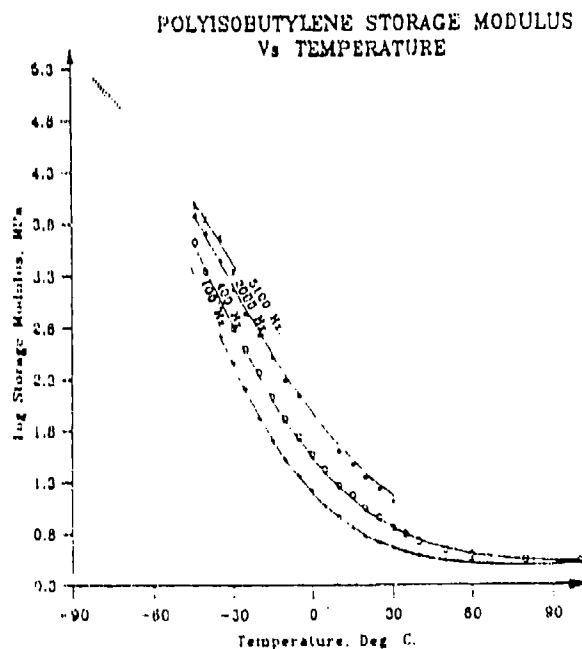


Figure 9. Convergence of polyisobutylene storage modulus versus temperature data at various frequencies.

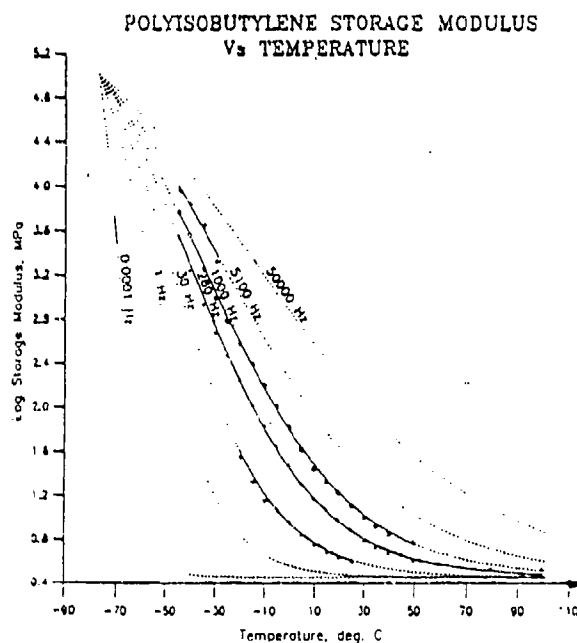


Figure 11. Extrapolation of polyisobutylene storage modulus data to a very low and high frequencies using our model.

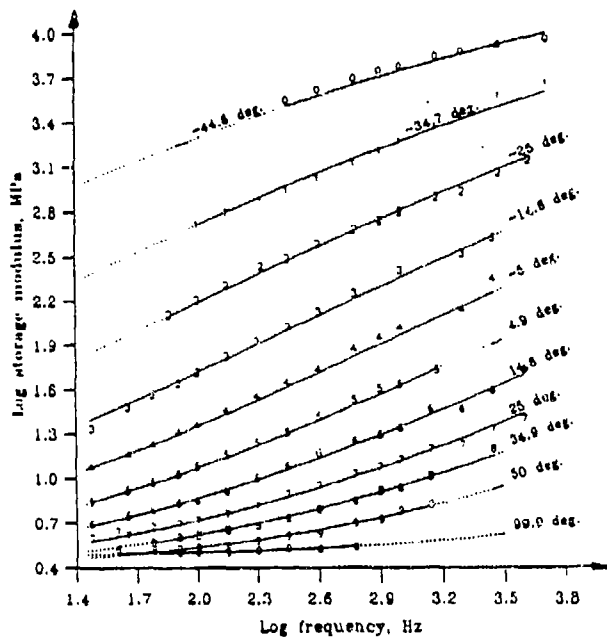


Figure 12. Comparison of polyisobutylene storage modulus data with model predictions.

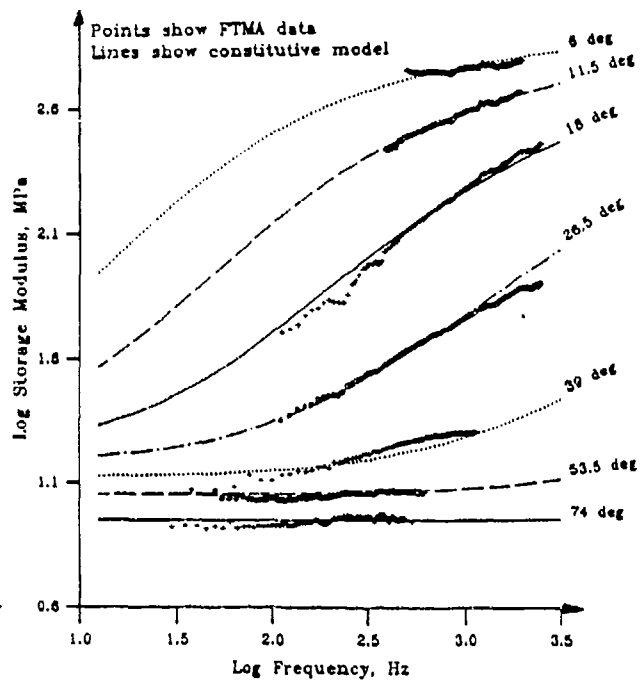


Figure 13. Comparison of NBR storage modulus data with model predictions.

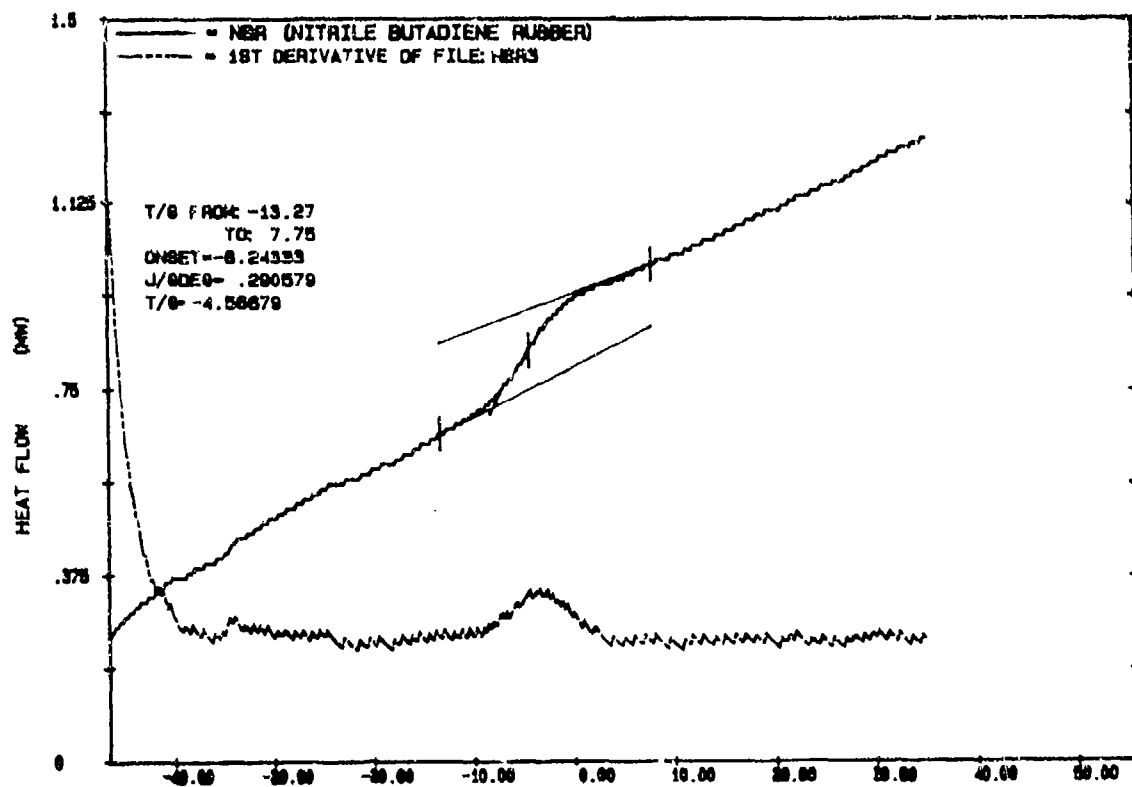


Figure 14. DSC scan of NBR using Perkin Elmer instrument.

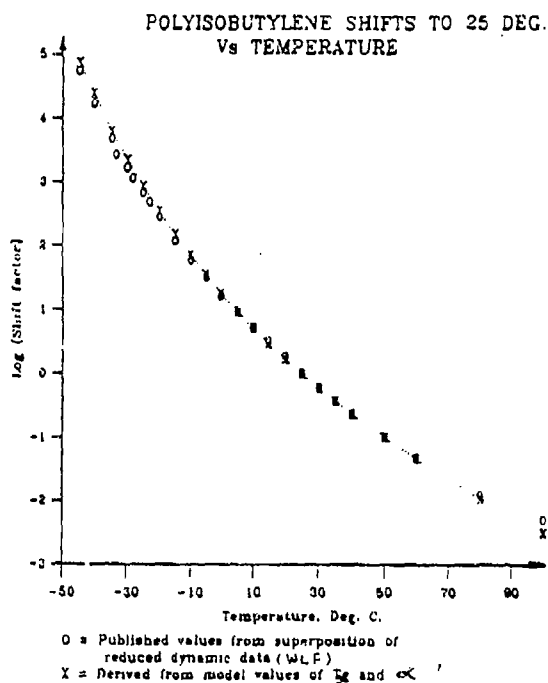


Figure 15. Comparison of polyisobutylene shift factors obtained using our constitutive equation and the WLF equation.

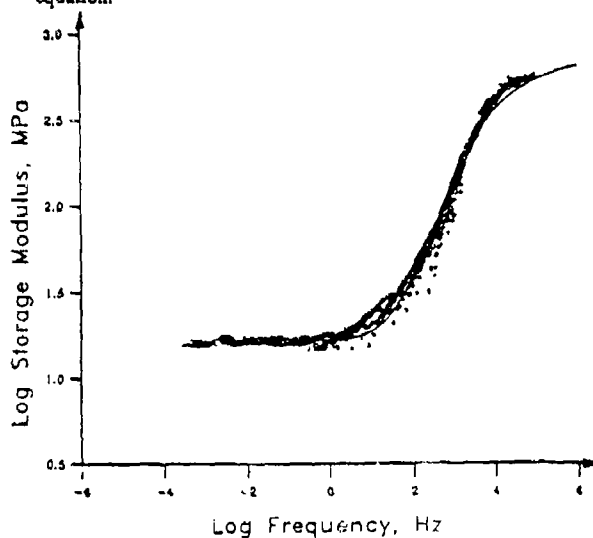


Figure 17. NBR storage modulus master curve at 20 C. obtained using the model shift factors.

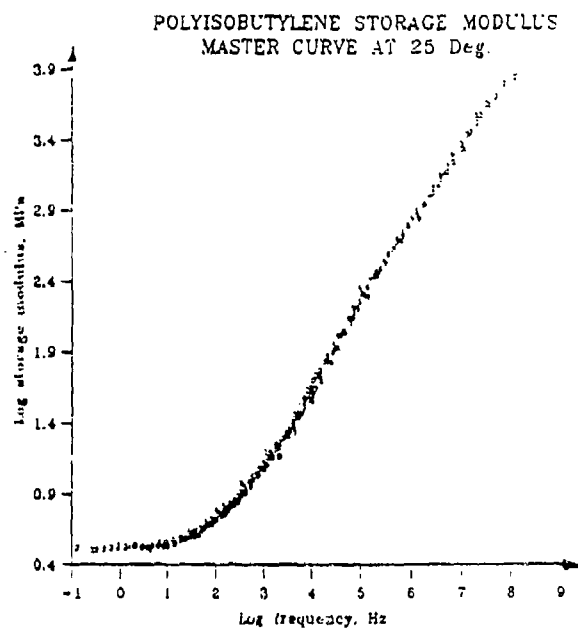


Figure 16. Polyisobutylene storage modulus master curve at 25 C. obtained using the model shift factors.

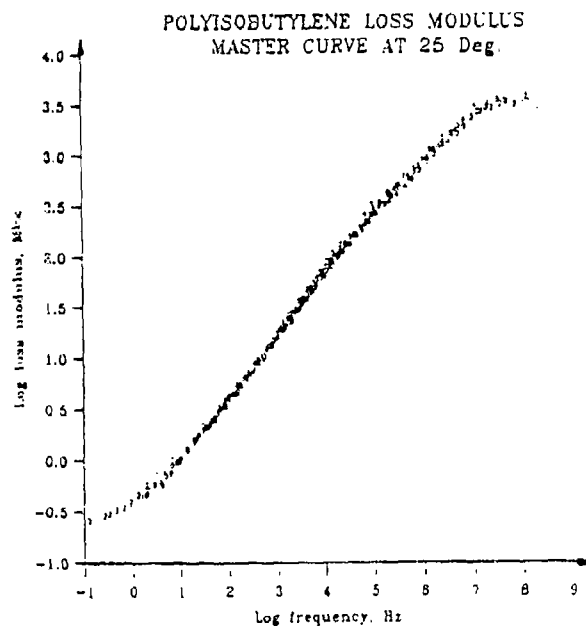


Figure 18. Polyisobutylene loss modulus master curve at 25 C. obtained using the model shift factors.



latter. The agreement of our shift factor with that of the WLF equation is an excellent verification of the constitutive equation. The model can be used further to obtain the master curves. Figures 16 and 17 are the storage modulus master curves for NBR and polyisobutylene at 25 C. The model parameters obtained using the storage modulus were used to compute the loss modulus. Figure 18 is the master curve for the loss modulus of polyisobutylene. The excellent representation provides another verification of our constitutive equation.

The glass transition phenomenon has certain universal features, as described earlier. The kinetics of the transition process is governed by the exponents of the power law spread function. We postulate that if the kinetics of the transition is governed by an universal process, then the exponent of both the polymers must have the same value. Figure 19 is a plot of spread factor as a function of temperature for both polymers. The slope of the curve is the exponent. It can be seen from the plot that both curves have the same slopes.

## DISCUSSION

The foregoing results clearly demonstrate that the constitutive model provides an excellent representation of the thermoviscoelastic behavior of two different classes of polymers NBR (a cross-linked network polymer) and polyisobutylene (linear polymer). The equation can be used to obtain other material functions such as creep compliance, stress relaxation modulus, and relaxation and retardation spectra using the relations given in references [5,8].

The most important feature of the model is the convergence of all isofrequency versus temperature curves at a low temperature. The thermodynamics formulation, described in the previous section, provides a basis and the reason for the convergence of data. The hyperbolic tangent and power law functions are consistent with the generally observed behavior of polymeric materials. It may be possible to represent the data using other mathematical functions. However, the convergence is an unique feature of our model and must not be confused with the form of the mathematical function used in the formulation. The hyperbolic tangent and power law functions were found to work very well with two materials tested. Sheaffer has proven that the hyperbolic tangent is the correct representation for a certain type of phase transitions.

A necessary condition for a good model is internal consistency. The phenomenological model meets this condition very well in the way it correlates the trends and features of loss factor with model parameters, the shift factor with the WLF equation, and the master curves. The excellent agreement with the Gibbs and DiMarzio theory is another vindication of our model. The exponent of the power law function is related to the kinetics of the glass transition phenomenon. The same value for the exponents for two different classes of polymers is consistent with the universality of glass transition

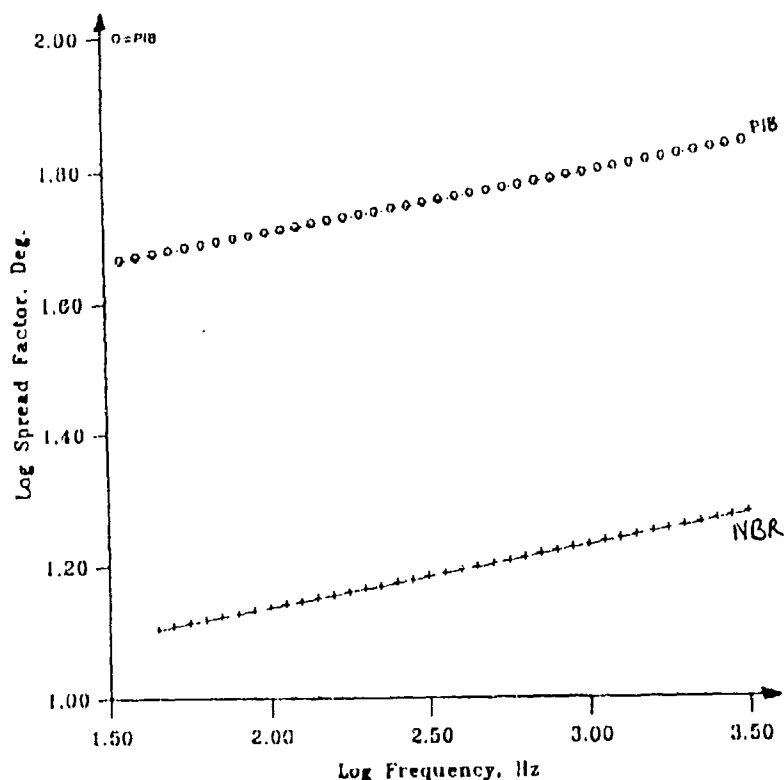


Figure 19. Comparison of model kinetic parameter  $\alpha$  for NBR and polyisobutylene.

process as discerned from the observations made over many years. This indeed is a strong result in support of the constitutive equation.

We believe that the convergence of isofrequency data and a model to determine its value represents a break through in the theory of amorphous material formation. Our model provides a simple procedure to study the glass transition phenomenon. The model can be used to obtain the molecular relaxation times as a function of temperature. The information may provide an understanding of an important topic of the physical aging of polymers. To the best of our knowledge, our model is the only model that can give an estimate of the thermodynamics second order transition temperature from the measured data. This could be very useful information. Note that it is impossible to attain the second order transition temperature by any experimental means.

The constitutive equation can be used to construct master curves. The model can be extended to include the effects of other variables of interest such as moisture content and plasticizer. Proceeding in this manner one can develop a predictive model incorporating parameters of interest.

## REFERENCES

1. Angell, C. A., MacFarlane, D. R., and Oguni, M., 1986, in *Dynamic Aspects of Structural Changes in Liquids and Glasses*, Eds. Angell C. A. and Goldstein, M., The New York Academy of Sciences, pp. 241-247.
2. Astarita, G., Paulaitis, M. E., Wissinger, R. G., 1989, "Thermodynamics of the Glass Transition," *Journal of Polymer Science: Part B: Polymer Physics*, Vol. 27, pp. 2105-2116.
3. Bagley, R. L., 1991, "The Thermorheological Complex Materials," in *Proceeding of Damping' 91*, J. Pearsol, and L. Rogers, Editors, Wright-Patterson Air Force Base, Ohio 45433, WL-TR-91-3078, Section-CBD.
4. Bagley, R. L., Torvik, P. J., 1983, *Journal of Rheology*, Vol. 30, No. 1, pp 133-155.
5. Christensen, R. M., 1982, *Theory of Viscoelasticity an Introduction*, 2nd. ed., Academic Press Inc., New York, Chs. 3,4
6. Ehrenfest V. P., 1933, *Proceeding Amsterdam Academy*, Vol. 36, pp. 155-157.
7. Ehrenfest, V. P., 1959, *Collected Scientific Papers*, Edited Klien, M. J., North-Holland Publishing Company, Amsterdam, pp. 628-632.
8. Ferry, J. D., 1980, *Viscoelastic Properties of Polymers*, 3rd. ed., John-Wiley & Sons Inc., New York, Chs. 6, 7, 11, 12.
9. Ferry, J. D., Child, W. C. Jr., Zand, R., Stern, D. M., Williams, M. L., and Landel, R. F., 1957, "Dynamic mechanical properties of polyethyl methacrylate," *Journal of Colloid Science*, 12, pp. 53-67.
10. Fitzgerald, E. R., 1989, Personal Communications, Dept. of Mech. Eng., Johns Hopkins University, Baltimore, Maryland.
11. Fitzgerald, E. R., Grandine, L. D., Ferry, J. D., 1958, "Dynamic Mechanical Properties of Polyisobutylene," *Journal of Applied Physics*, Vol. 24, No. 5, pp. 650-655.
12. Ganeriwala, S. N. "A new Model of Glass Transition Phenomenon," *Journal of Chemical Physics*, in communication.
13. Ganeriwala, S. N., and Hartung H. A., 1989, "Fourier Transform Mechanical Analysis and Phenomenological Representation of Viscoelastic Material Behavior," in *Sound and Vibration Damping with Polymers*, Eds. R. D. Corsaro and L. H. Sperling, ACS Symposium Series 424, American Chemical Society, Washington D. C.; also, J. Acoust. Soc. Am., in Progress.
14. Ganeriwala S. N. and Hartung H. A., "Developing a Constitutive Equation for Linear Thermoviscoelastic Materials," in *Constitutive Laws for Engineering Materials: Recent Advances and Industrial and Infrastructure Applications*, Eds. C. S. Desai, E. Krempl, G. Frantziskonis, and H. Saadatmanesh, ASME book Series, ASME Press, New York, pp. 347-351.
15. Gibbs, J. H., DiMargio, E. A., 1958, "Nature of the Glass Transition and the Glassy State," *The Journal Chemical Physics*, Vol. 28, pp. 373-383.
16. Kauzmann, W., 1948, "The Nature of the Glassy State and the Behavior of Liquids at Low Temperatures," *Chemical Review*, Vol. 43, pp. 219-256.

17. Krumhansl, J. A., Schrieffer, J. R., 1975, "Dynamics and Statistical Mechanics of a One-Dimensional Model Hamiltonian for Structural Phase Transition," *Physical Review B*, Vol. 11, 9, pp. 3535-3545.
18. Lee, E. H., 1974, "Thermo-Viscoelasticity", in *Mechanics of Viscoelastic Media and Bodies*, in J. Hult, ed. Symposium Gothenburg/Sweden, Springer-Verlag, Sept. 2-6, pp. 339-357.
19. Plazek, D. J., 1965, "Temperature dependence of the viscoelastic behavior of polymers" *The Journal of Physical Chemistry*, Vol. 69, pp. 3480- 3487.
20. Shen, M. C. and Eisenberg, A., 1970, "Glass transitions in polymers," *Rubber Chemistry and Technology*, Vol 43, pp. 95-155
21. Schwarzl, F., Staverman, A. J., 1952, "Time-temperature dependence of linear viscoelastic behavior," *Journal of Applied Physics*, Vol. 23, pp. 838-843.
22. Staverman, A. J., 1966, "Thermodynamic Aspect of the Glass-Rubber Transition," *Rheological Acta.*, Vol. 5, pp. 283-292.
23. Williams, M. L., Landel, R. F., Ferry, J. D., 1955, "The Temperature Dependence of Relaxation Mechanisms in Amorphous Polymers and Other Glass-forming Liquids," *J. of American Chem. Soc.*, Vol. 77, pp. 3701-3707.

# **SENSITIVITY ANALYSIS FOR ESTIMATION OF COMPLEX MODULUS OF VISCOELASTIC MATERIALS BY NON-RESONANCE METHOD**

Kwang-Joon Kim, Professor  
Tae-Kil Ahn, Graduate Student

Center for Noise and Vibration Control  
Dept. of Mechanical Engineering, KAIST

## **ABSTRACT**

One of the most influential factors to the complex modulus of a viscoelastic material is the frequency of vibration. Various techniques have been developed for the estimation of such frequency dependent characteristics, each of which has, of course, its own advantages as well as disadvantages. Non-resonance method is a technique to obtain the complex modulus over a wide range of frequency in a relatively short time. Sometimes, however, measurement noise problems make the complex modulus estimations by this method unreliable especially in the anti-resonance frequency regions.

In this study, the effects of the measurement errors on estimating the complex modulus by applying non-resonance method; transmissibility measurement approach to longitudinal vibration of rod-type specimen are investigated. Sensitivities of the Young's modulus and loss factor with respect to the measurement errors are derived for this approach based on mathematical model and subsequently a way to obtain the reliable frequency region for specified error bounds is shown. And these have been supported by experimental results.

---

Address : Center for Noise and Vibration Control (NOVIC)  
Department of Mechanical Engineering, KAIST  
Science Town, Taejon 305-701, KOREA

Phone : International - 82 - 42 - 869 - 3024

## 1. INTRODUCTION

Viscoelastic materials are useful for isolation and damping of noise, shock and vibration. For an efficient design of components or systems with such viscoelastic materials, first of all, it is necessary to have an accurate knowledge of the complex modulus of elasticity - that is, the dynamic Young's modulus and loss factor. It is well known that the complex modulus of these materials are basically dependent on frequency and temperature. Many techniques and instruments have been developed to measure the dynamic properties of viscoelastic materials, which can be classified into resonance and non-resonance methods [1,2].

In resonance method material properties are determined only at several resonance frequencies, while in non-resonance method the modulus are obtained in the overall frequency range of interest. In the first approach the estimations at the several resonance points might be inter- or extra-polated to obtain the properties at interim frequencies. However it would be definitely desirable to determine the viscoelastic modulus of the material directly at closely spaced frequencies, because there could be transitional intervals between the resonance points where the complex modulus change rapidly with respect to the frequency [3,4,5].

In the non-resonance method, complex modulus of viscoelastic materials are often obtained by subjecting a specimen to a single frequency sinusoidal excitation and sweeping the frequency. In this approach it may be difficult to obtain truly isothermal properties since dependence of the energy dissipation or temperature variation upon the frequency is not known a priori. In this aspect, random excitation can minimize the variations of temperature with respect to the frequency [2]. When, however, the complex modulus is estimated based on the random excitations, the measurement and data processing errors cannot be avoided to some extent. Thus, in this paper, we analyze the effects of the measurement errors on estimating the complex modulus in the non-resonance approach.

Non-resonance approach for rod-type specimens can be classified into the transmissibility and impedance methods [6]. Pritz and Buchanan analyzed the error effects in the transmissibility method [3,7,8]. However, Pritz dealt with an approximate model of the transmissibility function, and Buchanan was concerned mainly for the reasonable numerical calculations of the complex modulus from the measured transmissibility functions. In this paper, the transmissibility method is analyzed with respect to its sensitivity to the measurement errors. As the result of sensitivity analysis, confidence intervals of the estimated complex modulus are given, from which the reliable frequency ranges are extracted. Finally, experimental results are presented.

## 2. SENSITIVITY ANALYSIS IN TRANSMISSIBILITY APPROACH

### 2-1. PROCEDURE OF ESTIMATION OF MATERIAL PROPERTIES

The schematic diagram of the transmissibility approach for a rod-type specimen is shown in Fig.1. In deriving the governing equation of the specimen, it is assumed that the cross-section is constant, the material homogeneous and isotropic, plane cross-sections remaining plane, only axial stresses present and uniformly distributed over the cross-section, the bonded effects at the

specimen ends negligible, and the lateral dimension of the specimen sufficiently less than wavelength. The last two assumptions mean that the specimen is slim enough and the exciting frequency is restricted to be lower than a given value [9]. Under these assumptions, dynamic behavior of the specimen is described by the well-known one dimensional wave equation.

$$E(1+j\eta)\frac{\partial^2 u}{\partial x^2} - \rho\frac{\partial^2 u}{\partial t^2} = 0 \quad (1)$$

where  $E$  is the dynamic Young's modulus,  $\eta$  the loss factor,  $\rho$  the density,  $t$  the time, and  $j = \sqrt{-1}$ .  $u = u(x,t)$  is the axial displacement of the specimen at the longitudinal distance of  $x$  from the one end. The transmissibility function between the bottom and top of the specimen can be derived as follows:

$$\frac{U_2}{U_1} = \frac{1}{\cos \zeta^* - \gamma \zeta^* \sin \zeta^*} \quad (2)$$

where  $\gamma$  is the ratio of the loading mass which consists of the accelerometer and a rigid loading mass to the specimen mass and  $\zeta^*$  is a nondimensional parameter for the frequency defined by

$$\zeta^* = \frac{L}{\lambda} \frac{2\pi}{\sqrt{1+j\eta}} \quad (3)$$

In equation (3),  $\lambda$  is the wave length given by  $\lambda = \frac{2\pi}{\omega} \sqrt{\frac{E}{\rho}}$  and  $L$  the specimen length. Since equation (2) deals with complex numbers, substituting  $\zeta^* = \xi - j\beta$  and  $\frac{U_2}{U_1} = H \cos \phi + j H \sin \phi$  ( $\xi, \beta, H, \phi$ : real) into this equation yields two real equations as follows:

$$\cosh \beta \left( \cos \xi - \gamma \xi \sin \xi \right) + \gamma \beta \cos \xi \sinh \beta - \frac{\cos \phi}{H} = 0 \quad (4)$$

$$\sinh \beta \left( \sin \xi + \gamma \xi \cos \xi \right) + \gamma \beta \sin \xi \cosh \beta + \frac{\sin \phi}{H} = 0$$

Once the solution sets of  $\xi$  and  $\beta$  are obtained from equations (4) as functions of  $L/\lambda$ ,  $E$  and  $\eta$  are readily calculated from the following equations.

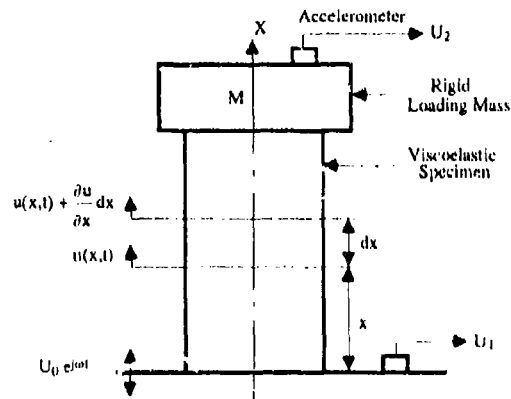


Fig.1 Schematic diagram of the transmissibility approach for a rod-type specimen

$$E = \rho \omega^2 L^2 \frac{\xi^2 - \beta^2}{(\xi^2 + \beta^2)^2} \quad (5)$$

$$\eta = \frac{2\xi\beta}{\xi^2 - \beta^2} \quad (6)$$

One problem with the equations (4) is that the solutions cannot be obtained in explicit form, but only can be solved numerically, e.g. by the Newton-Raphson method. Another problem is that the equations have infinite number of solutions, but that only one set of them is the physically relevant solution. The procedure of obtaining the physical solution is well described by Buchanan [3].

## 2-2. SENSITIVITY ANALYSIS

As could be seen in the above section, the complex modulus depends on  $H$ ,  $\phi$ ,  $\rho$ ,  $\gamma$ , and  $L$ . As  $\rho$ ,  $\gamma$  and  $L$  are measured under static conditions, the errors in measuring these values may be negligibly small. However, if the sensor and cable mass is not negligible in comparison with the rigid loading mass, the measurement error of  $\gamma$  may be large. Therefore, the effects of the errors in measuring  $\gamma$  as well as  $H$  and  $\phi$  on the estimation of  $E$  and  $\eta$  are investigated in this section.

The errors of  $E$  and  $\eta$  caused by uncertainties in  $H$ ,  $\phi$  and  $\gamma$  can be represented as follows :

$$\Delta E \approx \frac{\partial E}{\partial H} \Delta H + \frac{\partial E}{\partial \phi} \Delta \phi + \frac{\partial E}{\partial \gamma} \Delta \gamma \quad (7)$$

$$\Delta \eta \approx \frac{\partial \eta}{\partial H} \Delta H + \frac{\partial \eta}{\partial \phi} \Delta \phi + \frac{\partial \eta}{\partial \gamma} \Delta \gamma$$

The relative errors of  $E$  and  $\eta$  can be represented subsequently as follows :

$$\frac{\Delta E}{E} \approx D_{EH} \frac{\Delta H}{H} + D_{E\phi} \Delta \phi + D_{E\gamma} \frac{\Delta \gamma}{\gamma} \quad (8)$$

$$\frac{\Delta \eta}{\eta} \approx D_{\eta H} \frac{\Delta H}{H} + D_{\eta\phi} \Delta \phi + D_{\eta\gamma} \frac{\Delta \gamma}{\gamma}$$

where  $D$ 's represent the sensitivity coefficients defined as below.



$$D_{EH} = \frac{\partial E}{\partial H} \frac{H}{E}, \quad D_{E\phi} = \frac{\partial E}{\partial \phi} \frac{1}{E}, \quad D_{E\gamma} = \frac{\partial E}{\partial \gamma} \frac{\gamma}{E} \quad (9)$$

$$D_{\eta H} = \frac{\partial \eta}{\partial H} \frac{H}{\eta}, \quad D_{\eta\phi} = \frac{\partial \eta}{\partial \phi} \frac{1}{\eta}, \quad D_{\eta\gamma} = \frac{\partial \eta}{\partial \gamma} \frac{\gamma}{\eta}$$

As mentioned before,  $E$  and  $\eta$  can not be represented explicitly in terms of  $H$ ,  $\phi$  and  $\gamma$ . Thus we can not obtain the derivatives in equations (7) or (9) directly. The derivation of these derivatives in detail is given in the Appendix.

The sensitivity coefficients depend on  $H$  and  $\phi$ , which are functions of  $L/\lambda$ ,  $\gamma$  and the dynamic characteristics of the material investigated. In order to analyze the sensitivity of the estimated modulus to the measurement errors, the sensitivity coefficients have been calculated as functions of nondimensional factor  $L/\lambda$  for the following cases:  $E = \text{const.}$ ,  $\gamma = 1.0$ , and  $\eta = 0.01, 0.1, 1.0, 2.0$ . The transmissibilities are shown in Fig.2 and the values of the sensitivity coefficients are plotted in Fig.3 and 4 as functions of  $L/\lambda$ , from which the following characteristics can be observed.

In case of low loss factors ( $\eta = 0.01, 0.1$ ), the relative error of  $E$  depends on the errors in measuring  $H$  and  $\phi$  to a very high degree near  $L/\lambda \approx 0$ . In this range of  $L/\lambda$ ,  $|D_{EH}| \gg 1$  and  $|D_{E\phi}| \gg 1$  whereas  $|D_{E\gamma}| \approx 1$ . The sensitivity coefficients  $|D_{EH}|$  and  $|D_{E\phi}|$  decrease rapidly as  $L/\lambda$  increases from zero and the range of  $L/\lambda$  for  $|D_{EH}| > 1$  is wider than that for  $|D_{E\phi}| > 1$ , which means that  $\phi$  is less influential to  $E$  than  $H$ . In this region, the relative error of  $\eta$  influenced by the measurement error of  $\phi$  is larger than the one by  $\Delta H$ , while the error by  $\Delta \gamma$  is negligible. At frequencies near the first resonance ( $L/\lambda = 0.14$ ), the relative error of  $E$  by  $\Delta H$  or  $\Delta \phi$  is negligibly small compared with the one by  $\Delta \gamma$ , since  $|D_{EH}| \approx |D_{E\phi}| \ll 1$  whereas  $|D_{E\gamma}| \approx 1$ . In this region of  $L/\lambda$ , the relative error of  $\eta$  depends mainly on  $\Delta H$ , since  $|D_{\eta H}| \approx 1$  whereas  $|D_{\eta\phi}| \approx |D_{\eta\gamma}| \ll 1$ . Above the first

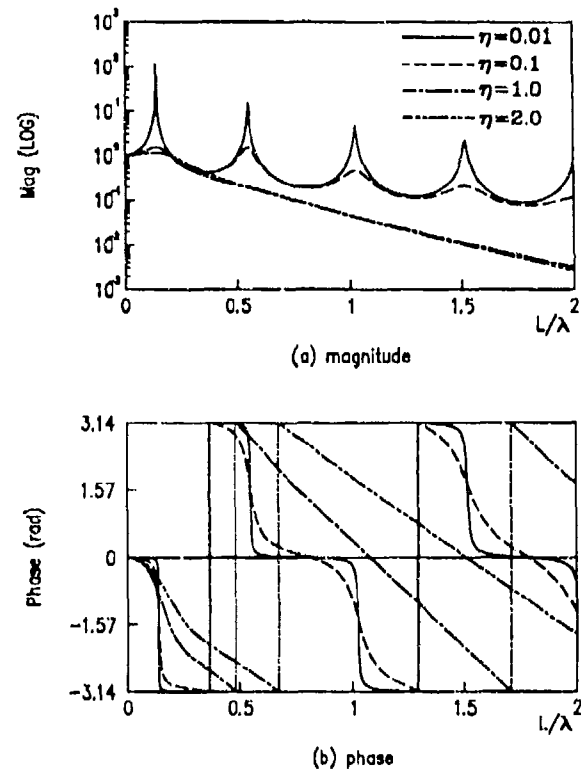


Fig.2 Transmissibilities in longitudinal vibration of rod-type specimens

resonance, the relative error of  $E$  is sensitive to the measurement errors  $\Delta H$ ,  $\Delta \phi$  and  $\Delta \gamma$  in the anti-resonance regions where  $H$  is locally minimum, whereas it is negligible at the resonances.

Also the degree of the sensitivity decreases globally as  $L/\lambda$  increases. In this range of  $L/\lambda$ , the relative error of  $\eta$  depends on the measurement errors  $\Delta H$  and  $\Delta \gamma$  to about the same degree at the resonances, since  $|D_{\eta H}| \approx |D_{\eta \gamma}| \approx 1$  whereas  $|D_{\eta \phi}| \ll 1$ . In the anti-resonance regions, the relative error in  $\eta$  is sensitive to all of  $\Delta H$ ,  $\Delta \phi$  and  $\Delta \gamma$ , but the range of  $L/\lambda$  where the error is significant by  $\Delta \phi$  is wider than the one by  $\Delta H$  and  $\Delta \gamma$ , meaning  $\phi$  is more influential to  $\eta$  than  $H$  and  $\gamma$ .

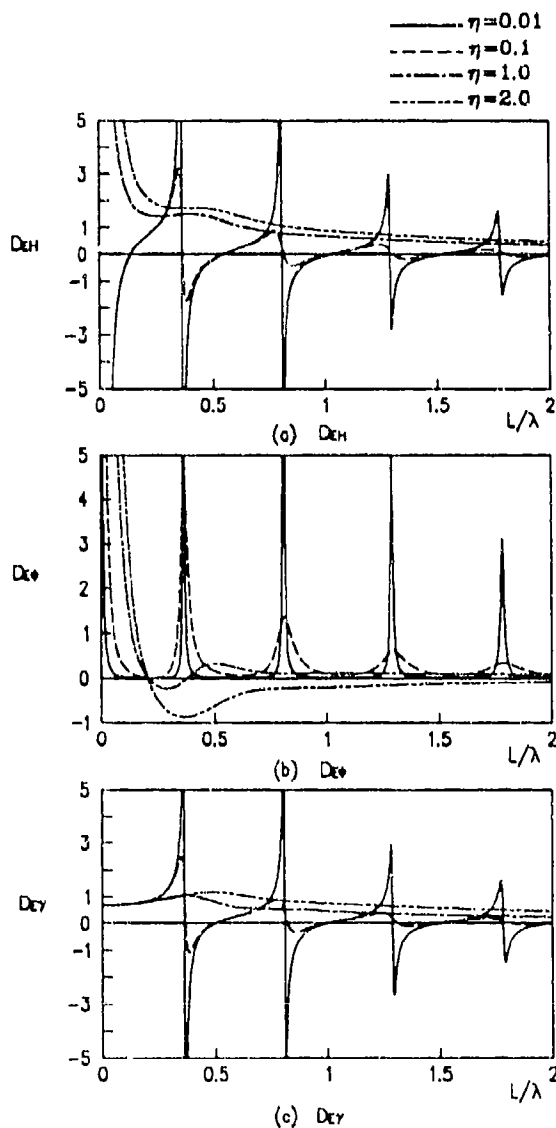


Fig.3 Sensitivity coefficients of the Young's modulus in the transmissibility approach

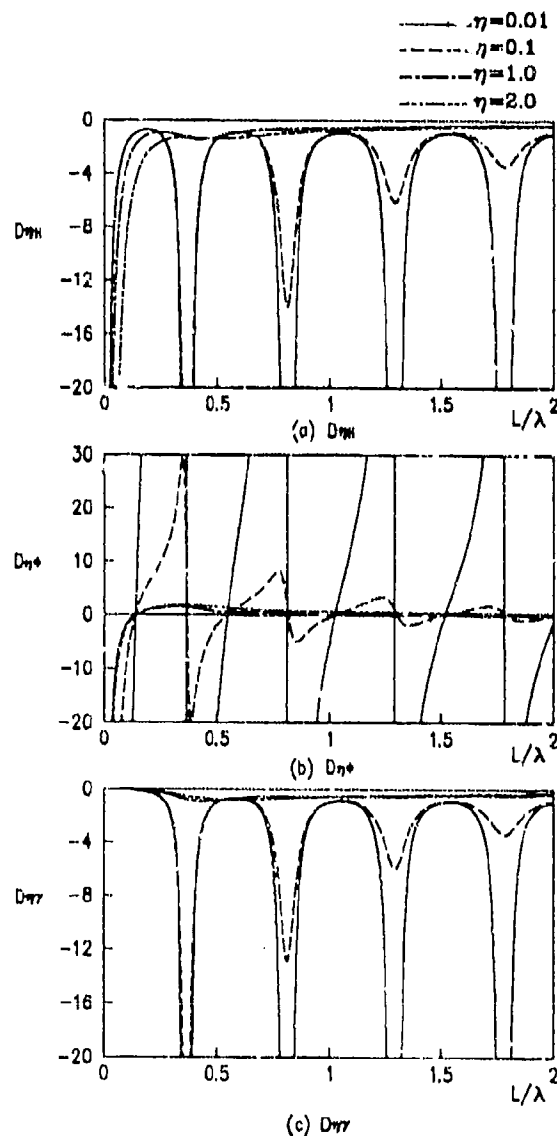


Fig.4 Sensitivity coefficients of the loss factor in the transmissibility approach

In case of high loss factors ( $\eta=1.0, 2.0$ ), near  $L/\lambda \approx 0$ , the relative errors of  $E$  and  $\eta$  seem similar to the case of low loss factors. At frequencies near the first resonance ( $L/\lambda=0.14$ ), dependence of the relative error of  $E$  on the errors in measuring  $H$  and  $\phi$  is almost the same and

larger than the one for  $\gamma$ . In this region of  $L/\lambda$ , the relative error of  $\eta$  depends mainly on the error in measuring  $H$ , since  $|D_{\eta H}| > 1$  whereas  $|D_{\eta \phi}| \approx |D_{\eta \gamma}| \ll 1$ . Above the first resonance, the relative errors in  $E$  and  $\eta$  are not so sensitive to the measurement errors, since  $|D_{EH}| \approx |D_{E\gamma}| \approx 1$ ,  $|D_{E\phi}| < 1$ , and  $|D_{\eta H}| \approx |D_{\eta \phi}| \approx |D_{\eta \gamma}| \approx 1$ .

In summary, the errors in estimating  $E$  and  $\eta$  near  $L/\lambda \approx 0$  are very sensitive to the measurement errors  $\Delta H$  and  $\Delta \phi$ , but not to  $\Delta \gamma$ , which is clearly due to the fact that the relative motion between the input and the output is negligible and the inertia effect of loading mass can be neglected in this range of  $L/\lambda$ . It is noted that, however, the measurement errors of  $H$  and  $\phi$  may cause a larger error in the estimation of  $\eta$  than in case of  $E$ , since  $|D_{\eta H}| > |D_{EH}|$  and  $|D_{\eta \phi}| > |D_{E\phi}|$  globally. It is observed that for low loss factor ( $\eta=0.01, 0.1$ ) the errors of  $E$  and  $\eta$  are sensitive to the measurement errors  $\Delta H$ ,  $\Delta \phi$  and  $\Delta \gamma$  in the anti-resonance regions, but that for high loss factor ( $\eta=1.0, 2.0$ ) it is not the case.

### 2-3. SIMULATIONS

In this section, the effects of the measurement errors  $\Delta H$  and  $\Delta \phi$  on the complex modulus estimation will be illustrated using examples. Although the errors  $\Delta H$  and  $\Delta \phi$  in general consist of random and bias components, we consider only random errors because the bias errors are not easily known. Two typical examples are simulated: one for a low loss material ( $\eta=0.05$ ) and the other for a high loss material ( $\eta=0.5$ ). The diameter, length and mass ratio of each specimen are 10 (mm), 30 (mm) and 1.0, respectively. The true values of Young's modulus and density are  $1 \times 10^7$  (N/m<sup>2</sup>) and 1335 (kg/m<sup>3</sup>), respectively. A white noise random signal was used for the input, and another white noise uncorrelated with the input was added to the system output as the measurement noise. The rms level of the output noise was 1.7% of that of the output in both cases. The transmissibility and coherence function were calculated by taking 10 averages and are shown in Fig.5, where it can be found that the smaller the magnitude of the transmissibility the more contaminated the transmissibility function by the output noise.

Fig.6 shows the complex modulus estimated

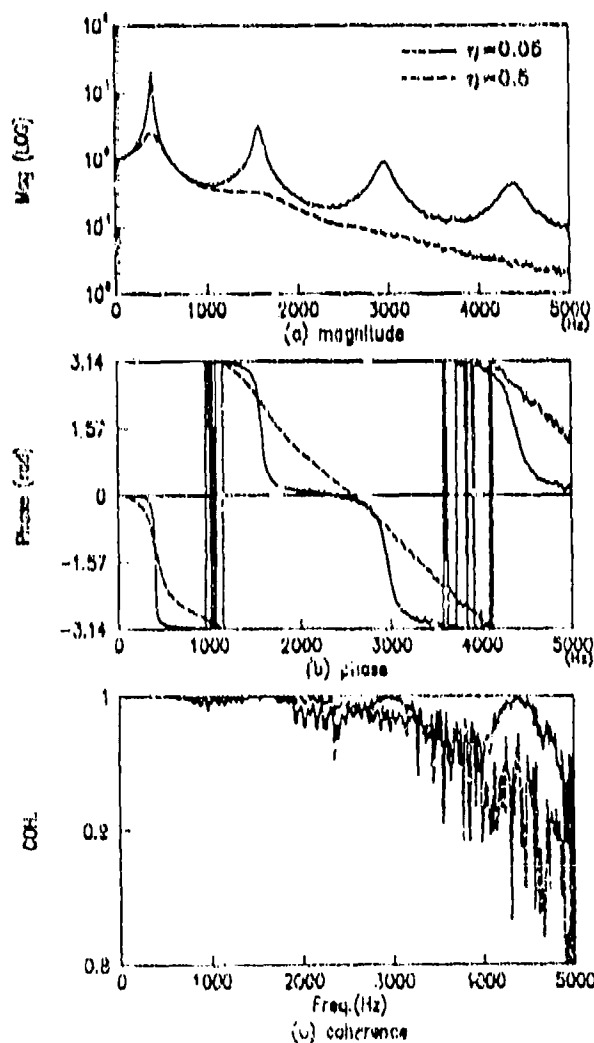


Fig.5 Transmissibility functions generated for simulation studies

from the transmissibility function for the low loss material. The estimated modulus is scattered near the zero frequency regions and around the anti-resonances. The scattering of  $\eta$  looks larger than that of  $E$ . Near the zero frequency, the scattering of the estimated modulus is very wide as can be expected. Between the resonances, the scattering degree of the calculated modulus does not much increase as the frequency increases, although the coherence is deteriorated.

Fig.7 shows the complex modulus estimated from the transmissibility function for the high loss material. The estimated modulus is far less scattered compared with the previous case except at the lowest frequency region below the first resonance, even if the measurement error is larger than that of the low loss material case. These coincide well with the results Figs.3 and 4 in the previous section.

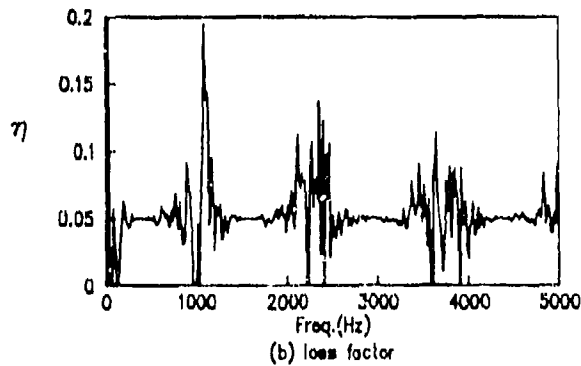
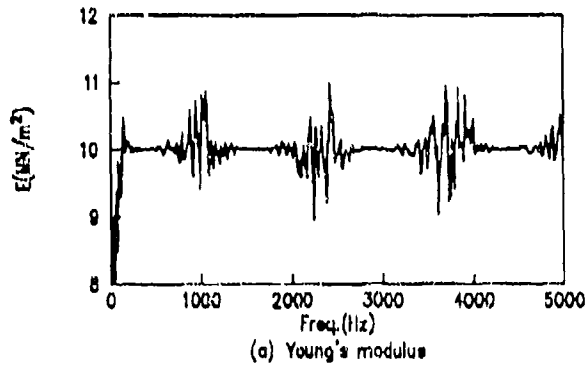


Fig.6 Estimated complex modulus for a low loss material ( $\eta=0.05$ )

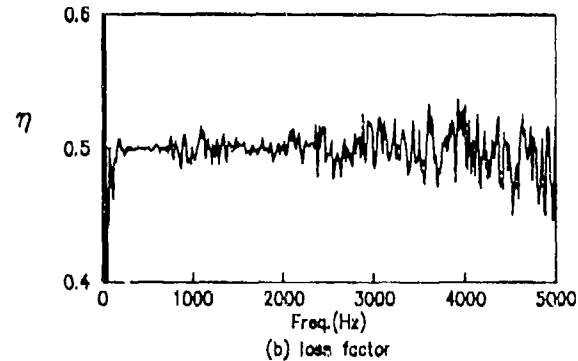
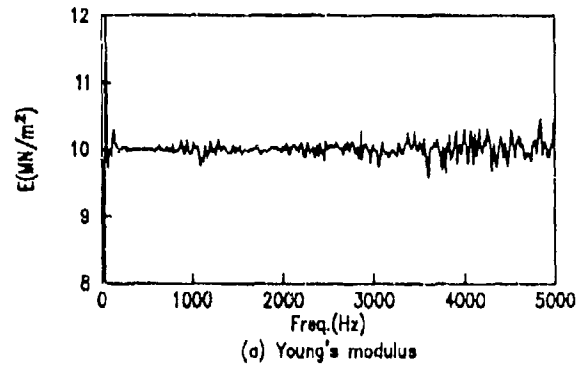


Fig.7 Estimated complex modulus for a high loss material ( $\eta=0.5$ )

For small random error, the 95% confidence intervals of  $\Delta H$  and  $\Delta \phi$  are given as follows [10] :

$$\left| \frac{\Delta H}{H} \right| \leq 2 \frac{\text{s.d.}[H(f)]}{H(f)} = 2 \frac{\left(1 - \gamma_{xy}^2\right)^{1/2}}{|\gamma_{xy}| \sqrt{2 n_d}} \quad (10)$$

$$\left| \Delta \phi \right| \leq 2 \text{ s.d. } \left[ \phi(f) \right] \approx 2 \frac{\left( 1 - \gamma_{xy}^2 \right)^{1/2}}{\left| \gamma_{xy} \right| \sqrt{2 n_d}}$$

where s.d. means the standard deviation,  $\gamma_{xy}^2$  the coherence and  $n_d$  the average number.

Figs.8 and 9 show the 95% confidence intervals for  $E$  and  $\eta$  estimated from equations (8) together with the true values, where it is observed that the confidence intervals include the true values in the almost entire frequency range. Thus, the frequency range where the estimations are within specified error bounds can be obtained from these confidence intervals.

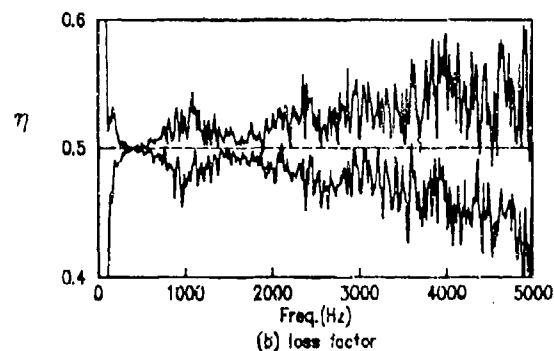
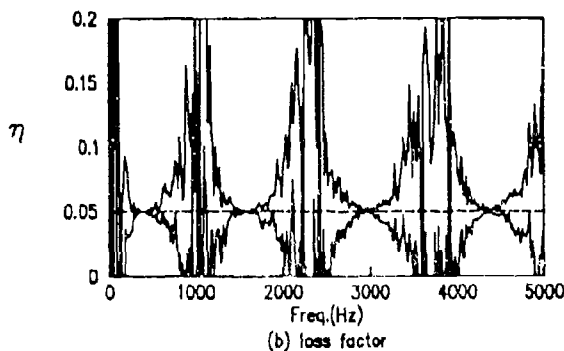
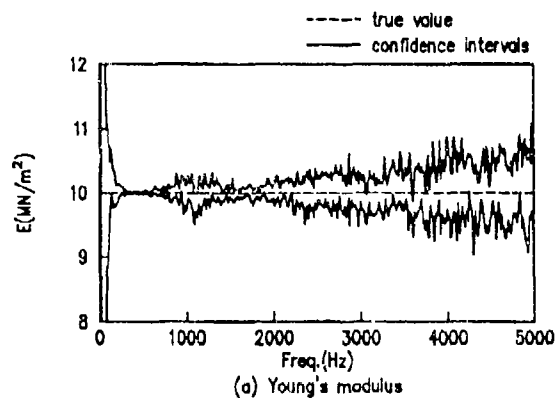
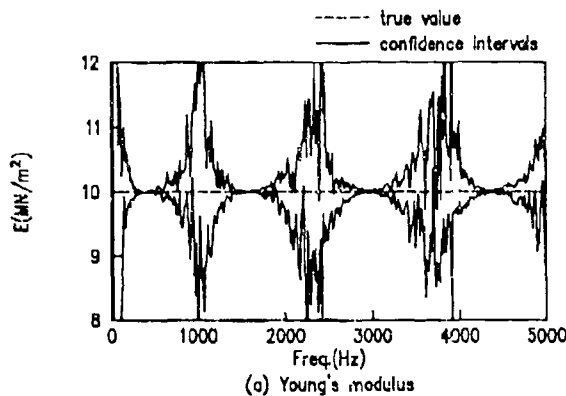


Fig.8 95% confidence intervals of the estimated complex modulus for a low loss material ( $\eta=0.05$ )

Fig.9 95% confidence intervals of the estimated complex modulus for a high loss material ( $\eta=0.5$ )

### 3. EXPERIMENTAL RESULTS

By the transmissibility approach discussed above, the complex modulus of a Neoprene rubber (DURO 60) was investigated. The specimen is a solid circular cylinder with diameter 25 (mm), and length 40 (mm). The material density is  $1354 \text{ (kg/m}^3\text{)}$  and the mass ratio is 1.925. Metal plate holding an accelerometer (PCB Type 303A02) was bonded to the top of the specimen. The other end of the specimen and the same type accelerometer were bonded to the table of an electromagnetic shaker (B&K Type 4808). The frequency range of random excitation was up to

3 kHz and the vibration level of the shaker was kept low enough to be in the linear range of the material and then the atmospheric temperature was 16°C.

The transmissibility and coherence were determined by taking 50 averages with a signal analyzer (HP3562A) and are shown in Fig.10. It can be found that the coherence is greater than 0.9 in the experiment frequency range except near zero frequency, which may be due to the characteristics of the piezo-type accelerometers and electrodynamic shakers. Above 1500 Hz, the coherence drops down rapidly with the increase of frequency, which may be ascribed to the fact that the output signal decreases as frequency increases.

Fig.11 shows the complex modulus estimated from the measured transmissibility function together with the 95% confidence intervals. The estimated complex modulus are very stable except near the zero frequency regions, which should be because the loss factor of the specimen is so high. These coincide well with the discussions in the previous section. The frequency range for 5% error bounds with 95% confidence is from 94 to 3000 Hz in case of Young's modulus and 187 to 2990 Hz in case of loss factor.

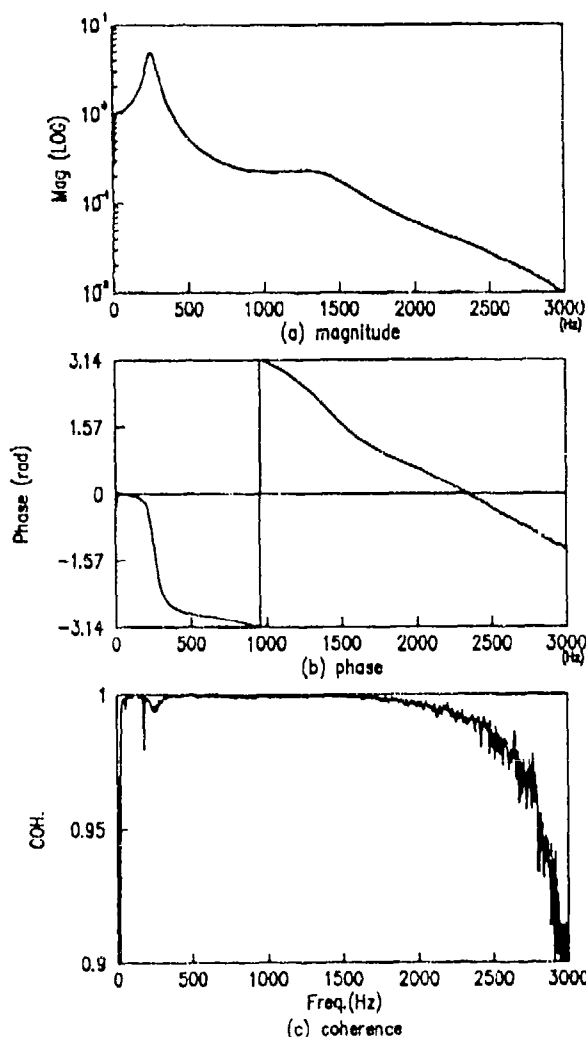


Fig.10 Transmissibility measurements for a Neoprene specimen

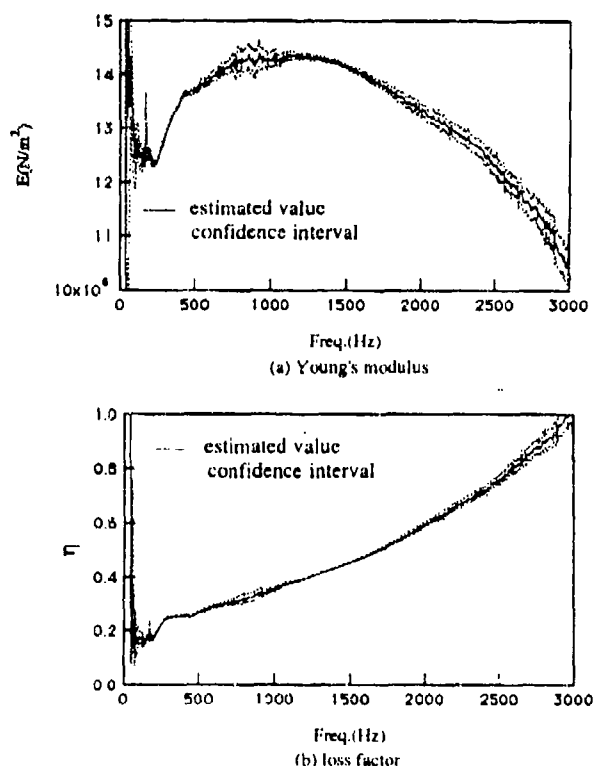


Fig.11 Estimated complex modulus of a Neoprene with 95% confidence intervals

The estimated Young's modulus decreases with frequency over 1200 Hz, which doesn't match the general characteristics of Young's modulus of viscoelastic materials increasing with frequency. This is believed to be the limitations of the elementary model used in subsection 2-1. There exist some techniques to compensate for such a phenomena [9].

#### 4. CONCLUSIONS

The transmissibility method has been analyzed by concentrating on the effects of the measurement errors on estimating the complex modulus of the viscoelastic materials. From the analysis the following conclusions can be drawn and these have been supported by experiment.

In the transmissibility approach, if the loss factor of the material is low, estimation of the complex modulus is very sensitive to the measurement errors both near  $L/\lambda \approx 0$  and in the anti-resonance regions. If the loss factor is high, estimation of the complex modulus is sensitive only near  $L/\lambda \approx 0$ . Generally, the degree of sensitivity decreases as  $L/\lambda$  increases and estimation of  $\eta$  (loss factor) is more sensitive to the measurement errors than the case of  $E$  (dynamic Young's modulus).

Since the confidence intervals on the estimated complex modulus can be defined based upon this sensitivity analysis, it would be useful in designing an experimental set-up as well as confirming the statistical reliability of the estimations by a testing facility.

#### ACKNOWLEDGMENTS

This has been partially supported by Agency for Defense Development of Korea.

#### REFERENCES

1. S. O. Oyadiji and G. R. Tomlinson 1985 Journal of Sound and Vibration 101(3), 277-298. Determination of the Complex Moduli of Viscoelastic Structural Elements by Resonance and Non-Resonance Methods.
2. S. N. Ganeriwala 1992 Second International Congress on Recent Developments in Air- and Structure-Borne Sound and Vibration, March 4-6, Auburn University, USA, 1379-1386. Dynamic Mechanical Properties of Viscoelastic Materials.
3. J. L. Buchanan 1987 Journal of the Acoustical Society of America 81(6), 1775-1786. Numerical Solution for the Dynamic Moduli of a Viscoelastic Bar.
4. J. D. Ferry 1970 Viscoelastic Properties of Polymers, New York: John Wiley & Sons, Second-edition.
5. J. C. Snowdon 1968 Vibration and Shock in Damped Mechanical Systems, New York: Wiley.
6. J. L. Edwards and D. R. Hicks 1972 Journal of the Acoustical Society of America 52(3), 1053-1056. Useful Range of a Mechanical Impedance Technique for Measurement of Dynamic Properties of Materials
7. T. Pritz 1980 Journal of Sound and Vibration 72(3), 317-341. Transfer Function Method for Investigating the Complex Modulus of Acoustic Materials: Spring-Like Specimen

8. T. Pritz 1982 Journal of Sound and Vibration 81(3), 359-376. Transfer Function Method for Investigating the Complex Modulus of Acoustic Materials: Rod-Like Specimen
9. T. Pritz 1981 Journal of Sound and Vibration 77(1), 93-100. Apparent Complex Young's Modulus of a Longitudinally Vibrating Viscoelastic Rod.
10. J. S. Bendat and A. G. Piersol 1986 RANDOM DATA: Analysis and Measurement Procedures, New York: Wiley - Interscience

## APPENDIX : DERIVATION OF THE ERROR COEFFICIENTS

Since the complex modulus  $E$  and  $\eta$  are functions of  $\xi$  and  $\beta$  as shown in equations (5) and (6), the relative errors of  $E$  and  $\eta$  can be represented as follows :

$$\begin{bmatrix} \frac{\Delta E}{E} \\ \frac{\Delta \eta}{\eta} \end{bmatrix} = \begin{bmatrix} \frac{\partial E}{\partial \xi} \frac{1}{E} & \frac{\partial E}{\partial \beta} \frac{1}{E} \\ \frac{\partial \eta}{\partial \xi} \frac{1}{\eta} & \frac{\partial \eta}{\partial \beta} \frac{1}{\eta} \end{bmatrix} \begin{bmatrix} \Delta \xi \\ \Delta \beta \end{bmatrix} \quad (a1)$$

The parameters  $\xi$  and  $\beta$  in the above equations are functions of  $H$ ,  $\phi$  and  $\gamma$  as shown in equation (4), which means that the error in  $\xi$  and  $\beta$  can be represented as follows :

$$\begin{bmatrix} \Delta \xi \\ \Delta \beta \end{bmatrix} = \begin{bmatrix} \frac{\partial \xi}{\partial H} & \frac{\partial \xi}{\partial \phi} & \frac{\partial \xi}{\partial \gamma} \\ \frac{\partial \beta}{\partial H} & \frac{\partial \beta}{\partial \phi} & \frac{\partial \beta}{\partial \gamma} \end{bmatrix} \begin{bmatrix} \Delta H \\ \Delta \phi \\ \Delta \gamma \end{bmatrix} \quad (a2)$$

Representing the left hand sides of the equations (4) by  $F_1(\xi, \beta ; H, \phi, \gamma)$  and  $F_2(\xi, \beta ; H, \phi, \gamma)$ , the following relations can be derived.

$$\begin{aligned} \frac{\partial F_1}{\partial \xi} \frac{\partial \xi}{\partial H} + \frac{\partial F_1}{\partial \beta} \frac{\partial \beta}{\partial H} + \frac{\partial F_1}{\partial H} &= 0 \\ \frac{\partial F_2}{\partial \xi} \frac{\partial \xi}{\partial H} + \frac{\partial F_2}{\partial \beta} \frac{\partial \beta}{\partial H} + \frac{\partial F_2}{\partial H} &= 0 \end{aligned} \quad (a3)$$

From equation (a3), the following relation is derived.



$$\begin{bmatrix} \frac{\partial \xi}{\partial H} \\ \frac{\partial \beta}{\partial H} \end{bmatrix} = - \begin{bmatrix} \frac{\partial F_1}{\partial \xi} & \frac{\partial F_1}{\partial \beta} \\ \frac{\partial F_2}{\partial \xi} & \frac{\partial F_2}{\partial \beta} \end{bmatrix}^{-1} \begin{bmatrix} \frac{\partial F_1}{\partial H} \\ \frac{\partial F_2}{\partial H} \end{bmatrix} \quad (a4)$$

if

$$\begin{bmatrix} \frac{\partial F_1}{\partial \xi} & \frac{\partial F_1}{\partial \beta} \\ \frac{\partial F_2}{\partial \xi} & \frac{\partial F_2}{\partial \beta} \end{bmatrix} \neq 0$$

The other derivatives can be obtained by the same procedure. So, the relative errors of E and  $\eta$  can be represented as follows :

$$\begin{bmatrix} \frac{\Delta E}{E} \\ \frac{\Delta \eta}{\eta} \end{bmatrix} = - \begin{bmatrix} \frac{\partial E}{\partial \xi} \frac{1}{E} & \frac{\partial E}{\partial \beta} \frac{1}{E} \\ \frac{\partial \eta}{\partial \xi} \frac{1}{\eta} & \frac{\partial \eta}{\partial \beta} \frac{1}{\eta} \end{bmatrix} \begin{bmatrix} \frac{\partial F_1}{\partial \xi} & \frac{\partial F_1}{\partial \beta} \\ \frac{\partial F_2}{\partial \xi} & \frac{\partial F_2}{\partial \beta} \end{bmatrix}^{-1} \begin{bmatrix} \frac{\partial F_1}{\partial H} & \frac{\partial F_1}{\partial \phi} & \frac{\partial F_1}{\partial \gamma} \\ \frac{\partial F_2}{\partial H} & \frac{\partial F_2}{\partial \phi} & \frac{\partial F_2}{\partial \gamma} \end{bmatrix} \begin{bmatrix} \frac{\Delta H}{H} \\ \Delta \phi \\ \frac{\Delta \gamma}{\gamma} \end{bmatrix} \quad (a5)$$